Title
Tailoring Nanoscale van der Waals Materials via Atomic Doping, Conversion, and Confinement

Author
Stonemeyer, Scott Lloyd

Publication Date
2021

Peer reviewed|Thesis/dissertation

Tailoring Nanoscale van der Waals Materials via Atomic Doping, Conversion, and Confinement

by

Scott Lloyd Stonemeyer

A dissertation submitted in partial satisfaction of the

requirements for the degree of

Doctor of Philosophy

in

Chemistry

and the Designated Emphasis

in

Nanoscale Science and Engineering

in the

Graduate Division

of the

University of California, Berkeley

Committee in charge:

Professor Alex Zettl, Co-Chair
Professor Felix R. Fischer, Co-Chair
Professor Peidong Yang
Professor Markita Landry

Spring 2021

Tailoring Nanoscale van der Waals Materials via Atomic Doping, Conversion, and Confinement

Abstract

Tailoring Nanoscale van der Waals Materials via Atomic Doping, Conversion, and Confinement

by

Scott Lloyd Stonemeyer

Doctor of Philosophy in Chemistry
with a Designated Emphasis in Nanoscale Science and Engineering

University of California, Berkeley

Professor Alex Zettl, Co-Chair
Professor Felix R. Fischer, Co-Chair

Control over the atomic structure of nanoscale materials allows for tailoring of their electronic and physical properties to enhance or alter their applications. The elemental and structural makeup of the nanomaterials dictates which methods of atomic control can be utilized to tailor their atomic structure. In this dissertation, we focus on nanomaterials comprised of low-dimensional building blocks, such as graphene, hexagonal boron nitride (h-BN), and transition metal chalcogenides (TMC), all members of the class of van der Waals (vdW) structures. We will leverage the 2-dimensional (2-D) and 1-D vdW nature of these nanomaterial systems to tailor their atomic and electronic structure through doping, conversion, or confinement.

Part I will open our discussion on targeted material growth, utilizing synthetic chemistry techniques to reconfigure a nanomaterial's atomic and electronic structure through doping and conversion. The work presented in **Chapters 1-5** focuses on the concept of dimensionality and how it relates to material structure, property, and applications. **Chapter 3** analyzes synthetic chemistry techniques used to alter the structure of graphene sheets and assemble those sheets into graphene-based macrostructures, such as doped-aerogels, for more meaningful applications. **Chapter 4** examines methods to utilize the robust lattice of graphene as scaffolding for the conversion of other porous, macroscopic systems built from other 2-D materials, such as h-BN nanofoams. **Chapter 5** explores the conversion method to access different compositions of porous structures beyond that of a layered material, breaking into the porous ceramics field.

Part II examines other vdW nanoscale materials from the TMC, such as the transition metal dichalcogenides (TMD) and trichalcogenides (TMT). However, techniques discussed in **Part I** are not easily applied to the TMD and TMT to tailor their atomic and electronic structure. Therefore, we pursue other means of atomic tailoring, specifically constrained material growth, where the atomic and electronic structure of materials can be reconfigured through drastic physical confinement of the crystals grown. **Chapters 8-14** studies how constraining the dimensions of these 2-D and 1-D vdW materials down to "atomic thinness" results in size quantization with profound consequences. Confinement through nanotube encapsulation of the TMD and TMT nanomaterials has resulted in several emergent phenomena ranging from structural distortions (**Chapters 8** and **9**) to newly stabilized crystalline structures (**Chapters 10, 11,** and **13**) to periodic superstructures (**Chapters 12** and **14**).

To my family and friends who have been there for me through all my successes and failures;
Your belief in me never faltered, and I appreciate you more than you will ever know.

To Theo, Murphy, and Mera, for the love, encouragement, and fun adventures.

Table of Contents

List of Figures

List of Tables

Acknowledgements

First, I have to thank my graduate advisor, Alex Zettl, for providing an inviting and open research group and environment to learn and be scientifically creative. Entering graduate school, I knew I would be exploring an entirely new research area with little background, and I am eternally grateful you were willing to take a chance on a chemistry student who had never even studied solid state physics (oops, did I not mention that in our initial interview?). I could not have asked for a better research advisor to work with; the open discussions and humor made for an amazing research and learning environment.

Alongside Alex, I owe many thanks to the members of the Zettl group who have been wonderful friends and collaborators over the years. Sally Turner, thank you for making me feel immediately welcomed in the group, allowing me to shadow you on so many projects, and being my chemistry buddy surrounded by physicists and materials scientists. You set a high standard for what an office buddy and friend should aspire to be, and I am so excited to see what you have been accomplishing post grad school. Thang Pham, thank you for taking me under your wing as a first year to help get me started on my projects. You were always fun to work with and patient in teaching, and I look forward to seeing what you do in the future. Jeff Cain and Amin Azizi, I really appreciate all the guidance over the years not only in research, but in life itself; your perspective was greatly appreciated. Matt Gilbert and Hu Long, even though we did not work on many projects together, I could always count on you to help me problem solve and brighten up my day running into you in the hallway or lab to chat and catch up. Derek Popple, I was very happy to get another chemistry buddy in the lab; we are slowly taking over the physics research groups. I always enjoyed chatting about experiments or our weekend plans and catching up over Zoom during the pandemic. JDeasy, graduate school is tough enough, so thank you for making my life so much easier whenever you could. I will miss stopping by your office for the dry humor. A special thank you to the undergraduate researchers I was lucky enough to work with over the years. Emilee Hall, Jonathan Kim, Malik Elasha, Markus Thiel, May Lorenzo, Austin Culp, and James Marquez, I am very excited to see what you all have been and will be doing after graduation and wish you all the best of luck!

Thank you to all my collaborators over the years. Marvin Cohen, Sehoon Oh, and Mehmet Dogan, thank you for your constant support and dedication to the projects over the years. I thoroughly enjoyed our conversations and was always excited by the work we were doing. Peter Ercius, thank you for being a fantastic mentor and research partner, I learned so much working with you and always enjoyed our one-on-one discussions. Marcus Worsley, I was very happy to poach Sally's projects when she left so we could continue working together. I enjoyed the monthly updates and creative project ideas I got to pursue with you.

I would also like to thank my undergraduate advisor, Sarah Petitto, for not only being an amazing instructor and mentor, but an amazing friend over the years. I am so grateful to have had the opportunity to work with you and stay connected over the years for your worldly and insightful advice. I cannot tell you how much I appreciate your support and honest opinions about surviving and thriving in academia and beyond. You set a high standard for what it means to be a mentor and advisor, and I am very fortunate to have had the opportunity to work with you and get to know you over the years.

To all of my Minnesota friends: Thank you for your nonstop support over the years. You made graduate school in another state difficult because I was always missing you, but I knew you were always cheering me on from a distance. To my California friends: Thank you for sharing in the craziness, triumphs, failures, and wild ride that is grad school. Julia, Ahmed, Kaity, Bethany, Naomi, Rachel, and David, I am very appreciative of the time spent commiserating over lunch hours, troubleshooting seemingly impossible tasks, and daydreaming about the opportunities that lay ahead of us.

Lastly, I want to thank my family for helping me reach this point. Mom and dad, thank you for the unwavering support while growing up. You instilled a sense of confidence and determination that I carry with me to this day. Nia and Melinda, thank you for the reality checks and meme support. You both kept me grounded and moving forward. Theo, I can never express enough gratitude or appreciation for how much you did for both of us, and the sacrifices made. I cannot wait for our next chapter and the exciting adventures that await us. I love you all.

Part I: Targeted Material Growth

Chapter 1: Introduction to van der Waals Materials and Dimensionality

Keywords: Graphene, Hexagonal Boron Nitride, Transmission Electron Microscopy, Diffraction Pattern, Raman Spectroscopy, X-Ray Photoelectron Spectroscopy, Energy Dispersive Spectroscopy, Scanning Electron Microscopy, Carbon Nanotubes, Boron Nitride Nanotubes

Part I will open our discussion on targeted material growth, where we can utilize synthetic chemistry techniques to reconfiguring a material's atomic and electronic structure. Before doing so, we first need to understand the fundamentals of the materials being targeted, specifically low dimensional van der Waals materials, such as graphene and hexagonal boron nitride. The concept of low dimensionality for studying condensed matter systems has exploded in importance since the Nobel Prize for work done with graphene was awarded back in 2010. Studying materials at their fundamental limit, or van der Waals limit, through exfoliation or encapsulation, has shown a staggering number of emergent phenomena in chemistry, physics, and materials science. This introductory chapter will set the reader up with the fundamentals behind the layered, van der Waals materials discussed in **Part I**, such as graphene and hexagonal boron nitride, and related instrumental techniques to study the structural and chemical composition of these systems. A second introductory chapter in **Part II** will explore other layered, van der Waals systems, namely the transition metal dichalcogenides and trichalcogenides, which will build on what is discussed here. All data presented in this dissertation are produced by the author unless otherwise noted.

1.1 Crystal Structure and Dimension

Much of the work presented in this dissertation will explore materials that have a crystal structure comprised of lower dimensional building blocks. From a chemistry perspective, bonding is often described in terms of very small molecules, such as water (H_2O) or perhaps benzene (C_6H_6). However, there is a whole class of solid-state materials that are comprised of infinitely many atoms bonded together in a 3-Dimensional (3-D) solid. The canonical example first described for these types of solid crystals is often table salt, or NaCl, as shown in **Figure 1.1**. Another common example, also shown in **Figure 1.1**, is diamond, which is an incredibly hard material due to the covalent bonding of the carbon atoms that makeup the crystal lattice. Even though NaCl and diamond are both crystalline solids, the bonding within the structure and geometries of their unit cell (or repeatable chemical unit) are drastically different. NaCl and diamond are just two common examples from thousands of different crystalline lattices, where the atomic arrangement, electronic structure, and resultant properties, can be tuned by changing the elemental composition of the structure or the bonding present.

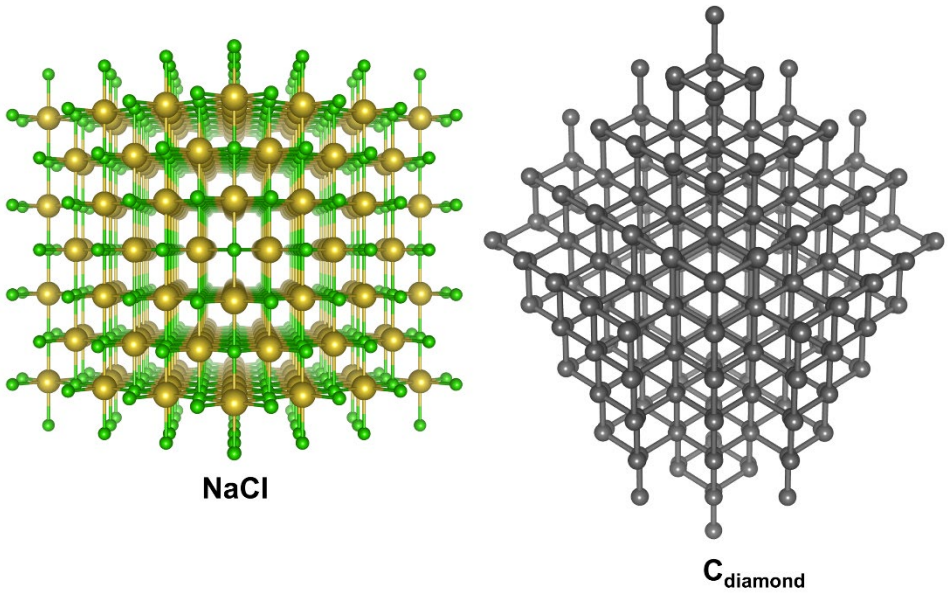

Figure 1.1 Crystalline solid examples. Left: Sodium Chloride (NaCl), with green and gold spheres representing the sodium cations and chlorine anions, respectively. Right: Diamond (C).

1.1.1 Carbon bonding

Carbon is an excellent example of how the atomic arrangement, electronic structure, and resultant properties can all be tuned by changing the bonding within the structure. The diamond structure shown in **Figure 1.1** is composed of all carbon atoms that are arranged in a tetrahedral geometry due to the bonding between atoms. For the carbon atoms in diamond, the three 2p orbitals hybridize with the 2s orbital to form 4 sp^3 bonding orbitals. For the bonding shown in **Figure 1.2**, these 4 sp^3 bonds are arranged in a tetrahedral geometry, giving diamond its unique shape, extreme hardness, and insulating behavior.[1] However, the fascinating characteristic of carbon is its flexibility in bonding hybridization. By changing the hybridization, the structural arrangement, and resulting properties, are drastically altered. When carbon hybridizes two 2p orbitals with the 2s orbital, forming 3 sp^2 bonds as shown in **Figure 1.2**, it forms a structure commonly referred to as graphene.

Graphene is a single layer of carbon atoms that are sp^2-bonded together. Looking at the sp^2 bonding in **Figure 1.2**, we see that the bonding orbitals form a trigonal planar geometry, where one p orbital is left unhybridized to form the double bonds between neighboring carbon atoms. Many graphene layers typically grow and stack on top of each other through van der Waals (vdW) forces, forming a more familiar compound, graphite. Graphite behaves drastically different than diamond. While diamond is translucent and an insulator, graphite is opaque and metallic, owed to the radically enhanced electron mobility from the double bonding within the graphene structure.[1] Even though diamond and graphene are identical in terms of chemical composition (only containing carbon atoms) the bonding and structural arrangement of the atoms has the final say in material properties.[2]

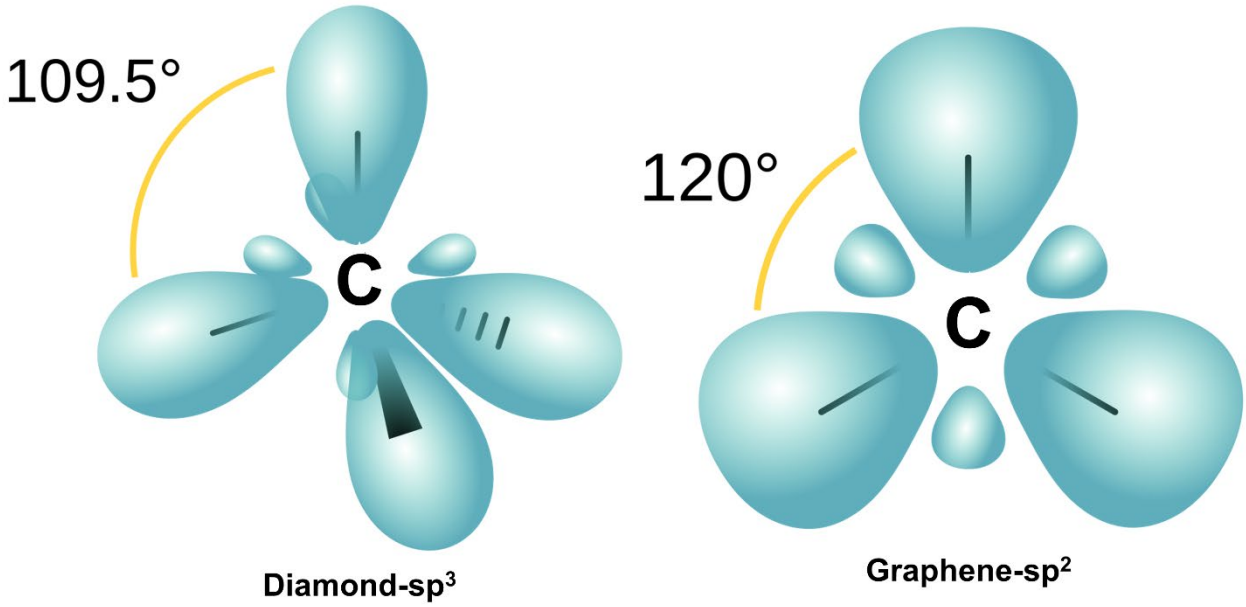

Figure 1.2 Different bonding hybridizations for carbon. Left: Diamond tetrahedral bonding, with sp^3 hybridization and associated bond angle shown. Right: Graphene trigonal planar bonding, with sp^2 hybridization and associated bond angle shown.

However, unlike diamond, because the bonding in graphene is all planar, the resulting structure is planar, with no covalent bonds between planes. Instead, the planar sheets of graphene are held together by vdW forces over longer length scales. **Figure 1.3** shows a model of graphene layers that have stacked together via vdW forces to form a 3-D crystalline solid of graphite. As seen clearly in **Figure 1.3**, there are no strong covalent or ionic bonds between the sheets of graphene, meaning graphite is just a 3-D crystalline solid comprised of 2-D building blocks (graphene). The layers of graphene are held together primarily by weaker vdW forces, as the sheets are very close in proximity to one another, roughly 3Å apart. These vdW forces extend across the entire surface area of the graphene sheets, providing strong interactions which hold the entire 3-D graphite solid together.

While graphite itself is relatively mundane, being used primarily as a refractory material, its individual components, graphene sheets, have proven anything but. The discovery of a single sheet of graphene garnered Andre Geim and Konstantin Novoselov the Nobel Prize in Physics in 2010, for their work on isolating and characterizing a single layer of graphene in 2004. They leveraged the fact that vdW forces are comparatively weak (as opposed to ionic or covalent bonding), meaning individual graphene layers can be separated from one another without breaking chemical bonds. The uncovering of a single atomic layer of graphene set the bar for what was possible with layered materials and laid the groundwork for a surge of scientific discoveries surrounding layered vdW materials in the years to come.

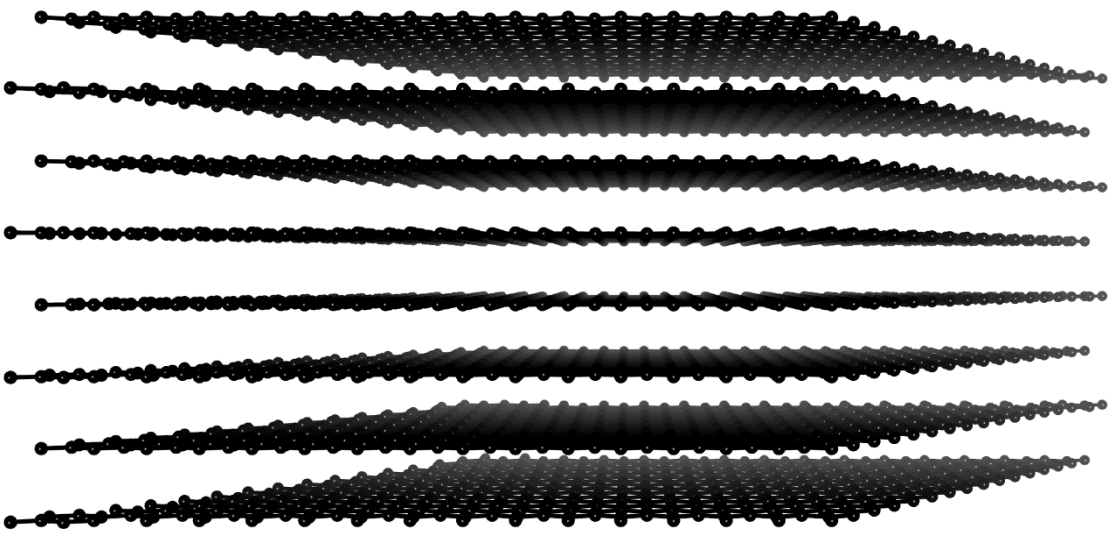

Figure 1.3 Stack of graphene sheets forming graphite.

1.2 Graphene and hexagonal boron nitride

Single-layer graphene has been thoroughly studied via theoretical and experimental means. The high symmetry of the graphene lattice, coupled with the monoatomic species comprising the lattice, generates very interesting electrical properties for single-layer graphene, such as a zero-gap energy band, massless Dirac fermions, and high carrier rates.[3] **Figure 1.4** shows the lattice of graphene, where A and B both represent carbon atoms arranged in a hexagonal geometry.[4] Also shown in **Figure 1.4** is the Brillouin zone of graphene, which is also hexagonal. The Brillouin zone of graphene has two high symmetry points, K and K', that are degenerate in energy.[4] If we look to the tight-binding model for the energy dispersion in graphene,

$$E_{\pm} = \frac{1}{2}(H_{AA} + H_{BB} \pm \sqrt{(H_{AA} - H_{BB})^2 + 4|H_{AB}|^2}) \qquad \textbf{(Eq. 1.1)}$$

we see that the onsite energies, H_{AA} and H_{BB}, are equivalent for both A and B sites, as they are both carbon atoms. Therefore, the radical simplifies to a single solution, meaning the energy of the two bands is degenerate at the K and K' points, leading to the zero-gap energy band.[4] **Figure 1.4** shows the conical intersection of these two bands at the high symmetry K and K' points.

Because of its metallic nature and flat surface, graphene has found application in an abundance of research, especially electronics. Field effect transistors capitalize on the high electron mobility in graphene, with low scattering.[3] Graphene has also been utilized to cap species in a conductive substrate for imaging, and protect those species from interaction with the environment.[5] More importantly, graphene continues to be an important part of vdW heterostructures, as it provides a conductive backbone for any devices constructed.[6]

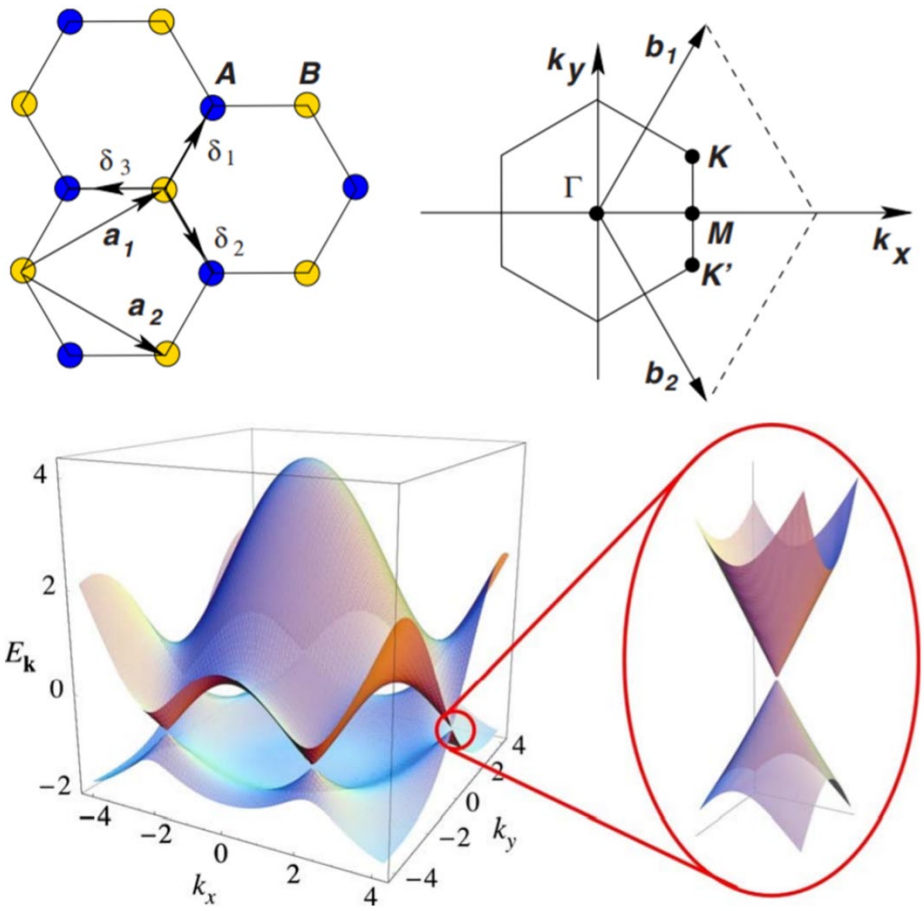

Figure 1.4 Graphene lattice, Brillouin Zone, and associated energy dispersion in reciprocal space. Adapted from reference 4.

However, if we could somehow make the lattice sites between A and B different, then the on-site energies would no longer be equivalent, and we could open a gap at the K and K' points, altering the electronic structure of the layered material. To accomplish this, however, chemical species that can form a layered material with planar bonding are required. One other similar, layered vdW material widely studied is hexagonal boron nitride (h-BN). Like graphite, h-BN is a bulk 3-D crystalline material comprised of individual 2-D atomic layers of boron and nitrogen atoms bonded together in a hexagonal lattice. Also like graphene, single layers of 2-D h-BN can be isolated from the 3-D bulk crystals with similar exfoliation techniques.[7]

Graphene and h-BN are very similar in structure because they have unit cells that are isoelectronic, where graphene's C-C unit has 8 valence electrons, and h-BN's unit has 8 valence electrons (3 from Boron and 5 from Nitrogen).[3] Because their unit cells have the same quantity of valence electrons for bonding, they adopt very similar atomic structures, even beyond the simple layered material, which we will discuss in later sections. However, even though they adopt identical structures and similar bonding, graphene and h-BN have polar-opposite electronic structures. While graphene is a zero-gap semimetal, the different on-site energies for h-BN separates the energy bands at the symmetric K and K' points, generating a wide-gap insulator of ~4.5 eV.[3] This affords h-BN monolayers very different applications than its graphene relative. Single layers of h-BN are a great dielectric and reduce substrate effects for various property

measurements.[8] Boron nitride can also be incorporated into devices to provide a chemically inert barrier to protect the inner materials from the external environment, enhancing their performance and creating high quality samples.[9]

Figure 1.5 showcases the similarities in the structure between graphene and h-BN. The lattice constants of graphene and h-BN are almost identical at 2.46Å and 2.50Å, respectively, resulting in the almost identical layered material. These structural similarities can be leveraged for interesting replacement of carbon with boron or nitrogen within the graphene lattice, further modulating and enhancing the properties of graphene. We will discuss the implications of doping the graphene lattice with foreign species in later chapters.

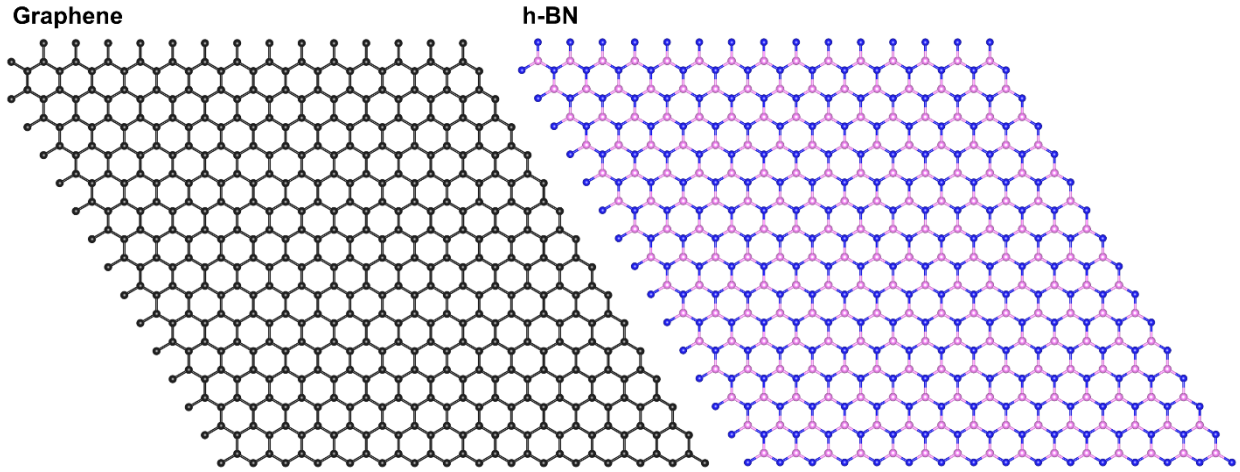

Figure 1.5 Structural models of graphene and h-BN. Black, blue, and pink spheres represent carbon, nitrogen, and boron atoms, respectively.

1.3 Graphene and h-BN, and their structural polymorphs

While the layers of graphene and h-BN have gained a lot of interest due to their atomic thinness, the study of these materials has uncovered other interesting features about these material systems. While graphene can be isolated from naturally grown graphite, there are other structure polymorphs, such as nanotubes, that can be synthesized under the appropriate conditions. While carbon can form several other polymorphs from graphene or diamond, the main structure we will focus on in this chapter and in **Part II** is carbon nanotubes (CNT). These cylindrical microtubules of graphene, or CNT, were discovered in 1991 by Sumio Iojima.[10] While these types of structures had been observed in previous experiments by other researchers, Iojima really called attention to their uniqueness and the reproducible synthesis using arc-discharge methods.[10] Most forms of CNT have very similar properties to graphene, with excellent transport properties, high chemical and thermal robustness, and high tensile strength.[11]

Following suit with a similar polymorph is h-BN, which can form boron nitride nanotubes (BNNT). BNNT were first theoretically predicted in 1993 by Dr. Marvin Cohen, and experimentally isolated in 1995 by Dr. Alex Zettl.[12,13] BNNT showed all of the same structural characteristics of CNT, such as high aspect ratios, single- to few-wall tubes, and narrow diameters.[12] Also similar to CNT, the BNNT held similar properties to the parent h-BN material, remaining highly insulating and thermally robust. While the synthesis of BNNT was not as standardized as CNT from the onset, the Zettl group went on the develop means of mass-producing large quantities of BNNT.[14] **Figure 1.6** shows a schematic of the CNT and BNNT in

comparison to the parent graphene or h-BN material, where the bonding remains the same, but the once flat, layered material is simply rolled into an interconnected cylinder.[15] **Figure 1.7** shows CNT and BNNT in powder and fiber form, where they optically resemble the parent material as well. Like graphene and graphite, CNT are very dark in color, while BNNT are bright white like h-BN.

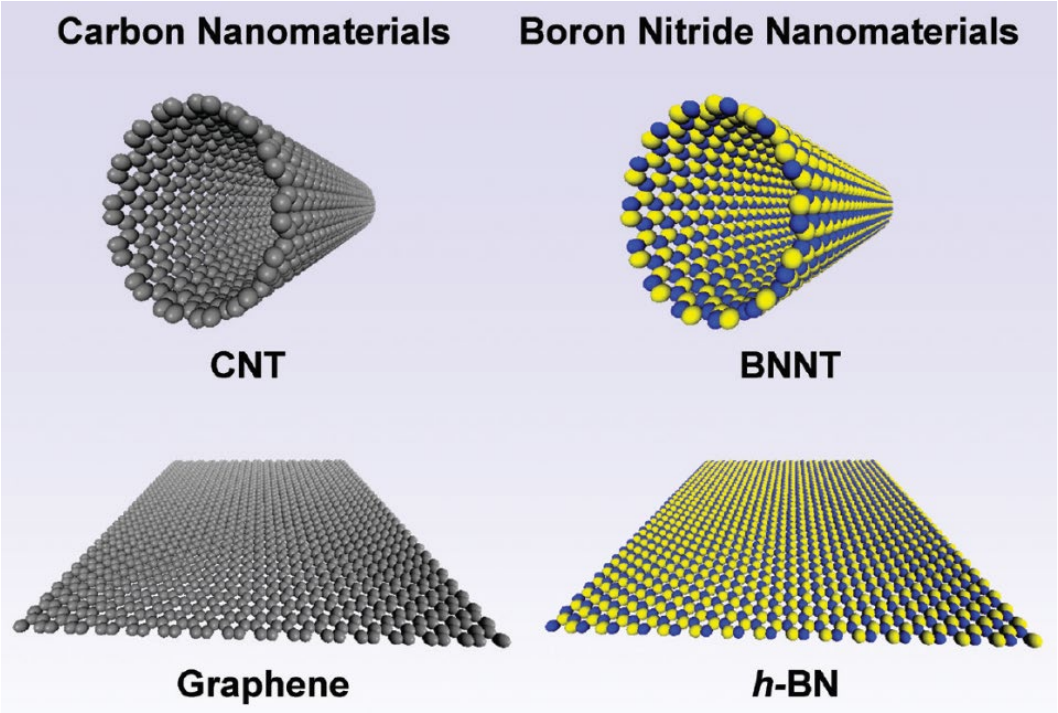

Figure 1.6 Schematic of carbon and boron nitride nanotubes in comparison to their parent material. Adapted from reference 15.

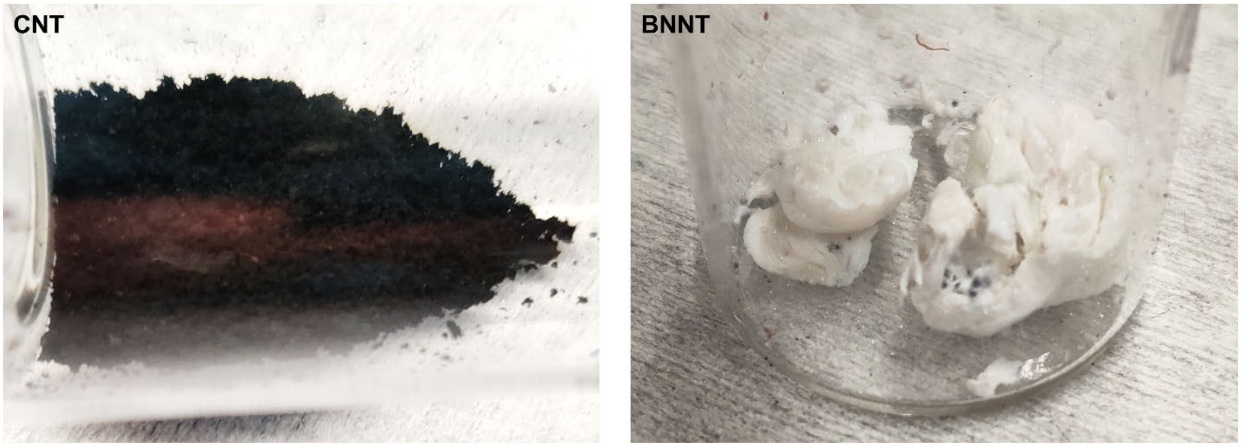

Figure 1.7 Optical images of carbon and boron nitride nanotubes.

1.4 Characterizing graphene and h-BN nanostructures

While the synthesis and initial isolation and identification of graphene, h-BN, and their related polymorphs is instrumental in the development of the 2-D vdW field of study,

characterizing these types of structures has drastically improved over the years. Various instrumental techniques have become standard procedure for characterizing not only the atomic structure of these nanomaterials, but also their chemical composition. Here, we will discuss some of the standard techniques and observed characteristics from said techniques, in relation to graphene, h-BN, and their associated nanotubes.

1.4.1 Raman Spectroscopy

Raman spectroscopy is a powerful tool to examine these layered systems because of their strong sp^2 bonding. Raman spectroscopy is a laser-based measurement to probe the vibrational modes of the material interest, which not only gives clues to the crystalline nature of the material being studied but can uncover compositional information as well. **Figure 1.8** shows a commercial experimental setup for Raman spectroscopy. As the entire system is enclosed, areas of interest have been labeled for convenience. In brief, an incident laser of specific energy is scattered off the surface of the material and recollected to a detector to record the shift in energy after interaction with a material. The laser light interacts strongly with vibrational modes within the material that produce strong polarization within the material, resulting in inelastic scattering of the laser light, which is recorded as a shift in energy, or wavenumber.[16]

A characteristic Raman spectrum of graphite is shown in **Figure 1.9**. There are two main peaks of interest, the G peak (~1590 cm^{-1}) and the 2D peak (~2680 cm^{-1}). Graphene exhibits similar vibrational modes, allowing for good comparison to the spectrum for graphite. The G peak arises from the strong, interplane vibrations from the sp^2 carbon bonds, hence the very high intensity of this peak. This process involves a vibrational transition within the Dirac cone at the high symmetry K and K' points discussed in previous sections.[17] The 2D peak is closely related to the G peak, however this mode is an intervalley transition between two neighboring Dirac cones.[17] While the G and 2D peak are directly related to the structure of graphene, the intensity of these peaks can provide great insight into the composition and crystallinity of graphene and graphite. For example, because the 2D peak is a two-step, phonon-assisted process, any defects, or dopant atoms, that are not carbon will scatter the 2D Raman process (as they change the vibrational energy within the lattice), drastically lowering the overall intensity of this peak. There are also additional peaks, such as the D peak, that will appear and change intensity based on defects and dopant atoms as well. We will discuss these changes in the Raman spectrum in **Chapter 3**.

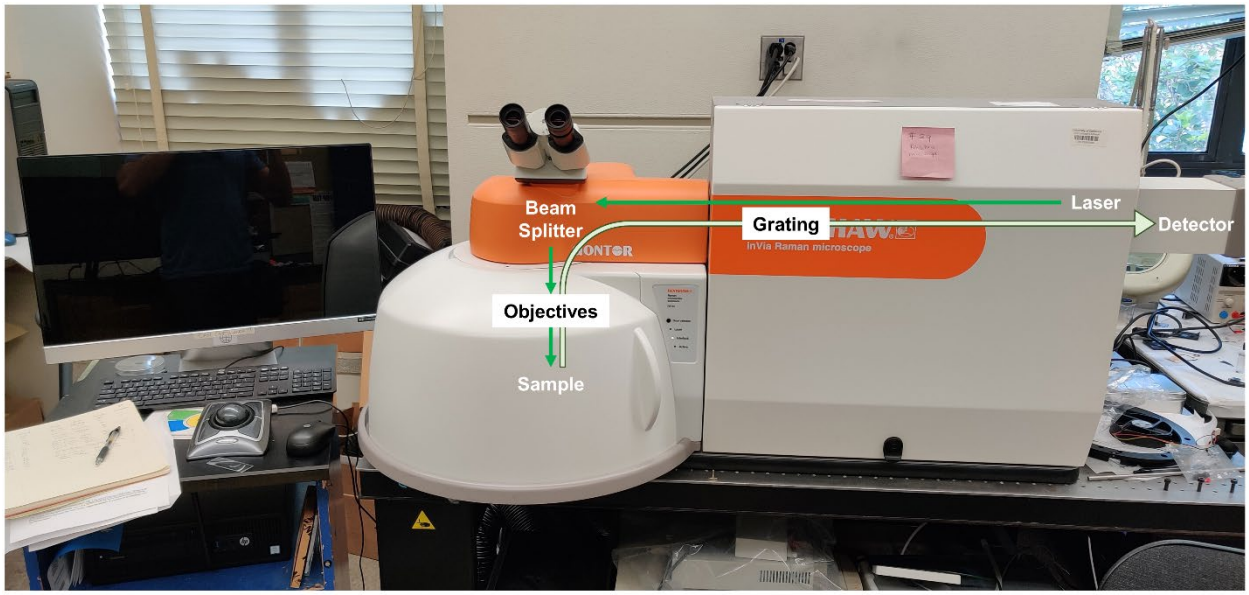

Figure 1.8 Raman spectroscopy setup in the Zettl group.

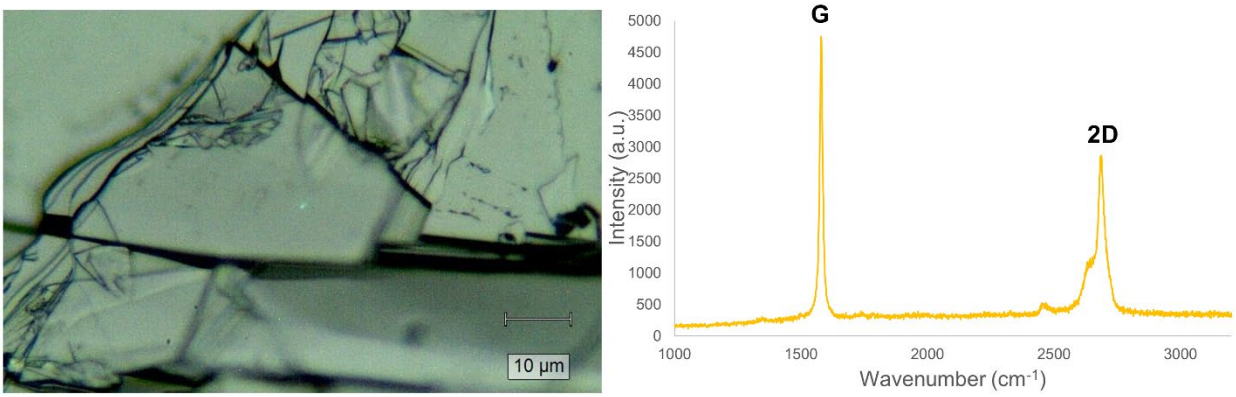

Figure 1.9 Left: Optical image of a graphite sample with green laser spot in center of flake. Right: Exemplary Raman spectrum for graphite, where a strong G peak (strong in-plane vibrations from sp^2 carbon bonds) and 2D peak (high crystallinity and low defect count) are readily apparent and labeled.

1.4.2 Scanning electron microscopy

While Raman can spectroscopically probe the structure of these nanomaterials, direct imaging of the structure is tricker with optical microscopes, especially with atomically thin samples or nanotubes only a few nanometers in diameter. Therefore, we turn to electron microscopy to view these atomically thin sheets at higher resolution to study their structure, and even chemical composition. Scanning electron microscopy (SEM) provides excellent overview of these material systems at the sub-micron level without excessive sample preparation needed. **Figure 1.10** shows a commercial experimental setup for SEM. As the entire system is enclosed, areas of interest have been labeled for convenience. In brief, an electron source thermionically emits electrons, which are condensed into an electron beam. This beam is scanned across the surface of the sample, which causes secondary electrons (electrons from the sample itself) to be

ejected and collected by the secondary electron detector.[18] By measuring the intensity of electrons collected and mapping it to the x- and y-coordinates of where the beam was located at that collection point, an image of varying intensity is generated.[18]

Examples of SEM images captured of CNT are shown in **Figure 1.11**. The CNT closer to the surface are higher in contrast due to the higher intensity of secondary electrons collected at those positions. The electrons emitted from CNT at the surface of the sample are not reabsorbed by the sample itself, meaning they have a higher chance of being detected and increasing overall intensity at that spatial point. The regions between the CNT also show lower intensity due to reduced amount of material present to emit any secondary electrons. As seen in **Figure 1.11**, much higher resolution can be obtained than typical optical microscopy, resolving feature sizes well under 500 nm. Typical microscope conditions use an accelerating voltage of 5keV to direct the electron beam towards the sample. The resolution obtained is related to the overall accelerating voltage and spot size used. A higher accelerating voltage will increase the energy of your electron beam, meaning more secondary electrons are emitted from the sample. Similarly, a smaller spot size will increase the number of secondary electrons emitted, as a concentrated electron beam increases the number of electrons hitting a specific region in the sample while it scans. However, the accelerating voltage and spot size must be balanced to preserve the sample and reduce damage to the sample from the electron beam while imaging.

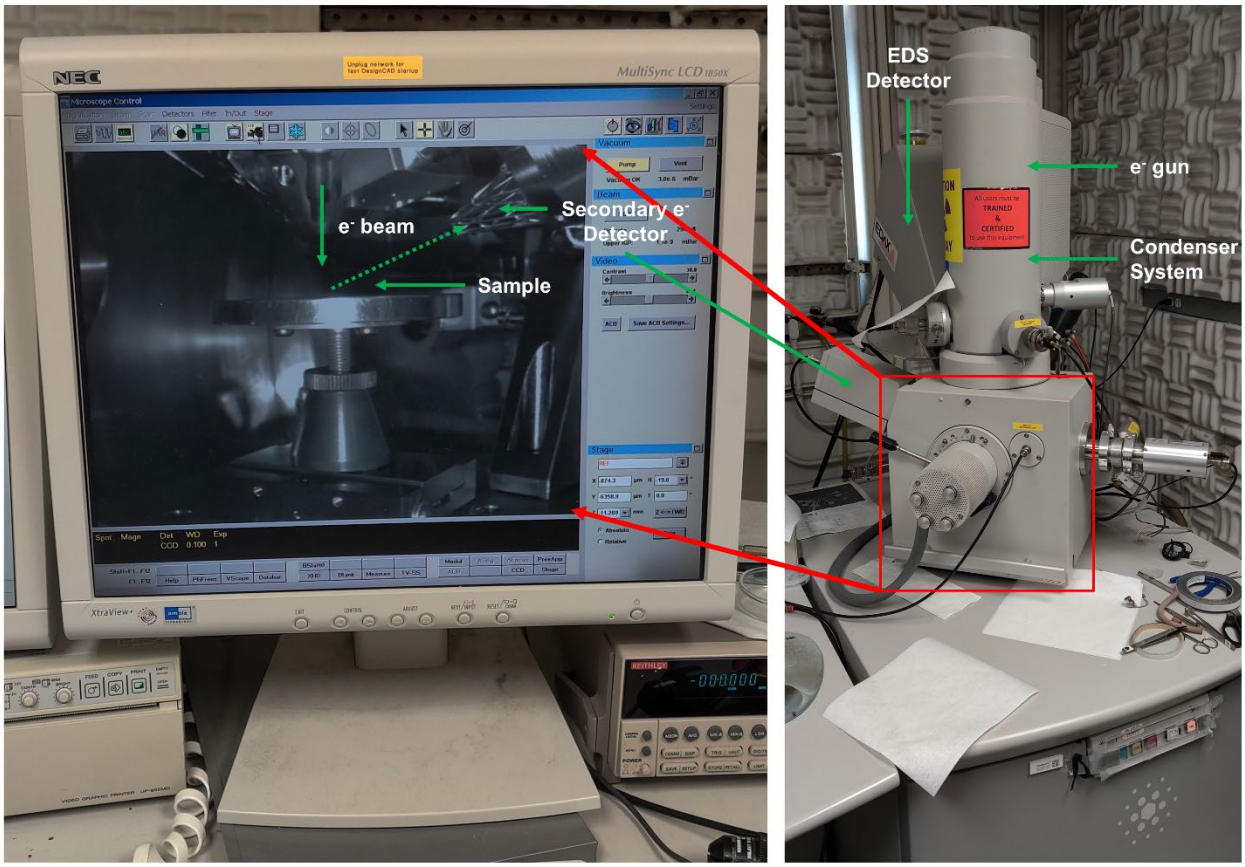

Figure 1.10 Scanning electron microscopy setup in the Zettl group.

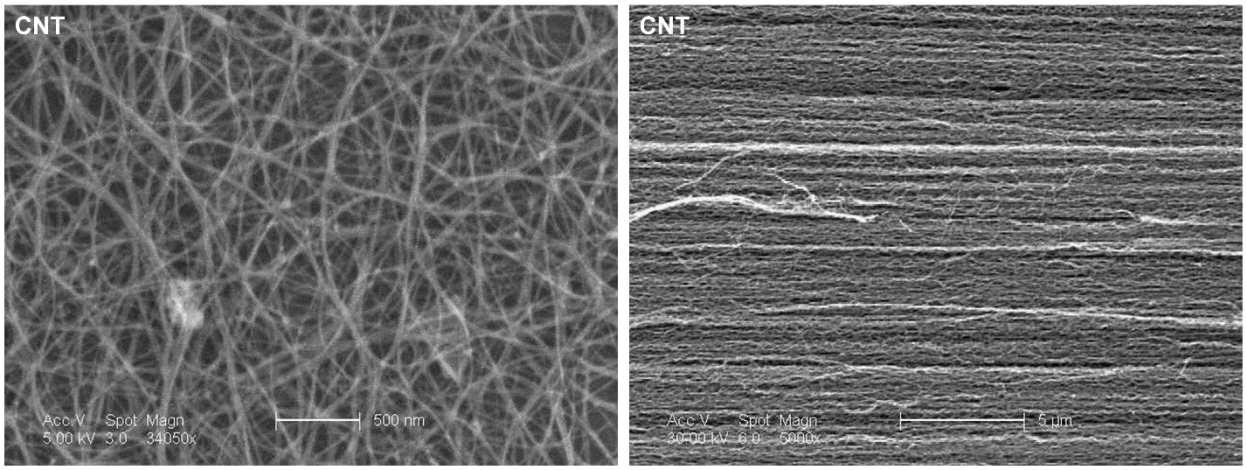

Figure 1.11 Scanning electron micrographs of bundles of carbon nanotubes. Scale bars measure 500 nm (left) and 5 μm (right).

1.4.3 Energy dispersive spectroscopy

SEM is fantastic for structural imaging of materials, but direct analysis of chemical composition of the structure is not immediately apparent from imaging. However, the imaging process performed with SEM can be utilized to obtain chemical information about the sample, providing both quantitative and qualitative analysis of material composition. This technique is energy dispersive spectroscopy (EDS), which uses the electron beam of the SEM as the probing source, and measures the x-rays emitted from the sample. As mentioned in the previous section, the electron beam causes electrons to be ejected from the sample. By drastically increasing the accelerating voltage and decreasing the spot size, as previously discussed, the number of electrons ejected from the sample drastically increases. If the energy of the incident electron is high enough, core level electrons can be ejected from the sample.[19] When this happens, an electron in a higher energy level will relax to the lower energy state, releasing an x-ray. The energy of this x-ray is characteristic of the elemental species present, due to atomic quantization of energy levels, and these x-rays can be used to identify elemental species present.[19]

The overall schematic of the EDS process is shown in **Figure 1.12**. The incident electron comes from the SEM electron beam, and the x-ray emitted is collected by a detector. The energy levels, labeled K, L, and M, correspond to the energy transitions of electrons transitioning between energy levels. These labels are used to identify specific peaks in EDS spectra for different elements. **Figure 1.13** shows characteristic peaks of an h-BN and graphene sample, respectively. For h-BN, we see two peaks, one corresponding to the boron Kα transition at 0.183 keV, and the other to the nitrogen Kα transition at 0.392 keV. In graphene, we only observe one strong peak corresponding to the carbon Kα transition at 0.277 keV. Lighter elements, such as boron, carbon, and nitrogen, only exhibit a single peak in EDS spectra, as they only have one core energy level to remove electrons from (1s), which corresponds to the K energy transition. However, in heavier elements, there are multiple core shells of electrons, and several higher energy electrons that could lower in energy, leading to several peak possibilities for higher Z elements. A limiting factor in EDS analysis is tied directly to the low spectral resolution, which is typically around 150 eV.[19] We will discuss the implications of this for systems containing both carbon and boron or nitrogen in later chapters.

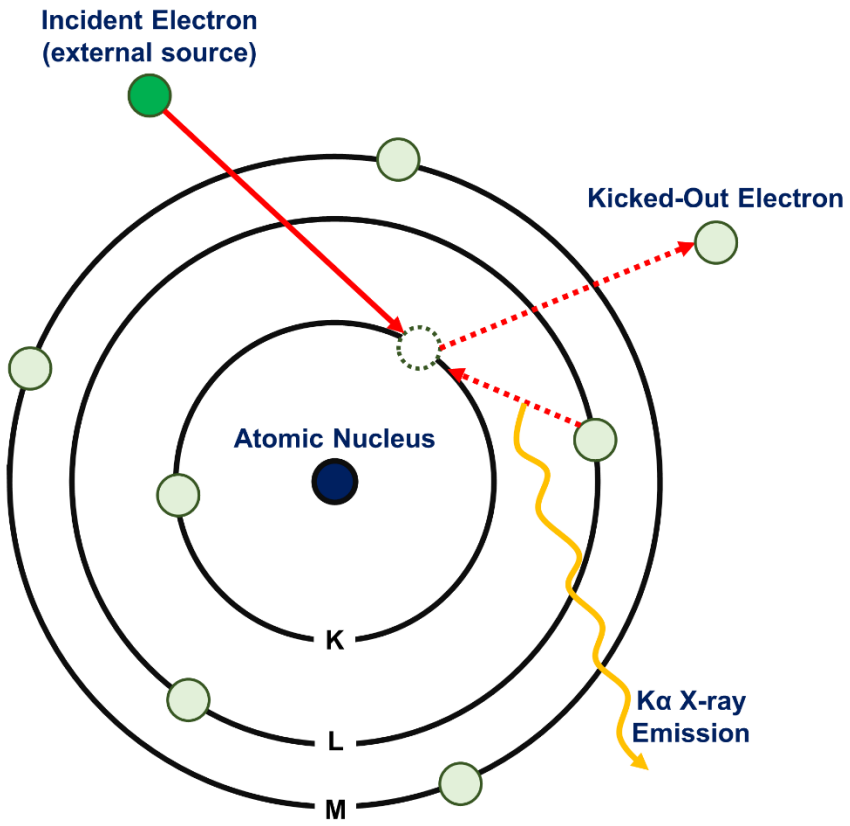

Figure 1.12 Schematic of the process for energy dispersive spectroscopy.

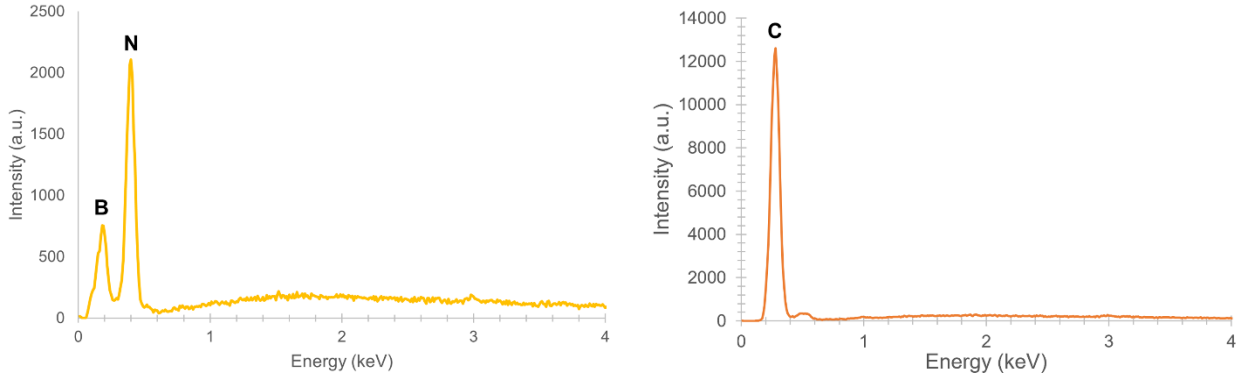

Figure 1.13 Example energy dispersive spectroscopy spectra for h-BN and graphene.

1.4.4 X-ray Photoelectron Spectroscopy

EDS provides excellent information into the chemical composition of materials, but the process is only sensitive to the identity of the element, but contains no other information, such as bonding of that element. Therefore, if we wanted to examine specific bonding in the material, we need to turn to x-ray photoelectron spectroscopy (XPS). While EDS uses incident electrons to generate x-rays, which are subsequently detected, XPS uses incident x-rays to generate electrons, which are subsequently detected. Because XPS uses x-rays as its spectroscopic probe, XPS is primarily used to study the surface of materials, as s x-rays cannot penetrate to the core of

materials.[20] **Figure 1.14** shows a schematic of the process involved for XPS. Briefly, x-rays are generated from an aluminum source, which are monochromatic in energy. These x-rays are then impinged upon the surface of the material. If the x-rays are high enough in energy, they will knock out electrons from the atom. These electrons are collected and detected based on their energy. As the initial energy of the incident x-ray (photon energy) is known to a high degree, and the energy of the detected electron (kinetic energy) is known, then the overall energy lost from the initial impact can be detected as follows:

$$Binding\ Energy = Photon\ energy\ (x-ray) - Kinetic\ energy\ (e^{-}) \qquad \textbf{(Eq. 1.2)}$$

The binding energy is the value reported in the resulting spectrum. However, because the binding energy of the electron is directly dependent upon its proximity to the atomic nucleus, and the distance to the atomic nucleus is highly dependent upon the oxidation state of the element, then the binding energy measured directly relates to the type of bonding the measured electron was participating in.[20] **Figure 1.15** shows an example of a survey spectra obtained from XPS on a graphene aerogel sample with nitrogen doping. An initial probe is performed on the sample to determine the elements present. Here, we see oxygen, nitrogen, and carbon are present in substantial quantities. Knowing the specific elements present, we can then collect higher resolution energy scans of specific regions, such as is shown in **Figure 1.16** for the nitrogen peak from **Figure 1.15**. From the higher resolution energy scan, the nitrogen peak that appeared to be a single peak in the survey spectra is seen to be comprised of two separate peaks, corresponding to two different types of nitrogen bonding present in the material. The different types of bonding will be discussed in more detail in later chapters.

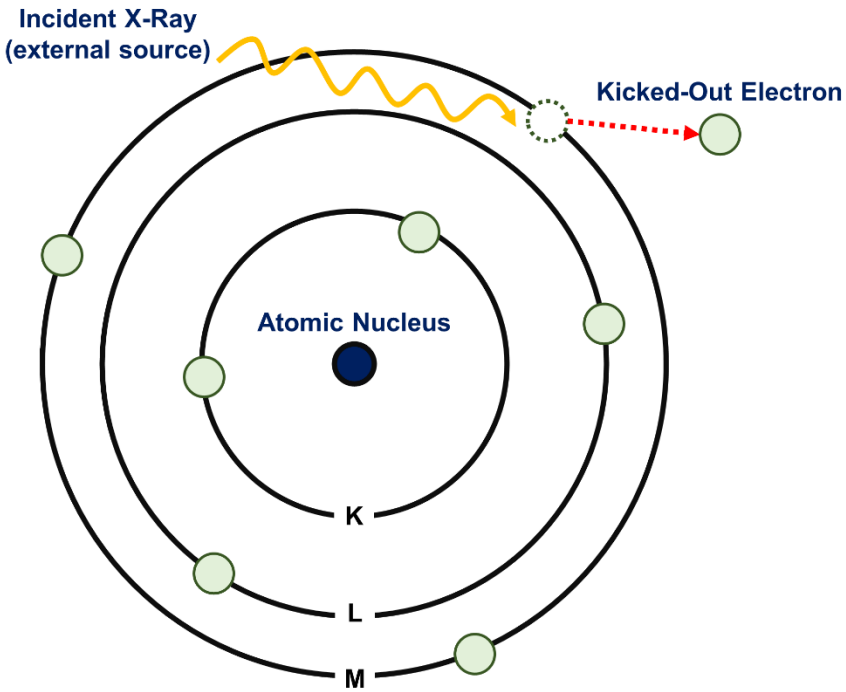

Figure 1.14 Schematic of the process for x-ray photoelectron spectroscopy.

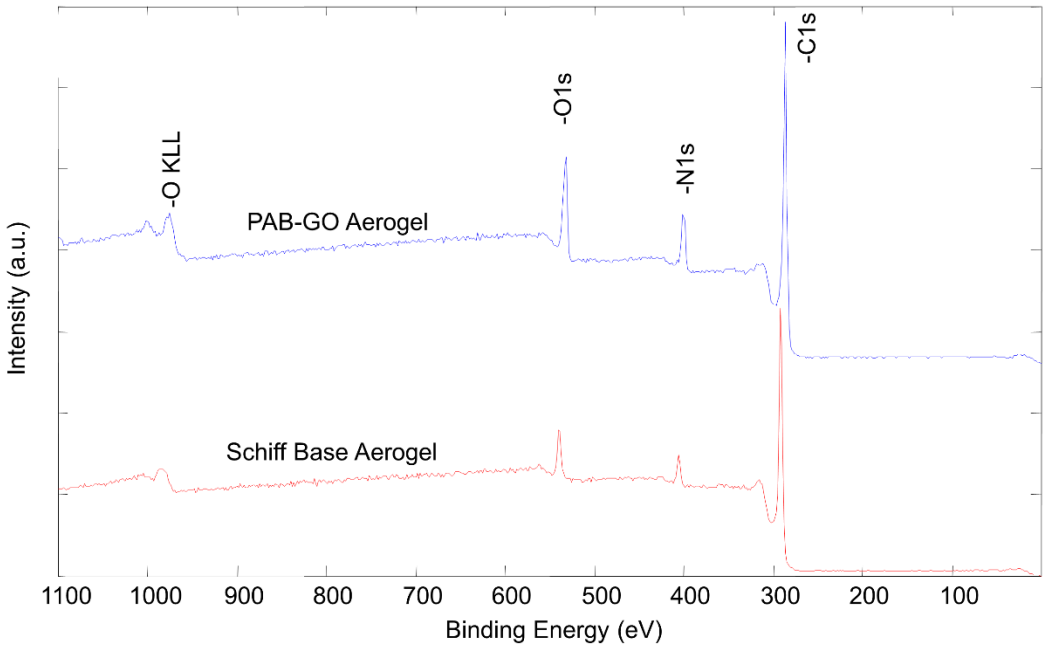

Figure 1.15 Example survey x-ray photoelectron spectra for graphene and carbon aerogels. Data collected in collaboration with Dr. Art Nelson.

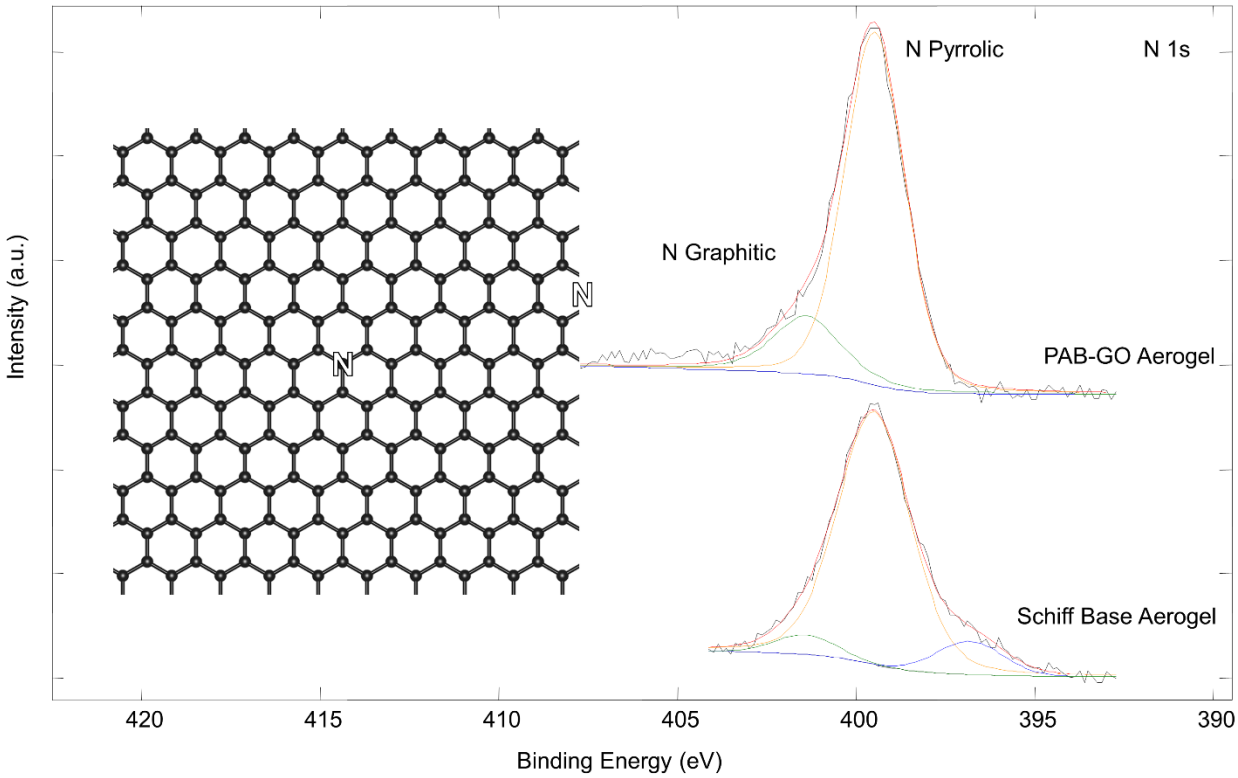

Figure 1.16 Example of a higher resolution energy spectrum for N1s to differentiate between types of bonding present. Data collected in collaboration with Dr. Art Nelson.

1.4.5 Transmission electron microscopy

While the previous techniques discussed provide great insight into the chemical composition of the materials, the spatial resolution of these techniques is still significantly large, considering graphene, h-BN, and their nanotube counterparts are atomically thin. Therefore, we can also explore transmission electron microscopy (TEM) as a technique to view the structure of these materials at the nanoscale, achieving spatial resolutions high enough to resolve different tube walls in a multi-walled CNT. **Figure 1.17** shows a commercial experimental setup for TEM. As the entire system is enclosed, areas of interest have been labeled for convenience. In brief, electrons are generated by a LaB_6 filament (e^- gun), which are accelerated down through the column to form an electron beam. These electrons can be accelerated from 80-300 kV, with similar considerations to be made as SEM, where high accelerating voltages can produce higher resolution images, but may destroy your sample in the process. With these atomically thin materials, they cannot survive high accelerating voltages without large numbers of defects being generated, so typical imaging is performed at 80 kV. Additionally, to enhance resolution and limit the interaction of the electron beam with gaseous species, the entire TEM column is under high vacuum, reaching pressures around 10^{-7} Torr.

As electrons are emitted from the filament, they are formed into a coherent electron beam as they pass through the lenses in the condenser system. A properly formed beam is symmetrical, has no astigmatism as the focus is adjusted, and is very stable and monochromatic in electron energy so there are no fluctuations. Once formed, the beam will pass through the sample, which has been properly prepared thin enough to be transparent to the electron beam (hence the transmission aspect of TEM). For graphene, h-BN, nanotubes, and many other nanomaterials, these samples in and of themselves are transparent to the electron beam without any alteration, so they can be directly prepared on a TEM grid. **Figure 1.17** also shows a couple different TEM sample grids, each of which has different utility. Typical TEM sample grids are made of a copper mesh, and overlayed with either a carbon film or holey carbon. The lacey carbon acts as a support to suspend nanomaterials over vacuum for TEM imaging. These grids are 3mm in diameter and are loaded onto the stage of the TEM holder, also shown in **Figure 1.17**. The sample holder is loaded into the column via a multi-step process as to not break vacuum, where the sample will ultimately be perpendicular to the electron beam for the beam to pass through.

As the electron beam passes through the sample, the electrons interact with the sample itself, and may diffract off crystal planes within the material being imaged, creating a diffraction pattern. After diffraction, the electrons are reconstructed through the projection lens, after which they strike a phosphorescent screen and produce an image of the sample. The screen can be 'lifted' to expose the electron beam directly to a detector, usually a CCD camera, and a digital image can be produced. **Figure 1.18** shows a standard TEM image of few-layer graphene, where darker contrast in the image indicates the electron beam interacted more with that region of the sample than vacuum (vacuum can be seen in the top left corner and bottom left-half of the TEM image).

While **Figure 1.18** shows a relatively wide view of the sample, the individual edges of the few-layer graphene can still be resolved easily to determine that there are 3 sheets of graphene stacked on one another. While the resulting image can show a large amount of detail about the structure of the material, the diffraction pattern generated by the electron beam can also uncover very useful information about the material itself. The lattice planes within a crystalline solid have very specific characteristics unique to each material, such as lattice spacing and

symmetry or geometry. The apertures labeled in **Figure 1.17** can be used to generate a selected area diffraction pattern, as shown in **Figure 1.18**. The diffraction pattern shown is from the selected region in the TEM image of the few-layer graphene. The planes diffracting the electron beam are the [001] planes in graphene, as noted. For more intricate solids that have 3-D bonding, diffraction patterns are a great tool to determine a variety of details about materials, such as orientation of the sample, alignment of multiple layers in a layered vdW setup, or the symmetry group of a new crystalline material that has been synthesized.[21–23] For graphene, we expect to see a six-fold symmetry in the diffraction pattern, a result of the hexagonal lattice of carbon atoms.

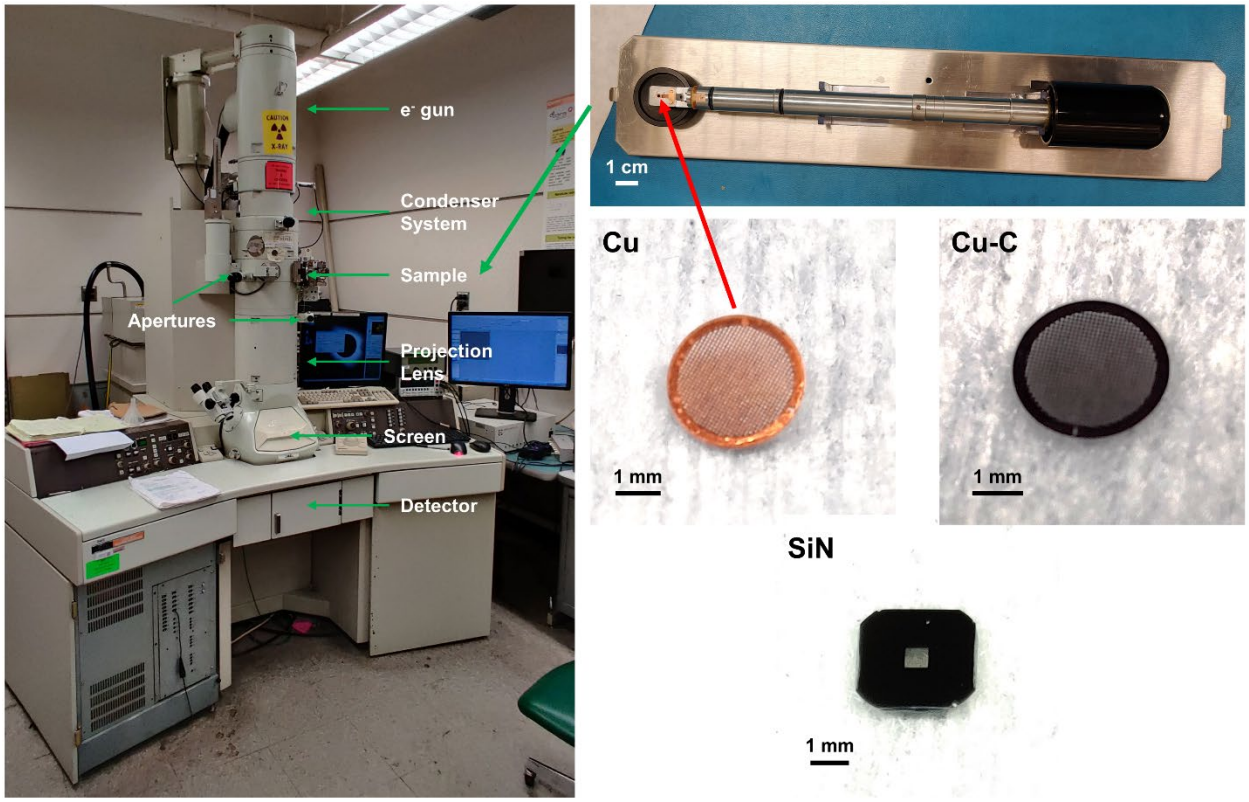

Figure 1.17 Transmission electron microscopy setup in the Zettl group.

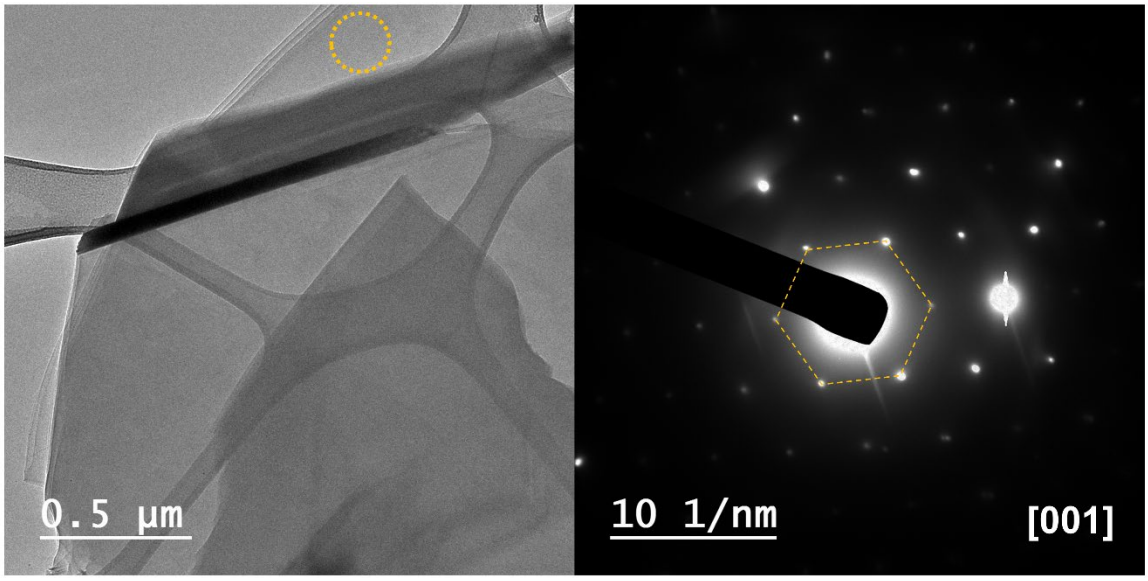

Figure 1.18 Transmission electron micrograph and associated selected area diffraction of few-layer graphene.

While the above TEM image shows a relatively broad view of a graphene sample, standard TEM can resolve features much smaller, such as the inner wall distance in nanotubes. **Figure 1.19** shows a couple of example images of BNNT at higher magnification, demonstrating the higher spatial resolution achieved with standard TEM imaging. In a multi-walled BNNT, the tube walls are ~3Å apart, which can be differentiated in the images. A later chapter will explore even higher resolution microscopy techniques, namely scanning transmission electron microscopy, which can resolve individual atoms in a material under the correct conditions.

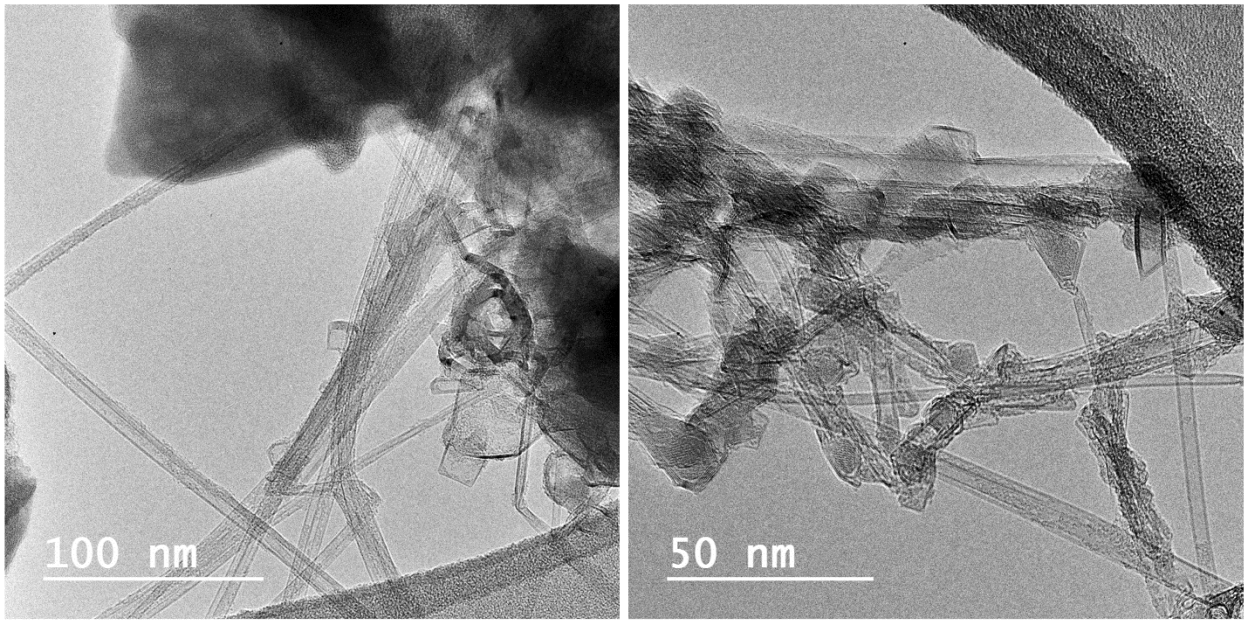

Figure 1.19 Transmission electron micrograph of boron nitride nanotubes.

1.5 Conclusion

Here, we explored the fundamentals behind vdW materials, and how their bonding and elemental composition ultimately determines their structure and properties. We then examined several analytical techniques to study both the surface structure (Raman, SEM, TEM), chemical composition (EDS, XPS), and underlying defects and crystal lattice (Raman, TEM diffraction) of these low-dimensional material systems. By developing strong methods of atomic structure and chemical composition analysis, we can correlate the property-structure relationship in these types of systems and leverage that relationship to tailor these materials through targeted material growth. The following chapters in **Part I** will explore synthetic chemistry techniques used to alter the structure of graphene sheets and assemble those sheets into graphene-based macrostructures, such as aerogels, for more meaningful applications. Additionally, we will explore how the robust lattice of graphene can act as scaffolding for the growth of other interesting material systems through conversion, such as h-BN nanofoams or porous ceramics.

Chapter 2: Aerogel Fundamentals

Keywords: Graphene, Hexagonal Boron Nitride, Aerogel, Hydrogel, Porosity, Surface Area, Scanning Electron Microscopy, Transmission Electron Microscopy, Raman Spectroscopy

Previously we discussed the significance and breakthroughs that have been achieved with the study of flat, van der Waals (vdW) materials, such as few- and single-layer graphene and hexagonal boron nitride (h-BN). The anisotropy of the graphene and h-BN sheets, chemical inertness of their basal plane, and high surface area makes these layered materials interesting for a range of applications. While the monolayer limit of graphene and h-BN has provided, and continues to uncover, a world of exciting chemistry and physics, the continued improvement of their integration into larger, macroscopic systems is vital towards expanding their utility. The following chapter will discuss the background and fundamentals behind graphene and h-BN aerogels, synthetic methods, associated characterization methods, and potential modifications to their basic structure.

2.1 History and applications of aerogels

Aerogels are porous, ultralight materials, whose properties and resulting applications are largely derived from the fundamental building blocks of the structure, generating many different structures with a wide range of applications across many fields.[24–29] Silica aerogels were some of the first aerogels to be studied widely in both research and industry. Silica aerogels were first developed back in the 1930s, but further development was delayed over half a century later, until their use for storage of fuel was explored in 1985.[30] Silica itself offers great thermal insulation, which directs its application towards heat management or acoustic barriers, however any applications requiring a conductive substrate find rare usage from silica-based aerogels.[30]

Fortunately, aerogels can be built out of materials beyond silica, making the world of aerogels an exciting area to explore more fully. Recently, aerogels built out of vdW materials, such as graphene and h-BN, have garnered a lot of attention for application in energy storage, gas sensing, and thermal management.[27,29,31] **Figure 2.1** shows the three common types of aerogels discussed so far: silica, graphene, and h-BN, all three of which have very different synthetic methods and resulting properties.[30,32,33] While the aerogels presented in **Figure 2.1** are built out of different materials, they have several characteristics in common regardless of chemical composition. High surface area (500-1200 m^2/g), high porosity (80-99.8%), and low densities (1.4-20 mg/cm^3) are just a few of the fundamental characteristics of aerogels.[24,30,32,34,35] Beyond the porosity and surface area of aerogels, additional properties and applications are derived from the specific building blocks comprising the aerogel. For example, graphene aerogels have high electrical conductivity and provide excellent scaffolding for energy applications, catalysis, and sensing applications.[25,31,36] On the flip-side, aerogels comprised of h-BN sheets are thermally insulating and provide excellent thermal management, or present a more oleophilic scaffold than graphene, thus showcasing improved absorption of certain gaseous and liquidous species.[29,37–39]

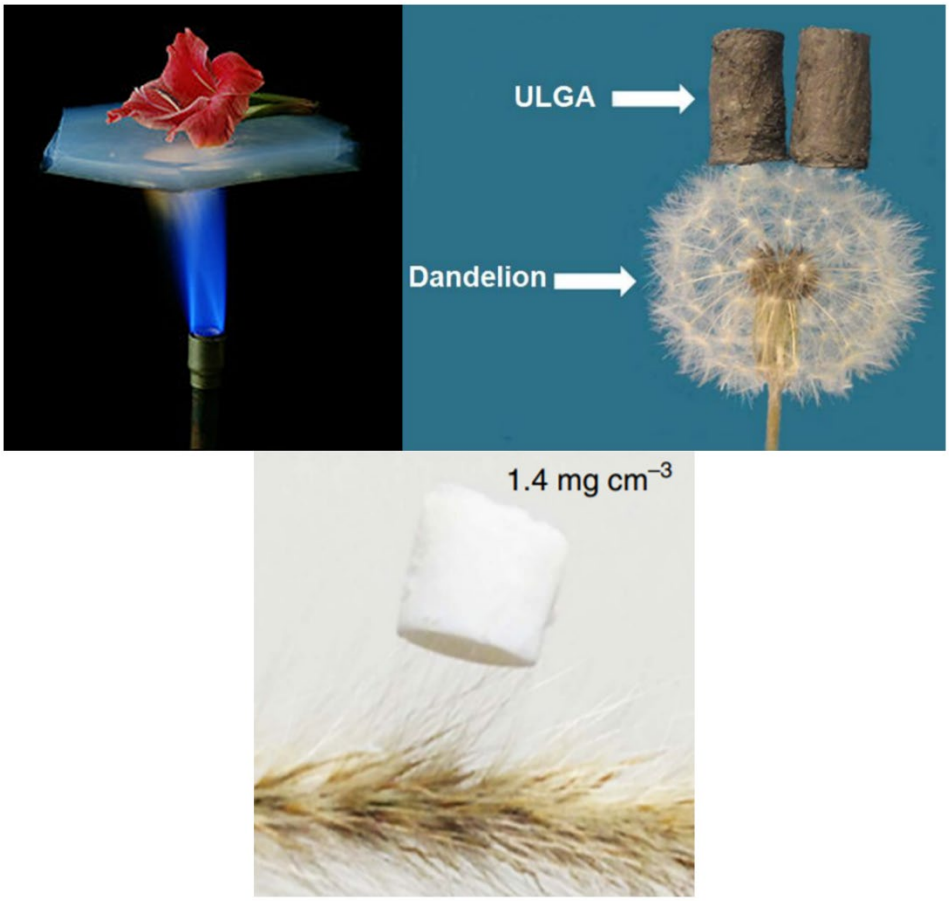

Figure 2.1 Three common types of aerogels. Top left: A silica aerogel supporting a flower, providing thermal protection from an open flame. Top right: A graphene aerogel resting on a dandelion. Bottom: An h-BN aerogel resting on wheat grass. Adapted from references 30,32,33.

The excitement surrounding the fabrication of aerogels out of vdW materials, such as graphene and h-BN, stems from the ability to incorporate massive amounts of the few- and single-layer material into a larger, macroscopic structure. In doing so, the resulting aerogels exhibit properties the benefit from the fundamental properties of the underlying building blocks. In the following sections, we will go into more detail about graphene and h-BN aerogels, specifically the synthetic techniques explored, characterization, and overall aerogel morphology.

2.2 Graphene aerogels

The first aerogel built from a vdW material we will explore is graphene aerogels. These aerogels are comprised of few-layer graphene sheets that have been cross-linked together, exhibiting high surface area and high porosity. However, additional properties are afforded to the graphene aerogel because of the underlying graphene sheets comprising the overall structure. Similar to the individual graphene layers, graphene aerogels have very high conductivity and structural robustness.[25,32] Additionally, as a result of their high conductivity, these aerogels find excellent application in gas sensing, mechanical flexibility, supercapacitors, and more.[27,31,32] **Figure 2.2** shows an optical image of graphene aerogels and highlights the ability to tune their overall shape and size.[35]

Figure 2.2 Graphene aerogels of varying sizes, from ~0.7 cm to 2.7 cm. Image credit to Dr. Sally Turner.[35]

2.2.1 Graphene aerogel synthesis

Graphene aerogels can be synthesized in a variety of ways, such as hydrothermal reduction, chemical reduction, or templated growth.[24] However, regardless of how the graphene aerogel is synthesized, in order to generate sufficient cross-linking of the graphene sheets to maintain a stable, macroscopic structure, we must start with graphene oxide. **Figure 2.3** shows a model of a graphene oxide (GO) sheet, along with the associated oxygen-containing functional groups (OCFG).[40] The OCFG provide the means of chemically cross-linking the graphene sheets through covalent bonds formed between two OCFG on neighboring GO sheets.

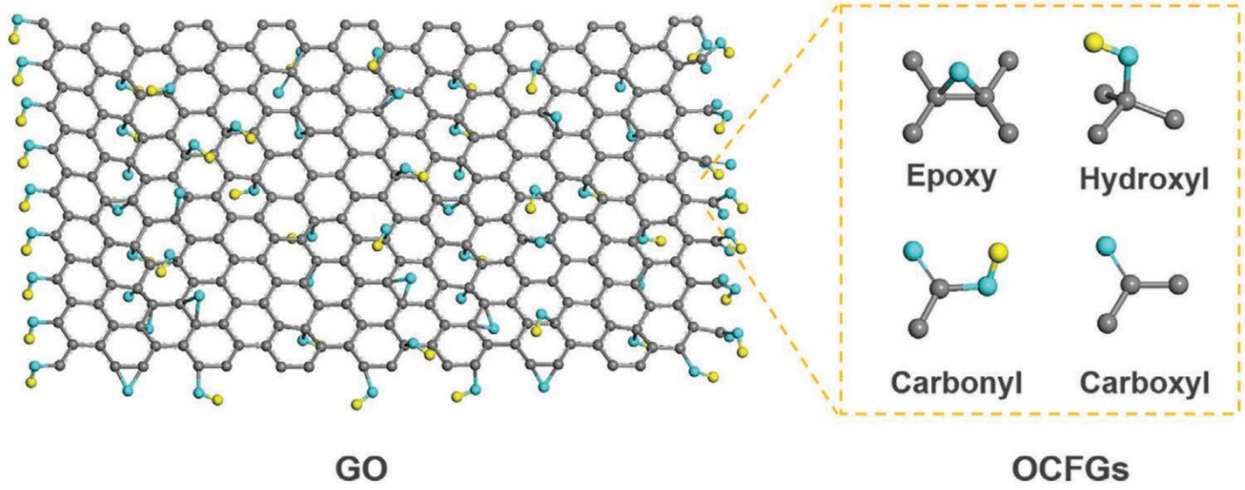

Figure 2.3 Atomic model of graphene oxide and the oxygen-containing functional groups adorning the surface and edges. The most common OCFG adorning the surface of graphene is typically epoxy groups or carbonyls, while the edges are typically functionalized by hydroxyls and carboxyls. Adapted from reference 40. Note: the Carbonyl and Carboxyl label are interchanged in the graphic.

The GO sheets can be chemically cross-linked through a variety of methods as previously mentioned. However, we commonly utilize a base-assisted gelation of the GO sheets, which provides excellent covalent cross-linking and results in structurally sound and reproducible aerogels. The base-assisted gelation of the GO sheets was developed by our colleague, Dr. Marcus Worsley, and is shown in **Figure 2.4**.[41]

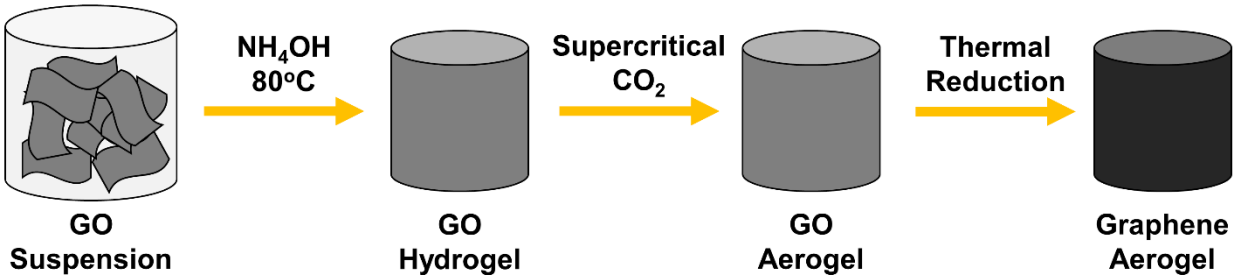

Figure 2.4 Schematic of the base-catalyzed synthesis of graphene aerogels. From left to right: Creation of GO suspension, gelation, critical point drying, and thermal reduction to graphene.

In more detail, the graphene aerogels are prepared by the gelation of a GO suspension, which undergoes chemical cross-linking, drying, and reduction to a final graphene aerogel. First, an aqueous suspension (~20mg/mL) of GO is prepared via bath sonication. The OCFGs on the surface and edge of the GO sheets interact strongly with water (a polar solvent) and allow for generation of relatively stable suspensions of GO. After sonication, the GO suspension is prepared for chemical cross-linking via basic conditions. Ammonium hydroxide (NH_4OH), a weak base, is added to the GO solution in a 1:6 ratio (NH_4OH:H_2O). The base-prepared GO solution is transferred to vials of desired shape and size. The resultant gels that form will take the shape (with some shrinking) of the reaction vessel, allowing for generation of aerogels of differing geometries, such as disks or cylinders.

Once distributed to vials of interest, the suspensions can be sealed tightly and placed in a furnace at 80°C for 3 days. During this time, the NH_4OH will catalyze reactions between the OCFG on neighboring GO sheets, resulting in chemical cross-linking and overall shrinkage of the final structure. This entire process of cross-linking and formation of structure is known as 'gelation'. Once gelation is complete, the original GO suspension will have formed a GO hydrogel, which is porous in nature, but with pores filled by water rather than air.

In order to obtain the porous GO structure as an aerogel, the water must be removed from the pores. However, due to the surface tension of water, normal drying in air would result in collapsed pores and a very dense final structure.[42] Therefore, the liquid inside of the pores must be removed without any surface tension. One method of achieving drying without surface tension is known as critical point drying, where the temperature and pressure of a system is controlled through the different phase regimes to achieve a supercritical fluid that behaves like a liquid and gas. One such substance that can form supercritical fluids is carbon dioxide (CO_2).

However, water and CO_2 are not miscible, so we must perform solvent exchanges to exchange the water in the pores with acetone (which is miscible with CO_2). Solvent exchange is achieved by submersion of the hydrogel (while in its original container) in the solvent of interest (in our case acetone) and left for 12-24 hours depending on the size of the hydrogel. To ensure all water is removed from the pores and fully exchanged with acetone, we typically perform 2 exchanges. Once the hydrogel has been fully exchanged, the gels (while in their containers) are placed in a pressurized vessel filled with acetone. The pressurized vessel is filled with liquid CO_2 while slowly draining the acetone. Once the acetone has drained completely, the system is left to exchange with the liquid CO_2. The vessel is then brought to the supercritical temperature and pressure of CO_2, where the liquid will leave the pores as a gas, keeping the porous structure intact. **Figure 2.5** shows the phase diagram and critical region of CO_2 for reference.[43]

Once the gels have been dried, we are now left with an aerogel. However, the graphene sheets, while chemically cross-linked through the OCFG, still have large amounts of unreacted OCFG on their surface and edges, resulting in a mostly GO-based aerogel. Therefore, to obtain the final desired graphene aerogel, the GO must be reduced. There are two ways of reducing and removing the OCFG: chemical or thermal reduction. Chemical reduction of the GO sheets can be achieved by several methods, such as acetic acid or Vitamin C.[44,45] Here, we commonly use thermal reduction of the GO structure to obtain the graphene aerogel, starting at 1050°C under Argon to remove the majority of the OCFG with some defects remaining. However, complete removal of OCFG and defects to obtain highly crystalline graphene aerogels requires annealing temperatures between 1500-2000°C.[46]

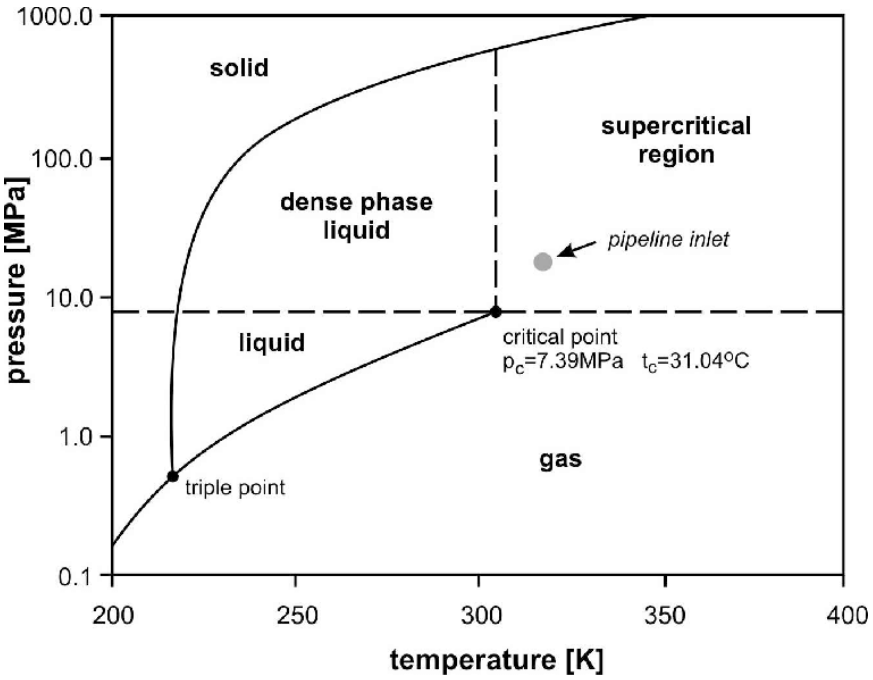

Figure 2.5 Phase diagram of carbon dioxide. Supercritical point marked at 7.4 MPa and 31°C. Room pressure and temperature are located at 0.1 MPa and 295 K, respectively. Adapted from open-source material.

2.2.2 Elemental characterization of graphene aerogels

Once the graphene aerogels have been successfully synthesized, we can begin characterization of their chemical composition and structural morphology. The chemical makeup of the graphene aerogels is simple, containing mainly carbon. However, the OCFG provide additional fingerprints to study the overall crystallinity of the resulting graphene aerogel. The structure morphology exhibits large, thin sheets of graphene chemically cross-linked with high porosity. This section will explore Raman spectroscopy and typical spectra observed for these aerogel structures.

A characteristic Raman spectrum of a thermally reduced (1050°C) graphene aerogel is shown in **Figure 2.6**. There are three main peaks of interest, the D peak (~1360 cm^{-1}), G peak (~1590 cm^{-1}), and the 2D peak (~2680 cm^{-1}). The fundamentals of Raman spectroscopy, specifically with graphene, were discussed in **Chapter 1**, but here we see some distinct

differences. While the G peak is of highest intensity and largest prevalence in this partially reduced aerogel, the D peak is substantially larger, and 2D peak is substantially reduced. These two peaks (and their ratio to the G peak) are good indicators of the overall crystallinity of the obtained aerogel. The 2D mode is an intervalley transition that requires two phonons and can be easily scattered by defects in the crystalline graphene network. Therefore, the overall intensity of this peak is inversely proportional to the number of defects (usually caused by OCFG).[17] The D peak is a resultant of a phonon scattered by a defect, so its intensity is directly proportional to the number of defects present in the material.[17] While the Raman spectrum in **Figure 2.6** indicates there are still substantial numbers of defects present in the graphene aerogel, additional thermal annealing at higher temperatures would remove these defects and drastically increase the overall crystallinity of the graphene aerogel.

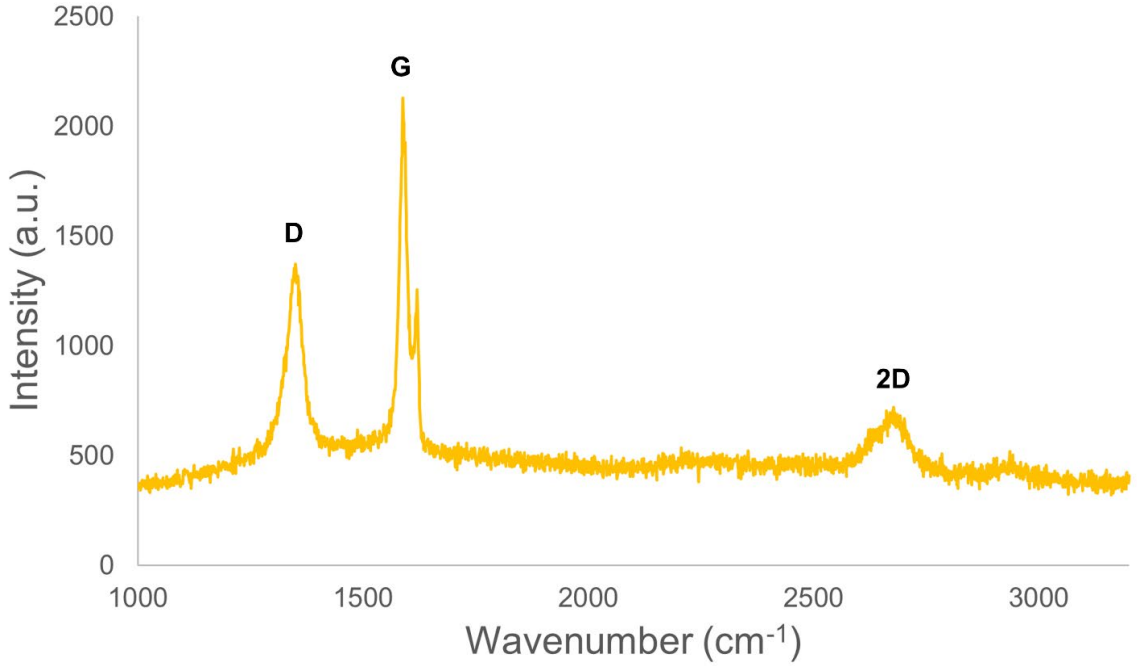

Figure 2.6 Raman spectrum of thermally reduced graphene aerogel. Three main peaks of interest have been labeled: D peak (~1360 cm^{-1}), G peak (~1590 cm^{-1}), and 2D peak (~2680 cm^{-1}).

There are other methods to analyze the chemical composition of aerogels other than Raman spectroscopy. To study the chemical composition of structures, energy dispersive spectroscopy (EDS) can be used. However, while atomic content can be uncovered, the specific functionality or bonding of the elements is unknown from EDS. For more bonding information, Fourier Transform – Infrared Spectroscopy (FT-IR) can probe the chemical makeup of aerogels and is a useful tool when trying to chemically modify sp^2-bonded structures, such as graphene and h-BN, with any specific functional groups. [44,47,48] However, while FT-IR provides an insight into bonding, it cannot provide any information on atomic content. If both atomic content and bonding information are required, then the best analytical tool is X-Ray Photoelectron Spectroscopy (XPS). FT-IR, EDS, and XPS as analytical tools will be explored further in **Chapter 3**.

2.2.3 Structural characterization of graphene aerogels

Beyond the chemical makeup of the graphene aerogels, we are also interested in their structural morphology, porosity, and crystallinity, all of which have significant impact on the resulting application of graphene aerogels. As the graphene aerogels are comprised of nanoscale sheets of graphene, we require electron microscopy to uncover the morphology of the cross-linked graphene sheets. This section will explore scanning electron microscopy, porosimetry measurements, and transmission electron microscopy.

Scanning electron microscopy (SEM) is an excellent tool to view the micron-scale features of the connected sheets and subsequent porous network of the graphene aerogel. **Figure 2.7** shows typical SEM images obtained of a graphene aerogel at different magnifications. The defining features of an aerogel under SEM are interconnected, semi-wrinkled sheets that are highly conductive (no charging under the electron beam) and assembled in a porous network. From **Figure 2.7**, we clearly see sheets on the order of 5-10 micron in size-scale, with pores on the order of sub-5 micron in size observed throughout. **Figure 2.7** (right) also shows the exterior of a graphene aerogel where an edge running down the center of the image is clearly visible.

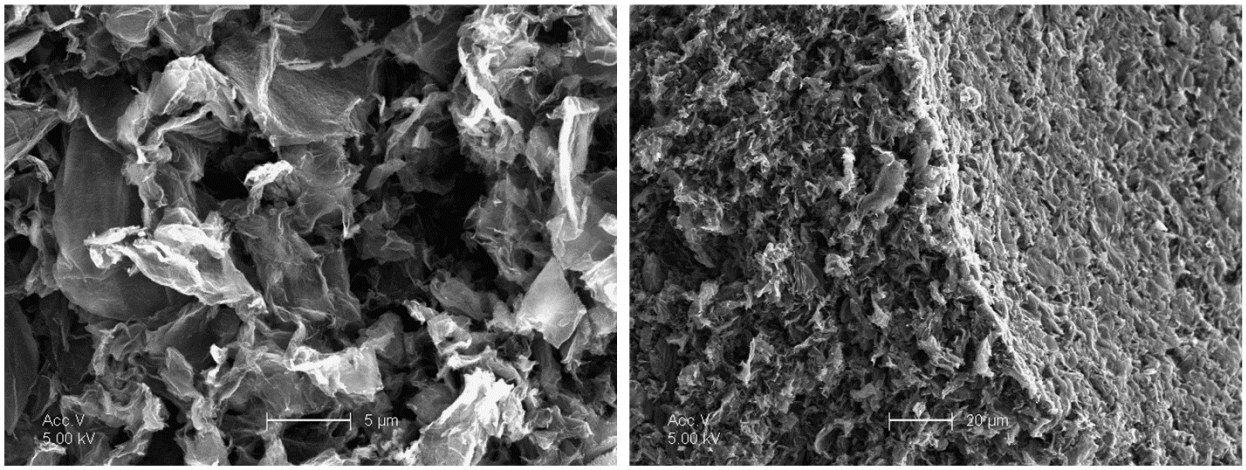

Figure 2.7 Scanning electron microscopy images of a graphene aerogel. Left: Interior of the graphene aerogel. Scale bar measures 5 µm. Right: Exterior of the graphene aerogel. Scale bar measures 20 µm. The sheets of graphene are microns in size (~5 µm) and consist of a few layers.

While the porous nature of the graphene aerogel can be qualitatively studied under SEM, quantitative data is more meaningful in the understanding of the assembly of the graphene sheets and resultant applications. **Figure 2.8** highlights typical isotherms collected for graphene aerogels, which also highlights nitrogen gas adsorption/desorption isotherms and the pore distribution of the graphene aerogel network.[25] The isotherms provide insight into the overall specific surface area of the graphene aerogel (584 cm^2/g in the case of the reference material), and the pore diameter range is seen to be between 10-100 nm (with a peak occurrence at 13 nm for the reference material).[25]

Surface area and porosimetry data is collected via the Brunauer-Emmett-Teller (BET) method. The BET method examines the adsorption process of gaseous species onto a solid substrate (and subsequent desorption), the results of which can be used to determine the specific surface area of the solid-state material and corresponding porosity. The theory behind BET is an extension of the Langmuir adsorption model, where we assume that a gas behaves ideally at

isothermal conditions (hence the isotherms commonly plotted for BET measurements).[49] The additional assumptions made for BET include the ability for gaseous molecules to form infinite layers, but the enthalpy of adsorption for the first layer is constant and greater than any additional layers.[49] It is the formation of this first layer that ultimately corresponds to the specific surface area of the solid being studied.

While the surface area is dependent upon the number of gaseous molecules required to form a monolayer on the exposed surface of the solid substrate, the porous structure requires additional adsorption data. For studying the fine pore structure of the material, the pressure is increased until liquid has condensed in all pores (i.e., the pores become saturated), at which point the pressure is incrementally decreased. The overall shape and hysteresis in the adsorption and desorption sections of the isotherm provide information on the fine pore structure of the solid sample.[49,50]

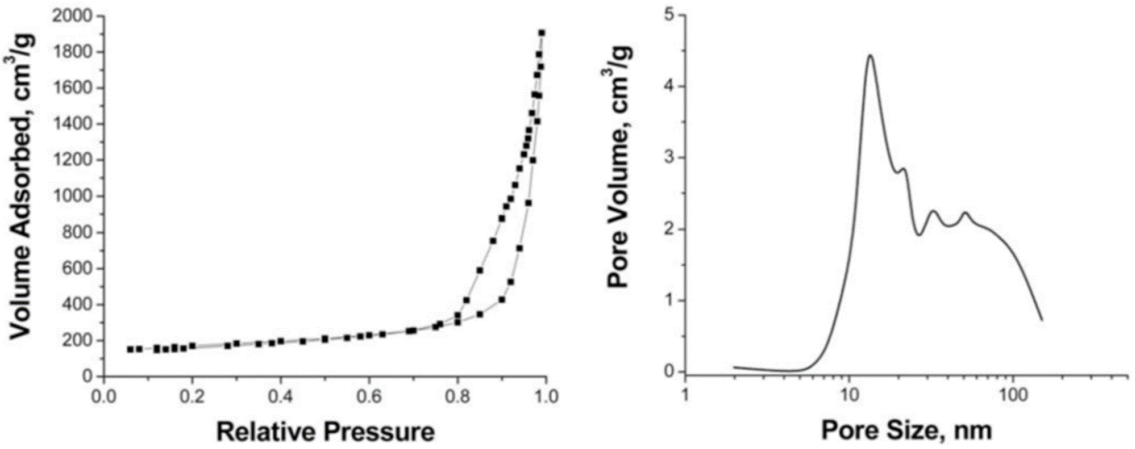

Figure 2.8 Nitrogen isotherm and pore distribution for a graphene aerogel. Image credit to Dr. Marcus Worsley.[25]

An additional source of structural characterization, aimed at the crystallinity of the material, is transmission electron microscopy (TEM). TEM is an excellent tool to view the atomic structure of the graphene sheets at the nanometer size-scale to see the morphology of the graphene sheets at an atomic scale. Under TEM, any wrinkles, edges, tears, or defects are readily apparent in the material.[31,51,52] An added benefit to the study of crystallinity in the TEM, is that electron diffraction can be obtained simultaneously. **Figure 2.9** shows standard TEM imaging and electron diffraction obtained for highly crystalline graphene layers. Readily apparent in the TEM image is the overall flatness and high crystallinity of the few-layer graphene. This is further confirmed by the electron diffraction shown, where a six-fold spot pattern is highlighted. Additionally, only one set of diffraction spots is observed, indicative of a single crystal orientation of the graphene layers from the selected region. The well-defined, single set of diffraction spots confirms the underlying crystalline nature of the graphene sheets.[53]

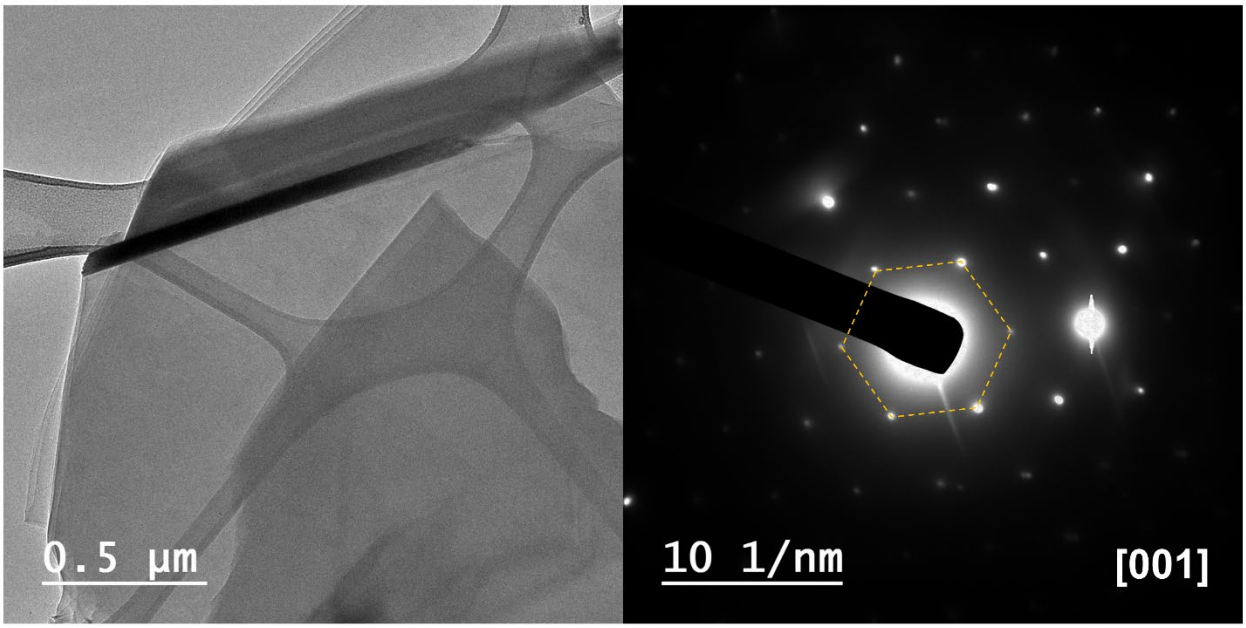

Figure 2.9 Standard transmission electron microscopy imaging of graphene sheets and associated electron diffraction. Left: TEM image of few-layer graphene. Scale bar measures 500 nm. Right: Selected area diffraction pattern of few-layer graphene. The six-fold symmetry of the diffraction spots has been highlighted by the gold dashed lines.

In **Figure 2.9**, we show the diffraction of the graphene sheets along the [001] plane (the basal plane of the graphene), where we look for six-fold symmetry, a result of the underlying hexagonal lattice of graphene. In addition to the overall symmetry of the obtained diffraction pattern, we gain additional information based on the intensity of the diffraction spots. Layers thicker than monolayer will have different intensities of the lower- and higher-order diffraction spots.[21] However, in our diffraction pattern seen in **Figure 2.9**, there is a very bright higher-order diffraction spot to the right of the [000] spot, and some slight asymmetry in the overall brightness in the diffraction pattern. This indicates that the alignment of the diffraction plane is slightly off the zone axis and would require some small tilting to obtain perfectly symmetric intensity of the diffraction spots. Because of the slight asymmetry, no additional knowledge about the number of layers can be gleaned from the diffraction pattern, however the TEM image shows clear edges of the overlapping layers and appears to be at least trilayer graphene.

2.3 Boron nitride aerogels

The second family of vdW-built aerogels we will explore here are h-BN aerogels. While these aerogels are comprised of few-layer h-BN sheets, these sheets were first cross-linked together as graphene aerogels, and subsequently converted to h-BN, which will be further explored in the synthetic section. The h-BN aerogels still exhibit high surface area and high porosity. However, additional properties are afforded to the h-BN aerogel because of the underlying h-BN sheets comprising the overall structure. Similar to the individual h-BN layers, h-BN aerogels provide great thermal management and hydrophobic characteristics.[54–56] Additionally, these aerogels find excellent application in gas adsorption, oil absorption, and sensing.[28,37,38,57] **Figure 2.10** shows an optical image of a graphene aerogel that has been

converted to its h-BN counterpart. The optical difference between the two aerogels comes from the electronic structure of the underlying components, where graphene is conductive and appears black, while h-BN is insulating and appears white. The small black specks on the h-BN aerogel are small particles of carbon fiber from the conversion process. The h-BN aerogel has been broken to show complete conversion throughout the entire structure.

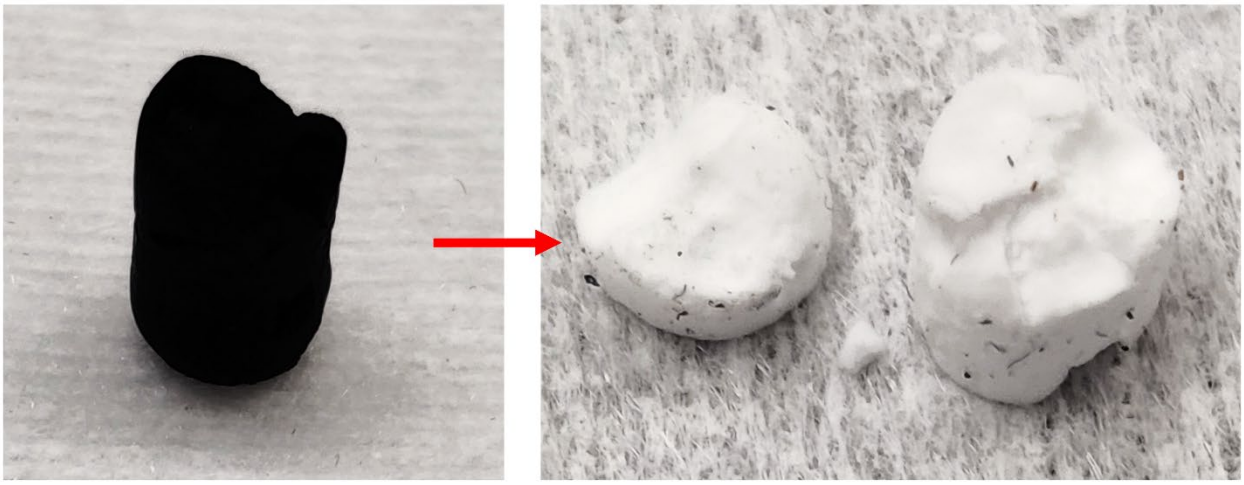

Figure 2.10 (Left) Graphene aerogel that was converted to an (right) h-BN aerogel. Overall scale of the aerogels is roughly 10 mm in height.

2.3.1 Boron nitride aerogel synthesis

The synthetic routes for boron nitride aerogels are not as straightforward as graphene aerogels due to the smaller library of chemistries involving h-BN. However, there are still a variety of methods used to obtain h-BN aerogels, such as cross-linking of functionalized h-BN sheets, drying of suspensions created from h-BN containing polymers, or foaming of precursor materials.[29,38,57] The aerogels generated from these methods have many similarities to their graphene aerogel counterparts, such as high specific surface areas, unique distribution of pore sizes, and varying mechanical properties. In this section, we will discuss a different approach to the synthesis of h-BN aerogels, which is direct conversion of a graphitic network to that of boron nitride through carbothermic reduction.

In general, a carbothermic reduction starts with the reduction of an oxide by carbon atoms from a carbon source. For h-BN carbothermic conversion, the oxide source is boron oxide and the carbon source is the graphene-based structure we wish to convert to BN. During the reduction process, nitrogenization (from high temperature N_2 gas) of the products can be simultaneously incorporated to produce a final BN product. While the carbon structure and boron oxide are solid reagents, the B_2O_3 vaporizes and becomes a gaseous reagent alongside the N_2 during heating. The carbothermic reduction and nitrogenization occurs at the atomic sites of the carbon source, which generally means the carbon source is gradually replaced by BN. In the case of aerogel conversion, the carbon source is the hexagonal carbon lattice of the graphene aerogel, which is gradually replaced with an h-BN lattice:[58]

$$\frac{3}{2}C(s) + B_2O_3(g) + N_2(g) \xrightarrow{\Delta} 2BN(s) + \frac{3}{2}CO_2(g) \qquad \textbf{(Eq. 2.1)}$$

The reaction described in **(Eq. 2.1)** likely preferentially starts at defect sites in the carbon materials, such as surface functional groups, wrinkles, grain boundaries, vacancies, and edge atoms, where there is weaker bonding compared to the flat surface of a pristine sheet of sp^2-bonded carbon atoms.[59,60] As the reaction proceeds, the carbon lattice is gradually replaced by that of h-BN. Conversion of carbon species to that of a BN network has been performed on innumerable substrates, such as nanotubes, aerogels, foams, and more.[56,59,61,62] The benefit of direct conversion of the carbon lattice to that of BN is the retention of overall morphology, surface, and macrostructure. In conventional carbon templating the bulk and nanoscale structural morphology of the parent carbon-based material is maintained in the final BN product. This follows naturally from the isoelectronic hexagonal structure of graphene and h-BN, and the near-identical lattice parameters. For many of the previously studied carbon materials, such as carbon nanotubes or graphene aerogels, the material is comprised of micron- or nano-sized features with a large active surface area, containing many pathways for the boron- and nitrogen-containing gaseous reactant species to approach the graphitic structure and react.[56] In **Chapter 4** we will explore how the reaction pathway differs for closely packed carbon structures, such as graphite, and resultant changes in morphology between the native graphite and resulting h-BN material.

The conversion of graphitic species to BN is done in an induction furnace, heated by AC currents. The setup involves a large diameter quartz tubing as the overall reaction housing, which is heated by conduction coils, as shown in **Figure 2.11a**. The brass fitting at the top of the inlet valve in **Figure 2.11a** is where the nitrogen gas is flowed in at the top for the nitrogenization of the carbon product. Any excess nitrogen or gases evolved during the heating and reaction process are exhausted through the tubing coming out the top of the quartz tubing (slightly off center in **Figure 2.11a**). The entire quartz tubing setup is sealed with gaskets and can be run through pump-purge cycles (pumping under vacuum and then the system is refilled with nitrogen) to remove excess oxygen from the overall setup. A graphite crucible, shown in **Figure 2.11d**, is used to hold the carbon species of interest (such as a graphene aerogel), as well as the boron oxide. Graphite must be used as it is inert at very high temperatures (it will not cross-contaminate the sample) and can structurally survive repeated high-temperature heating and cooling cycles. After the graphite crucible has been used many times, the crucible itself will start to convert to BN, as shown in **Figure 2.11c**.

A schematic of the graphite crucible shown in **Figures 2.11c** and **2.11d** is shown in **Figure 2.12**. The top portion of the crucible (the longer shaft/inlet and disk filled with holes) shown in **Figures 2.11c** and **2.11d** is removable and is shown as the basket in **Figure 2.12**, which has the inlet for N_2 and holds the graphene aerogel. The boron oxide is loaded as a powder into the bottom of the crucible, away from the carbon being converted. The boron oxide will melt and vaporize, being carried by the flowing N_2 to the surface of the graphene aerogel, where the carbothermic reduction and simultaneous nitrogenization can occur. As the carbon structure is only exposed to gaseous reagents, the overall structure is maintained with little physical damage from the conversion process.

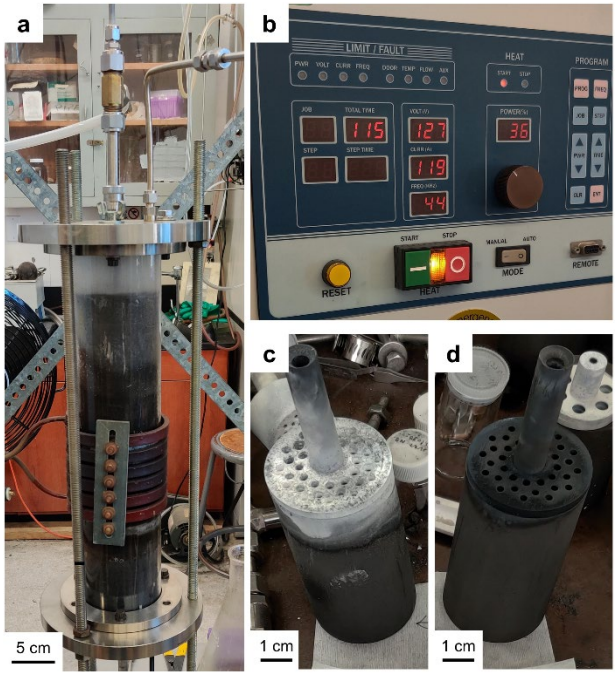

Figure 2.11 Induction furnace setup for BN conversions. (a) Reaction chamber where the induction coils heat the external quartz tubing, inside of which a graphite crucible and reactants are placed. (b) Control panel where the time, voltage, current, frequency, and power are controlled. (c) Graphite crucible after many BN conversions, where the carbon of the crucible has started to be converted itself and replaced by BN. (d) Graphite crucible before being subjected to many conversions.

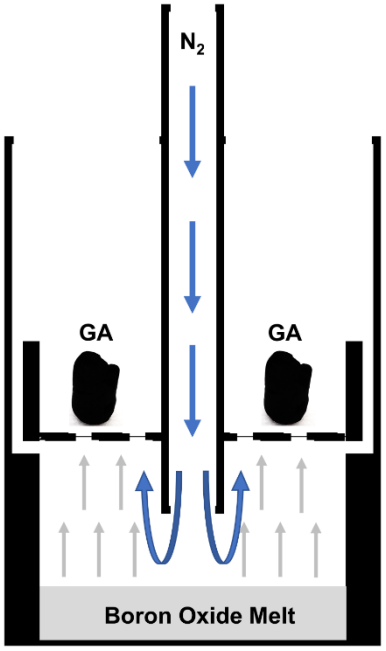

Figure 2.12 Schematic for the conversion of a graphene aerogel. The overall container is the graphite crucible, containing the boron oxide powder, graphene aerogel, and inlet for the nitrogen gas.

The most important takeaway from the conversion process, is that the overall structure, size, and shape of the h-BN aerogel is entirely dependent upon the starting graphene aerogel. Therefore, any structure or shape desired for the h-BN aerogel must be designed into the graphene aerogel before conversion. The benefit of using the conversion process to obtain h-BN aerogels, is that there has been significantly more exploration into the reaction chemistries to design and control the surface morphologies and obtainable structures in graphene aerogels vs. h-BN systems. Therefore, the final structure of an h-BN aerogel is not limited by our current ability of functionalizing BN sheets to build h-BN aerogels from the ground-up.

2.3.2 Elemental characterization of boron nitride aerogels

Once the h-BN aerogels have been successfully converted, we can begin characterizing their chemical composition. The chemical makeup of the h-BN aerogels is simple, containing only boron and nitrogen. The structure morphology exhibits large, thin sheets of h-BN that were cross-linked as graphene sheets, which exhibit the same large surface area and high porosity as the initial graphene aerogel. This section will explore Raman spectroscopy and typical spectra observed for these aerogel structures.

A characteristic Raman spectrum of a chemically converted h-BN aerogel is shown in **Figure 2.13**. There is only one main peak of interest, the E_{2g} peak (~1365 cm^{-1}). The E_{2g} peak of h-BN is similar to the G peak of graphene, where the vibrational mode activated is the in-plane vibration of the sp^2-bonded boron and nitride atoms. One interesting aspect about the spectrum for the converted h-BN aerogels (and other converted systems) is that the Raman signal can have a very high background count. **Figure 2.13** shows an average background count of ~7,500 for h-BN (signal to background ratio of ~5), while **Figure 2.6** shows an average background count of ~400 for graphene (signal to background ratio of ~5.5). Typically, fluorescence from the sample or impurities in the sample is much larger in signal than the Raman scattering, which gives rise to large background counts.[63] The large background count could indicate there are impurities in the h-BN structure after the conversion from graphene. **Figure 2.14** shows a Raman spectrum of a partially converted graphene structure, which has extremely high background count (as compared to the spectrum in **Figure 2.6**), with the D, G, and 2D peaks of graphene still visible. In some cases, the background counts can completely obscure the signal of interest, so further processing of the h-BN aerogel could be necessary to remove impurities, such as additional thermal annealing.

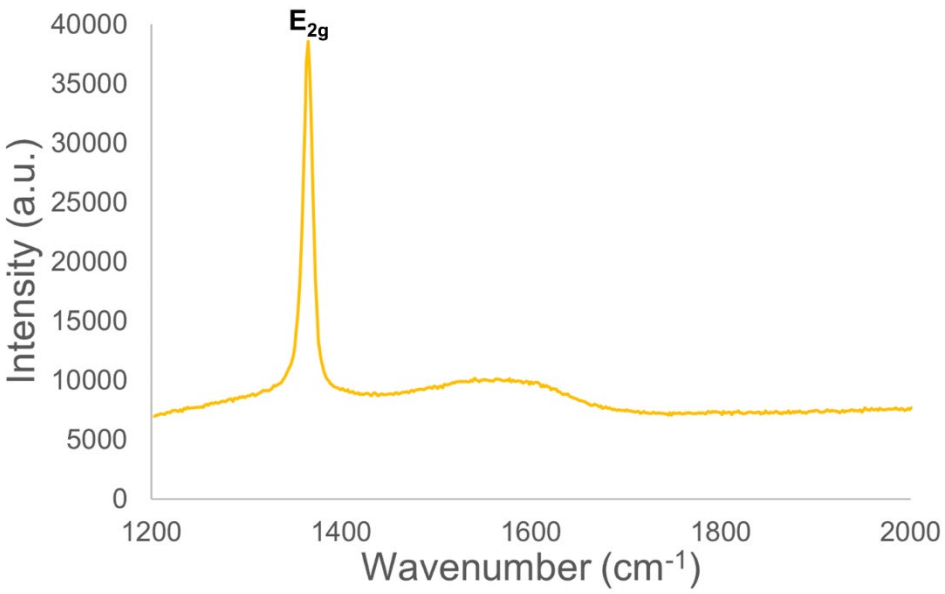

Figure 2.13 Raman spectrum of converted h-BN aerogel. The main peak of interest has been labeled: E_{2g} peak (~1365 cm^{-1}).

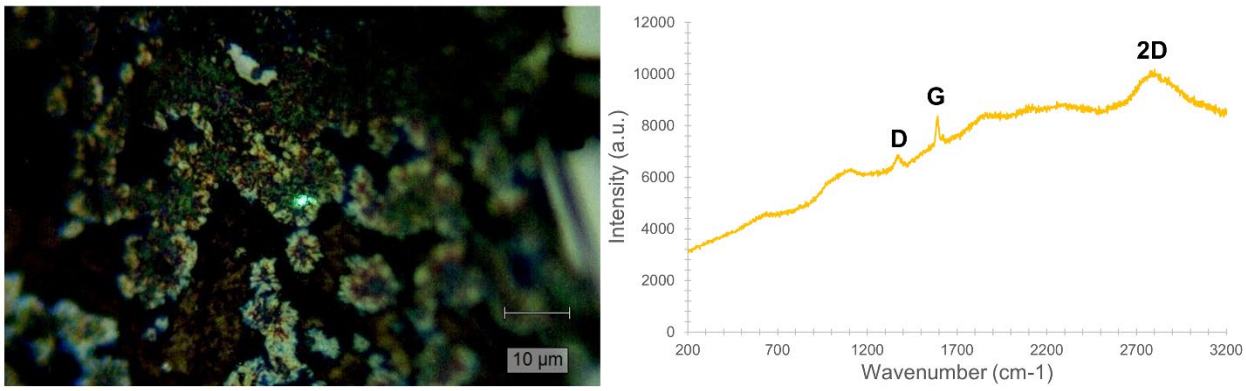

Figure 2.14 Raman spectrum of partially converted graphene aerogel. The three main peaks of interest for graphene are still visible and have been labeled: D peak (~1360 cm^{-1}), G peak (~1590 cm^{-1}), and 2D peak (~2680 cm^{-1}).

2.3.3 Structural characterization of boron nitride aerogels

Beyond the chemical makeup of the h-BN aerogels, we are also interested in their structure morphology, porosity, and crystallinity, all of which have significant impact on the resulting application of h-BN aerogels. Additionally, we would like to compare the morphology, porosity, and crystallinity to the graphene aerogels from which the h-BN aerogels were converted. This section will explore scanning electron microscopy, porosimetry measurements, and transmission electron microscopy of the h-BN aerogels and typical images observed for these aerogel structures.

Scanning electron microscopy (SEM) is an excellent tool to view the micron-scale features of the connected sheets and subsequent porous network of the h-BN aerogel. **Figure 2.15** shows typical SEM images obtained of an h-BN aerogel at similar magnifications. The

defining features of an h-BN aerogel under SEM are interconnected, semi-wrinkled sheets that are assembled in a porous network. Because h-BN itself is insulating, the surface can charge from the incident electrons used for imaging, affecting the ability to capture clear images. In order to reduce the charging, lower accelerating voltages, large spots sizes, or sputtering with a conductive material may be of use. Another route is to break the h-BN aerogel apart and mount it on a conductive surface, such as carbon tape, to reduce charging. From **Figure 2.15**, we clearly see h-BN sheets on the order of 5-10 micron in size, similar to the sheets of graphene from the graphene aerogel. The pore size also appears to be on the order of sub-5 micron in size observed throughout. The edges of the h-BN nanosheets appear to have similar roughness to the graphene sheets shown in **Figure 2.7**.

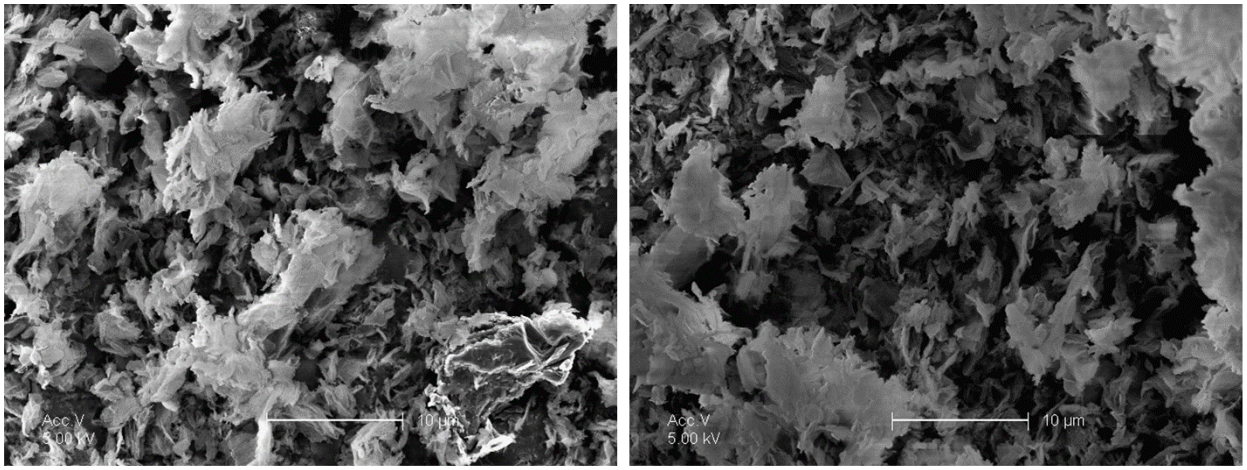

Figure 2.15 Scanning Electron Microscopy images of an h-BN aerogel. Both show the interior of the aerogel. Scale bars measure 10 µm. The sheets of h-BN are microns in size (~5 µm) and consist of only a few layers.

While the porous nature of the h-BN aerogel can be qualitatively studied under SEM, quantitative data is more meaningful in the understanding of the assembly of the graphene sheets and resultant applications. **Figure 2.16** shows a simple comparison of typical isotherms collected for a graphene aerogel and h-BN aerogel.[56] The nitrogen gas adsorption/desorption isotherms are similar in their overall shape and hysteresis, however the h-BN isotherm has much lower specific volume adsorption. As will be seen in the TEM images, the h-BN sheets tend to contain more layers than the graphene aerogel, meaning the overall h-BN aerogel could be denser in nature and would lead to a decrease in overall specific volume adsorption.[56]

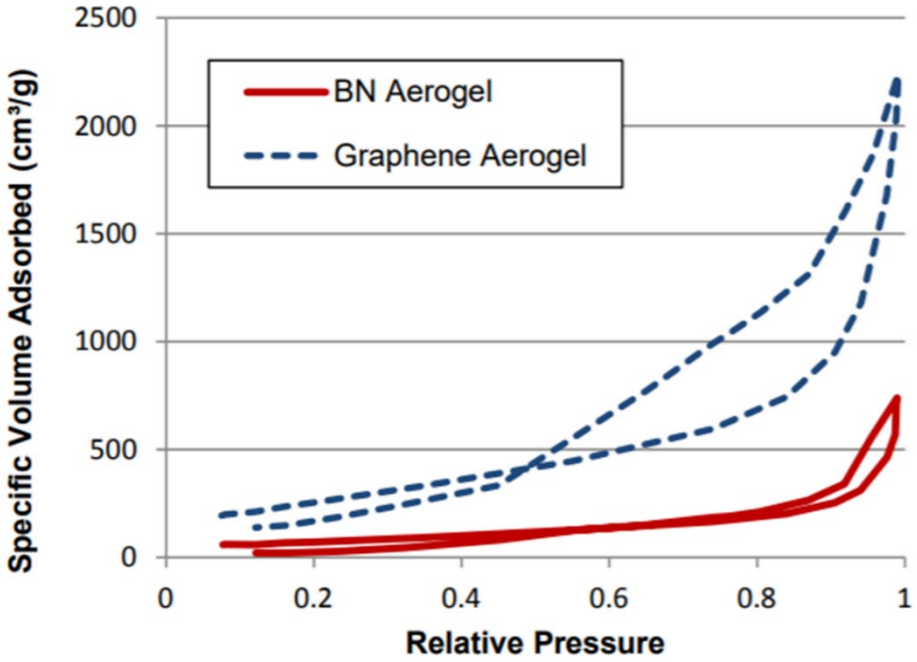

Figure 2.16 Nitrogen isotherms for a graphene and h-BN aerogel. The decrease in the specific volume adsorbed for the h-BN aerogel is attributed to the small increase in layer numbers of the h-BN sheets after conversion, leading to a denser aerogel. Image credit to Dr. Thang Pham.[56]

To study the underlying crystallinity of the converted h-BN sheets, we employ TEM. Under TEM, we observe a large increase in the number of wrinkles and edges in the h-BN over the parent graphene sheets observed in **Figure 2.9**. **Figures 2.17a** and **2.17b** shows standard TEM images of the resultant converted h-BN sheets. **Figures 2.17c** and **2.17d** show standard electron diffraction obtained for the crystalline h-BN aerogel. Readily apparent in the TEM image is the layered structure of the h-BN sheets, which, although is crinkled in appearance, is highly crystalline. This is further confirmed by the selected area diffraction pattern of the marked region in **Figure 2.17b**, where distinct six-fold patterns are observed. Several six-fold spot patterns are highlighted and subsequently marked in **Figure 2.17d**. Because multiple sets of diffraction spots are observed, we know there are multiple orientations of the sheets of h-BN within the aerogel. We can measure the offset of two sets of the diffraction patterns to determine the orientation of the h-BN sheets in relation to one another. As shown in **Figure 2.17d**, two of the sheet domains are misaligned by ~14^{o}.

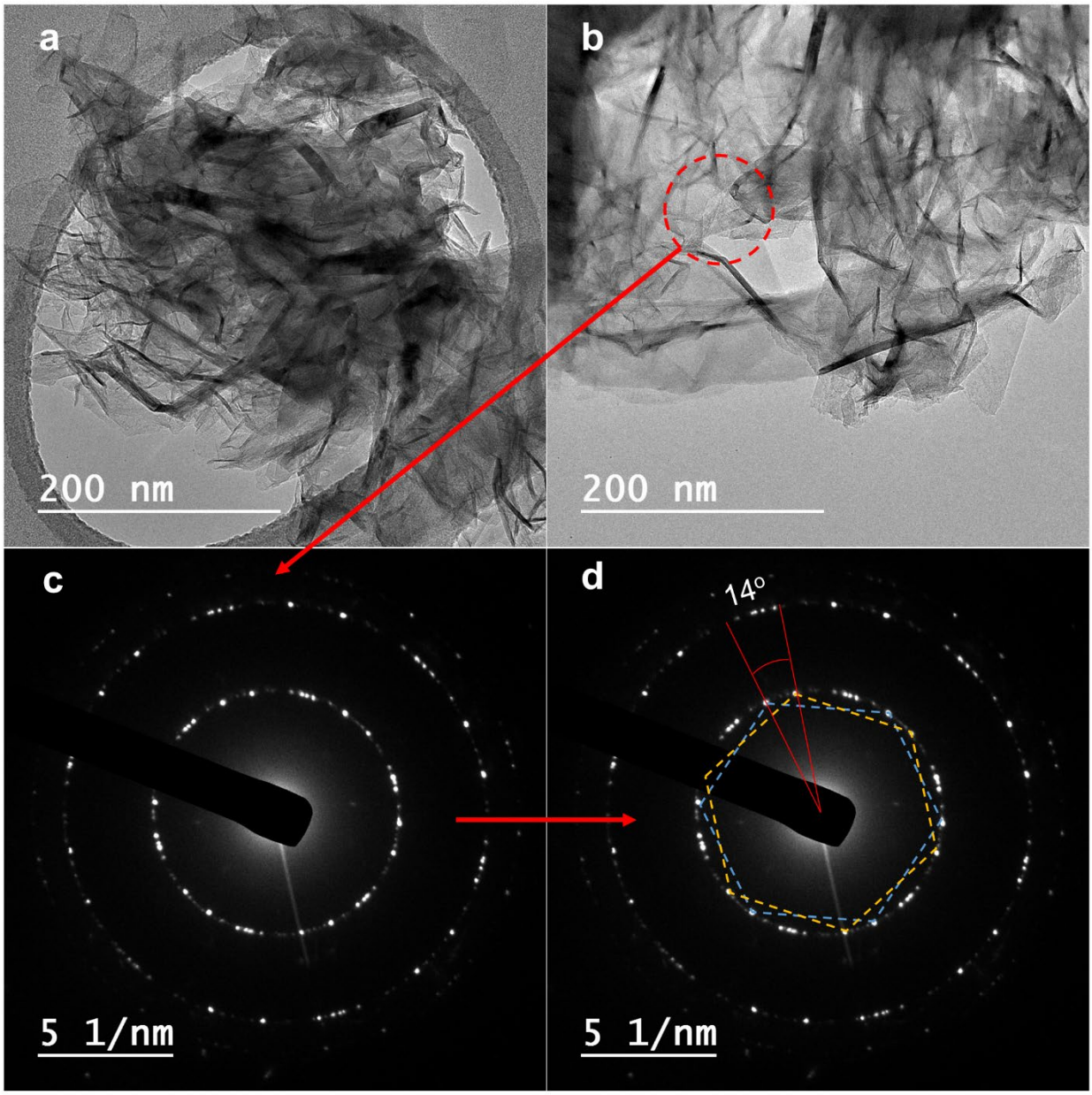

Figure 2.17 Standard transmission electron microscopy imaging and associated electron diffraction of h-BN sheets from an aerogel. (a/b) TEM image of few-layer h-BN. Scale bars measure 200 nm. (c/d) Selected area diffraction pattern of the few-layer h-BN from the marked region in (b). The six-fold symmetry of two sets of diffraction spot have been highlighted by the gold and blue dashed lines. The orientation of these two sets of diffraction spots shows a misalignment of 14°.

2.4 Modification of aerogel structures

While graphene and h-BN aerogels have been studied for a variety of applications based off the inherent properties of the highly crystalline, defect free sheets, additional modifications to the aerogel structure can be made to customize the utility of the aerogels. For instance, doping of

the aerogel with nanoparticles can enhance catalytic or sensing activity based on the nanoparticles used.[28,64,65] Another route to modifying the structure of the aerogels is based on the manipulation of the fundamental building blocks of the aerogels themselves: the graphene and h-BN sheets. Modifying the sheets of graphene or h-BN themselves, either from atomic doping or defect incorporation, allows for interesting surface states to be incorporated, which can lead to enhanced sensing or catalytic properties.[31,66,67] Previous work completed by my colleague Dr. Sally Turner showcases the ability to incorporate boron within the graphitic network of a graphene aerogel. Subsequent removal of the boron dopants generated targeted defects, leading to enhanced sensing of NO_2 molecules.[31] **Figure 2.18** shows an overall schematic of the modification of the graphene network, which involves post treatment of a graphene aerogel with a triphenylboron solution and thermal annealing. We will explore the beginnings of some experimental work to incorporate nitrogen into the network of a graphene aerogel through modification of the starting GO suspension in **Chapter 3**.

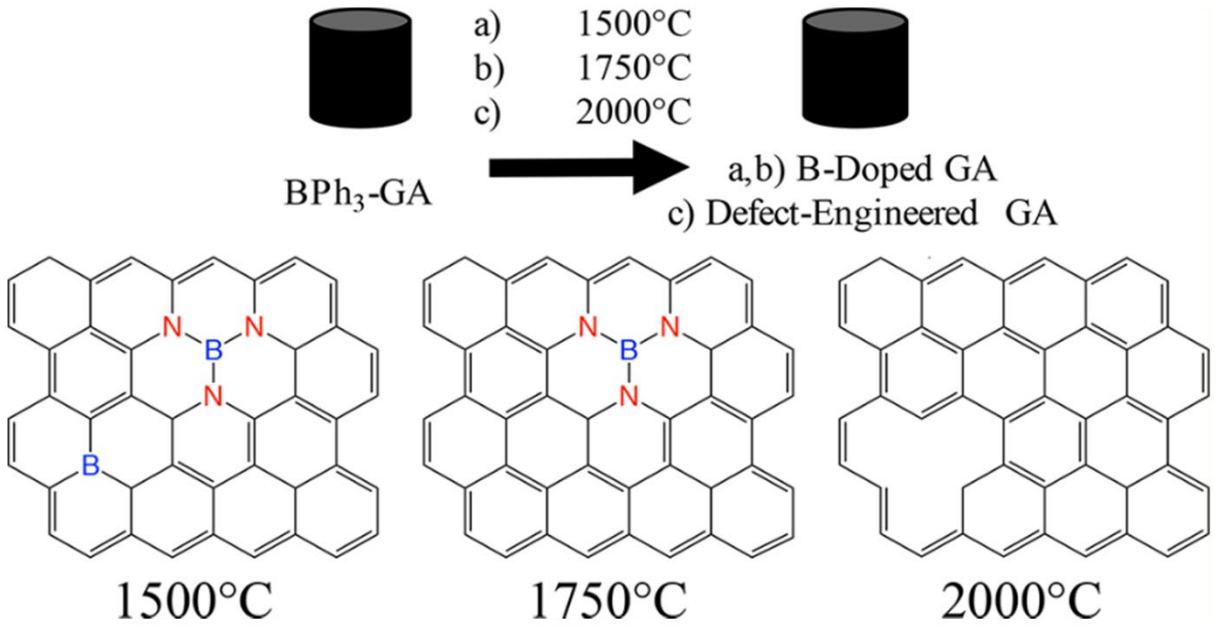

Figure 2.18 Dopant and defect engineering possibilities of aerogels through manipulation of the comprising layered material. Graphene aerogels can be doped by boron through a post-treatment of the aerogel with a boron-species containing solution. The boron doping can be thermally annealed out of the graphitic structure, leaving behind defect structures. Image credit to Dr. Sally Turner.[31]

2.5 Conclusion

This chapter explored the fundamentals of aerogels, from their synthesis, elemental composition, and structural characterization. While aerogels can be built out of many materials beyond silica, we focused on aerogels built out of vdW materials, such as graphene and h-BN, which have garnered a lot of attention for application in energy storage, gas sensing, thermal management, and so much more. The resulting applications are dictated by the properties of the comprising layered material chosen, allowing for customizable aerogels. The synthetic methods explored in this chapter covered that of graphene and h-BN aerogels. Graphene aerogels are

constructed from chemically cross-linked GO sheets, where a base-assisted gelation of the GO sheets provides excellent covalent cross-linking and results in structurally sound and reproducible aerogels. For h-BN aerogels, we employ a carbothermic reduction and nitrogenization of a graphene aerogel for direct conversion of a graphene aerogel to an h-BN aerogel. By utilizing a conversion method for obtaining h-BN aerogels, the overall structure, size, and shape of the h-BN aerogel can be designed through the initial graphene aerogel.

Characterization of both types of aerogels follow similar standard procedures. Composition can be determined by the vibrational modes observed in Raman spectroscopy. Furthermore, peak intensity and background of the spectrum provides additional insight into the overall defect structure and purity of the sample. Structural morphology can be analyzed by SEM to view the micron-scale features of the connected sheets and subsequent porous network of the aerogels. Quantitative data on the specific surface area and porosimetry is collected via the BET method, which examines the adsorption process of gaseous species onto a solid substrate. The crystallinity of the aerogel sheets is further examined by TEM and electron diffraction, where any wrinkles, edges, tears, or defects are readily apparent in the material, and misalignment of the sheets can be determined.

While the fundamentals of the synthesis and characterization of graphene and h-BN aerogels are well understood, there is still more to explore for the creation of other interesting porous structures. **Chapter 3** discusses initial research into the doping of the graphene sheets for added functionality. **Chapter 4** goes into greater detail about the conversion process for BN structures, and how this process can be utilized to explore porous structures of other types, such as nanofoams. **Chapter 5** explores the conversion method to access different compositions of porous structures beyond that of a BN network.

Chapter 3: The Power of Small Molecules – Nitrogen-Doped Graphene Aerogels

Special thank you to James Marquez, Dr. Marcus Worsley, and Dr. Art Nelson for their support on this project.

Keywords: Graphene, Aerogels, Doping, Nitrogen, Scanning Electron Microscopy, FT-IR, Energy Dispersive Spectroscopy, Schiff Base

We explored the fundamentals behind graphene aerogel synthesis in the previous chapter and touched on the possibilities of further enhancement or alteration via doping or defect engineering of the graphitic structure. While graphene itself presents an interesting and useful aerogel for a variety of applications, the control over atomic species incorporated within the lattice provides additional expansion and improvement of said applications. This chapter will continue to explore the advantages of atomic doping, associated chemistries involved, and subsequent characterization of such structures.

3.1 Motivation behind doping of graphene aerogels

Aerogels are excellent materials for applications that require high surface area, porous networks, and low densities. These applications range from thermal management, to fuel storage, to gas sensing, to adsorption of certain species, all of which capitalize on the ability of small molecules to easily migrate through the aerogel structure.[30,57,64,68] In addition to the surface area and porous structure, graphene aerogels (GA) provide a conductive scaffolding which allows for a plethora of applications, from gas sensing, to catalysis, to energy storage, and more.[24,25,27] However, the overall performance of these pure graphene systems is held back by the smooth and relatively inert surface of graphene, and enhancement of these properties can be aided by addition of species other than carbon.[24,28,69]

While nanoparticles or adatoms have shown an ability to improve or alter the performance of GA, a more robust method to tune the properties of GA is through atomic doping within the carbon lattice.[24,69,70] As previously discussed in both **Chapters 1** and **2**, there are a couple elements (boron and nitrogen) that are similar enough to carbon in terms of size and type of bonding that can be inserted into the lattice and replace carbon atoms directly.[56,71,72] In low quantities, this structural replacement of carbon atoms with another elemental species is referred to as doping, and has powerful implications on the local electronic and chemical environment for the graphene sheet. Previous work was completed by my colleague, Dr. Sally Turner, focusing on the doping of GA with boron, and subsequent removal of those dopant atoms to create defect sites. In their work, Dr. Turner demonstrated how these dopant-engineered GA showed drastically improved sensitivity and limit of detection for sensing NO_2 in air.[31]

In this work, I focus on the doping of the graphene lattice with nitrogen. Nitrogen has been of high interest for doping graphene systems to improve their overall performance in energy and reaction applications, specifically catalytic activity and batteries.[66,73–76] These nitrogen(N)-doped graphene systems show enhanced performance for these applications, because the small molecule interactions with the surface of graphene are enhanced by the N-dopants within the sheet. Ultimately, the free energy for the adsorption and desorption of the small molecules from the surface is drastically lowered by the N-doped site, improving the overall interaction of small molecular species with the aerogel structure.[66] Incorporating nitrogen into carbon and graphitic

species has been done in a multitude of systems, from carbon nanotubes, to carbon fibers, to some porous carbons.[77,78] However, one system that has been lacking substantial improvement for N-doping is GA. Therefore, in this chapter, we will discuss an approach to functionalize and dope the graphene sheets before they are assembled into an aerogel, preserving their high surface area and overall porous structure.

3.2 Synthetic approaches towards doped graphene aerogels

Many of the previously doped systems mentioned, such as carbon nanotubes, fibers, and sheets, are synthesize from gaseous precursors to dope the system.[77] However, GA cannot be built from gaseous precursors, but instead are fabricated through a liquid-phase gelation process, previously discussed in **Chapter 2**. Therefore, we must employ other synthetic routes to incorporate nitrogen into the GA system. **Figure 3.1** shows the overall schematic of the traditional synthesis of GA through the base-assisted gelation process previously described. Below that, an alternative route to synthesize GA is proposed, where an additional small molecule species is introduced to the solution of graphene oxide (GO) to incorporate additional functionality into the graphene sheets.

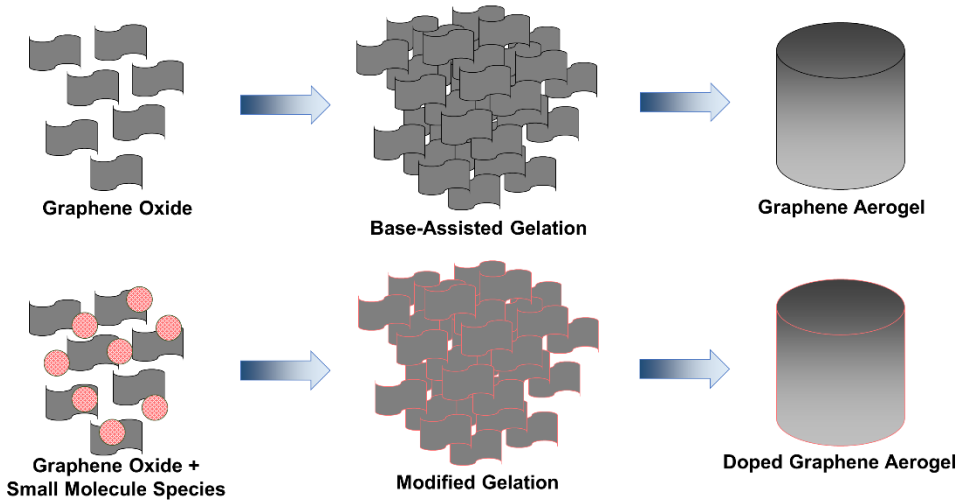

Figure 3.1 Schematic of small molecule incorporation for doped aerogels. Top: Standard gelation and assembly of graphene oxide nanosheets. Bottom: Gelation of graphene oxide nanosheets and accompanying small molecule species, resulting in additional cross-linking reaction chemistries.

3.2.1 Schiff Base Reaction for nitrogen doping

To ensure the small molecule added to the solution of GO will in fact incorporate itself into the graphitic network, we need to identify reaction mechanisms that will ultimately lead to the cross-linking between the functional groups on the GO and the groups present in the small molecule. **Figure 3.2** highlights one such reaction mechanism, known as a Schiff-base reaction, which demonstrates a remarkably reproducible method to cross-link nitrogen-containing functional groups to that of an oxygen-containing functional group.[73,79] This reaction process is very amenable to the standard fabrication of GA because of the solvent environment used in GA fabrication. In **Figure 3.2**, the first step of the reaction process is nucleophilic addition, where

the deprotonated amine group (nucleophile) attacks the electrophilic carbon from the oxygen-containing functional group. Ultimately, the oxygen functional group is removed via a dehydration in step 2, resulting in the covalent cross-linking of nitrogen to carbon.

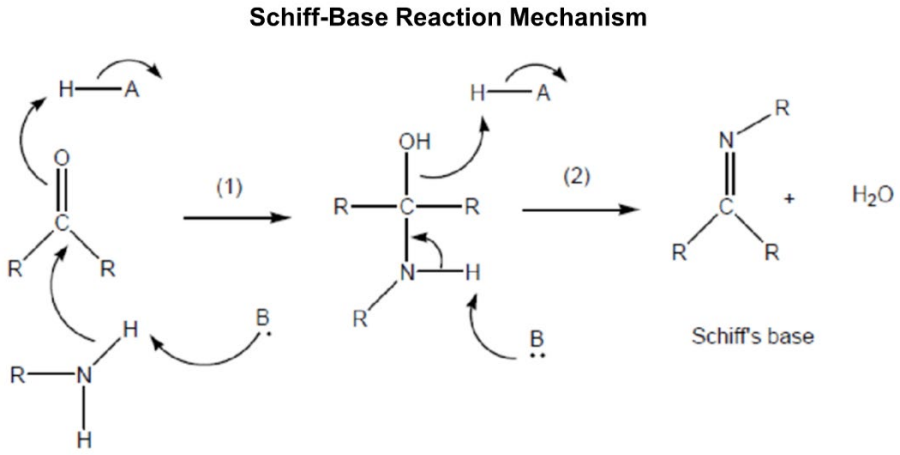

Figure 3.2 Schiff-Base reaction mechanism overview. Step (1): Nucleophilic addition. Step (2): Dehydration. Adapted from reference 79.

In the case of our modified GO gelation process, the oxygen functional groups will serve a dual purpose. They will provide the backbone of cross-linking necessary to gel the graphene sheets together and build the macrostructure needed, while also providing the electrophilic carbons due to the many oxygen containing functional groups, as shown in **Figure 3.3**. The amine (nucleophile) groups that will cross-link with the carbon atoms within the graphene sheets and provide a nitrogen source for N-doping come from the Pararosaniline Base (PAB) also shown in **Figure 3.3**.

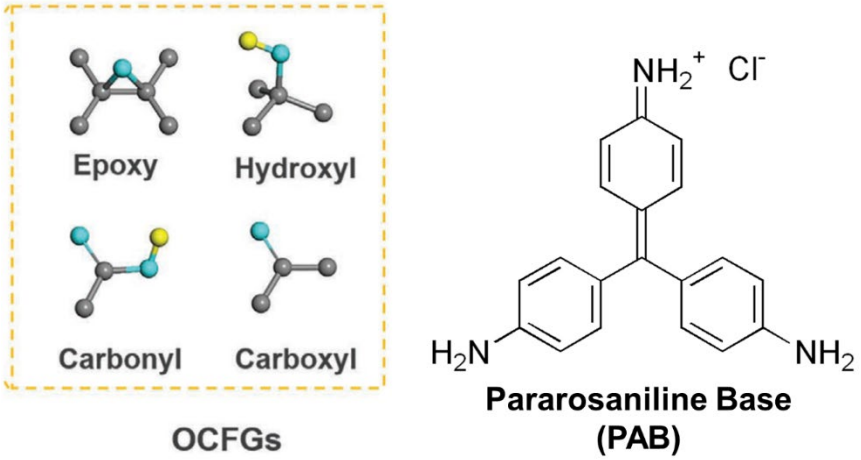

Figure 3.3 The Schiff Base precursors used in this study. The OCFGs on graphene oxide act as the carbonyl compound, while the pararosaniline base (PAB) acts as the aromatic amine. Adapted from reference 40.

The incorporation of PAB into the GO suspension is done at various mass ratio loadings to see how the addition of PAB could affect the gelation of the GO sheets. Too much PAB, and

the cross linking of the nitrogen with the graphene sheets could interfere with the cross linking of the GO sheets, destroying the macrostructure of the aerogel. Ultimately, the mass loading ratios we studied all led to nicely formed hydrogels that could be subsequently critically dried to obtain aerogels. **Figure 3.4** shows vials containing the standard GO suspension, which is very black in color, as well as different mass ratio loadings of the PAB molecule, which is a red dye and colors the suspension upon addition.

Figure 3.4 Reaction vials of standard graphene oxide suspension and PAB+GO suspensions. Far left: Standard GO suspensions. Right three: Varying mass ratios of PAB added to GO suspensions. Vials are 15 mm in diameter.

3.3 Structural characterization of the N-doped graphene aerogel

The structure of the N-doped GA is explored with scanning electron microscopy and FT-IR spectroscopy. Structural morphology imaging was obtained using scanning electron microscopy (FEI Sirion XL30, operated by myself and James Marquez). FT-IR spectroscopy is carried out on a Nicolet 6700 FT-IR Spectrometer. A comparison structure was needed for these studies to see how the incorporation of PAB could alter the structure or spectrum of bonding in FT-IR. **Figure 3.5** shows the control Schiff Base Aerogel (SBA) used in this study. Again, PAB was the amine nucleophile, while isophthalaldehyde was the carbonyl compound. The right-hand image is a scanning electron micrograph of the resulting SBA after gelation and drying of the reacted PAB and isophthalaldehyde.

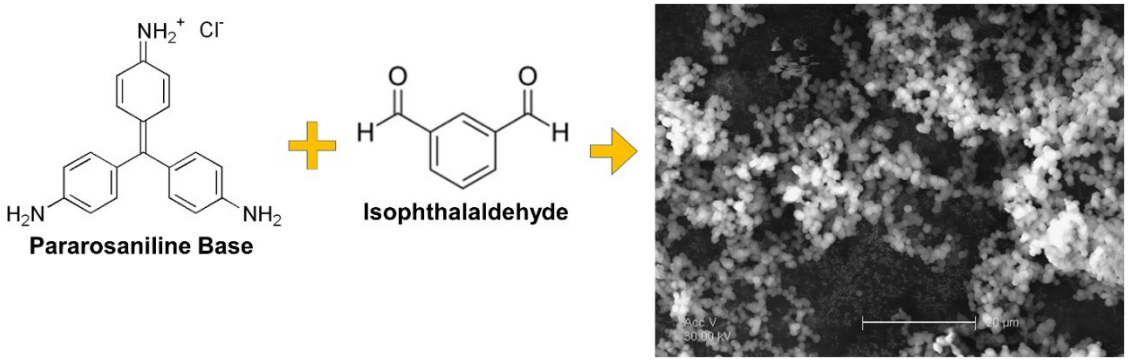

Figure 3.5 Control Schiff Base Aerogel. Left: Pararosaniline base (amine group) and Isophthalaldehyde (carbonyl group). Right: Scanning electron microscopy image of the gelled and dried aerogel. Scale bar measures 20 µm.

3.3.1 FT-IR spectroscopy control experiment

The first structural analysis we can explore is the type of cross-linking and bonding present in the aerogels formed. FT-IR spectroscopy provides information on the bonding present through vibrational frequencies of the parent material. **Figure 3.6** shows three FT-IR spectra for the SBA control, a standard GO-aerogel with no PAB addition, and the N-doped PAB-GO aerogel. There are several characteristic peaks associated with nitrogen bonding in organic systems that would be an excellent fingerprint to identify whether the nitrogen has successfully cross-linked with the GO sheets. Nitrogen-carbon sp^2 single bond vibrations fall within the 1000-1350 cm^{-1} region, while the nitrogen-hydrogen bond vibrations fall higher, between the 3100-3500 cm^{-1} region. Unfortunately, due to the high concentration of oxygen functional groups remaining within the graphitic structure, those wavenumber regions can be obscured by bonding from carbonyls, carboxyls, and hydroxyls, all three of which are prevalent within the GO structure.

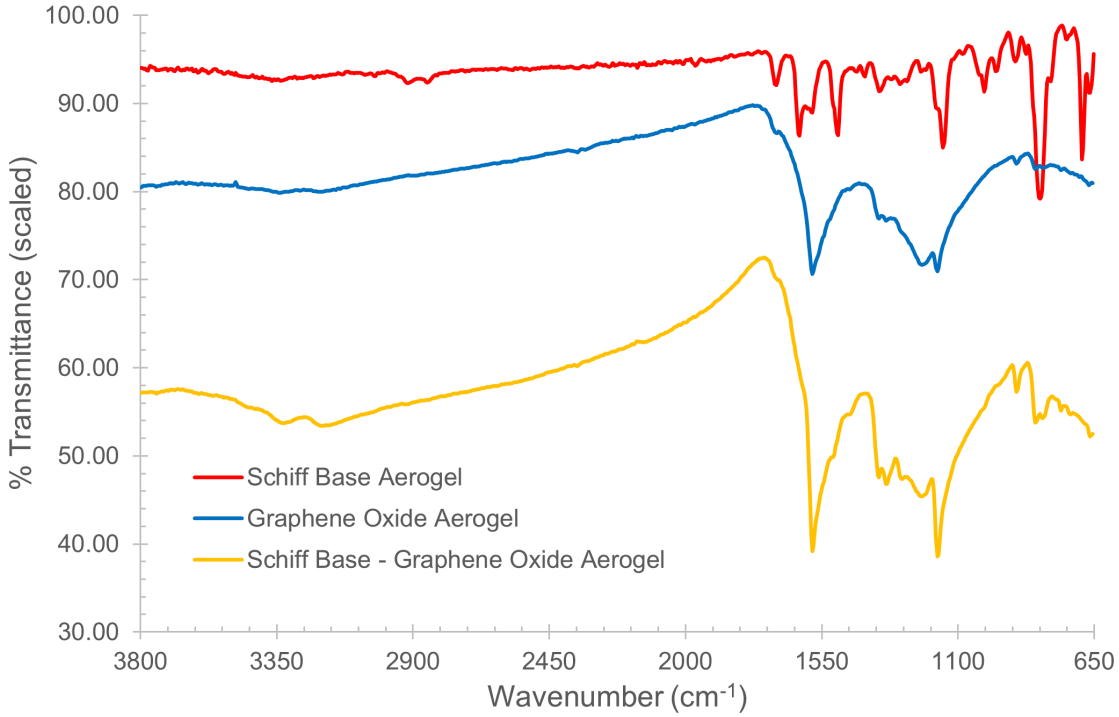

Figure 3.6 FT-IR spectra of three control experiments. Red curve: Schiff Base Aerogel control. Blue curve: GO aerogel control. Gold curve: PAB+GO aerogel.

As we can see from the three spectra shown in **Figure 3.6**, there are several key peaks in the SBA spectra that could help identify additional nitrogen bonding in the PAB-GO aerogel, however there are almost no differences between the PAB-GO aerogel and GO aerogel spectra. At this current time, there are too many functionalities within the aerogel materials to identify fingerprint regions in the FT-IR spectra. Coupled with the larger than normal background from the graphene backbone for the GO-based aerogels, the characteristic nitrogen peaks may be

harder than expected to identify. Therefore, the next section will explore other methods of characterizing the structure and bonding within the aerogels.

3.3.2 Surface structure of the N-doped graphene aerogel

While we saw successful gelation of the GO solution with the PAB molecule added, **Figure 3.5** shows how these Schiff Base systems can form more particle-like moieties when reacted. Therefore, we need to characterize the surface structure of the PAB-GO aerogel to ensure we do not see any additional structures other than the anticipated crinkled, porous interconnected sheets of graphene. **Figure 3.7** shows an SEM image of the PAB-GO aerogel. Within the structure, we only see the fluffy, connected sheets of graphene that we expect, with no clumping or particle-like formations observed. From a broad structural view of the aerogel, the PAB molecule did not interfere with the formation of the aerogel upon gelation. Therefore, we can turn to elemental compositional analysis to determine how much nitrogen is retained by the structure, and how the nitrogen is incorporated within the system. The PAB molecule could have cross-linked with the oxygen functional groups in the GO, but we need to analyze the bonding present to determine if the nitrogen present is within the graphene lattice as a dopant, or as an external functionalization of the graphene sheet.

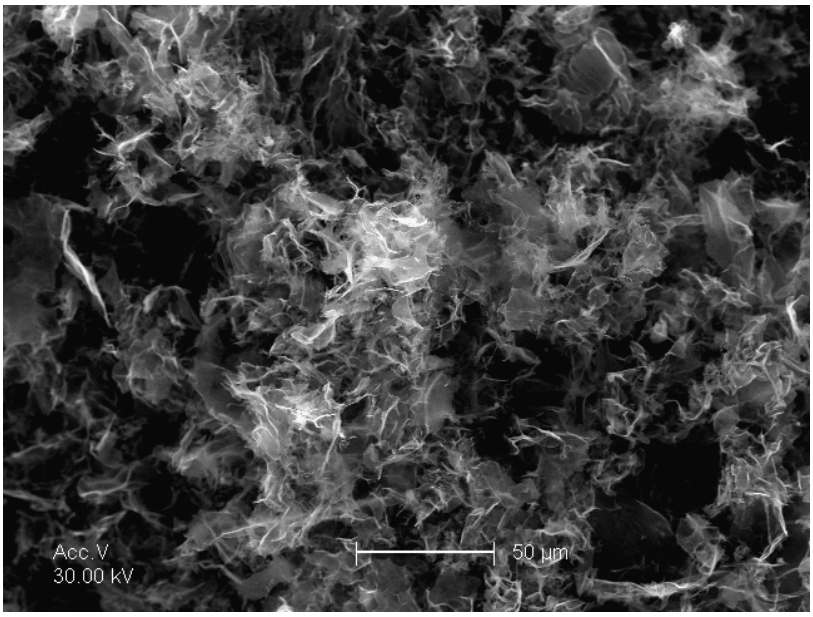

Figure 3.7 Scanning electron micrograph of the N-doped aerogel. Scale bar measures 50 µm.

3.4 Chemical analysis of the N-doped graphene aerogel

The chemical composition is verified via Energy Dispersive Spectroscopy (EDS) and X-Ray Photoelectron Spectroscopy (XPS). Chemical composition with electron microscopy was obtained via EDAX on an FEI Sirion XL30. Bonding information was obtained through XPS analyses performed with Al Kα, 200 µm spot, performed by Dr. Art Nelson at Lawrence Livermore National Laboratory.

3.4.1 Elemental composition

Initial analysis of the elemental composition of the N-doped GA can be done with EDS in the SEM. It is important to note here, however, that EDS is not necessarily the most appropriate measurement for quantification of the elemental composition, as our sample consists of purely light-Z elements, specifically nitrogen and carbon, which overlap in energies for EDS. However, we can use EDS as a first-order analysis and pursue additional spectroscopy techniques to probe the chemical makeup of the porous structure, as shown in later sections.

Figure 3.8 shows the EDS spectrum obtained from the PAB-GO aerogel studied previously with FT-IR and surface imaging, as shown in **Figures 3.6** and **3.7**. The EDS spectrum could be obtained simultaneously with imaging, and the corresponding region imaged and analyzed spectroscopically is shown in **Figure 3.8**. The main feature observed in the EDS spectrum is the carbon peak at 0.277 keV, labeled as such. There is a small peak to the right of the carbon peak which corresponds to remnant oxygen functionalities from the GO sheets. The lack of a nitrogen peak in the EDS spectrum does not immediately indicate no incorporation of nitrogen within the graphene sheets. The sensitivity of EDS is inversely related to the surface roughness of the sample scanned.[19] Graphene aerogels have incredibly high surface roughness, therefore sensitivity for minor species is drastically reduced. Furthermore, the lower energy resolution of EDS means the nitrogen and carbon peaks overlap, and the overall intensity of those peaks differs drastically for the same scan rate.[19] For example, the carbon peak shown in **Figure 3.8** is just shy of 13,000 counts for a specified dose and time of data collection. The same dose and time of data collection performed on h-BN may result in a nitrogen peak with intensity over 4-fold lower in intensity. Therefore, when examining structure that have both carbon and nitrogen, the nitrogen peak could be lost entirely, especially when it is a minority species.

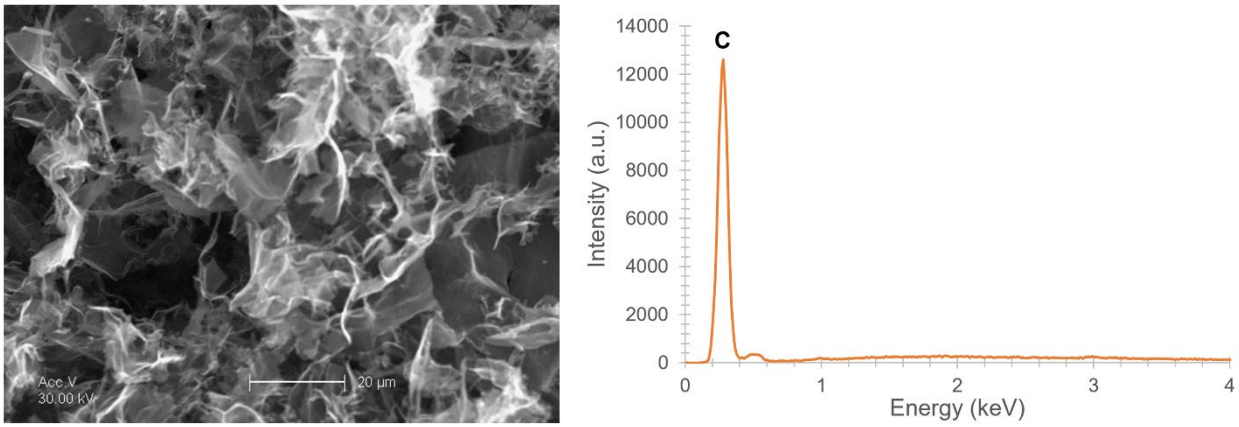

Figure 3.8 Scanning electron micrograph of the N-doped aerogel and associated energy dispersive spectroscopy spectrum. Scale bar measures 20 µm. Carbon peak is labeled in the EDS spectra, with a small, unmarked oxygen peak visible to the right.

3.4.2 Bonding characteristics

To determine the amount of nitrogen doped into the GA, as well as the type of doping acquired, we need a more sensitive measurement: XPS. **Figure 3.9** shows the survey spectra of the PAB-GO aerogel and the SBA for comparison. The spectra have been offset in the y-axis direction to display both simultaneously. Each spectrum is labeled with the specific sample

analyzed, and each peak is labeled in terms of which energy emission is observed (C1s for example). Higher resolution scans are shown in following figures, where we can see the specific type of bonding present in nitrogen. Both the PAB-GO aerogel and SBA aerogel were analyzed to see how the type of nitrogen bonding evolved between the two systems, and if there was more graphitic-type bonding in the PAB-GO aerogel sample. From the survey spectra shown in **Figure 3.9**, we see the presence of a strong N1s peak in both the PAB-GO aerogel sample and the SBA sample. Therefore, while we could not identify or confirm any nitrogen composition from EDS or FT-IR, there is indeed significant nitrogen incorporation from the addition of the PAB small molecules in the beginning of the synthetic process before gelation of the GO sheets.

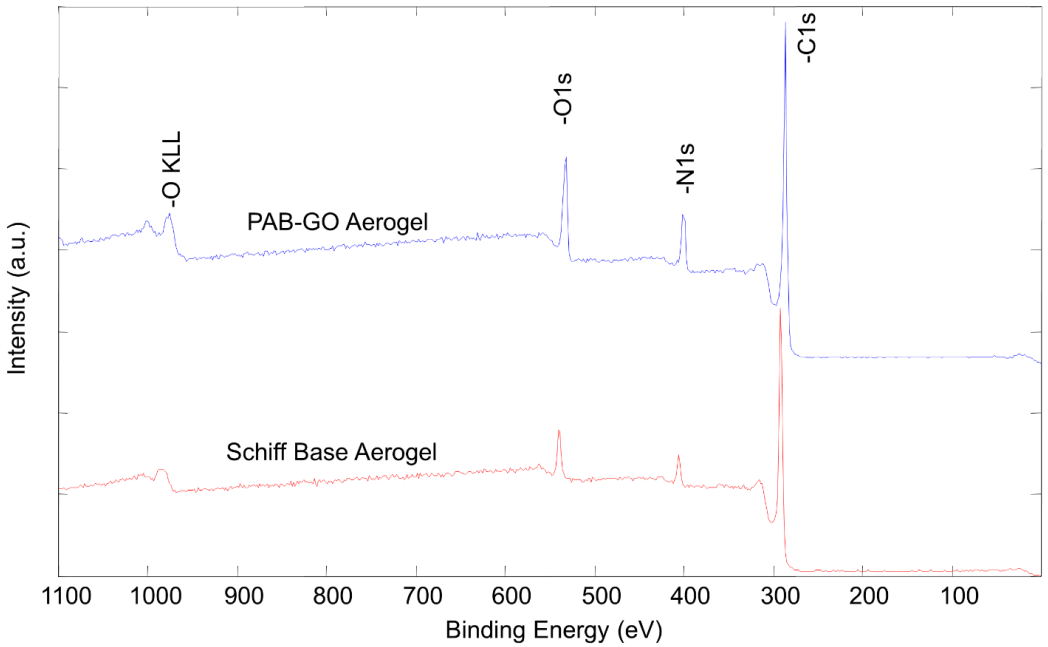

Figure 3.9 Survey X-Ray photoelectron spectra for the PAB -GO aerogel and Schiff Base Aerogel. Data collected in collaboration with Dr. Art Nelson.

With confirmation that nitrogen is in fact present somewhere within the structure of our PAB-GO aerogel, the next step is to determine the type of bonding present. For instance, these small molecules could remain adhered to the surface of the GO sheets or trapped within small pores through the gelation and drying process, which would lead to a false sense of N-doping. Therefore, we look at a higher resolution scan for our XPS spectrum to identify the bonding from nitrogen, shown in **Figure 3.10**.

Figure 3.10 shows the N1s spectra for the PAB-GO aerogel and SBA for comparison, with an inset of a graphene lattice schematic for the type of nitrogen bonding observed in the PAB-GO aerogel. For both the PAB-GO and SBA aerogel, the main type of nitrogen bonding is in the form of pyrrolic bonding, or 5-membered rings containing a nitrogen atom. That type of bonding within the graphene sheets could occur along the edge of the sheet, as shown in the schematic by the N label along the edge. While this type of bonding is not the traditional dopant we would expect within the 6-membered rings of graphene, even these edge sites would provide an interesting landscape for small molecules to interact with while being contained by the graphene sheets. Furthermore, there is a substantial peak corresponding to graphitic N-doping in the PAB-GO aerogel sample, significantly higher than that of the SBA. Therefore, while the

majority of nitrogen bonding for the PAB-GO aerogel within the sample is pyrollic in nature, there is a significant amount incorporated directly within the graphene lattice, which is exactly the type of N-doped GA that would enhance property measurements.

Table 3.1 lays out the atomic content of each species, namely carbon, nitrogen, and oxygen, in each type of sample. The composition results were slightly surprising in terms of which sample showed higher amounts of nitrogen. The SBA was expected to show higher amounts of nitrogen, because the entire structure is built of small molecules, with more opportunity for cross-linking of the amine groups to occur. However, the PAB-GO showed significantly more nitrogen incorporated (~9.4%) within the structure, as compared to roughly 5.9% in the SBA. When comparing other N-doped carbons, 9% doping is comparatively high. Most carbon systems achieve doping from <1% to 10%, with many systems leveling out at ~4% N-dopant levels.[77] The amount of nitrogen doped into the GA structure is expected to decrease slightly as we anneal the structure to remove the remaining oxygen functional groups, which contribute to about 10% of the atomic content.

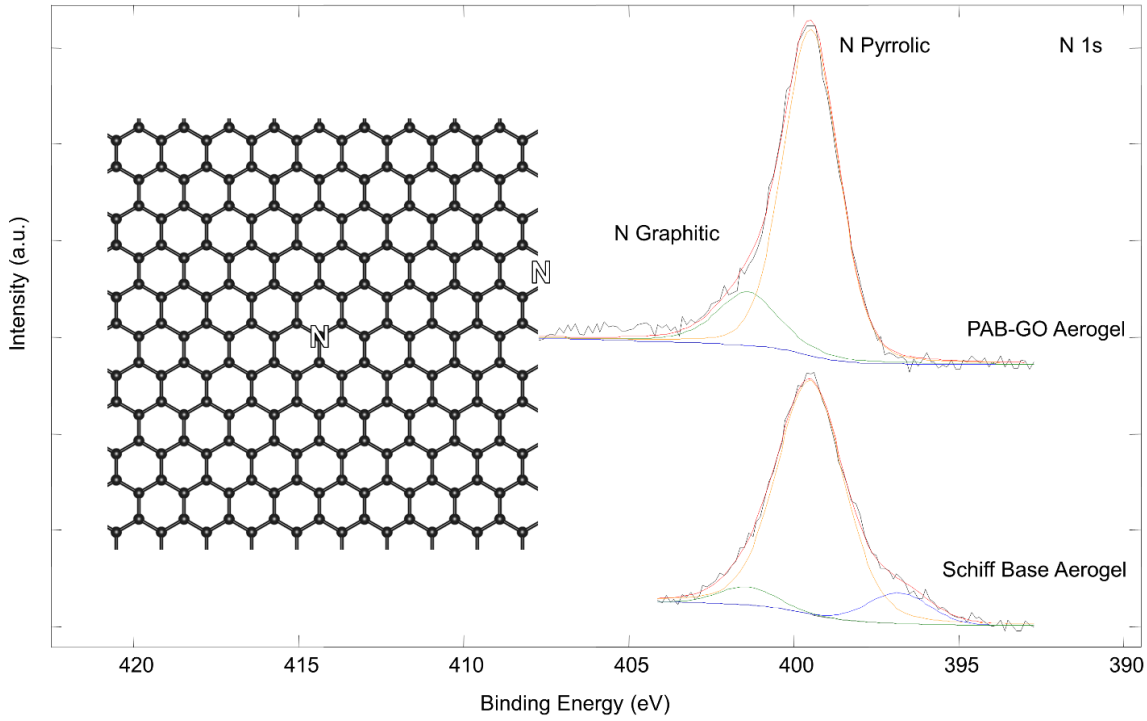

Figure 3.10 Nitrogen 1s XPS spectra for the PAB-GO aerogel and Schiff Base Aerogel. Inset in the spectra is a schematic of the two types of nitrogen bonding observed for the PAB-GO Aerogel. Data collected in collaboration with Dr. Art Nelson.

Table 3.1 Atomic percent of Carbon, Nitrogen, and Oxygen for the Schiff Base Aerogel and PAB-GO Aerogel. Amounts are reported in atomic percent. Data collected in collaboration with Dr. Art Nelson.

Sample	C (at.%)	N (at.%)	O (at.%)
Schiff Base Aerogel	86.60	5.83	7.57
PAB-GO Aerogel	79.87	9.37	10.76

3.5 Conclusion

This chapter discussed the benefits of doping graphitic systems, such as graphene aerogels, with atoms that can bond fully within the graphene lattice. Nitrogen presents itself as an interesting doping species, as the nitrogen site lowers the binding energy of small molecules to the surface of graphene, resulting in enhance performance for applications ranging from sensing to energy storage. We explore a reaction mechanism commonly used to produce Schiff Bases, which covalently cross-links nitrogen containing functional groups to a carbonyl compound through nucleophilic addition. The large amounts of oxygen present within graphene oxide sheets act as the carbonyl compound, while a pararosaniline base molecule, with three amine groups, provides the nitrogen content to dope the graphene sheets. After production of the PAB-GO aerogel, XPS measurements show that the nitrogen is in fact bonded within the graphene sheets comprising the aerogel, and we achieve comparatively large amounts of nitrogen doping, currently capping out around 9.4%.

Chapter 4: Approaching Porous Structures from the Top-Down – One-step Conversion of Graphite to Crinkled Boron Nitride Nanofoams for Hydrophobic Liquid Absorption

Special thank you to Dr. Thang Pham and James Marquez for their support on this project.

Key Words: Nanofoam, Hexagonal Boron Nitride, Oleophilic, Graphite, Surface Area, Electron Microscopy, Carbothermic Reduction, Crinkled Sheets

The previous chapter discussed methods in obtaining macroscopic, porous structures from the assembly and chemical cross-linking of nano-scale materials, such as graphene sheets and small molecules. While these 'bottom-up' approaches provide an excellent route for true customization of the fundamental building blocks of the overall macrostructure, the synthetic processes often contain many reaction steps. Even for the standard graphene aerogels presented in the introduction, there are many steps involved in obtaining the final product: creation of a suspension, catalytic gelling, solvent exchanges, critical point drying, and finally reduction to a graphitic system. Additional steps are required if any modifications or doping of the aerogel system are desired, further complicating the process. Generating larger amounts of samples without such time intensive processes could benefit from a top-down approach. Instead of carefully crafting the structure from the ground-up, we can utilize pre-existing macrostructures and induce large modifications to their morphology through chemical conversions. This chapter furthers our discussion and understanding of chemical conversion processes for top-down methods, to convert macrostructures (such as graphite) to some type of porous system with similar attributes to typical aerogels.

4.1 Motivation behind generating porous structures from macroscopic systems

Three-dimensional, porous, macroscopic structures such as aerogels and rigid foams have shown great efficacy in a wide range of applications, from energy storage, to gas sensing, to thermal management for heat transfer, to the absorption of oleophilic species in aqueous systems.[27,28,31,38,39,80] Interestingly, such open structures can be derived not only from conventional three-dimensional materials such as oxides, but also from low-dimensional building blocks, such as graphene, h-BN, and transition metal dichalcogenides.[26,56,81] The properties of the final structures are controlled not only by the inherent material properties of the building blocks, but also by the connectivity chemistry and geometry, which ultimately affect the porosity, surface area, and chemical and thermal stability of the aerogels and foams.[25,31,39,56]

We have discussed the impressive array of graphitic aerogels and activated carbon foams (all carbon-based) in previous sections, where the synthesis exploits well-known carbon chemistries.[25,81] Many of the synthetic approaches are of the "bottom-up" variety, where either small particles or molecules are functionalized and covalently bound together to form the macroscopic structure, such as the pararosaniline base aerogel we explored in **Chapter 3**.[24] For carbon, there is a veritable treasure trove of molecular precursors and synthetic routes to choose from, allowing for wide-ranging creativity in aerogel and nanofoam design.[31,34,40,68,77,82]

4.1.1 Exploiting structural similarities between graphene and h-BN

An exciting complement to carbon, h-BN has also been explored in various macrostructures. Indeed, h-BN aerogels and foams have been produced and they indicate impressive efficacy in chemical sensing, gas adsorption, atomic sequestering, and membrane composites.[37,38,83,84] Unfortunately, the diverse synthetic routes endemic to carbon do not typically carry over to h-BN systems, due to a reduced number of boron- and nitrogen-derived starting materials, and generally higher reaction activation barriers. Nevertheless, important contributions have been made in the functionalization of boron nitride nanosheets to allow for covalent crosslinking of the sheets to generate networks, as well as the direct synthesis of BN structures (such as foams) from molecular precursors of boron- and nitrogen-containing compounds.[37,38,84]

In order to bypass the need for molecular precursors, "top-down" synthetic methods, or conversions, can be pursued. Due to the structural similarity between graphene and h-BN, h-BN macrostructures, such as nanotubes, aerogels, activated powder, and foams, can be synthesized from a sacrificial carbon structure, provided that the carbon is pre-formed precisely into the desired final structural geometry.[39,56,60,84,85] However, following such a delicate "two step" process can be extremely time- and energy-intensive, especially for aerogels and similar porous graphite structures that require multi-step synthetic processes.

In this chapter, I present a robust, scalable, and facile approach to "leapfrog" the two-step conversion process from a graphitic to h-BN structure. This is accomplished through a one-step conversion method to generate crinkled h-BN nanofoam quickly and directly from raw graphite, as highlighted in **Figure 4.1**. The single-step synthetic approach utilizes the simultaneous carbothermic reduction and nitrogenization of boron oxide powder, with graphite fragments acting as both a source of carbon for the reduction process and instantly a rough template for the growth of the final h-BN product. High-resolution transmission electron microscopy and electron diffraction demonstrate that the final converted h-BN nanofoam is crystalline at the atomic scale but has substantial crinkling of the h-BN sheets at the nanoscale. An overall porous, foam-like macrostructure is produced that is very amenable to oil absorption due to the drastic increase in surface area from the original starting graphitic material. The operative conversion mechanism from flat carbon precursors to crinkled boron nitride sheets is proposed. Crinkled h-BN nanofoam shows a surface area over 60 times larger as compared to the graphitic scaffold, leading to improved oil absorption capabilities (up to 325 wt%).

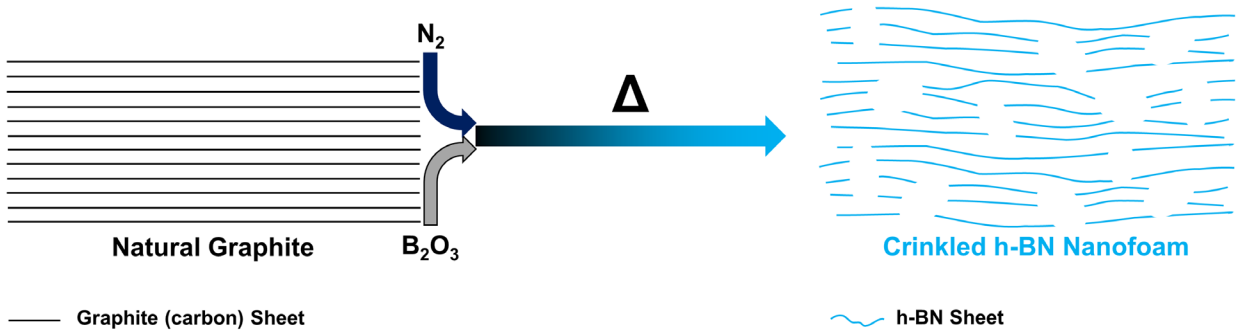

Figure 4.1 Schematic of single-step 'leapfrog' synthesis of crinkled h-BN nanofoam from natural graphite.

4.2 Carbothermic reduction synthesis protocol

The high-temperature carbothermic-reduction synthesis method for crinkled h-BN nanofoam uses components of a synthesis method for BN aerogels, as reported elsewhere.[39,56] Briefly, a pure and un-restructured graphite precursor is placed together with boron oxide in a custom machined graphite crucible and heated to between 1650-1850 °C in an induction furnace under a pure nitrogen gas flow. The synthesis of the converted nanofoams was carried out by Dr. Thang Pham, James Marquez, and myself, with assistance from Dr. Hu Long to develop the "time" experiment to observe partial conversion.

Several different graphite precursors are examined with different domain sizes and crystallinity, namely highly ordered pyrolytic graphite (HOPG), Kish graphite, few-micron-sized graphite flake powder, and centimeter-sized graphite fragments. Typically, up to 0.5 grams of graphite is loaded in the graphite crucible, together with excess boron oxide, usually 5-10 grams depending on the amount of graphite material being converted. Nitrogen gas is flowed through the system at 1500 sccm, and total reaction time is 45-60 minutes to ensure a complete conversion. The converted h-BN nanofoam obtained from the different graphite precursors all show comparable results, so for simplicity and consistency, all data presented in this report are obtained from the conversion of naturally occurring graphite fragment powder (Alfa Aesar, Graphite flake, 325 mesh, 99.8% (metal basis)), with a "time" exploration experiment utilizing larger naturally occurring graphite fragments (NGS Naturgraphit, Graphenium Flakes, size 5-10mm).

4.3 Characterizing the crinkled h-BN nanofoams

The atomic structure of the crinkled h-BN nanofoams is explored with electron microscopy, while the chemical composition is verified via Raman spectroscopy and Electron Energy Loss Spectroscopy (EELS). Raman spectroscopy was performed by Dr. Thang Pham and myself using a Renishaw inVia spectrometer with 514 nm laser excitation. Structural morphology and atomic imaging were obtained using scanning electron microscopy (FEI Sirion XL30, operated by myself), and transmission electron microscopy (JEOL JEM 2010, and aberration-corrected TEAM 0.5, both operated at 80 kV, operated by Dr. Thang Pham, Dr. Matt Gilbert, and myself), respectively. Nitrogen porosimetry, for analysis of surface area and

porosimetry, was carried out by Dr. Marcus Worsley. The analysis was carried out via the Brunauer–Emmett–Teller (BET) method using an ASAP 2020 surface area analyzer (Micromeritics Instrument Corporation).

4.4 Retaining overall macroscale shape after conversion to h-BN

The 'leapfrog' conversion of graphite to crinkled, h-BN nanofoam, achieved through high temperature carbothermic reduction of graphite and boron oxide, is highlighted in **Figure 4.2**. As illustrated, the overall dimensions of the graphite fragment are retained following conversion (**Figures 4.2a** and **4.2b**), but there is a striking change in color upon conversion, from black to white, indicative of a dramatic chemical modification and a change in the electronic band structure of the material. **Figure 4.2c** shows, for the converted material, the unique Raman signature of the E_{2g} in-plane vibrational mode of sp^2-bonded h-BN, at 1367 cm^{-1}.[39] No other peak is observed, consistent with a complete chemical conversion from graphite to h-BN. The resulting h-BN nanofoam expands because of the difference in morphology from the starting graphite material, and it is qualitatively much more compressible than the parent graphite. Small deformations appear to be reversible, but large deformations lead to a fracturing of the material, not unlike some graphene-based aerogel materials.[32]

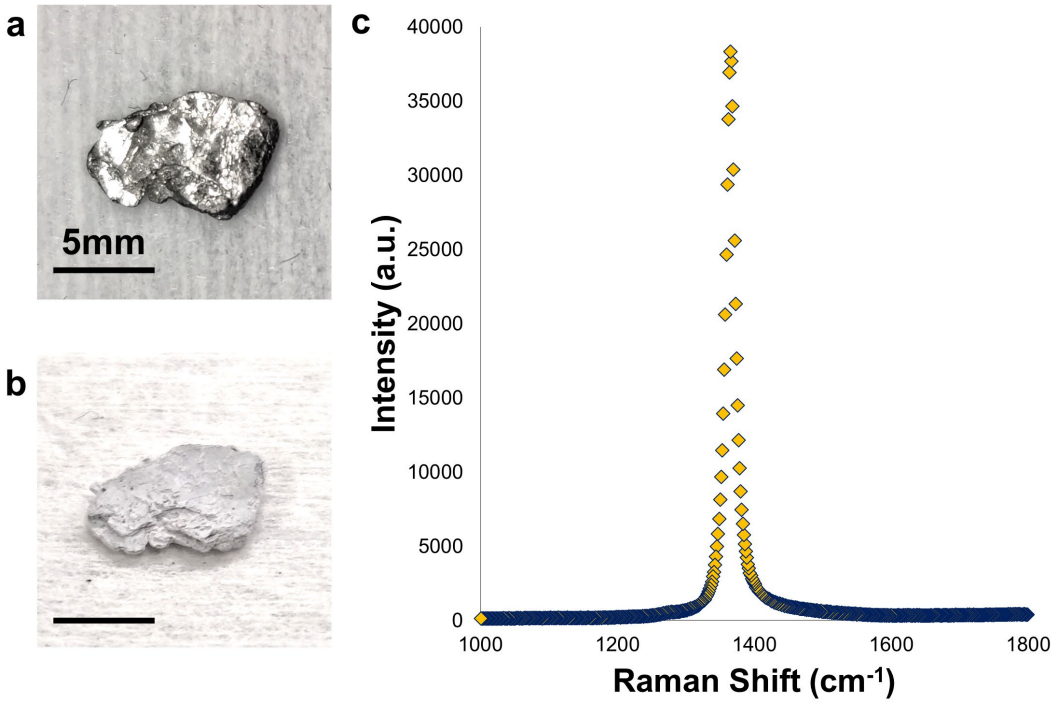

Figure 4.2 Conversion of graphite fragment to crinkled h-BN nanofoam. Prior to the conversion reaction (a), the graphite fragment is shiny black. After conversion (b), the fragment retains its overall geometry, but changes color to bright white. Scale bars in (a) and (b) measure 5mm. (c) Raman spectrum of the converted h-BN fragment, with a peak at 1367 cm^{-1} corresponding to the E_{2g} in-plane vibrational mode of sp^2-bonded BN. Data collected in collaboration with Dr. Thang Pham.

4.5 Drastic morphology changes on the nanometer-size scale

The structure of the converted material is examined using secondary electron microscopy (SEM), where the conversion from flat graphite to a crinkled h-BN nanofoam can be readily seen. The scale of the folds, crinkles, and curvature of the sheets is examined in more detail in **Figure 4.3**, where SEM images are compared at different magnifications of the starting graphite fragment to those obtained (at identical magnification) for the converted crinkled h-BN nanofoam.

Figure 4.3a shows the macroscopic view of a graphite flake, where several wrinkles in the sheet are readily observed (they appear as bright lines). These wrinkles are anywhere from 20 to 100 microns in length and separated by tens of microns. At higher magnification, seen in **Figures 4.3b** and **4.3c**, at the 2 micron and 500 nm size scale, regions between the global wrinkles are easily found, and no additional interesting features are observed in graphite. **Figure 4.3d** shows a macroscopic view of the h-BN nanofoam, where similar wrinkles (again appearing as bright lines) ranging from 20 to 100 microns in length are observed, similar to the graphite precursor. However, in sharp contrast, **Figures 4.3e** and **4.3f** shows that for the converted h-BN material, the apparently flat morphology at the 20-micron scale, is actually composed of a highly porous nanofoam structure at the 2-micron and 500-nm size scale. At the higher magnification, we see that the character of the h-BN sheets is actually of a porous, foam-like nature, with characteristic pores and linkers on the order of 500 nm to 1 micron in length. This new porous morphology covers the entire surface of the h-BN nanofoam. We refer to the overall surface of the h-BN as crinkled to delineate between a specific isolated large-scale wrinkle in the material and the overall surface morphology of the nanofoam. The pores vary somewhat in size, but are typically 500 nm across, as shown in **Figure 4.3f**, with high areas of curvature surrounding the pores, leading to the crinkled effect.

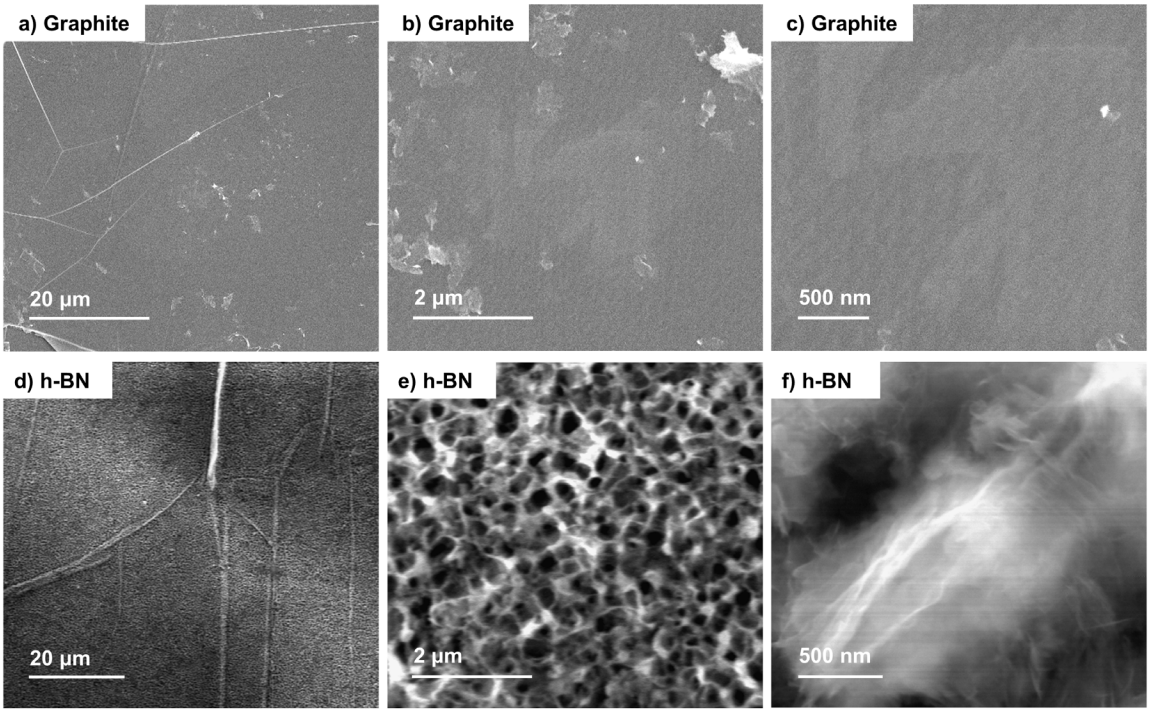

Figure 4.3 Scanning electron microscopy images of different size-scales for the native graphite flake and resulting crinkled h-BN nanofoam. SEM images of (a-c) a graphite fragment and (d-f) converted h-BN. The macroscopic morphology of the graphite fragment (a) is maintained in the converted BN (d), where the surface overall is very flat in nature, and even large macroscopic edges and wrinkles can be observed in both (a) and (d). The flat, pristine nature of the layers in the unconverted graphite fragment is maintained at high magnification, as shown in (b) and (c). (e) A higher magnification image highlighting the spongey, foam-like nature of the converted h-BN. (f) High magnification SEM image of the h-BN where the crinkled nature of the h-BN sheets is readily visible. Data collected in collaboration with Dr. Thang Pham.

In contrast to the more conventional carbon-to-h-BN templating conversion process, the simplified one-step conversion method presented here apparently completely leapfrogs the need for first preparing a porous carbon intermediary. In most previous carbon-to-boron-nitride conversions, such as C-to-BN nanotubes, C-to-BN aerogels, and C-to-BN activated powder, both the macroscopic *and* nanoscopic structures of the carbon precursors are maintained in the corresponding BN products.[39,56,60,85] Hence, the carbon-based starting material must first be configured into the desired "end form". Here, the converted h-BN has a similar *macroscopic* structure as the starting graphite (i.e. layered 'sheets' of material) but displays drastically different *nanoscopic* structure (i.e. crinkled nanofoam). In discussion below, we examine the likelihood that a nanoporous carbon intermediate structure is involved but is "automatically" locally formed within the graphite and then quickly templated and converted to crinkled nanoporous h-BN foam.

4.6 Resultant properties of the crinkled h-BN nanofoam

In addition to the change in structure from conversion of graphite to h-BN nanofoam, we are also interested in how the properties of the resulting crinkled nanofoam differ from the graphitic precursor. Native graphite has an incredibly low surface areas of roughly 0.6 m^2/g, and is moderately hydrophilic in nature.[86,87] We find that the crinkled nature of the h-BN nanofoam presented in this study exhibits surface areas of 41.2 ± 0.8 m^2/g, an increase in surface area over 60 times from the graphitic precursor. The surface area of this single-step converted, crinkled h-BN nanofoam is well within the desired range of other h-BN foams (30 to 130 m^2/g), and substantially higher than carbon-based nanofoams from other commonly used carbon precursors (0.16 to 3.3 m^2/g), all without requiring an involved, multi-step synthesis process.[37,57,88] Along with a drastic increase in surface area, the crinkled h-BN nanofoams are more hydrophobic than graphite, allowing for improved oil absorption capabilities. We find oil absorption rates up to 325 wt%, twice as efficient as other commonly used activated carbon alternatives.[39,80]

4.7 Study of the overall crystallinity of the crinkled sheets

The crystallinity and chemical makeup of the crinkled h-BN sheets forming the nanofoam are examined further using transmission electron microscopy (TEM). **Figure 4.4** shows typical TEM images of graphite sheets before conversion and h-BN sheets after conversion, using the one-step conversion process. **Figure 4.4a** shows a TEM image of the starting graphite sample (mechanically exfoliated to facilitate TEM imaging); it displays the well-known flat graphene structure. The corresponding selected area electron diffraction (SA-ED, **Figure 4.4a** inset) shows that the few-layer graphene sheets are single crystal, evidenced by a unique set of six bright spots representing graphene's hexagonal lattice. The atomic morphology of the converted h-BN sheets is shown in **Figures 4.4b-d**. Here, although sheet-like structure is clearly still evident, the sheets are no longer flat but possess various degrees of crinkling. The SA-ED inset in **Figure 4.4b** correspondingly exhibits many sets of spots with six-fold symmetry, indicating atomic crystallinity but with changing of stacking sequences and rotation of the sheets due to the severity of the crinkling.

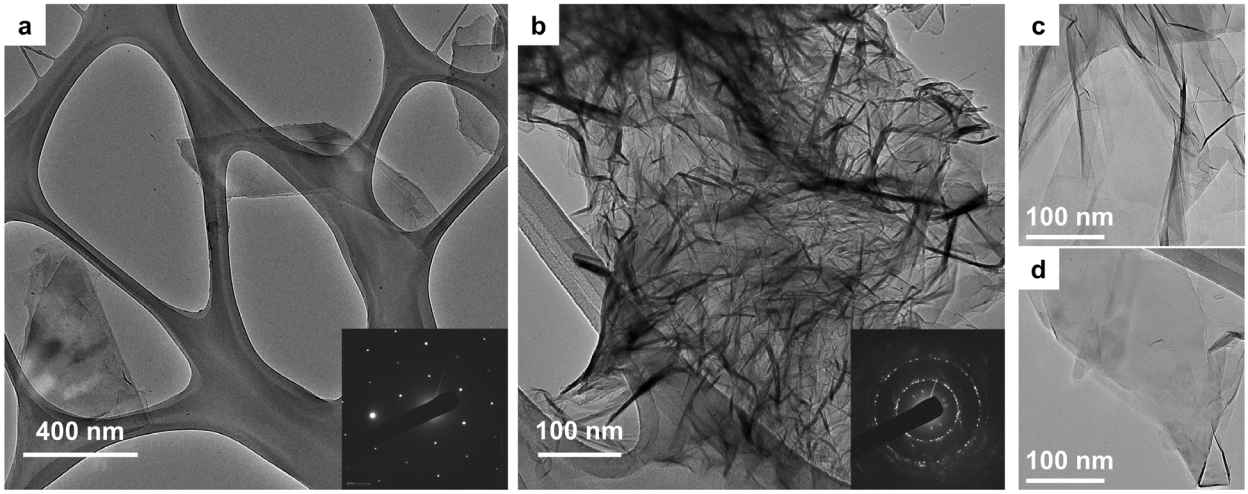

Figure 4.4 Transmission electron microscopy images of sheets of the starting graphene material and resultant crinkled h-BN sheets. (a) HR-TEM image of flat and well-stacked graphene sheets. (Inset) Corresponding SA-ED pattern showing a unique set of six-spots, indicating single crystal graphene sheets. (b) HR-TEM image of crinkled, few-layered h-BN from the converted nanofoam. (Inset) Corresponding SA-ED pattern showing several sets of six-spot patterns, indicating rotational and translational stacking in the layered, crinkled sheets. Additional HR-TEM images highlighting (c) mildly crinkled h-BN sheets and (d) almost perfectly flat h-BN sheets from the same h-BN nanofoam sample.

At the size scale shown in **Figure 4.4**, sheets from the h-BN nanofoam may exhibit different degrees of curvature in their crinkling. Some regions have very high curvature (**Figure 4.4b**), medium curvature (**Figure 4.4c**) and almost no curvature (**Figure 4.4d**). However, the overall morphology of the crinkled h-BN nanofoam is uniform in distribution of these various degrees of crinkling. A crinkled piece of paper would exhibit similar differences in morphology at small size scales, where the crinkling of the paper is globally uniformly distributed across the surface, but regions of almost perfectly flat surface will be found between regions of extremely high curvature.

4.7.1 The atomic scale and elemental analysis of the crinkled sheets

We then employ aberration-corrected (AC)-TEM and electron energy loss spectroscopy (EELS) to probe in greater detail the crystallinity and chemical purity of the converted h-BN material. Results are shown in **Figure 4.5**. AC-TEM imaging (**Figure 4.5a**) clearly shows the hexagonal lattice in the sheets of the converted h-BN nanofoam. At the edge of the sheets, where there are approximately three layers of hexagonal BN, the layers stack perfectly in the conventional AA' order, evidenced by the well-aligned hexagons of B and N atoms, with N-terminated zig-zag edges.[89] We also observe the signature triangular electron-induced defects commonly seen in h-BN during electron microscopy imaging.[51] Interestingly, moving towards the center of the sample (towards the top right corner of the AC-TEM image) several Moiré patterns are observable, indicative of the changing of stacking sequences, either by a translational or rotational shifting of the top sheets with respect to the bottom ones.[89,90] The

change in stacking sequence is a result of the crinkling observed in the h-BN sheets. The corresponding EELS spectrum (**Figure 4.5b**) shows that the converted h-BN sheets contain only B and N atoms, with an atomic ratio of 1B:1N. There is no C edge found in the spectrum, confirming the chemical purity of the sample. These studied confirm the complete conversion from crystalline, flat graphite fragment to atomically crystalline, crinkled h-BN nanofoam.

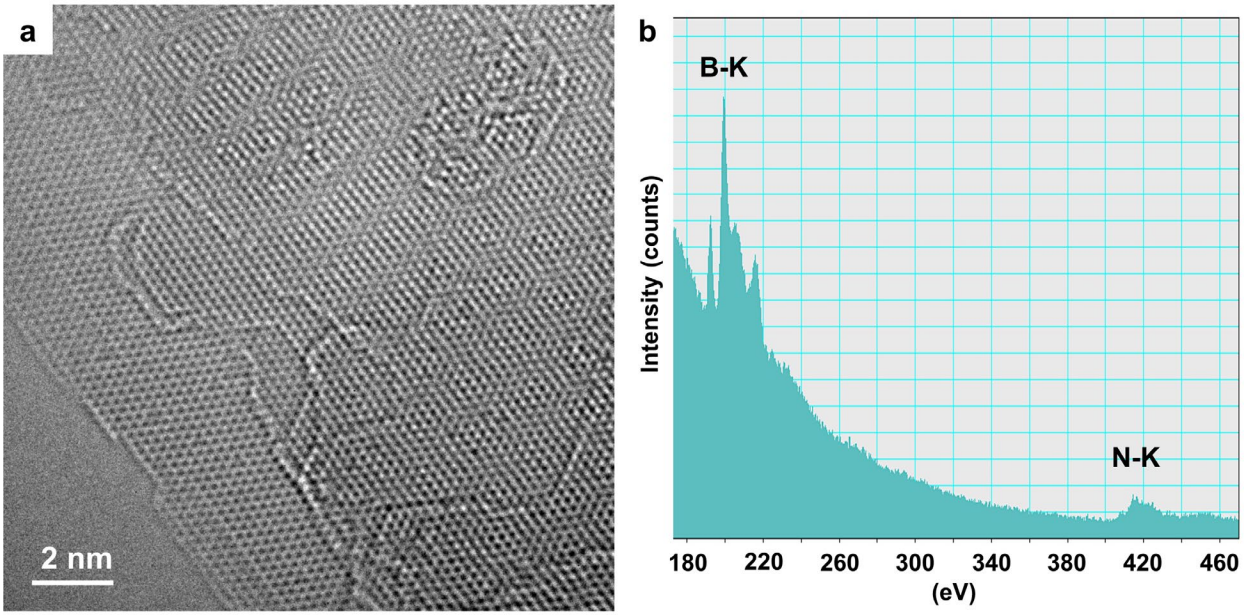

Figure 4.5 Electron microscopy images obtained from the TEAM 0.5 microscope of crinkled nanosheets. (a) Aberration-corrected atomic-resolution TEM image of converted few-layer h-BN taken from the crinkled nanofoam, showing a single-layered edge and triangular defects, as well as a Moiré pattern in the few-layered region. (b) Elemental composition confirmed by corresponding EELS spectrum displaying K-edges of boron (B) and nitrogen (N). The extracted atomic ratio is 1B:1N. Data collected in collaboration with Dr. Matt Gilbert.

4.8 Uncovering the conversion mechanism from graphite to crinkled h-BN nanofoams

We now examine the formation mechanism of the crinkled h-BN nanofoam. As mentioned previously, in conventional carbon templating the bulk and nanoscale structural morphology of the parent carbon-based material is maintained in the final BN product. This follows naturally from the isoelectronic hexagonal structure of graphene and h-BN, and the near-identical lattice parameters. An interesting question is what reaction path is followed in the present one-step conversion process, where the morphology is clearly dramatically altered, at least at the nanoscale.

In general, a carbothermic reduction starts with the reduction of an oxide, in this case boron oxide, by carbon atoms from a carbon source, in this case graphite. During the reduction process, nitrogenization of the products can be simultaneously incorporated to produce a final BN product. While the graphite flakes and boron oxide are solid reagents, the B_2O_3 vaporizes and becomes a gaseous reagent alongside the N_2 during heating. The carbothermic reduction and nitrogenization occurs at the atomic sites of the carbon source, which generally means the carbon

source is gradually replaced by BN. In the case of this experiment, the carbon source is the hexagonal carbon lattice of graphite, which is gradually replaced with an h-BN lattice:[58]

$$\frac{3}{2}C(s) + B_2O_3(g) + N_2(g) \xrightarrow{\Delta} 2BN(s) + \frac{3}{2}CO_2(g) \qquad \textbf{(Eq. 4.1)}$$

The reaction described in **(Eq. 4.1)** likely preferentially starts at defect sites in the carbon materials, such as surface functional groups, wrinkles, grain boundaries, vacancies, and edge atoms, where there is weaker bonding compared to the flat surface of a pristine sheet of sp^2-bonded carbon atoms.[59,60] For many previously studied carbon materials, such as carbon nanotubes or graphene aerogels, the material is comprised of micron- or nano-sized features with a large active surface area, containing many pathways for the boron- and nitrogen-containing gaseous species to approach the graphitic structure and react.[56] In contrast, for thick high-quality graphite fragments many hundreds of microns in size, the only accessible sites for the incoming gaseous reactant is the undersaturated bonds on the carbon atoms at edges or the relatively rare wrinkles in the sheets of the graphite layers. We hypothesize that, as a result, the conversion reaction preferentially starts from the edges of the graphite layers, and to some extent the top and bottom surfaces of the layers as well, and proceeds inwards from there.[58]

The crinkling of the layers occurs throughout the conversion process, as the final product (h-BN) and any intermediate products have different thermal expansion coefficients and lattice mismatches compared to the supporting graphite layers.[91–93] As mentioned, the graphite flakes are comprised of many layers of micron-sized graphene sheets densely stacked together, resulting in step-wise conversion from outside-in. As a result, at elevated reacting temperatures, the expansion mismatch between the lattice of graphene vs. h-BN and any intermediates in a densely packed and micron-sized system would induce buckling and crinkling of the sheets. The pores of the h-BN nanofoam are created as the sheets crinkle during the conversion process. Because the pores are formed by the sheets crinkling, which is controlled by the difference in thermal expansion of the graphene layers, h-BN layers, and any intermediates, the pore size is relatively fixed and provides consistency between the samples synthesized and analyzed.

4.8.1 Studying partial conversion of the h-BN nanofoams

In order to test this hypothesis and to better understand how the conversion process migrates through the graphite layers, a related conversion experiment is performed on a relatively large graphite fragment ~1cm in size. The larger graphite fragment is intentionally only partially converted to h-BN by limiting the boron oxide present in the system and reducing the reaction time. The partially converted sample is then cleaved to identify regions of different degrees of conversion, with regions near the center of the sample showing the lowest degree of conversion and regions near the edges showing the highest degree of conversion.

We note that large samples such as this can be completely converted through the entirety of the flake, but the diffusion of the gaseous reagents is the time-limiting factor. If standard diffusion of the gaseous reagents is assumed, then the time the conversion takes scales (assuming standard diffusion theory) as the square of the size of the sample. So, as an example, if the 5 mm sample of **Figure 4.2** is converted in one hour, a 10 mm sample (such as the one in **Figure 4.6**) would take 4 hours for complete conversion. If this leapfrog conversion technique were applied

to a 50 mm sample, the overall reaction time might take up to 100 hours. We see no evidence that long processing times degrade already converted material (say at the outer surface of the specimen, where conversion first occurs). On the other hand, the h-BN nanofoam expands throughout the conversion process, further aiding the diffusion of the gaseous reagents to penetrate the sample, thus speeding up the conversion process. In our current experimental setup reaction times can be long, but the limited availability of boron oxide would prevent full conversion of very large samples. Of course, the experimental setup could be reconfigured to a flow-type system, where boron oxide could be heated separately from the graphite flake, and subsequently flowed in, which would present itself as a more ideal system for large-scale conversion.

Figure 4.6 presents results from the conversion progression experiment. **Figure 4.6a** is an optical microscope image of the large, partially converted graphite fragment. After cleaving, the fragment retains its white edges, suggestive of complete conversion to h-BN, while the center is black, suggestive of unconverted graphite. Off-center regions are gray, suggestive of a carbon-boron-nitride mixture. **Figures 4.6b-e** show SEM images for material taken from different regions of the sample, with **Figure 4.6b** taken from the center region and **4.6e** from the edge region. **Figures 4.6c** and **4.6d** are for intermediate regions. The upper halves of **Figures 4.6b-e** are illustrative schematics of the nanoscale structure of the corresponding regions, with black representing carbon-based material and blue representing BN-based material. The letters C, CBN, and BN stand for carbon, carbon-boron-nitride mixture, and pure boron nitride, respectively. In a sense, the progression from **Figure 4.6b** to **4.6e** represents a time progression of the reaction from ‘start’ to ‘end’, hence our addition of a “time” arrow in the figure, whose color gradually changes from black to blue.

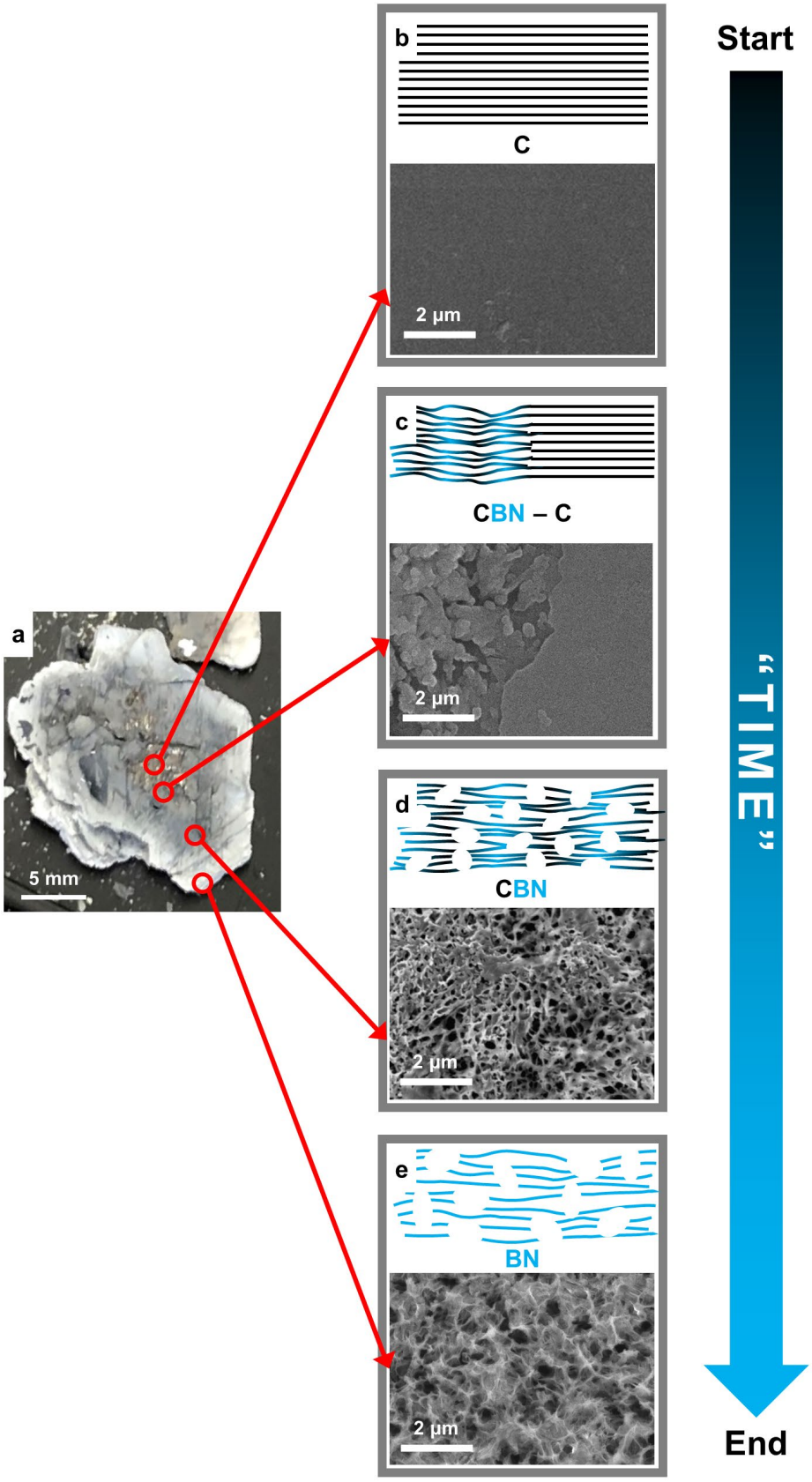
a
5 mm
b
C
2 µm
c
CBN – C
2 µm
d
CBN
2 µm
e
BN
2 µm
Start
"TIME"
End

Figure 4.6 Bulk graphite to crinkled h-BN nanofoam reaction progression. The conversion of a single large graphite fragment is interrupted midstream such that only the outer surface of the fragment is fully converted, while further in the sample is partially converted, and, at the very core, still pristine and unconverted. Materials taken from different regions thus present a "time" series of the conversion reaction. (a) Optical photograph of the bulk fragment. (b) - (e) SEM images for material taken from the core (b), mid-regions (c and d), and outer edge (e). Schematics above each SEM image represent the nanostructure and chemical composition, ranging from flat planes of pure carbon graphite in (b) to fully converted, high-porosity crinkled sheets of h-BN nanofoam in (e); they suggest a likely conversion pathway (see main text). Black color in the schematics represents carbon, while blue represents BN. The letters C, CBN, and BN represent pure carbon, a carbon-boron-nitride mixture, and pure boron nitride, respectively.

The conversion process produces intermediate CBN material, with different atomic ratios throughout the sample, depending on progression of the reaction. The largely unconverted graphite material of **Figure 4.6b** is smooth and featureless with well-ordered carbon-based parallel planes. The beginnings of h-BN conversion are seen in the intermediate structure of **Figure 4.6c**, where a boundary exists between the graphitic carbon and crinkled BN. Macroscopically, the material now appears gray. **Figure 4.6d** represents further progression into the conversion reaction. The material continues to appear gray, but the conversion of the sheets to crinkled h-BN has progressed, and numerous nanoscale pores have appeared. The material resembles a foam. For the fully converted material, **Figure 4.6e**, the product consists of crinkled, pure h-BN nanofoam, strikingly white in color. These observations reinforce an outside-in conversion mechanism and pathway, where the graphite is converted at an extremely local level to crinkled h-BN nanofoam.

4.9 Conclusion

In this study, we introduced a 'leapfrog' conversion method as a single-step, cost-effective, and scalable method of preparing crinkled h-BN nanofoam for oil absorption via the carbothermic reduction and nitrogenization of boron oxide and graphite. The crinkled h-BN nanofoam maintains some aspects of the macroscopic properties of the precursor graphite, namely a sheet-like surface of large domains with wrinkles and edges. But, critically, the surface exhibits a dense network of pores on the nanometer size-scale, reflecting pure h-BN nanofoam, and results in a significantly higher surface area for the nanofoam as compared to the graphitic starting species. The crystallinity and chemical makeup of the h-BN nanofoam is confirmed by AC-TEM and EELS. A conversion pathway is presented for flat graphite sheets to crinkled-sheet h-BN nanofoam. The resultant h-BN nanofoams find significant improvement in the absorption of oil as compared to other activated carbon species, and the increased surface area could find use in other applications, such as chemical sensing, gas storage/capture, and membrane composites.

Chapter 5: Porous Ceramics – An Extension of the Carbothermic Reduction of Macrostructure Carbon Precursors

Special thank you to Dr. Marcus Worsley and Dr. Art Nelson for their support on this project.

Keywords: Boron Carbide, Porous, Ceramic, Scanning Electron Microscopy, Energy Dispersive Spectroscopy, X-Ray Photoemission Spectroscopy, Raman, Carbothermic Reduction

The previous chapter explored the creation of nanofoams through conversion methods, which exhibit much higher surface areas than the precursors from which they are made. The h-BN nanofoams explored also exhibited properties similar to aerogels, such as excellent oil absorption based on the hydrophobic nature of the comprising h-BN sheets. While the manipulation of h-BN itself is more complicated than graphene under certain conditions, obtaining h-BN nanofoams from the conversion of carbon precursors allows us to customize the nanofoam through the carbon starting material. For example, the macroscopic structure of the nanofoam, such as overall size and shape of the foam, can be designed into the material from the starting graphitic material. The concept of converting graphite in a top-down manner to a similar, yet wildly different material such as h-BN, can be extended to other systems that may present more challenging bottom-up approaches of synthesis. Here, we will explore the synthesis of boron carbide from graphite, using some of the key principles of carbothermic conversion, while investigating the differences in macro- and micro-scale of the material and resultant change in material properties.

5.1 Motivation behind porous ceramics

Boron carbide is a unique material that exhibits a wide range of interesting properties for a material comprised of low-Z elements. High melting point, extreme hardness, excellent wear resistance, and low density are just some of the useful properties exhibited by boron carbide.[94–96] Because of these properties, boron carbide is classified as a ceramic, which presents itself useful at both room- and high-temperature environments.[94] Due to its abundance of different uses, boron carbide also has many different synthetic routes to achieve the desired morphology and structure of the final ceramic obtained.[94,97,98] While many studies have looked at the densification of boron carbide for high-impact or neutron absorber applications, there are many applications, such as ceramic armor or wear-resistance, that would benefit from a less dense, porous boron carbide structure.[94,95,99]

Previously explored examples of low density, porous materials are graphene and h-BN aerogels. While aerogels present an interesting porous and light structure to explore for boron carbide, the production of the aforementioned aerogels tends to rely on small-molecule chemistry, which is largely inaccessible for boron carbide or other ceramic structures.[24,30,33] Therefore, other methods of creating porous ceramics have focused on generating structures from pre-formed ceramic particles via sintering.[100] The desired ceramic is mixed within a polymer network, which is later removed by high thermal treatment. The removal of the polymer network creates a porous structure of the remaining ceramic material. The density and size of pores can be controlled by the polymer slurry.[100] However, the size-scale of the pore structure created is massive compared to the graphene or h-BN aerogels, only reaching pore sizes as small as 2.2 mm.[100]

Therefore, there is much room for improvement to achieve micron-size scale porous networks of boron carbide. Here, we will explore the direct synthesis of porous boron carbide from a carbothermic reduction method, which results in pore sizes as small as 1 μm in size. The overall structure is completely porous in nature and is a fully interconnected network of boron carbide 'nodules' and pores, without additional sintering required. As a result of the porous network, the density of the porous boron carbide is reduced to 0.389 g/cm^3, as compared to the bulk density of boron carbide, which is reported at ~2.5 g/cm^3, a decrease of almost 85% in density.[96] The porous boron carbide also presents an interesting macrostructure for the absorption of oil, resulting in an incredibly hard material, often utilized for high-wear applications, that can absorb up to 148 wt% of a lubricating oil.

5.2 The conversion of graphite to porous boron carbide

The high-temperature carbothermic-reduction synthesis method for porous boron carbide ceramics uses components of a synthesis method for BN aerogels, as reported elsewhere.[39,56] Briefly, a pure and un-restructured graphite precursor is placed together with boron oxide in a custom machined graphite crucible and heated to between 1650-1850 °C in an induction furnace under a pure argon gas flow. Typically, up to 0.5 grams of graphite is loaded in the graphite crucible, together with excess boron oxide, usually 5-10 grams depending on the amount of graphite material being converted. Argon gas is flowed through the system at 1500 sccm, and total reaction time is 45-60 minutes to ensure a complete conversion. The converted porous boron carbide is obtained from conversion of naturally occurring graphite fragments (NGS Naturgraphit, Graphenium Flakes, size 5-10mm).

5.2.1 Carbothermic reduction of boron oxide

In general, boron carbide requires extremely high temperatures to achieve successful synthesis, especially at the stoichiometric ratio of B_4C. The typical reaction process followed is the carbothermic reduction of boron oxide. This process is similar to the carbothermic production of h-BN structures from other graphitic species, such as nanotubes, aerogels, and nanofoams, where high temperature and volatile, gaseous species replace the carbon lattice of the parent graphitic material.[56,58,62] However, in the case of boron carbide, there is no simultaneous nitrogenization of the carbon sheets with the reduction of boron oxide. Therefore, the resulting structure will only be comprised of B and C bonding. Boron carbide is formed following the overall carbothermic reduction reaction of boron oxide.[101]

$$2B_2O_3(s) + 7C(s) = B_4C(s) + 6CO(g) \qquad \textbf{(Eq. 5.1)}$$

In **(Eq. 5.1)** we see that the carbothermic reduction of boron oxide produces 1 mol of the desired boron carbide per 6 moles of gaseous carbon monoxide.[101] This removal of carbon from the carbon lattice in graphite results in the overall porous structure observed in later Figures, and will be explored in more detail in terms of elemental composition and bonding. While the overall entropic changes in **(Eq. 5.1)** are extremely favorable, ΔH = +400 Kcal/mol, meaning **(Eq. 5.1)** is very endothermic and requires much higher reaction temperatures than standard production of other aerogel species, such as graphene aerogels, which can successfully obtained at 80ºC with chemical reduction.[24,45,102] For boron carbide, the Gibbs Free Energy reaches a value of 0 at ~1500ºC, so reaction temperatures achievable in an induction furnace can successfully produce boron carbide.

Typically, the carbothermic reduction process is done with powder boron oxide and powder, amorphous forms of carbon, such as carbon black, carbon char, or spongey cokes.[94,99,103] The resultant boron carbide obtained is a crystalline powder of varying sizes, ranging from sub-100 nm to a few micron in size.[97,103] However the resultant boron carbide results in micro or nanostructures physically isolated from one another (i.e. no inter-particle bonding). While these powders may be porous in structure, they require additional processing to make pellets or films, which involves additional energy input and a denser final product. In the work I present here, we examine a method using highly crystalline graphite (rather than amorphous carbon) to produce an interconnected network of boron oxide nodules of ~500nm in size, while retaining the overall shape and structure of the starting graphite material, resulting in a porous macrostructure of boron carbide. **Figure 5.1** shows the schematic for the conversion of graphite to a porous boron carbide structure though high temperature carbothermic reduction of boron oxide.

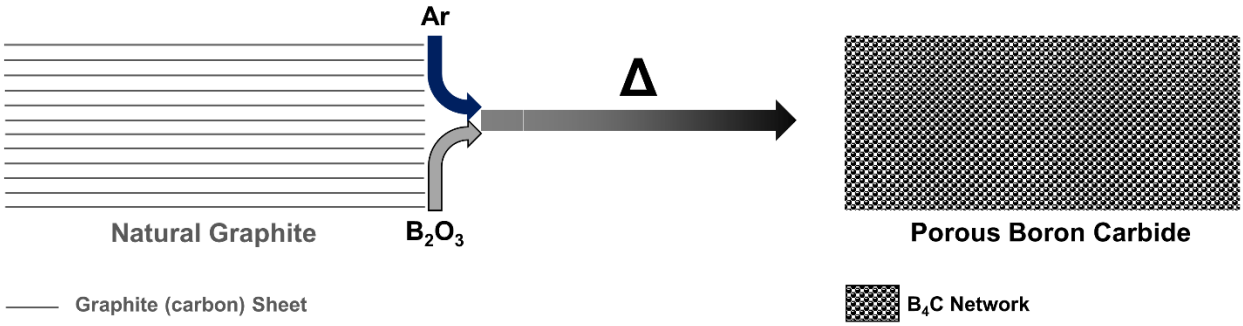

Figure 5.1 Reaction schematic of the conversion of graphite to porous boron carbide.

5.2.2 The partial conversion of graphite

The exploration into porous boron carbide started from our initial studies into the carbothermic conversion of graphite to h-BN materials. In **Chapter 4**, we explored the conversion of graphite to an h-BN nanofoam, which showed drastic alteration to the nanometer size-scale of the material from the parent graphite material. In an effort to better understand the drastic change in structural morphology, I began exploring the conversion mechanism through control syntheses, to see what each component of the overall reaction could contribute. In doing so, one of the control reactions ran was boron oxide and graphite under argon, to see if the reaction conditions (temperature, vapor pressure of boron oxide, time, etc.) resulted in any chemical conversion on its own. Similar to the work in **Chapter 4**, the reaction between graphite and boron oxide came to partial completion, because the size of the graphite precursor left the boron oxide as the limiting reagent.

Figure 5.2 shows a scanning electron microscopy image of the converted graphite, highlighting a partially converted region studied. We see an island of converted material surrounded by the native, flat, crystalline graphite. **Figure 5.2** shows how removal of the carbon lattice as carbon monoxide, along with the drastic change in lattice constants between graphite and boron carbide, results in the porous network being built from the crystalline graphitic material.[40,96] Complete conversion of the graphite studied is easily achieved with a thin enough sample, as diffusion of the gaseous reagents is aided by the structural evolution throughout the conversion process.

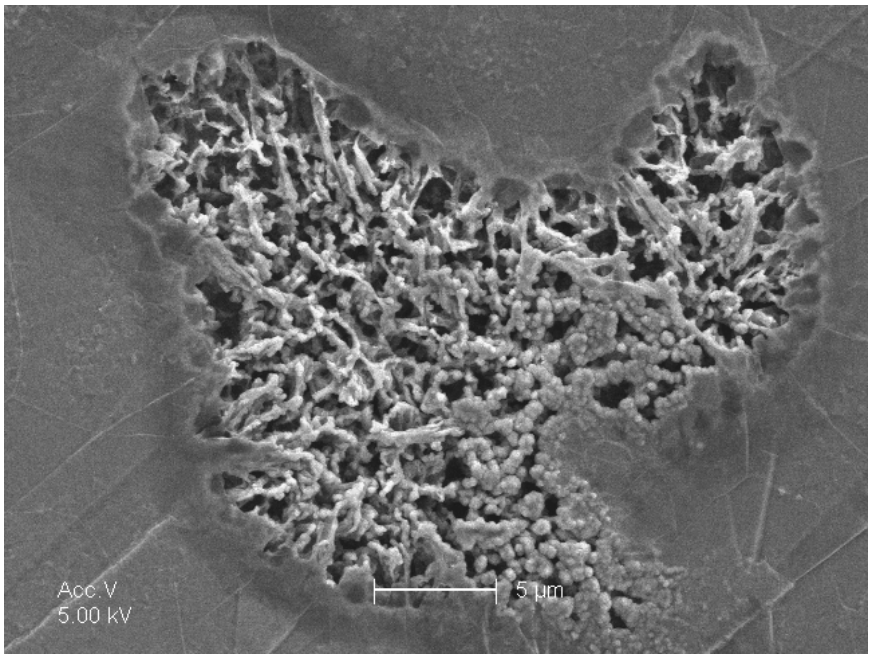

Figure 5.2 Scanning electron microscopy image of an island of conversion within a graphite sheet. Scale bar measures 5 µm. A thick graphite specimen exhibited partial conversion within the interior surface, where islands of conversion could be found.

5.3 Structural characterization of porous boron carbide

The structure of the porous boron carbide is explored with electron microscopy, and surface morphology studied via nitrogen adsorption studies. Structural morphology imaging was obtained using scanning electron microscopy (FEI Sirion XL30), and transmission electron microscopy (JEOL JEM 2010, operated at 80 kV). Nitrogen porosimetry, for analysis of surface area, was carried out by Dr. Marcus Worsley. The analysis was carried out via the Brunauer–Emmett–Teller (BET) method using an ASAP 2020 surface area analyzer (Micromeritics Instrument Corporation).

5.3.1 Retaining the overall macroscale shape after conversion to boron carbide

As previously mentioned, the conversion of large flakes of crystalline graphite to boron carbide not only results in an interconnected, porous structure, but the overall shape and size is controlled by the starting graphite material, shown in **Figure 5.3**. As illustrated, the overall dimensions of the graphite fragment are retained following conversion, but there is a striking change in color upon conversion, from shiny gray (**Figures 5.3a** and **5.3c**) to dull black (**Figures 5.3b** and **5.3d**), indicative of a dramatic chemical modification and change in the surface morphology of the material. Graphene is a flat semimetal, resulting in a shiny surface. Boron carbide is a semiconductor, and the porous structure is texturally rough, resulting in more scatting of incident light and a blacker appearance. **Figure 5.3** also highlights the ability to convert millimeter-sized crystals of graphite to porous boron carbide, indicating a large-scale reaction for the conversion of graphite to boron carbide.

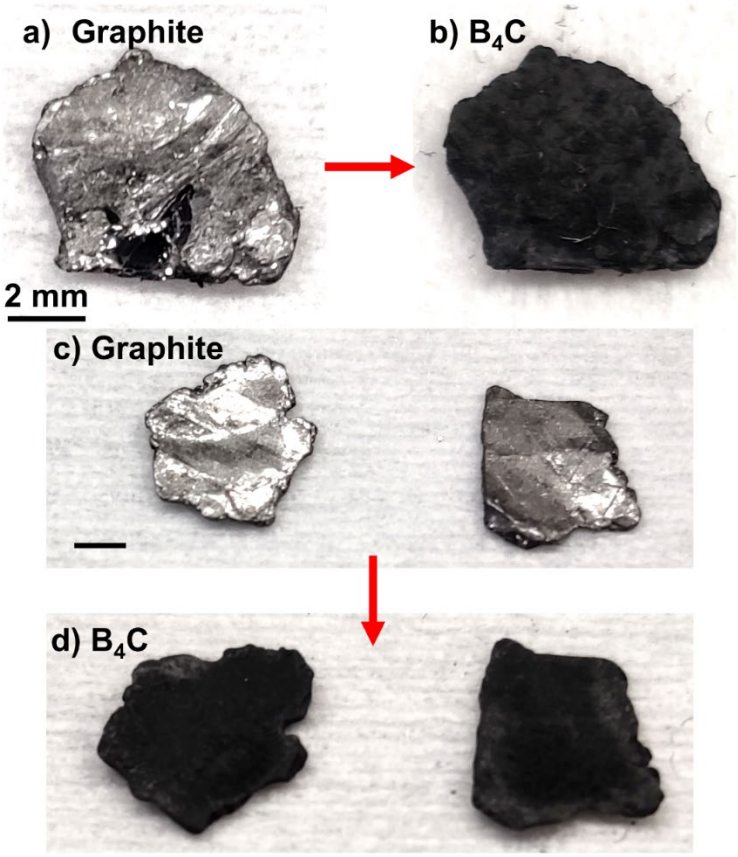

Figure 5.3 Conversion of graphite to porous boron carbide. The overall shape and size of the starting graphite is maintained. Scale bars measure 2 mm.

5.3.2 Drastic morphology changes on the nanometer-size scale

While the macroscopic structure appears the same to the eye, the microscopic structure exhibits drastic changes in the overall morphology. The structure of the converted material is examined at the micron size-scale using secondary electron microscopy (SEM), where the conversion from flat graphite to a porous boron carbide can be readily seen. **Figure 5.4** shows the microscopic view of a graphite flake, where the overall sheet is very flat and crystalline, with maybe some small amounts of debris on the surface. As discussed in **Chapter 4**, the macroscopic view of graphite flakes can show larger scale wrinkles and edges, in the starting graphitic material, which are ultimately carried over to the converted product. The scale of the porous structure is examined in more detail in **Figure 5.5**, where SEM images are compared at different magnifications to examine different length-scales of the product.

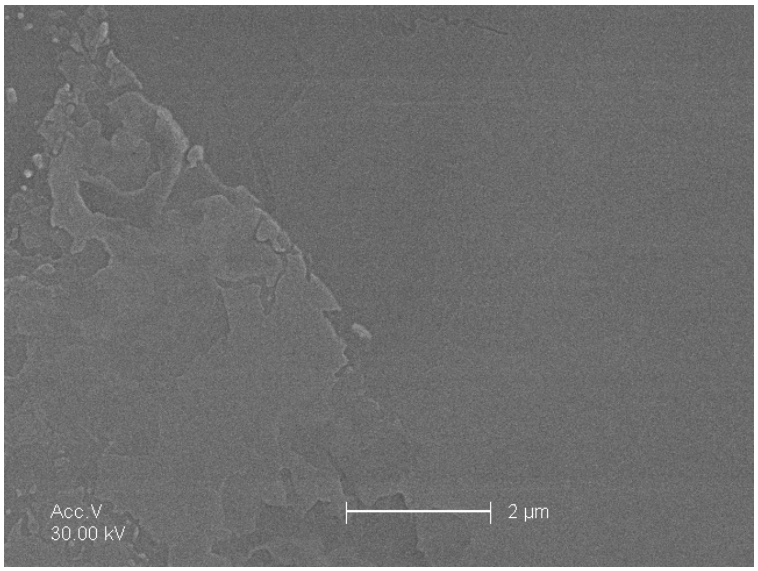

Figure 5.4 Scanning electron micrograph of flat graphite. Scale bar measures 2 µm.

Figure 5.5 showcases the porous surface of the converted porous boron carbide from **Figures 5.3b** and **5.3d**. The top SEM images showcase the wrinkles and edges that are often found in the large, millimeter-sized graphite flakes, and are maintained through the conversion process. The porous boron carbide is comprised of particle-like, 'nodules' of boron carbide, which are all structurally interconnected and form the complete porous structure. In the bottom SEM images in **Figure 5.5**, we inspect the 'nodules' and pores more closely. The nodules of boron carbide material are ~500 nm in size, with pores roughly 1-2 µm in size.

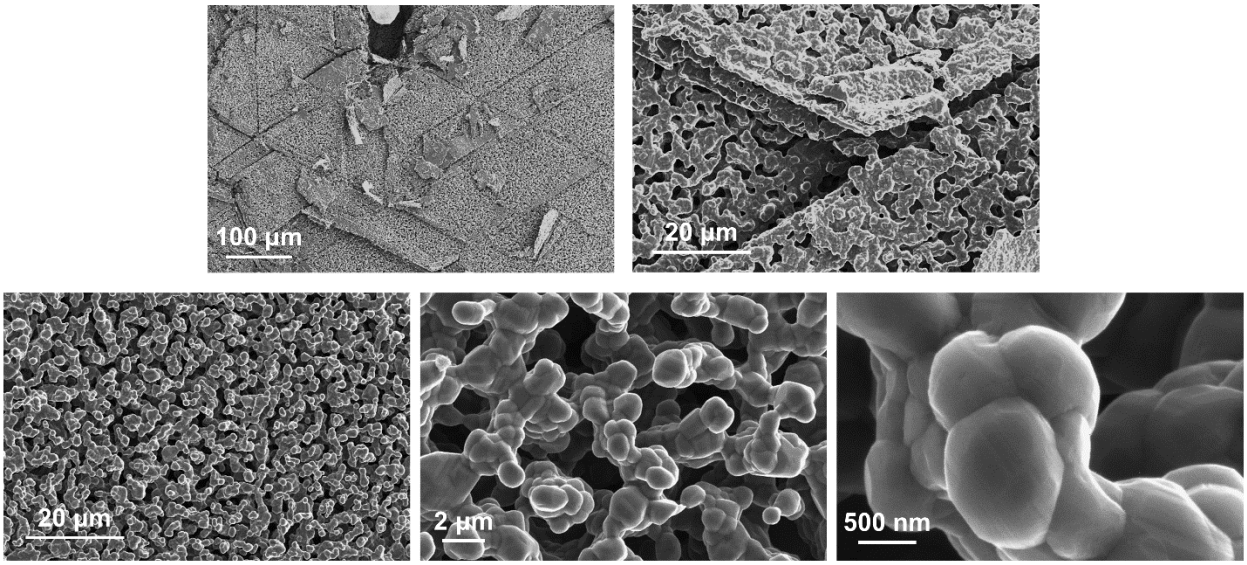

Figure 5.5 Scanning electron microscopy images of different size-scales for the porous boron carbide. Top: Larger length-scale SEM images of porous boron carbide, showcasing how wrinkles and edges of the native graphite flake are carried over to the porous boron carbide product. Bottom: Higher magnification of the surface of the porous boron carbide, showcasing the small porous features and interconnected boron carbide 'nodules'.

Figure 5.6 shows transmission electron microscopy (TEM) of one of the boron carbide 'nodules' and associated electron diffraction. Under TEM, we see the nodules can be isolated from one another through mechanical separation (i.e. scraping and bath sonication). The selected area diffraction patterns shows a cubic pattern associated with rhombohedral lattices, such as boron carbide or hematite, with only one set of strong diffraction spots observed.[93,104,105] Therefore, while the boron carbide nodules may differ in orientation or size, they are highly crystalline in nature, indicating appropriate synthesis conditions for achieving highly crystalline boron carbide.

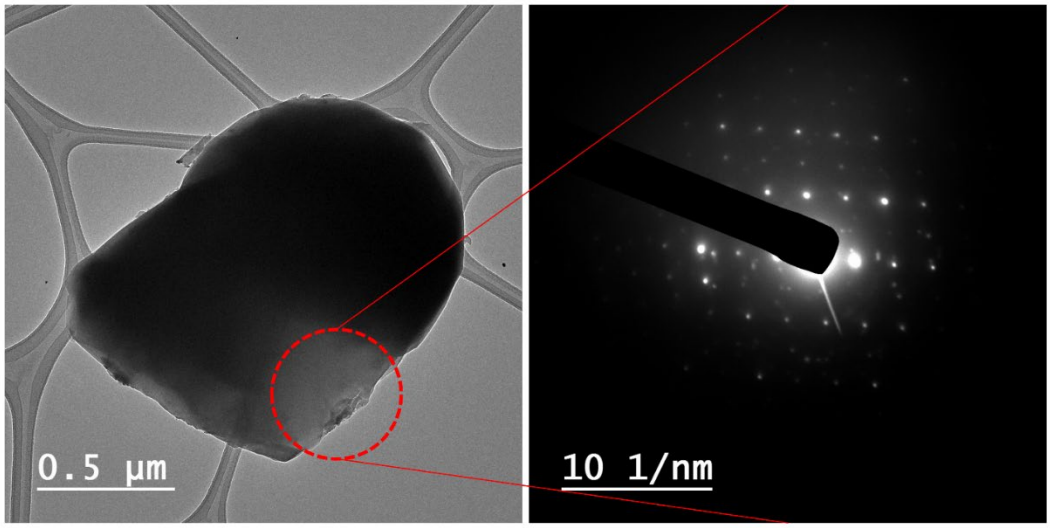

Figure 5.6 Transmission electron microscopy of a boron carbide 'nodule'. TEM micrograph captures a single boron carbide 'nodule' that was separated from the interconnected porous network via mechanical separation. Selected area diffraction pattern from selected region shows a single pattern of strong diffraction spots, indicating single crystalline material.

5.4 Resultant properties of the porous ceramic

The formation of a porous network indicates a much less dense material than sintered nanoparticles, as is usually for other synthetic methods.[94,95,99,106] The density of boron carbide can range from ~1.8 to 2.5 g/cm^3, depending on sintering conditions.[98] Here, the density of the porous boron carbide is roughly 0.389 g/cm^3, as compared to the bulk density of boron carbide, which is reported at ~2.5 g/cm^3, a decrease of almost 85% in density. In addition to the change in density due to the structural change from conversion of graphite to porous boron carbide, we are also interested in how the properties of the resulting porous ceramic differ from the graphitic precursor. Native graphite has an incredibly low surface areas of roughly 0.6 m^2/g, and is moderately hydrophilic in nature.[86,87] We find that the porous boron carbide has a surface area of 4.3 ± 0.3 m^2/g, an increase in surface area over 7 times from the graphitic precursor. Along with a drastic increase in surface area, the porous yet interconnected boron carbide allows for improved oil absorption and retainment capabilities. We find oil absorption rates up to 148 wt%.

5.5 Chemical analysis of the porous boron carbide

The chemical composition is verified via Raman spectroscopy, Energy Dispersive Spectroscopy (EDS), and X-Ray Photoelectron Spectroscopy (XPS). Raman spectroscopy was performed with a Renishaw inVia spectrometer with 514 nm laser excitation. Chemical composition was obtained via EDAX on an FEI Sirion XL30. Bonding information was obtained through XPS analyses performed with Al Kα, 200 μm spot, performed by Dr. Art Nelson at Lawrence Livermore National Laboratory.

5.5.1 Elemental composition

Initial analysis of the elemental composition of the porous boron carbide can be done with EDS in the SEM. It is important to note here, however, that EDS is not necessarily the most appropriate measurement for quantification of the elemental composition, as our sample consists of purely light-Z elements, specifically boron and carbon, which overlap in energies for EDS. However, we can use EDS as a first-order analysis and pursue additional spectroscopy techniques to probe the chemical makeup of the porous structure, as shown in later sections.

We can first examine the starting graphite material for our base-level understanding of the chemical composition (which we expect to be fully carbon). **Figure 5.7** shows the EDS spectrum obtained from the natural graphite fragments used in the conversion process, also seen in **Figures 5.3a** and **5.3c**. This spectrum could be obtained simultaneously with the imaging done in **Figure 5.4** to correlate the spectrum with the surface structure. Here we see only flat, crystalline graphite with no morphology change, and maybe some slight contamination, evidenced by the small oxygen peak neighboring the carbon peak. The main feature seen is the carbon peak at 0.277 keV, labeled as such.

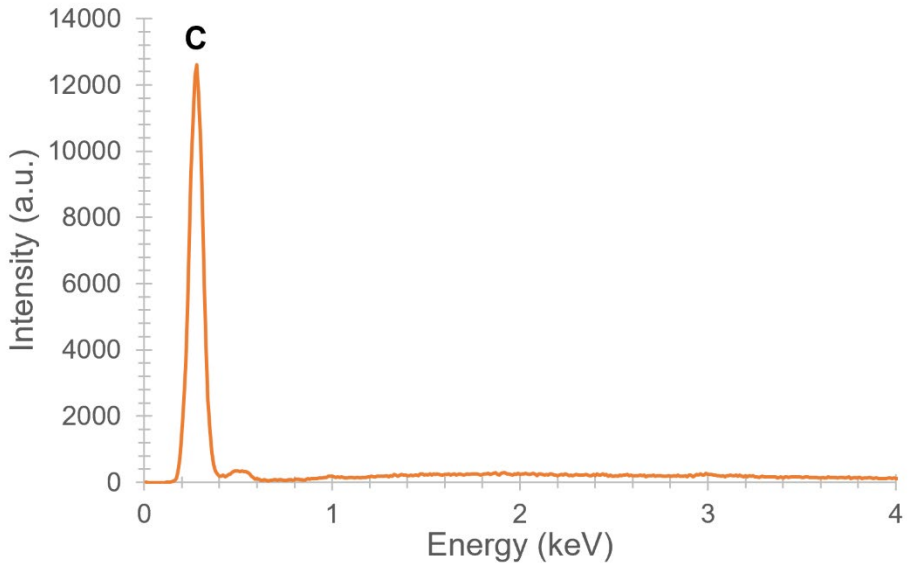

Figure 5.7 Energy dispersive spectroscopy of graphite. Spectrum obtained on the natural graphite fragment used in the conversion process, where the main peak of Carbon is easily observed. A small neighboring peak of oxygen can be seen, which can come from surface functional groups or contamination from handling.

We then analyze the porous boron carbide for the elemental composition. **Figure 5.8** shows the EDS spectrum obtained from the converted, porous boron carbide specimen from **Figures 5.3b** and **5.3d**. This spectrum could be obtained simultaneously with the imaging done in **Figure 5.5** to correlate the spectrum with the surface structure. While the main peak observed is still that of carbon, there is a shoulder easily seen in **Figure 5.8** that is indicative of boron within the sample. As previously mentioned, the energies of boron and carbon in EDS overlap, with boron at 0.183 keV and carbon at 0.277 keV. In standard detectors for EDS, the energy resolution is roughly 130-140 eV, meaning samples containing both carbon and boron will exhibit difficulty in resolving between the two energy peaks.[19] Therefore, the asymmetry in the carbon peak can be attributed to the signal from boron, however, quantification is less straightforward.

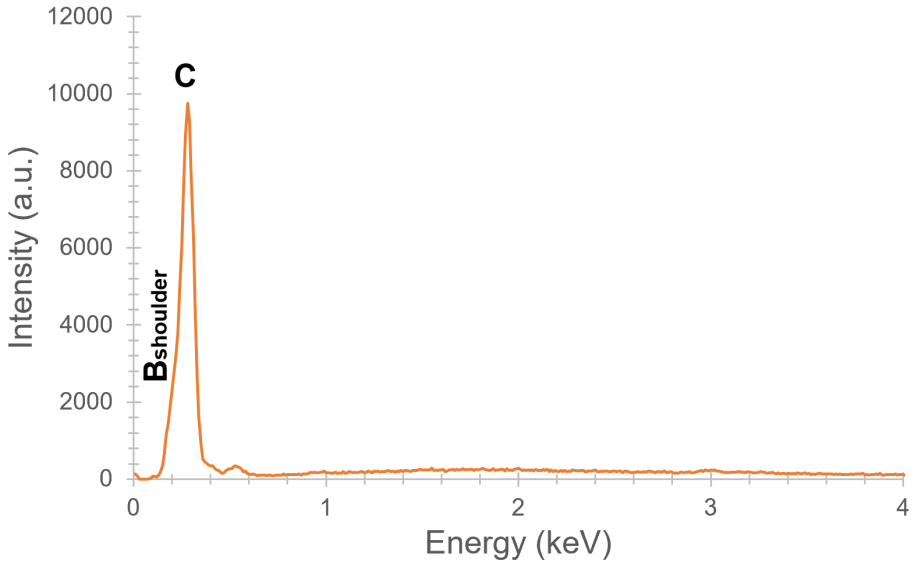

Figure 5.8 Energy dispersive spectroscopy of porous boron carbide. Spectrum obtained on the converted, porous boron carbide. The main carbon peak is still apparent, but with slight asymmetry in the gaussian distribution, indicative of boron signal.

5.5.2 Bonding Characteristics

In order to ascertain the stoichiometry of the porous boron carbide specimen, as well as the associated bonding, we can turn to XPS. We perform XPS on a partially converted graphite sample to see how the bonding evolves over the course of conversion. **Figure 5.9** shows an optical image of the sample used for XPS measurements. The regions have been labeled, and three specific regions were analyzed for any difference observed throughout the conversion process. **Figure 5.9a** is analyzing an unconverted region of the graphite flake and appears shiny. **Figure 5.9b** is an attempt to analyze the border region between the native graphite and porous boron carbide. However, as seen in **Figure 5.2**, these regions can be comprised of many different structures, so analysis may be inconclusive. **Figure 5.9c** analyzes the fully converted porous boron carbide.

The results of the XPS scans of the three labeled regions are shown in the full XPS spectra in **Figure 5.10**. The spectra have been offset in the y-axis direction to display all three simultaneously. Each spectrum is labeled with the specific region from where it was collected.

Each element is labeled in terms of which energy emission is observed (B1s for example), and higher magnifications scans are shown in following figures, where we can see the specific type of bonding present in each element.

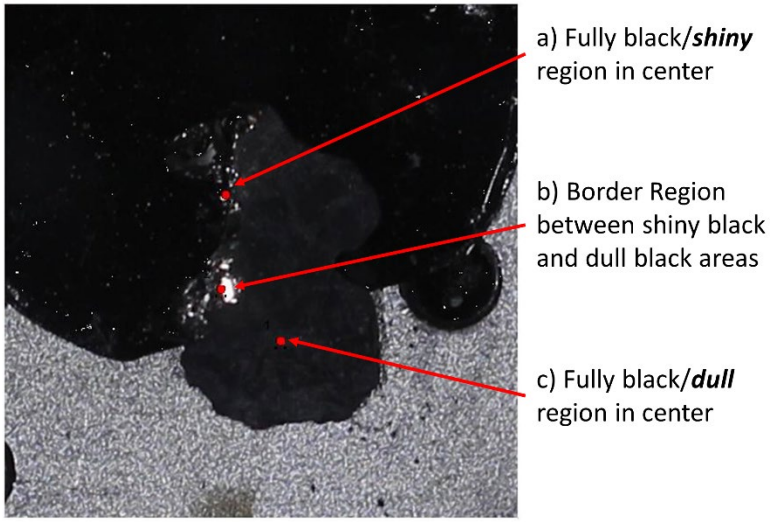

Figure 5.9 Optical image of partially converted porous boron carbide flake. X-Ray Photoelectron Spectroscopy was performed on three distinct regions. (a) Fully shiny black region of unconverted graphite. (b) Border region between the native graphite and porous boron carbide. (c) Fully dull black region of converted porous boron carbide. Data collected in collaboration with Dr. Art Nelson.

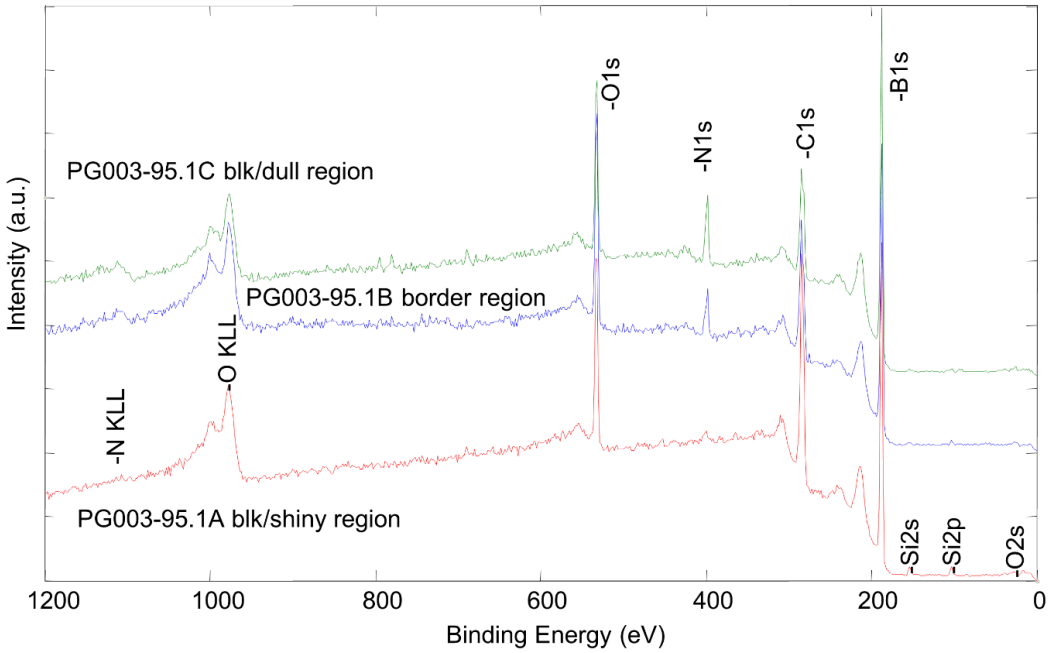

Figure 5.10 X-Ray photoelectron spectroscopy survey spectra for the three different regions in the partially converted graphite. The spectra are labeled by the sample number and end in the region (A = black/shiny, B = border, C = black/dull). Data collected in collaboration with Dr. Art Nelson.

The XPS spectra collected provide information about the chemical makeup of the porous boron carbide material, along with structural information about the bonding present. **Table 5.1** summarizes the results of the atomic content in each region scanned. In the regions where unconverted graphite was visible, the amount of carbon present is much higher, but still outweighed by the content of boron. The sample analyzed is inhomogeneous throughout due to partial conversion. Coupled with a relatively large scanning spot of 200 μm, the analysis completed in regions a and b could have undesired signal from surrounding regions of the sample. For example, the partially converted graphite exhibited large areas of flat, crystalline material, with small islands of conversion, such as those seen in **Figure 5.2**, scattered throughout occasionally. This could explain the larger than expected amounts of boron observed in the unconverted or partially converted regions.

Table 5.1 Atomic percent of Boron, Nitrogen, Carbon, and Oxygen for each region in the partially converted porous boron carbide. Amounts are reported in atomic percent. Data collected in collaboration with Dr. Art Nelson.

Region	B (at.%)	N (at.%)	C (at.%)	O (at.%)
a	56.90	0.91	33.14	9.05
b	60.63	3.33	24.16	11.88
c	66.54	4.68	19.62	9.16

For the chemical composition of the final porous boron carbide product, we look to Region c, where full conversion is observed. This row has been highlighted in **Table 5.1**. Here, we see a stoichiometry of B:C of 3.4:1, close to the desired ratio of 4:1 for boron carbide. However, if we look at the phase diagram of boron carbide in **Figure 5.11**, we see that certain regions, depending on the amount of carbon present, can result in boron carbide with excess graphite.[93,97] For our carbothermic reduction conversion process, our temperature is below the 2000 ºC mark on **Figure 5.11**, so we will certainly not be approaching any of the liquidous regions marked at extremely high temperatures. As for atomic content of carbon, our carbon and boron oxide source are separated from one another, meaning our sample exists within the higher concentration regime of carbon, which will ultimately result in boron carbide + graphite. Based on the ratio determined for Region c, there is an abundance of carbon present, and we could assume that our sample consists of boron carbide + graphite based on the phase diagram.[97] Therefore, assuming we have successfully converted the graphite to boron carbide (B_4C) as our final product and readjusting the ratio for a 4:1 of B:C, then there is a very small amount (~3%) of excess carbon present. We will discuss additional chemical composition measurements performed via Raman spectroscopy in a later section, which will further verify our assumption as correct, where we see strong signal for the desired 4:1 ratio of boron carbide (B_4C).

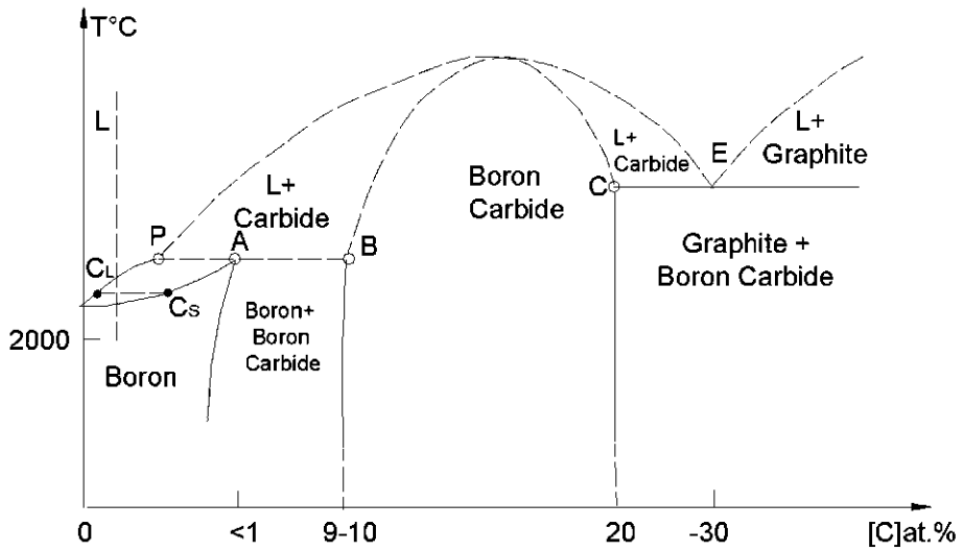

Figure 5.11 Phase diagram of boron carbide at varying atomic concentrations of carbon. Boron carbide regions are of stoichiometry 4:1 of B:C. Adapted from reference 97.

The bonding information for boron is provided via the B1s spectra in **Figure 5.12** for each region. Between the three different regions, very similar bonding is present, with two main peaks present. The first main peak observed at ~187.5 eV is associated with crystalline B-C bonding. The second main peak observed at ~189 eV is associated with amorphous B-C bonding.[107] There is the whispers of a peak observed at ~ 191.5 eV, which can be attributed to B-O bonding. Therefore, from the bonding present in the B1s spectra, the vast majority of the boron content present in Region c is from boron carbide, albeit some regions may be more amorphous than originally anticipated. This could indicate that reaction conditions may need to occur at higher temperatures so that all the boron carbide domains are no longer amorphous.

The carbon bonding presented in **Figure 5.13** is much busier than that of boron. The peak at ~282.5 eV is associated with C-B bonding, indicating the formation of boron carbide as well.[107] The peaks present in **Figure 5.13** above 286 eV can all be attributed to C-O type bonding, indicating the remaining carbon is heavily functionalized by oxygen containing groups, or there are surface oxides on the material. Typically, C-C bonding from graphite comes between 284 and 285 eV, as is seen in Region a, indicating that the carbon in Regions b and c could not be graphitic in nature after the conversion process, but rather graphene oxide. Again, higher reaction temperatures would anneal these functional groups out of the material and leave behind more crystalline material.

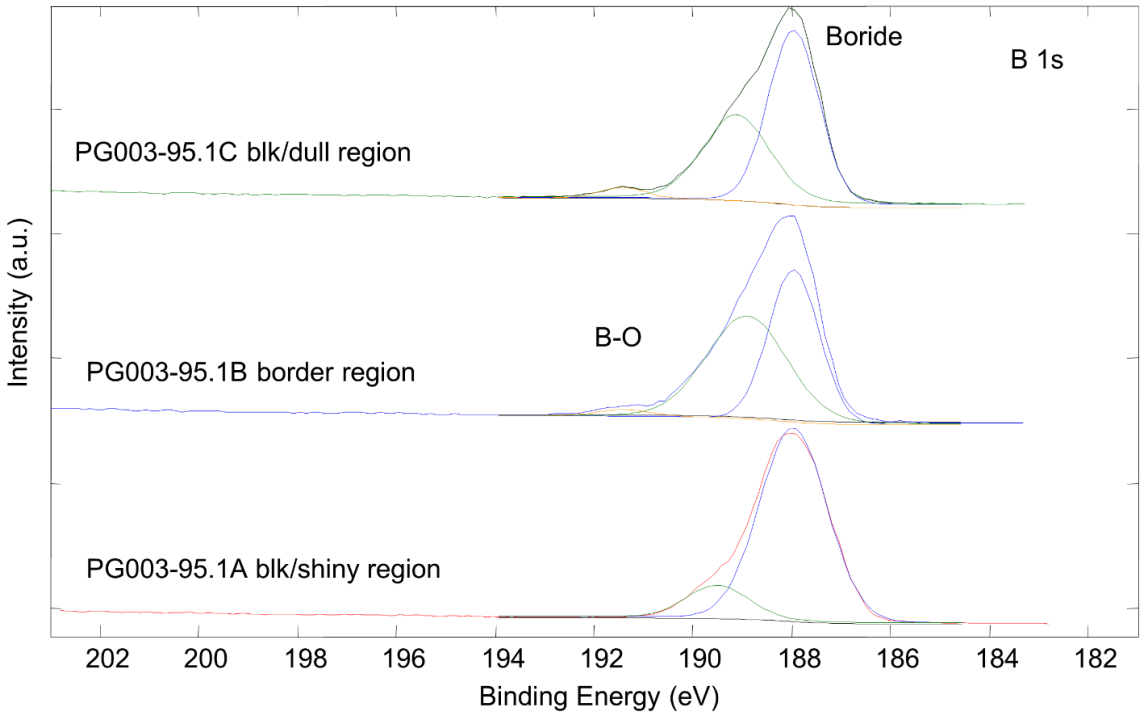

Figure 5.12 B1s XPS spectra of the porous boron carbide. Data collected in collaboration with Dr. Art Nelson.

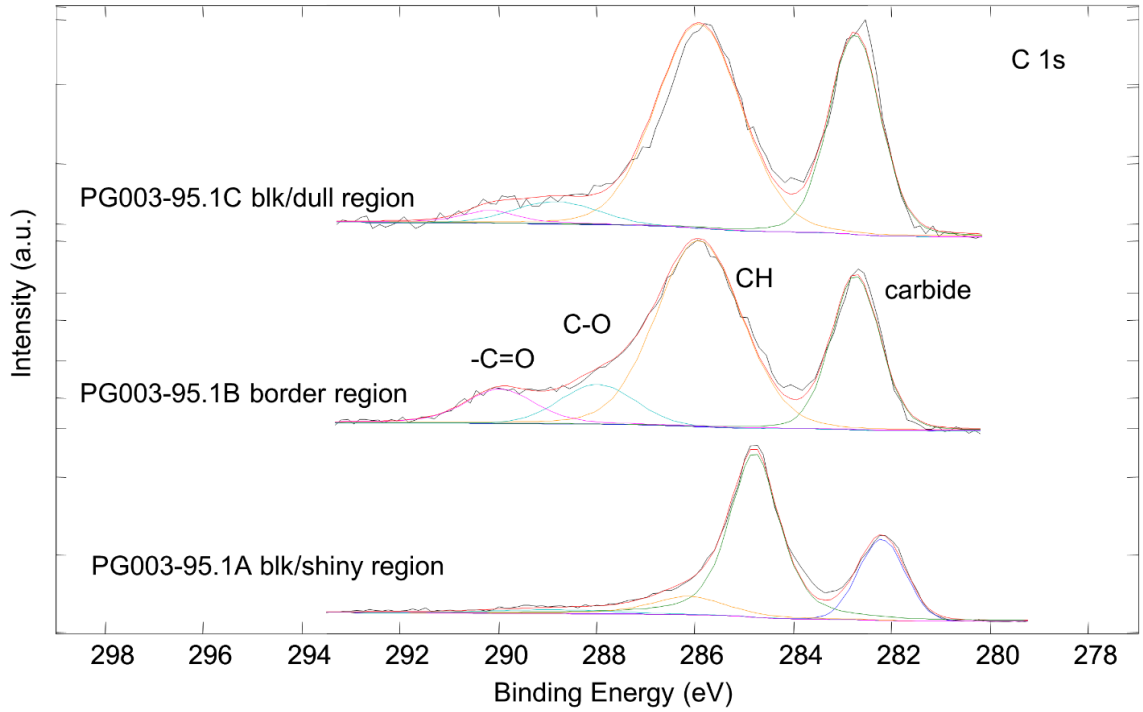

Figure 5.13 C1s XPS spectra of the porous boron carbide. Data collected in collaboration with Dr. Art Nelson.

We also see small amounts of nitrogen and oxygen present in the sample, shown in **Figures 5.14** and **5.15**, respectively. The amounts present vary slightly depending on which region of the sample we examine. Depending on the bonding present, we can determine where these contaminants come from, and the type of bonding is labeled on each spectrum. The nitrogen is likely contamination from the experimental setup, as the same carbothermic reduction equipment as shown in **Chapter 4** for the conversion of graphite to h-BN nanofoams is used for the carbothermic synthesis of boron carbide. Another likely source of contamination would be from nitrogen present in the system during the conversion process, however pump-purge procedures are followed to ensure an atmosphere as rich as possible in argon. The majority of the nitrogen contamination is present as carbon nitride, as seen by the highest peak present in **Figure 5.14** for N-C bonding.

Oxygen is likely contamination from some limited functionalization of the parent graphite material as hydroxyl groups, labeled in **Figure 5.15** as OH-. However, much of the increase in oxygen for Regions b and c appears to be from H_2O, as compared to the OH- and O= peaks present (and their relative intensity) in Region a. As the porous boron carbide is expected to drastically increase the overall exposed surface area as compared to the unconverted graphite, additional water would have adhered to the surface of the porous boron carbide after conversion, resulting in additional oxygen signal from water.

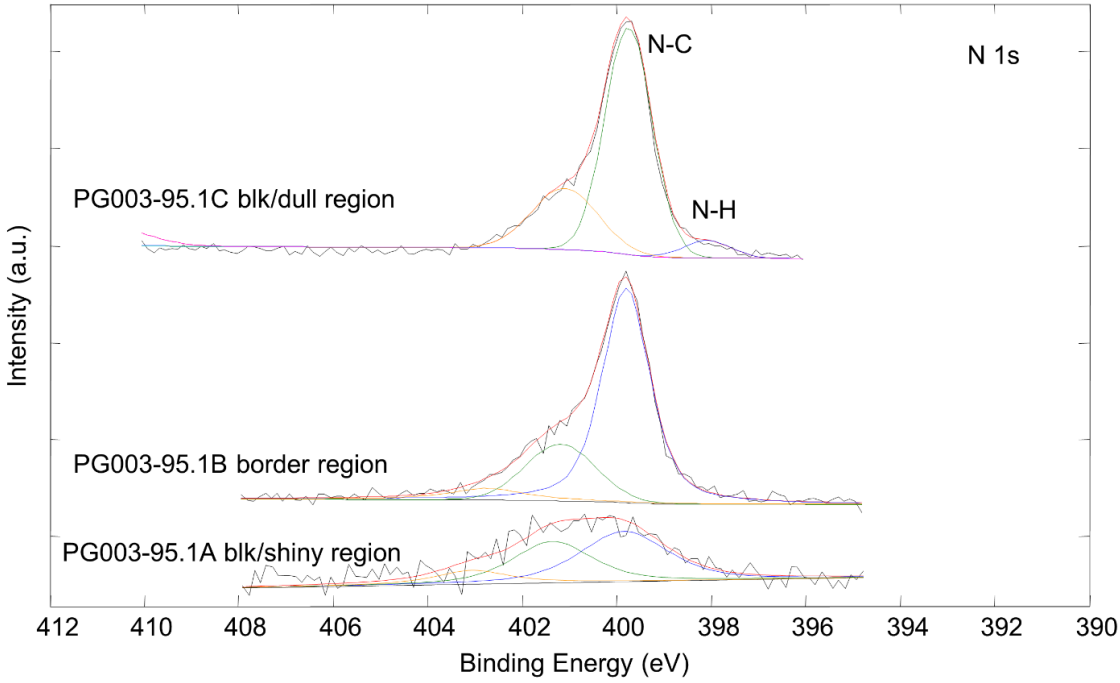

Figure 5.14 N1s XPS spectra of the porous boron carbide. Data collected in collaboration with Dr. Art Nelson.

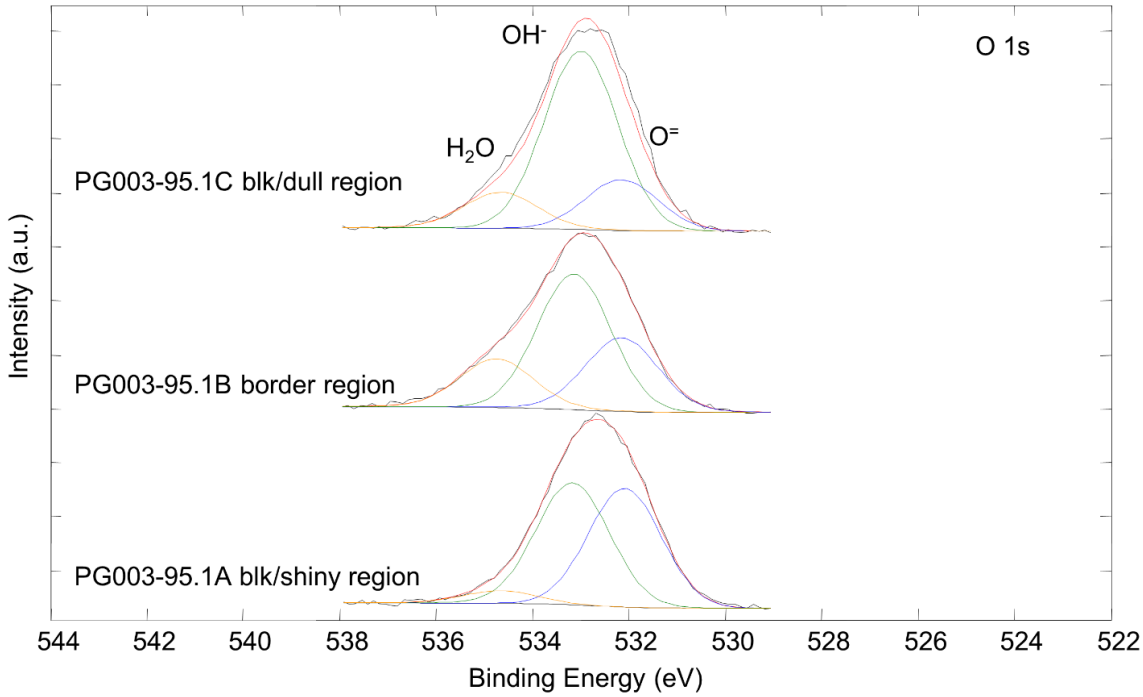

Figure 5.15 O1s XPS spectra of the porous boron carbide. Data collected in collaboration with Dr. Art Nelson.

5.5.3 Macrostructure characterization

While the data presented from XPS supports the formation of the desired 4:1 ratio of boron carbide (B_4C), there is still some ambiguity for the amorphous and crystalline bonding energies observed in **Figure 5.12** for the boride bonding. To escape the ambiguity of bond-specific information, we pursue more broad spectroscopic methods that will probe macroscale bonding properties of the material, such as vibrational modes within the porous boron carbide. Therefore, we next examine Raman spectroscopy of the porous boron carbide. **Figure 5.16** shows the Raman spectrum obtained from the porous boron carbide, with the background subtracted from the spectrum. All peaks observed correspond directly to boron carbide as previously studied, with no extraneous peaks present from impurities or substrate.[96] As such, individual peaks have not been labeled. If carbon were present in an abundance as a graphitic structure, a strong peak somewhere around 1590 cm^{-1} would have been readily observed, and if functionalized graphene (or graphene oxide) were present in massive quantities, then a strong peak around 1350 cm^{-1} would have been observed.[31] Therefore, the excess carbon present is likely in an amorphous, oxidized form, and could be easily removed via post treatment or higher reaction temperatures.

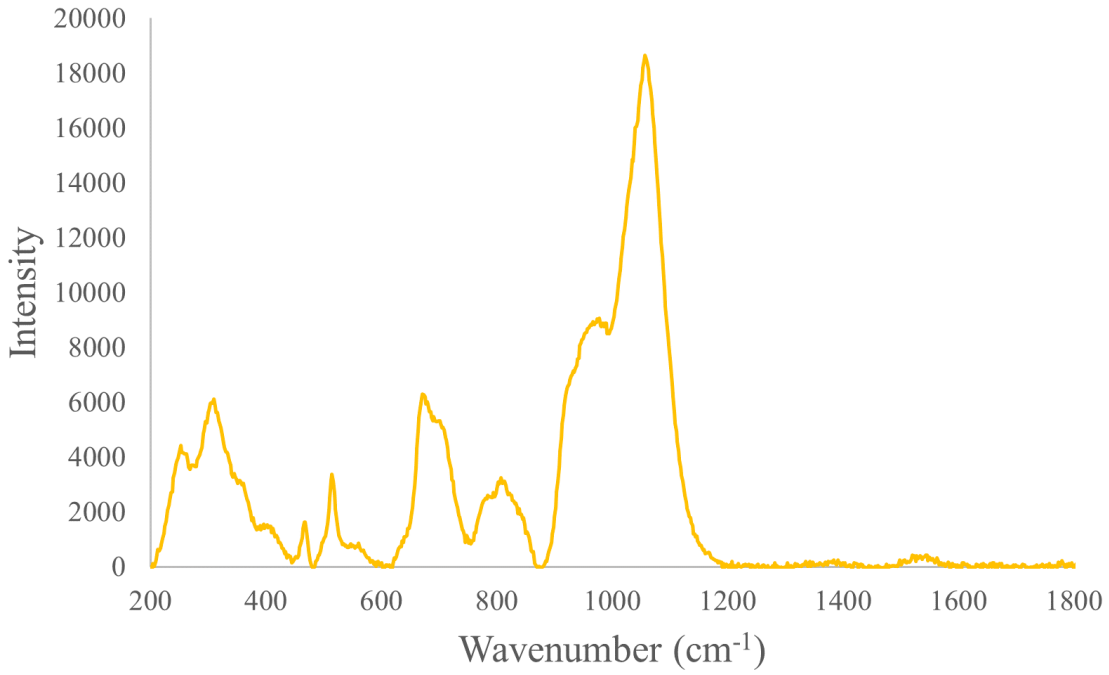

Figure 5.16 Raman spectrum of the porous boron carbide. Individual peaks have not been labeled as all peaks observed correspond directly to the boron carbide, with no interference from any impurities or substrate.

5.6 Conclusion

Here, we discussed a facile route to achieve customizable porous boron carbide ceramics with an interesting interconnected, particle-like network of B_4C. The size-scale of the pore network is magnitudes smaller than other routes to achieve porous ceramics, reaching pores as small as 500 nm, where previously reports were on the millimeter scale. We achieve a porous ceramic via a direct synthesis method through carbothermic reduction of boron oxide, using large, crystalline graphite as the carbon substrate for conversion. XPS and Raman spectroscopy confirm the stoichiometry of B_4C for the final structure. The resulting structure is completely porous in nature and fully interconnected, without additional sintering required. As a result of the porous network, the density of the porous boron carbide is reduced to 0.389 g/cm^3, as compared to the bulk density of boron carbide, which is reported at ~2.5 g/cm^3. In addition to the change in density, the porous boron carbide has a surface area of 4.3 ± 0.3 m^2/g, an increase in surface area over 7 times from the graphitic precursor. As a result, the porous boron carbide also presents an interesting macrostructure for the absorption of oil, resulting in an incredibly hard material often utilized for high-wear applications, that can absorb up to 148 wt% of a lubricating oil. The work presented in this chapter expands upon the conversion of graphite to other structures of varying elemental composition, and presents another simple, effective route to produce large amounts of desired material with minimal synthetic steps required.

Chapter 6: Continued Work – Aerogels, Doping, and Conversion

The first part of this work presented in **Chapters 1-5** focused on the concept of dimensionality, and how it relates to material structure, property, and applications. The chapters in **Part I** explored targeted material growth of material systems, focusing on doping and conversion methods. **Chapter 3** studied synthetic chemistry techniques used to alter the structure of graphene sheets and assemble those sheets into graphene-based macrostructures, such as doped-aerogels, for more meaningful applications. **Chapter 4** examined methods to utilize the robust lattice of graphene as scaffolding for the growth of other porous, macroscopic systems built from other 2-D materials, such as h-BN nanofoams. **Chapter 5** explored the conversion method to access different compositions of porous structures beyond that of a layered material, breaking into the porous ceramics field.

Part I examined robust methods of atomic structure and chemical composition analysis, which allows for correlation between the property-structure relationship in these types of layered systems. In doing so, we were then able to leverage that relationship to tailor these materials through targeted material growth, either through doping or conversion. Aerogels were the first example we explored, where the atomic thinness of graphene and h-BN is leveraged to produce porous, ultralight materials with a wide range of applications across many fields.[24–29] These aerogels typically show excellent behavior for energy applications, catalysis, sensing applications, or thermal management, depending on the parent material comprising the aerogel.[25,29,31,36–39] Even though aerogels could be designed out of a variety of 2-D materials, the most explored system is graphene aerogels, owed to the larger library of possible synthetic methods to chemically cross-link graphene oxide sheets. However, the overall performance of these pure graphene aerogel systems is hindered by the smooth and relatively inert surface of graphene, and enhancement of properties can be aided by addition of species other than carbon.[24,28,69]

Chapter 3 explored a couple elements, specifically boron and nitrogen, that are similar enough to carbon in terms of size and type of bonding, that can be inserted into the graphene lattice structure and replace carbon atoms directly.[56,71,72] In low quantities, this structural replacement of carbon atoms with another elemental species is referred to doping, and has powerful implications on the local electronic and chemical environment for the graphene sheet. We focused on the doping of the graphene lattice with nitrogen, as these nitrogen(N)-doped graphene systems show enhanced performance in energy and reaction applications, specifically catalytic activity and batteries.[66,73–76] To achieve N-doping into the graphene aerogel, we explored a reaction mechanism commonly used to produce Schiff Bases, which covalently cross-links nitrogen containing functional groups to a carbonyl compound through nucleophilic addition. Incorporation of a small pararosaniline base molecule into the graphene oxide suspension before gelation produced a covalently cross-linked system with comparatively high amounts of nitrogen doping, currently capping out around 9.4%.

There are still some questions we are working to answer related to the incorporation of nitrogen into these aerogel systems. For starters, there were still oxygen-containing functional groups within the graphene aerogel, which could be annealed out of the structure by higher temperatures. However, the nitrogen dopants can also be annealed out of the graphene lattice at high enough temperatures, so studies need to be performed at different annealing temperatures to see how the nitrogen content is impacted. Additionally, high temperature annealing will 'graphitize' the bonding of the carbon atoms more, increasing the overall crystallinity of the

aerogel structure. This could positively impact the N-doping as well by increasing the overall amount of graphitic nitrogen bonding within the doped structure. We are also studying the level of control maintained over the content of N-doping in the final graphene aerogel based on the amount of pararosaniline base incorporated into the graphene oxide suspension before gelation. While 9.4% doping of nitrogen is high, we are still not sure about the maximum limit that can be achieved through this process. Finally, while the doping content of nitrogen and type of bonding observed is very promising and exciting, there is much to be explored for how this doping affects the aerogel properties. For N-doped graphene aerogels, the performance in gas-sensing, supercapacitors, or graphene electrode measurements should show considerable improvement over the standard graphene aerogel counterparts.[77]

Chapter 4 sought to explore macrostructures built from a 2-D material other than graphene. However, many of the synthetic approaches for graphene aerogels are of the "bottom-up" variety, where either small particles or molecules are functionalized and covalently bound together to form the macroscopic structure, such as the pararosaniline base aerogel we explored in **Chapter 3**.[24] We explored a robust, scalable, and facile "leapfrog" conversion process for a "top-down" synthetic approach, in order to bypass the need for molecular precursors, obtaining porous h-BN macrostructures from a graphitic system. Overall, a porous, crinkled h-BN foam- was produced that showed a surface area over 60 times larger as compared to the graphitic scaffold, leading to improved oil absorption capabilities (up to 325 wt%).

While the conversion mechanism from graphite flakes produced very crystalline crinkled h-BN nanofoams, there are still some interesting implications of the conversion process that would be interesting to study in more detail. In the work presented in **Chapter 4**, a 'time' study was performed, where a very large piece of graphite was partially converted to examine how the conversion process migrated through the system. There are fascinating boundary regions that form throughout the conversion process, where untouched, perfectly flat graphite can be seen with a sharp edge transition to a semi-crinkled network. These boundary regions could contain interesting incorporation of boron, carbon, and nitrogen into a single crystalline lattice. These BCN structures have their own fascinating properties, such as a tunable bandgap dependent upon stoichiometry.[108] Further control of the conversion process to isolate a BCN structure would provide a very powerful tool to further manipulate the structure of these porous structure and further tune their properties and applications.

Chapter 5 explored our first attempts at expanding the conversion method to achieve structures beyond that of h-BN. In doing so, we were able to access the direct synthesis of porous boron carbide, a unique material that exhibits high melting point, extreme hardness, excellent wear resistance, and low density.[94–96] The structure achieved via carbothermic conversion from graphite is completely porous in nature and fully interconnected without additional sintering required. As a result of the porous network, the density of the porous boron carbide is reduced to 0.389 g/cm^3, a decrease of almost 85% as compared to the bulk density of boron carbide (~2.5 g/cm^3), beneficial for applications in ceramic armor or wear-resistance.[94–96,99] In addition to the change in density, the porous boron carbide has a surface area of 4.3 ± 0.3 m^2/g, an increase in surface area over 7 times from the graphitic precursor. As a result, the porous boron carbide also presents an interesting macrostructure for the absorption of oil, resulting in an incredibly hard material, often utilized for high-wear applications, that can absorb up to 148 wt% of a lubricating oil.

Further study into the conversion of a pure carbon structure to that of B_4C could provide needed insight into the full possibilities for these porous ceramic networks. Interestingly, subjecting a graphene aerogel to the same conversion process as graphite results in a very similar looking material, with 'nodules' of B_4C interconnected in a porous network. However, converting aerogels could be an interesting method to further tune the density of the final material. The conversion of other unique carbon systems, such as nanotubes or fullerenes, would undoubtedly result in equally fascinating B_4C structures. The possibilities are still wide open to explore what is fully possible with this conversion mechanism, and how ceramic materials could have shape or structure designed into them through an easier to process material system, such as graphene, graphene aerogels, or graphite.

Part I focused mainly on the manipulation of the 2-D layered material systems, especially graphene and h-BN, through targeted material growth. This manipulation imparts additional utility into the material systems, such as doping for enhanced molecular interaction or conversion to access a new material class. However, while graphene and h-BN have garnered the most attention as materials whose low dimensionality adds a unique experimental handle to tune material properties, there are other low-dimensional systems to explore. The transition metal dichalcogenides (TMD) and transition metal trichalcogenides (TMT) are two closely related systems that, like graphene and h-BN, are also comprised of low-dimensional building blocks. Unfortunately, the chemistries surrounding the TMD and TMT are nowhere near similar to that of carbon, so similar doping or conversion techniques are not accessible to manipulate or tailor their material properties. Therefore, **Part II** will explore other means of tailoring material properties through extreme atomic confinement.

Part II: Constrained Material Growth

Chapter 7: Introduction to Low-Dimensional Transition Metal Chalcogenides and Extreme Atomic Confinement

Keywords: Transition Metal Dichalcogenide, Transition Metal Trichalcogenide, Transmission Electron Microscopy, Scanning Transmission Electron Microscopy, Electron Energy Loss Spectroscopy, Monolayer, Single-chain, Encapsulation, Crystal Field Splitting, Octahedral, Trigonal Prismatic, Atomic Confinement

Part I of this dissertation discussed the important discoveries that have been made with the 2-D van der Waals (vdW) materials, focusing on the manipulation of graphene and hexagonal boron nitride (h-BN) for the targeted growth of materials using synthetic chemistry techniques. The low-dimensional nature of these two structures have afforded systems comprised of graphene or h-BN a wide range of applications. However, graphene and h-BN are on two opposite ends of the 2-D layered materials spectrum, with graphene being highly conductive and h-BN a wide-gap insulator. Here, in **Part II**, we will discuss another class of low-dimensional materials with properties intermediate to graphene and h-BN. The materials of interest, namely transition metal dichalcogenides and transition metal trichalcogenides, show a host of interesting and unique properties for 2-D and 1-D systems, respectively. However, similar synthetic chemistry techniques are not easily applied to these systems to tailor their atomic and electronic structure. Therefore, we pursue other means of tailoring, specifically constrained material growth, where the atomic and electronic structure of materials can be reconfigured through drastic physical confinement of the crystals grown. All data presented in this dissertation are produced by the author unless otherwise noted.

7.1 Transition metal chalcogenide material family

While most of the initial research and discovery of the vdW limit of 2-D atomically thin sheets of crystalline materials focused on graphene and h-BN, there are additional material systems which form crystalline solids comprised of low-dimensional building blocks. The transition metal chalcogenide (TMC) material family is one such material system that exhibits a wide range of structures, many of which are comprised of low-dimensional building blocks held together by vdW forces, such as the transition metal dichalcogenides (TMD) and transition metal trichalcogenides (TMT). These TMC systems can be isolated and studied down to their vdW limit, similarly to graphene and h-BN, and have a much richer variety of atomic and electronic structures due to the tunability in elemental composition and stoichiometry.[109] The elemental composition of TMC is easily changed through exchange of the transition metal and/or chalcogenide for an entirely new chemical formula, resulting in entirely new material properties. The stoichiometry of the TMC determines the resulting structure obtained, and allows for tuning between 2-D layered TMD (like graphene or h-BN) or lower dimensional 1-D chain-like TMT.[109,110]

The two main TMC material families we will focus our study on in this dissertation are TMD and TMT. **Figure 7.1** shows an atomic model for common examples of the TMD and TMT structures, highlighting the vdW nature of these 3-D bulk crystalline materials. Following sections will describe the TMD and TMT structure in more detail, however it is important to note the structural similarity between graphene/h-BN and the TMD. As seen in **Figure 7.1a**, the structure of Molybdenum Disulfide (MoS_2), a commonly studied 2-D TMD, shows a similar

layered structure of atomically thin sheets stacked by vdW forces. **Figure 7.1b** shows an even lower-dimensional vdW system, Titanium Trisulfide (TiS_3), where the 1-D chain-like structure is readily apparent. Due to the structural similarity to graphene, many members of the TMD family have been isolated and studied at the monolayer limit. However, while the TMT materials are vdW species, their additional quantization to a 1-D chain has hindered the true isolation and study of a single chain. **Part II** of this dissertation will discuss an encapsulation technique developed to aid in the isolation and study of the TMT family at the few- and single-chain limit, and well as other interesting vdW structures observed.

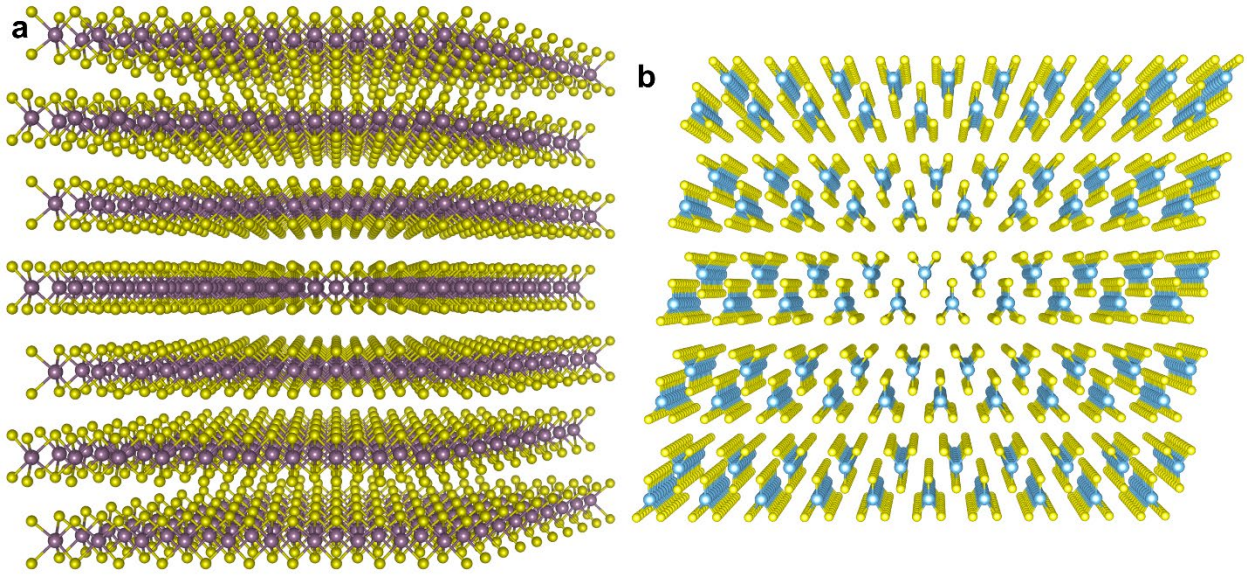

Figure 7.1 Crystal structure model for (a) 2-D layered transition metal dichalcogenides and (b) 1-D chain-like transition metal trichalcogenides. The transition metal atoms are represented by the purple and blue spheres, while the chalcogenide is represented by yellow spheres.

Because of the ability to exchange the transition metal or chalcogenide in the TMC systems of interest, there is a large library of vdW-based transition metal chalcogenides we can study. In brief, the TMD and TMT have the chemical formula of MX_2 and MX_3, respectively, where M is a transition metal and X is a chalcogen. The MX_2 structure consists of 2-D sheets of material, while the MX_3 structure consists of 1-D trigonal prismatic chains of material. The low-dimensional sheets or chains are assembled into a 3-D bulk crystal through vdW forces. **Table 7.1** shows the various transition metal and chalcogenide combinations of the materials we will examine throughout this dissertation. We focus mainly on the Group IVB and VB transition metals and present all combinations of the chalcogenides for completeness. While not all combinations have been successfully synthesized or characterized, by the end of this dissertation we will see how the techniques described here allow us to access some members of the TMT family that were previously unknown. As a point of interest, a brief descriptor of the defining material property for each TMD and TMT combination has been presented in **Table 7.1** as well.

Table 7.1 Different combinations of TMD and TMT from the Group IV and V transition metal block. The di- and tri-chalcogenide are listed across the top for each transition metal. All combinations have been listed for completeness, even if no bulk synthesis has been reported. The temperatures listed in the table are the transition temperatures.

		Chalcogen					
		S_3	S_2	Se_3	Se_2	Te_3	Te_2
		Bulk	*Bulk*	*Bulk*	*Bulk*	*Bulk*	*Bulk*
Group IV Transition Metal	Ti	Semicond.	Semimetal	No Reported Synthesis	CDW (200K)	No Reported Synthesis	Semimetal
	Zr	Semicond.	Semicond.	Semicond.	Semicond.	SC (2K)	Semimetal
	Hf	Semicond.	Semicond.	Semicond.	Semicond.	SC (1.4-2K), CDW (70-93K)	Semimetal
Group V Transition Metal	V	No Reported Synthesis	Metallic	No Reported Synthesis	CDW (110K)	No Reported Synthesis	Metallic
	Nb	Semicond., CDW (450-475K)	SC (2-6K)	CDW (145K, 59K)	CDW (26K), SC (7.2K)	No Reported Synthesis	SC (0.7K)
	Ta	CDW (210-220K)	CDW (220, 280, 350K), SC (0.5-2.2K)	SC (2.1K)	CDW (90K), SC (0.1K)	Reported Synthesis, No Characterization	CDW (170K)

Key: Semicond. = Semiconductor/Insulator; CDW = Charge Density Wave; SC = Superconducting

7.2 Bonding in transition metal complexes

Before we dive into the TMD and TMT material systems and why we are so interested in studying them at their vdW limit, we first need to discuss the bonding within these material systems and how that impacts atomic and electronic structure. For this section, we will be borrowing terminology and descriptions from inorganic chemistry to study these 2-D and 1-D extended solid-state systems at a 'molecular' limit. While a molecular unit would behave drastically different than a system with extended bonding on the micron size-scale, the geometries and energies described at the 'molecular' limit translate nicely to the phenomena observed at the macroscale for our systems.

To describe our TMD or TMT system as a molecule, we can reduce the macrostructure down to a coordination complex. A coordination complex consists of a central atomic species, which is usually metallic and is termed the 'coordination center'. Surrounding the coordination center are any number of atoms or small molecules bound through covalent chemistry and are typically referred to as ligands. For our argument here, the coordination center of our complexes are transition metal atoms, and the ligands are chalcogens of a single species. For the TMD and TMT systems, typically the transition metals being studied are in Group IVB, VB, and VIB, as the transition metal will need to reach a relatively high oxidation state to coordinate with several chalcogen ligands.[111] Because of a higher oxidation state, the transition metal center can take on

higher numbers of ligands, which for both TMD and TMT, is 6 total ligands. With a coordination number of 6, there are two main geometric arrangements or conformations of these ligands: octahedral and trigonal prismatic. **Figure 7.2** shows both the octahedral and trigonal prismatic conformation of a 6-coordinated transition metal complex. An octahedral conformation is the most symmetric orientation, occupying the space group of O_h. The trigonal prismatic conformation is essentially the octahedral conformation, but with a plane of 3 ligands rotated to match the other plane of 3 ligands. The rotation breaks inversion symmetry of the complex and reduces the symmetry of the trigonal prismatic conformation to the space group of D_{3h}.

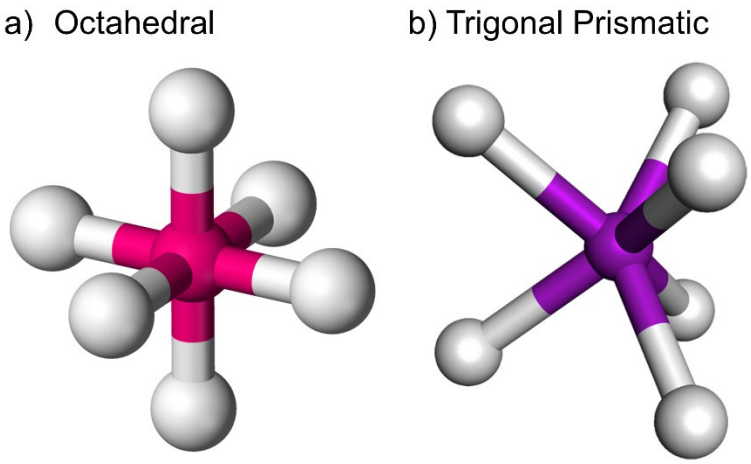

Figure 7.2 The two main conformations of a 6-coordinated metal center: (a) Octahedral and (b) Trigonal Prismatic. The pink and purple spheres are the transition metal center, surrounded by the 6 ligands, represented by white spheres.

While higher symmetry conformations tend to be more stable and lower in energy, the total energy of the system is dictated by the filling of the orbitals with electrons and can be the deciding factor for an octahedral or trigonal prismatic conformation. The filling of orbitals and relative energies of each orbital to be filled is an important concept in ligand field theory. For the TMD and TMT systems, the main driving force behind the atomic structure and resulting electronic structure can be viewed through the lens of ligand field theory. In short, ligand field theory describes the bonding and geometry of metal complexes as a result of the interaction between the molecular orbitals from the metal atom center and surrounding ligands.[112] Because we are focused on transition metal complexes, the orbitals of interest are the d-orbitals. **Figure 7.3** shows the 5 d-orbitals for the transition metal centers, with an additional schematic of how these orbitals break degeneracy for an octahedral complex.

The transition metals have 5 d-orbitals that are all degenerate in energy for when existing in elemental form. However, when ligands (or chalcogenides) bond and form complexes with the transition metal, the degeneracy of these d-orbitals is broken, and the way in which those orbital levels split is entirely dependent upon the conformation of the ligands. For an octahedral complex, if we drew an x-y-z coordinate system through the complex (in a way which preserves the highest symmetry), we would see that the ligands are oriented perfectly along the x-, y-, and z-axes. The bonding orbitals from the ligands are then interacting most strongly with the d_z^2 and d_x^2-$_y^2$ orbitals, and form degenerate bonding and anti-bonding molecular orbitals. Therefore, these two d-orbitals are split into a lower and higher energy level, where the higher energy level remains near the original energy of the d orbitals before splitting. The remaining d-orbitals, d_{yz},

d_{zx}, and d_{xy}, will typically form degenerate non-bonding orbitals and are the first to fill with any remaining d electrons. It is important to note that the splitting of the d-orbitals shown in **Figure 7.3** is purely schematic to show that the resulting molecular orbitals are separated by some energy gap, ΔE, and may remain degenerate with one or two other orbitals. How far above or below the molecular orbitals are in comparison to the original d-orbitals is entirely dependent upon the ligands in the system and the resulting oxidation state of the transition metal center.

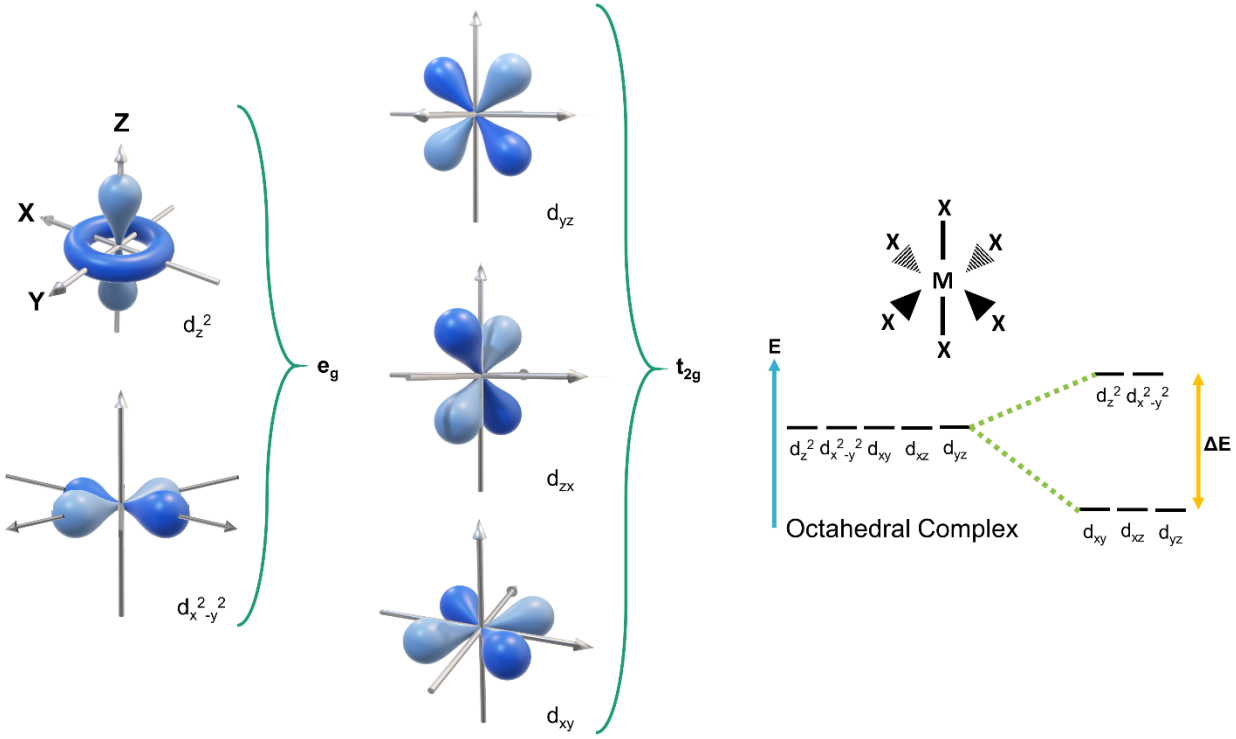

Figure 7.3 Ligand field theory used to describe the bonding and geometry in transition metal complexes. The splitting shown for the octahedral complex is purely schematic and not to scale for direction or magnitude of splitting.

The trigonal prismatic conformation of a 6-coordinated complex will undergo different splitting of the d-orbitals and affects the overall filling of those orbitals differently. The implications of different splitting and subsequent filling will be discussed in a later section, as well as how these two conformations can strongly influence the final properties of the extended TMC structure. There are also considerations to be made about the packing of these two different conformations in an extended network, which will be touched on in later sections as well.

7.3 Synthesis of transition metal chalcogenides

Before studying the atomic and electronic structures of the TMC material systems, we first need to synthesize them. Synthesis of single crystals of both TMD and TMT follow similar chemical vapor transport (CVT) synthetic protocols, where stoichiometric amounts of elemental transition metal and chalcogenide reagents are mixed (possibly with a transport agent) and sealed under vacuum in a quartz ampoule. The ampoule is then subjected to high reaction temperatures (between 600 and 900°C) and finally brought to room temperature through controlled cooling or

quenching, depending on the desired phase of the material.[113,114] In addition to single crystals, some drastic improvements have been made to directly synthesize a single layer of TMD material through chemical vapor deposition (CVD). This typically requires a growth substrate and a two-zone furnace, as the transition metal and chalcogenide have very different melting and boiling temperatures.[115] By controlling the amount of vaporized precursor, single-layer regions of a TMD can be grown on the substrate. For studies presented in this dissertation, the synthetic technique pursued follows CVT protocols, with an additional species required to study the vdW limit of TMD and TMT, which will be outlined in a later section. **Figure 7.4** shows an overall view of the experimental setup which can be utilized for both the CVT and CVD growth protocols. For CVT, only the tube furnace is required, because the reagents are contained in a sealed ampoule. For CVD, mass flow controllers will control the flow of gas to carry vaporized reagents to a growth substrate inside of the tube furnace, with any remaining volatile species removed from the system through a bubbler.

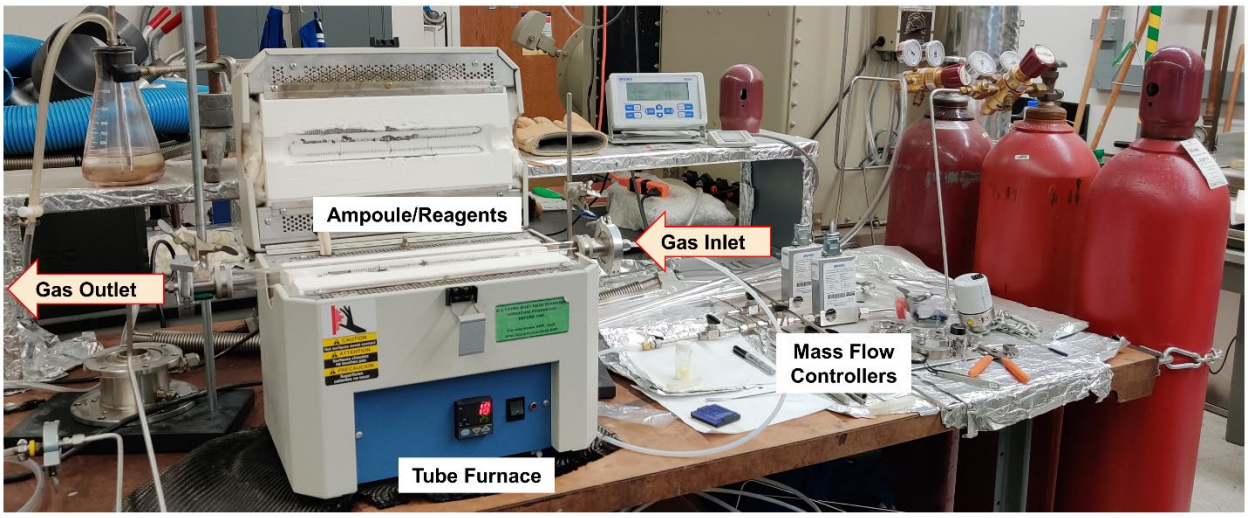

Figure 7.4 Experimental set up of a tube furnace which can be used for both chemical vapor transport and deposition growth protocols for transition metal dichalcogenides and transition metal trichalcogenides. Important regions have been labeled.

7.4 Transition metal dichalcogenides

The first TMC material family we will explore is one of the most popular in current condensed matter research on 2-D systems: Transition metal dichalcogenides. The excitement from the study of TMDs stems initially from the similarities to graphene, namely the 2-D, atomically thin sheets comprising the TMD crystal, which can be isolated in similar means as graphene.[116,117] Unlike graphene, there is more freedom of choice in terms of the chemical makeup of the layers of TMD crystal. Graphene forms its layered structure through flat sp^2 bonds, with no interconnecting bonds between sheets of material. To maintain the flat sp^2 bonding, the only other elements that can be completely exchanged into a similar lattice are boron and nitride to form h-BN. TMD, on the other hand, exhibits a different type of bonding, as described in **Section 7.2**, that is more akin to transition metal complexes. Therefore, we have a whole library of transition metals to insert as the coordination center and three different chalcogen species to insert as our 'ligands'. **Figure 7.5** shows the atomic model of a common TMD, Molybdenum Disulfide, for reference.

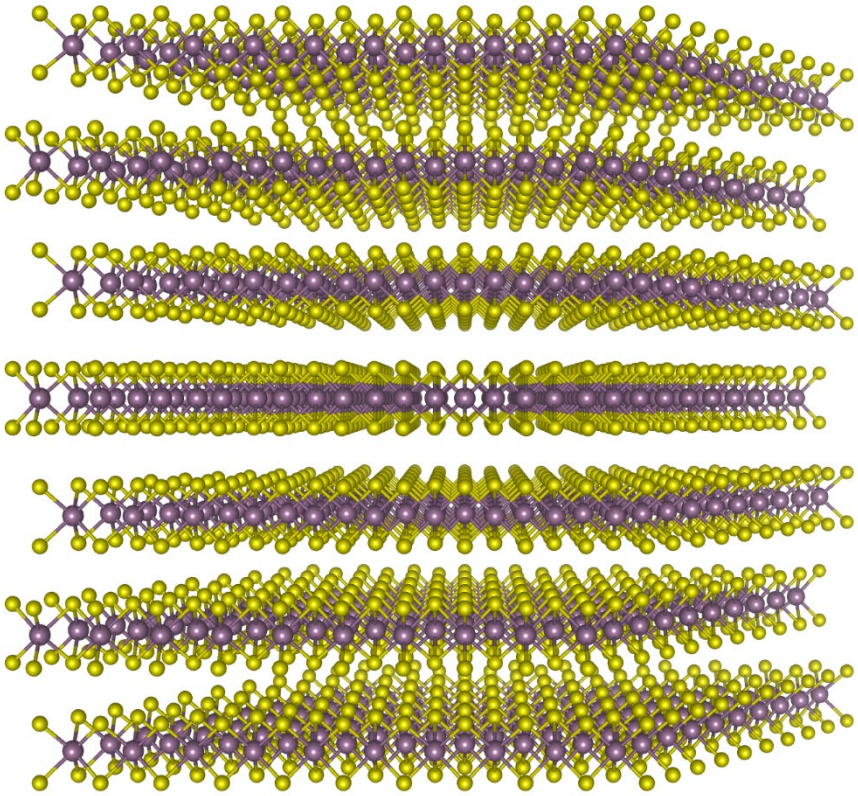

Figure 7.5 Atomic model of a layered transition metal dichalcogenide, MoS_2. Molybdenum and sulfur are represented by the purple and yellow spheres, respectively.

TMD have the chemical formula of MX_2, where M is a transition metal and X is a chalcogen. Typically, as briefly mentioned before, the transition metal groups we focus on for TMD are the Group IVB, VB, VIB, and occasionally VIIB. The MX_2 structure consists of strong bonding within a plane of atoms, forming 2-D sheets of material, which are assembled into a 3-D bulk crystal through vdW forces. In total, there are roughly 11 transition metals that readily form the TMD stoichiometry, and while not all transition metals form a TMD with every chalcogen, the family of TMD is relatively large and diverse.[109,113] Aside from varying chemical composition, the other main difference between graphene and TMD is their atomic structure. Graphene is perfectly flat and truly atomically thin due to its sp^2 bonding, however from **Figure 7.2**, we saw that TMD will have more of a sandwich structure, as evidenced in **Figure 7.6**. **Figure 7.6** shows both the basal plane (or top-down view) of a monolayer of TMD and the edge view of a monolayer of TMD, with one example from each of the two most common phases, 2-H and 1-T, shown. The nomenclature commonly used refers to the way the unit cell is built, where 2-H indicates the unit cell is comprised of a hexagonal lattice (H) from two layers (2), and 1-T indicates the unit cell is comprised of a trigonal unit cell (T) from one layer (1).

While the structure of TMD is not perfectly atomically thin like graphene, all bonding present is within the plane of a single sheet of TMD, resulting in a structure held together by vdW forces. Monolayers of TMD can be isolated and studied, showing more structural variation than graphene or h-BN. From the basal plane view in **Figure 7.2a** and **7.2b**, we see high symmetry of the crystalline lattice (3- or 6-fold), with the 2-H phase in **Figure 7.2a** almost looking identical to that of h-BN, with two different atomic sites present in a purely hexagonal

lattice. However, upon examination of the edge-view, we see that these materials are not purely one atom thick, but rather 3 layers of atoms thick, forming a sandwich structure. The middle layer, comprised of the transition metal, is sandwiched on top and bottom by the chalcogen layer.

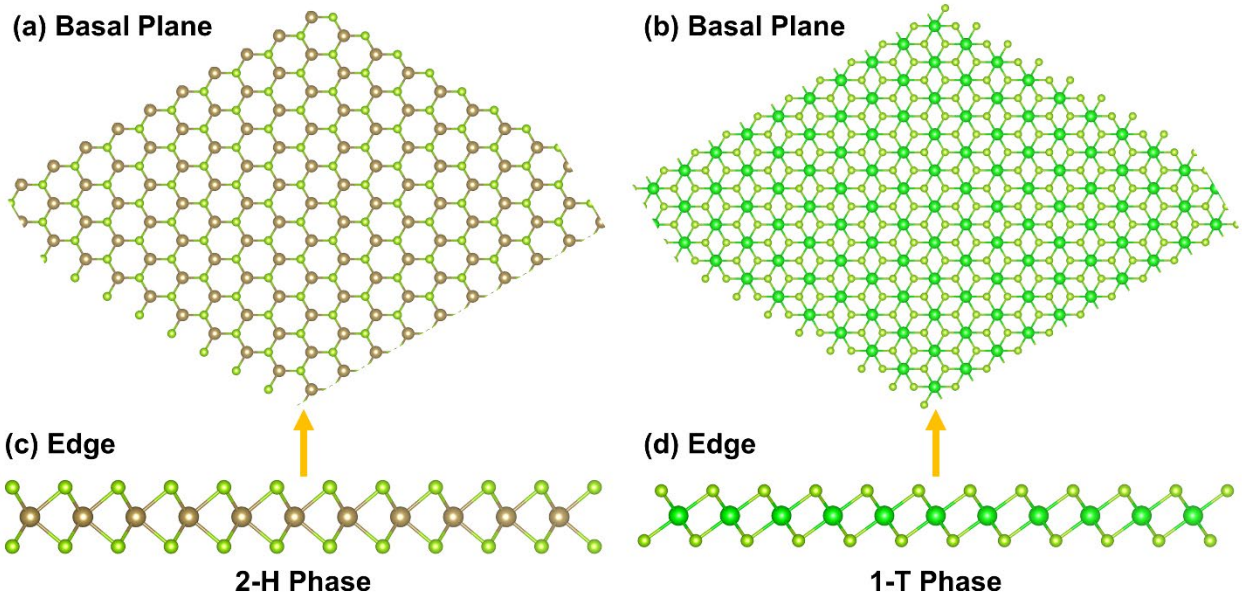

Figure 7.6 Atomic model of two common phases of transition metal dichalcogenides, both showing a sandwich structure. (a/b) Basal plane view of a single layer of a transition metal dichalcogenides in the 2-H and 1-T phase, respectively. (c/d) Edge view of the 2-H and 1-T phase, respectively.

With the transition metal central to the surrounding chalcogen layers, we see how the breakdown of this extended network can be approximated by a coordination complex as presented in **Section 7.2**. **Figure 7.6** also shows how the two different conformations presented earlier (octahedral and trigonal prismatic) result in the two commonly found phases. The 1-T phase retains an inversion symmetry and is best approximated by an octahedral coordination complex conformation, while the 2-H phase has lost its inversion symmetry, similar to the trigonal prismatic conformation. **Figure 7.7** shows a schematic which looks at how the difference in phase (or structure) results in different splitting of the degenerate d-orbitals, and ultimately alters the material property.

Figure 7.7a shows the octahedral conformation, which corresponds to the 1-T phase of TMD, and associated splitting of the d-orbitals, as discussed in an earlier section. From this schematic, we see that there is a single energy gap between the new molecular orbitals after splitting of degeneracy. **Figure 7.7b** shows the trigonal prismatic conformation, which corresponds to the 2-H phase of TMD, and associated splitting of the d-orbitals. From this schematic, we see that there are two energy gaps between the new molecular orbitals after splitting of degeneracy. But how do we know which combination of transition metal and chalcogenide will result in which phase, and why do some transition metals prefer one phase over the other? This question is answered easiest by looking at examples of each phase and how the d-orbitals would be filled with the d electrons. It is important to note that we assume empty, half-filled, and filled orbital energy levels are the most stable.

For the 1-T phase, a common TMD example would be $HfTe_2$, which is easily grown in thin films through molecular beam epitaxy and preferentially grows in the 1-T phase.[118] For the TMD, with a composition of MX_2, we assume the chalcogenide (Te) will have an oxidation state of -2, giving us an oxidation state for our metal (Hf) of +4. When working with $HfTe_2$, Hf only has 4 valence electrons, so as a TMD, Hf has 0 valence electrons. Therefore, when the split d-orbitals are 'filled', they actually remain empty because of the high oxidation state of Hf. Therefore, the preferred conformation would be octahedral, or 1-T phase, because of the high crystal structure symmetry and high number of degenerate orbitals.[112] As a result of the empty d bands, most of the Group IVB TMD are semiconducting in nature, as the lower energy orbitals will be completely filled, and electrons will need to be promoted to higher energy levels for transport.[109,119]

For the 2-H phase, a common TMD example is MoS_2, which has been extensively studied as a photoconductive and catalytically active material.[120,121] Again, as a TMD, we assume the chalcogenide (S) will have an oxidation state of -2, giving us an oxidation state for our metal (Mo) of +4. Mo has 6 valence electrons, so as a TMD, Mo will have 2 remaining valence electrons to fill the split d-orbitals. If MoS_2 had the 1-T structure, we see from **Figure 7.7** that the split d-orbitals would only be partially filled and would not be the most stable filling of empty, half, or full. However, the structure can adjust its symmetry slightly to the 2-H phase and create different splitting of its d-orbitals. Thinking back to ligand field theory, the splitting of the d orbitals is a result of the interaction between the molecular orbitals on the transition metal center and surrounding chalcogen 'ligands'. These interactions drastically change with the conformation change from octahedral to trigonal prismatic, resulting in a different splitting of the d-orbitals. Now, there is one orbital lowest in energy which would be filled first with the 2 remaining valence electrons from Mo. These two electrons would completely fill the d_z^2 orbital, thus creating a more stable structure than the 1-T phase.[112] This also correlates to the properties observed in MoS_2, where the valence d band is completely filled, resulting in semiconducting properties.[119]

Some research has recently been focused on altering the phase of a TMD obtained through electron doping. If a driving force in obtaining 2-H phase MoS_2 has to do with completely filling the d_z^2 orbital, then what would happen if we put an additional electron into the unit cell, giving Mo 3 valence electrons and the ability to fill all of the lowest energy d-orbitals in the octahedral splitting? It turns out the answer aligns well with what could be expected by looking at the molecular orbital filling: With an extra valence electron through doping, MoS_2 can be made to shift its phase from 2-H to 1-T, as all three d-orbitals of lowest energy could be half-filled in an octahedral conformation. Experiments using chemical doping with alkali metals have shown these phase changes.[122–124] This also drastically impacts the properties, where 1-T MoS_2 now has a half-filled band and is metallic in behavior, becoming a better conductor and enhancing certain properties such as supercapacitors.[125,126]

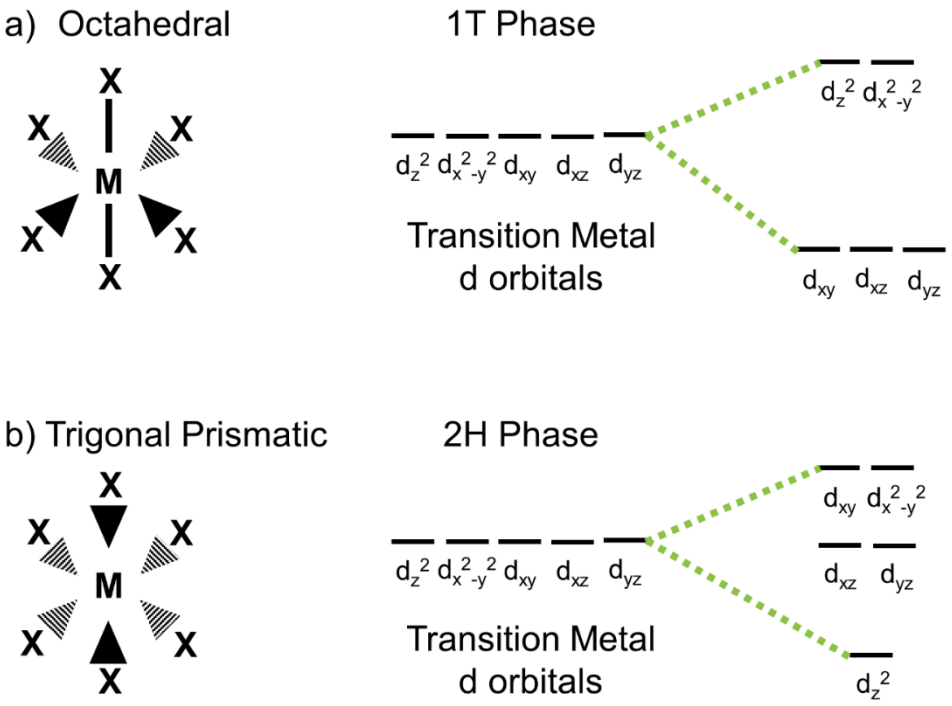

Figure 7.7 Schematic of the two different conformations of 6-coordinated complexes, and their relation to common phases of transition metal dichalcogenides observed. (a) Octahedral conformation typified by the 1-T phase of transition metal dichalcogenides. Associated splitting of the once-degenerate d orbitals. (b) Trigonal prismatic conformation typified by the 2-H phase of transition metal dichalcogenides. Associated splitting of the once-degenerate d orbitals.

However, an important distinction to make here is that the phase and electronic properties of the material may depend on the filling of the d-orbitals, but the size of the transition metal and size of the chalcogenide can also play a role in the structure or phase obtained as well. Smaller transition metals and smaller chalcogenides pack differently than the larger transition metals and larger chalcogenides, and different combinations thereof will require different space to occupy without strain.[112]

The possibility of a phase change is another degree of freedom that TMD exhibit and graphene does not and has powerful ramifications. Multiple phase types allow for further control and tailoring of material properties through the fine atomic structure. Understanding the different mechanisms through which these structural changes can happen, and if they are reversible or not, broadens the extent to which multiple types of these structures can be combined to create heterostructures that benefit from the properties of each underlying material.[6] The fine control over the atomic structure mentioned for MoS_2 is typically only observed at the monolayer limit, as there is more freedom of movement without additional layers interacting. Therefore, it is important we make a clear distinction between the monolayer or 2-D limit of the TMD materials family vs. their bulk crystal counterpart. We will explore this in more detail in **Section 7.6**.

7.5 Transition metal trichalcogenides

A close relative of the transition metal dichalcogenides is the transition metal trichalcogenides family. The TMT have the chemical formula of MX_3, where M is a transition

metal and X is a chalcogen. Typically, as briefly mentioned before, the main transition metal groups we focus on for TMT are the Group IVB, VB, and VIB, although the Group VIB TMT are more amorphous in nature.[114,127,128] In total, there are roughly 7 transition metals that readily form the TMT stoichiometry, with a wide array of material properties, from semiconductors that are photoactive, to charge density wave and superconducting materials.[128,129] Similar to the TMD material family, TMT are also a vdW structure, but of different dimensionality. The MX_3 structure consists of strong bonding within a chain of atoms, forming 1-D trigonal prismatic chains of material (instead of 2-D sheets), which are assembled into a 3-D bulk crystal through vdW forces.[128]

Figure 7.8 shows the crystal structure of the TMT material family. **Figure 7.8a** readily shows the vdW nature of the makeup of these crystalline materials, where the individual chains of atoms do not exhibit any strong interchain bonding (bonding between two different chains). However, **Figure 7.8b** highlights the strong intrachain bonding (bonding within the same chain) along the chain axis. While the bonding within these chains is similar to the bonding observed in TMD, and even some nomenclature (trigonal prismatic chains) carries over, there are some subtle differences that prevent us from making similar comparisons to the molecular orbital splitting described in **Figure 7.7**. As seen in **Figure 7.8a**, while there is no interchain bonding, there is some intrachain bonding that is rather different, specifically the bond between two of the chalcogen atoms themselves. The main implication of this chalcogen-chalcogen bond is the resulting oxidation state of the metal center, as there is some electron sharing happening 'outside' of this metal-chalcogen bonding.[130] Not every TMT exhibits these chalcogen-chalcogen bonds; they are entirely depending upon the size and overlap of the transition metal/chalcogenide combination.[112] The geometry and vdW bonding is not affected by these chalcogen bonds.

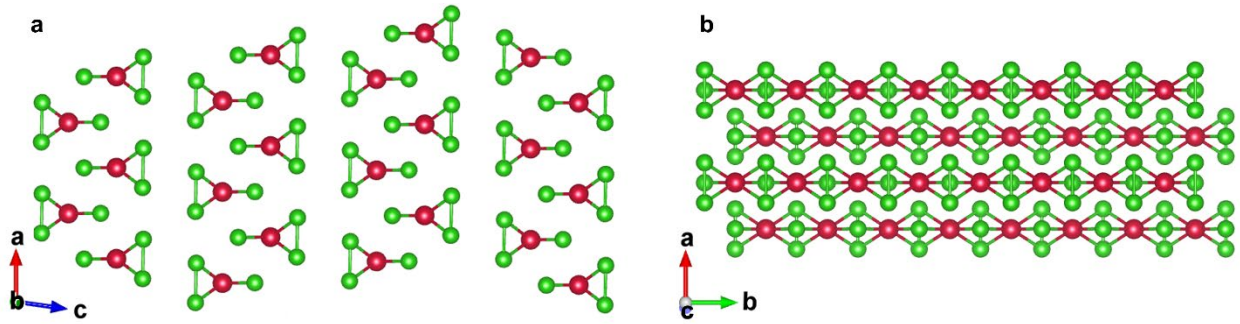

Figure 7.8 Atomic model of the crystal structure of a transition metal trichalcogenide, comprised of trigonal prismatic chains. (a) End-view of the trigonal prismatic chains, showing the vdW gap between each chain. (b) Side-view of the trigonal prismatic chains showing the strong bonding along the chain axis. The transition metal center and surrounding chalcogens are represented by the red and green spheres, respectively.

Unlike the TMD, which present two common phases (2-H and 1-T), the TMT only bond as trigonal prismatic chains in their bulk crystalline form. There has been impactful research describing the possibilities and effects of tuning between two phases in TMD, resulting in a drastically different atomic structure and resultant electronic structure.[131] Similar results have not been shown for the TMT material family in bulk form, and up until recently, no work had achieved the isolation and study of single atomic chains of TMT. We will explore the study of single chains of TMT in **Section 7.6**.

7.6 The van der Waals limit of transition metal chalcogenides

Because of their elemental and structural diversity, TMD have exhibited a relatively large array of interesting properties and applications, from catalysis to energy production.[125,132–135] The array of properties are exhibited in bulk crystals of TMD, however their interesting geometry as atomically thin sheets also presents an interesting aspect to their application, allowing for the creation of atomically thin devices.[23,121,136,137] For this reason, the TMD are regularly synthesized or isolated to their vdW limit as a monolayer. Initially, the TMD presented themselves as another interesting, layered material that could be isolated at the monolayer limit like graphene. However, because the sheets are built of relatively heavier atoms, and have a finite thickness to them, isolating TMD to the monolayer limit can impact their electronic structure as well. One of the seminal results demonstrating the ability to tune material properties based on layer number was work done by Feng Wang's group at UC Berkeley. In their work, the group demonstrated a strong enhancement of the photoluminescence of MoS_2 at the monolayer limit, indicating an indirect-direct bandgap evolution.[138]

These results created a flurry of excitement, as layer number was a unique handle of the TMD material family to tune and alter their material properties and was purely based on size confinement of the material, with no chemical alteration required. Fortunately for TMD, there are well-developed exfoliation techniques that can be used to isolate the monolayer limit (developed through the study of graphene and h-BN), and CVD growth techniques previously mentioned to directly grow a monolayer of TMD. **Figure 7.9** shows electron microscopy images of the monolayer limit of MoS_2 (**Figure 7.9a**) and bulk crystals of TiS_2 (**Figure 7.9b**). The monolayer of MoS_2 forms triangular crystal domains, representative of the 3-fold symmetry in the monolayer 2-H phase presented in **Figure 7.6.** Bulk crystals of TiS_2 are hexagonal, representative of the 6-fold symmetry present in the bulk 2-H phase. An important note here is that even as a monolayer, the TMD are readily isolated and characterized through standard synthesis and analytical methods. At atomic thinness, the resulting monolayer can be hundreds of nanometers in width, allowing for easy optical identification of the layers.

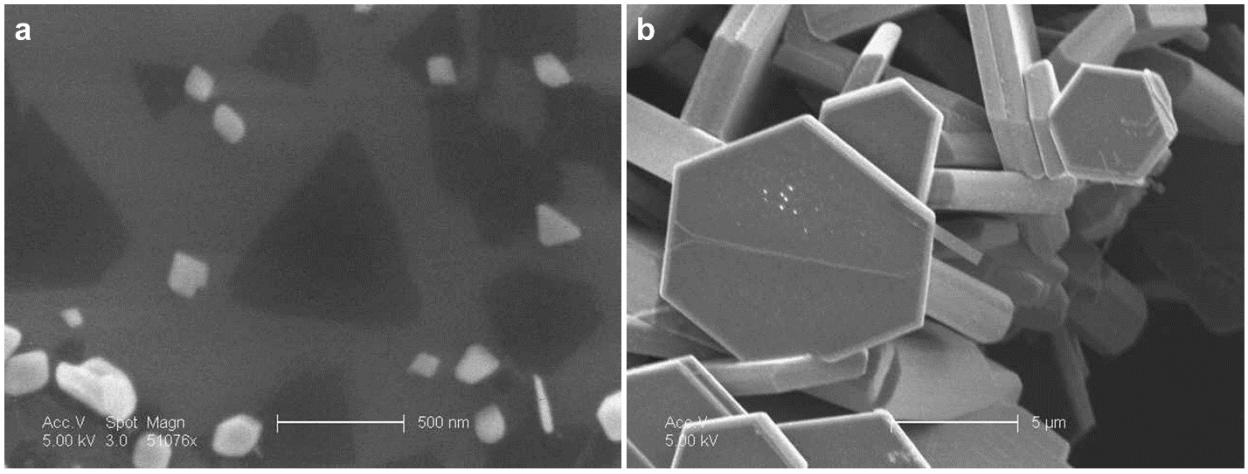

Figure 7.9 Electron microscopy images of transition metal dichalcogenides grown through (a) chemical vapor deposition and (b) chemical vapor transport. (a) Single layer MoS_2 forming triangular domains. Scale bar measures 500 nm. (b) Bulk single crystals of TiS_2 forming hexagonal platelets. Scale bar measures 5 µm.

The TMT material family is tricker to study at the true vdW limit as a single chain. While comprised of weaker vdW bonding in the 3-D structure, these atomic chains interact with many neighboring chains, which stabilizes their structure and prevents them from breaking or degrading. Furthermore, as the trigonal prismatic chains are quantized in two dimensions, characterizing the exfoliation or isolated growth of a single chain is difficult and would require high resolution microscopy techniques instead of typical optical microscopy. Some work has been attempted at thinning down the TMT to atomic thinness, with results getting down to sub-5 nm in thickness.[110] Even electron transport on $NbSe_3$ samples sub-20 nm in thickness have showed interesting modulation of the charge density wave transition temperatures, indicating that size quantization of TMT could result in additional modification and a method to tailor TMT material properties through size quantization as well.[139]

Figure 7.10 shows electron microscopy images of two common TMT materials: ZrS_3 and $ZrTe_3$. Both show a quasi-1-D needle-like crystal, a result of the 1-D trigonal prismatic chains comprising the bulk crystalline material. While small crystals of material can be easily formed, as seen in **Figure 7.10a**, they are nowhere near the single-chain limit. **Figure 7.11** shows an atomic model of what the single-chain limit could look like for a TMT. However, the overall structure, as will be described throughout this dissertation, can alter dramatically without vdW interactions from neighboring chains. To study those structural changes and behavior of single atomic TMT chains, the isolation and characterization of an atomically thin 1-D chain of material needed to be developed, similar to initial work required to isolate and study atomically thin 2-D sheets of graphene or TMD.

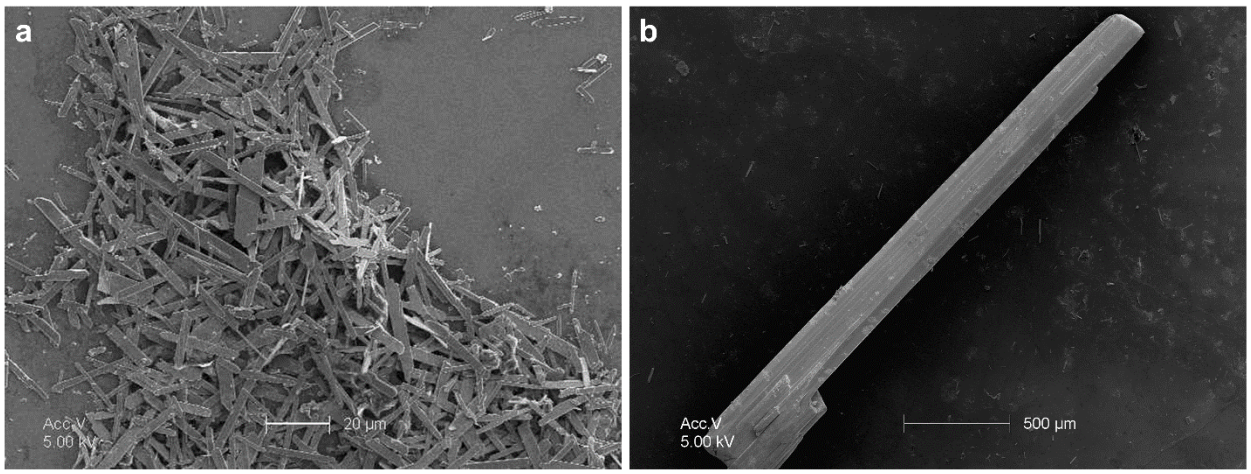

Figure 7.10 Electron microscopy images of transition metal trichalcogenides grown through chemical vapor transport. (a) Small, needle-like bulk crystalline ZrS_3. Scale bar measures 20 µm. (b) Large, bulk crystalline $ZrTe_3$. Scale bar measures 500 µm.

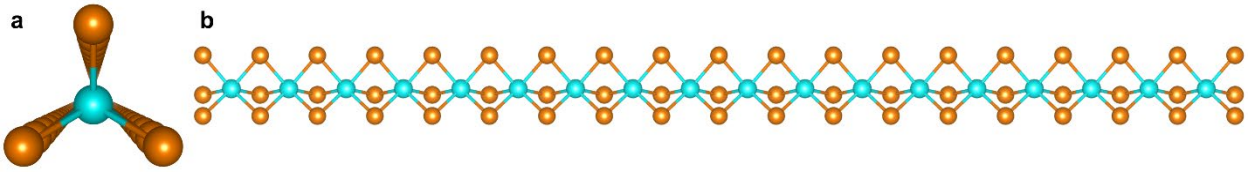

Figure 7.11 Atomic model of a single chain of TMT isolated from bulk. (a) End-view of the trigonal prismatic chain. (b) Side-view of the trigonal prismatic chain. The transition metal center and surrounding chalcogenides are represented by the blue and orange spheres, respectively.

7.7 Encapsulation technique

In order to study the single-chain limit of TMT, we first have to develop a method to isolate a single chain. Classic exfoliation methods, or "top-down", techniques used to study monolayer TMD have been attempted before, but could never achieve single-chain TMT.[110,139] Therefore, we can instead turn to "bottom-up" approaches, and start with elemental reagents. To isolate a single chain, however, we need to stop the growth of additional chains after a single chain has formed. One route to do so would be to physically confine the material growth space so that there would only be enough physical space for a single chain to grow (which would be smaller than 1 nm). A material that could physically confine the TMT chains to less than 1 nm is carbon nanotubes (CNT), which have a hollow cavity that has been filled with a host of different materials prior to these studies.[140–142] Many of these filling methods utilize solution-phase filling of species that are dissolved in a solvent, which is then taken into the hollow cavity of CNT through capillary forces.[142] Unfortunately, the TMT materials are not soluble in solvents, and are typically grown via high temperature CVT, as discussed in **Section 7.3**. Some results had been shown to be able to fill CNT with chalcogenides at elevated temperatures through vapor-phase filling.[143]

My colleague, Dr. Thang Pham, was the first to extend the vapor-phase filling of CNT to the TMT material family, and showed the successful filling and isolation of a single chain of $NbSe_3$ inside the hollow core of CNT and boron nitride nanotubes.[144] **Figure 7.12** shows a simplified schematic of the filling of CNT with TMT. Typically, vaporized transition metal and chalcogenide elemental precursors will migrate and fill the CNT, whereupon they react and form the TMT chains directly inside of the CNT. An added benefit of encapsulating the chain of TMT within nanotubes, is that the chains are protected from environmental degradation, allowing for easier material handling and sample preparation. **Figure 7.13** shows high-resolution TEM images of $NbSe_3$ chains encapsulated within nanotubes. The structure of numerous (~20) chains encapsulated by a CNT of inner diameter 3.86 nm resembles that of the bulk crystal with signature one-dimensional chains oriented along the axis of the nanotube. The number of $NbSe_3$ chains isolated is dictated strictly by geometrical constraint, meaning nanotubes with smaller inner diameters can access fewer and fewer chains. In doing so, we see that triple-, double-, and single-chain $NbSe_3$ can be encapsulated within nanotubes with successively smaller inner diameters of 2.49 nm, 1.87 nm, and 1.21 nm, respectively. **Figure 7.13** demonstrates, rather remarkably, that isolated single chains of TMTs can indeed be stabilized, isolated, and studied to the extent of the TMD family.

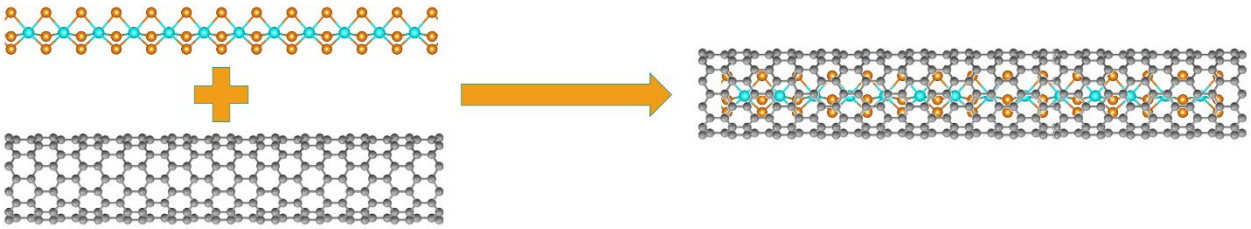

Figure 7.12 Simplified filling schematic of transition metal trichalcogenide chains inside of carbon nanotubes.

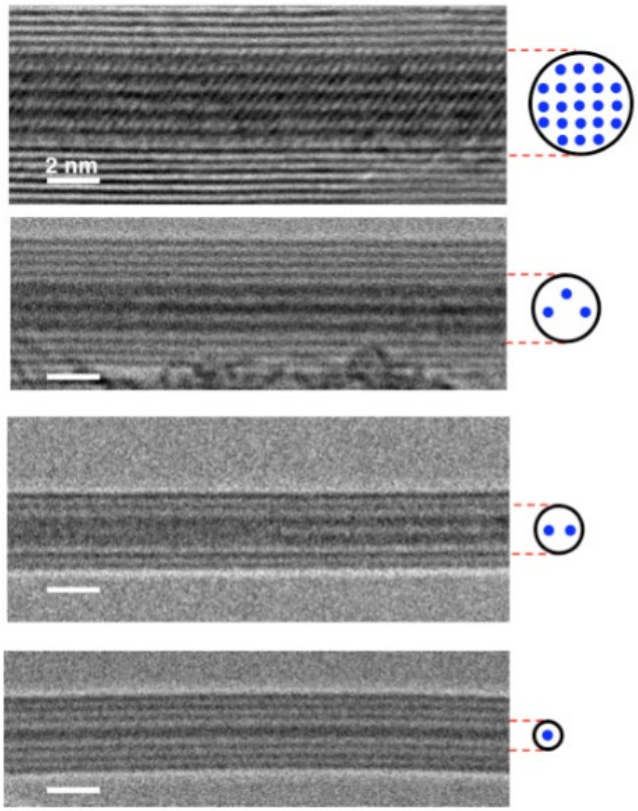

Figure 7.13 Isolation of 1-D TMT materials down to single-chain limit. High-resolution TEM images of many (A), triple (B), double (C) and single chain (D) of prototypical TMT $NbSe_3$ encapsulated within CNT (multi-, triple-, and double-chain filling) or a BNNT (single-chain filling). The simplified cross- sectional schematics show different numbers of chains encapsulated in tubes with different inner diameters. In the multi-chain filling, atoms appear bright (over-focus); in the triple-, double-, and single-chain limit, atoms appear dark (under-focus). Image credit to Dr. Thang Pham.[144]

In addition to the varying number of TMT chains isolated, other structural changes in the few- and single-chain limit of $NbSe_3$ were observed, such as few-chain spiraling and charge-induced torsional wave instabilities of single chains.[144] These results were incredibly impactful and insightful into the possibility of structural manipulation of atomic chains through encapsulation, which should ultimately result in altered electronic structure and properties. Additionally, the filling of CNT through a vapor-phase technique greatly benefits the study of the few- and single-chain limit of TMT, as all TMT members can be synthesized through high

temperature CVT methods. Therefore, the CNT encapsulation process presented here is a robust and transferrable method to study the few- and single-chain limit of TMT. The following chapters in this dissertation will utilize this transferrable technique to access the growth of a whole host of unique chain-like and related structures inside the hollow core of CNT. Characterization of the atomic and electronic structures will be described in greater detail in each chapter as it relates to the specific material of interest, as well as the associated modifications to the atomic and electronic structure associated with the extreme physical confinement of the TMT chains.

7.8 Characterizing encapsulated species

Once the encapsulated chains of TMT have been successfully synthesized, the next step is to characterize and elucidate the filled structure. Because of the extreme atomic confinement of these systems, we rely heavily on electron microscopy techniques to achieve the spatial resolution necessary for resolving the encapsulate TMT chains. Typical analysis of the as-synthesized TMT@CNT (TMT-filled CNT) is first examined with standard transmission electron microscopy, then atomic-resolution scanning transmission electron microscopy. Potential characterization of the elemental composition can be followed up by energy dispersive spectroscopy or electron energy loss spectroscopy.

7.8.1 Transmission electron microscopy

The first technique we employ to study these encapsulated systems is transmission electron microscopy (TEM). The theory behind TEM is described in **Part I**, but in brief, as the electron beam passes through the sample, the electrons interact with the sample itself. After interacting with the sample, the electrons are reconstructed and strike a phosphorescent screen to produce an image of the sample. **Figure 7.14** shows a standard TEM image of an encapsulated TMD system, where filled CNT regions have been marked on the image. Even in standard TEM, we can begin to see the underlying crystal lattice of the encapsulated material, as evidenced by the patterned filling observed. Because the structure follows the walls of the CNT, we can confidently state the crystalline structure is inside the hollow core of the CNT. More details about the encapsulated TMD systems will be discussed in **Chapters 12**, **13**, and **14**. A standard TEM image of an encapsulated TMT system can be seen in **Figure 7.15**. The chain-like nature of the filling is readily apparent, and both filled and empty sections of the CNT have been labeled to highlight the easily spotted difference between an encapsulated structure and a still-empty CNT. More details about the encapsulated TMT systems will be discussed in **Chapters 8**, **9**, **10**, and **11.**

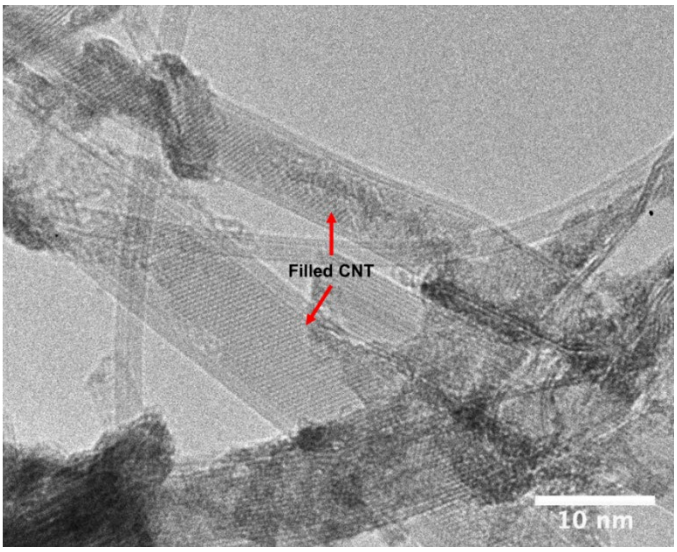

Figure 7.14 Standard transmission electron microscopy image of a carbon nanotube filled with a transition metal dichalcogenide nanoribbon. Data collected in collaboration with Derek Popple.

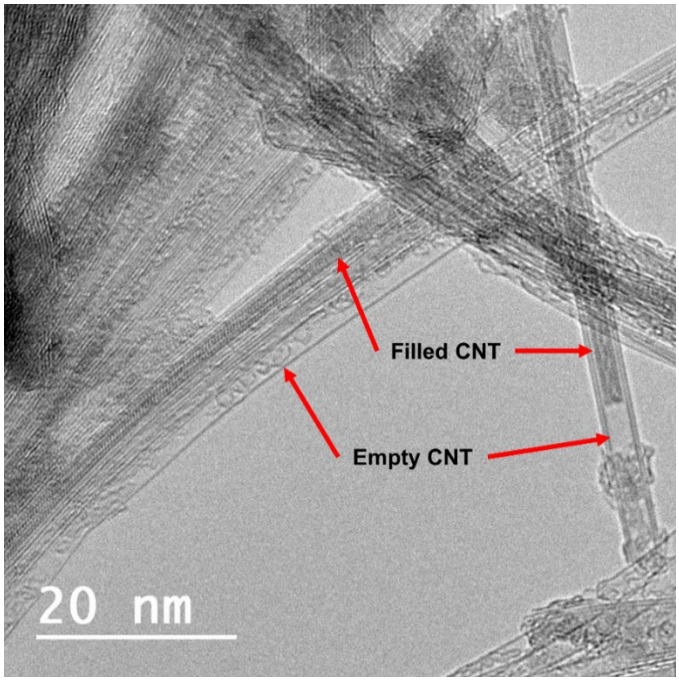

Figure 7.15 Standard transmission electron microscopy image of a carbon nanotube filled with transition metal trichalcogenide chains.

7.8.2 Scanning transmission electron microscopy

TEM gives us a good overview of the filling achieved utilizing the encapsulation technique. However, if we want to study the atomic structure in greater detail to see what effects encapsulation has on the interior structure, then we must pursue atomic-resolution imaging. Scanning transmission electron microscopy (STEM) is a similar technique to TEM, where an electron beam is formed, passed through a sample, and the interactions of the electron beam with

the sample is used to produce an image. However, in STEM, instead of a parallel beam of electrons that is exposed to the entire sample at once, the electron beam is focused into a probe, which scans across the sample to form an image (similar to scanning electron microscopy).

Figure 7.16 shows a schematic of the imaging process in STEM. The electron beam scans back and forth across the sample surface in small, pre-determined steps depending on the probe size. At each position on the sample, depending on the composition of the sample, different levels of scattering of the electron beam occurs. If there is no sample where the beam is present, the beam transmits without incidence, as indicated by the Bright Field (BF) transmission line.[145] When the beam interacts with a portion of the sample, the beam is diffracted as indicated by the Dark Field (DF) and High-Angle Annular Dark Field (HAADF) transmission lines. The difference between DF and HAADF diffraction depends on the elemental composition of the sample, where heavier Z elements typically scatter the electron beam more, resulting in more HAADF signal, and lighter elements scatter the electron beam less, resulting in more standard DF signal.[145] In STEM, the image produced is a reconstruction of only portions of the electron beam that scatters to the angles selected for the detector, typically HAADF. Therefore, by changing the angle of the detector, we select differently scattered electrons transmitting through the sample, and can block out the BF transmission (which is only indicative of no sample). In doing so, our images have reverse contrast to standard TEM images, where the background (no sample) is dark, and heaver Z regions of the sample are brighter in contrast. The spatial resolution of the image is dictated by the size of the electron beam probe formed, where a smaller probe interacts with more finite regions of the sample and increases resolution.[145] The microscope used in our experimental studies is the TEAM 0.5 microscope at the National Center for Electron Microscopy, more details for which can be found in later chapters.

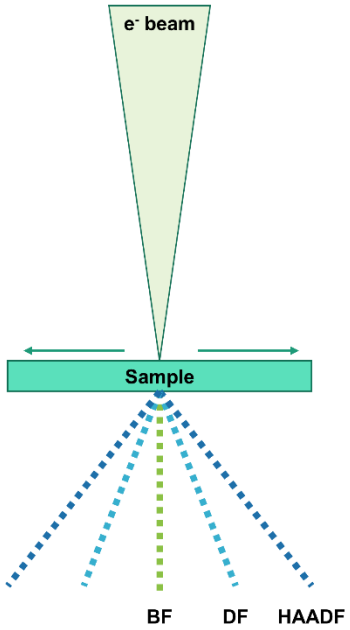

Figure 7.16 Schematic of the probe formation and scattering in scanning transmission electron microscopy.

For the TMT and TMD systems being studied in this dissertation, we are imaging relatively high Z elements, especially compared to the carbon that forms the nanotubes.

Therefore, HAADF detectors allow for easy imaging of these encapsulated species and provides detailed information about the atomic structure that cannot be obtained through standard TEM. **Figure 7.17** shows standard STEM images of encapsulated structures. **Figure 7.17a** shows an encapsulated TMD structure, where the atomic resolution allows for easy identification of the specific phase of the material (1-H monolayer). **Chapter 12** will discuss this structure in more detail. **Figure 7.17b** shows encapsulated chains (triple-chain to be exact) of $ZrTe_3$. Spiraling of the few-chain limit can be seen, which will be discussed in **Chapter 9**.

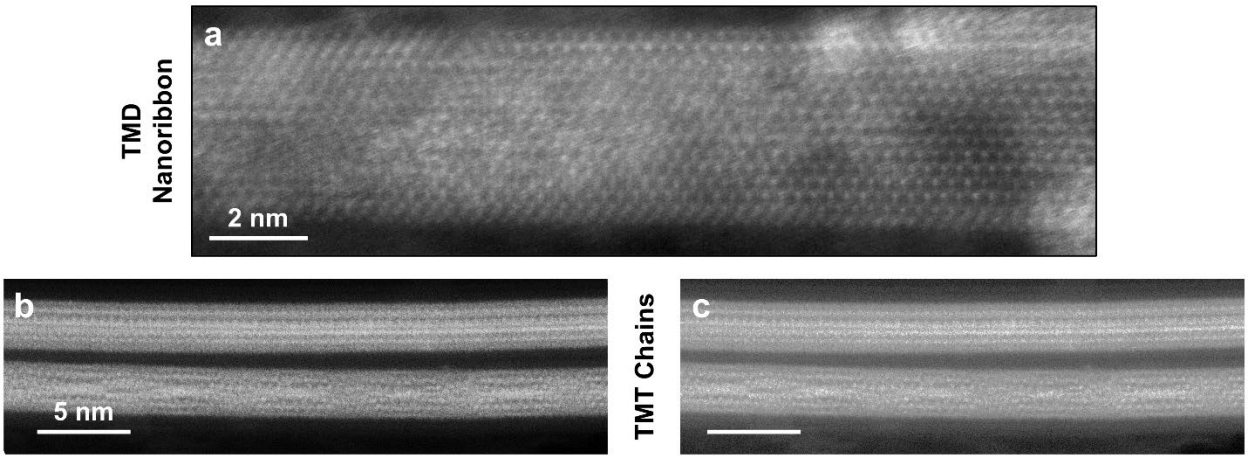

Figure 7.17 Standard scanning transmission electron microscopy images of carbon nanotubes filled with (a) transition metal dichalcogenide nanoribbon and (b/c) transition metal trichalcogenide chains. The images shown in (b) and (c) are of the same sample, but with different image contrasts to show the carbon nanotube walls in (c). Data collected in collaboration with Dr. Jeff Cain.

7.8.3 Electron energy loss spectroscopy

The atomic structure of the encapsulated structures can be elucidated in great detail via STEM imaging. Additional chemical information can be obtained through the same process utilized to generate STEM imaging, but instead of selecting for different diffraction angles, we focus instead on the energy of the electrons before and after interaction with the sample. As the electrons interact with the sample, they scatter either inelastically (energy lost) or elastically (energy conserved).[146] The inelastically scattered electrons typically lose energy equivalent to certain energetic transitions unique to each atomic species. Measuring the energy loss of these electrons is done through electron energy loss spectroscopy (EELS). The electrons that scatter elastically contribute to a zero-loss peak in the spectrum, which is usually cut out of the energy range as no identifying information is found in this peak.[146] However, the electrons that inelastically scatter interact strongly with the electron cloud surrounding each atomic species within the sample. Energy from the electron beam will be transferred to an electron of the atomic species, and if the interaction is strong enough, the electron within the atomic species will be knocked free from its orbital, ionizing the atomic species.[146] The energy required to remove an electron from an atomic orbital is unique to each atomic species, so the measured electron energy loss is indicative of the elemental species present which could generate such an energy transition.

Figure 7.18 shows a typical energy window observed for EELS. The material being studied contained titanium and tellurium, for which the peaks are labeled. Two distinct peaks are

seen that correspond to titanium, while there is a more broad, subtle peak observed for tellurium. Unfortunately, while the TMD and TMT materials are excellent species to analyze via STEM due to their high Z contrast, EELS is not as sensitive for these heavier Z elements as it is for lighter elements. Typically, the sensitivity (or sharpness) of EELS peaks observed starts to deteriorate for elements beyond the 3d transition metals.[147] Therefore, any quantified data is tough to obtain for the TMD and TMT systems, especially at their vdW limit, but EELS can provide some clarification about certain species present. For heavier elements, energy dispersive spectroscopy can provide clearer information for identification, and is the spectroscopy typically utilized for these systems. Even still, the small size of these encapsulated structures provides very little signal, pushing the capabilities of both spectroscopic techniques. The following chapters of **Part II** will explore the spectroscopic identification of these encapsulated systems and how the low signal can still generate meaningful data to work with.

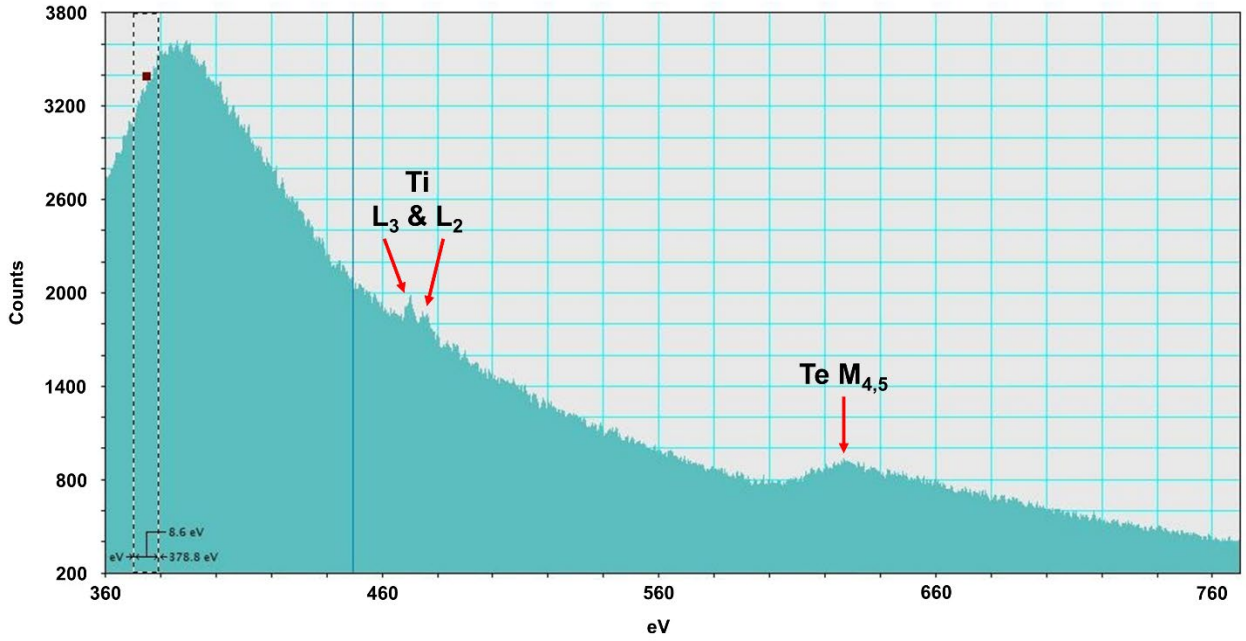

Figure 7.18 Standard electron energy less spectrum of a sample containing titanium and tellurium. The edges of titanium and tellurium have been labeled. Data collected in collaboration with Dr. Jeff Cain.

7.9 Conclusion

Here, we explored the fundamentals behind the isolation and study of single atomic layers of TMD, which benefitted from previous work completed on graphene and h-BN. However, similar methods of isolation and study do not extend readily to TMT, which should exhibit just as rich a field of emergent phenomena at the vdW limit, as initially shown for the single-chain limit of $NbSe_3$. We explored the encapsulation process developed to confine the material growth of TMT down to the few- and single-chain limit, and the associated analytical techniques required to study these encapsulated systems in more detail. The processing-structure-property relationships in solid-state vdW materials are explored to greater detail in the following chapters. The work presented in **Part II** extends the encapsulation work to material systems of TMT chains, TMD nanoribbons, and exotic variations therein. Following the work presented

here, we will redefine the expectations for isolating systems down to the sub-nanometer size limit, and the vast array of emergent phenomena waiting to be discovered through atomic confinement of vdW systems, such as TMD and TMT.

Chapter 8: Inducing Drastic Electronic Structure Changes via Physical Confinement – Metal-Insulator Transition in Quasi-One-Dimensional HfTe3 in the Few-Chain Limit

Special thank you to Dr. Thang Pham and Dr. Sehoon Oh for their assistance on this project.

Keywords: Hafnium Tritelluride, Encapsulation, Transmission Electron Microscopy, Scanning Transmission Electron Microscopy, Density Functional Theory, Metal-Insulator Transition, Electronic Structure, Atomic Structure

The initial encapsulation study performed by Dr. Thang Pham set the stage for pursuing the 1-D vdW limit of the transition metal trichalcogenide family. The encapsulation technique provides much more than the physical confinement of the material of interest. The surrounding nanotube provides a physical barrier between the interior material and the surrounding environment, greatly improving the material handling and stability. For this reason, we can begin to explore material systems, such as hafnium tritelluride, that have suffered from their instability in ambient environments. The encapsulation technique provides a means of furthering the study of materials plagued by their own degradation, while simultaneously exploring their atomic and electronic structure at the vdW limit.

8.1 Motivation to pursue encapsulation of other transition metal trichalcogenides

Constraining the physical size of solids can dramatically influence their electrical, optical, magnetic, thermal, and mechanical properties. Intrinsically low-dimensional materials, including van der Waals (vdW) bonded quasi-two-dimensional compounds (exemplified by graphite, hexagonal boron nitride, and transition metal dichalcogenides (TMD)) and quasi-one-dimensional vdW compounds (exemplified by transition-metal trichalcogenides (TMT)), are particularly intriguing, in that the bulk state already presents weakened inter-plane or inter-chain bonding, which leads to strong structural, electronic, and phononic anisotropy.[6,148] Constraining the dimensions of these 2-D vdW materials down to "atomic thinness" can result in various degrees of additional size quantization with profound consequences.

Therefore, it is a reasonable expectation that the 1-D vdW TMT materials would exhibit additional size quantization phenomena with novel and unexpected properties when isolated down to the few- and single-chain limit. As discussed in the introductory chapter, the prototypical quasi-one-dimensional TMT conductor $NbSe_3$ was successfully synthesized in the few- to single-chain limit by my colleague Dr. Thang Pham, and unusual torsional wave instabilities were observed.[144] The driving force for the instabilities was proposed to be charging of the chains, which suggests that other TMT compounds with closely related crystal structure might exhibit similar torsional wave instabilities in the few- or single-chain limit.

8.2 Material fundamentals of the quasi-one-dimensional $HfTe_3$

Here we report the successful synthesis and structural characterization of $HfTe_3$ within the hollow cores of multiwall carbon nanotubes (MWCNT). The selectable inner diameter of the MWCNT constrains the transverse dimension of the encapsulated $HfTe_3$ crystal and thus, depending on the inner diameter of the nanotube, $HfTe_3$ specimens with many chains (~20), down to few chains (3 and 2), and even single isolated chains, are obtained. The MWCNT sheath

simultaneously confines the chains, prevents oxidation in an air environment, and facilitates characterization *via* high resolution transmission electron microscopy (TEM) and scanning transmission electron microscopy (STEM). Together with complementary first-principles calculations, we find a coordinated interchain spiraling for triple and double chain $HfTe_3$ specimens, but, in sharp contrast to $NbSe_3$, long-wavelength intrachain torsional instabilities are markedly absent for isolated single chains. Instead, $HfTe_3$ shows a structural transition via a trigonal prismatic rocking distortion to a new, unreported crystal phase, concomitant with a metal-insulator transition, as the number of chains is decreased below four.

$HfTe_3$ is an intriguing, but little studied, Group IVB TMT with a trigonal prismatic linear chain structure very similar to that of the Group VB TMT $NbSe_3$.[110,149,150] **Figure 8.1** shows the quasi-one-dimensional crystal structure of $HfTe_3$. Each chain distributes the Te atoms in an isosceles triangle, with the unit cell of $HfTe_3$ containing two trigonal prismatic chains with an inversion center. A characteristic that has inhibited extensive study of $HfTe_3$ is extreme air sensitivity, even for bulk single crystals.[151] Some studies suggest that metallic $HfTe_3$ supports a charge density wave (CDW) and possibly filamentary superconductivity, but there are significant discrepancies between reports. [129,151] Single crystal specimens likely undergo a CDW phase transition at T_P=93 K, while T_P for polycrystalline specimens is ~80 K. Although single crystals have not shown superconductivity down to 50 mK, polycrystalline samples can apparently undergo a superconducting phase transition at T_c=1.7 K.[129,151]

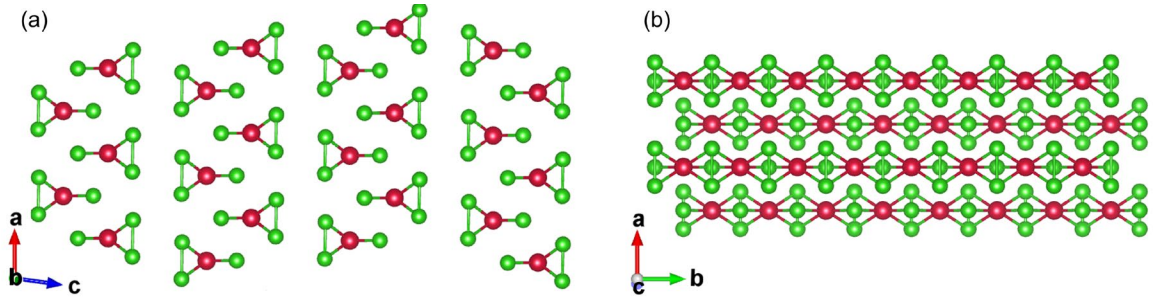

Figure 8.1 Crystal structure of $HfTe_3$ chains in bulk. Crystal view along the (a) *b* axis and (b) *c* axis, highlighting the quasi-one-dimensional nature of the trigonal prismatic $HfTe_3$ chains. Hf and Te atoms are represented by red and green spheres, respectively.

8.3 Synthesis methods of $HfTe_3$@CNT

$HfTe_3$ is synthesized within carbon nanotubes using a procedure similar to that outlined previously for $NbSe_3$,[144] following $HfTe_3$ growth-temperature protocols.[151] Typically, stoichiometric amounts of powdered Hf along with Te shot (~560 mg total), together with 1-4 mg of end-opened MWCNTs, and ~5 mg/cm^3 (ampoule volume) of I_2 are sealed under vacuum in a quartz ampule and heated in a uniform temperature furnace at 520 ºC for 7 days, then cooled to room temperature over 9 days. Energy dispersive spectroscopy (EDS) confirms a 1:3 stoichiometry of encapsulated $HfTe_3$ chains (25.14 at.% Hf, 74.86 at.% Te), with no statistical variations in stoichiometry along the chain observed. Carbon nanotubes are purchased from CheapTubes (90% SW-DW CNTs), Hafnium powder from Fisher Scientific (99.6%, 325 mesh), Tellurium shot from Sigma-Aldrich (99.999%, 1-2mm), and Iodine from Spectrum Chemicals (99.8%, resublimed).

8.4 Experimental structural observations of $HfTe_3$@CNT

After synthesis, filled $HfTe_3$@CNT samples are cast onto lacey carbon TEM grids for characterization. A JEOL 2010 microscope, operated at an accelerating voltage of 80 kV, is used for high-resolution imaging (HR-TEM). Elemental analysis is carried out on a Titan-X operated at an accelerating voltage of 80 kV for energy dispersive spectroscopy (EDS), and atomic resolution STEM imaging is done on the aberration corrected TEAM 0.5 microscope at the National Center for Electron Microscopy, at an accelerating voltage of 80 kV, both with assistance from Dr. Thang Pham and Dr. Peter Ercius.

8.4.1 Electron microscopy

Figure 8.2 shows high-resolution TEM images of representative $HfTe_3$ samples encased within MWCNTs, together with simplified side view and cross-sectional view schematics. In **Figure 8.2a**, a 3.85 nm-wide (inner diameter) MWCNT encases ~20 $HfTe_3$ chains, where the number of chains is estimated based on the carbon nanotube diameter and a close-packing configuration of the chains. **Figures 8.2b-d** show three, two, and one $HfTe_3$ chain(s) within MWCNTs of inner diameters 2.50 nm, 1.81 nm, and 1.19 nm, respectively. We thus successfully achieve the single-chain limit of $HfTe_3$. **Figure 8.3** shows atomic resolution STEM images of the few- and single-chain limit of $HfTe_3$ samples encased within MWCNTs, with an atomic model representation of the double- and single-chain limit. **Figures 8.3a-c** show a triple, double, and single chain of $HfTe_3$ confined within MWCNTs of inner diameters 2.51 nm, 1.69 nm, and 1.21 nm, respectively. Approximately 65% of CNT are filled, and of those filled, the total length of the chains ranges from 100 nm to over 1 μm in length.

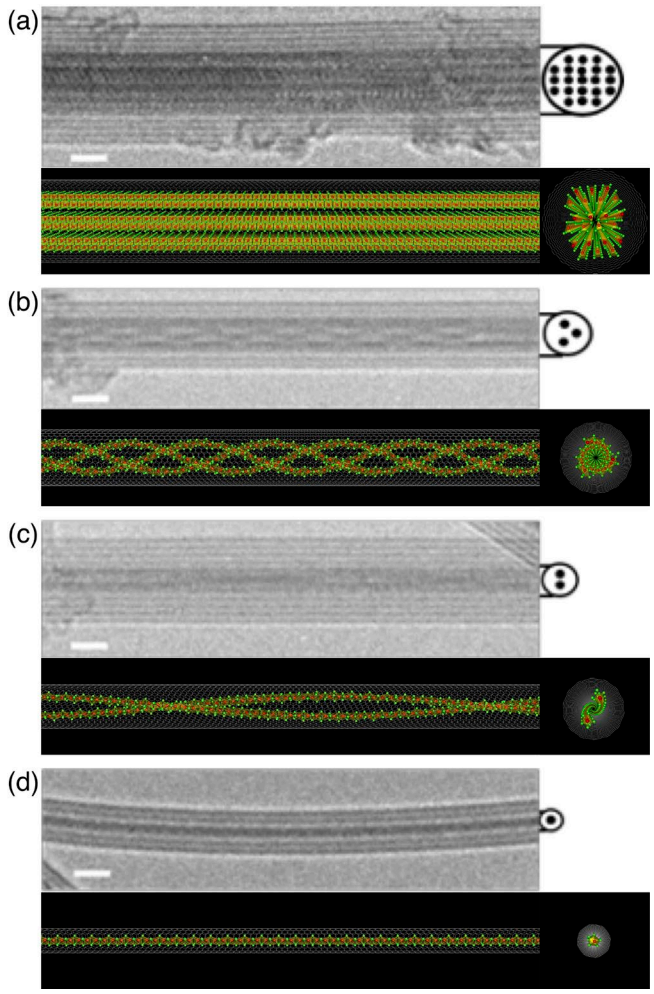

Figure 8.2 Encapsulation series from many- to single-chain limit of $HfTe_3$. High resolution transmission electron microscopy images of (a) many- (b) triple- (c) double- and (d) single-chain limits of $HfTe_3$ encapsulated within a carbon nanotube. A simplified cross-sectional representation of the filled carbon nanotube is shown to the right of each image, with a model of the chains' filling behavior shown below each image. Scale bars measure 2 nm. All images are underfocused, where Hf and Te atoms appear dark.

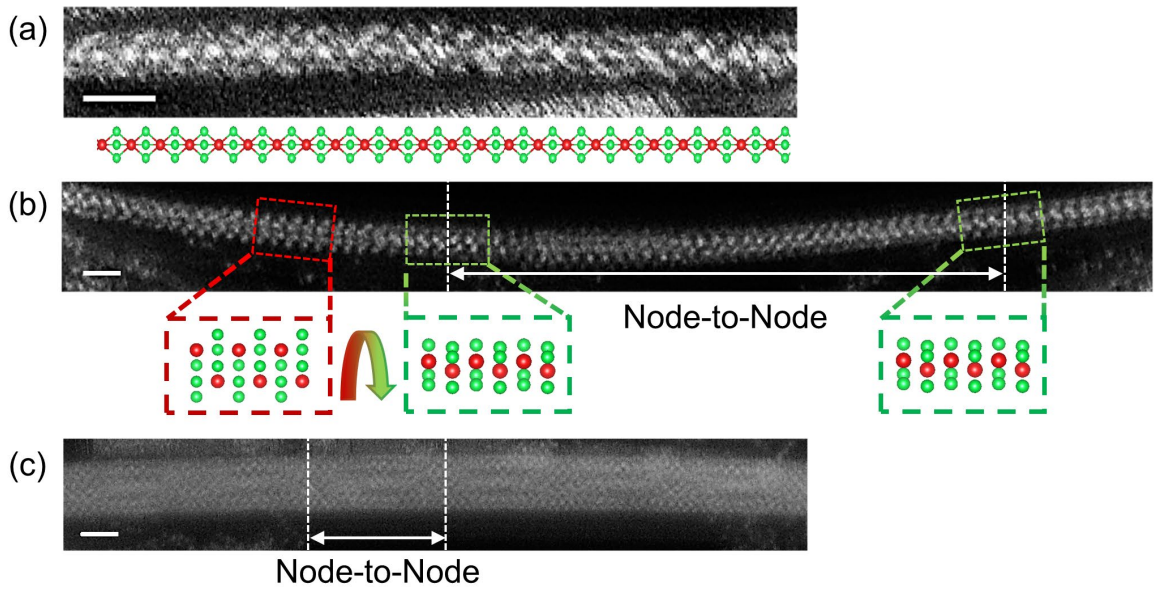

Figure 8.3 High-resolution images of encapsulated single, double, and triple $HfTe_3$ chains. Scanning transmission electron microscopy image of (a) single, (b) double, and (c) triple $HfTe_3$ chains encapsulated within a carbon nanotube. Hf and Te atoms appear white in the images. Atomic models below (b) and (c) demonstrate the orientation of the chains, where Hf and Te atoms are red and green, respectively. The node-to-node length of the spiraling in (a) and (b) is marked by white dashed lines. Scale bars measure 1 nm.

For the related material $NbSe_3$ in the few-chain limit, 3 or 2 chains spiral around each other in a helical fashion, and in the single chain limit the trigonal prismatic units comprising the chain gradually twist azimuthally as one progresses along the chain axis, comprising a single-chain torsional wave. **Figures 8.2b, 8.2c, 8.3a,** and **8.3b** show clearly that $HfTe_3$ displays the same spiraling behavior in the triple- and double-chain limit. For triple $HfTe_3$ chains, the spiraling node-to-node distance ranges from 3.05 to 4.44 nm (**Figures 8.2b** and **8.3a**), while for double $HfTe_3$ chains, the node-to-node distance ranges from 10.60 to 11.07 nm (**Figures 8.2c** and **8.3b**). These observations demonstrate that interchain spiraling, for low chain number, is not unique to $NbSe_3$—it appears to be a general feature of confined TMTs, independent of the chemical composition of the chain. The difference in node-to-node distance of the $HfTe_3$ chains, which is significantly longer when compared to the node-to-node distance for $NbSe_3$ (1.45 to 1.85 nm in triple chain $NbSe_3$, 1.90 to 2.30 nm in double chain $NbSe_3$), is in large part due to the larger tellurium atoms sterically preventing as tight of a spiraling overlap between the chains.[112,144]

8.5 Atomically resolved single-chain $HfTe_3$@CNT

An intriguing question is, does a single chain of $HfTe_3$ encapsulated within a MWCNT support a torsional wave (as does a single chain of $NbSe_3$)? We answer our question by applying high resolution aberration corrected HAADF STEM imaging at 80 kV to encapsulated $HfTe_3$. **Figure 8.3a** (shown above) shows a STEM image of an encapsulated single chain of $HfTe_3$, along with an atomic model, where the contrast setting does not show the CNT walls. **Figure 8.4** (shown below) shows additional encapsulated single-chain $HfTe_3$, along with a higher contrast

image to show the CNT walls. No long-wavelength torsional wave is observed in the single-chain limit of $HfTe_3$. Despite common interchain spiraling observed in triple and double chains of both $NbSe_3$ and $HfTe_3$, the single-chain charge-induced torsional wave (CTW) observed for $NbSe_3$ is absent in $HfTe_3$, which points to a fundamental difference between single chains of $NbSe_3$ and $HfTe_3$. In addition, as we show below, the chains themselves in few-to-single-chain specimens of $HfTe_3$ display a completely different kind of structural distortion, that of intracell rocking, which, in sharp contrast to $NbSe_3$, results in a size-driven metal-insulator transition.

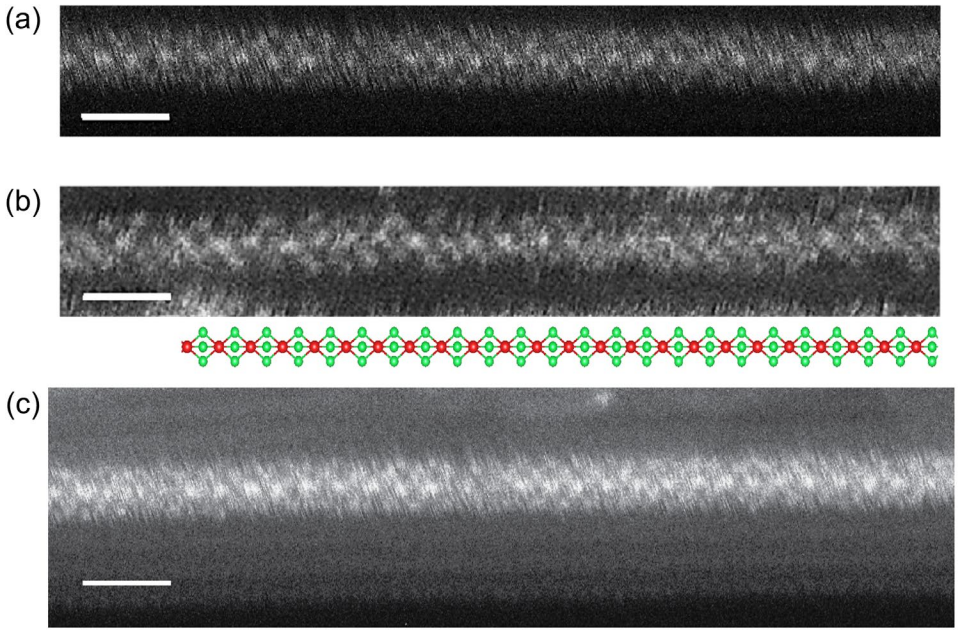

Figure 8.4 Encapsulation of single $HfTe_3$ chains. Scanning transmission electron microscopy image of (a-c) single $HfTe_3$ chains encapsulated within a carbon nanotube. (a) and (c) show the same single-chain $HfTe_3$, however (c) is shown in low contrast where the CNT walls are visible. Hf and Te atoms appear white in the images. An atomic model below demonstrates the orientation of the chain in both A and B, where Hf and Te atoms are red and green, respectively. Scale bars measure 1 nm.

8.6 Theoretical study of single-chain $HfTe_3$@CNT

First principles density functional theory (DFT) calculations are then employed to aid in the study of the few- and single-chain limit of $HfTe_3$. The calculations and analysis in the following sections are completed by Dr. Sehoon Oh, with supervision from Dr. Marvin Cohen. For the calculations performed below, we use the generalized gradient approximation,[152] norm-conserving pseudopotentials,[153] and localized pseudo-atomic orbitals for the wavefunction expansion as implemented in the SIESTA code.[154] The spin-orbit interaction is considered using fully relativistic j-dependent pseudopotentials[155] in the l-dependent fully-separable nonlocal form using additional Kleinman-Bylander-type projectors.[156,157] We use 1×512×1 Monkhorst-Pack k-point mesh for finite chains, and 40×64×24 for bulk. Real-space mesh cut-off of 1000 Ry is used for all of our calculations. The van der Waals interaction is evaluated using the DFT-D2 correction.[158] For finite chains, a vacuum region of 50 Å × 50 Å perpendicular to the chain is

used and dipole corrections are included to reduce the fictitious interactions between chains generated by the periodic boundary condition in our supercell approach.[159]

8.6.1 Building a model for the single chain

To further study the single-chain limit of $HfTe_3$, we began constructing candidate structures of encapsulated chains to determine the most stable structure. To start, we isolated a single chain from a bulk crystal of $HfTe_3$ without altering any bonding or structural orientation, and encapsulated this single chain within a carbon nanotube, as shown in **Figure 8.5**. The energy of this system was relaxed, with little alteration to the structure. Surprisingly, even from this initial study of the single chain, we see a drastic alteration of the electronic band structure, as highlighted in **Figure 8.5d**. However, we pursue a deeper understanding of the energetics in single-chain $HfTe_3$, as we know from its relative, $NbSe_3$, that a totally isolated single chain has much more freedom to distort its structure and minimize its energy even further.

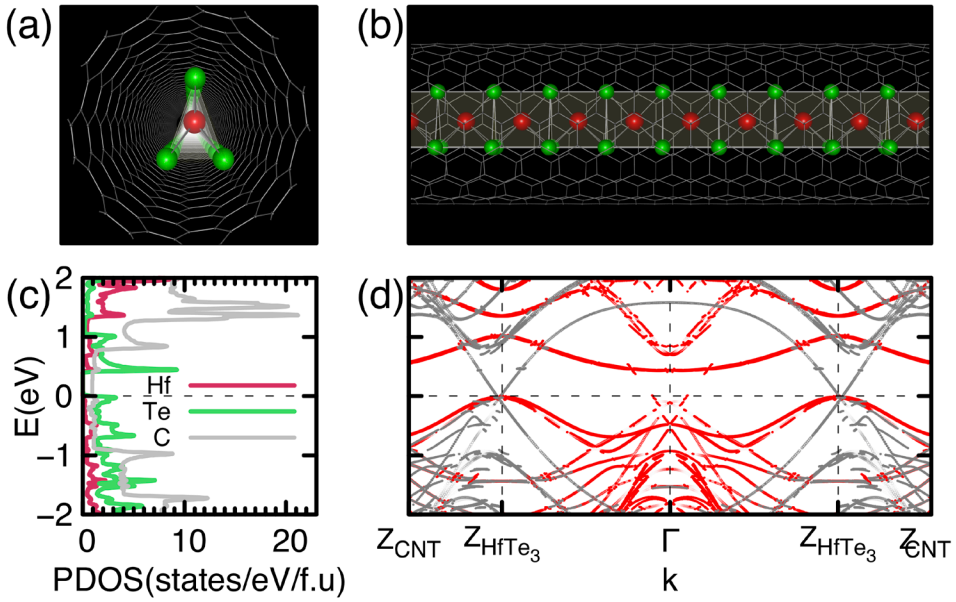

Figure 8.5 Calcuated atomic and electronic structures of TP geometry single-chain $HfTe_3$ encapsulated a CNT. (a-b) The atomic and (c-d) electronic structures of TP geometry single-chain $HfTe_3$ encapsulated in an (8,8) CNT are presented. The atomic structure is obtained with a constraint to force the TP symmetry in the atomic structure optimization. In (c-d), the Fermi energy is set to zero and marked with a horizontal dashed line. In (d), the bands represented by red and grey line are projected onto the chain and CNT, respectively, and unfolded with respect to the first Brillouin zone of the unit cells of the single-chain and CNT, where zone boundaries for the chain and CNT are denoted as Z_{HfTe3} and Z_{CNT}, respectively. Data collected in collaboration with Dr. Sehoon Oh.

8.6.2 Uncovering the trigonal antiprismatic rocking distortion

Employing the above parameters, we began studying the structural distortions of few- to single-chain $HfTe_3$ more fully. From the isolated chain studied in **Figure 8.5**, we begin to

investigate the atomic and electronic structures of a single chain of $HfTe_3$ isolated in vacuum more carefully. From the atomic positions of the chains comprising bulk solid, we construct candidate structures using supercells with various length from $1b_0$ to $12b_0$ to investigate possible twisting behavior, where b_0 is the distance between the nearest Hf atoms. These varying supercells were of initial interest because of the charge-induced torsional wave observed in $NbSe_3$.[144] From the constructed candidate structures, atomic structures are optimized by minimizing the total energy.

Unexpectedly, all investigated atomic structures of single-chain $HfTe_3$, except for a periodicity $\lambda=1b_0$ (i.e. no twist at all), show a short-wavelength rocking distortion from a trigonal prismatic (TP) unit cell (**Figure 8.6c**) to a trigonal antiprismatic (TAP) unit cell (**Figure 8.6h**). This is in sharp contrast to the long-wavelength torsional wave observed in single-chain $NbSe_3$. **Figures 8.6a-b** and **8.6f-g** show the atomic structure and the corresponding electronic structure of single-chain $HfTe_3$ in TP geometry obtained with a periodicity of $\lambda=1b_0$, and rocked TAP geometry with $\lambda=2b_0$. As shown in **Figures 8.6i-j**, the calculated electronic structure of the single-chain indicates a semiconducting transition upon isolation of a single chain, with a significant energy gap of 1.135 eV opening. Additionally, the rocked TAP structure of the $HfTe_3$ chains is observed in chain systems of 3 chains or fewer, leading to a band gap opening, as will be discussed in subsequent sections. This TAP rocking distortion is the first observed case of a different structural arrangement in the TMT material family, and is reminiscient of the two different phases observed in the TMD family, which will be discussed in following sections.

Next, we investigate the atomic and electronic structures of single-chain $HfTe_3$ encapsulated inside a carbon nanotube (CNT). The initial candidate structures of both TP and rocked TAP geometry single chains are constructed using the separately relaxed atomic positions of single-chain $HfTe_3$ isolated in vacuum, and those of an empty (8,8) CNT (indices chosen for convenience). From the candidate structures, the atomic positions of the chain are relaxed by minimizing the total energy, whereas atomic positions of the CNT are fixed, as the CNT does not interact strongly with the chain, as discussed below. We calculate the binding energy E_b of a single-chain $HfTe_3$, which is defined as:

$$E_b = E_{HfTe3} + E_{CNT} - E_{HfTe3/CNT} \qquad \textbf{(Eq. 8.1)}$$

where E_{HfTe3} is the total energy of the isolated TAP single-chain $HfTe_3$, E_{CNT} is the total energy of an empty CNT isolated in vacuum, and $E_{HfTe3/CNT}$ is the total energy of the joint system of the TP or TAP single-chain $HfTe_3$ encapsulated inside the CNT. The calculated binding energies of TP and TAP single chains are 0.964 and 1.23 eV per $HfTe_3$ formula unit (f.u.), respectively, confirming that the encapsulated single-chain $HfTe_3$ inside CNT also adopts a TAP geometry as in the isolated case. Because of the extremely short wavelength of the rocking TAP distortion and low signal for any diffraction studies of the chain, we were unable to resolve the TAP rocking experimentally via (S)TEM in this experiment. However, the TAP rocking distortion is ultimately resolved in another material, as discussed in detail in **Chapter 11**.

Figures 8.6k-l and **8.6m-n** show the calculated atomic structure of single-chain $HfTe_3$ with TAP geometry encapsulated in the CNT and the corresponding electronic structure. The Fermi energy lies at the energy level of the Dirac point of the CNT, which is inside the gap of the single-chain. As shown in **Figures 8.6e-f** and **8.6i-j**, the states of single-chain $HfTe_3$ near the Fermi energy are not altered appreciably by the confinement, indicating there is no charge transfer between the $HfTe_3$ chain and CNT (unlike the case of encapuslated $NbSe_3$).

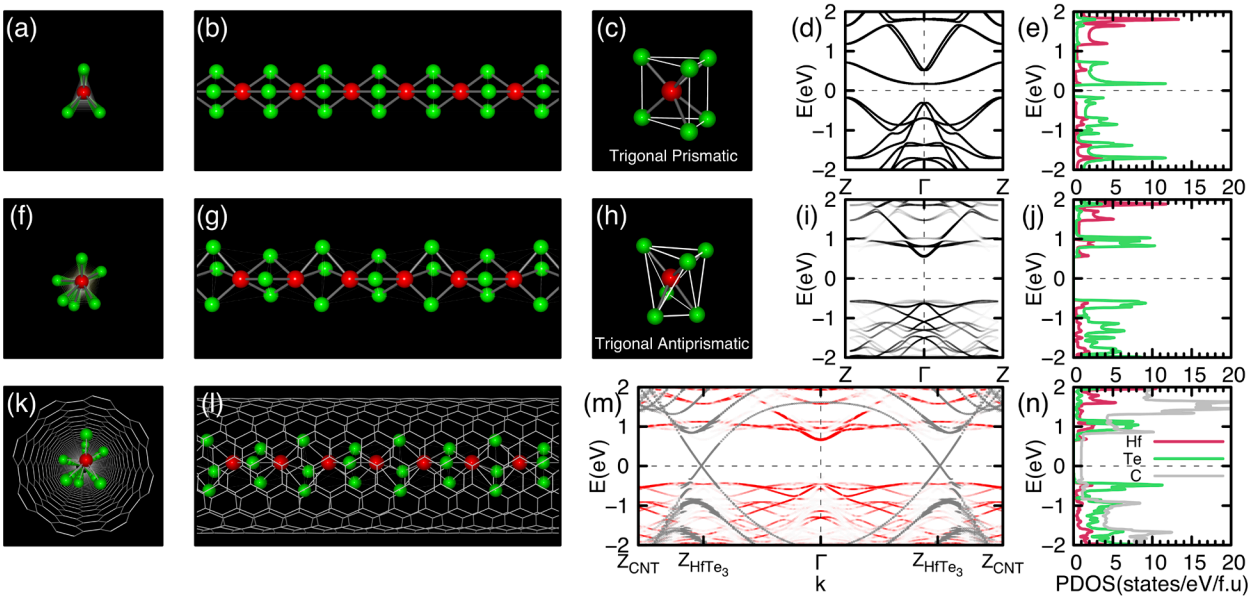

Figure 8.6 Calculated atomic and electronic structures of single-chain $HfTe_3$. The atomic and electronic structures of single-chain HfTe3 isolated in vacuum with (a-e) TP and (f-j) TAP geometry, and (k-n) the TAP single-chain encapsulated inside a (8,8) CNT are presented. In the atomic structure, the red and green spheres represent Hf and Te atoms, respectively. The basic units of (c) the TP and (h) TAP geometry are shown for comparison. In the band structures, the chemical potential is set to zero and marked with a horizontal dashed line. In (m), the bands represented by red and grey lines are projected onto the single-chain $HfTe_3$ and CNT, respectively, and unfolded with respect to the first Brillouin zone of the unit cell of the single-chain with periodicity $\lambda=b_0$ and the CNT, where zone boundaries for the chain and CNT are denoted as Z_{HfTe3} and Z_{CNT}, respectively. Data collected in collaboration with Dr. Sehoon Oh.

8.7 Understanding the trigonal antiprismatic rocking distortion of single-chain TMT

The TAP rocking in single-chain $HfTe_3$ vs. the long-wavelength torsional wave instability observed in single-chain $NbSe_3$ is the most notable difference between the two systems. To explore the mechanism dictating such a drastic difference observed at the single-chain limit, two factors are key: (i) the geometry of the unit cell of the chain and (ii) the electronic structure of a single chain in each system.

While the stability of the TP vs. TAP single chain was thoroughly investigated, we also needed to account for any changes in the ligand field surrounding the Hf transition metal due to the reduction of neighboring chains. Therefore, we further studied the distribution of the Te atoms within the chain, to compare the stability of an isosceles vs. equilateral distribution of the Te atoms in $HfTe_3$, as shown in **Figure 8.7a-c**. Calculation results from the TP single-chain $HfTe_3$ with equilateral distribution of the Te atoms indicates that the chain is metallic and has 0.193 and 0.672 eV/f.u. higher total energy than the semiconducting isosceles distribution of Te atoms in TP and TAP single-chain $HfTe_3$, respectively.

Because the Te atoms in $HfTe_3$ are distributed as an isosceles triangle in a trigonal prismatic chain, the 3-fold symmetry of the chain is broken, and the inversion center of the unit cell is lost when the single-chain limit of $HfTe_3$ is reached. This causes the Te bands near the chemical potential to split. Splitting of the bands reduces the energies of the occupied Te band

near the chemical potential and creates a semiconducting gap of 0.341 eV in a single $HfTe_3$ chain, as shown in **Figures 8.7d-f**. However, the total energy of the single chain of $HfTe_3$ can be further lowered by rocking the Te atoms between each Hf metal center into a TAP chain, splitting the Te bands near the chemical potential even more than the TP chain, as shown in **Figures 8.7g-i**. The rocked TAP structure of single-chain $HfTe_3$ has 0.479 eV/f.u. lower total energy than the TP single chain, with the energy gap enlarging from 0.341eV to 1.135 eV in the final rocked TAP structure. We note that we have also investigated an equilateral distribution of the Te atoms, similar to the Se atoms in single-chain $NbSe_3$, shown in **Figure 8.7a-c**, and thereby confirmed that the isosceles distribution in $HfTe_3$ continues to be the energetically preferred structure for all chain numbers.

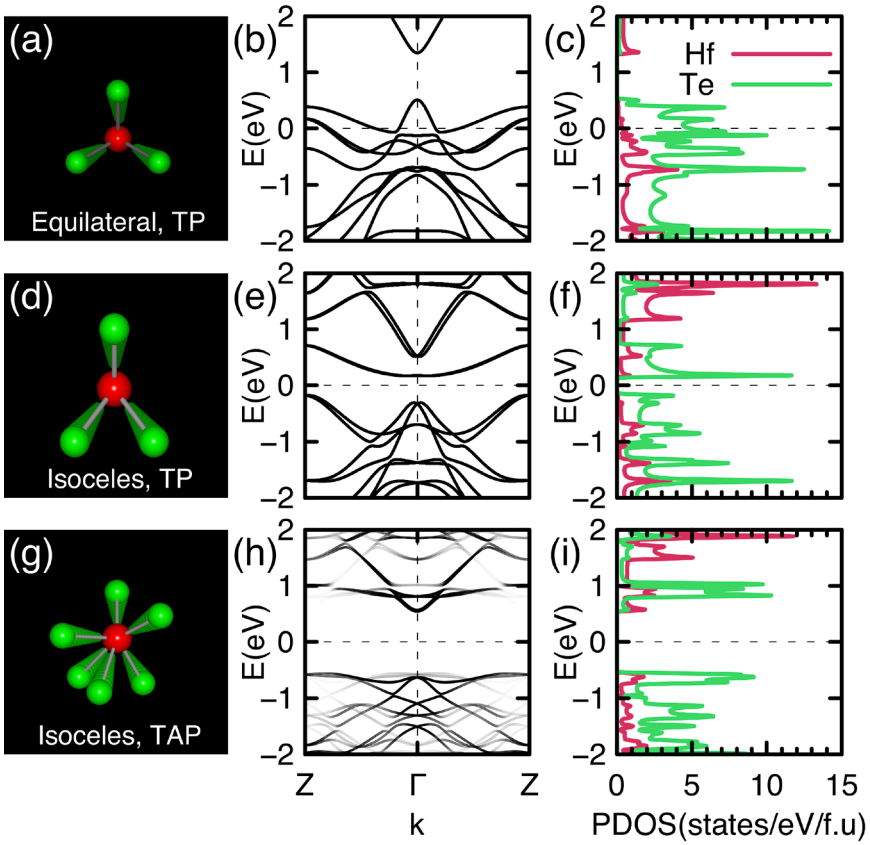

Figure 8.7 Calcuated atomic and electronic structures of TP and TAP geometry single-chain $HfTe_3$ with Te atoms forming equilateral and isoceles triangles. The atomic and electronic structures of single-chain $HfTe_3$ isolated in vacuum are presented. (a-c) The TP single-chain $HfTe_3$ with an equilateral triangle distribution of Te atoms, (d-f) the TP and (g-i) TAP single-chain HfTe3 with an isosceles triangle distribution of Te atoms. In the axial view along the *b*-axis of the unit cell, the red and green spheres represent Hf and Te, respectively. In the band structures, the chemical potential is set to zero and marked with a horizontal dashed line and the Brillouin zone center and the edge are denoted as Γ and Z, respectively. In (h), the bands are unfolded with respect to the first Brillouin zone of the unit cell of the single-chain with length of b_0. Data collected in collaboration with Dr. Sehoon Oh.

Splitting of the Te bands in the TAP chain is possible because the single chain of $HfTe_3$ has an even number of electrons in the unit cell. A single chain of $NbSe_3$ has an odd number of electrons in the unit cell, preventing any splitting of the bands, and allowing a metallic band structure with 3-fold symmetry even down to the single-chain limit. Therefore, for single-chain TMTs, we observe either a TP ($NbSe_3$) or TAP ($HfTe_3$) structural arrangement of the chalcogen atoms, depending on elemental composition, leading to metallic or insulating behavior, respectively. The structural difference between $NbSe_3$ and $HfTe_3$ is analogous to the transition-metal dichalcogenides, where some materials (such as MoS_2) prefer the trigonal prismatic (1H) structure showing insulating behavior, while others (such as WTe_2) prefer the trigonal antiprismatic (1T or 1T') structure showing metallic behavior.

8.8 Examining multi-chain $HfTe_3$@CNT

8.8.1 Parallel chains of $HfTe_3$

While the single-chain specimen of $HfTe_3$ underwent very interesting TAP rocking distortions, we also observed interesting phenomena in the multi-chain specimen and their spiraling motifs observed in **Figures 8.2** and **8.3**. To fully understand the implications of these drastic structural changes, we first isolate and investigate bulk and finite numbers of $HfTe_3$ chains that are parallel aligned, as seen in **Figure 8.8**. In doing so, we are able to more clearly examine how the spiraling motif observed in double- and triple-chain $HfTe_3$ alters the electronic band structure. Units of many, four, triple, double, and single chains of $HfTe_3$ are isolated from the bulk crystal, and the energy of the system is relaxed. **Figures 8.8a-c** shows $HfTe_3$ in bulk, with the expected metallic nature of the bands. **Figures 8.8d-f** examine a multi-chain bundle of chains, where the structure of the chains does not change in any noticeable form when relaxed. **Figures 8.8g-i** examine the four-chain limit and **Figures 8.8j-l** examine the triple-chain limit, where still there is no noticeable alteration to the structure when relaxed. However, the density of states shown in **Figures 8.8i** and **8.8l** begin to show very different projections, indicating that this level of quantization is starting to alter the electronic band structure, likely a result of the changing symmetry from the alteration of the unit cell. Once we reach the double-chain limit, even without the spiraling structural change, we begin to see more drastic modifications to the atomic structure when the system is relaxed, highlighted in **Figure 8.8j**, where the alignment of the Te atoms is deformed fairly dramatically. The single chain is similar to that shown in **Figure 8.7d**, for easy comparison to the few- and multi-chain counterparts.

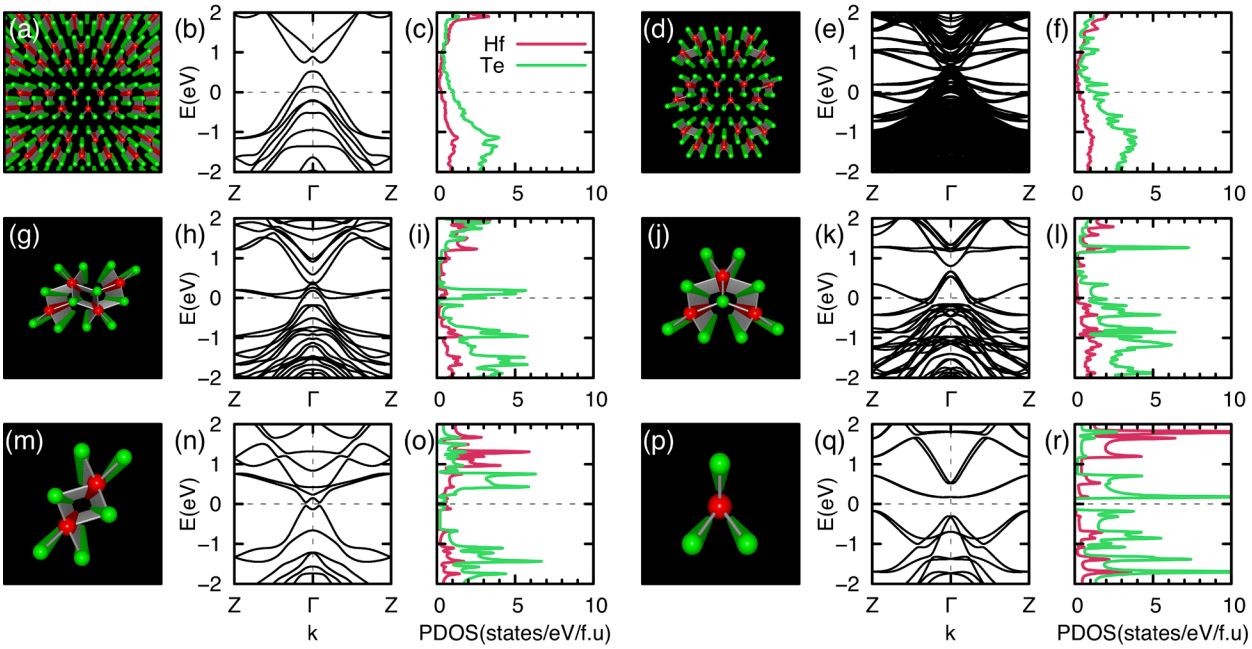

Figure 8.8 Calcuated atomic and electronic structures of $HfTe_3$ bulk and finite parallel chains. The atomic and electronic structures of $HfTe_3$ bulk crystal and parallel finite chains with TP geometry isolated in vacuum are presented. (a-c) The bulk crystal, (d-f) 22-chain, (g-i) quadruple-chain, (j-l) triple-chain, (m-o) double-chain, and (p-r) single-chain. In the axial view along the *b*-axis of the unit cell, the red and green spheres represent Hf and Te atoms, respectively. In the band structures, the chemical potential is set to zero and marked with a horizontal dashed line and the Brillouin zone center and the edge are denoted as Γ and Z, respectively. Data collected in collaboration with Dr. Sehoon Oh.

8.8.2 Spiraling double and triple chains

With a better understanding of the atomic and electronic structure of the few-chain limit from simple energy minimizations, we then turn to the drastic spiraling structure observed in the double- and triple-chain limit. To investigate multi-chain spiraling and possible on-chain rocking of double- and triple-chain $HfTe_3$, we construct several candidate structures isolated in vacuum using the atomic positions of the chains comprising bulk solid with the diameters and periodicities of the spiral wave obtained from experimental evidence and minimize the total energy to determine the fully relaxed atomic structure. **Figures 8.9a-c and 8.9d-f** show the relaxed atomic structure, electronic band structure, and projected density of states (PDOS) of the spiraling double- and triple-chain $HfTe_3$, respectively. As shown in **Figures 8.9a and 8.9d**, the individual chains comprising the spiral double- and triple-chain also rock into the TAP geometry, similar to the single-chain $HfTe_3$, to minimize the total energies of each chain. In turn, each TAP chain spirals around the others in a helical fashion. The obtained electronic structures of spiraling double- (**Figures 8.9b-c**) and triple-chain (**Figures 8.9e-f**) $HfTe_3$ resemble that of the TAP single-chain (**Figures 8.9i-j**). Spiraling double- and triple-chain $HfTe_3$ has energy gaps of 1.020 and 1.018 eV, respectively, comparable to that of the TAP single-chain, 1.135 eV.

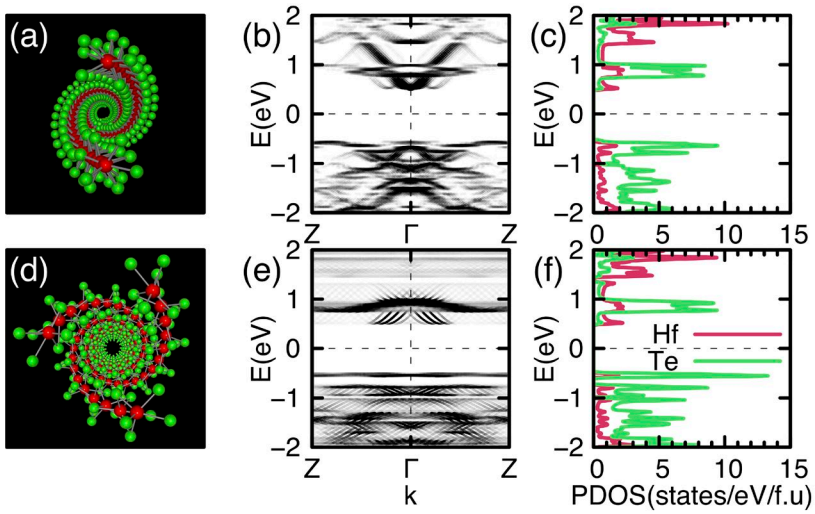

Figure 8.9 Calculated atomic and electronic structures of spiraling double- and triple-chain $HfTe_3$. Atomic and electronic structures of spiral (a-c) double and (d-f) triple chains of $HfTe_3$ isolated in vacuum are presented. In the axial view along the *b*-axis of the unit cell, red and green spheres represent Hf and Te atoms, respectively. In (b, e) the band structures, the chemical potential is set to zero and marked with a horizontal dashed line and unfolded with respect to the first Brillouin zone of the single-chain unit cell with periodicity $\lambda=b_0$, where the Brillouin zone center and edge are denoted as Γ and Z, respectively. The individual chains comprising triple- and double-chain rock into TAP geometry. Data collected in collaboration with Dr. Sehoon Oh.

To understand the preferred spiraling pattern and on-chain rocking of double- and triple-chain $HfTe_3$, the competing interactions that exist among free-standing parallel chains and the interactions among encapsulated spiraling chains are analyzed. In bulk down to quadruple chains, strong interchain vdW interactions between the Hf centers and Te atoms on neighboring chains allow for the largest energy stabilization, and this is the largest determining factor in the parallel orientation of the chains. Metallic behavior is maintained from bulk to quadruple chains, as described above in **Figure 8.8**. Once the triple- and double-chain limit is reached, however, the chains undergo two physical changes. First, the Te ligands rock to form the TAP unit within each chain, which lowers the total chain energy and opens the energy gap. Second, the chains spiral around one another in a helical fashion. Interestingly, spiraling of the double- and triple-chain systems of $HfTe_3$ does not significantly alter the band gap; the rocking distortion into the TAP chain conformation remains the main driving force behind the metal-insulator transition in the few-chain limit of $HfTe_3$.

8.9 Conclusion

In summary, on-chain rocking of $HfTe_3$ chains into the TAP geometry drives a metal-insulator transition for chain systems of three or fewer. Quadruple- and higher-chain systems have more neighboring chains with a larger number of interchain vdW interactions between the Hf centers and Te atoms on those neighboring chains, preventing the chains from rocking into the TAP geometry, which maintains the metallic behavior. Encapsulation of the triple- and double-chain limit within a CNT promotes the spiraling of the chains. The spiraling enhances the vdW interactions between the chains and the CNT inner wall and further stabilizes the chains.

Chapter 9: Broadening the Search for the vdW Limit of Transition Metal Chalcogenides – The Trials, Triumphs, and Tribulations on the Road to Discovery

Special thank you to Malik Elasha and Markus Thiel for their assistance on this project.

Keywords: Transition Metal Trichalcogenides, Single Crystal Synthesis, Encapsulation, Trisulfide, Triselenide, Tritelluride

Modifying the dimensions of solid-state materials is a powerful and unique method to control the atomic and electronic structure of the material. Controlling the atomic dimensions of a material affords us the opportunity to further study the modulation of the physical properties for these material systems, and explore the possibilities of unique material geometries and emergent phenomena at the atomic scale.[7,23,137,144,160,161] The continued exploration and isolation of vdW materials down to their fundamental limit has sparked a surge of research in the materials science and condensed matter physics fields and continues to be an exciting avenue towards modulation of material properties.[137,162,163] We know from the previous work reported on $NbSe_3$ and $HfTe_3$ that the transition metal trichalcogenides (TMT) could show just as rich a variety of properties to explore at the vdW limit, similar to those explored with the transition metal dichalcogenides (TMD).[109,128,144,163]

9.1 Motivation to reach the vdW limit of more transition metal trichalcogenides

One family of materials that commonly gets lumped in with other systems, but never as a standout on its own, is the transition metal trichalcogenides (TMT). Often researchers will refer to the TMT as layered materials, similar to their close cousin, the transition metal dichalcogenides (TMD).[110,128,148] However, as discussed in **Chapter 7**, the TMT family is comprised of linear chain-like compounds with the chemical formula MX_3, where M is a transition metal (typically Group IVB or VB) and X is a chalcogen (S, Se, or Te). As mentioned in the **Chapter 7**, their chain-like structure induces high anisotropy in their crystal structure, which affects their electron transport properties, such as photoconductivity, charge density wave transitions, and superconductivity.[128,129,164]

The anisotropy of the TMT crystal structure can be used to our advantage, as shown in **Chapter 7** and **8**. The 1-D nature of the trigonal prismatic chains bodes well for encapsulation within the 1-D hollow cavity of carbon nanotubes (CNT), and has shown surprising and exciting results for the $NbSe_3$ and $HfTe_3$ system isolated down to the single-chain limit.[144,163] What is even more exciting, is the structural motif of the $NbSe_3$ and $HfTe_3$ systems exist in the whole family of TMT materials. **Table 9.1** shows a similar table presented in **Chapter 7**, with all Group IVB- and Group VB-based TMT shown, along with a one-word descriptor of their electronic structure. Note that all of the TMT members shown in **Table 9.1** may or may not exist in bulk form, which has been denoted by "No Reported Synthesis". All transition metals from Group IVB and VB have been included for completeness, even if they are not generally considered part of the TMT family.

As seen in the TMT family table, there are 11 total members that have been studied in bulk form, two of which have been discussed at the few- and single-chain limit. Therefore, there are still 9 reported members of the TMT family that are worth pursuing at the vdW limit to determine how their atomic and electronic structures could evolve as few- and single-chains.

There are an additional 7 TMT members that have not been synthesized or studied in any meaningful manner, showcasing just how large the TMT family is, and how diverse the atomic and electronic structures at the vdW limit, and associated properties, waiting to be uncovered truly are. In the following sections, we will explore the synthetic trials and parameters surrounding each member of the TMT family, along with the triumphs and tribulations encountered for each additional member studied.

Table 9.1 Transition metal trichalcogenide family and corresponding attributes. All Group IVB and VB transition metal trichalcogenides. The property listed for each is a brief descriptor of their electronic structure.

		Chalcogen		
		S_3	Se_3	Te_3
		Bulk	*Bulk*	*Bulk*
Group IV Transition Metal	Ti	Semicond. (~1.05 eV)	No Reported Synthesis	No Reported Synthesis
	Zr	Semicond. (~1.87 eV)	Semicond. (~0.68 eV)	SC (2K)
	Hf	Semicond. (~1.90 eV)	Semicond. (~0.59 eV)	SC (1.4-2K), CDW (70-93K)
Group V Transition Metal	V	No Reported Synthesis	No Reported Synthesis	No Reported Synthesis
	Nb	Semicond. (~1.07 eV), CDW (450-475K)	CDW (145K, 59K)	No Reported Synthesis
	Ta	CDW (210-220 K)	SC (2.1K)	Reported Synthesis, No in-depth characterization

Key: Semicond. = Semiconductor/Insulator; CDW = Charge Density Wave; SC = Superconducting

9.2 Exploring the encapsulated transition metal trichalcogenide family

To begin exploring the vdW limit of the TMT family, we need to start from the single crystal growth conditions for each TMT structure, similar to the synthetic protocols used for the isolation of $NbSe_3$ and $HfTe_3$ chains. In fact, the successful isolation of the few- and single-chain limit of $HfTe_3$ followed the single crystal synthetic conditions almost exactly, with some forgiveness in the reaction temperature and time. **Table 9.2** shows an overview of the growth conditions for 10 of the 11 known TMT family members ($HfTe_3$ is absent, however we discussed the growth of this material in **Chapter 8**).[148] One important note to make is that the single crystal synthesis is not necessarily the end-all, be-all, of obtaining encapsulated structures, as will be thoroughly discussed in this chapter. Rather, the single crystal growth techniques give us a starting point, but the temperature and time of synthesis is a large parameter space to explore and changes for the encapsulated species. While $HfTe_3$ followed the single crystal growth parameters

almost exactly, encapsulated $NbSe_3$ could be obtained at slightly lower temperatures than the single crystal growth.[129,163]

Table 9.2 Reaction conditions for single-crystal synthesis of transition metal trichalcogenides. Adapted from reference 148.

Crystals	Temperature (°C)		Transporting agents	Best conditions	
	Source	Growth		(°C)	Agent
TiS_3	600–500	500–450	I_2, S_2Cl_2, ICl_3, S	550–500	ICl_3
ZrS_3	850–650	800–600	I_2, S_2Cl_3, ICl_3	750–730	S_2Cl_3
				650–600	I_2
	950–750	725–550	I_2	650–600	I_2
$ZrSe_3$	750–650	700–600	I_2, Se_2Cl_2	650–600	I_2
$ZrTe_3$	800–650	700–600	I_2, $TeCl_4$	650–600	I_2
HfS_3	850–650	800–600	I_2, S_2Cl_2	650–600	I_2
$HfSe_3$	700–650	650–600	I_2, Se_2Cl_2	650–600	I_2
NbS_3	700–650	700–600	I_2, S_2Cl_2, S	670–610	10%S
$NbSe_3$	750–650	700–600	I_2, S_2Cl_2, Se, ICl_3	720–710	10%Se
				680–660	ICl_3
TaS_3	700–650	550–450	I_2, S_2Cl_2, S	550–500	S_2Cl_2, 30%S
$TaSe_3$	750–650	710–600	I_2, ICl_3, Se	700–680	10%Se

9.2.1 Synthesis of the encapsulated transition metal trichalcogenides

Each TMT species is synthesized within CNT following a similar synthetic route, highlighted in **Figure 9.1a** for the overall reaction schematic. First, CNT must be prepared for filling of inorganic species. Carbon nanotubes are purchased from CheapTubes (90% SW-DW CNTs) and opened by oxidation in air (515ºC for 15 minutes). Once opened, the CNT are ready to be coated in the ampoule. Quartz ampoules (4mm ID and 6mm OD) are used for the high temperature synthesis of the TMT. Before filling of TMT precursors, the ampoules must be prepared with the now-opened CNT. The interior of the ampoule is wetted with DI water, with excess water drained, and 1-4mg of end-opened CNT are then poured into the wetted ampoule. The CNT thoroughly coat the inner walls of the ampoule through adhesion, for easier removal after the crystal growth process.

Once the CNT-coated ampoules are prepared, the inorganic precursors can be added. Typically, stoichiometric amounts of powdered transition metal (Ti, Zr, Hf, Nb, or Ta) along with chalcogenide powder or shot (S powder or Se/Te shot) are massed and added to the ampoule (~560 mg in total mass). As seen in **Table 9.2**, some type of chemical transport agent is necessary to generate volatile species of transition metal. In our studies, we use iodine (I_2) as the chemical transport agent, as most transition metals easily form some type of volatile transition metal halide with iodine.[114,148] Generally, ~5 mg/cm^3 (ampoule volume) of I_2 are added along with the elemental precursors. Once all reagents are added, the ampoule is sealed under vacuum (~10^{-6} Torr) with an HHO torch. The sealed ampoule is then heated in a uniform temperature clamshell furnace. The reaction temperature, reaction time, and cool-down parameters were changed for each species, and will be discussed in more detail in the following sections.

9.2.2 Characterization of the encapsulated transition metal trichalcogenides

Each TMT species is characterized in a similar manner using electron microscopy, highlighted in **Figure 9.1b** for the overall sample preparation and characterization schematic. After synthesis, the quartz ampoule is cracked open to access the filled CNT and prepare TEM grids for electron microscopy analysis. Because of the ampoule preparation, substantial amounts of CNT would remain adhered to the quartz walls, making isolation of the CNT from any bulk crystals straightforward. Small pieces of the quartz ampoule with adhered CNT would be placed in a scintillation vial with high-purity isopropyl alcohol. The CNT would then be suspended into the solution via bath sonication at high power for 30-60 minutes. The filled TMT@CNT sample solution is then cast onto lacey carbon TEM grids (Cu, 300 mesh) for characterization. A JEOL 2010 microscope, operated at an accelerating voltage of 80 kV, is used for high-resolution transmission electron microscopy imaging (HR-TEM).

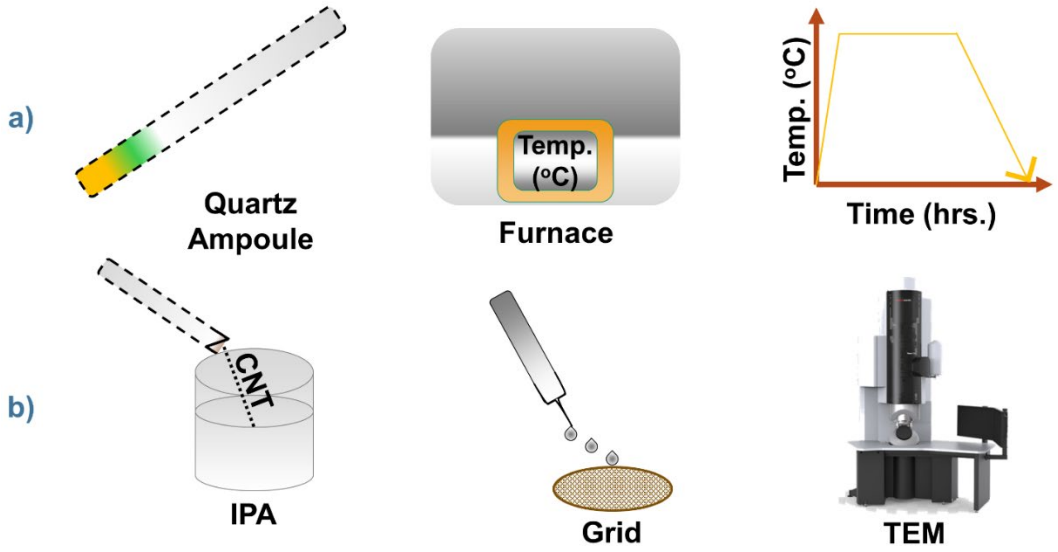

Figure 9.1 Synthesis and characterization scheme for encapsulated species. (a) Overall schematic of the synthesis process. From left to right: Quartz ampoule with the powder CNT adhered to the inner walls (black dotted lines), elemental transition metal (yellow), and elemental chalcogen (green). The sealed ampoule is then placed in a single-zone, clamshell furnace and heated following a predetermined heating, holding, and cooling regiment, as indicated by the temperature vs. time plot. b) Overall schematic of the sample preparation and characterization process. From left to right: Quartz ampoule is cracked, and pieces with adhered CNT are sonicated in isopropyl alcohol (IPA) to create a suspension. The suspension is then drop-cast onto a lacey carbon TEM grid and imaged in a JEOL 2010 TEM.

The following sections utilize the synthetic protocols, sample preparation, and characterization techniques presented in **Figure 9.1**. Each section explores a single transition metal and the corresponding trichalcogenides. Here, I only explore the members of the TMT family that have been synthesized and studied in bulk before, such as TiS_3, and will address the TMT members that have not been reported, such as $NbTe_3$, in the last section and **Chapter 11**. Most attempted syntheses of the TMT family are reported, regardless of the successful or unsuccessful encapsulation of chains, with commentary on the type of encapsulated species

observed. As the TMT family consists of many different species and stoichiometries, I will include any observations about potential structures observed that may not necessarily be the desired TMT but could be an interesting stoichiometry and structure to study in more detail. Initial synthetic trials were performed for each individual TMT studied, and only those that showed some type of filling, regardless of crystallinity, were studied in greater detail with additional modifications to the synthetic parameters. As a point of reference, TEM imaging is the primary characterization technique used to evaluate the success and potential modifications for synthetic parameters in each TMT system. As the TMT are chain-like in nature, we look for chain-like filling of the CNT, as was observed in the $NbSe_3$ and $HfTe_3$ systems.[144,163] If amorphous filling or other crystalline filling was observed, the reaction was considered semi-successful, and warranted further modification of the synthetic parameters.

9.3 Hafnium trichalcogenides

Following the successful synthesis and subsequent encapsulation of $HfTe_3$, the first transition metal trichalcogenide group explored for additional encapsulated members is hafnium, specifically HfS_3 and $HfSe_3$. Both HfS_3 and $HfSe_3$ are semiconductors, with the trisulfide having a medium bandgap of ~1.90 eV and the triselenide ~0.60 eV, and have both been studied as visible light detectors.[165–167] As shown in **Table 9.2**, both HfS_3 and $HfSe_3$ follow very similar single crystal synthetic parameters, so we can start with the same reaction protocol for both, as shown in **Figure 9.2**.

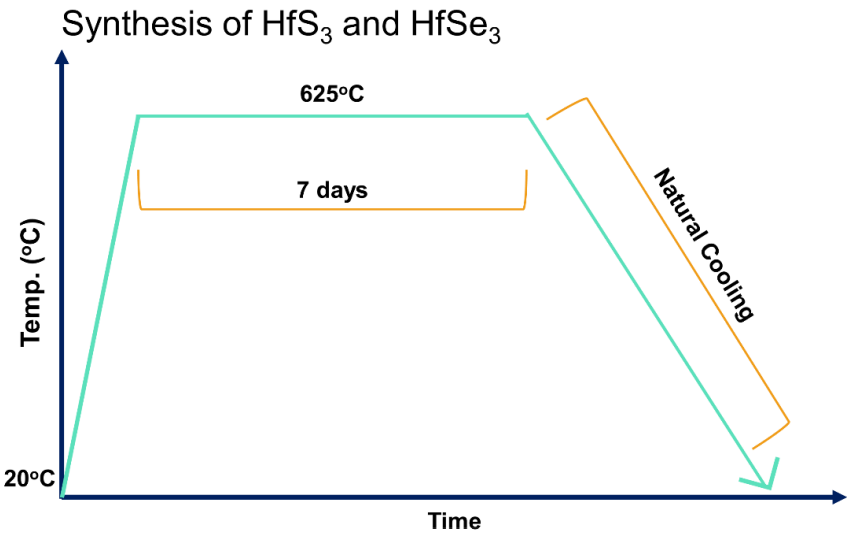

Figure 9.2 Initial synthetic protocol for the growth of encapsulated HfS_3 and $HfSe_3$ chains. Starting from room temperature, the furnace is set to run at 625°C for 7 days (heating naturally and reaching temperature within 30 min.), then left to cool naturally to room temperature in the furnace (the furnace is essentially turned down to room temperature and left).

Upon initial inspection of the ampoules, there was considerable bulk crystal growth in the HfSe system, showing long, needle-like crystals, an attribute common to all TMT members, indicating successful growth of $HfSe_3$. A scanning electron microscopy image of these crystals is shown in **Figure 9.3** for reference. However, the crystals for the HfS system did not seem fully formed, and the resulting product, while very different in color, did not present any large

crystals, indicating HfS_3 synthesis could be incomplete. Both the HfSe and HfS system were prepared for TEM analysis.

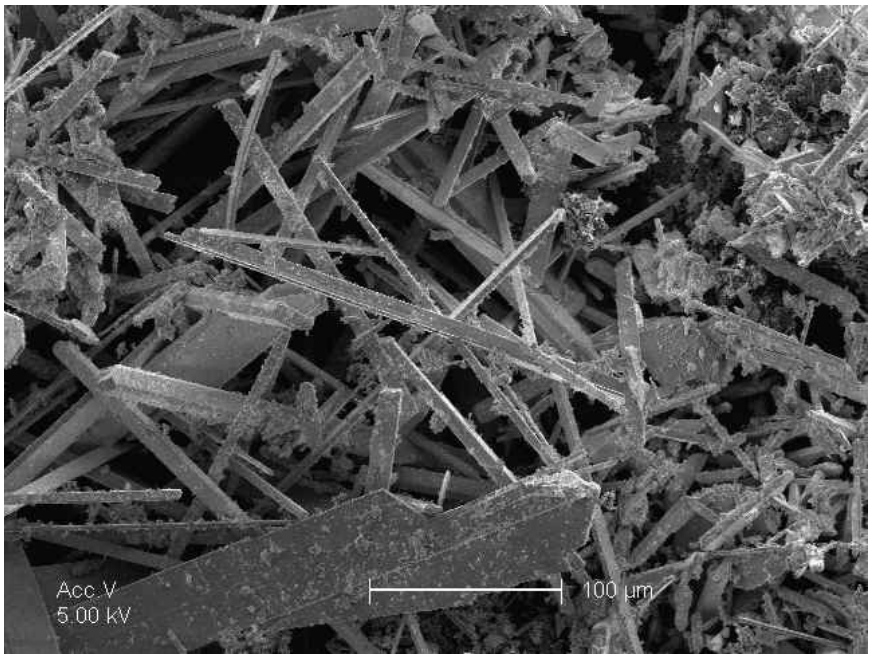

Figure 9.3 Scanning electron microscopy image of long, needle-like crystals of $HfSe_3$. Scale bar measures 100 µm.

Both the HfS and HfSe system are prepared for imaging under TEM. No TEM images for the HfS system are presented, as no filling of any type was observed in the CNT. Efforts were focused on the HfSe system because of some very interesting filling observed, as shown in **Figure 9.4**. Some CNT were filled with a dark, amorphous substance, which can generally be attributed to amorphous chalcogen filling.[143] Even amorphous chalcogen filling is promising, as this is indication that reaction temperature and time were sufficient for vaporized species to migrate into the CNT and condense. However, there are two crystalline fillings observed that are of great interest and warranted further exploring. The first type of interesting crystalline filling observed, also shown in **Figure 9.4**, was not chain-like in nature, and at first pass this structure remained unidentified. However, as our expertise in identification and synthesis of various filling-types within CNT has grown, this type of crystalline structure appears very thin and ribbon-like, which we generally attribute to a nanoribbon, probably $HfSe_2$. Encapsulated TMD nanoribbons, as will be discussed in **Chapters 12, 13, and 14**, are also of great interest and show just as rich modulation to their atomic and electronic structure as the encapsulated TMT. The nanoribbon structure observed warrants additional investigation beyond the scope of the information presented here.

The second type of filling observed is the type of structure we are after for the TMT, which is the linear chain-like filling, shown in **Figure 9.4**. However, the chains observed are very short in length, reaching only ~ 50 nm in length, and the frequency of these structures observed was very low. Because multiple filling structures were observed, and the overall size scale of the desired chain-like structure was very short, we can note that the reaction conditions were not quite finely tuned enough to encourage high filling ratios of the CNT, or to encourage

filling of a single type of structure. Therefore, the synthetic parameters were modified from initial conditions presented in **Figure 9.2**.

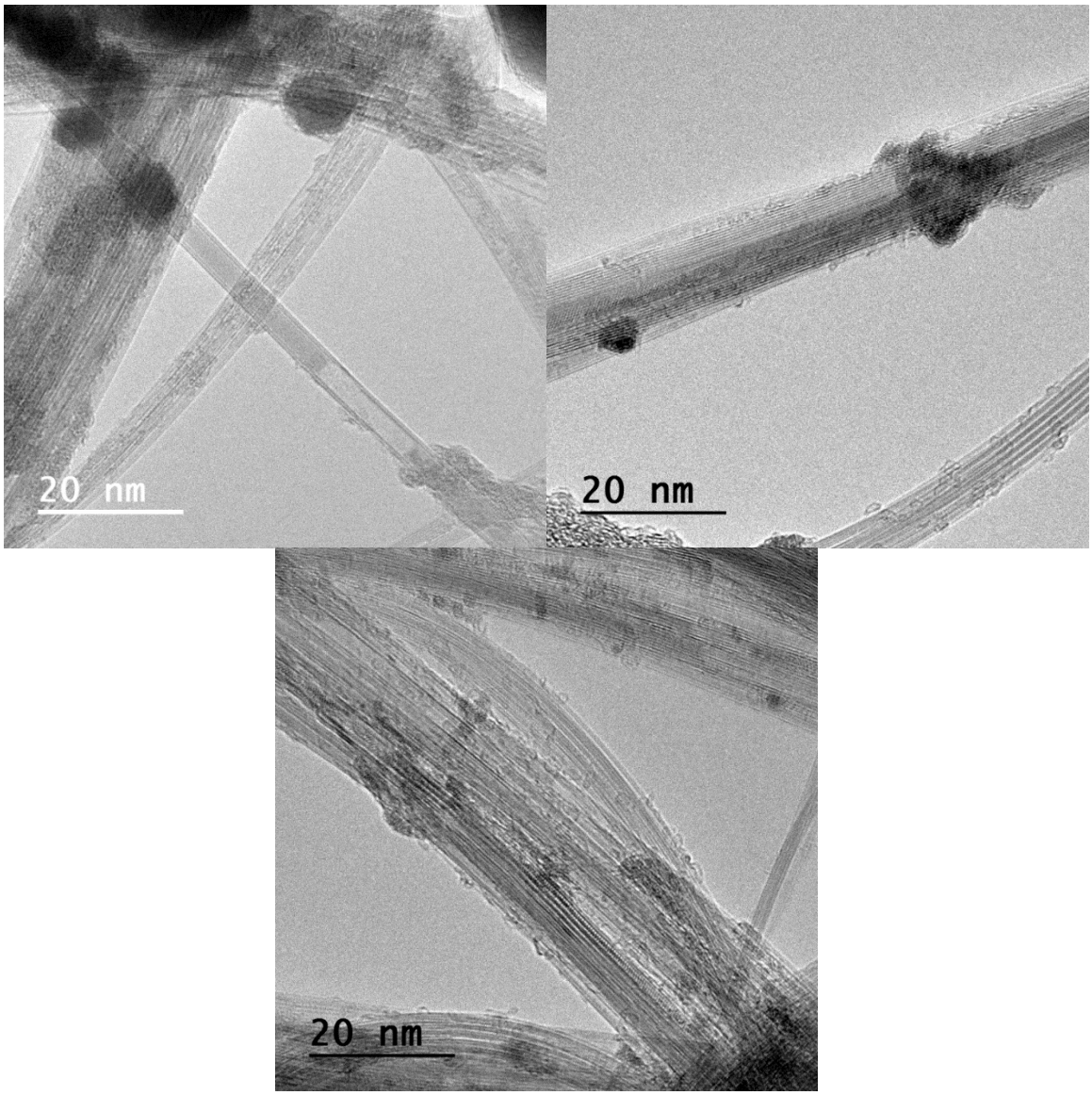

Figure 9.4 Representative TEM images of observed filling structures in the HfSe system. Top left: Amorphous filling of the HfSe system, presumed to be amorphous Se. Top right: Flat, narrow crystalline filling of the HfSe system, presumed to be a nanoribbon of $HfSe_2$. Bottom: Chain-like crystalline filling of the HfSe system, consistent with TMT filling, indicating potentially successful growth and isolation of $HfSe_3$.

As we are working within the Hf family, the first modifications to the synthesis were to follow that of $HfTe_3$, as presented in **Figure 9.5**. These synthetic parameters were at a lower reaction temperature with more control over the cooling of the crystals, which could potentially favor a specific stoichiometry of the crystal structure and preferentially grow a single encapsulated crystalline structure. As no filling was observed for the HfS system, only the HfSe system was pursued for modified syntheses.

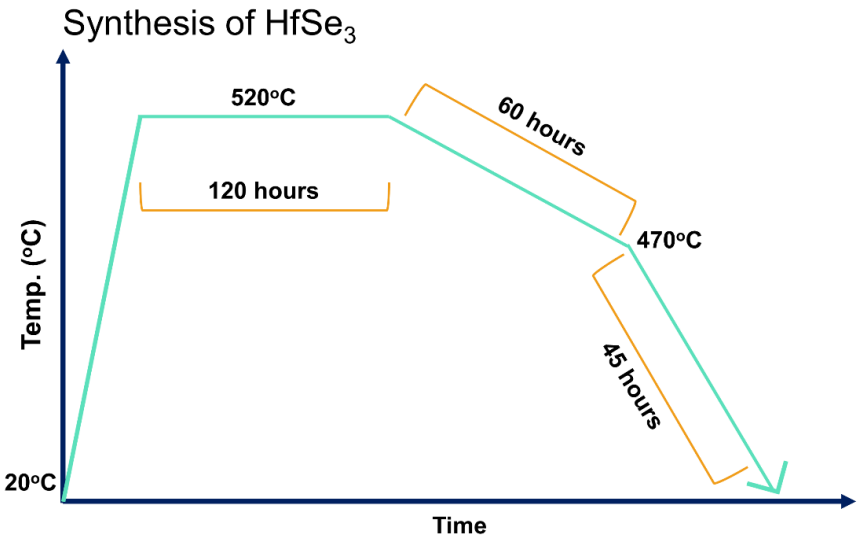

Figure 9.5 Modified synthetic protocol for the growth of encapsulated $HfSe_3$ chains.

Following the modified synthetic protocols, TEM imaging was performed to see how the change in reaction temperature and cooling rate affected the overall growth of encapsulated HfSe species. As shown in **Figure 9.6**, the lower reaction time and extended cooling did not have a favorable impact on the type of filling observed. While the amount of filling observed was substantially greater, the only type of filling observed was amorphous in nature. The reaction temperature was more than likely too low in this case and could not form crystalline species. Therefore, higher reaction temperatures were pursued in subsequent reaction growths.

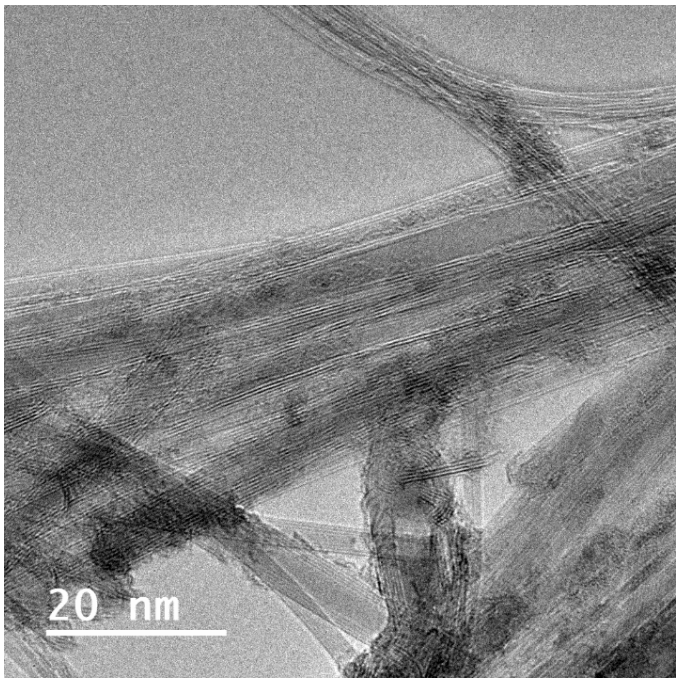

Figure 9.6 Representative TEM image of observed filling structures in the HfSe system after revised synthesis conditions.

Several modified synthetic parameters were pursued for the successful growth of encapsulated $HfSe_3$ chains. The modified parameters are presented in **Figure 9.7**, where the reaction temperature and reaction time are modified to see if an increase in filling and an increase in crystalline species can be obtained. Unfortunately, none of these modified reactions presented any meaningful improvement in the filling observed, and eventually the HfSe system was put on pause to pursue other transition metal families. The initial synthetic parameters shown in **Figure 9.2** produced the most exciting results for the encapsulation of the HfSe system, and absolutely warrants further exploration. There is still plenty of parameter space for the various combinations of reaction temperature, reaction time, and cooling methods to explore.

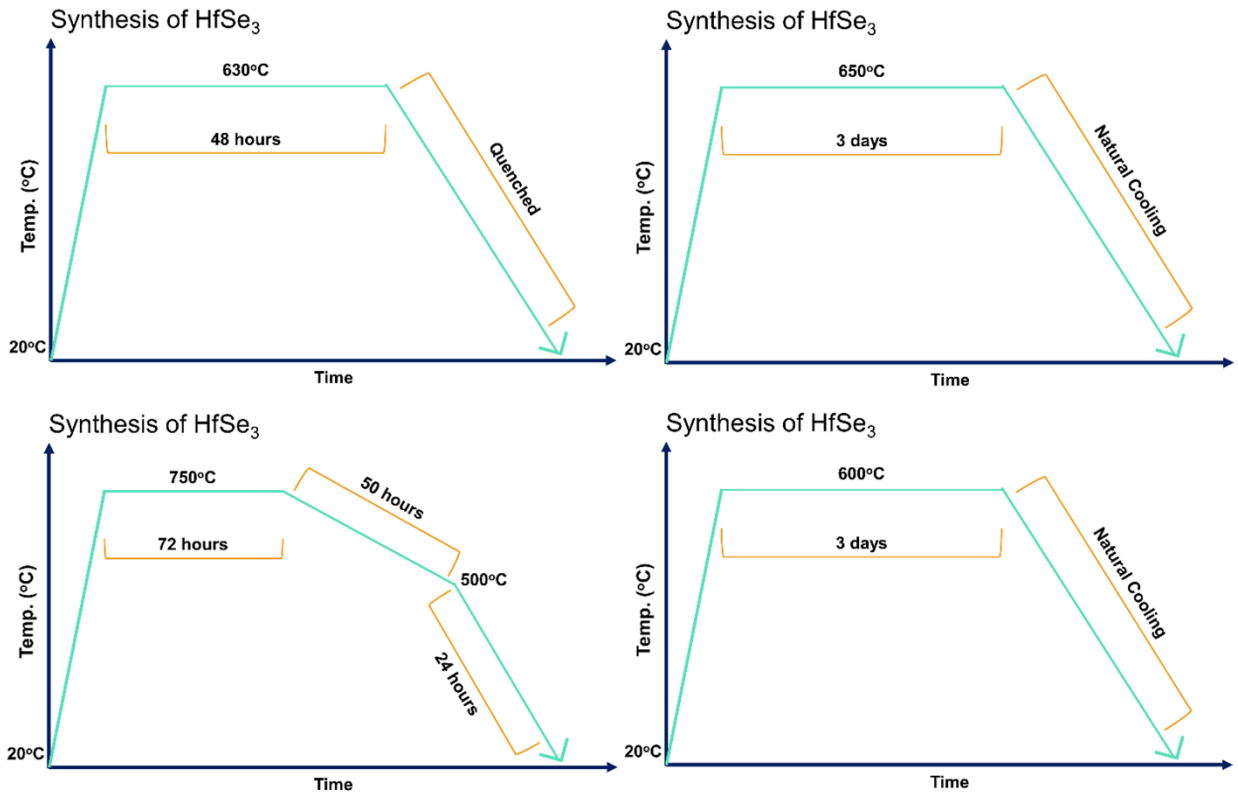

Figure 9.7 Additional modified synthetic protocol for the growth of encapsulated $HfSe_3$ chains.

9.4 Niobium trichalcogenides

Following exploration of the hafnium family, the niobium family was next in pursuit. $NbSe_3$ was the first successful TMT explored down to the vdW limit, studied as few- and single-chain entities. In bulk, NbS_3 is a semiconductor (~1.0 eV), and **Table 9.2** shows that the synthetic protocol for NbS_3 is very similar to some of the other sulfides and that of $NbSe_3$.[148,167] **Figure 9.8** shows the initial synthetic parameters developed for the synthesis of NbS_3 encapsulated species.

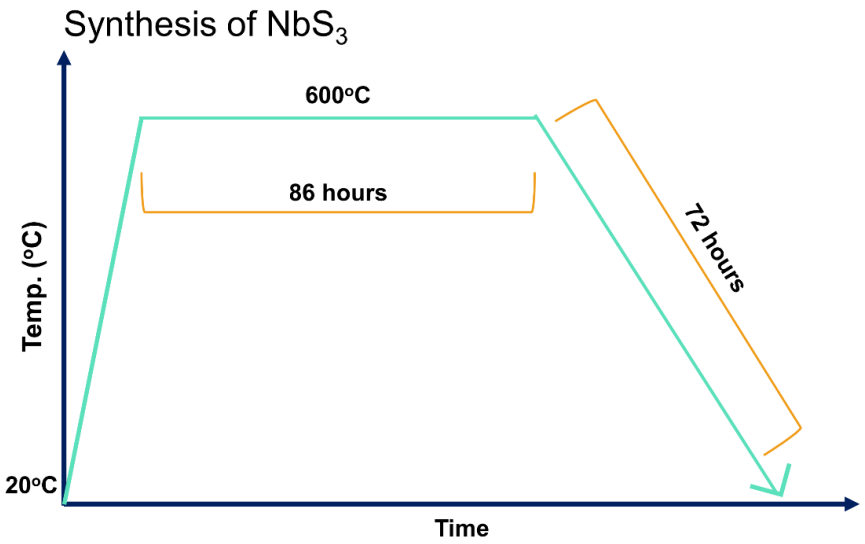

Figure 9.8 Initial synthetic protocol for the growth of encapsulated NbS_3 chains.

Following the synthesis of NbS_3, bulk needle-like crystals were observed, a promising sign for the successful growth and encapsulation of species from the NbS system, similar to the macroscopic observations for the HfSe system. Unfortunately, upon preparation of the NbS sample and viewing under electron microscopy, there was no filling species of any type observed. No TEM images are posted here, as nothing of interest was noticed in the sample. Due to the broad parameter space that exists for the synthesis of these encapsulated species, and the difficulties observed in the hafnium family to narrow down which parameters affect filling and crystallinity, we leave the NbS system open for exploration to examine other TMT families.

9.5 Tantalum trichalcogenides

Closely related to the niobium family, the tantalum family, specifically TaS_3 and $TaSe_3$, was an ideal next candidate. Dr. Jeff Cain led the pursuit of encapsulated Tantalum systems for the trisulfide and triselenide. Ultimately, no chain-like filling was observed in either of these systems after many modifications to the synthetic parameters. However, crystalline filling was observed for the TaS system, similar to what was observed in the HfSe system in **Figure 9.4**, specifically the thin and narrow filling of potential nanoribbons. **Figure 9.9** shows a TEM image of the high contrast, crystalline filling observed. Unlike the HfSe system, however, the TaS system showed greater filling ratio of the CNT and much longer filling lengths of the crystalline material, warranting further study of these observed structures. These crystalline species are explored further in **Chapter 12** and show fascinating defect structures never observed in any bulk TMD before. Additionally, in **Chapter 14**, we will discuss the encapsulation of the telluride species of the tantalum family, which also present very interesting crystalline filling of multiple stoichiometries within CNT. As presented in **Table 9.1**, structures in the TaTe system had been previously reported in literature, but no substantial follow up studies had been performed.

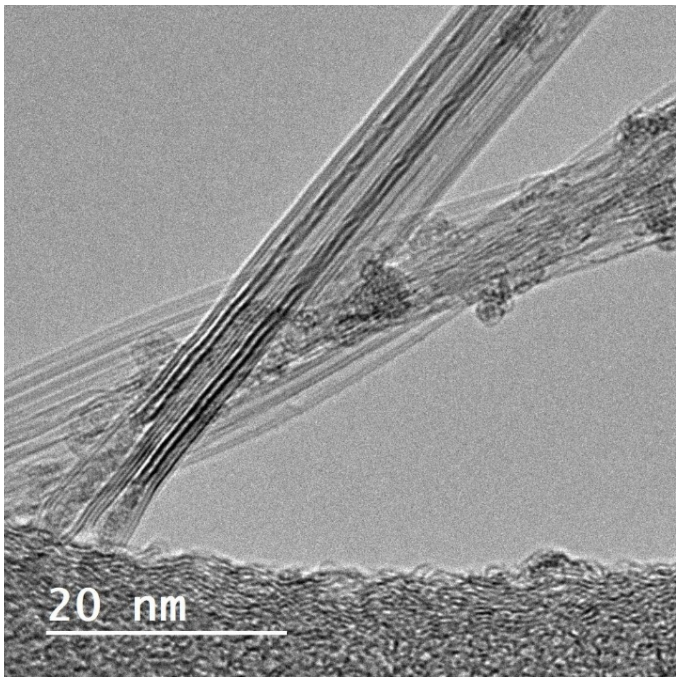

Figure 9.9 Representative TEM image of observed filling structures in the TaS system.

9.6 Titanium trichalcogenides

Following the initial exploration of niobium and tantalum, the known members of the Group VB TMT have been pursued to varying extents based on initial observations. As vanadium-based TMT have not been synthesized or studied in prior research, we can focus our attention on the remainder of the Group IVB TMT. The titanium family is only comprised of one known member, TiS_3. TiS_3 has garnered a lot of interest in study, being a semiconductor (~1.05 eV) and showing great application as an anisotropic photoconductor.[167,168] The synthetic conditions shown in **Table 9.2** highlight a lower overall reaction temperature required, similar to $HfTe_3$.[148] During the process of generating ampoule samples of the TiS system for study, a sample of TiSe was generated as well. Even though no bulk crystal synthesis has been realized for $TiSe_3$, more successful encapsulation of the selenide-based transition metal compounds, rather than the sulfide-based, had been observed up to this point. **Chapter 11** will explore the experimental study of previously unknown members of the TMT family. **Figure 9.10** shows the initial synthetic protocols pursued for the isolation of TiS_3 chains within CNT, and some type of crystalline TiSe species.

Both the TiS and TiSe system were prepared for imaging under TEM. No filling of any type was observed in the CNT for the TiS system. **Figure 9.11** shows dark, amorphous filling observed for the TiSe system, which is generally attributed to amorphous chalcogen filling. As mentioned previously, even amorphous chalcogen filling is promising, as this is indication that reaction temperature and time were sufficient for some vaporized species to migrate into the CNT and condense. However, as the $TiSe_3$ system has not been studied in bulk, no further modification of the synthetic space for the TiSe system was pursued.

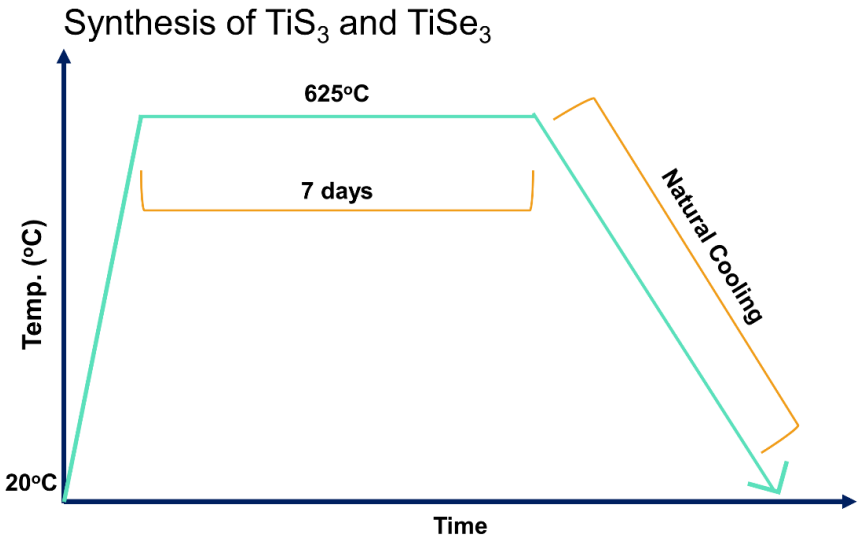

Figure 9.10 Initial synthetic protocol for the growth of encapsulated TiS_3 and $TiSe_3$ chains.

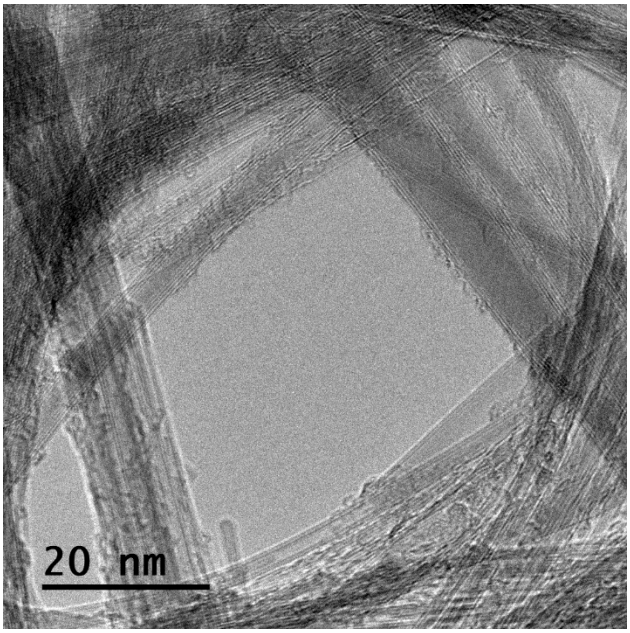

Figure 9.11 Representative TEM image of observed filling structures in the TiSe system.

Even though initial synthetic parameters did not yield any encapsulated species for the TiS system, several modifications to the synthetic parameters were pursued to realize some form of encapsulated system from the TiS family. **Figures 9.12** and **9.13** show two different modifications to the synthetic parameters for the synthesis of encapsulated TiS species. The main difference between these synthetic changes is the overall reaction time. Sulfur is the most volatile chalcogen out of the three commonly used, so longer reaction and cool down times were explored to see how time affected overall crystallization of volatile species. Samples prepared from the shorter reaction times in **Figure 9.12** did not yield any encapsulated species, however increasing the reaction time in **Figure 9.13** produced some species inside of the CNT. **Figure 9.14** shows the observed filling, where again only a dark, amorphous structure was observed.

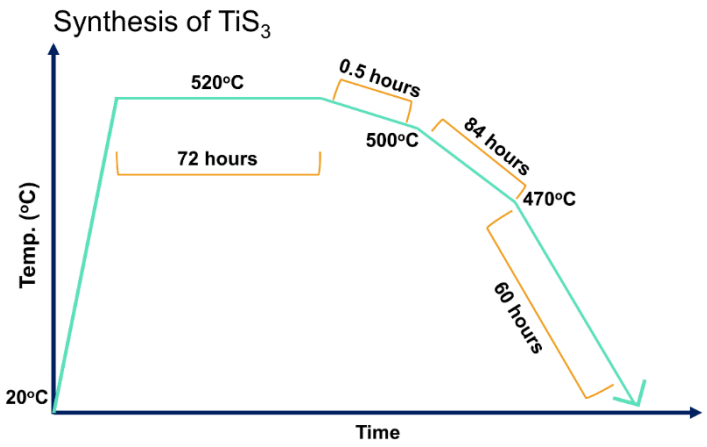

Figure 9.12 Modified synthetic protocol for the growth of encapsulated TiS_3 chains.

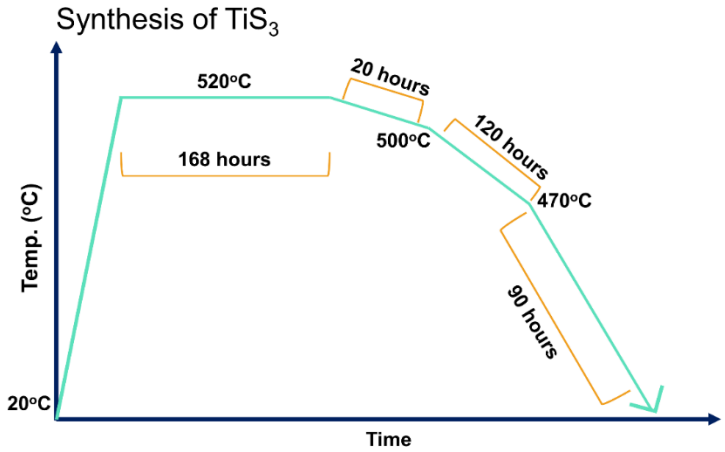

Figure 9.13 Additional modified synthetic protocol for the growth of encapsulated TiS_3 chains.

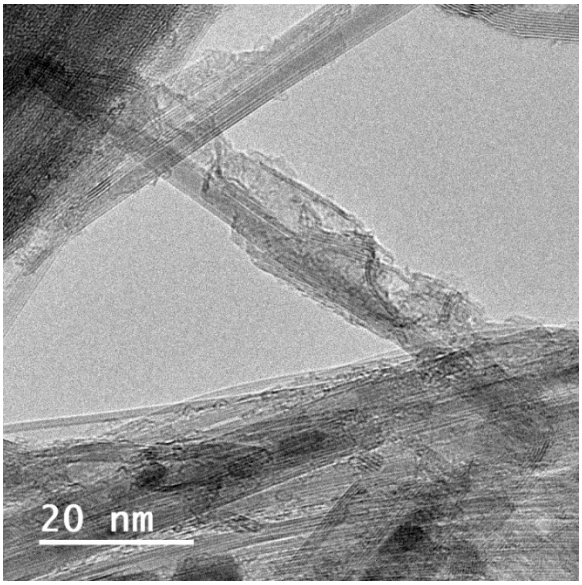

Figure 9.14 Representative TEM images of observed filling structures in the TiS system after revised synthesis conditions.

Successful isolation of any chain-like or other crystalline species for the TiS system has yet to be realized, however successful filling of the CNT with amorphous species seems to be aided by extended reaction times and cooling. As no crystalline structure seems to have formed, the overall reaction time probably did not play a large role in the filling, but rather the extended cooling time could have aided the condensation of species inside of the CNT. A trend we started to notice was the initial difficulty in observing encapsulated structures for any of the sulfide TMT, as compared to the selenides or tellurides, which we will address to some extent at the end of this chapter.

9.7 Zirconium trichalcogenides

The last remaining transition metal system to explore for the TMT family is that of zirconium. Zirconium is one of two transition metals that forms trichalcogenide structures with all three chalcogens, the other being hafnium. However, unlike hafnium, all three of the zirconium-based TMT are well-studied and have shown a variety of applications, from photodetectors, to current generators in nanoelectronics, to catalysts.[165,169,170] The synthetic conditions surrounding the successful growth of the three Zr-based TMT seem to be better understood, and from **Table 9.2**, the most ideal synthetic conditions for all three are essentially identical. Therefore, **Figure 9.15** highlights the initial synthetic parameters explored for all three TMT.

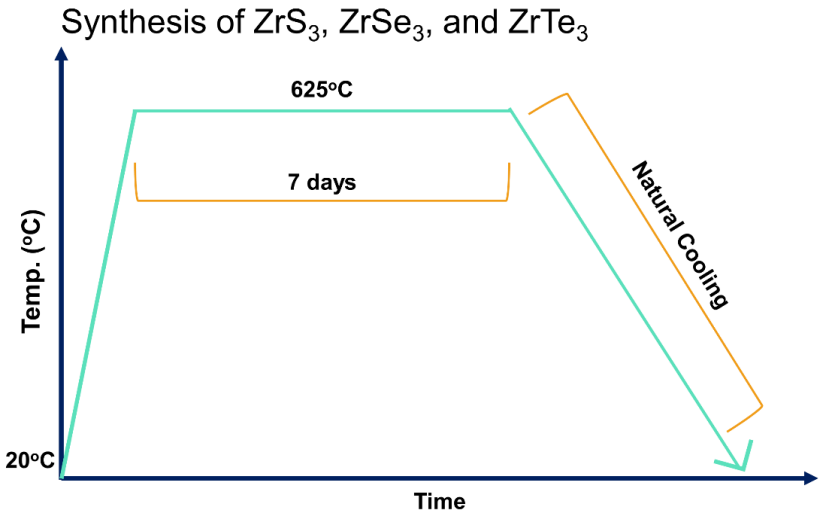

Figure 9.15 Initial synthetic protocol for the growth of encapsulated ZrS_3, $ZrSe_3$, and $ZrTe_3$ chains.

The ZrS, ZrSe, and ZrTe systems were prepared for imaging under TEM. The ZrS system did not exhibit any type of filling in the CNT. **Figure 9.16** shows dark, yet crystalline filling observed for the ZrSe system, indicating the initial synthetic parameters were fit for some filling of the CNT and condensation of crystalline material. However, the filling is not chain-like in nature, meaning the parameters were not ideal for the growth of encapsulated $ZrSe_3$. **Figure 9.17** shows the high contrast, linear chain-like filling we hope to observe for $ZrTe_3$. However, the filling ratio is low and overall length-scale is extremely short. The results in **Figures 9.16** and **9.17** are significant improvements over the observations made for other TMT systems.

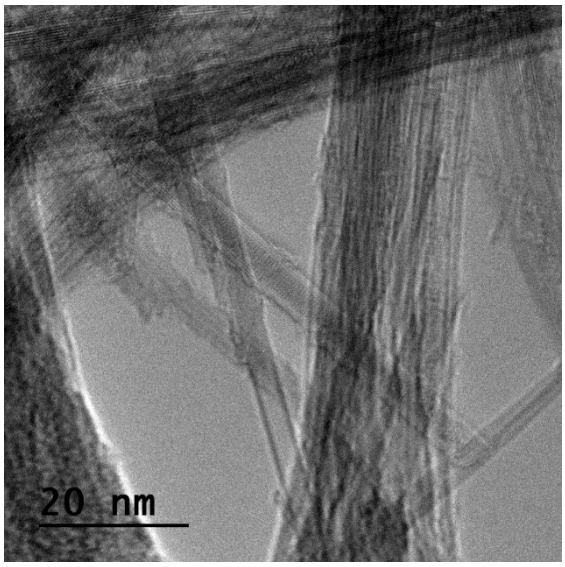

Figure 9.16 Representative TEM image of observed filling structures in the ZrSe system.

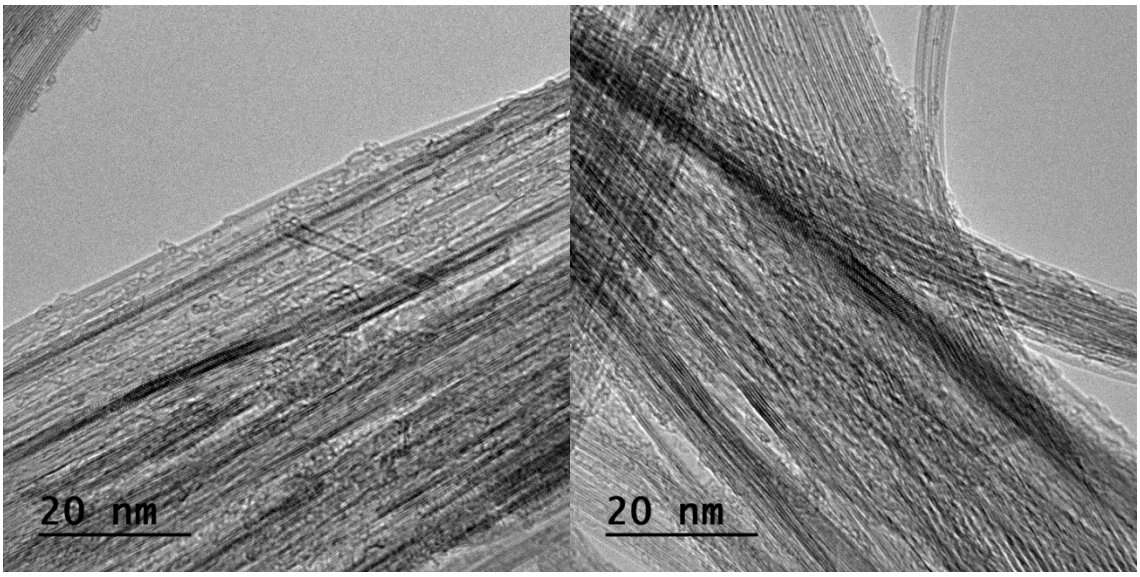

Figure 9.17 Representative TEM images of observed filling structures in the ZrTe system.

The effect of reaction temperature on the filling of species in CNT still needs more exploration, especially if temperatures for encapsulated species could deviate from the single-crystal growth conditions. The first route of modification was increasing the reaction temperature in an attempt to increase the crystallinity and filling ratio of the encapsulated ZrSe and ZrTe systems, shown in **Figure 9.18**. We also continue to explore the synthesis of encapsulated ZrS systems as well, since the single crystal synthetic parameters closely match those of ZrSe and ZrTe. A prolonged cooling protocol was also followed for the modified synthesis in **Figure 9.18**. Extended cooling has shown some improved filling, albeit not always of crystalline species, of the CNT with some amorphous sulfide species, and showed improved filling capabilities of the $HfTe_3$ species inside of CNT. The cooling of the system could play a dual role in the overall filling of the CNT and the resulting phase of the material.

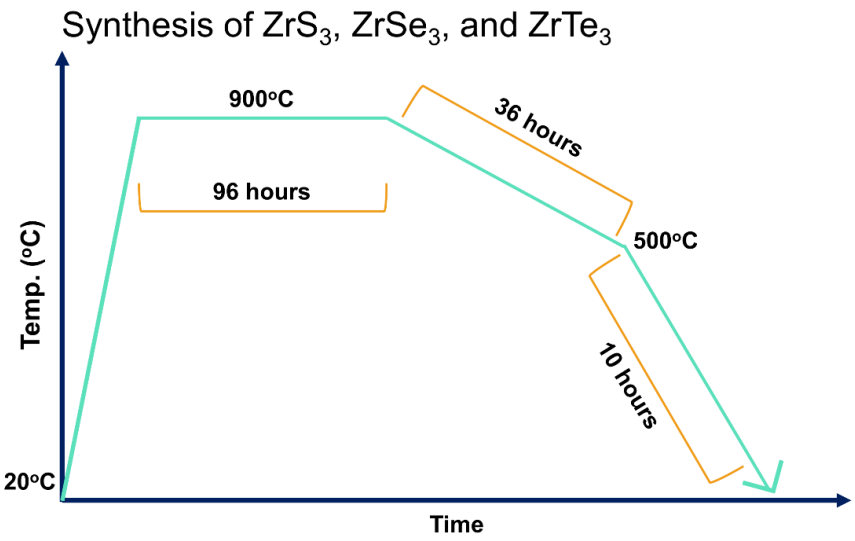

Figure 9.18 Modified synthetic protocol for the growth of encapsulated ZrS_3, $ZrSe_3$, and $ZrTe_3$ chains.

The overall filling scheme of vapor species inside of CNT is in a constant state of motion. At the high reaction temperatures of these TMT systems, the reactive vapor species are constantly entering and leaving the CNT.[143] If the cooling is too slow, then the reactive species can remain volatile for extended periods of time and could condense and crystallize as larger bulk crystals outside of the CNT.[171] However, if cooling is too fast, then the reactive species may not have enough time to continue to migrate inside of the CNT to condense and form crystalline systems. Cooling rate needs to be such that volatile species have enough energy and motion to enter the CNT, but then lose enough energy to condense inside of the CNT and form a seed particle for other vapor species to continue the growth.[172] An additional factor to balance is the specific stoichiometry of material we are trying to synthesize in the first place, and how stable that stoichiometry is. For example, $HfTe_3$ requires slow cooling for the bulk crystal, as the ditelluride and tritelluride phase are in direct competition with each other for stability, and rapid cooling will preferentially form the ditelluride.[129]

Figures 9.19, 9.20, and **9.21** show the observed filling species of the ZrS, ZrSe, and ZrTe systems, respectively. Higher contrast filling is observed in the ZrS system, reminiscent of the TaS system. However, this crystallinity was rarely observed in the sample, and the filling fraction was incredibly low, so the ZrS system was not studied in further detail. Higher reaction temperature and more control of the cooling parameters does seem to have benefitted the encapsulation of some species from the ZrS system, which could be the key for accessing other encapsulated sulfide members of the TMT family.

Unlike the lower reaction temperature and faster cooling, the ZrSe system showed only dark, amorphous filling at higher temperatures and longer cooling times. The only improvement over the initial synthetic conditions is that the overall filling fraction drastically increased with the modified parameters, so perhaps one of the two modifications (reaction temperature and cooling time) could play a role in the encapsulation of the selenide-based systems. Under the modified synthetic parameters, the ZrTe system showed growth and encapsulation of linear chain-like species, indicating the successful isolation of $ZrTe_3$ inside of the CNT. As $ZrTe_3$ showed the most successful and exciting results for the Zr family, we will continue to focus on $ZrTe_3$ for further study.

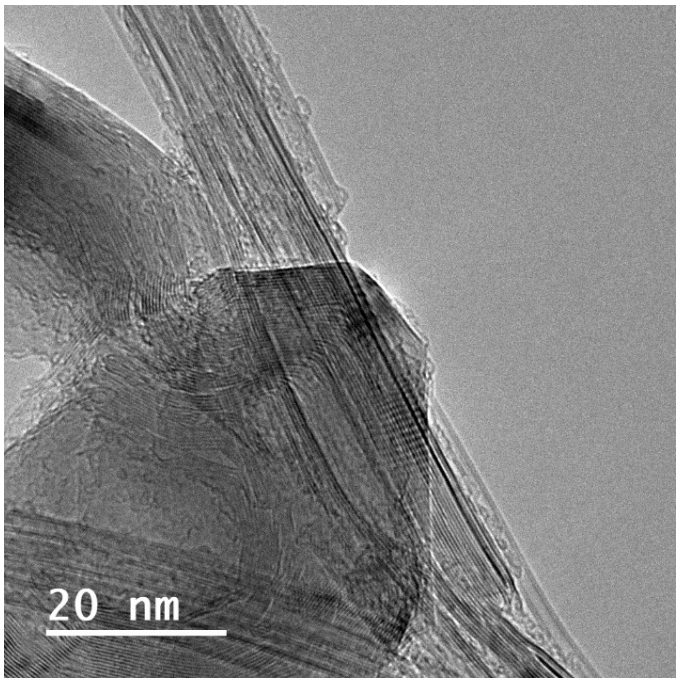

Figure 9.19 Representative TEM image of observed filling structures in the ZrS system after revised synthesis conditions.

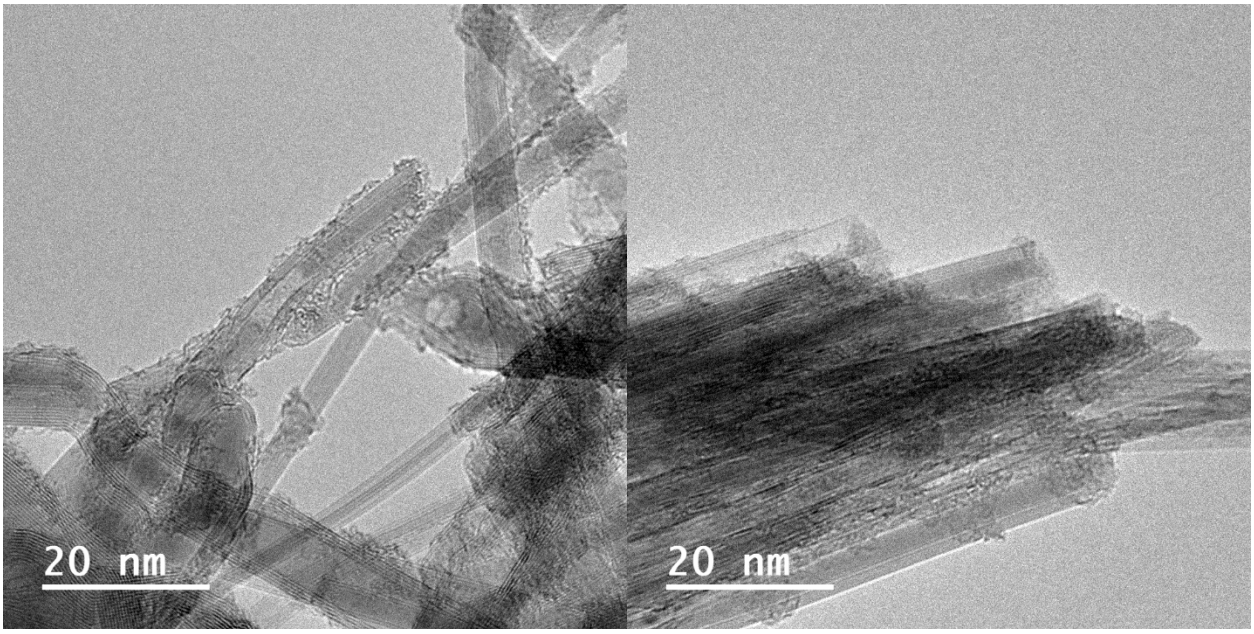

Figure 9.20 Representative TEM image of observed filling structures in the ZrSe system after revised synthesis conditions.

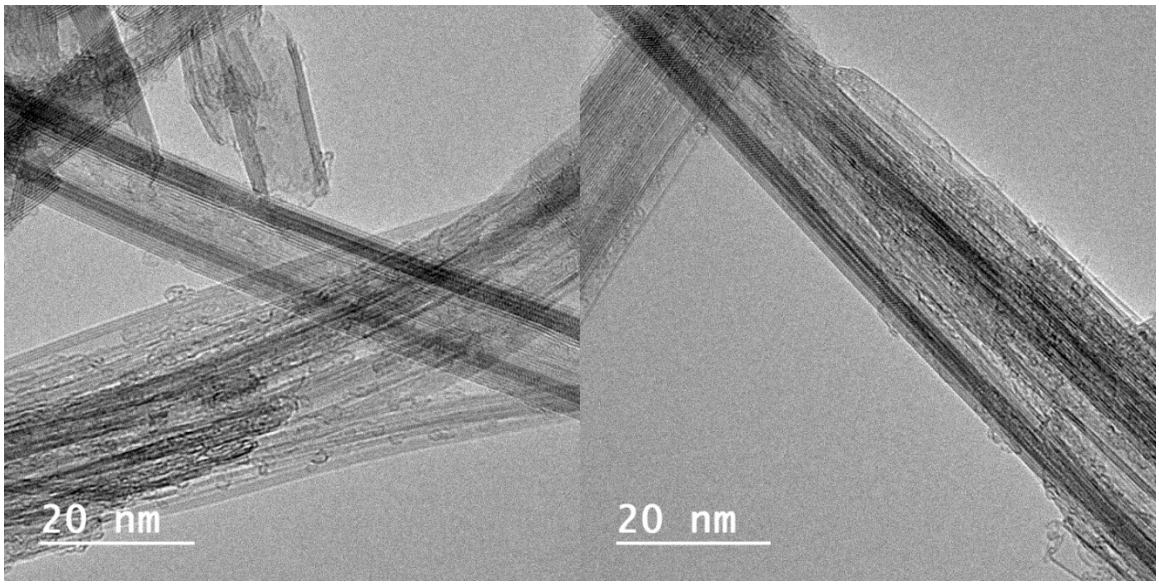

Figure 9.21 Representative TEM image of observed filling structures in the ZrTe system after revised synthesis conditions. Linear chain-like filling suggesting successful filling of the tritelluride.

An interesting species observed other than the linear chain-like compounds sought for indication of $ZrTe_3$, were some flatter, narrower species. These crystalline structures, shown in **Figure 9.22**, were similar to those observed in the HfSe and TaS systems, good indication that these structures are encapsulated nanoribbons. Very few of these moieties were observed, so we will not pursue their study or isolation in more detail. However, this nanoribbon structure, presumably $ZrTe_2$, could be of interest for future studies on the successful growth and isolation of TMD nanoribbons.

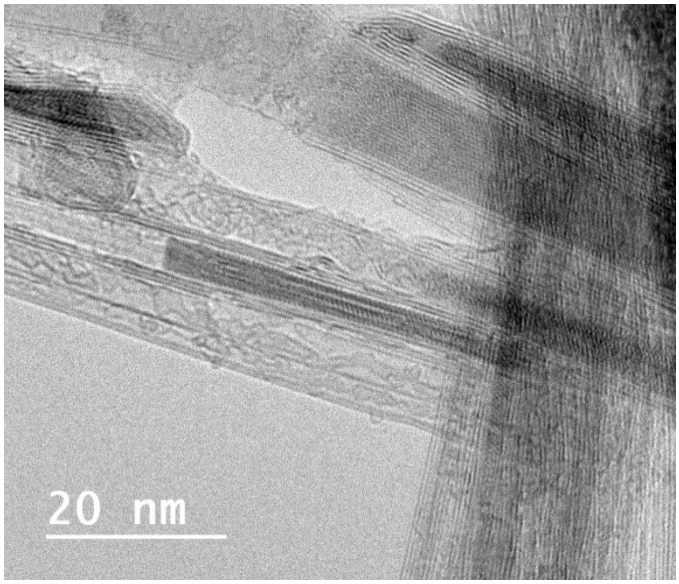

Figure 9.22 Additional TEM image of interesting observed filling structures in the ZrTe system. Flat, crystalline lattice observed in a CNT roughly 15 nm wide. Possible nanoribbon filling.

Fairly dramatic differences were observed in the overall filling ratio and crystallinity of species inside of the CNT between the initial synthetic parameters explored in **Figure 9.15** and the modified parameters in **Figure 9.18**, especially for the ZrSe and ZrTe systems. Therefore, additional synthetic trials were performed to explore how different parameters affect the overall growth of the encapsulated species. **Figure 9.23** shows an additional modified parameter space for the ZrSe and ZrTe systems, where the overall reaction temperature has been lowered but extended cooling is still pursued, and even extended beyond initial modifications.

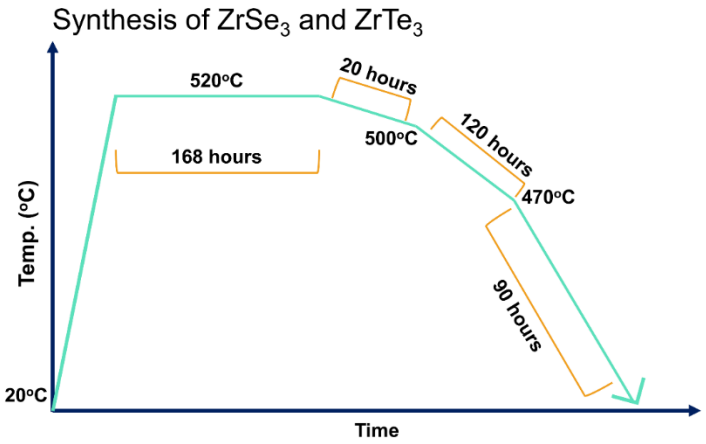

Figure 9.23 Modified synthetic protocol for the growth of encapsulated $ZrSe_3$ and $ZrTe_3$ chains.

Both the ZrSe and ZrTe system samples were prepared for TEM imaging, however no filling was observed for the ZrTe system at these lower temperatures. As seen in **Figure 9.24**, successful filling of the CNT for the ZrSe system was observed, however the filled species remain as dark, amorphous filling with no crystallinity observed. The overall filling ratio is similar to that of the higher reaction temperature pursued in **Figure 9.18**, which is good indication that extended cooling seems to be beneficial to the overall filling of selenide-based materials. The parameter that needs to be explored further is the overall reaction temperature, which could have the most control over the crystallinity of the encapsulated system.

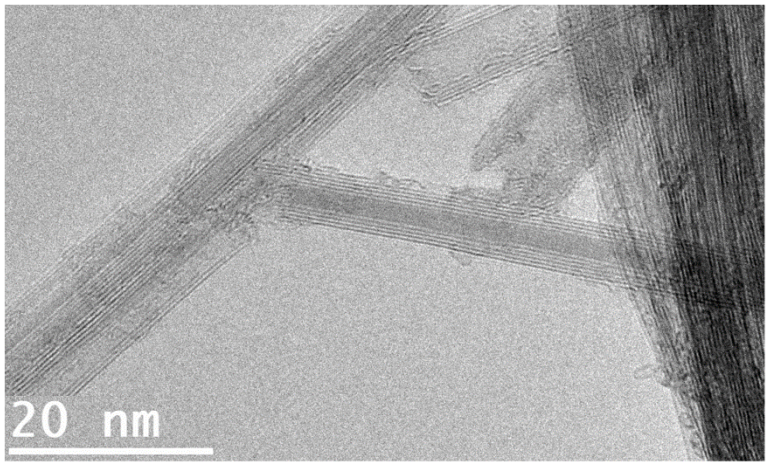

Figure 9.24 Representative TEM image of observed filling structures in the ZrSe system after revised synthesis conditions.

The reaction temperature in **Figure 9.23** proved too low for $ZrTe_3$. So, we can begin exploring higher reaction temperatures while maintain longer periods of cooling to aid in the overall filling ratio of the CNT. **Figure 9.25** shows the modified synthetic parameters explored with slightly higher reaction temperatures and prolonged cooling, which resulted in the successful synthesis and encapsulation of $ZrTe_3$ at higher filling fractions.

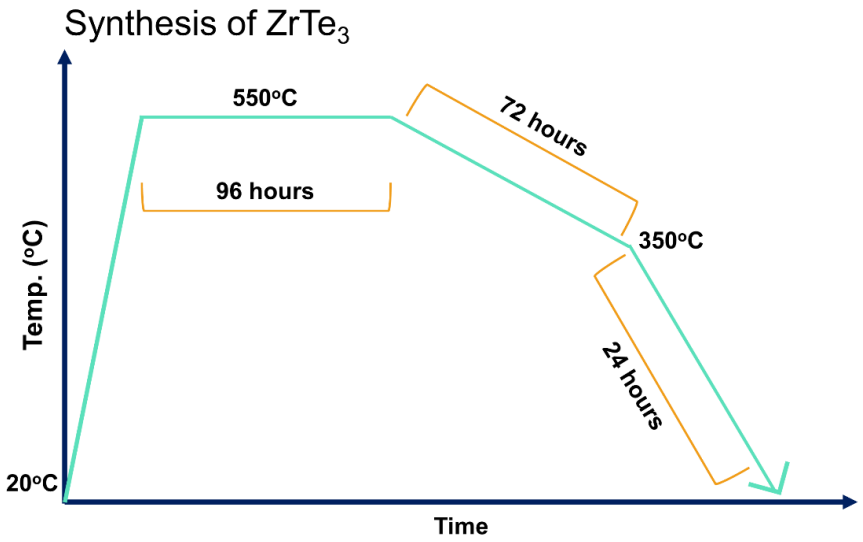

Figure 9.25 Modified synthetic protocol for the growth of encapsulated $ZrTe_3$ chains.

Figure 9.26 shows the improved filling and encapsulation of linear chain-like compounds of $ZrTe_3$. While the chain-like filling is indicative of the successful growth of a TMT, at the few-chain limit, spiraling of the chains can often be observed. Following previous synthetic protocols, spiraling chains of $ZrTe_3$ had not been observed. However, at the modified reaction temperature in **Figure 9.25**, few-chain spiraling structures were very abundant in the sample and showcases similar behavior of the few-chain limit of $ZrTe_3$ to that of $HfTe_3$ and $NbSe_3$.[144,163] We also observe several instances of the double-chain limit of $ZrTe_3$, shown in **Figure 9.26**.

Alongside the standard chain-like filling observed, there were a few instances of drastically higher contrast filling, also chain-like in nature, as shown in **Figure 9.27**. The filling shown in **Figure 9.27** is reminiscent of the filling observed in the TaS system, which later was found to be encapsulated nanoribbons. Therefore, the ZrTe system could also easily form encapsulated TMD nanoribbon structures, as is supported, and evidenced, by the structures observed in **Figure 9.22** and **Figure 9.27**. The nanoribbon-type filling was not commonly observed, so the synthetic parameter space must continue to be explored to preferentially form these ribbon-like structures of a TMD over the chain-like structures of a TMT.

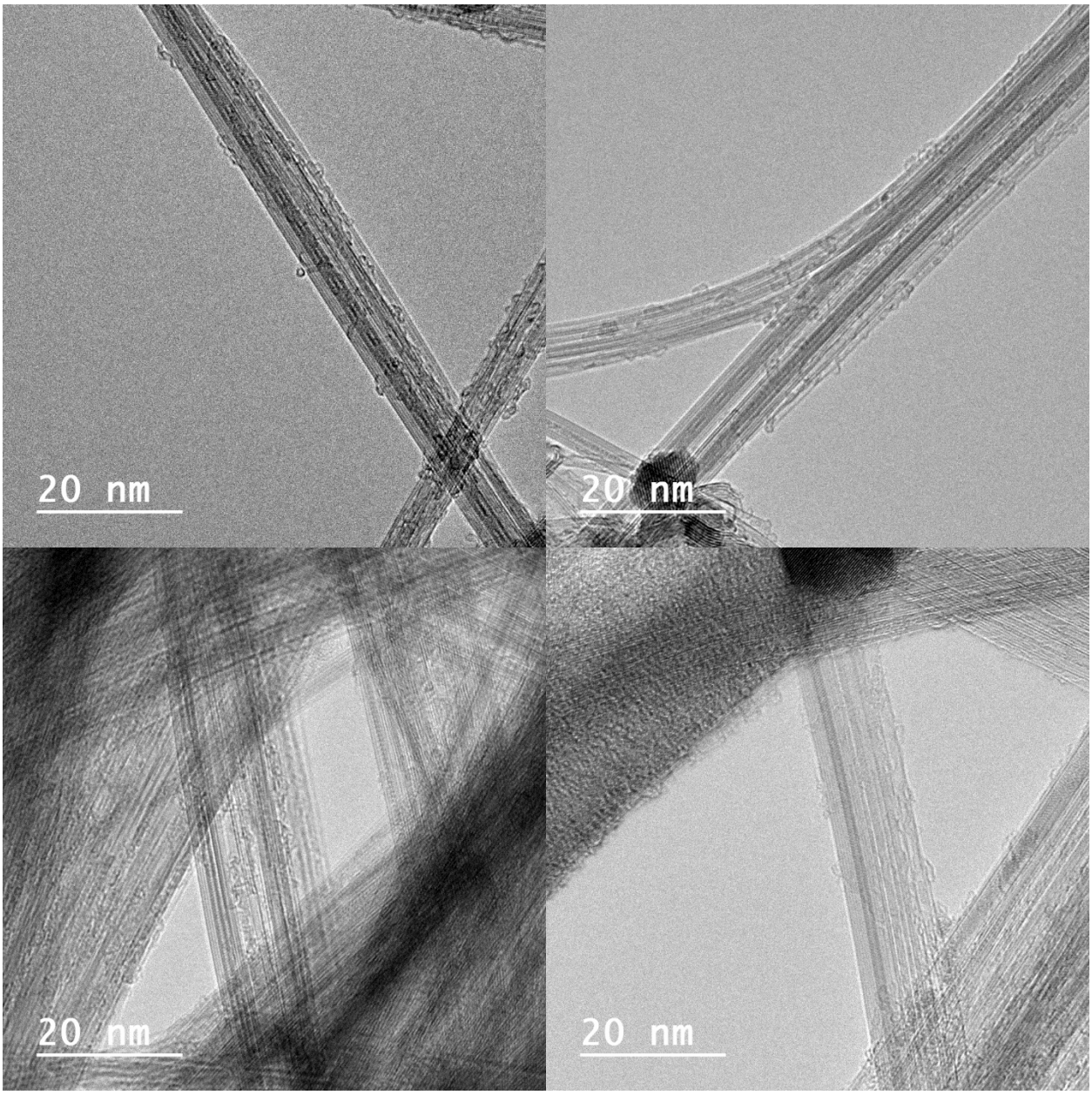

Figure 9.26 Representative TEM images of observed filling structures in the ZrTe system after revised synthesis conditions. Linear chain-like filling suggesting successful filling of the tritelluride. Top images also showcase the tell-tale sign of few-chain spiraling samples.

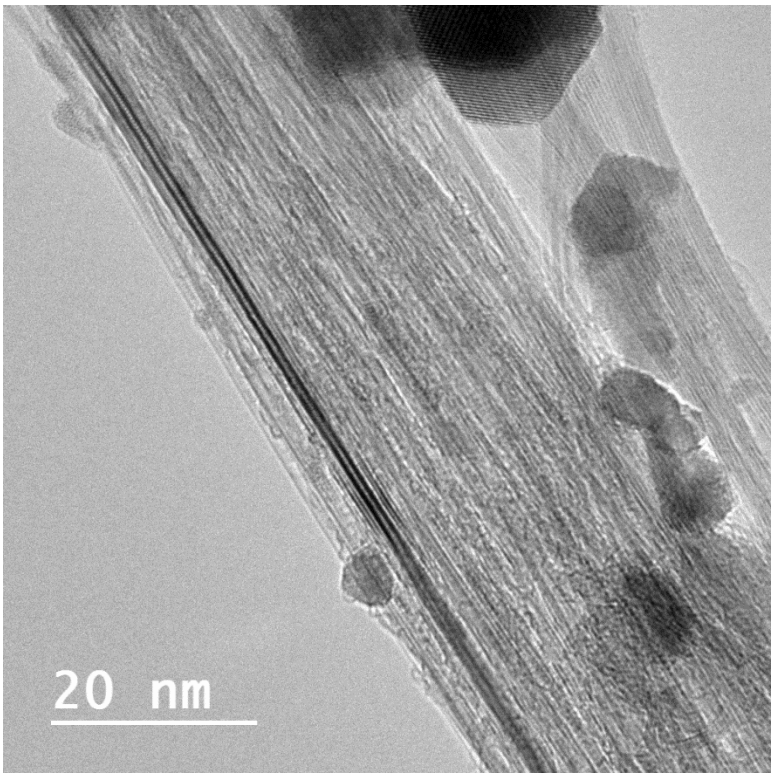

Figure 9.27 Representative TEM image of additional observed filling structure in the ZrTe system after revised synthesis conditions.

9.7.1 Analyzing the atomic structure of encapsulated $ZrTe_3$

Due to the increase in filling ratio and stabilized spiraling chain structures observed, $ZrTe_3$ was an ideal candidate for further study with atomic-resolution microscopy. Working with Dr. Jeff Cain, we employed scanning transmission electron microscopy (STEM) to obtain structural imaging of the encapsulated chains, which is highlighted in **Figure 9.28**. $ZrTe_3$ showcased incredibly nice structures to image, with straight triple chains and spiraling triple chains found often in tandem. The periodicity of the spiraling chains is roughly 5 nm, and surprisingly not always present in the triple-chain specimen. More study is required to understand what drives the preferential spiraling of the chains, however from studies performed on $HfTe_3$, the spiraling enhances the energy relaxation of the system due to structural changes at the single-chain limit.[163]

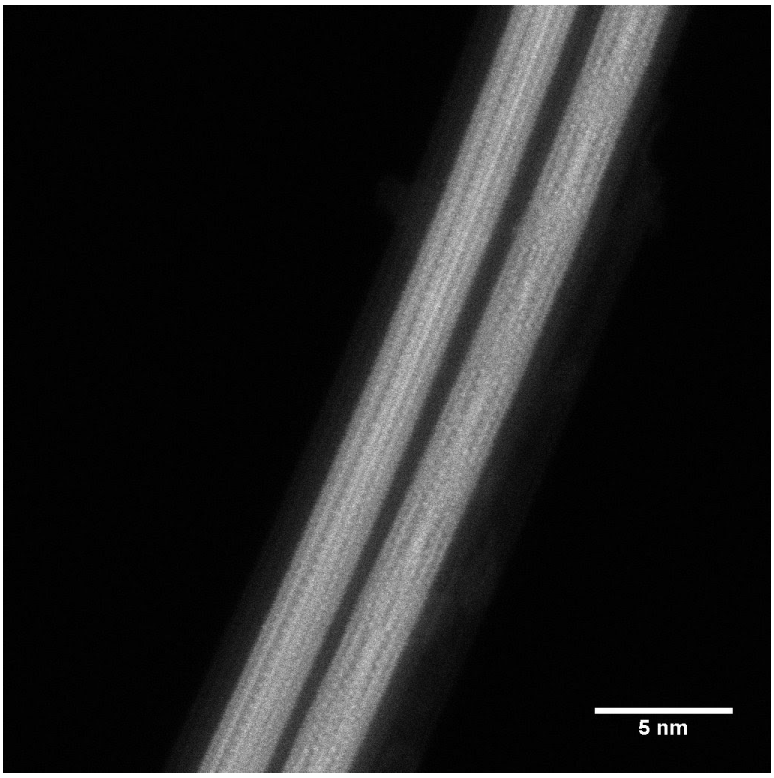

Figure 9.28 Representative scanning transmission electron microscopy image of encapsulated $ZrTe_3$. Exemplary image of two different encapsulated chain systems. Straight triple chains (left) and spiraling triple chains (right) observed in two neighboring double-walled carbon nanotubes.

We were interested in this inherent difference between the spiraling of triple-chain $ZrTe_3$ vs. $HfTe_3$, as they are both Group IVB transition metal tritellurides, so their atomic and electronic structure should be similar. From an inorganic coordination complex perspective, the overall size of Zr and Hf is identical (the covalent radius of both is 175 pm), and their electronegativity is identical (Pauling Scale: 1.3), so the bonding and geometry of their orbitals should be roughly the same.

To better understand the difference in the spiraling observed, we sought additional information on the single-chain limit of $ZrTe_3$ so we could compare the structure to that of single-chain $HfTe_3$. **Figure 9.29** shows the calculation results generated by Dr. Sehoon Oh, following similar procedures outlined in **Chapter 8** for the theoretical study of $HfTe_3$.[163] The atomic structure is almost identical to that of $HfTe_3$, where again the single-chain limit energetically prefers a trigonal antiprismatic (TAP) distortion, which results in an overall opening of the band structure around the Fermi level. The only immediately noticeable difference for the $ZrTe_3$ single chain is the size of the gap that opens. While the TAP distortion in $HfTe_3$ results in a gap of over 1.1 eV opening, $ZrTe_3$ shows a smaller gap of just over 0.5 eV. Therefore, there could be energetic competition between the energy relaxation from spiraling of the triple-chain limit, and how much energy is required to break the vdW interactions along the axis of the chain to induce spiraling. Additional study would be needed to examine the energetic transition from parallel alignment to a spiraling system and could provide exciting insight into the overall energetics of these fascinating structural moieties observed at the few-chain limit that would never occur in bulk crystals.

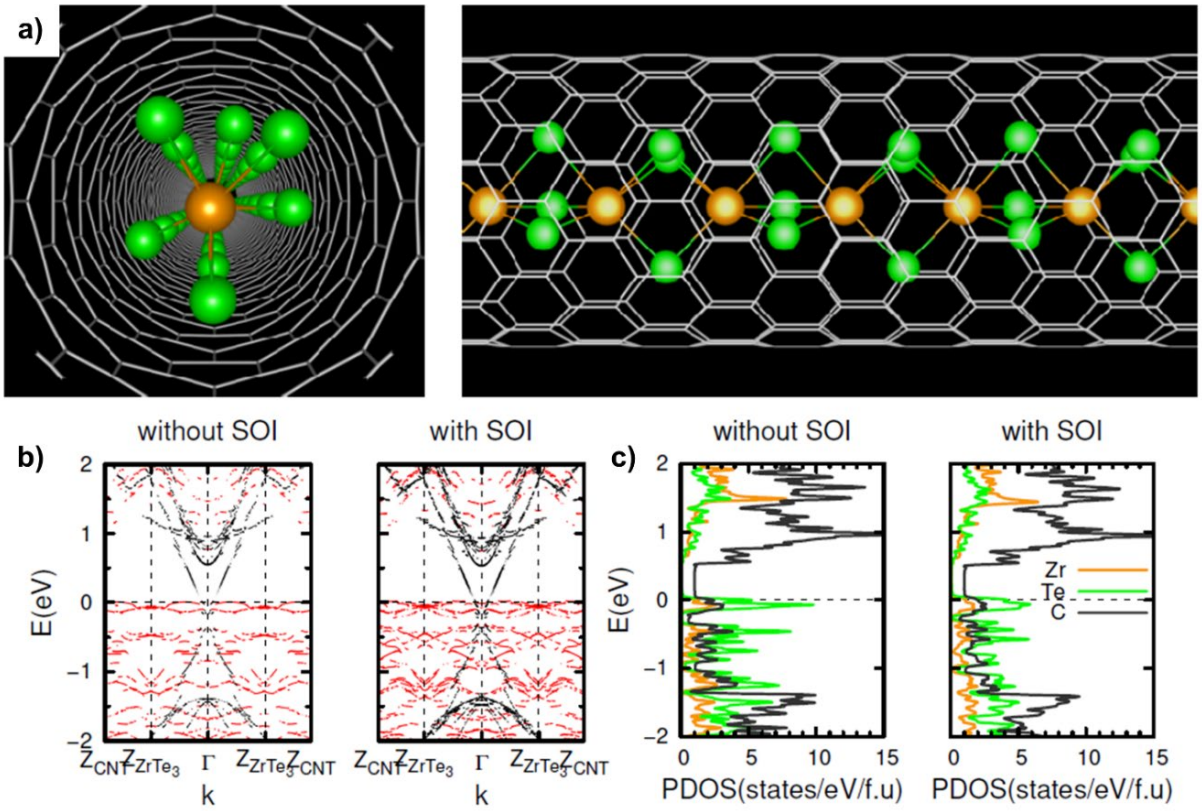

Figure 9.29 Atomic and electronic structure of single-chain $ZrTe_3$. a) Atomic structure of an encapsulated single chain of $ZrTe_3$. The white lattice is that of a single-wall carbon nanotube, with the Zr and Te atoms represented by orange and green atoms, respectively. b) Electronic structure of the encapsulated chain without and with spin orbit interaction (SOI). The red lines represent the bands of the $ZrTe_3$, while black lines are those of the carbon nanotube. c) Projected density of states (pDOS) of the encapsulated chain without and with SOI. The orange line represents the states of zirconium, green for tellurium, and black for the carbon nanotube. Data collected in collaboration with Dr. Sehoon Oh.

9.8 Exploring spectroscopic analysis of encapsulated $ZrTe_3$

While exploring encapsulated $ZrTe_3$ at the few-chain and single-chain limit provides interesting insight into the stability of the TMT at their vdW limit, we wanted to continue improving our analytical techniques of these encapsulated structures and their associated emergent phenomena at the ultra-confined limit. Similar to the TMD family, most of the TMT family that are well-studied exhibit unique spectroscopy spectra (such as Raman modes) due to their anisotropic structure. This unique signature in their spectra could provide an additional method of confirming filling of CNT with the desired material. Additionally, we could expect to see interesting differences in their spectra at the few- and single chain limit, due to the more dramatic modification to the atomic structure. Raman spectroscopy could provide insight into how their vibrational modes area altered due to the modified environment of the encapsulated chains, and photoluminescence could start to probe the electronic structure of the encapsulated species.[173]

9.8.1 Background on Raman spectroscopy of $ZrTe_3$

In order to probe these nanostructures with spectroscopic tools, we collaborate with Dr. Sebastian Heeg at Freie University in Berlin. Dr. Heeg is an expert on the spectroscopic study of encapsulated species within CNT, utilizing Raman spectroscopy to probe linear chains of encapsulated carbon atoms.[174–176] We first pursued the study of encapsulated many and few chains of $ZrTe_3$, to see if enough signal could be obtained from the encapsulated structures before pursuing the study of single-chain $ZrTe_3$. **Figure 9.30** shows the vibrational modes present in bulk $ZrTe_3$ crystals.[177] Based on the spectra shown in **Figure 9.30**, we expect the Raman modes of $ZrTe_3$ chains to occur at frequencies between 35 cm^{-1} and 220 cm^{-1}. However, the Raman modes can be classified into low and high frequency sets. The low frequency set (37 – 86 cm^{-1}) was assigned to external crystal modes (translational modes and "libration" modes) of the chains forming a bulk crystal, which are the vibrational modes of highly fixed chains (i.e. in bulk crystals).[178] The high frequency modes above 100 cm^{-1} are associated with the internal vibrations of the chains (intrachain vibrations). The low frequency vibrational modes that arise from the rigid nature of the chains would either decrease in intensity or disappear altogether at the few-chain limit, therefore we proceed with Raman studies focused on the higher frequency vibrational modes (over 100 cm^{-1}).

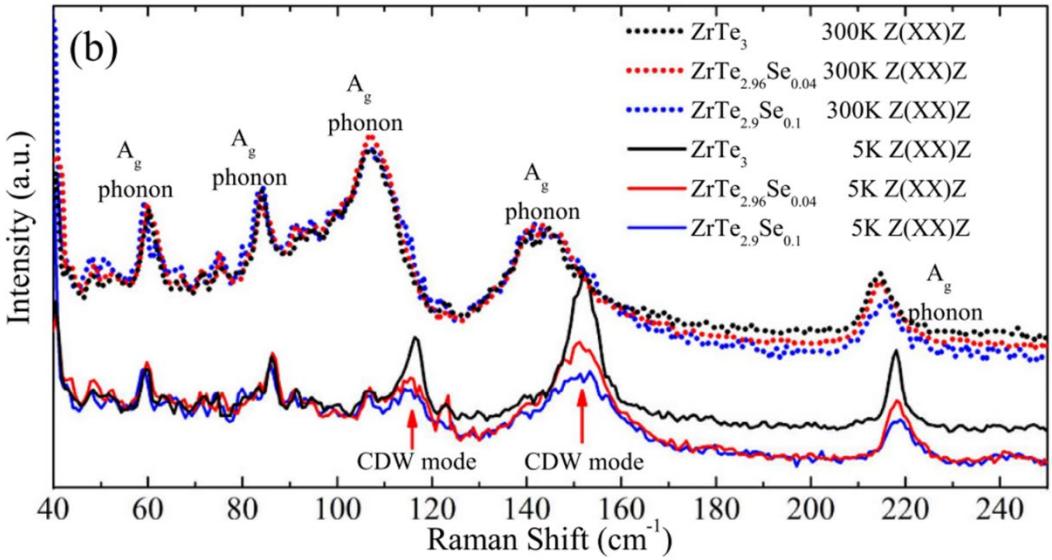

Figure 9.30 Raman spectra of $ZrTe_3$. Phonon modes of interest are above 100 cm^{-1}. Adapted from reference 177.

9.8.2 Experimental Raman measurement of encapsulated $ZrTe_3$

Samples of encapsulated $ZrTe_3$@CNT were prepared in the Zettl lab following the protocol explored in previous sections. Screening of the CNT was performed using TEM to ensure high filling ratios and desired many- and few-chain specimen. For Raman, samples were prepared on Si/SiO_2 substrates. In short, the suspended $ZrTe_3$@CNT sample was drop cast on an Si/SiO_2 substrate, dried and viewed under SEM to ensure relatively disperse distribution of the CNT. Once the samples were prepared, they were shipped to Dr. Heeg for measurement.

The $ZrTe_3$@CNT sample was measured at various locations on the sample with two different laser wavelengths (532nm and 633nm) to scan for Raman signatures of the $ZrTe_3$ chains from inside of the CNT. To generate representative spectra, spatial maps of the same 10x10 μm region were taken and averaged over individual lines of the scan. **Figure 9.31a** shows typical Raman spectra of CNT with very strong signals indicating a high density of CNT sample. There were no features that are unusual for CNT spectra, and no immediate signature of the $ZrTe_3$ chains was observed.

Figure 9.31b shows averaged line spectra for the two laser wavelengths, with the expected $ZrTe_3$ modes indicated by dashed lines. In some of the spectra, there is some matching of the obtained spectra and the expected signal from $ZrTe_3$. While there is possible matching between the spectra, unfortunately we cannot conclusively say whether this signal is generated by encapsulated $ZrTe_3$ chains. The issue has to do with the frequency range we would observe signal from both the $ZrTe_3$ *and* CNT. CNT exhibit strong lattice vibrations due to the sp^2 bonding, as denoted by the G- and D-band in **Figure 9.31a**, similar to graphene (as discussed in the **Chapter 1)**. However, CNT also exhibit strong vibrational modes in the lower frequency range, up to 300 cm^1, from the radial vibration of the nanotube (expanding and contracting of the tube radially from the center). The frequency range where we expected to observe the Raman modes of the $ZrTe_3$ chains overlaps with the radial breathing modes (RBMs) frequency of the CNT in the sample. The CNT sample used also has a broad diameter distribution, meaning the RBM observed will also have a broad distribution of frequencies.

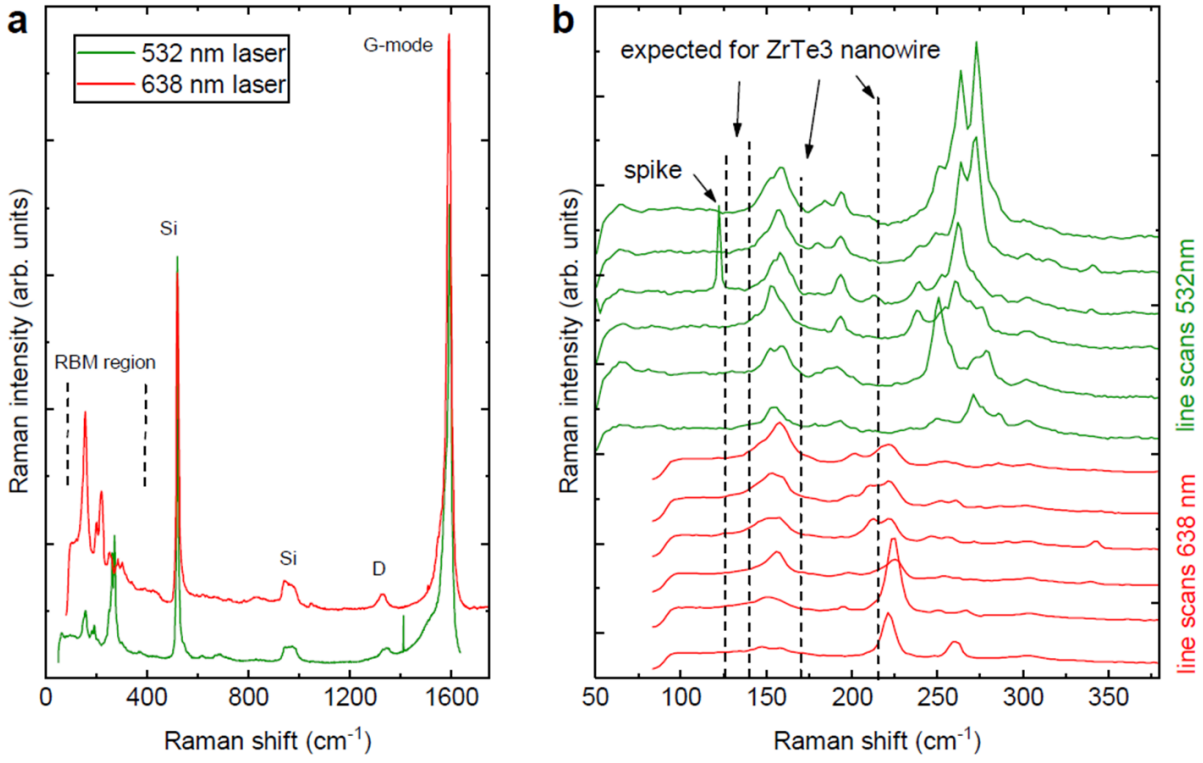

Figure 9.31 Experimental Raman on $ZrTe_3$@CNT sample. a) Typical spectra collected of the CNT sample. No extraneous or unexpected signal obtained. b) Averaged line spectra of the $ZrTe_3$@CNT sample, with measurements from the 638 and 532 nm lasers indicated by the red and green lines, respectively. Data collected in collaboration with Dr. Sebastian Heeg.

In addition to the overlap of frequencies, the strong and resonant Raman response of the CNT most likely dominates the Raman signal obtained and would obscure the Raman signal of the $ZrTe_3$ chains (assuming we can detect the $ZrTe_3$ in principle). Based on the signal-to-noise ratio of the spectrum shown in **Figure 9.30**, the $ZrTe_3$ Raman signal looks extremely weak, most likely orders of magnitude below that of the CNT.

One route to circumvent this issue of signal is to use CNT with small diameters and a very narrow diameter distribution, possibly monochiral CNT (i.e. (6,5) tubes), whose RBMs do not overlap with the spectral region where we expect the $ZeTe_3$ signals.[179] In general, CNTs with diameters ≤ 0:85nm exhibit RBM frequencies ≥ 275 cm^{-1}, plenty removed from the highest frequency phonon observed in $ZrTe_3$. Pursuing solely single-chain specimen of encapsulated $ZrTe_3$ in ultranarrow, monochiral CNT is absolutely feasible and an excellent course for future study. I also recommend looking for other encapsulated materials that exhibit vibrational modes at much higher frequencies than the RBM of the encapsulating CNT. Some of the nanoribbon-like TMD species observed within the CNT would be another excellent point of study for spectroscopic probing of encapsulated species.

9.9 Observed variations in filling of the different chalcogenide species

Throughout the exploration of encapsulated TMT, noticeable trends of filling emerged. The chalcogens did not always follow their single-crystal growth parameters, nor did each chalcogen show similar structures at similar conditions. While the tritelluride TMT were fewest in number and least-studied, they showed the highest affinity for filling of the CNT at the many-, few-, and single-chain limit, and provided fantastic samples to work with and explore via atomic-resolution electron microscopy. The sulfide- and selenide-based TMT exhibited much different types of filling if they showed filling at all.

More systematic studies are needed to better understand the mechanism of filling for each chalcogen responsible for the differences in filling observed between sulfur, selenium, and tellurium systems. However, currently, we can think broadly about the main differences between sulfur, selenium, and tellurium that could attribute to these filling and structure differences. One major difference between the three chalcogenides is their melting and boiling point, which directly affects their overall vapor pressure. **Table 9.3** shows the melting point and boiling point of each chalcogenide for reference.

Table 9.3 Phase-change physical data for sulfur, selenium, and tellurium.

Chalcogenide	Melting Point (°C)	Boiling Point (°C)
Sulfur	115	445
Selenium	221	685
Tellurium	450	988

The key point to notice is the boiling point of sulfur in comparison to the single crystal synthesis for each TMT, and the initial synthetic parameters chosen. In short, for the synthesis of the TMT, the reaction temperature is well above the boiling point of sulfur, and not necessarily always above the boiling point of selenium or tellurium. Therefore, the vapor pressure of sulfur will be considerably higher than that of selenium or tellurium in a similar reaction. The vapor

pressure of the gaseous species plays a role in how mobile these species are, and whether or not they will migrate and successfully condense within the CNT. Due to the higher vapor pressure of sulfur in these reactions, I hypothesize that extended cooling times for the sulfur-based TMT (or even TMD for that matter) could play a large role in the successful crystallization and encapsulation of desired stoichiometric species.

9.10 Conclusion

In this chapter, we have gone through a deep dive of the synthetic parameters surrounding the various TMT systems, observations made for how each system initially filled CNT, and the various levels of success and failure. For the Hafnium TMT system, no filling was observed for HfS, however the synthetic protocols following **Figure 9.2** produced the most exciting results for the encapsulation of the HfSe system, and absolutely warrants further exploration. Following the synthesis of NbS_3, bulk needle-like crystals were observed, however, upon preparation of the NbS sample and viewing under electron microscopy, there was no filling species of any type observed. The Tantalum systems for the trisulfide and triselenide ultimately showed no chain-like filling after many modifications to the synthetic parameters. However, crystalline nanoribbon-like filling was observed for the TaS system, and warranted further exploration, detailed further in **Chapter 12**.

The Ti system proved even more difficult for encapsulation. Successful isolation of any chain-like or other crystalline species for the TiS system has yet to be realized, however successful filling of the CNT with amorphous species seems to be aided by extended reaction times and cooling and could benefit from further study. The Zr system showed the most promising results amongst all of the TMT family members. Alongside the standard chain-like filling observed for $ZrTe_3$, there were a few instances of drastically higher contrast filling of ZrTe, reminiscent of the filling observed in the TaS system, which later was found to be encapsulated nanoribbons.

For all TMT family members, there is still plenty of parameter space that has not been explored. The overall reaction temperature, reaction time, and cooling methods can affect the extent of filling within the CNT, the overall crystallinity of encapsulated species, and the stoichiometry of the resulting structure obtained. There is also much to be learned about the filling mechanism of the CNT, and how it relates to the differences in filling observed between sulfur, selenium, and tellurium. Systematic studies of filling CNT could provide fundamental insight into the crystal formation of encapsulated species under confined environments.

Chapter 10: Stabilizing lower-dimension forms of a transition metal chalcogenide – Emergence of Topologically Non-trivial Spin-polarized States in a Segmented Linear Chain

Special thank you to Dr. Thang Pham and Dr. Sehoon Oh for their leadership on this project.

Keywords: van der Waals, Segmented, Topological Insulator, Transition Metal Chalcogenide, Scanning Transmission Electron Microscopy, Density Functional Theory, Mirror Symmetry

An added benefit of the pursuit of encapsulated 1-D vdW structures is the stabilizing environment of the carbon nanotubes used to physically confine materials. The physical barrier formed by the carbon nanotube can isolate and stabilize structures that could never exist on their own in bulk form, leading to new and exciting low-dimensional structures. Here, we will discuss one such structure observed in our pursuit of low-dimensional hafnium telluride.

10.1 Motivation to stabilize a low-dimensional vdW material

The synthesis of new materials with novel or useful properties is one of the most important drivers in the fields of condensed matter physics and materials science. Discoveries of this kind are especially significant when they point to promising future basic research and applications. Van der Waals (vdW) bonded materials comprised of lower-dimensional building blocks have been shown to exhibit emergent properties when isolated in an atomically thin form.[7,137,144,163,180–183] While standard material exploration is achieved in bulk crystalline form, here we explore the discovery of a transition metal chalcogenide in a heretofore unknown segmented linear chain form. The basic building blocks each consist of two hafnium atoms and nine tellurium atoms (Hf_2Te_9), which are vdW bonded end-to-end. Although the stabilization of these molecular building blocks is interesting in and of itself, first-principle calculations based on density functional theory reveal striking crystal-symmetry-related features in the electronic structure of the segmented chain. Among some of the features are giant spin splitting and nontrivial topological phases of selected energy band states, which are explained in more detail in later sections. VdW-bonded segmented linear chain transition metal chalcogenide materials could open up new opportunities in low-dimensional, gate-tunable, magnetic and topological crystalline systems.

10.2 Exploring the family of hafnium telluride materials

The isolation of single layers of vdW bonded sheet-like materials has launched a new era of two-dimensional (2D) materials exploration, with the discovery of intriguing physical phenomena such as the fractional quantum Hall effect in graphene and an indirect-to-direct bandgap transition for monolayers of the transition metal dichalcogenide MoS_2.[137,180] As discussed in **Chapters 7, 8,** and **9**, chain-like transition metal trichalcogenides (TMTs) have been examined at the one-dimensional (1D) limit inside carbon or boron nitride nanotubes. The ultra-confinement of these systems has uncovered a whole host of emergent phenomena, for example charge-induced torsional waves appearing in single-chain $NbSe_3$.[144] Learning from these previous studies of vdW-type materials at their vdW limit (single sheets or chains), we must continue pushing the exploration of other transition metal chalcogenide family members to their vdW limit.

Here, we investigate a different transition metal chalcogenide (TMC) family, hafnium telluride (Hf-Te). As is common with other TMC materials, the hafnium telluride family has a host of different stoichiometries that are supported in bulk form. Bulk $HfTe_2$ is a semimetal comprised of 2D layers with vdW bonds between layers, while bulk $HfTe_3$ is a metal composed of 1D trigonal prismatic chains with vdW bonds between the chains.[118,129,164,182] At their vdW limit, however, we see their material properties are modulated by the extreme confinement of the crystal structure. Isolation of a monolayer of $HfTe_2$ shows flattening of the valence band, while encapsulation of chains of $HfTe_3$ within carbon nanotubes (CNTs) results in a size-driven metal-insulator transition as the chain number passes from 4 to 3.[163,182] A single chain of $HfTe_3$ encapsulated within a CNT supports a short-wavelength trigonal antiprismatic rocking distortion that drives a significant energy gap, but the chain is otherwise structurally robust.[163]

Through encapsulation, we show here that an entirely new low-dimensional form of the Hf-Te family is possible. The new form consists of structurally coherent zero-dimensional "blocks", each comprised of two Hf atoms and nine Te atoms (i.e. Hf_2Te_9), arranged end-to-end in a *segmented linear chain*, with vdW bonds linking the blocks or chain segments. The segmented chain resides inside the hollow core of a CNT, which protects the chain from oxidation and facilitates experimental characterization. First principles calculations reveal an especially rich electronic structure for the segmented chain. The bands near the chemical potential are fully spin-polarized in one direction and *k*-dependent giant spin splitting (GSS) of the bands occurs due to one mirror symmetry which is broken by crystal momentum *k,* and another mirror symmetry which is preserved for all *k*. Calculated Zak phases of the bands suggest externally tunable topological invariance.

10.3 Synthesis method of Hf_2Te_9@CNT

The synthesis procedure of the segmented linear procedure is similar to that previously reported for $HfTe_3$, however the inner diameter of the CNT is more critical to the successful growth and isolation of the vdW chain.[163] In general, multiwalled carbon nanotubes (CNTs) (Cheap Tubes) are annealed in air at 515 °C for 20 minutes to open the end-caps before the filling step. The as-prepared CNTs (~1-4 mg) together with a stoichiometric amount of Hf powder and Te shot (~ 560 mg in total), and ~5 mg/cm^3 (ampoule volume) of iodine powder (transport agent) are sealed under high vacuum (10^{-6} torr) in a 4mm inner diameter quartz ampoule. The sealed ampoule is kept at 520 °C for 7 days, and then gradually cooled to room temperature (over 9 days). Control syntheses were also performed, in which the precursor powders contained either only one material (i.e., only Hf, Te, or I_2), or any combination of two reagents (e.g., only Hf and I_2). We found no evidence of a segmented chain structure within the CNTs in these control experiments, confirming these vdW structures require Hf-Te reaction chemistries, with I_2 as a transport agent. Important to note is that the vdW segmented chains are isolated solely in the narrowest CNT (no more than ~1.1 nm inner diameter) within the sample, suggesting the segmented chain can only be stabilized to the single-chain limit.

10.4 Experimental characterization of Hf_2Te_9@CNT

To prepare the synthesized Hf_2Te_9@CNT for characterization, the product is dispersed in isopropanol by bath sonication for 30 minutes, then drop-cast onto a copper grid for STEM investigation, with assistance from Dr. Thang Pham and Dr. Jeff Cain. The imaging and

spectroscopy are carried out using TEAM 0.5 operating at 80 keV at the National Center for Electron Microscopy (NCEM) under the guidance of Dr. Chengyu Song. STEM simulations were generated by Dr. Peter Ercius using PRISM code developed by Dr. Ophus at NCEM (available online) for comparison to the experimental STEM images. The average-cell calculation, completed by Dr. Brian Shevitski, is done by the template matching technique written in Python to increase the signal-to-noise ratio and quality of the STEM image.

10.4.1 Electron microscopy characterization of Hf_2Te_9@CNT

Figure 10.1 shows an overview of atomic-resolution high-angle annular dark-field (HAADF) scanning transmission electron microscopy (STEM) images of the chains. Shown are bundles of CNT, each of which are filled with a segmented chain of vdW blocks. The chains are clearly and strikingly segmented into regularly spaced blocks, each with distinct substructure, which we examine more closely in following sections. The segmented chains observed are stable under the electron beam, with minimal damage observed, as seen in **Figure 10.1b**.

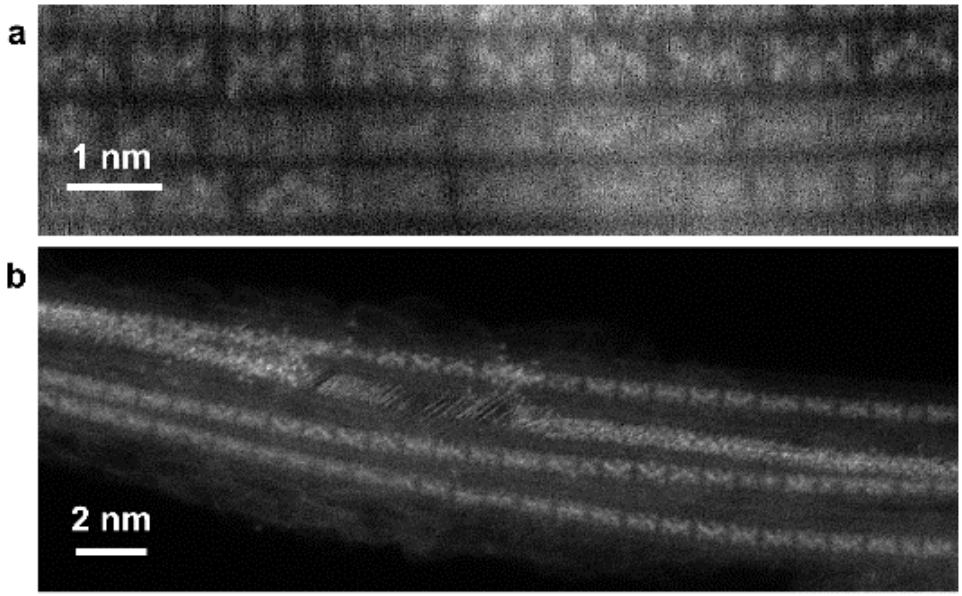

Figure 10.1 Encapsulated segmented chains of Hf_2Te_9. (a,b) Aberration-corrected high-angle annular dark field (HAADF) STEM image of bundles of CNT, each encapsulating a segmented chain of Hf_2Te_9 encapsulated within a CNT. The bright white spots are the atoms, while the walls of the CNT are not readily visible due to the contrast of the images. The structure consists of regularly spaced segments. Data collected in collaboration with Dr. Thang Pham.

10.4.2 Electron energy loss spectroscopy

While imaging under electron microscopy, electron energy loss spectroscopy (EELS) can also be performed on the segmented chain samples, shown in **Figure 10.2**. The Te M-edges of the EELS spectra are consistent with the atomic structure shown in **Figure 10.1**, and the M-edge is known to have a delayed onset and diffuse peak for heavier elements.[146] However, EELS can really only provide qualitative data, rather than any quantification of the segmented blocks, due to the incredibly low signal acquired. We note that previous studies have shown that CNTs can

be filled by pure metals and pure chalcogens, for which we need to control.[141,143] As described in the synthesis section, in order to investigate the filling nature of the metals or chalcogens present in this study, we performed control experiments and found no evidence for segmented chain structure within CNTs using only Hf, Te, or I_2, or any combination thereof, as feedstock.

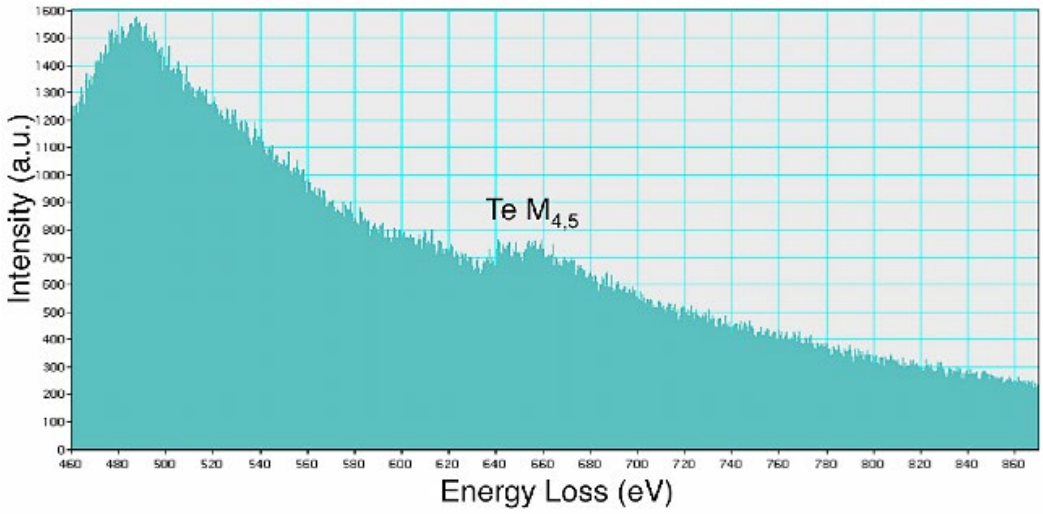

Figure 10.2 Electron energy loss spectrum of the segmented chain. Tellurium $M_{4,5}$ edges observed from a linear chain of Hf_2Te_9 blocks.

10.5 Theoretical study of the atomic structure of the vdW segmented chain

Density functional theory (DFT) calculations are then employed to aid in the identification of the precise atomic structure of the blocks. The calculations and analysis in the following sections are completed by Dr. Sehoon Oh, with supervision from Dr. Marvin Cohen. First, several candidate structures of the segmented chain with various chemical formulae are constructed in a vacuum (no CNT), and the atomic positions of the candidate structures are fully relaxed by minimizing the total energy. Using the relaxed atomic positions of the segmented chain isolated in vacuum and those of a pristine (8,8) CNT (chosen for both convenience and its inner diameter of 1.1 nm), we construct the atomic structure of the segmented chain encapsulated inside the (8,8) CNT. The atomic positions of the segmented chain are relaxed further by minimizing the total energy, while those of the CNT are fixed, as the CNT structure is stable and fixed due to the strong sp^2 bonding.[184] During this process, the atomic structure of the segmented chain is not altered appreciably, meaning the encapsulation is more than likely acting as physical stabilization, as opposed to chemical stabilization (no strong interaction between the CNT and encapsulated segmented chain). Among all of the candidate structures investigated, only one relaxed structure, with a chemical formula of Hf_2Te_9, matches well with the experimental data.

10.5.1 DFT calculation methods

In more detail, calculation methods utilize the generalized gradient approximation, norm-conserving pseudopotentials, and localized pseudo-atomic orbitals for the wavefunction expansion as implemented in the SIESTA code.[152–154] The spin-orbit interaction is considered using fully relativistic j-dependent pseudopotentials in the l-dependent fully-separable nonlocal

form using additional Kleinman-Bylander-type projectors.[155–157] We use 1×1×512 Monkhorst-Pack *k*-point mesh and 1000 Ry real-space mesh cut-off for all of the calculations. The van der Waals interaction is evaluated using the DFT-D2 correction.[158] Dipole corrections are included to reduce the fictitious interactions between chains generated by the periodic boundary condition in our supercell approach.[159]

10.5.2 Atomic structure in vacuum

Figure 10.3 shows the atomic structure of the segmented chain Hf_2Te_9 obtained from DFT calculation. The atomic structure has mirror planes in the unit of Hf_2Te_9 denoted as M_y and M_z, perpendicular to *y*- and *z*-axis, respectively. The length of a block is 7.89 Å, and blocks are separated by 3.65 Å. Each block connects to each other, forming a linear chain as shown in **Figure 10.3a**. **Figures 10.3b-d** show the basic building block of the structure, along the *x*-, *y*-, and *z*-axis, respectively. Each block has two Hf atoms and nine Te atoms, with sequence Te_3-Hf-Te_3-Hf-Te_3 along the chain (*z*) direction. Each Hf atom is surrounded by six Te atoms in a trigonal prismatic form. The adjacent Te atoms form isosceles triangles. The triangle at the center of the block is on the mirror plane perpendicular to the chain direction, while those on the sides of the block cant toward the center of the block.

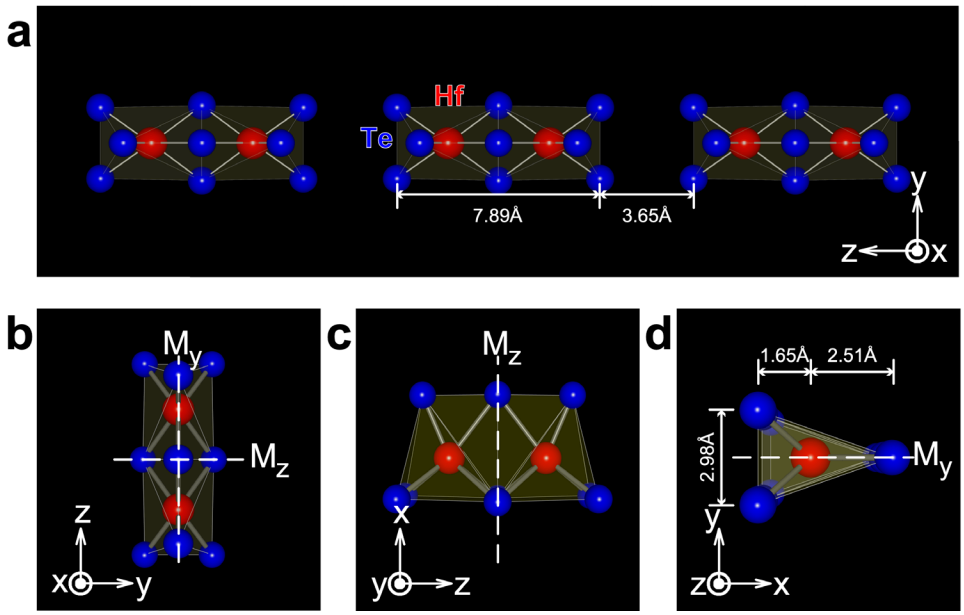

Figure 10.3 Atomic structure of the single-atomic segmented chain of Hf_2Te_9 obtained from DFT calculation. (a) The obtained atomic structure of the segmented single chain is shown, where Hf and Te atoms are represented as red and blue spheres, respectively, and chain direction is set to *z*-direction. (b-d) The atomic structure of the segmented chain of Hf_2Te_9 unit in side views along (b) *x*-axis and (c) *y*-axis, and (d) the axial view along *z*-axis, where the mirror planes in the unit perpendicular to *y*- and *z*-axes are represented by white dashed lines and denoted as M_y and M_z, respectively. Data collected in collaboration with Dr. Sehoon Oh.

An important distinction to note here is that single-chain transition-metal trichalcogenides (TMTs) materials prefer either trigonal prismatic or antiprismatic structures depending on the composition, similar to the way some transition-metal dichalcogenide (TMD) materials prefer

the trigonal prismatic (1H) structure while others prefer the trigonal antiprismatic (1T or 1T') structure, as discussed in **Chapter 7** on TMD and TMT materials. Therefore, both the trigonal prismatic and antiprismatic structures were included in the candidate structures. Energetically, the segmented chain prefers a trigonal prismatic structure, unlike the continuous single-chain $HfTe_3$, which prefers an antiprismatic structure.[163] The total energy of the segmented chain in the prismatic form is ~0.8 eV lower total energy per Hf_2Te_9 formula unit (f.u.) than the antiprismatic form. The preference for the trigonal prismatic structure in the segmented chain is more than likely a resultant of the canting of the tellurium atoms on the end of the segments. This can be more thoroughly explained if we look at the charge density within each segmented block. be due to the canting of the tellurium atoms on the end of the segments.

10.5.3 Charge density

We next examined the charge density of the segmented chain, to study the interactions within each segmented block and how they drive the trigonal prismatic structure preference and vdW interactions. **Figure 10.4** shows the calculated charge density of the single-atomic segmented chain of Hf_2Te_9. As seen in **Figures 10.4a-b**, the charge density between the two end Te atoms that cant inwards and the center Te atom has significant overlap, indicating stronger interaction between those three Tellurium atoms, which ultimately would 'hold' the blocks in the trigonal prismatic structure. **Figure 10.4b** clearly shows a gap in the charge density between the bottom Te atoms, while the charge density function overlaps across the top three Te atoms. The charge density between the blocks is very low and has minimum value at the middle point between the blocks, meaning that the blocks are vdW bonded, not covalently bonded. The real-space wavefunction of all the occupied states are also examined, $\psi_{nk}(r)$, showing no occupied states between the blocks, confirming the vdW bonding of the blocks.

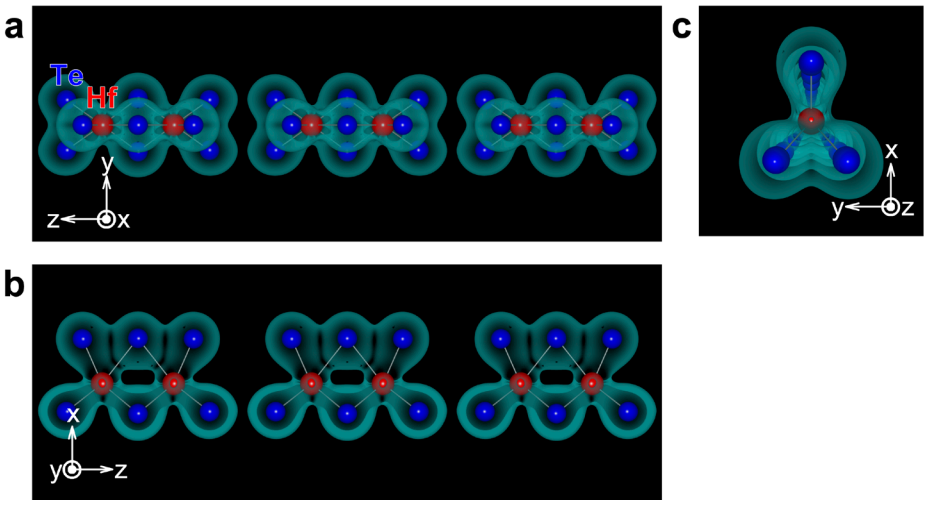

Figure 10.4 Charge density of the single-atomic segmented chain of Hf_2Te_9. Isosurface plots of the calculated charge density along with the atomic structures. Side views along (a) *x*-axis, (b) *y*-axis, and (c) axial view along *z*-axis. Hf and Te atoms are represented as red and blue spheres, respectively, and the isosurfaces are shaded in cyan. Data collected in collaboration with Dr. Sehoon Oh.

10.5.4 Verification of calculations against experiment

We then compare the observed experimental structures with the resultant theoretical atomic structure solved for theHf_2Te_9 building blocks. **Figure 10.5** shows more detailed structural characterization of the experimental and theoretical comparison of a segmented Hf_2Te_9 chain encapsulated within a CNT. **Figure 10.5a** shows an atomic-resolution high-angle annular dark-field (HAADF) scanning transmission electron microscopy (STEM) image of the chain. The inner diameter of the CNT host (not easily visible in **Figure 10.5a**) is 1.1 nm. The chain is clearly and strikingly segmented into regularly spaced blocks, each with distinct substructure. **Figures 10.5b-c** show the theoretically predicted structure of the segmented chain encapsulated inside the (8,8) CNT. **Figure 10.5b** shows the segmented chain together with the CNT, while **Figure 10.5c** shows the detailed structure of a single block, as was shown in **Figure 10.3**. The length of a block is 7.89 Å, and blocks are separated by 3.65 Å, consistent with a typical vdW gap. The block atomic structure has two mirror symmetries and the mirror planes perpendicular to the *y*- and *z*-axis are respectively denoted as M_y and M_z in **Figure 10.5c**. Each block has two Hf atoms and nine Te atoms, with sequence Te_3-Hf-Te_3-Hf-Te_3 along the chain (*z*) direction. Each Hf atom is surrounded by six Te atoms forming a trigonal prismatic structure.

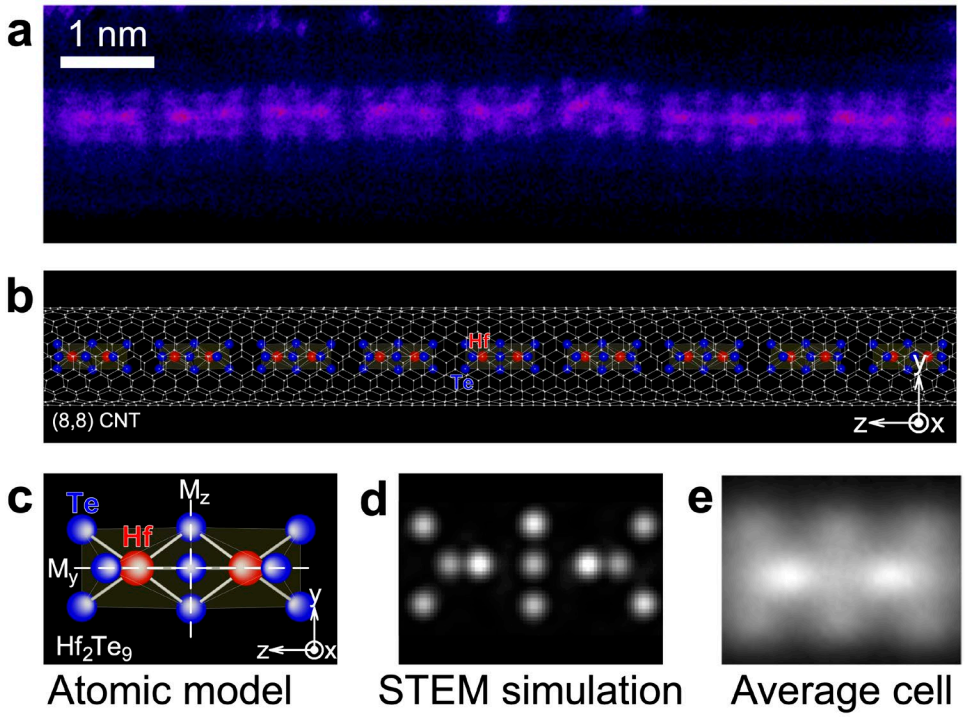

Figure 10.5 The single-atomic segmented chain of Hf_2Te_9. (a) Aberration-corrected high-angle annular dark field (HAADF) STEM image of a segmented chain of Hf_2Te_9 encapsulated within a double-walled CNT. A false color (Fire in the Look up Table (LUT) of ImageJ) is applied to visually aid the analysis. The structure consists of regularly spaced segments of Hf_2Te_9 (or Te_3-Hf-Te_3-Hf-Te_3). (b-c) Atomic structure of the single-atomic segmented chain of Hf_2Te_9 obtained from DFT calculation. (b) The obtained atomic structure of the segmented single chain inside an (8,8) single wall CNT is shown, where Hf and Te atoms are represented as red and blue spheres, respectively, and chain direction is set to *z*-direction. (c) The building block of a Hf_2Te_9 unit is shown without CNT for clearer presentation of the atomic structure, where the mirror planes perpendicular to *y*- and *z*-axes are represented by white dashed lines and denoted as M_y and M_z, respectively. (d) Multislice simulated STEM image using the proposed atomic structure. (e) Composite STEM image generated from the average cell structure of each segment. Data collected in collaboration with Dr. Sehoon Oh.

To further validate the proposed block atomic structure, we simulate a block STEM image, as shown in **Figure 10.5d**. To compare this prediction to experimental STEM data, we first generate a composite STEM image by averaging 227 orientationally-similar experimental STEM single-block images, as shown in **Figure 10.5e**. Comparison of **Figures 10.5d** and **10.5e**, as well as the dimensions of a block and the separation gap, shows good agreement between theory and experiment.

10.5.5 Hf_2Te_9 as a molecule

We also wanted to investigate the stability of an isolated Hf_2Te_9 molecule (a single isolated block) using DFT calculation, to further understand its stability. We constructed candidate structures of the isolated molecule both in vacuum and encapsulated inside CNT using the atomic positions from the segmented chain, and the atomic positions are relaxed by

minimizing the total energy. **Figures 10.6** and **10.7** show the obtained relaxed atomic structure of the isolated Hf_2Te_9 molecule in vacuum and in CNT, respectively. For both cases, the atomic structure of the molecule shows no significant change when it is isolated from the chain, except that the isosceles triangles of Te atoms on edges cant toward the center slightly more compared to the segmented chain configuration. We investigate possibilities for the molecule to change its shape to antiprismatic form, and to 'decompose' to other small molecules or atoms. No additional possible atomic structure configurations could be found which have lower energy than that of the structure shown in **Figures 10.6** and **10.7**.

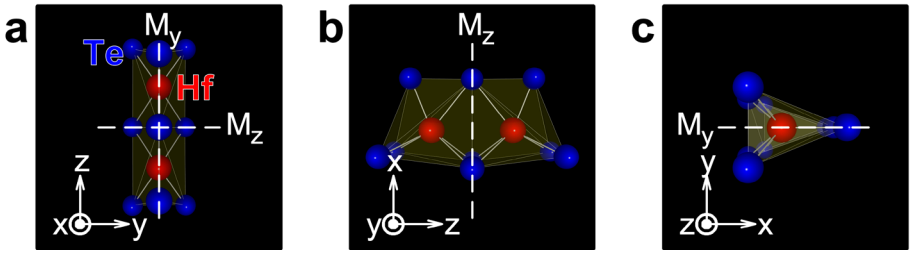

Figure 10.6 Hf_2Te_9 molecule isolated in vacuum. The atomic structure of the molecule is shown. Side views along (a) *x*-axis, (b) *y*-axis, and (c) axial view along *z*-axis. Hf and Te atoms are represented as red and blue spheres, respectively. Data collected in collaboration with Dr. Sehoon Oh.

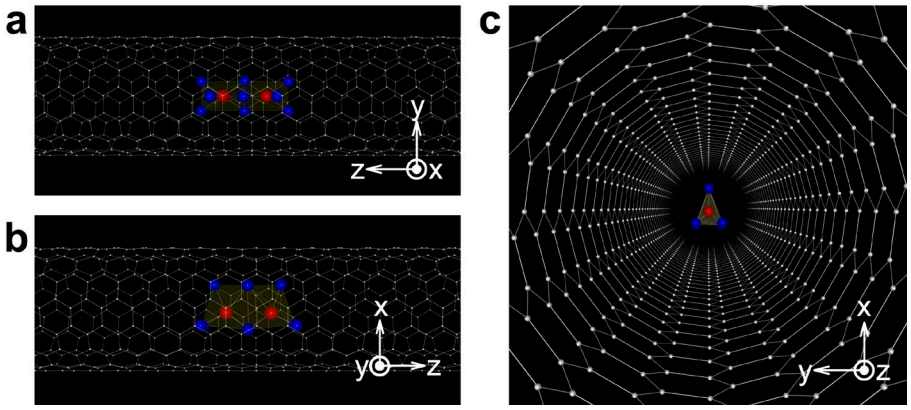

Figure 10.7 Hf_2Te_9 molecule encapsulated inside an (8,8) CNT. The atomic structure of the Hf_2Te_9 molecule encapsulated within the CNT is shown. Side views along (a) *x*-axis, (b) *y*-axis, and (c) axial view along *z*-axis, where Hf, Te and C atoms are represented as red, blue and white spheres, respectively. Data collected in collaboration with Dr. Sehoon Oh.

10.6 Theoretical study of the electronic structure of the vdW segmented chain

10.6.1 Orbital Angular Momentum

We investigate the electronic structure of the segmented Hf_2Te_9 chain by DFT calculation. Because of the presence of the mirror symmetry with respect to M_y plane (**Figures 10.3b** and **10.5c**), which is not broken by the crystal momentum *k*, the *x*- and *z*-components of spin and orbital angular momentum (OAM) with respect to the atomic positions on the plane should be zero regardless of *k*.[185] On the base level, the OAM is defined as the sum of the orbital

angular momenta from each of the electrons present, with magnitude $\sqrt{\mathrm{L}(\mathrm{L}+1)}(\hbar)$ in which L is an integer. The possible values of L depend on the individual *l* values and the orbital orientations possible within the atom. Using Hafnium as an example, the valence electrons of interest live in the 5d orbital. Therefore, $l = 2$, giving us possible angular momentum values of $-\sqrt{6}\,\hbar$ to $\sqrt{6}\,\hbar$. Often, though, the OAM is assumed to be quenched (i.e. the OAM is nonexistent) due to the symmetry and degeneracy of the orbitals, in Hafnium's case, the *d* orbitals. While some of the OAM can be assumed to be quenched in the segmented chain here, some of the OAM can have finite value, as described below. As previously discussed in **Chapter 7**, these transition metals exist as coordination complexes, with bonding to the chalcogenides similar to a ligand field. This crystal field causes splitting of the *d* orbitals, meaning they are no longer degenerate, giving rise to finite values of OAM.[186]

Therefore, in regard to the segmented chain presented here, the crystal momentum *k* breaks the mirror symmetry with respect to the M_z plane, and the energy eigenstates are not the eigenstates of M_z, so the *y*-component of the OAM of the states can have finite value (the *x* and *z* are assumed to be quenched) except for the time reversal invariant momentum (TRIM) points, the center, and the edge of the Brillouin zone ($k = 0, \pi/a$, where *a* is the unit cell length).

10.6.2 Spin-orbit interaction – Rashba effect

Figures 10.8a and **10.8d** show the electronic band structure of the segmented chain isolated in vacuum, obtained without considering spin-orbit interaction (SOI). The bands in **Figure 10.8d** are colored with the expectation values of the *y*-component of local OAM of the states $|\psi_{nk}\rangle$, with the band index *n* and the crystal momentum *k*, integrated over all the atoms in the unit cell,

$$< L_y >= \sum_{i \in cell} < L_y^i > \qquad \textbf{(Eq. 10.1)}$$

where $< L_y^i >$ is the expectation value of the *y*-component of local OAM with respect to the *i*-th atom of the states $|\psi_{nk}\rangle$. **Figures 10.8b** and **10.8e** show the electronic band structure of the chain isolated in vacuum obtained with considering SOI. The bands in **Figure 10.8e** are colored with the expectation value of the *y*-component of spin, $< S_y >$, of the states. We only focus on the two bands closest to the fermi energy, as this segmented chain is still a crystalline solid, and while the SOI tend to be small, they play an important role in the bands surrounding the fermi level. We are also working with a low-dimensional, asymmetric crystal lacking an inversion center, which splits the spin degeneracy and further enhances the SOI effect at the fermi level.[185,187,188]

The unquenched L_y of the states near the chemical potential combined with the SOI, causes a Rashba-type spin-splitting of the bands proportional to L_y, resulting in fully spin polarized states in the *y*-direction. Because the states with opposite *k* have opposite spin polarization, directional currents can be generated using circularly polarized light as demonstrated through valley-photon coupling in 2D transition metal dichalcogenides.[189,190] The calculated band gap is 100.3 meV, and the states near the chemical potential mostly derive from Te atoms, as shown in **Figures 10.8c** and **10.8f**.

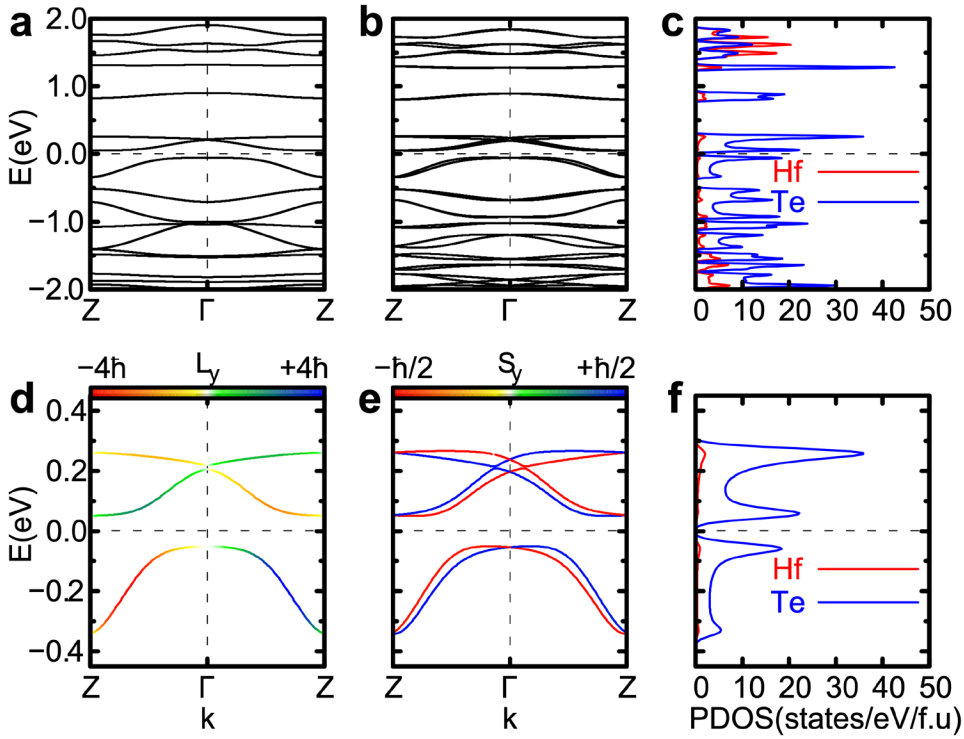

Figure 10.8 Calculated electronic structures of the single-atomic segmented chain of Hf_2Te_9. (a-c) The electronic structure of an isolated segmented chain of Hf_2Te_9. The band structures obtained (a) without and (b) with considering SOI, and (c) PDOS obtained with SOI. (d-f) The electronic structure of the segmented chain of Hf_2Te_9 near the chemical potential. The band structures obtained (d) without and (e) with considering SOI, and (f) PDOS obtained with SOI. (d-e) The color of the band lines represents the expectation value of the *y*-component of OAM $\langle L_y \rangle$ (in (d)), and spin $\langle S_y \rangle$ (in (e)). In (a-f), the chemical potential is set to zero and marked with a horizontal dashed line. Data collected in collaboration with Dr. Sehoon Oh.

Figure 10.9 shows the calculated atomic and electronic structures of the segmented chain encapsulated inside an (8,8) CNT. The encapsulation does not alter the electronic structure of the segmented chain significantly except for the band repulsion at ~0.3 eV above the Fermi energy. The states near the chemical potential remain fully spin-polarized in the *y*-direction, and the energy difference between the top of the highest occupied band and the bottom of the lowest unoccupied band remains at ~100 meV, similar to that of the chain isolated in vacuum. No appreciable covalent bonding between the chain and CNT is found. Mülliken charge analysis reveals that the amount of charge transferred from the CNT to the segmented chain is 0.118 e/Hf_2Te_9 formula unit (f.u.), where e is the electron charge.[191] The binding energy of the chain, E_b, is calculated to be 3.32 eV/f.u., which is defined as

$$E_b = E_{Hf2Te9} + E_{CNT} - E_{Hf2Te9/CNT} \qquad \textbf{(Eq. 10.2)}$$

where E_{Hf2Te9}, E_{CNT} and $E_{Hf2Te9/CNT}$ are the total energies of the segmented chain isolated in vacuum, an empty CNT, and the joint system of the chain encapsulated inside the CNT, respectively.

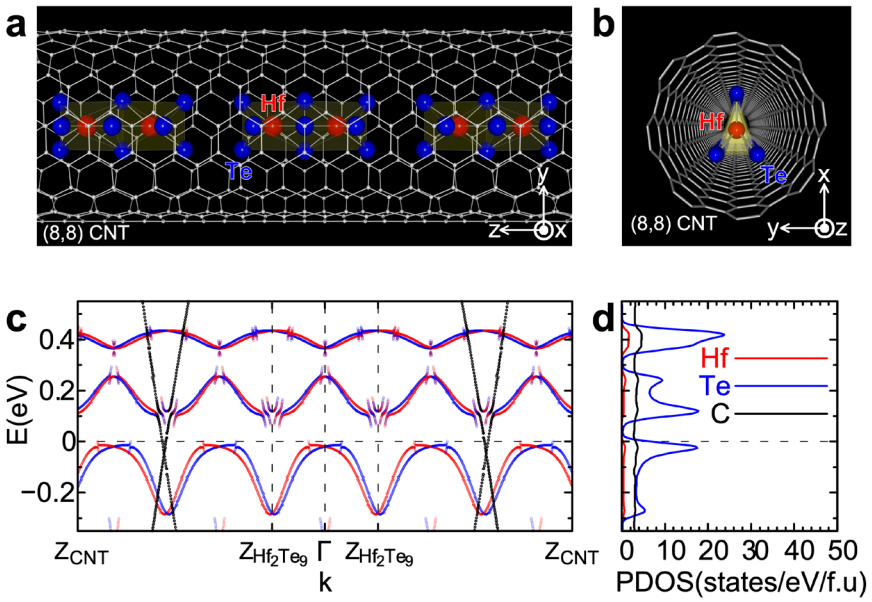

Figure 10.9 Calculated atomic and electronic structures of a single-atomic segmented chain of Hf_2Te_9 encapsulated in an (8,8) CNT. (a,b) Atomic structure of a segmented chain of Hf_2Te_9 encapsulated within a CNT in (a) side view and (b) axial view, where Hf, Te, and C atoms are represented as red, blue and white spheres, respectively. (c,d) Electronic structure of the segmented chain of Hf_2Te_9 encapsulated in the CNT. (c) Band structure and (d) PDOS obtained with SOI. In (c, d), the Fermi energy is set to zero and marked with a horizontal dashed line. In (c), band structures represented by red and blue dots are projected onto spin up and spin down, respectively, in the *y*-direction of the segmented chain and unfolded with respect to the first Brillouin zone of the unit cell of the segmented chain, while the bands represented by black dots are projected onto the CNT and unfolded with respect to the first Brillouin zone of the unit cell of the CNT. The center of the Brillouin ($k = 0$) is denoted by Γ, while Z_{Hf2Te9} and Z_{CNT} denote the zone boundaries for the segmented chain and the CNT, respectively. Data collected in collaboration with Dr. Sehoon Oh.

10.7 Emergent topological properties of a vdW segmented chain

In the world of insulators, the topology of the energy states (those closest to the fermi level) are of great interest, because they not only define the bulk properties, but they can define any interesting or unique properties. While the topology in general refers to the bulk, global properties, which in an insulator's case would be an energy gap that cannot be closed by any small perturbations, there are invariants within the material (such as edge states, surface states, or defects) that can alter the local properties.[192,193] A very exciting example of this can be found in graphene nanoribbons, which are globally semiconducting in nature, but if designed properly, protected spin states can be created within the nanoribbon, creating a new class of material.[194,195] By defining or altering the unit cell of a crystalline solid, or creating junctions of two different unit cells, the boundaries of the unit cells or junctions can populate interesting, localized states. The overall topology of one-dimensional crystals can be examined via the Zak phase, an integration over the first Brillouin zone, which reveals the number of states present along the edge.[196] What makes the Zak phase an interesting approach to study the topology, is that it is

highly dependent on the unit cell of the system, meaning small structural changes can have drastic impacts on the overall Zak phase.[194]

10.7.1 Topology of the Segmented Chain

We now consider the topological properties of the segmented chain. Because of the presence of time-reversal symmetry and mirror symmetry with respect to M_z, it is relatively straightforward to determine the Zak phase of our system.[197] In our case, the Zak phase of the n-th band, γ_n, is quantized to 0 or π (mod 2π), corresponding to a topologically trivial or nontrivial band, respectively.[198] The symmetry-protected topological invariance, Z_2, can be obtained by

$$(-1)^{Z_2} = e^{i\sum_{n\in I}\gamma_n} = e^{2\pi i P^I/e} \qquad \textbf{(Eq. 10.3)}$$

where the sum of the Zak phase is over the occupied bands in only one channel $\{u^I_{nk}\}$ out of two time-reversal channels $\{u^s_{nk}\}$, s=I,II, and P^I is the partial polarization over the channel I.[197,199]

We calculate the Zak phases of the n-th bands of the channel s

$$\gamma_n^S = i\int_{-\pi/a}^{\pi/a} dk\, \langle u^s_{nk}|\partial_k|u^s_{nk}\rangle \qquad \textbf{(Eq. 10.4)}$$

for all of the occupied states of the segmented chain isolated in vacuum by integrating the Berry connection, across the 1D Brillouin zone, where u^s_{nk} is the periodic part of the electron Bloch wave function with band index n and crystal momentum k of the channel s, and s = I, II are the time-reversal channels. Because of the presence of the time-reversal symmetry and the mirror symmetry with respect to M_z, γ^s_n is quantized to 0 or π (mod 2π), corresponding to a topologically trivial or nontrivial band, respectively. Explicitly, we calculated

$$\gamma_n^S = Im\left[ln\prod_{i=1}^{N}\langle u^s_{nk_i}|u^s_{nk_i+1}\rangle\right] \qquad \textbf{(Eq. 10.5)}$$

using the discretized k points, where Im […] is the imaginary part of […], k_i with i=1,…,N, $k_{N+1}=k_1$, and a periodic gauge, in which the following is used:

$$u^s_{nk_{N+1}}(z) = u^s_{nk_1}(z)e^{-i2\pi z/a} \qquad \textbf{(Eq. 10.6)}$$

Since the sum of Zak phase over one channel is nothing but the partial polarization of the channel, the Z_2 invariance can be obtained alternatively by

$$Z_2 = 2P^I/e = Q \bmod 2 \qquad \textbf{(Eq. 10.7)}$$

where Q is the end charge of the finite-length chain[18,19]. We verify this topological richness with an explicit calculation of Z_2 invariance for an h-doped chain as discussed below.

10.7.2 Tuning the Topological Invariance

By tuning the fermi level of the segmented chain, different bands can be accessed, and could potentially allow for tuning of the topology for the segmented chain. Therefore, we need to examine both the neutral and hole-doped cases of the segmented chain. We obtain the symmetry protected topological Z_2 invariance by

$$(-1)^{Z_2} = e^{i\sum_n \gamma_n^I} \qquad \textbf{(Eq. 10.8)}$$

where the sum is over the occupied bands only in channel I. That is, the Z_2 invariance is determined by the number of nontrivial occupied bands in one time-reversal channel.

Specifically, odd and even numbers of nontrivial occupied bands mean $Z_2 = 0$ and 1, respectively. We obtain the Z_2 for the neutral case and for the hole-doped case, where two electrons per formula unit are subtracted in the DFT calculation, as shown in **Figure 10.10**. For the neutral case, $Z_2 = 0$, corresponding to a trivial insulator, while $Z_2 = 1$ for the h-doped case, corresponding to a topological mirror insulator. The calculated Zak phase of the highest occupied band is π. As the h-doped chain has two fewer electrons per unit cell than the neutral chain, the total Zak phase of the h-doped chain must differ from that of the neutral chain by π, owing to emptying of the highest occupied band, and provided the Hamiltonian of the h-doped system may be obtained adiabatically from the neutral system without closing the band gap.

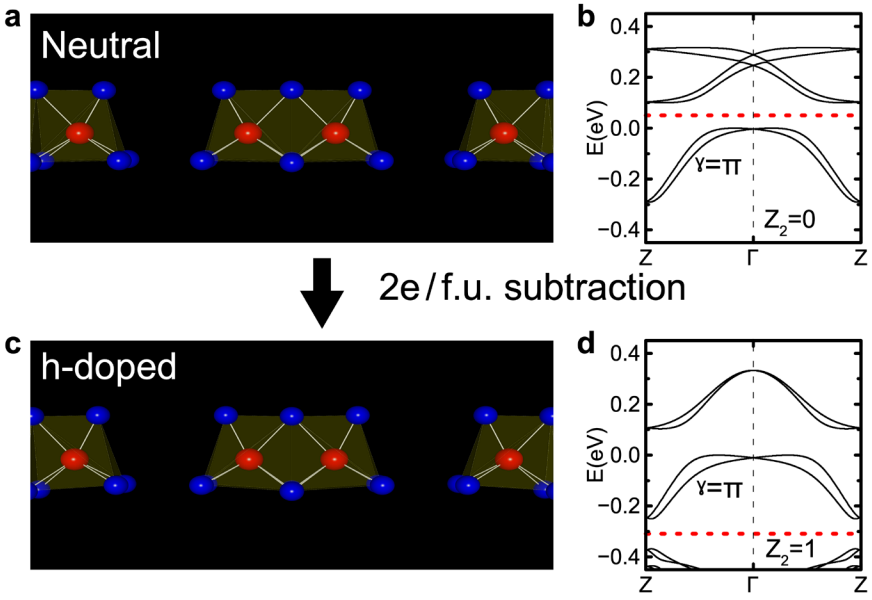

Figure 10.10 The single-atomic segmented chain of Hf_2Te_9 with chemical potential changed. (a, b) The atomic and electronic structure of the segmented chain of Hf_2Te_9 without chemical potential change (neutral) are shown for the comparison. (c, d) The atomic and electronic structure of the segmented chain of Hf_2Te_9 with two electron per formula unit subtracted in the DFT calculation (h-doped). In (a, c), Hf and Te atoms are represented as red and blue spheres, respectively. In (b, d), the energy level of the highest occupied band is set to zero, and the chemical potential is represented by red dashed line. Data collected in collaboration with Dr. Sehoon Oh.

Since the sum of the Zak phase over one channel is nothing more than the partial polarization of the channel, the Z_2 invariance can be obtained alternatively again by

$$Z_2 = 2P\,{}^{I}\!/_{e} = Q \bmod 2 \qquad \textbf{(Eq. 10.9)}$$

where Q is the end charge of the finite-length chain and e is the electron charge. We make finite chains (~15 nm) for both neutral and the h-doped system. We define the end charge of a system as the net deviation of the charge of the finite chain of the blocks on both edges from the average charge of the infinite length chain in two units. Explicitly,

$$Q = \rho_L + \rho_R - 2\overline{\rho} \qquad \textbf{(Eq. 10.10)}$$

where ρ_L (ρ_R) is the charge of the finite chain in the block on the left (right) edge and $\overline{\rho}$ is the charge of infinite length chain in one unit. For neutral case, $Q = 0$, meaning trivial insulator while $Q = 3e$ for the h-doped case, meaning topological mirror insulator.[199,200]

Due to the change in value for Q, we find that the topological invariance Z_2 of the segmented chain can be tuned by doping. As shown in **Figures 10.11a-b**, in the neutral state Z_2 = 0 for the infinite length Hf_2Te_9 segmented chain, meaning the chain is a trivial insulator. On the other hand, the highest occupied band is nontrivial and well separated from other bands, as shown in **Figure 10.11b**. Therefore, if the system is hole-doped (h-doped) so that the chemical potential lies between the energy levels of the highest and the second highest occupied band, as illustrated in **Figures 10.11c-d**, it becomes a topological mirror insulator, provided that the Zak phases of the bands remain unchanged and that the Hamiltonian of the h-doped system may be obtained adiabatically from the neutral chain without closing the band gap. In other words, the number of nontrivial occupied bands in one channel changes from even to odd, and the sum of the Zak phase of the h-doped chain in one channel differs from that of a neutral chain by π, owing to the emptying out of the nontrivial highest occupied band. Hence, upon doping, Z_2 changes from 0 to 1, meaning the segmented chain experiences a transition from a trivial insulator to a topological mirror insulator.

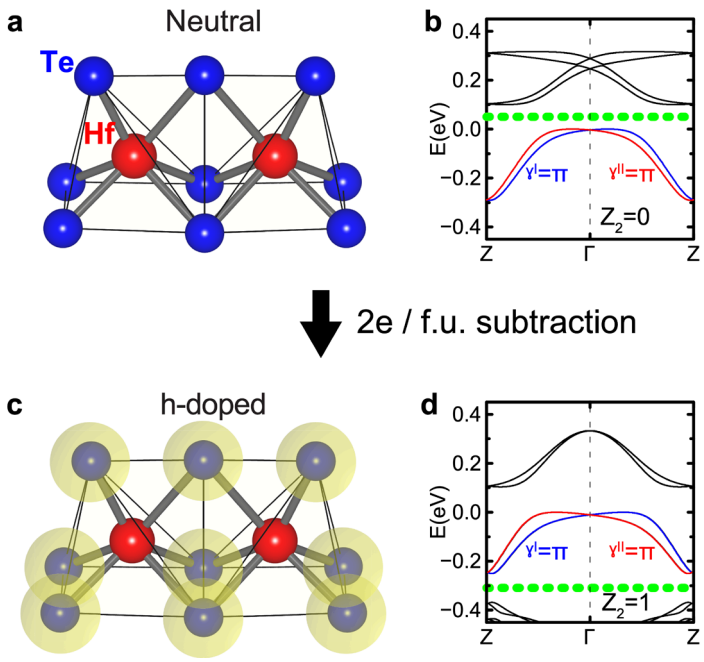

Figure 10.11 Topological properties of single-atomic segmented chain of Hf_2Te_9 with various chemical potential. (a,b) The atomic and electronic structures of the segmented chain of Hf_2Te_9 without chemical potential change are shown for the comparison. The highest occupied band is nontrivial. (c,d) The atomic and electronic structure of the segmented chain of Hf_2Te_9 with 2*e* / f.u. subtracted in the DFT calculation. In (a,c), Hf and Te atoms are represented as red and blue spheres, respectively. In (c), the subtracted charge is schematically represented by yellow spheres. In (b,d), the energy level of the top of highest occupied band is set to zero for easy comparison, and the chemical potential is represented by green dashed lines. Two time-reversal channels of the highest occupied bands, s=I, II, are represented by blue and red lines, respectively. The symmetry-protected topological invariance, Z_2, is 0 for neutral system, and 1 for the h-doped system. Data collected in collaboration with Dr. Sehoon Oh.

Many studies for related systems have shown that the chemical potential can be readily altered by chemical doping, electrostatic gating, or application of pressure.[7,194,201–205] This suggests that segmented chain Hf_2Te_9 represents a versatile, highly unusual, externally tunable topological material. We note that the Hf_2Te_9 segmented chain is, to our knowledge, the first example of a vdW-bonded crystalline material with spatial-symmetry topological invariants.[206,207] Our discovery thus expands the class of realized topological states of matter.

10.8 Conclusion

In conclusion, a TMC-based, vdW-bonded segmented linear chain material has been synthesized within a protective CNT cage, and its structure determined via STEM analysis and complementary DFT calculations. Theory also reveals giant spin splitting, which is promising for applications such as spintronic devices or tunable topological properties. The segmented linear chain is a realization of a TMC in the quasi-0D limit, where 0D blocks are vdW end-to-end bonded in a linear chain. This quasi 0D material completes the family of dimensionally-reduced TMCs, where bulk MX_2 compounds are typically quasi-2D and MX_3 compounds are typically quasi-1D (M=transition metal, X=chalcogen).

Chapter 11: Expanding the Family of Known Transition Metal Chalcogenides – Stabilization of $NbTe_3$, VTe_3, and $TiTe_3$ *via* Nanotube Encapsulation

Special thank you to Dr. Jeff Cain, Markus Thiel, Malik Elasha, Dr. Amin Azizi, and Dr. Peter Ercius for their assistance on this project.

Keywords: Transition Metal Trichalcogenide, Scanning Transmission Electron Microscopy, Energy Dispersive Spectroscopy, Trigonal Antiprismatic Chain, Simulation

While previous chapters have explored known members of the transition metal trichalcogenide (TMT) family at the single-chain limit, there remain some TMT members (many of which are tellurides) that have yet to be synthesized, even in bulk form. From the work discussed in **Chapter 8** and **10**, I have stressed the importance of the stabilizing cavity of the carbon nanotube for studying the 1-D limit of materials. Furthermore, especially in the $HfTe_3$ system, we have discussed at great length how the isolation of these TMT chains to the few- and single-chain limit allows for drastic structural evolution, resulting in entirely new phases of the TMT family. This new phase of TMT could be the key to unlocking the additional TMT members that have yet to be discovered.

11.1 Motivation behind uncovering additional members of the TMT family

One of the primary objectives of nanoscience is the precise control over the processing-structure-property relationship intrinsic to traditional materials science. As reported in previous chapters, the concept of dimensionality, and the engineering of materials' structure and properties *via* changes in dimensionality, has emerged as an additional degree of freedom within this paradigm. To this end, the isolation of single atomic-planes (*e.g.* graphene and the transition metal dichalcogenides) and chains (*e.g.* transition metal trichalcogenides, TMTs) from quasi-low-dimensional materials has been extremely fruitful.[7,138,144] There is an ever-growing list of materials being isolated down to their fundamental van der Waals (vdW) building blocks, and existing low-dimensional materials (*e.g.* nanotubes, graphene) have been excellent templates for the synthesis and stabilization of new low-dimensional materials and structures.[208–210]

Carbon nanotubes (CNTs) and boron nitride nanotubes (BNNTs) have been used as nano reaction vessels for the synthesis of a variety of materials, including elemental metals, halides, and chalcogenides.[141,183,211,212] The CNT sheath enables the study of 1D nanostructures that are not air-stable, by protecting them from oxidation. In some cases, the nanoconfined growth can induce the formation of crystal structures and morphologies unrealized in bulk counterparts, such as 1D HgTe, helices in 1D cobalt iodide, and twisting in single-chain monochalcogenides.[183,213–215] Encapsulation of materials inside small-dimeter nanotubes has become a unique route towards new quasi-1D nanostructures.

The encapsulation of materials inside nanotubes has also proven a straightforward and accessible route to studying already known quasi-1-D nanostructures, such as the few- and single-chain limit of TMT. The structure of MX_3 transition metal trichalcogenides (TMTs, with M a transition metal and X a chalcogen) is typified by one-dimensional (1D) chains weakly bound together *via* van der Waals interactions. The 1-D nature of the TMT structure is very amenable to the encapsulation process inside an already 1-D nanomaterial such as nanotubes. The MX_3 structural motif is common across a range of M and X atoms (*e.g.* $NbSe_3$, $HfTe_3$,

TaS_3), but not all M and X combinations are stable. In fact, many of the tellurium members of the TMT family have eluded synthesis in bulk form, even throughout the decades of study devoted to other TMT materials.

11.2 The transition metal tritelluride family

The archetypal quasi-1D materials family is the TMTs, commonly referred to as MX_3 compounds with M a transition metal and X a chalcogen. Typically for these materials 1D MX_3 chains are weakly coupled by interchain vdW interactions to form coherent, but highly anisotropic, three-dimensional crystals. The bulk synthesis and properties of the TMTs has been well explored and they are canonical examples of superconductors and charge density wave materials.[129,216] Recently, TMTs have also been isolated in the few- and single-chain limit, where they exhibit unique spiral chain structure and torsional instabilities, induced by the added dimensional constraint.[144,163] Based on chemical trends, one might expect the quasi-1D crystal structure seen in the TMTs to be present in all MX_3 compounds with M=Ti, Zr, Hf, Nb, or Ta, and X=S, Se, or Te. While this holds true for many of the possible combinations (*e.g.* $NbSe_3$, TaS_3, $HfTe_3$), specimens of many telluride-based TMTs have not been previously synthesized, and are likely not stable in bulk.[217]

The tritelluride's elusion of synthesis in bulk form stems mainly from the loss of directionality in the Te bonding.[217,218] While many studies of the transition metal chalcogenides and comparing stability of the sulfides vs. selenides vs. tellurides is viewed through the dichalcogenides, many of the findings can be extended to the trichalcogenides family as well. As described in **Chapter 7**, the increase in size of the Te atoms and varying charges associated with the Te-Te bonding within the crystalline network decreases the 'directionality' of the bonding within the Te network, increasing the preference of Te compounds to form more 3-D structured bonding networks.[218,219] However, for the formation of the linear-chain TMT compounds, we need directional bonding of the crystalline network to maintain the 1-D chain structure. Therefore, the proclivity of Te atoms to form a 3-D extended network is the main hurdle in stabilizing transition metal chalcogenides into a directionally bonded 1-D crystalline structure, such as the TMT family.

Here, we demonstrate the successful synthesis of three previously unreported MX_3 TMT compounds: $NbTe_3$, VTe_3, and $TiTe_3$. The three new members of the MX_3 family which are not stable in bulk can be synthesized in the few- to single-chain limit *via* nano-confined growth within the stabilizing cavity of multi-walled carbon nanotubes (MWCNTs). Depending upon the inner diameter of the encapsulating MWCNTs, specimens ranging from many chains to few chains (2-3), and even single chains, can be isolated and studied. The MWCNT sheath stabilizes the chainlike morphology, enabling synthesis and characterization with electron microscopy. Transmission electron microscopy (TEM) and atomic-resolution scanning transmission electron microscopy (STEM) reveal the chain-like nature and the detailed atomic structure. It is found that few-chain specimens of the new TMTs can exhibit a coordinated interchain spiraling, while the single-chain limit exhibits a trigonal anti-prismatic (TAP) rocking, behaviors seen previously in the few chain limit of $NbSe_3$ and $HfTe_3$.[144,163] First principles density functional theory (DFT) calculations give insight into the crystal structure and stability of the materials, the integral role that the encapsulating CNT plays in stabilization, as well as the electronic structure of the new materials.

11.3 Synthesis methods of MTe_3@CNT

The stabilized chains of $NbTe_3$, VTe_3, and $TiTe_3$ are synthesized within CNTs using a procedure similar to that outlined previously for $NbSe_3$ and $HfTe_3$, with assistance from Malik Elasha and Markus Thiel.[144,163] Stoichiometric quantities of powdered transition metal along with Te shot (~450 mg total), together with 1-2 mg of end-opened MWCNTs (CheapTubes, 90% SW-DW CNTs) and ~5 mg/cm^3 (ampoule volume) of I_2 are sealed under vacuum in a quartz ampoule and heated in a uniform temperature furnace at 520 – 625 ^{o}C for several days, then cooled to room temperature over 3-7 days.

11.4 Study of the stabilized MTe_3 chains

11.4.1 Electron microscopy details

After synthesis, filled CNT are cast onto TEM grids (Cu grid, 300 mesh, Lacey Carbon) for characterization. Initial imaging for confirmation and analysis of filling characteristics is done on a JEOL 2010 microscope (TEM, accelerating voltage of 80 kV). Elemental analysis was performed by Dr. Amin Azizi on an aberration-corrected FEI Titan3 (60−300) equipped with a SuperX energy dispersive X-ray spectrometer (EDS, accelerating voltage of 80 kV). The specimen measured were the few-chain TMT limit to acquire enough signal for determination of atomic species present. Atomic-resolution STEM imaging for identification of the few chains and TAP single chains is completed, with assistance from Dr. Jeff Cain, at the National Center for Electron Microscopy on TEAM 0.5, which is a Titan 80-300 with a ultra-twin pole piece gap, DCOR probe aberration corrector and was operated at 80 kV and semi-convergence angle of 30 mrad. Images were acquired using the ADF-STEM detector with an inner angle of 60 mrad and a beam current of approximately 70 pA, under guidance from Dr. Chengyu Song.

11.4.2 STEM simulation details

STEM simulations were performed by Dr. Peter Ercius, using EJ Kirkland's autostem program with parameters that matched the experiments. In detail for each simulation, we used a 21.48 Å square simulation box, 80 kV accelerating voltage, 30 mrad convergence semi-angle, 256-pixel sampling, 1 Å slice size, and 50 frozen phonon calculations. After completion, the multislice data was convolved with a 1.3 Å source size to match the contrast seen in the experiment images. Noise was added following Poisson counting statistics to match the 70 pA experimental beam current. This allowed us to interpret the positions of atoms based on the approximate Z-contrast in the images and to compare the projection images to the DFT simulated structures.

11.4.3 Characterization of the encapsulated MX3 species

Figure 11.1 shows high-resolution TEM images of representative samples from all three stabilized species encapsulated within MWCNTs, in which their 1D, chain-like nature is evident. In **Figure 11.1a**, ~14 $TiTe_3$ chains are encapsulated within a 3.47 nm-wide (inner diameter) MWCNT, where the number of enclosed chains is estimated based on the carbon nanotube diameter and a close-packing configuration of the chains. **Figure 11.1b** exhibits triple-spiraling

chains of VTe_3 within a 2.46 nm MWCNT, while **Figure 11.1c** shows straight triple chains of $NbTe_3$ within a 2.57 nm-wide MWCNT. **Figure 11.1d** shows a double chain example of $TiTe_3$ within a 2.04 nm MWCNT and **Figure 11.1e** highlights the single-chain limit of $NbTe_3$ encapsulated within a 0.99 nm wide MWCNT. These results demonstrate that a confined growth environment allows for the stabilization and characterization of many-, few-, and single-chain limits of $NbTe_3$, VTe_3, and $TiTe_3$.

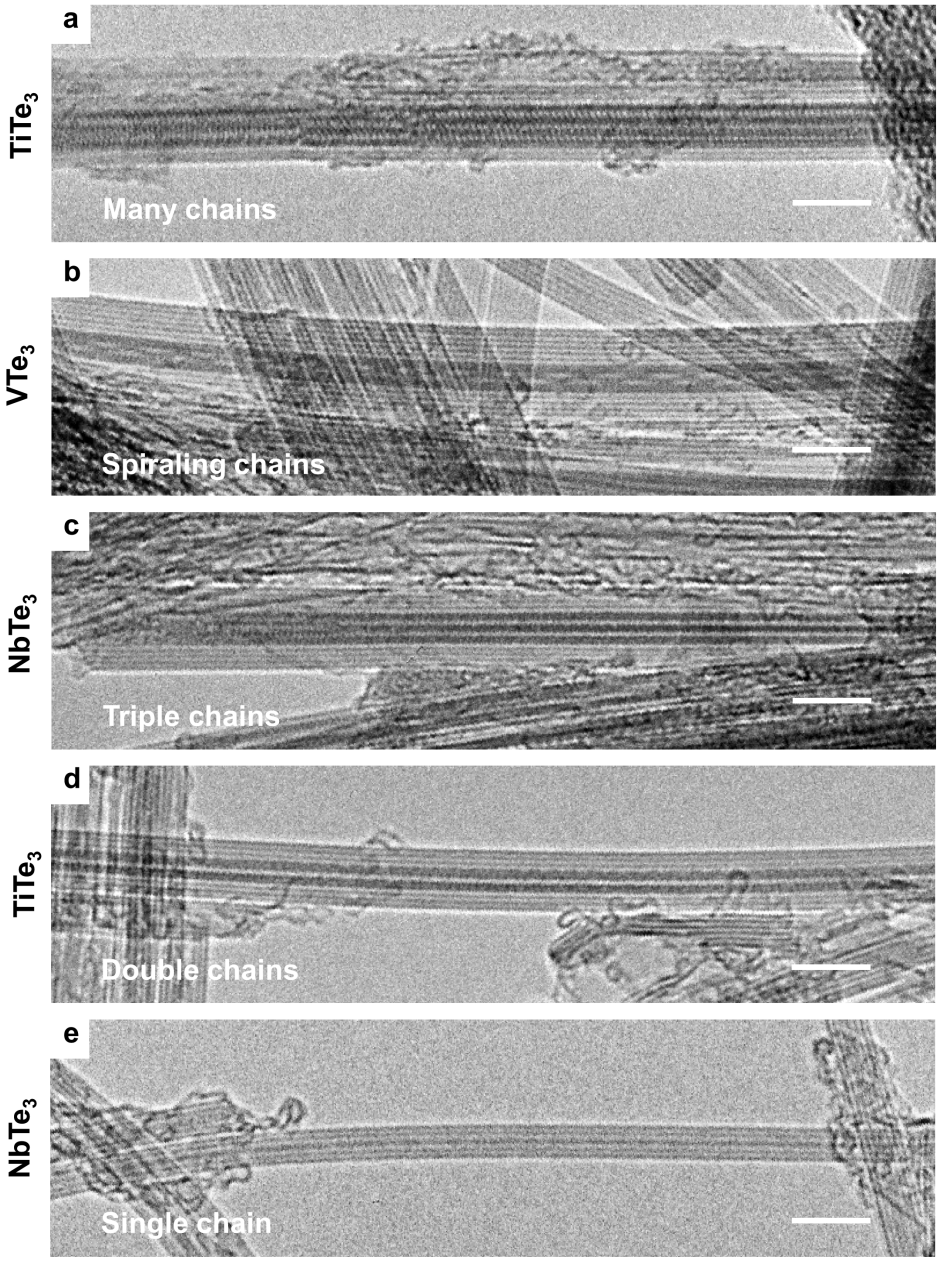

Figure 11.1 Representative samples of many- to single-chain limit of $TiTe_3$, VTe_3, and $NbTe_3$. Transmission electron microscopy images of (a) many chains of $TiTe_3$, (b) triple spiraling chains of VTe_3, (c) triple chains of $NbTe_3$, (d) double chains of $TiTe_3$, and (e) the single-chain limit of $NbTe_3$. All images are underfocused, where atoms appear dark. Scale bars measure 5 nm.

As seen in the TEM images in **Figure 11.1**, $NbTe_3$, VTe_3, and $TiTe_3$ adopt very similar behaviors when encapsulated, reminiscent of behaviors reported previously for $NbSe_3$ and $HfTe_3$. The most noticeable similarity in these encapsulated chain-like species is the spiraling in the few-chain limit, which is evident as shown in **Figure 11.1b** and **Figure 11.2**. The spiraling of encapsulated TMT chains has become an expected tell-tale sign of the few-chain limit of these systems. The spiraling motif is easily identified and a prominent feature to look for and expect when exploring new members of the TMT family. As discussed in **Chapter 8**, strong interchain vdW interactions between the transition metal centers and the chalcogen ligands (in this case Te atoms) on neighboring chains allow for the largest energy stabilization, and this is the largest determining factor in the parallel orientation of the chains. Once these neighboring chains are stripped away and we reach the few-chain limit, spiraling of the chains can, in some cases, stabilize the chains further by increasing the overall vdW interactions of said chains, both between the chains and the inner walls of the CNT. However, in all encapsulated species examined to-date, there is no strong-bonding interaction between the CNT and inner chains (i.e. zero bonding or covalency), and is purely vdW in nature, with the occasional transfer of charge in the case of $NbSe_3$.[144,163]

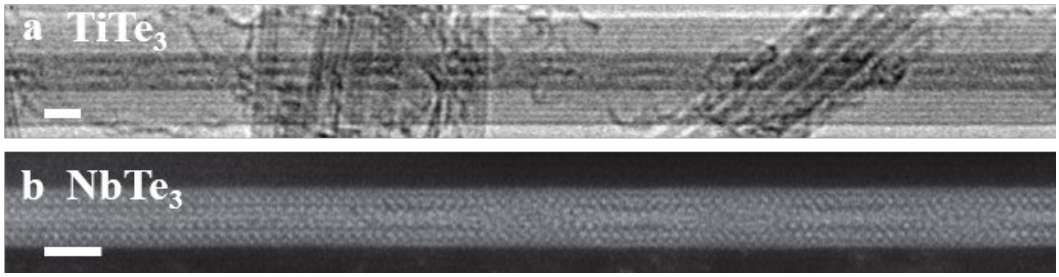

Figure 11.2 Tell-tale spiraling of the few-chain limit. (a) TEM image of few-chain twisting of $TiTe_3$ encapsulated within a MWCNT. (b) STEM image of few-chain twisting of $NbTe_3$ encapsulated within a MWCNT. Scale bars measure 2 nm.

11.4.4 Chemical analysis of the MTe_3 chains

Chemical analyses of the new materials by means of energy-dispersive X-ray spectroscopy (EDS) are shown in **Figure 11.3**, with accompanying spectra in **Figure 11.4**. **Figures 11.3a-c** show annular dark-field scanning transmission electron microscope (ADF-STEM) images of few-chain specimen of $NbTe_3$, VTe_3, and $TiTe_3$, respectively, as well as corresponding EDS line scans. EDS mapping is used to distribute the dose, and the maps are summed vertically to increase the signal to noise. The EDS line scans in **Figures 11.3a-c** confirm distribution of the transition metal, Nb, V, or Ti respectively, and Te atoms across the few-chain crystal within the carbon nanotube. The peak maximums for the associated transition metal and tellurium in each line scan spatially correspond to the material observed in the ADF-STEM image and is localized within the carbon signal (indicating encapsulation). The EDS spectra collected from individual few-chain $NbTe_3$, VTe_3, and $TiTe_3$ are presented in **Figure 11.4**. The spectra clearly show peaks of Nb and Te for $NbTe_3$, V and Te for VTe_3, and Ti and Te for $TiTe_3$.

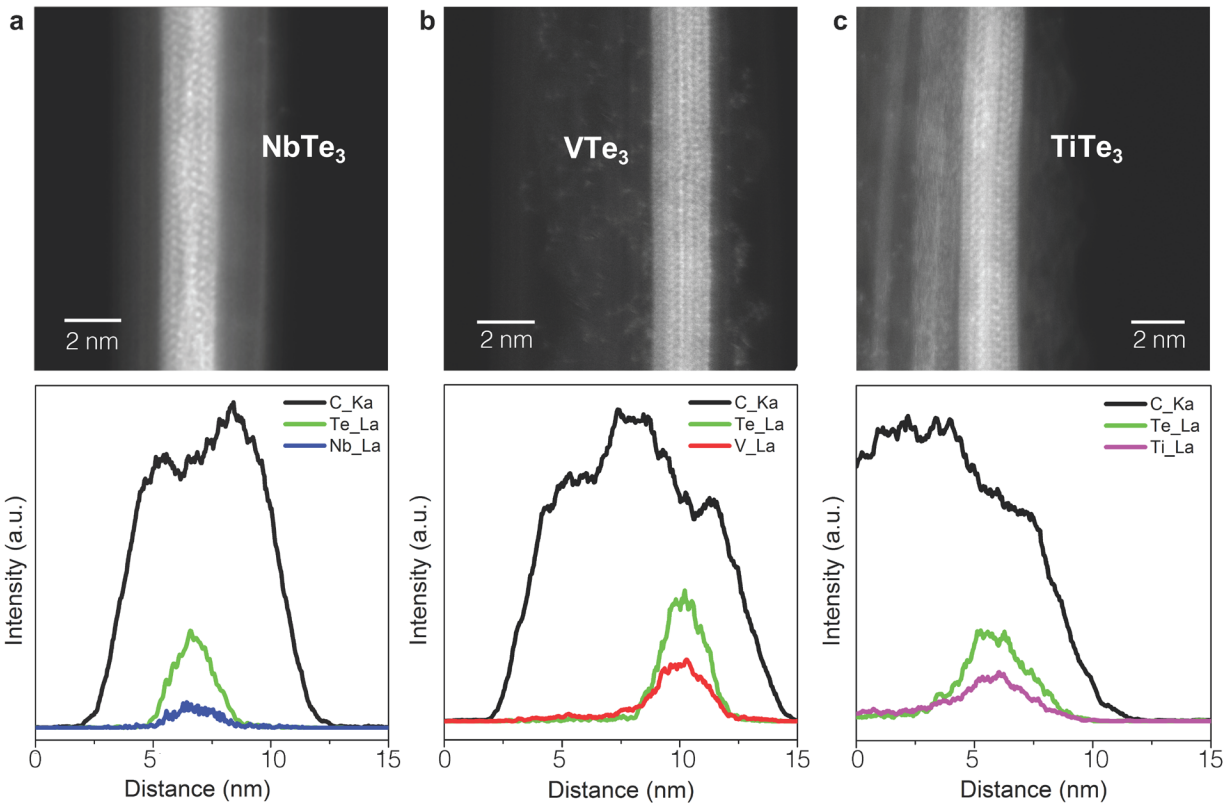

Figure 11.3 Elemental analysis of encapsulated few-chain $NbTe_3$, VTe_3, and $TiTe_3$. ADF-STEM images (top) of few-chain specimen and corresponding EDS line scans (summed vertically) for (a) $NbTe_3$, (b) VTe_3, and (c) $TiTe_3$. EDS line scans (bottom) show distribution of the transition metal and tellurium carbon within the carbon nanotube. Data collected in collaboration with Dr. Amin Azizi and Dr. Peter Ercius.

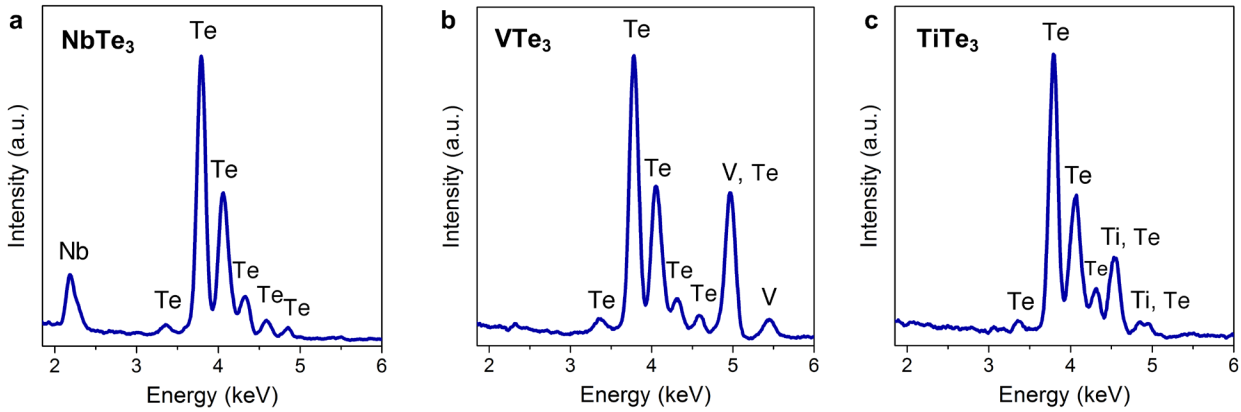

Figure 11.4 Energy Dispersive Spectroscopy Spectra. EDS spectra collected on few-chain specimen for (a) $NbTe_3$, (b) VTe_3, and (c) $TiTe_3$, with relevant peaks labeled. Data collected in collaboration with Dr. Amin Azizi.

It is important to note here that we do not employ EDS mapping for the purpose of identifying the spatial placement of signal received for each element, but rather the line scan and summation of signal. The encapsulated chains are filled with very little material, even in the few-

chain limit, giving very little signal in our EDS measurements. Due to the low signal to noise ratio, simply utilizing chemical mapping to 'locate' the atoms of interest cannot be done with a high enough confidence level.

Figure 11.5 demonstrates the elemental mapping generated by plotting a pixel in the spatial location signal is measured, while comparing the spatial location of the elemental mapping to a standard STEM image. **Figure 11.5a** is the ADF-STEM image taken of the portion of the few-chain specimen measured. In **Figures 11.5b-d**, each pixel of color represents a 'count' of measured intensity at that location. As seen in **Figure 11.5b**, there are hundreds of pixels measured for the carbon intensity, because the sample is encapsulated within a MWCNT several nanometers wide, providing substantial carbon signal that can be confidently mapped. In **Figures 11.5c** and **11.5d**, individual pixels can be identified and counted from the mapping, indicating too low of measured signal for niobium or tellurium for confident mapping. However, rather than doing elemental mapping, we can increase the signal-to-noise ratio by summing the intensities measured and produce the elemental line scans shown above in **Figure 11.3**. The line scans in **Figure 11.3a** are generated from the data shown in **Figure 11.5**, rotated 90°, with significantly more intense signal than the mapping, drastically improving confidence in semi-resolving the spatial location of the EDS signal.

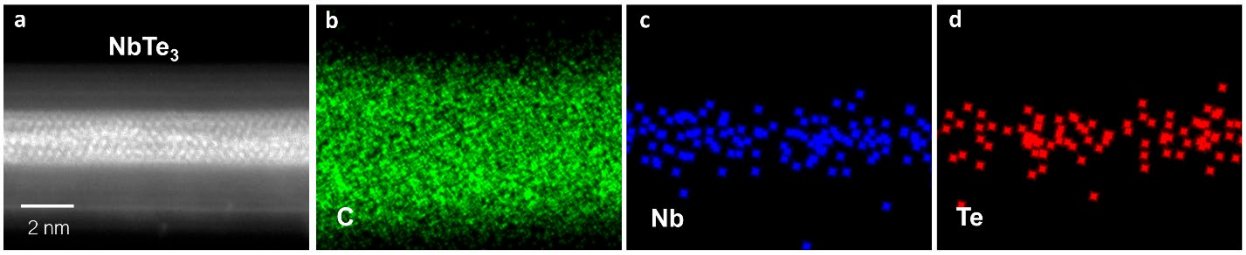

Figure 11.5 Elemental mapping demonstration for $NbTe_3$. Figure 2: (a) ADF-STEM image of a few-chain $NbTe_3$ and EDS maps of (b) C, (c) Nb, and (d) Te, showing homogeneous distributions of carbon within the carbon nanotube and niobium and tellurium only within the few-chain $NbTe_3$. Data collected in collaboration with Dr. Amin Azizi.

11.5 Experimentally resolving the TAP rocking distortion

The new TMT compositions are stable down to the single-chain limit. We examine the single-chain structure of these previously unreported chemistries using atomic-resolution annular dark field (ADF-) STEM imaging and STEM image simulation, highlighted in **Figure 11.6**. The STEM simulations are generated from the structures obtained by DFT calculations, as discussed in later sections. The left-hand section of the simulation shows the raw multislice output, and the right-hand section of the simulation incorporates noise from Poisson counting statistics according to the experimental dose.[220] The structure and contrast of atomic species observed in the simulations matches the experimental images for each of the single TMT chains, and highlights the ability of the high angular (HA)-ADF-STEM to distinguish the different atomic species in the single chains. In **Figure 11.6a-c**, single chains of $NbTe_3$, VTe_3, and $TiTe_3$, are seen encapsulated within a 1.11 nm, 1.02 nm, and 1.05 nm wide double-wall CNT, respectively. **Figure 11.6d** shows an atomic model of the single-chain TMT encapsulation process in a single-walled CNT, where the CNT clearly visible in the model may not be readily visible in the STEM images because of the contrast difference of the carbon atoms. The most striking aspect of all

three compounds' structure in **Figures 11.6a-c**, is what appears to be the intrachain rocking of the Te ligands along the chain axis. Such a rocking distortion was previously suggested by theory for few- and single-chain $HfTe_3$, but had not been experimentally resolved due to the spatial resolution necessary to observe such a small structural variation.[163] The enhanced experimental resolution in the present study allows for direct confirmation of such a rocking distortion for $NbTe_3$, VTe_3, and $TiTe_3$.

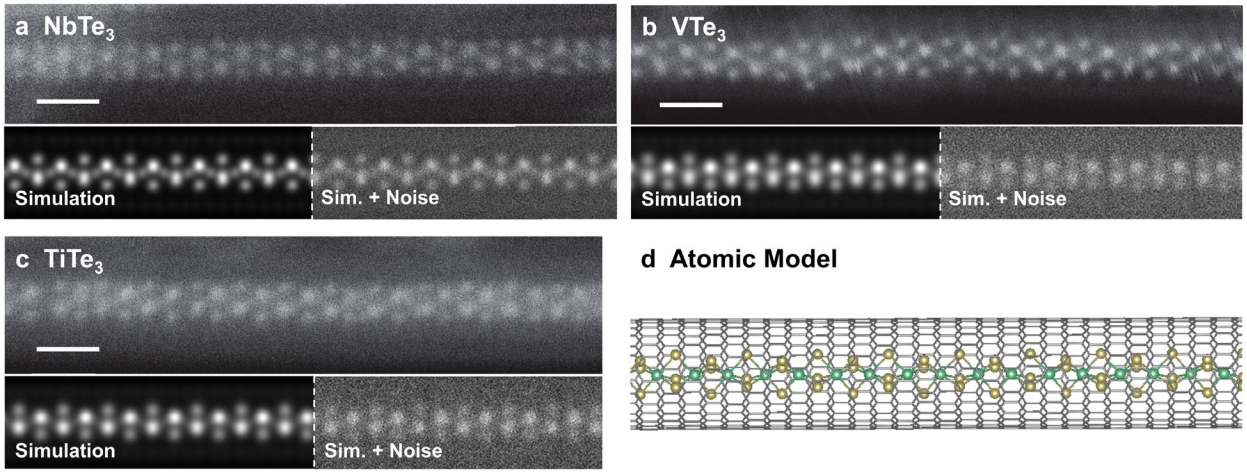

Figure 11.6 Single-chain STEM imaging, STEM simulation, and atomic structure of $NbTe_3$, VTe_3, and $TiTe_3$. STEM images of single chains of encapsulated (a) $NbTe_3$, (b) VTe_3, (c) $TiTe_3$. Below each STEM image is the corresponding STEM image simulations (left), with appropriate noise from microscope conditions added (right), from the structures obtained by DFT calculations (see **Figure 11.4**). Scale bars measure 1 nm. (d) Atomic structure and schematic of a single chain of transition metal tritelluride encapsulated within a carbon nanotube, where the gold and green atoms represent Tellurium and the corresponding transition metal (Nb, V, or Ti), respectively, and the gray lattice represents the encapsulating CNT. Data collected in collaboration with Dr. Jeff Cain.

The intrachain rocking of the Te ligands distorts the trigonal prismatic (TP) chains into a trigonal antiprismatic (TAP) chain structure. This is relatively unsurprising for the single chain of encapsulated $TiTe_3$, as titanium and hafnium are in the same group on the periodic table, so chemical trends imply this behavior. However, the TAP distortion seen in $NbTe_3$ and VTe_3 is surprising, as a previously studied encapsulated TMT in the same group, $NbSe_3$, did not show the TAP distortion, but rather a charge-induced torsional wave (CTW). Therefore, the TAP distortion seen in all three of these isolated structures could be closely related to their stability (or lack thereof) in bulk crystals, or indicate this behavior is innate to the single-chain limit of transition metal tritellurides, which is studied in following sections.

11.6 Confirming the stability of the TAP phase

11.6.1 Computational methods

The calculations and analysis in the following sections are completed by Dr. Sehoon Oh, with supervision from Dr. Marvin Cohen. As reported in previous chapters, we use the generalized gradient approximation, norm-conserving pseudopotentials, and localized pseudo-

atomic orbitals for the wavefunction expansion as implemented in the SIESTA code.[152–154] The spin–orbit interaction is considered using fully relativistic j-dependent pseudopotentials in the l-dependent fully-separable nonlocal form using additional Kleinman-Bylander-type projectors.[155,156] We use 1×1×128 Monkhorst-Pack *k*-point mesh for single chains, and about 32 mesh per $Å^{-1}$ of the reciprocal vector for bulk materials. Real-space mesh cut-off of 500 Ry is used for all of our calculations. The van der Waals interaction is evaluated using the DFT-D2 correction.[158] Dipole corrections are included to reduce the fictitious interactions between chains generated by the periodic boundary condition in our supercell approach.[159]

11.6.2 Building atomic models for the new MTe_3

As there are no previous experimental or theoretical reports on the stabilized $TiTe_3$, VTe_3, and $NbTe_3$, we need to pursue a full study of the stability of various structural compositions, distortions, and resulting electronic band structures for the new TMT members. We further investigate the structural makeup and the related TAP distortions of single-chain $TiTe_3$, VTe_3, and $NbTe_3$ *via* first-principles calculations based on density functional theory (DFT). As no bulk crystalline data are available for these TMT structures, we construct candidate structures for the chains with various symmetries including the TP and TAP phases, similar to the construction followed in the discussion about $HfTe_3$ and highlighted for reference in **Figure 11.7**. As there is no crystal structure data for atomic positioning in the chains, we extracted the atomic spacing from the atomic-resolution STEM images. From the constructed candidate structures, the atomic structures are optimized by minimizing the total energy. In the optimization, the atomic positions are relaxed with the fixed value of the distance between the nearest transition metal atoms, b_0^{MTe3} (M=Ti, V, and Nb), extracted from the STEM images shown above in **Figure 11.6**.

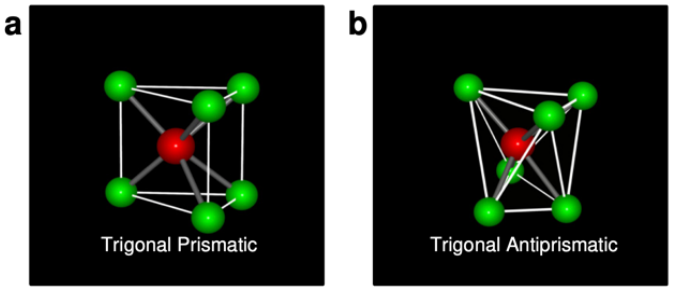

Figure 11.7 The geometry of the TP and TAP unit cell. The basic units of (a) the TP and (b) TAP geometry are shown for comparison.

11.6.3 Comparison of the TP and TAP phases in vacuum

We first consider the atomic and electronic structures of the single chains of $TiTe_3$, VTe_3, and $NbTe_3$ isolated in vacuum. The obtained atomic and electronic structures of the TP and TAP single chains isolated in vacuum are shown in **Figures 11.8** and **11.9**, respectively. All three of the TP single chains shown in **Figure 11.8** are metallic with the Te bands crossing the Fermi level. For the TAP chains, shown in **Figure 11.9**, the short-wavelength rocking distortions of Te ligands from a TP to a TAP unit cell, which was initially observed in the ADF-STEM images highlighted in **Figure 11.6**, lead to the splitting of the Te bands near the chemical potential. As a result, semiconducting band gaps of 0.690 and 0.486 eV in single chains of $TiTe_3$ (**Figures 11.9c**

and **11.9d**) and $NbTe_3$ (**Figures 11.9k** and **11.9l**) are created, respectively, while VTe_3 single chain remains metallic (**Figures 11.9g** and **11.9h**).

We note that the TAP structure of the single-chain $TiTe_3$ in vacuum has 0.652 eV/formula unit (f.u.) lower energy than the TP structure in vacuum, while the TAP structures of the single chains of VTe_3 and $NbTe_3$ isolated in vacuum have 0.015 and 0.142 eV/f.u. higher energies than the TP structures in vacuum, respectively. From initial calculations of the structures in vacuum, it is very clear that single-chain $TiTe_3$ is significantly more energetically relaxed in the TAP geometry, while VTe_3 and $NbTe_3$ are slightly more energetically relaxed in the TP geometry. As we experimentally observe the TAP geometry in all three single-chain specimens, we then turn to encapsulated models to see how the CNT may influence the energetics of the system.

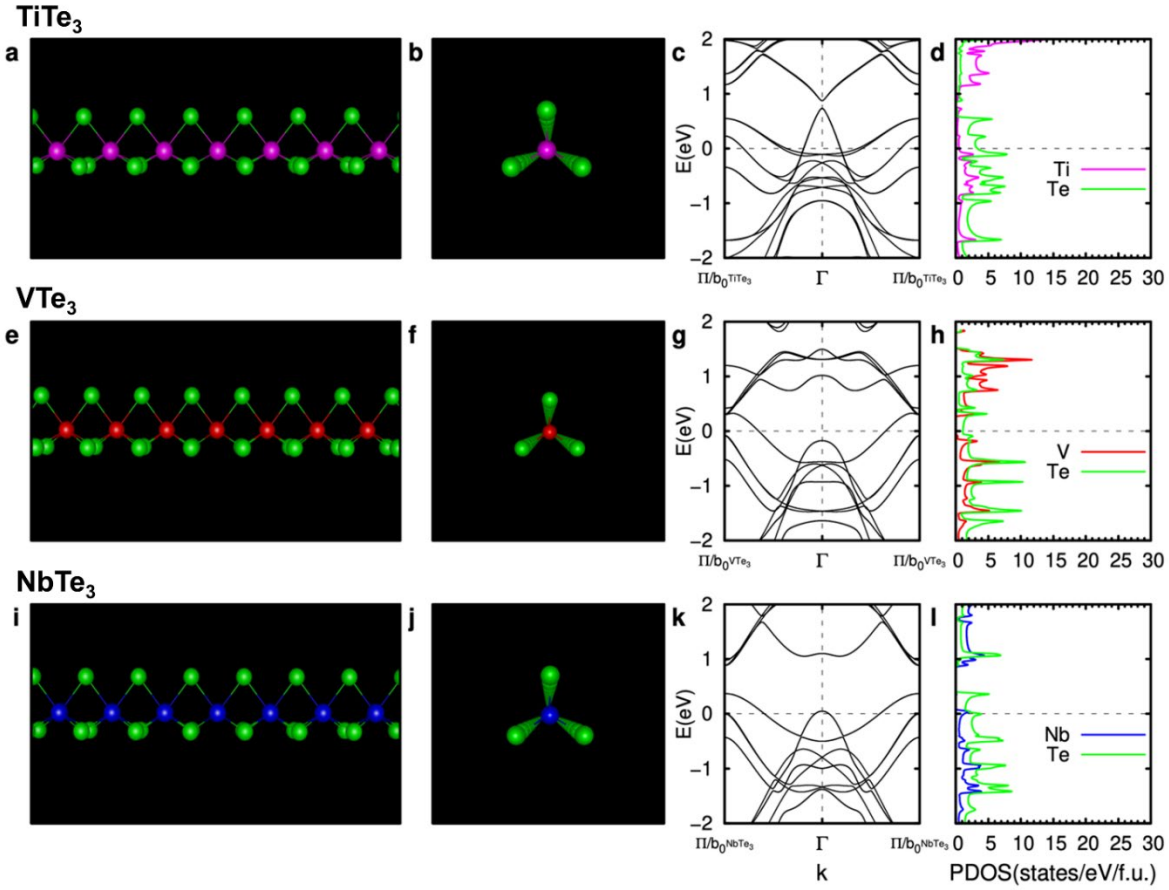

Figure 11.8 Calculated atomic structure and electronic structures for TP single-chain MTe_3 (M=Ti, V, and Nb) isolated in vacuum. (a-d) $TiTe_3$, (e-h) VTe_3, and (i-l) $NbTe_3$. In the 1st and 2nd columns, TP single-chain isolated in vacuum are presented side-on and end-on, respectively. In the atomic structure, the magenta, red, blue, and green spheres represent the Ti, V, Nb, and Te atoms, respectively. In the band structures, the chemical potential is set to zero and marked with a horizontal dashed line, and the zone boundaries for the chains are denoted as π/b_0^{MTe3}, where b_0^{MTe3} is the distance between the nearest transition metal atoms. In d, h, and l, the density of states projected onto Ti, V, Nb, and Te atoms are presented by magenta, red, blue and green lines, respectively. Data collected in collaboration with Dr. Sehoon Oh.

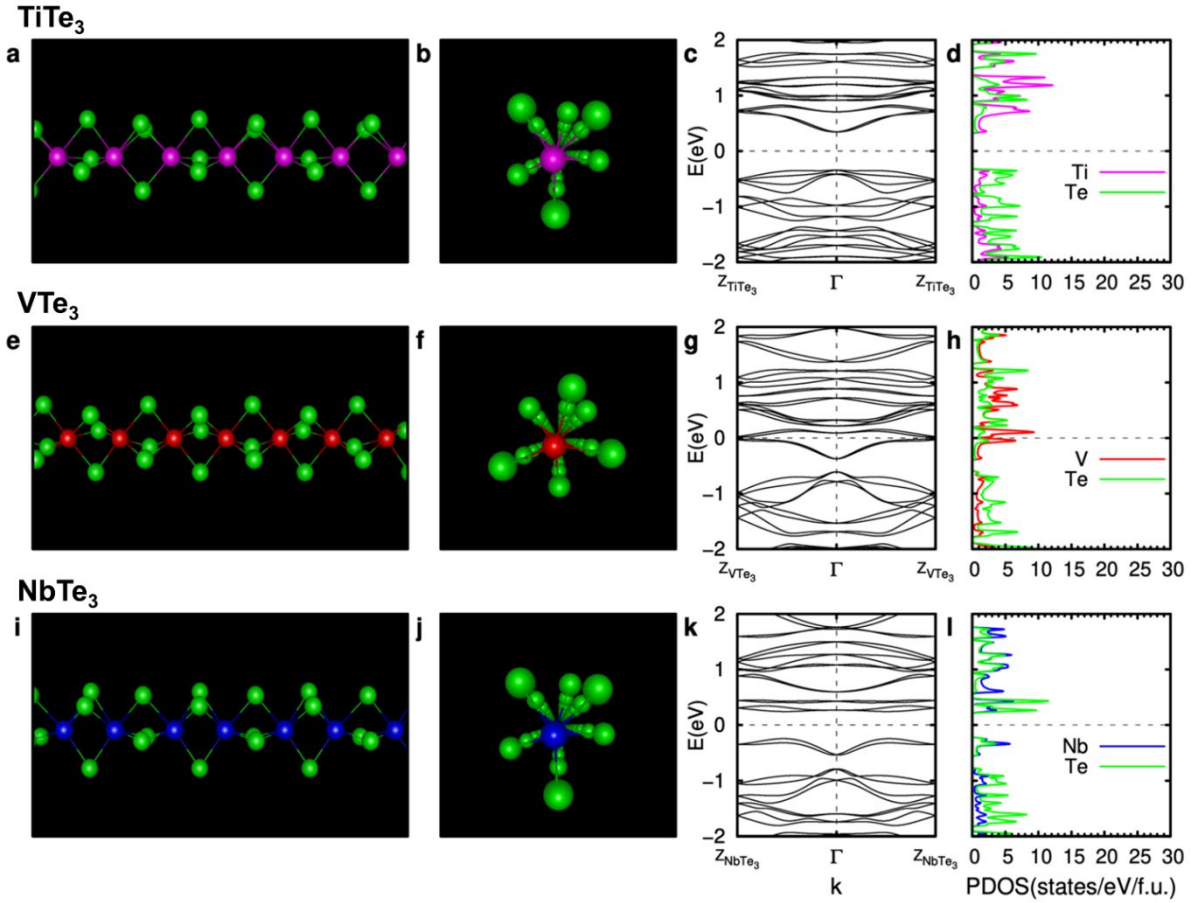

Figure 11.9 Calculated atomic structure and electronic structures for TAP single-chain MTe_3 (M=Ti, V, and Nb) isolated in vacuum. (a-d) $TiTe_3$, (e-h) VTe_3, and (i-l) $NbTe_3$. In the 1st and 2nd columns, TAP single-chain encapsulated isolated in vacuum are presented side-on and end-on, respectively. In the atomic structure, the magenta, red, blue, and green spheres represent the Ti, V, Nb, and Te atoms, respectively. In the band structures, the chemical potential is set to zero and marked with a horizontal dashed line, and the zone boundaries for the chains are denoted as Z_{MTe3}. Here, the lengths of the first Brillouin zones of the TAP chains are half of those in the corresponding TP chains because of the doubled real-space unit cell length of the rocking chains, i.e. $Z_{MTe3} = \pi/2 \cdot b_0^{MTe3}$ where b_0^{MTe3} is the distance between the nearest transition metal atoms. In d, h, and l, the density of states projected onto Ti, V, Nb, and Te atoms are indicated by magenta, red, blue and green lines, respectively. Data collected in collaboration with Dr. Sehoon Oh.

11.6.4 Comparison of encapsulated TP and TAP phases

Next, we investigate the atomic and electronic structures of the single-chain TMT encapsulated inside a (14,0) CNT (indices chosen for convenience). We construct the candidate structures using the atomic positions of the single chains isolated in vacuum and those of the empty CNT. As was done in previous chapters studying encapsulated TMT, the atomic positions of the candidate structure chains are relaxed by minimizing the total energy, whereas the atomic positions of the CNT are fixed. The obtained atomic and electronic structures of the TP and TAP single chains of TMT species encapsulated in the CNT are shown in **Figure 11.10** and **Figure 11.11**, respectively. For the TP chain geometry, all three of the MX_3 single chains remain

metallic, and the encapsulation does not alter the electronic structure of the chains significantly except for the Fermi level shift due to the charge transfer between the chains and CNT as shown in **Figures 11.8** and **11.10**. **Figure 11.11** shows the obtained atomic structures, the electronic band structure, and the projected density of states (PDOS) for the TAP single-chain MX_3 encapsulated in the CNT. For the TAP single chains of the MX_3, the encapsulation does not alter the electronic structure significantly, except for the chemical potential shift and the gap opening in the single-chain VTe_3 (**Figures 11.9** and **11.11**). The encapsulated $TiTe_3$ and $NbTe_3$ chains remain semiconducting with bandgaps of 0.680, and 0.339 eV, respectively, for the electron transfer within the chains. For VTe_3, the encapsulation-driven band repulsion at the Fermi level around the zone boundary, Z_{VTe3}, opens a bandgap of 0.062 eV as shown in **Figures 11.11g** and **11.11h**, leading to a transition from metal to semiconductor.

We note that the TAP structures of single-chain $TiTe_3$ and VTe_3 encapsulated in the CNT have 0.648 and 0.016 eV/formula unit (f.u.) lower energy than the TP structure encapsulated in the CNT, respectively, while the TAP structures of single-chains $NbTe_3$ encapsulated in the CNT has 0.162 eV/f.u. higher energies than the TP structures encapsulated in the CNT. While the energies of the encapsulated chains show favorable formation of the TAP structure for $TiTe_3$ and VTe_3, $NbTe_3$ still shows relatively lower energy for the TP system. As one final check of energy stabilities, we can turn to binding energy of the entire CNT and MTe_3 chain system.

We also calculate the binding energy, E_b, of the single-chain MX_3, which is defined as

$$E_b = E_{MX3^{chain}} + E_{CNT} - E_{MX3/CNT} \qquad \textbf{(Eq. 11.1)}$$

where E_{MX3}^{chain} is the total energy of the isolated single-chain MX_3, E_{CNT} is the total energy of an empty CNT isolated in vacuum, and $E_{MX3/CNT}$ is the total energy of the joint system of TP or TAP single-chain MX_3 encapsulated inside the CNT. The calculated binding energies of the TAP (TP) single chains of $TiTe_3$, VTe_3, and $NbTe_3$ are 1.378 (1.381), 1.165 (1.134), and 1.384 (1.404) eV/f.u., respectively. The relative binding energies, which in this case is the comparison of an MTe_3 chain in its encapsulated vs vacuum state, show a lower energy for the $NbTe_3$ chain in the TAP geometry as opposed to the TP geometry, which could account for the experimental observation of $NbTe_3$ in the TAP phase.

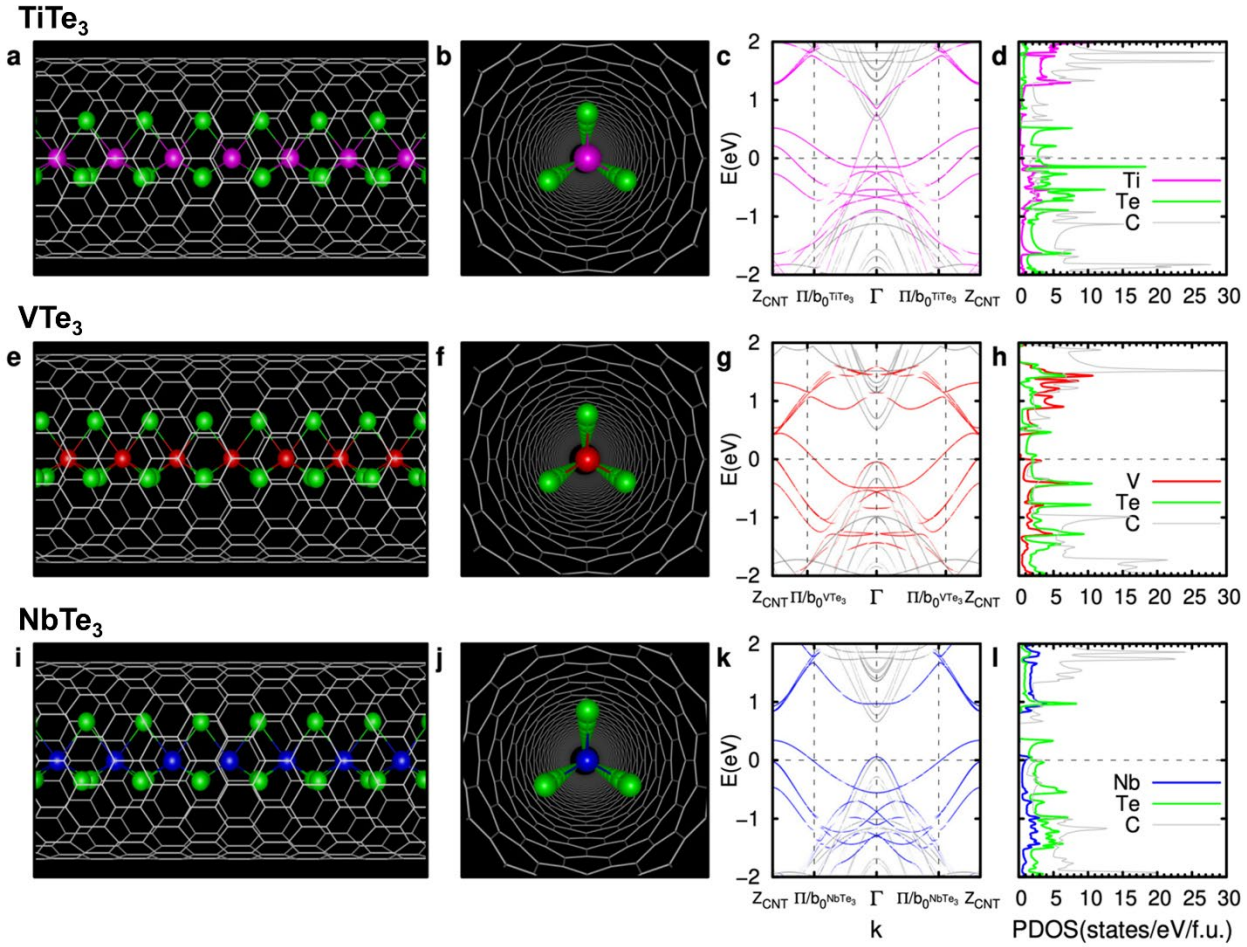

Figure 11.10 Calculated atomic structure and electronic structures for TP single-chain MTe_3 (M=Ti, V, and Nb) encapsulated in CNT. (a-d) $TiTe_3$, (e-h) VTe_3, and (i-l) $NbTe_3$. In the 1st and 2nd columns, TP single-chain encapsulated inside a (14,0) CNT are presented side-on and end-on, respectively. In the atomic structure, the magenta, red, blue, and green spheres represent the Ti, V, Nb, and Te atoms, respectively. In the band structures, the chemical potential is set to zero and marked with a horizontal dashed line. In c, g, and k, the bands represented by magenta, red, blue and gray lines are projected onto the single-chain $TiTe_3$, VTe_3, $NbTe_3$ and CNT, respectively. The bands are then unfolded with respect to the first Brillouin zone of the unit cell of the single chain and the CNT, where zone boundaries for the chain and CNT are denoted as π/b_0^{MTe3} and Z_{CNT}, respectively, and b_0^{MTe3} is the distance between the nearest transition metal atoms. In d, h, and l, the density of states projected onto Ti, V, Nb, Te, and C atoms are presented by magenta, red, blue, green, and gray lines, respectively. Data collected in collaboration with Dr. Sehoon Oh.

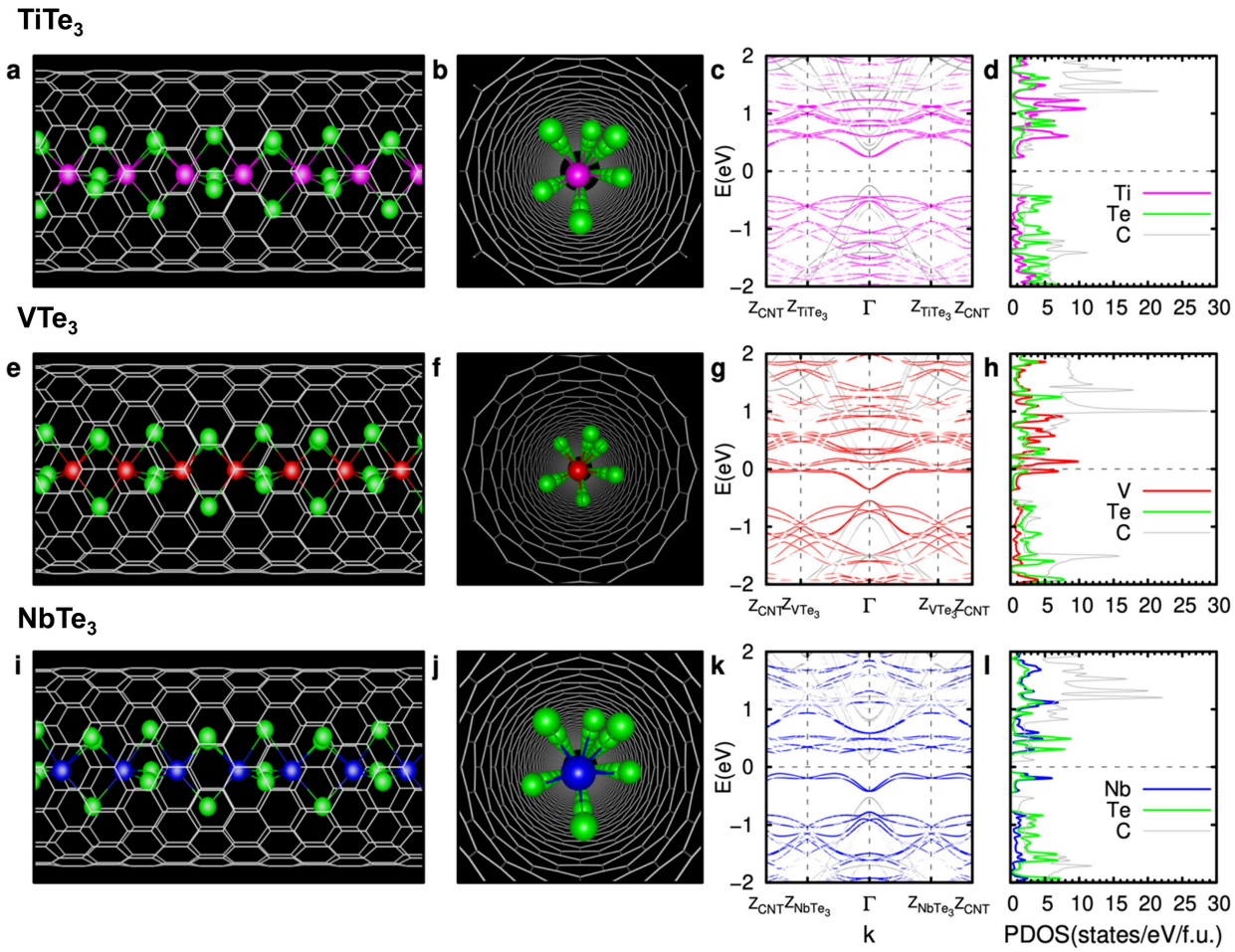

Figure 11.11 Calculated atomic structure and electronic structures for TAP single-chain MTe_3 (M=Ti, V, and Nb) encapsulated in CNT. (a-d) $TiTe_3$, (e-h) VTe_3, and (i-l) $NbTe_3$. In the 1st and 2nd columns, TAP single-chain encapsulated inside a (14,0) CNT are presented side-on and end-on, respectively. In the atomic structure, the magenta, red, blue, and green spheres represent the Ti, V, Nb, and Te atoms, respectively. In the band structures, the chemical potential is set to zero and marked with a horizontal dashed line. In c, g, and k, the bands represented by magenta, red, blue, and gray lines are projected onto the single-chain $TiTe_3$, VTe_3, $NbTe_3$, and CNT, respectively. The bands are then unfolded with respect to the first Brillouin zone of the unit cell of the single chain and the CNT, where zone boundaries for the chain and CNT are denoted as Z_{MTe3} and Z_{CNT}, respectively. Here, the lengths of the first Brillouin zones of the TAP chains are half of those in the corresponding TP chains because of the doubled real-space unit cell length of the rocking chains, i.e. $Z_{MTe3} = \pi/2 \cdot b_0^{MTe3}$ where b_0^{MTe3} is the distance between the nearest transition metal atoms. In d, h, and l, the density of states projected onto Ti, V, Nb, Te, and C atoms are presented by magenta, red, blue, green, and gray lines, respectively. Data collected in collaboration with Dr. Sehoon Oh.

11.7 Comparing stabilities of the dichalcogenides vs. trichalcogenides

Finally, we investigate the stability of the TMT families, including these new materials, by calculating the Gibbs free energies of formation, δG, of the MX_3, which are defined as

$$\delta G = \epsilon_{MX3} - n_M\epsilon_M - n_X\epsilon_X \qquad \textbf{(Eq. 11.2)}$$

where ϵ_{MX3}, ϵ_M and ϵ_X are the total energies per atom of the bulk MX_3, the bulk transition metal (M = Ti, Zr, Hf, V, Nb, and Ta), and the bulk chalcogen (X = S, Se, and Te), respectively, and n_M and n_X are the mole fractions of the M and X atoms, respectively, as shown in **Table 11.1**. In general, a more negative δG indicates a more stable product, and can equate (sometimes) to an 'easier' means of synthesis, as the energy of the final product is smaller than the energy of the individual reactants. An overall lowering of energy of products indicates favorable changes and balance in enthalpy (heat of reaction) and entropy (disorder of reaction).

The calculated δG increases in the order of sulfide, selenide, and telluride compounds, possibly due to the size effect of the chalcogen atoms. The calculated δG of VTe_3 and $NbTe_3$ are -0.156 and -0.312 eV/atom, respectively, notably higher than those of the experimentally observed telluride materials, $ZrTe_3$ and $HfTe_3$, which are -0.653 and -0.522 eV/atom, respectively, while that of $TiTe_3$ is -0.506 eV/atom, comparable with those of $ZrTe_3$ and $HfTe_3$. We compare the stability of an MX_3 configuration with those of an MX_2 configuration by calculating ΔE, which is defined as

$$\Delta E = E_{MX3^{bulk}} - E_{MX2^{bulk}} - E_{X^{bulk}} \qquad \textbf{(Eq. 11.3)}$$

where $E_{MX3}{}^{bulk}$, $E_{MX2}{}^{bulk}$, and $E_X{}^{bulk}$ are the total energies of the bulk MX_3, MX_2 and X, respectively. The calculated ΔE of $TiTe_3$, VTe_3, and $NbTe_3$ are 0.193, 0.292, and 0.110 eV/f.u., respectively, meaning the MX_3 configurations are less stable than the MX_2 configurations, while those of TaS_3, $NbSe_3$, and $ZrTe_3$ are -0.155, -0.063, and -0.011 eV/f.u., respectively, meaning the MX_3 configurations have higher or comparable stability compared to the MX_2 configurations. The relative stability of $TiTe_2$, VTe_2, and $NbTe_2$ as compared to their trichalcogenide counterparts, would account for the successful synthesis and experimental studies of those dichalcogenide systems.[221–223] Based on the calculated δG and ΔE, VTe_3 has the lowest δG and highest ΔE, implying it is the hardest to achieve in bulk form. However, $NbTe_3$ and $TiTe_3$ are also difficult to realize in their bulk form due to low δG and ΔE, respectively. This is consistent with there being no reports of successful bulk synthesis of these materials.

Table 11.1 Energetic property of MX_3 bulk. The Gibbs free energies of formation, δG, of the MX_3, defined as $\delta G = \epsilon_{MX3} - n_M\epsilon_M - n_X\epsilon_X$, where ϵ_{MX3}, ϵ_M, and ϵ_X are the total energies per atom of the bulk MX_3, the bulk transition metal M (M = Ti, Zr, Hf, V, Nb, and Ta) and the bulk chalcogen X (X = S, Se, and Te), respectively, and n_M and n_X are the mole fractions of the M and X atoms, respectively. The unit of δG is eV/atom.

	Ti	Zr	Hf	V	Nb	Ta
S	-1.042	-1.110	-1.082	-0.650	-0.666	-0.690
Se	-0.829	-0.895	-0.870	-0.464	-0.560	-0.514
Te	-0.506	-0.653	-0.522	-0.156	-0.312	-0.163

11.8 Conclusion

In summary, in this chapter, we demonstrated the few-chain limit synthesis of three new members of the quasi-1D TMT family, *via* encapsulation within the hollow cavity of MWCNTs. The nanotube sheath stabilizes and protects the materials, allowing access to hitherto unseen

compositions and crystal structures, specifically $NbTe_3$, VTe_3, and $TiTe_3$. We investigated the structures of the new materials with atomic-resolution electron microscopy, revealing helical twisting of chains in multi-chain specimens and an experimentally resolved trigonal antiprismatic rocking distortion in single chain specimen. DFT calculations illuminate the electronic properties of single chains of the materials encapsulated in MWCNTs and quantify the stability of these materials in their bulk form and in the single-chain limit. Analyzing the Gibb's Free Energy of these systems sheds additional light on the overall balance between the stability of the trichalcogenide systems vs. their dichalcogenide counterparts and explains some of the disparities in previous reports of synthesis and/or characterization of certain material families. Our study lays further groundwork for the study of confinement-stabilized non-equilibrium materials and associated emergent physical phenomena.

Chapter 12: Applying Encapsulation to other Material Families – Ultra-Narrow TaS_2 Nanoribbons

Special thank you to Dr. Jeff Cain, Dr. Sehoon Oh, and Dr. Amin Azizi for their leadership on this project.

Keywords: Two-Dimensional Materials, Nanoribbons, Transition Metal Dichalcogenides, Scanning Transmission Electron Microscopy, Flat Bands, Nanotubes, Tantalum Disulfide, Defect Array, Periodic Superstructure

While the previous chapters highlight the achievements in pushing the isolation of 1D vdW materials down to their fundamental limit (such as transition metal trichalcogenides), in **Chapter 9** highlighted how widely accessible the encapsulation technique developed is to many other families of materials. As the nanotubes provide physical confinement of the interior species, the quasi-1-D nature of the nanotube can also direct other materials to grow in a quasi-1-D structure, even if the material itself is not comprised of 1-D building blocks. Previous work by the Zettl group in 2016 has shown the ability to fill nanotubes with other crystalline species that can be directed into 1-D nanorod shapes due to the confinement within the nanotube.[141] Even other groups have shown the ability to grow nanoribbon-like materials inside the cavity of nanotubes, such as MoS_2.[224] However, previously reported techniques of these filling methods for other quasi-1-D structures has involved some type of wet-filling method, which requires precursors that are soluble in a solvent. This restriction has severely limited the progress of the study of quasi-1-D nanoribbon systems at the nanometer size-scale because few inorganic species have soluble precursors for solution-procession. In the following chapters, we apply the synthetic methods for encapsulating crystalline species to the transition metal dichalcogenides (TMD).

12.1 Motivating the confinement of 2-D materials

In step with the resurgent interest in 2D materials, there have been extensive efforts toward engineering additional levels of confinement, and thus lower dimensionality, in few- and monolayer van der Waals (vdW) bonded 2D structures. The greatest successes have been achieved in the fabrication and synthesis of graphene nanoribbons (GNRs), where rational bottom-up synthesis has been accomplished using the self-assembly of molecular precursors.[225,226] This has enabled the growth of GNRs with specific edge structures and atomically-precise widths, as well as single GNR heterojunctions with engineered band alignment and topology.[195,227–229] Exciting physics is similarly predicted to arise when 2D transition metal dichalcogenides (TMDs) are further constrained towards one-dimension (1D), including the emergence of metal-insulator transitions, enhanced thermoelectric performance, ferromagnetism, and tunable band gaps.[162,230–232]

While imposing additional confinement in two-dimensional (2D) materials has been proven to yield further control over their electronic, optical, and topological properties, the synthesis or fabrication of TMD nanoribbons (NRs) has lagged far behind that of GNRs both in terms of quality and width control. Past studies have relied upon top-down fabrication methods that require lithography and etching processes, which results in NRs with widths greater than 50 nm - too large to observe quantum confinement effects - and with a high degree of structural disorder.[233–235] Molecular beam epitaxy has been used for the fabrication of ultra-narrow $MoSe_2$

NRs, but this method has little flexibility in implementation (e.g. substrate choice).[236] Other bottom-up techniques, including chemical vapor deposition and vapor-liquid-solid growth, have recently been used to grow MoS_2 NRs, resulting in ribbons with average widths > 50 nm, again too large to access predicted quantum phenomena.[237,238] Some success has been found using solution-processed precursors to grow NR below the 5nm width limit, however the extent of filling is significantly lower than reports for vapor-phase filling of CNT, and the solution-processing is very limited in regards to the material systems that can be accessed through soluble precursors.[224,239]

12.2 Fundamentals behind TaS_2

While the templated growth of 1D nanomaterials using multi-walled carbon nanotubes (MWCNTs) has been successfully demonstrated for a variety of materials including elemental metals, halides, trichalcogenides, and molecular chains, where the synthesis generally results in nanowire- or chain-like structures, there is need to extend this templated growth to other material systems.[141,144,163,208,215] Here, we extend the encapsulation method using chemical vapor transport to achieve ribbon-like morphologies and demonstrate the growth of 2H-TaS_2 NRs. TaS_2 is a metallic TMD which hosts multiple charge-density-wave (CDW) phases, a Mott insulator state and possible quantum spin liquid, making it a unique material for the study of strongly correlated physics under extreme dimensional constraint.[240–243]

We achieve TaS_2 NRs with thicknesses down to the monolayer limit (typical layer numbers are between 1 and 3), widths as low as 2.5 nm, and lengths greater than 100 nm. The MWCNT sheath fully encapsulates the TaS_2 NR, protecting it from interaction with the environment. The growth produces NRs with controllable widths, clean NR surfaces and edges, and enables easy handling (e.g. solution-based post processing) and subsequent study of the structure and detailed atomic registry of NRs with transmission electron microscopy (TEM) and aberration-corrected annular dark-field scanning transmission electron microscopy (ADF-STEM). Furthermore, we observe and investigate previously unknown and unique periodic atomic superstructures defined by ordered defect arrays. First-principles calculations are used to elucidate the electronic structure of the NRs and atomic superstructure, revealing the presence of flat bands localized at the defect boundaries and edges. The synthesis of these ultra-narrow TMD NR is achieved utilizing vapor-phase growth conditions, an accessible and common synthesis route for many members of the TMD family. Nanotube-templated synthesis represents a unique, transferable, and broadly deployable route toward ultra-narrow TMD NR growth.

12.3 Synthesis method of TaS_2@CNT

TaS_2 NRs in the 2H phase are grown within MWCNT (CheapTubes) using chemical vapor transport (CVT). MWCNT were opened via oxidation at high temperature (515 ℃) for 1 hour in air, before the filling step. The opened nanotubes are then coated onto the inner surface of a 4 mm inner diameter quartz ampule, which is filled with elemental Ta and S powder, an iodine transport agent, and sealed under vacuum (10^{-6} Torr).[244] Synthesis is carried out in a gradient furnace in a manner similar to that used for single crystal TMD growth via CVT, the main reaction region of the ampoule being held at 760 ℃ for 1 week, then cooled to room temperature naturally. Synthesis of the samples was carried out by Dr. Jeff Cain, Markus Thiel, and myself.

12.4 Experimental characterization of TaS_2 nanoribbons

12.4.1 Electron microscopy details

Dr. Jeff Cain led the experimental characterization of the TaS_2@CNT samples, from sample prep to electron microscopy imaging. The filled CNTs are dispersed in isopropyl alcohol by bath sonication for 1 hour and drop-cast onto lacey carbon transmission electron microscope grids for imaging. Transmission electron microscope imaging was carried out on a JEOL 2010 microscope at an accelerating voltage of 80 keV. Scanning transmission electron microscopy was done on the TEAM 0.5 microscope at the National Center for Electron Microscopy at Lawrence Berkeley National Laboratory operating, which is a Titan 80-300 with a ultra-twin pole piece gap, DCOR probe aberration corrector and was operated at 80 kV and semi-convergence angle of 30 mrad. Images were acquired using the ADF-STEM detector with an inner angle of 60 mrad and a beam current of approximately 70 pA, under guidance from Dr. Chengyu Song. An aberration-corrected FEI Titan3 (60−300) equipped with a SuperX EDS system at 80 kV was also used for the imaging and spectroscopy, performed by Dr. Amin Azizi. Elemental mapping was performed in the STEM mode at 80 kV with a 7 min acquisition time.

12.4.2 STEM simulation details

STEM simulations were performed by Dr. Peter Ercius, using Prismatic's prism algorithm with parameters that matched the experiments.[245] In detail for each simulation, we used a 52.92 Å square simulation box, 80 kV accelerating voltage, 30 mrad convergence semi-angle, 0.04 Å/pixel sampling, 1 Å slice size, interpolation factor 4 and 50 frozen phonon calculations. After completion, the simulation data was convolved with a 1.3 Å source size to match the contrast seen in the experiment images. Noise was added following Poisson counting statistics to match the 70 pA experimental beam current. This allowed us to interpret the positions of atoms based on the approximate Z-contrast in the images and to compare the projection images to the DFT simulated structures.

12.4.3 Characterization of the encapsulated nanoribbon species

Figure 12.1a shows a schematic of a monolayer TaS_2 NR within a carbon nanotube for reference of the encapsulated species (for simplicity, a single-wall nanotube is shown), in both plan and end views. **Figures 12.1b-d** show electron microscopy images of the as-synthesized material. **Figure 12.1b** shows a plan view TEM image of a 5nm wide NR, while **Figure 12.1c** shows an edge view TEM image of a 3-layer NR. The dashed yellow lines in **Figure 12.1b** and **12.1c** delineate the inner walls of the MWCNT. The strong contrast, dark lines in **Figure 12.1c** are due to the edge-on orientation of the TaS_2 atomic planes, resulting in greater sample thickness. The measured interlayer distance (~0.7 nm) matches well with that of bulk TaS_2 (0.7 nm).[246] **Figure 12.1d** is an ADF-STEM image (plan view) of a monolayer TaS_2 NR approximately 4nm wide. The high crystallinity and uniform width of the NR is immediately apparent. It should be noted that **Figures 12.1b** and **12.1c** (TEM) have the reverse contrast of **Figure 12.1d** (STEM).

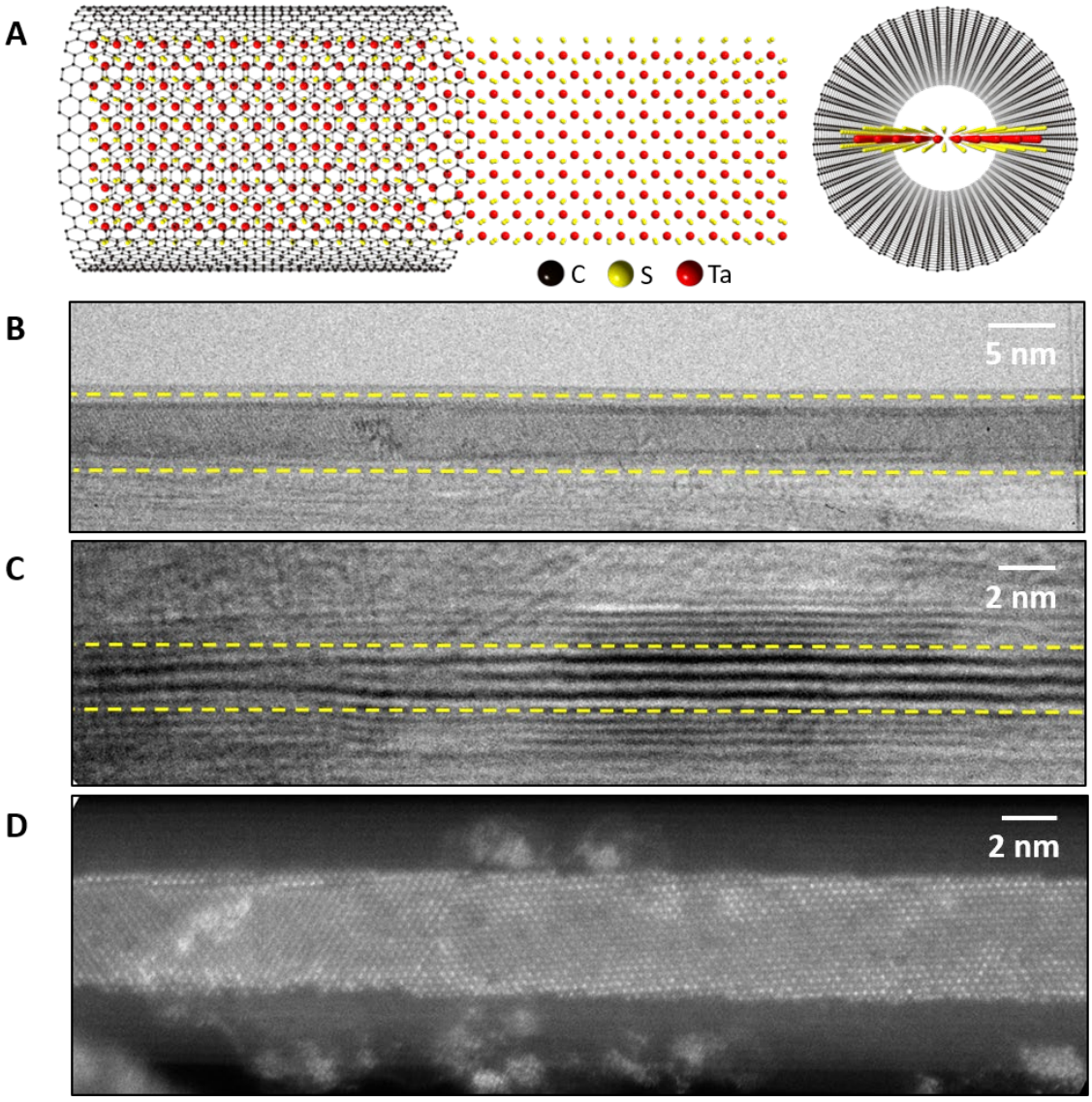

Figure 12.1 Electron microscopy imaging of encapsulated ultra-narrow TaS_2 nanoribbons. (a) Schematic of TaS_2 nanoribbons templated by carbon nanotubes in (left) plan view and (right) end view. (b) Plan view TEM image of 5 nm wide TaS_2 nanoribbon. (c) Side-view TEM image of a multilayer 2H-TaS_2 nanoribbon. (d) High-resolution ADF-STEM image of a pristine TaS_2 nanoribbon with ~4nm width. Data collected in collaboration with Dr. Jeff Cain.

12.5 Exploring the atomic scale and elemental composition of ultra-narrow nanoribbons

We further explore the detailed atomic structure and phase of the TaS_2 NR using atomic-resolution ADF-STEM imaging. A pristine NR with a width of 3.8 nm is presented in **Figure 12.2a**, where the hexagonal lattice characteristic of (monolayer) 2H-TaS_2 is clearly visible. A higher magnification portion of the ADF-STEM image of the NR in **Figure 12.1d** is also shown in **Figure 12.2b**. **Figure 12.2c** is a simulated STEM images of a monolayer of 2H-TaS_2. **Figure 12.2d** compares the line intensity profile along the dashed green box in the experimental image of **Figure 12.2b** and that of along the dashed orange box of the simulated STEM image of

monolayer 2H-TaS_2 in **Figure 12.2c**. There is excellent matching between the intensity of the line profile between the experimental and simulated image, indicating the sample consists of a monolayer 2H-TaS_2 NR, and further, is inconsistent with simulations performed on bi-layer TaS_2.

While the atomic structure of the observed NR matches that of the modeling and simulations, further analysis is needed to confirm the chemical makeup of the NR. The composition of the NRs is further supported by energy dispersive x-ray spectroscopy (EDS) (**Figures 12.2g-i**), which shows, over the width and length of the NR, a reasonably uniform distribution of Ta and S atoms. The (wider, as expected) carbon contribution is from the MWCNT. The EDS spectrum collected from the TaS_2 NR, shown in **Figure 12.3**, also clearly shows peaks of Ta and S. We also observe peaks for oxygen (likely due to contamination), as well as Si and N (from the substrate), which are not shown in the displayed energy range. The elemental mapping and spectrum further confirm the identity of the NR material.

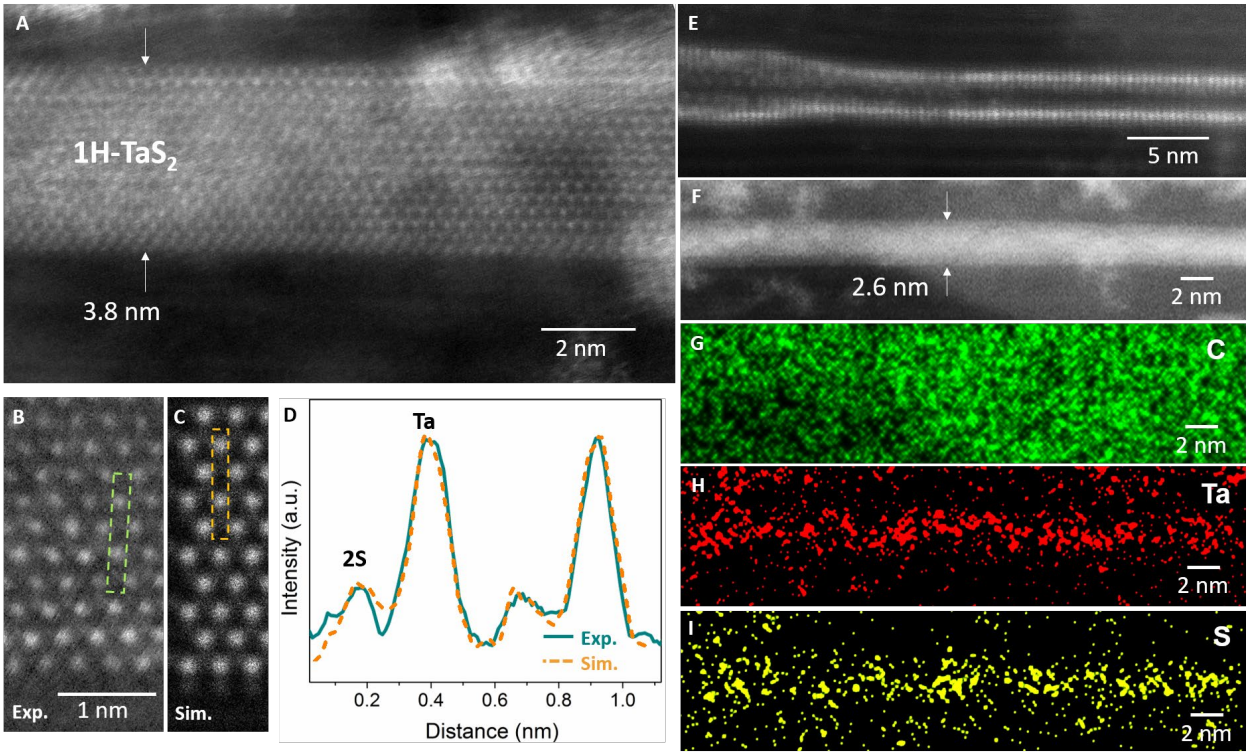

Figure 12.2 Atomic-resolution imaging of ultra-narrow, monolayer TaS_2 nanoribbons. (a) and (b) Atomic resolution ADF-STEM images of 2H-TaS_2 nanoribbons. (c) STEM simulation of 2H-TaS_2 monolayer nanoribbon (d) Line scan intensity profile comparison of the experimental (green) and simulated (orange) STEM images. (e) Side-view ADF-STEM image showing nanoribbon folding. (f-i) ADF-STEM reference image and EDS maps of C, Ta, S, respectively. Data collected in collaboration with Dr. Jeff Cain and Dr. Amin Azizi.

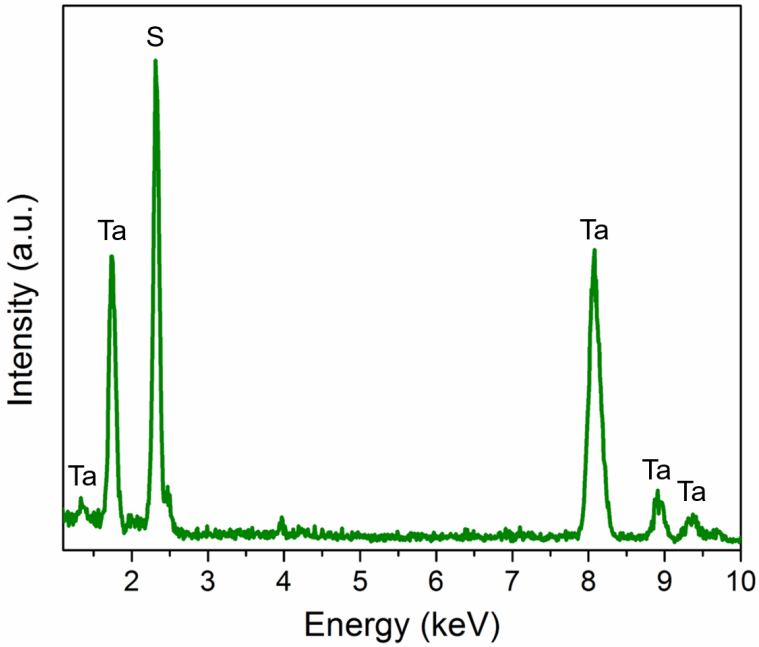

Figure 12.3 Energy dispersive x-ray spectroscopy spectrum. Elemental analysis of the encapsulated nanoribbons, confirming the presence of both Tantalum and Sulfur.

In addition to the phase and elemental composition of the NR, overall diameter is of great interest, as we are hoping to access very narrow confinement of NR. The smallest NR width we have observed is 2.5nm, and lengths on the order of 100nm is not uncommon. The widest NR observed is 6 nm wide, and the average NR width is 3.8 nm. A histogram of NR widths is shown in **Figure 12.4**. In addition to strictly planar morphologies, some NRs also show curling at the edges (**Figure 12.2e**, plan view), presumably facilitated by the MWCNT confinement. Any deformation or variation of the inner walls in an encapsulating CNT can cause the encapsulated NR to deform as well, which could lead to the curling observed in some specimen.

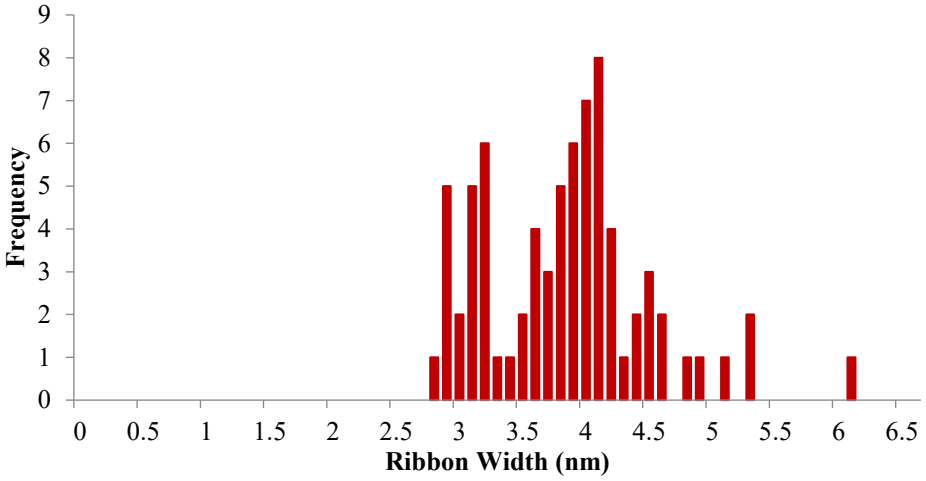

Figure 12.4 Histogram of TaS_2 nanoribbon widths. There is a relatively narrow distribution of nanoribbon widths between 2.5 nm and 6 nm, dictated by the inner diameter of the encapsulating nanoribbon. Majority of the nanoribbons observed were of 3 nm or 4 nm in diameter.

12.6 Uncovering a periodic defect array superstructure

As discussed in previous chapters, the encapsulation of vdW materials at their fundamental limit can stabilize unforeseen and novel atomic structure or deformations. These structural deformations or rearrangement of the material can drastically alter the electronic structure of the encapsulated material, giving rise to unexpected phenomena. In addition to the clean, atomically defined encapsulated NR, we find that TaS_2 NRs can form striking periodic atomic superstructures, an example of which is presented in **Figure 12.5**. **Figure 12.5a** shows an atomic-resolution ADF-STEM image of a 3.3 nm wide TaS_2 NR containing an ordered, "zig-zag" like superstructure characterized by triangular domains of ideal TaS_2 lattice interrupted by boundaries of low STEM contrast. The zig-zag structure is dramatically highlighted in a bandpass filtered version of the same image, presented in **Figure 12.5b**. The period of the perturbation is ~9 unit cells. These zig-zag periodic array superstructures are explored in more detail through calculations and simulation, some of which can be seen in **Figure 12.5**. The origin of this defect array is explained in more detail in following sections.

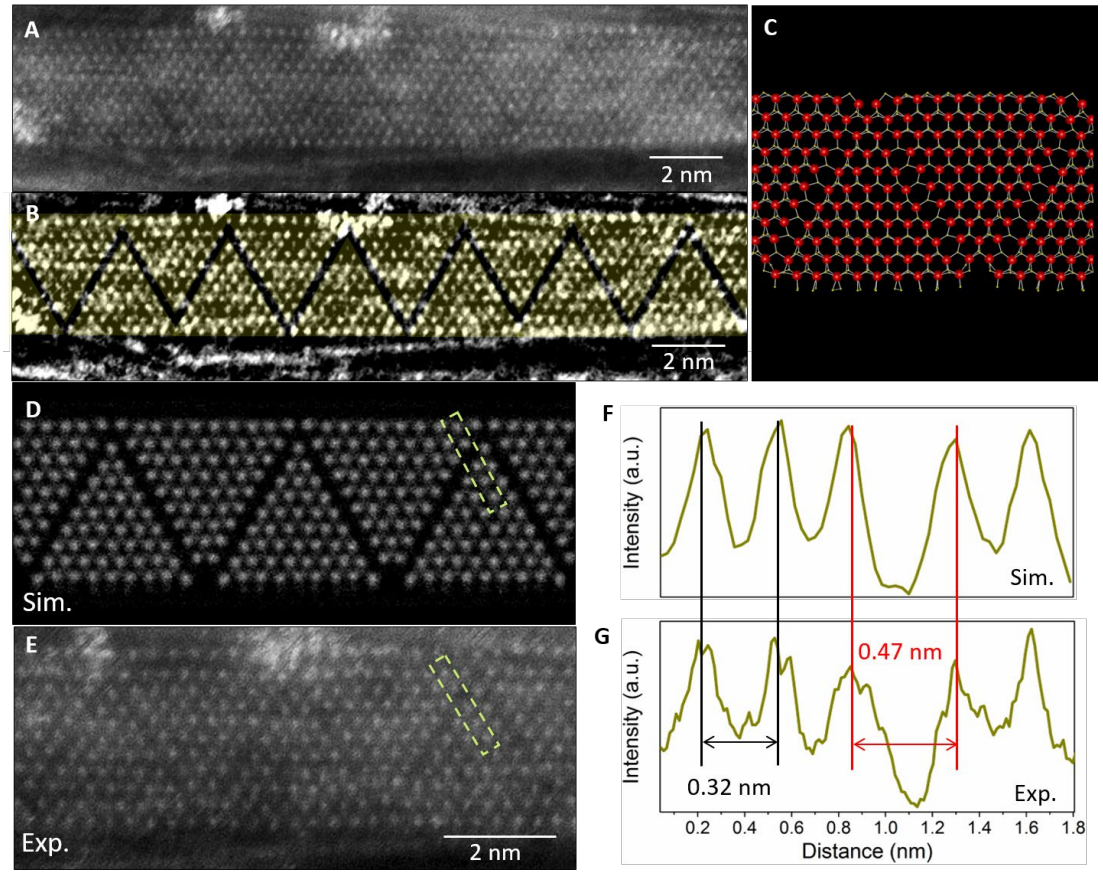

Figure 12.5 Zig-zag periodic superstructure in TaS_2 nanoribbons. (a) ADF-STEM image and (b) its filtered version showing presence of zig-zag like atomic superstructure. The superstructure is identified as defect line arrays, with lines of missing S atoms. (c) Calculated atomic structure of defect line arrays in monolayer TaS_2 nanoribbons. (d) Simulated an (e) experimental STEM images of defect line arrays. Line intensity scans of (f) the simulated and (g) experimental images across the defect boundary along the dashed green boxes.

In addition to the zig-zag periodic array superstructures observed, we also saw some parallel defect structures stabilized in some of the nanoribbons, as shown in **Figure 12.6**. These parallel superstructures are not as well understood and were also not observed nearly as frequently as the zig-zag motif. The origin of this parallel alignment is still under investigation, so the main superstructure under investigation for the remainder of this chapter will be the zig-zag periodicity shown in **Figure 12.5**.

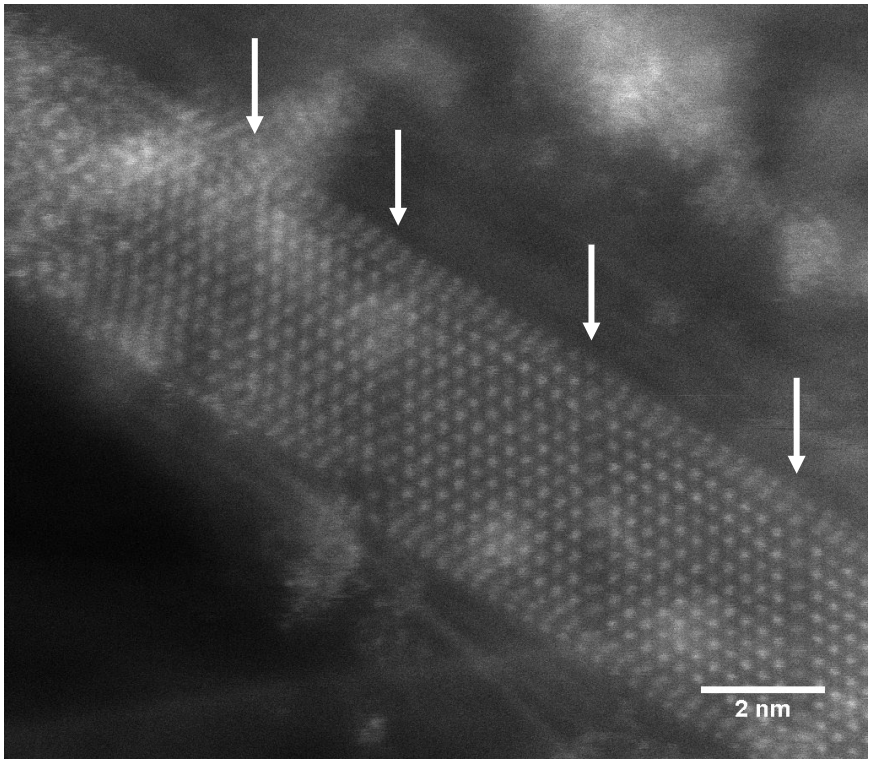

Figure 12.6 Parallel periodic superstructure in TaS_2 nanoribbons. (a) ADF-STEM image showing presence of parallel atomic superstructure, denoted by the white arrows. The origin of this superstructure is still under investigation, and less is known about its origin.

As we discuss in more detail below, the 2H-TaS_2 NRs considered here appear to support charge density waves (CDWs), but the CDW amplitudes are small and CDWs are not the origin of the dramatic zig-zag superstructure. Rather, the superstructure arises from line defect arrays. The atomic structure of the defect arrays is calculated via first principles calculations (see below), and the relevant candidate structure is shown in **Figure 12.5c**. The structure is characterized by zig-zag tracks of linearly-formed S vacancies. A STEM simulation of this structure is shown in **Figure 12.5d** for comparison with the experimental image in **Figure 12.5e**. The simulation is generated from the proposed structure discussed in subsequent sections. Intensity line profiles across the boundary (along the dashed green box) in both the simulated (**Figure 12.5f**) and experimental images (**Figure 12.5g**) match, showing a Ta-Ta distance of ~0.47 nm at the boundary versus ~0.32 nm within the ideal TaS_2 lattice. There is very good matching between the line scans highlighted in **Figure 12.5f** and **12.5g**, indicating the linearly-formed sulfur vacancies are a reasonable causation of the zig-zag defect arrays observed.

12.7 Exploring the zig-zag periodic superstructure in TaS_2 nanoribbons

12.7.1 Computational Methods

The calculations and analysis in the following sections are completed by Dr. Sehoon Oh and Dr. Mehmet Dogan, with supervision from Dr. Marvin Cohen. Similar to previous chapters, we use the generalized gradient approximation, norm-conserving pseudopotentials, and localized pseudo-atomic orbitals for the wavefunction expansion as implemented in the SIESTA code.[152–154] The spin–orbit interaction is considered using fully relativistic j-dependent pseudopotentials in the l-dependent fully-separable nonlocal form using additional Kleinman-Bylander-type projectors.[155,156] We use 64×64×18 Monkhorst-Pack k-point mesh for 2H-bulk, 64×64×36 for 1T-bulk, 64×64×1 for 1H- and 1T-MLs, 1×64×1 for 1H- and 1T-NRs without boundaries, and 1×9×1 for 1H- and 1T-NRs with boundaries. Real-space mesh cut-off of 1000 Ry is used for all of our calculations. The vdW interaction is evaluated using the DFT-D2 correction.[158] Dipole corrections are included to reduce the fictitious interactions between layers generated by the periodic boundary condition in our supercell approach.[159]

12.7.2 Atomic and electronic structure of bulk vs. monolayer TaS_2

We expand on our first-principles calculations based on DFT. We investigate the atomic and electronic structures of TaS_2 bulk and ML, and the obtained atomic and electronic structures of the 2H-bulk and ML configurations, shown in **Figure 12.7**, are consistent with other studies.[247,248] Of significant difference here (as compared to previous chapters) is that the monolayer limit of TaS_2 does not show any substantial alteration to its atomic or electronic structure. The only noticeable difference is an increase in the density states of the bonding orbitals for the sulfur, as seen in **Figure 12.7f**. Otherwise, the monolayer confinement of TaS_2 is not enough to induce any structural or electronic structure changes of the material, highlighting the need for ultra-confinement of some TMD species to access emergent properties of these materials.

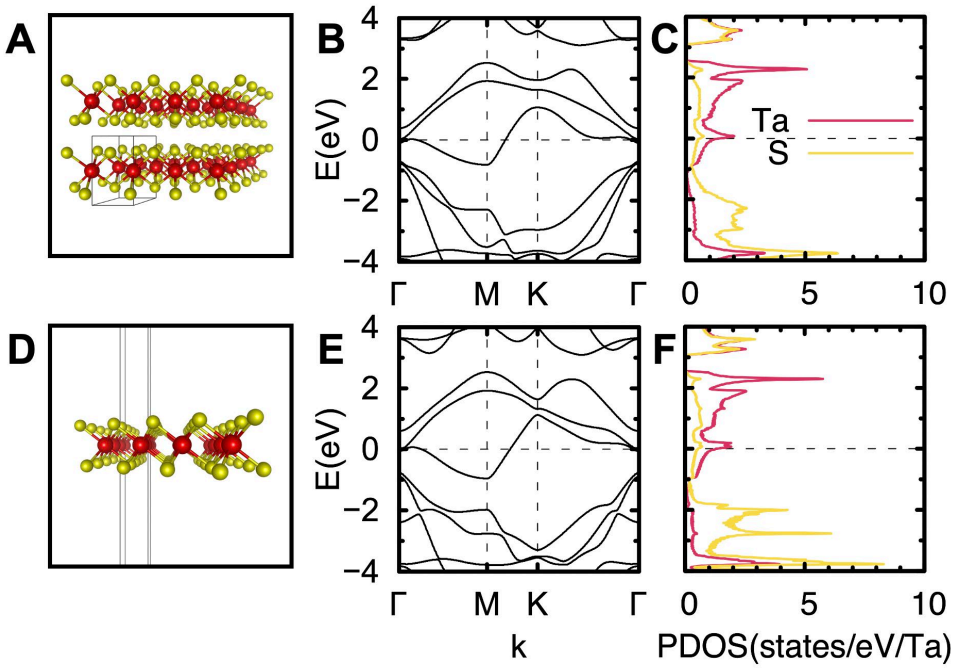

Figure 12.7 Atomic and electronic structures of the TaS_2 bulk and monolayer (ML). The atomic and electronic structures of (A-C) 2H-bulk, and (D-F) 1H-ML are shown. In the 1st column, the atomic structures obtained from density functional theory (DFT) calculations are shown where Ta and S atoms are represented by red and yellow spheres, respectively, and the unit-cell is represented by black frames. In the 2nd column, the electronic band structures are shown where the Fermi energy is set to zero. In the 3rd column, the projected density of states (PDOS) is shown, where the density of states projected to Ta and S atoms are represented by red and yellow lines, respectively. Data collected in collaboration with Dr. Sehoon Oh.

12.7.3 Building atomic models of narrow TaS_2 nanoribbons

With an understanding of the atomic and electronic structure of the bulk and ML TaS_2 material, we can then investigate the atomic and electronic structure of NRs with various widths. A CDW type of distortion is investigated because of the propensity for TaS_2 systems to undergo several distortions related to a CDW transition, and these structural distortions are very periodic in nature.[241,246] Because of their periodic nature, we explored the distortions possible from a CDW system as the possible cause of a periodic superstructure arising at the 1-D limit. Therefore, one of the first structural distortions we consider in the NR, without any vacancies or defects, is possible CDW distortions. In some of the lower T_C CDW transitions, the charge density modulation is commensurate with the underlying atomic structure, which could have interesting implications at an ultra-confined 1-D limit in the instance of a nanoribbon, as previous work on bulk vs. 2-D monolayers of TMD has shown modulation of the CDW transition temperatures and periodicity of distortion.[109] It is also worth emphasizing the calculated size of the partial gaps due to CDW-type distortions is ~0.1 eV, implying that the CDW distortions would persist at room temperature.

First, we start with the NRs without structural defects (i.e. no vacancies, substitutions, or adatoms) to see what type of distortions in a 1-D system could present themselves from CDW transitions. We construct candidate structures with various periodicity for considering possible

CDW type distortions. The atomic positions of all the constructed structures are relaxed by minimizing the total energy. The obtained atomic and electronic structures of a NR (W = 2.99 nm) are shown in **Figures 12.8a-c**. Because of the metallicity and 1D nature, CDW-type distortions and corresponding partial gap openings are found in all structures of varying widths. **Figure 12.8a** incorporates the CDW distortions, but the amplitude of the distortions is too small to be readily apparent, and furthermore, the CDW distortions are not commensurate with the experimentally observed zig-zag pattern. While the CDW does incorporate some structural distortions, they are not of significant magnitude, and would consequently not be measurable in the current experimental setup. Therefore, we exclude the possibility that the zig-zag superstructure originates from CDW-type distortions without structural defects.

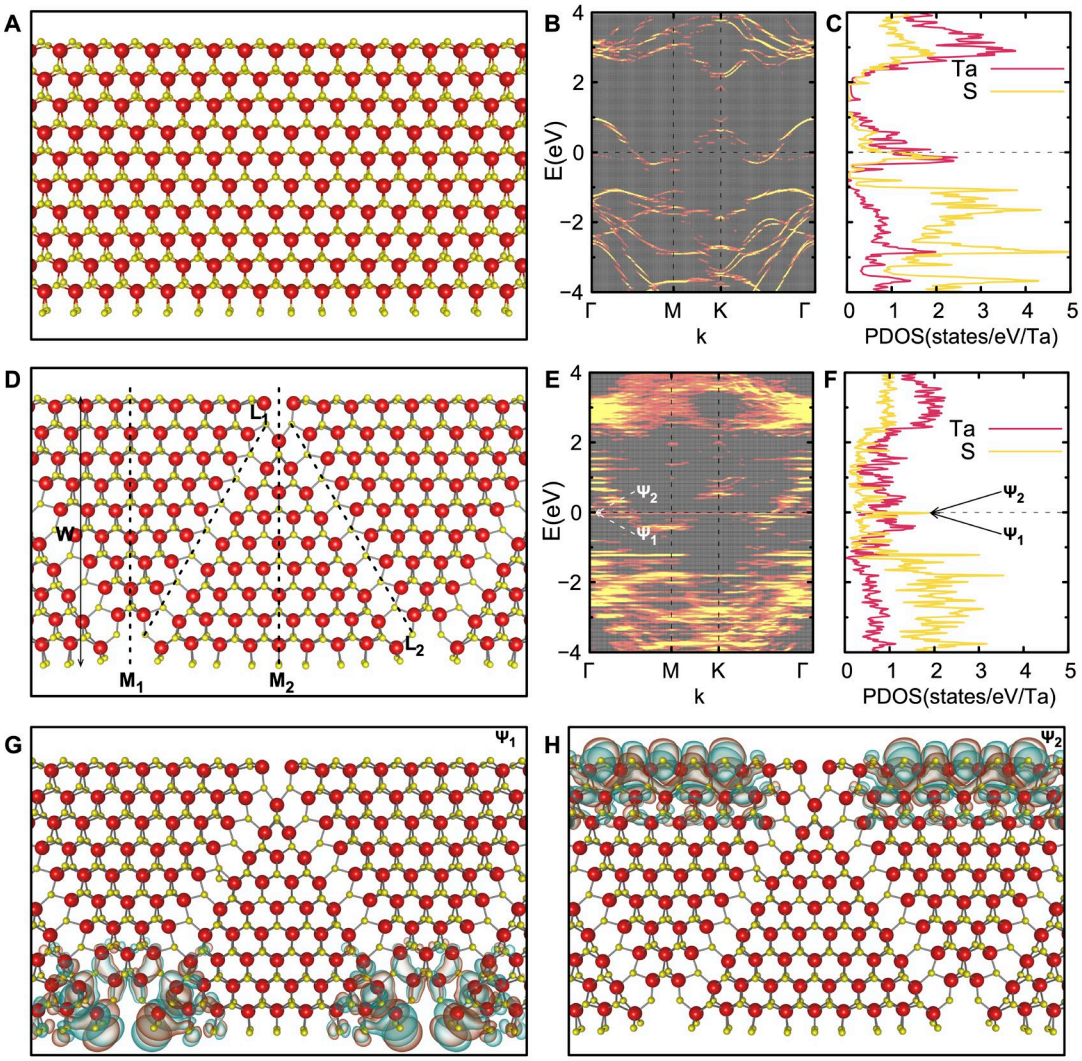

Figure 12.8 Atomic and electronic structure of TaS_2 NRs without and with defect line arrays. (a-c) The atomic and electronic structures of the 2H-NR of W=2.99 nm without the zigzag defect are shown. The structure does have CDW distortions, but the distortion amplitude is too small to be seen by eye in (a). (a) shows the atomic structure in planar view, (b) the electronic band structure, and (c) the PDOS of the NR. (d-h) The atomic and electronic structures of 2H-NR of W=3.08 nm with zigzag defect array are shown. (d) The atomic structure of the NR is shown in the planar view, where the zigzag boundaries of S vacancies are represented by black dashed lines denoted as L1 and L2, and the mirror planes are represented by vertical black dashed lines denoted as M1 and M2. (e) The electronic band structure and (f) the PDOS of the NR. The localized edge states are marked by arrows and denoted as ψ1 and ψ2. (g-h) The real-space wavefunctions of the localized edges states ψ1 and ψ2. The isosurfaces for the positive and negative values of the real-space wavefunctions are shaded in cyan and orange, respectively. In the atomic structures, Ta and S atoms are represented by red and yellow spheres, respectively. The bands in (b) and (e) are unfolded with respect to the unit-cell of the primitive 2H-ML. The density of states projected to Ta and S atoms are represented by red and yellow lines, respectively. The Fermi energy is set to zero. Data collected in collaboration with Dr. Sehoon Oh and Dr. Mehmet Dogan.

12.7.4 Elucidating the emergence of the zig-zag boundary defects

Because the zig-zag periodic superstructure cannot be explained by any type of CDW transition, we must explore other types of defect structures that could explain these arrays observed. We therefore construct and optimize numerous new candidate structures of the NRs with various types of structural defects for the zig-zag boundaries. The atomic positions of all the constructed candidate structures are relaxed again by minimizing the total energy. Among the various candidate structures, we find a defect structure of NRs with various widths that is energetically favored compared to other candidate structures and matches well with the experimental STEM data. After careful analysis of the energetics of all the obtained structures, which is described below, and comparison with the STEM data, we conclude that the zigzag boundaries are linearly-formed S vacancies in the NRs.

As described above, **Figure 12.5** shows the obtained atomic structures of a 2H-TaS_2 NR with a width (W) =3.34 nm, the experimental STEM data, and the STEM simulation using the structures obtained by DFT for comparison, which agree well with each other. **Figures 12.8D-H** show the atomic and electronic structures of a NR with the zigzag defect array (W = 3.08 nm) in vacuum. In **Figure 12.8d**, the atomic structure is presented with the zigzag defect array denoted by L1 and L2, and the mirror planes denoted by M1 and M2. **Figures 12.8E-F** show the band structure unfolded with respect to the unit-cell of the primitive 2H-ML and the projected density of states (PDOS), respectively. A partial gap opening around the K-point is observed as shown in **Figure 12.8e** and there are two flat bands near the Fermi energy, EF, (0.020 eV and 0.007 eV below EF), denoted as $\psi 1$ and $\psi 2$, respectively, in **Figures 12.8E-F**. The real-space wave function of the flat bands reveals that they are localized edge states as shown in **Figures 12.8g-h**. The state $\psi 1$ is localized at the lower edge and has odd parity with respect to the mirror symmetries M1 and M2, while $\psi 2$ is at the upper edge and has even parity with respect to the mirror symmetries as shown in **Figures 12.8G-H**. A similar analysis is also performed on pristine and defective NRs of width 3.29 nm, the results of which are shown in **Figure 12.9**.

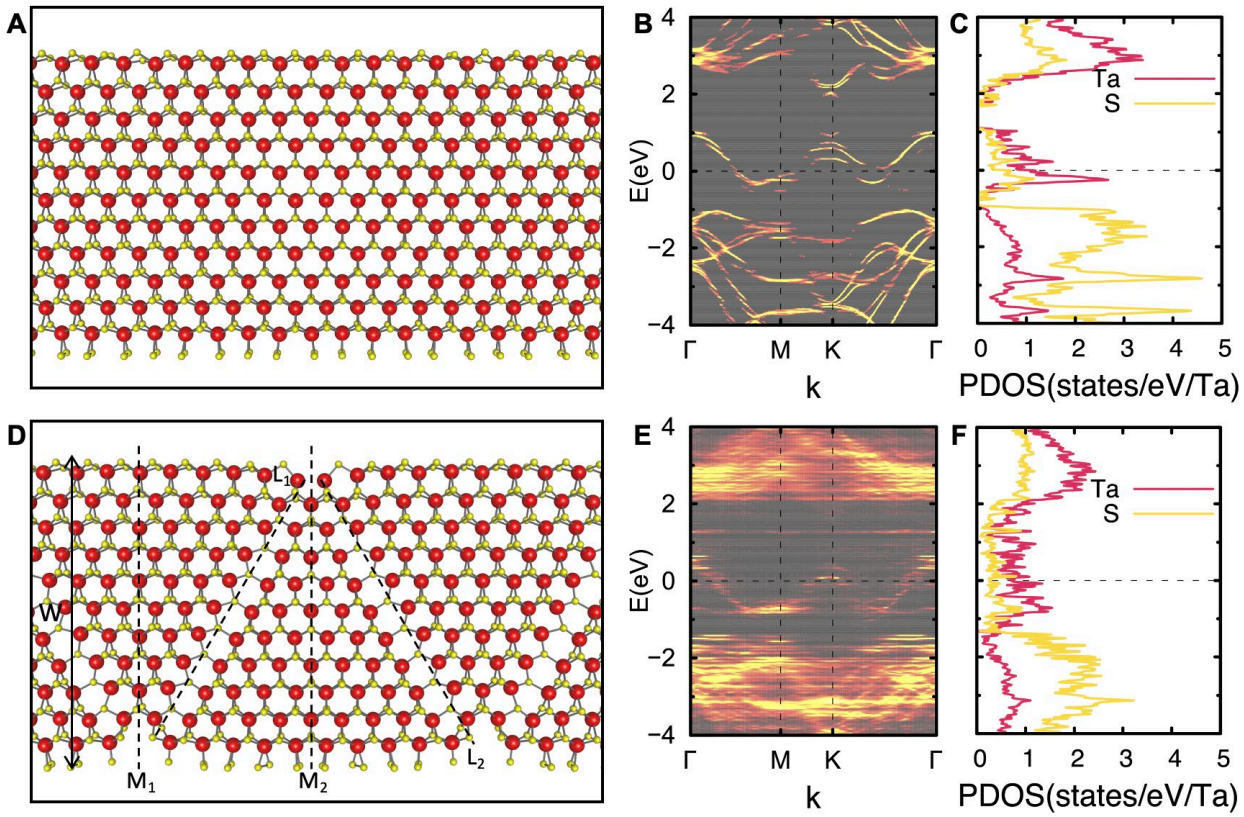

Figure 12.9 Atomic and electronic structure of TaS_2 NRs without and with defect arrays. (A-C) The atomic and electronic structures of the 1H-NR of W=3.29 nm without the zigzag defect are shown. (A) The atomic structure in planar view, (B) the electronic band structure and (C) the PDOS of the NR are shown. (D-H) The atomic and electronic structures of 1H-NR of W=3.34 nm with zigzag defect array are shown. (D) The atomic structure of the NR is shown in the planar view, where the zigzag boundaries of S vacancies are represented by the dashed lines denoted as L1 and L2, and the mirror planes are represented by vertical dashed lines denoted as M1 and M2. (E) The electronic band structure and (F) the PDOS of the NR are shown. In the atomic structures, Ta and S atoms are represented by red and yellow spheres, respectively. The bands in (B) and (E) are unfolded with respect to the unit-cell of the primitive 1H-ML. The density of states projected to Ta and S atoms are represented by red and yellow lines, respectively. The Fermi energy is set to zero. Data collected in collaboration with Dr. Sehoon Oh and Dr. Mehmet Dogan.

12.8 Examining the stability of the ultra-narrow TMD nanoribbons

To analyze the stability of the NRs with various numbers of atoms in the unit-cell, we calculate the Gibbs free energy of formation, δG, of the obtained structures, which is defined as

$$\delta G = ENR + nTa\mu Ta + nS\mu S \qquad \textbf{(Eq. 12.1)}$$

where ENR is the total energy per atom of the NR, nTa and nS are the mole fractions of Ta and S atoms, respectively, and μTa and μS are the chemical potentials of Ta and S, respectively. We choose μTa and μS as the binding energies per atom of the α-Ta bulk and crown-shaped S_8 molecule, respectively. We find an interesting tendency that the structures with more S vacancies

become more stable. For a quantitative analysis, we measure the ratio R of the number of Ta atoms to that of S atoms, which is defined as

$$R = nS / nTa \qquad \textbf{(Eq. 12.2)}$$

The NRs without structural defects have R_{NR} = 2.14~2.20, which is greater than that of bulk TaS_2 (R_{bulk} = 2.0), because the NR edges are S-terminated, and the confined nature of the NR increases the ratio of edge to basal plane. The presence of S vacancies reduces R, and the stable calculated structures agreeing well with the experimental data have R = 2.00~2.01, as shown in **Table 12.1**. We note that other kinds of defect ordering, such as Ta adatoms, can also reduce R and thereby enhance structural stability. We speculate that stabilization of the structure afforded by driving R → 2 is the main driving force of the formation of the zigzag defects with S vacancies.

Table 12.1 Structural and energetic properties of TaS_2 NRs. The structure phase, boundary shape, type of defects, symmetry, and the width, W, of two TaS_2 NRs obtained with DFT calculations. The number of Ta (S) atoms in the unit cell, NTa (NS), and the ratio of NTa to NS atoms, R. The Gibbs free energy of formation, δG, is defined as ENR + nTaμTa + nSμS, where ENR is the total energy per atom of the NR, nTa and nS are the mole fractions of Ta and S atoms, respectively, and μTa and μS are the binding energies per atom of the α-Ta bulk and crown-shaped S_8 molecule, respectively. Data collected in collaboration with Dr. Sehoon Oh and Dr. Mehmet Dogan.

	NR-1	NR-2
Phase	2H	2H
Boundary shape	Zigzag	Zigzag
Defects	S vacancies	S vacancies
Symmetry	Mirror	Mirror
W (nm)	3.08	3.34
NTa	99	120
NS	198	240
R	2.00	2.00
δG (eV)	-0.573	-0.633

12.8.1 Determining effects of confinement on TMD nanoribbons

As with any confined species, the effects of the encapsulating environment must be considered for any other strong interactions that could play a role in stabilizing the internal structure. To investigate the effects of encapsulation of the TaS_2 NR inside the CNTs, separately relaxed atomic positions of TaS_2-NRs isolated in vacuum and empty CNTs are used. Further relaxations are not performed. We then calculate the charge transfers between NRs and CNTs. The calculated charge transfer (q) from CNTs to 1H-TaS_2 NRs is 0.0192 e/Ta atom, where e is the electron charge. Note that q is much smaller than those for the transition metal

tricalcogenides such as $NbSe_3$, $HfTe_3$, and Hf_2Te_9 molecular chain.[144,163,208] This small transfer of charge would result in a very small change in the E_F for the electronic structure. The charge transfer is significantly smaller than other encapsulated systems, and those systems are well-understood to not interact strongly with the CNT. We conclude the CNT in this study merely provide physical boundary conditions for the material growth and no additional stabilization effects.

As additional points of interest, we finally study the magnetic and topological properties of these NR, as extreme quantum confinement can induce changes in the magnetic or topological characteristics of the confined material.[208,239] We perform fully magnetic calculations with spin–orbit interaction. We start with various magnetic moments in the self-consistent calculation but find no significant magnetic moment in any of the converged calculation results. After carefully checking the magnetic moments, we perform self-consistent calculations again assuming the time-reversal symmetry. No significant magnetic moment is found in all the fully magnetic calculations with spin–orbit interaction. However, the presence of the time-reversal symmetry and mirror symmetry in 2H- phase indicates the potential for interesting topological properties in these NRs. A combination of mirror and time-reversal symmetry in 1H-TaS_2 NRs results in quantized Zak phases of the bands.[198] For a TaS_2-NR with a finite total gap, which is not the case in this study but might be the case with smaller width, the topological invariance of the NR can be tuned by controlling the charge state using doping or gating as reported in recent studies.[194,208]

12.9 Conclusion

In summary, we have demonstrated a method that enables the synthesis of ultra-narrow TMD NRs via a simple and broadly deployable gas phase process, using MWCNTs to template their growth. Our method results in 2H-TaS_2 NRs with widths below 3 nm, and lengths greater than 100 nm, while reaching the ML limit. Further, the nanoconfined growth of the NRs results in the stabilization and formation of ordered arrays of linear defects in the TaS_2 lattice. DFT calculations reveal the characteristics of the defect arrays with spatial symmetries and electronic structures with localized edge and boundary states. The reported nanotube templated growth represents a versatile platform for the synthesis of ultra-narrow TMD NRs and the exploration of the materials under constraint in multiple dimensions.

Chapter 13: Exploring $ZrSe_2$ and $HfTe_2$ nanoribbons – Expanding the Study of Transition Metal Dichalcogenide Nanoribbons beyond the Sulfides

Special thank you to Derek Popple for his leadership on this project.

Keywords: Semiconductor, Semimetal, Transition Metal Dichalcogenides, Carbon Nanotubes, Electron Microscopy, Nanoribbons, Zirconium Diselenide, Hafnium Ditelluride, Encapsulation

Chapters 8, 10, 11, and 12 have shown first-hand how the continued exploration of other material systems at the 1-D chain and nanoribbon limit continues to provide exciting and unexpected results. Part of the excitement stems from the flexibility of our synthetic and characterization techniques to related members of the transition metal dichalcogenide (TMD) and trichalcogenide (TMT) family with few alterations required. In **Chapter 12**, we discussed in detail how the encapsulation method of transition metal chalcogenides could be expanded beyond the TMT family and now include quasi-1-D nanoribbons of TMD. While TaS_2 has shown surprising results as a quantized nanoribbon, from clean, atomically defined edges to defect-array superstructures, it is important that we establish the efficacy of our encapsulation technique to other related TMD structures, especially beyond the disulfides, which we explore here.

13.1 Motivation behind increasing the study of nanoribbons

While the effects of quantum confinement are well-understood for isolated monolayers of the 2D materials, there is still much work to be done on exploring the tunability of atomically thin 2D material properties through increased quantum confinement. Reducing one of the lateral dimensions of a 2D material leads to a quasi-one-dimensional (1D) morphology known as a nanoribbon (NR). NR can have unrestricted lengths but are confined in their width, on the scale of nanometers, leading to an atomically thin material with a high aspect ratio. Current work on organic and inorganic NR has shown that confining materials to a quasi-1D form is an effective technique for modulation of the material's atomic and electronic structure, providing a synthetic handle for tuning electronic properties such as the bandgap.[239,249–252]

13.1.1 Difficulties in expanding synthesis of nanoribbons to other material families

However, there are large disparities in the research completed on graphene-based NR and inorganic NR, largely in part to the very different synthetic protocols needed to obtain each type. There are two main routes of synthesizing NR, each with their own benefits and deficits. Top-down fabrication techniques via electron beam lithography or ion milling are more transferrable to a variety of materials, as they are not so dependent on the chemical species present, allowing for a larger library of unique NR with a variety of properties to be created. However, these top-down techniques can be difficult to scale for large production of NR and are limited by the resolution of the lithographic technique, sometimes resulting in rough edges and unintended defects within the material at a detriment to any intended material performance.[233,253,254] Bottom-up fabrication of NR from molecular precursors has been successful for graphene NR, showcasing a variety of structural motifs and associated properties.[195,226,249,250] Unfortunately, the techniques and chemistries developed for graphene NR cannot be easily applied to inorganic

systems, such as the TMDs, thus new synthetic routes will need to be developed to create a library of TMD NR.

In **Chapter 12**, we discussed how ultra-confinement of a TMD material down to the sub-5nm limit could induce drastic alterations to the atomic structure of the native TMD material, resulting in interesting defect states and localized edge states.[252] These periodic defect states and localized edge states are very exciting because we show similar behavior and control of that behavior on the atomic scale, similar to graphene NR, which are built from bottom-up.[195,226,227] This bottom-up technique employed is the encapsulation of the TMD inside the hollow cavity of a carbon nanotube (CNT), which has proven effective in creating atomically defined species.[144,163,255,256] In this scheme, the width of the TMD NR is controlled by the diameter of the CNT and any emergent atomic distortions are protected and stabilized.

Filling of nanotubes with species has been demonstrated for TMD before, specifically MoS_2 and WS_2. However these methods utilized liquid-filling techniques which are not readily applicable to many other members of the TMD family, and generally only applies to the sulfides, leaving many other TMD inaccessible.[224,239] Even in our previous work, we demonstrated the filling of another disulfide TMD, TaS_2.[252] While the encapsulation of TaS_2 NR via vapor-phase material growth is a much needed development and utilization of the encapsulation technique, we need to explore the accessibility and transferability of our encapsulation technique to the diselenide and ditelluride TMD NR family. To demonstrate the efficacy and broad applicability of our technique to grow TMD NR, we look towards two new material systems, $ZrSe_2$ and $HfTe_2$. These two TMD are excellent complementary systems to study how encapsulating TMD NR could affect different structure types and associated properties.

13.2 Exploring $ZrSe_2$ and $HfTe_2$

13.2.1 Fundamentals of $ZrSe_2$

The first material, $ZrSe_2$, presents an interesting target to pursue in NR form. $ZrSe_2$ is a semiconducting member of the TMD family, with a bulk band gap of ~1.0 eV, and prefers the 1-T phase.[257,258] However, there is some experimental evidence suggesting the monolayer limit of $ZrSe_2$ induces a small increase in the bandgap, up to ~1.2 eV.[257] However, this very mild increase in bandgap seems to be within experimental error of the measurements and calculations performed, so the tunability of $ZrSe_2$ bandgap through layer number is still up for debate. Fortunately, layer number is not the only parameter than can be manipulated in the layered TMD, as we have shown in **Chapter 12**. Theoretical predictions have already been made for $ZrSe_2$ NR, which indicate that the band gap is highly dependent on the width of the NR, but relatively independent of the layer number.[259] These characteristics provide the advantage of being able to tune the material's bandgap by controlling the NR width without having to isolate a single monolayer.

Figure 13.1 shows an atomic model of a 1-T monolayer $ZrSe_2$ NR. According to the density functional theory (DFT) calculations performed by Li *et al*., there is a critical width of NR that must be achieved to see dramatic change in the electronic structure.[259] It is important to note that the DFT calculations performed are inherently inaccurate for the absolute value of the band gap, however the overall trend still holds true. This was made apparent in another study on $HfSe_2$ (semiconductor TMD), where the experimentally measured bandgap is known to be ~1.1 eV, however DFT calculations predicted a gap of 0.5 eV.[260] The study on $ZrSe_2$ NR found that

the bandgap of the NR was inversely proportional to the NR width, with the bandgap of the NR diverging from the bandgap of the monolayer once the ribbon width is reduced to less than 6 nm (N = 16). A key takeaway from this work is that the realized NR must have widths smaller than 6 nm to access the regime of controllable bandgaps.

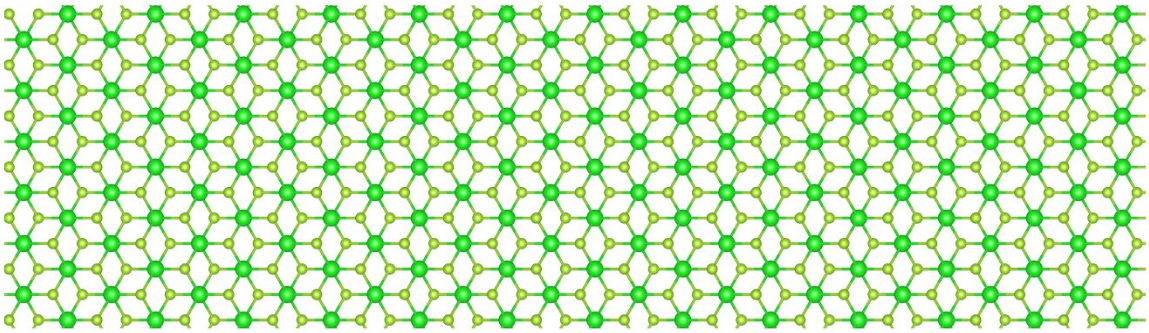

Figure 13.1 Atomic model of a 1-T monolayer $ZrSe_2$ nanoribbon. Zirconium and selenium atoms are represented by the green and yellow spheres, respectively.

13.2.2 Fundamentals of $HfTe_2$

The second material, $HfTe_2$, is an interesting member of the TMD family due to its different stable phases. In the 2-H phase, $HfTe_2$ is a semiconductor with a bulk band gap of ~1.55 eV, but in the 1-T phase is a semimetal member of the TMD family.[118,261] Typically, these two different phases are stabilized by the reaction of the temperature, and has little to do with the dimensionality of the synthesized crystal.[118] There is significant interest in targeting specific phases of $HfTe_2$ in order to control the electronic structure of the material and study charge density wave transitions, superconductivity, and band structure tuning via dimensionality constraints.[182,262] Molecular beam epitaxy has proven to be the most effective method in gaining control over the phase and dimensions of $HfTe_2$, however the true monolayer limit has yet to be realized in any of the phases.[118] Encapsulation of the $HfTe_2$ material would shed light on both the nature of the monolayer limit of $HfTe_2$, i.e. what phase is preferred as a monolayer, as well as provide additional insight into the quantum confinement of $HfTe_2$ on the nanometer scale and what impact could be had on the overall electronic structure.

One of the more effective studies that has been performed on $HfTe_2$ layers observes drastic changes in the electronic structure of bulk $HfTe_2$ due to alkali metal intercalation.[182] The doping of alkali metals is an effective route to separate the layers of the 2-D material, while adding additional charge to the system. **Figure 13.2** shows an atomic model of a monolayer of 2-H phase $HfTe_2$. Previous work reported by Nakata *et al*. highlights experimental work studying layers of $HfTe_2$, where the bands become more quantized at lower layer numbers.[182] An important distinction to make with the quantization of the bands is the noticeable difference in binding energy from bulk to bilayer and monolayer, of almost 1 eV in difference. The valence bands crossing the fermi energy, leading to the semimetal nature of $HfTe_2$, appear to be the most drastically affected by the layer numbers, indicating the monolayer limit of $HfTe_2$ could potentially lead to a drastic shift of metallicity.[182]

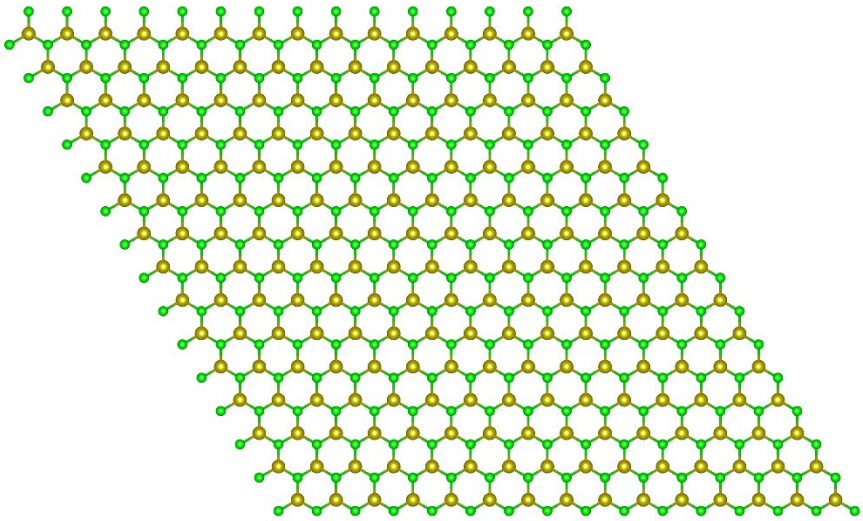

Figure 13.2 Atomic model of a 2-H $HfTe_2$ monolayer. Hafnium and tellurium atoms are represented by the gold and green spheres, respectively.

13.3 Synthesis method of $ZrSe_2$@CNT and $HfTe_2$@CNT

Synthesis of $ZrSe_2$@CNT: Carbon nanotubes (CheapTubes) were opened with thermal oxidation by heating in air at 510 °C for 15 minutes. The walls of a quartz ampoule were coated with approximately ~10 mg of opened CNT, then loaded with elemental zirconium, selenium, and 1 mg of iodine per volume (mL) of ampoule. Ampoules were loaded with reagents inside a glovebox then removed and sealed under vacuum ($<10^{-5}$ torr). Once sealed, the ampoule was placed in a tube furnace and heated at static heating of 575°C for 3 days followed by natural cooling back to room temperature. Synthesis of the samples was carried out by Derek Popple, Tony Vo Hoang, and Oh Byung Kwon.

Synthesis of $HfTe_2$@CNT: Carbon nanotubes (CheapTubes) were opened with thermal oxidation by heating in air at 510 °C for 15 minutes. The walls of a quartz ampoule were coated with approximately ~10 mg of opened CNT, then loaded with elemental hafnium, selenium, and 1 mg of iodine per volume (mL) of ampoule. Ampoules were loaded with reagents inside a glovebox then removed and sealed under vacuum ($<10^{-5}$ torr). Once sealed, the ampoule was placed in a tube furnace and heated at static heating of 900°C for 3 days followed by natural cooling back to room temperature. Synthesis of the samples was carried out by Derek Popple and myself.

13.4 Electron microscopy details

The filled CNTs were dispersed in 10-20 mL of isopropyl alcohol by bath sonication for 30-45 minutes at high power. After sonication, the solution turned into a dark gray or black color indicating a high concentration of suspended CNT. Several drops of the suspension were transferred to a copper TEM grid with a lacey carbon support (Ted Pella) and dried overnight before imaging. Derek Popple led initial characterization *via* transmission electron microscopy (TEM), performed on a JEOL-2010 electron microscope operated at an accelerating voltage of 80 kV in order to confirm filling of the nanotubes. For high resolution imaging, high angle annular dark field scanning transmission electron microscopy (HAADF-STEM) was performed

on the TEAM 0.5 microscopy at the National Center for Electron Microscopy (NCEM) at an accelerating voltage of 80 kV. Dr. Amin Azizi performed elemental mapping *via* energy dispersive X-ray spectroscopy (EDX) at Penn State using an aberration-corrected FEI Titan3 (60-300) operated at 80 kV with a 115 mm camera length and a SuperX EDX detector. EDS mapping was done in STEM mode with a beam current of 0.14 nA and an acquisition time of 5 minutes.

13.5 Characterizing the filling of $ZrSe_2$ nanoribbons

13.5.1 Overview of the $ZrSe_2$ nanoribbons

Figure 13.3 shows transmission electron microscopy (TEM) images highlighting the $ZrSe_2$ NR encapsulated within CNT. In the micrographs, the parallel lines arise from the walls of the multiwalled nanotubes used in the synthesis, while the darker region in the center of the tubes is the inorganic lattice corresponding to the $ZrSe_2$ NR. As shown in **Figure 13.3**, the synthesized NR had widths as low as 3.8 nm and could attain lengths of greater than 100 nm. The NR grow to fill the entire inner cavity of the CNT, indicating that NR widths are entirely dependent on the inner diameter of the CNT used. While the basal plane of the NR was most easily located and imaged, occasionally the edges of the NR were oriented parallel to the electron beam. In **Figure 13.3d**, a region of polycrystalline filling is observed, showing both the basal plane and edges of the NR. Imaging of edges gives an indication of the number of layers present in these samples.

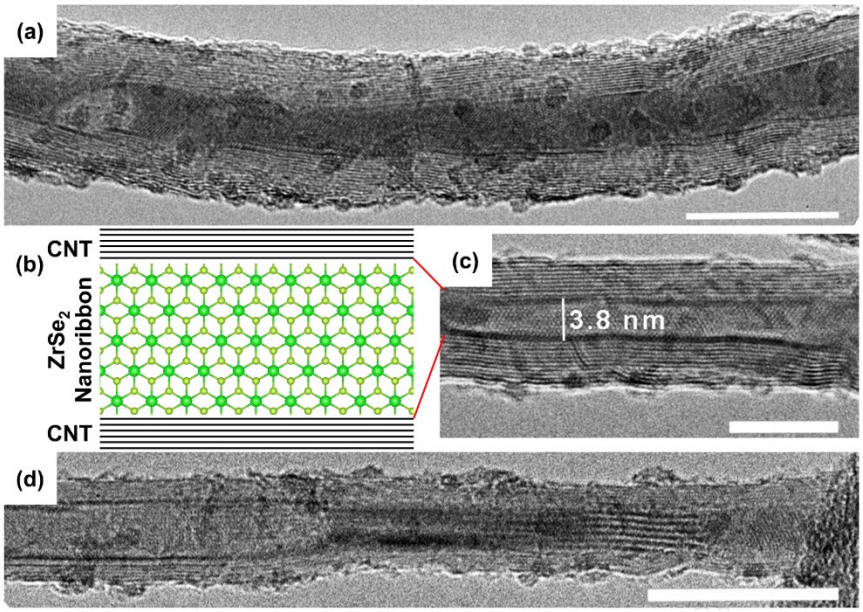

Figure 13.3 TEM of $ZrSe_2$@CNT. (a) Low magnification TEM image of a filled multiwall nanotube. (b) Schematic of a $ZrSe_2$ (1-T phase) nanoribbon encapsulated inside of a MWCNT. Zr and Se atoms are represented by bright green and yellow green atoms, respectively, with the black lines indicating the walls of the CNT. (c) TEM image of smallest nanoribbon observed. (d) TEM image of polycrystalline region of nanotube showing both basal plane and edges of nanoribbons. Scalebar measures (a and d) 20 nm and (c) 10 nm. Data collected in collaboration with Derek Popple.

13.5.2 Studying the atomic structure of encapsulated $ZrSe_2$ nanoribbons

Once the dimensions of the NR were characterized, the sample was imaged via HAADF-STEM to gain greater insight into the atomic structure of the NR. Due to the greater resolution of the aberration-corrected microscope and the increased Z contrast characteristic to HAADF-STEM, the atomic structure of the NR is more easily visualized compared to the nanotube. **Figure 13.4** shows a couple STEM images of the NR, along with a bandpass-filtered micrograph and Fast Fourier Transform (FFT) of one of the ribbons. **Figure 13.4b** shows a bandpass-filtered micrograph of **Figure 13.4a**, where the NR basal plane clearly shows the hexagonal structure of $ZrSe_2$. A portion of this NR is likely monolayer due to the clarity of the atomic lattice, although this is difficult to say conclusively in current experiments.

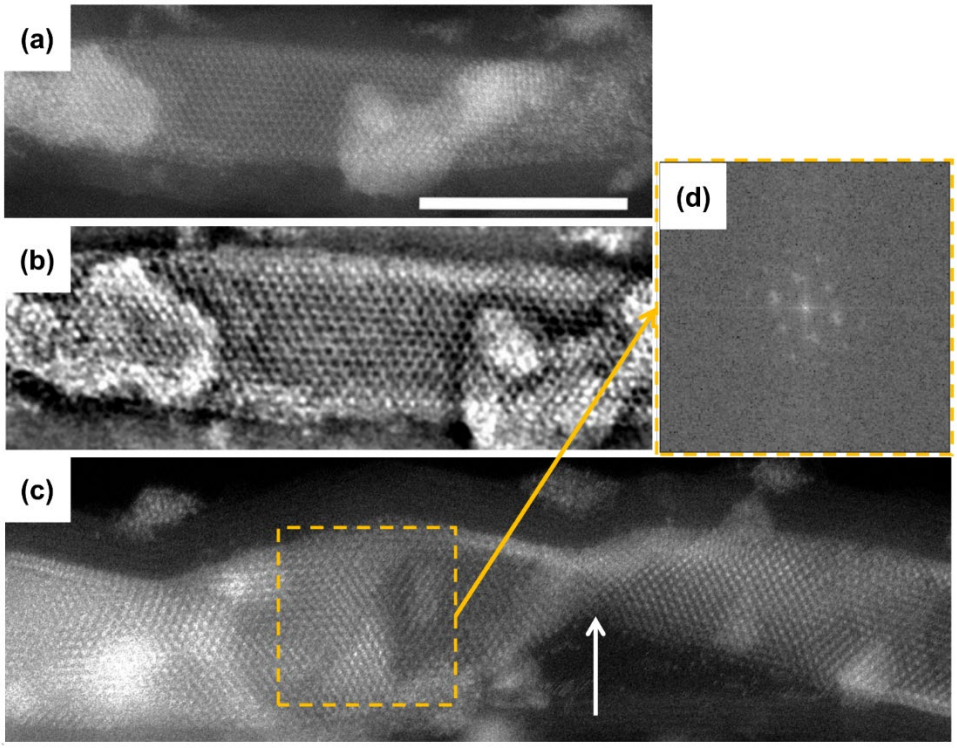

Figure 13.4 Basal plane structure of $ZrSe_2$ nanoribbons@CNT. (a) STEM image of $ZrSe_2$ nanoribbon. (b) Bandpass-filtered STEM image of (a), showcasing the hexagonal lattice of the $ZrSe_2$@CNT basal plane. (c) Twisted nanoribbon, with full rotation marked by the white arrow. (d) FFT of region encompassed by dashed box, with 6-fold symmetry present. Scale bar measures 10 nm.

In **Figures 13.4a** and **13.4c**, an increase in intensity near the edges of the ribbon can be seen, likely caused by the NR curling upward or downward due to the confinement imposed by the nanotube. Curling up or down leads to more atoms along the path of the electron beam, making the sample appear thicker in that region. This compression effect, as well as gradual twisting of the NR, could be employed for strain engineering to further modulate the bandgap of NR TMD materials.[117,167] **Figure 13.4c** highlights the most dramatic curling of NR observed to-date, where the white arrow denotes a complete 180° rotation of the NR around its lateral axis.

Figure 13.4d is an FFT of the NR, where 6-fold symmetry is readily observed in the highest intensity spots of the FFT, which is expected for the family of TMD materials.

As a result of the curling of the edges of the NR, it is difficult to conclusively determine whether the NR are terminated by zigzag or armchair edges. However, by examining the hexagonal pattern of the basal plane in **Figure 13.4b** it is evident that the hexagons with shared edges run parallel, rather than perpendicular, to the nanotube. This observation suggests that the NR are terminated by zigzag edges, although it is not known whether the edges are passivated. This hypothesis also agrees with computational results from Li *et al.* which showed the zigzag terminated NR are more stable than the armchair-terminated NR based on the cohesive energy.[259]

In addition to observing the internal structure of the encapsulated NR, we also need to confirm elemental composition of the NR. **Figure 13.5** shows energy dispersive spectroscopy (EDS) of the $ZrSe_2$ NR. Peaks for Zr and Se are readily observed, alongside trace iodine peaks (the chemical transport agent), likely an external contaminant that has been deposited on the outside of the CNT. Additional elemental analysis will be required to prove stoichiometry, however the encapsulated species thus far have proven to produce too little signal for quantitative analysis, so other means of confirmation are needed, such as structural confirmation from STEM, as discussed below.

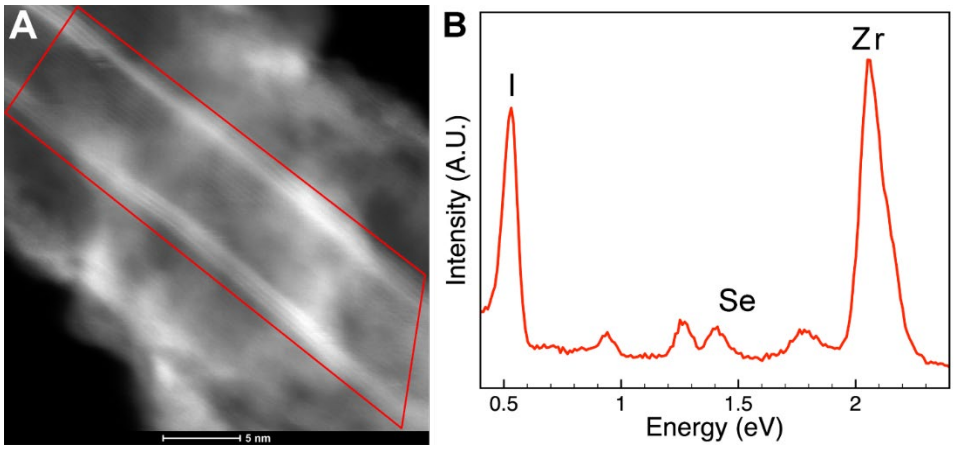

Figure 13.5 EDS spectrum of $ZrSe_2$ nanoribbons. (a) HAADF-STEM image of $ZrSe_2$ nanoribbon in multiwall carbon nanotube with area used for EDS quantification outlined in red. (b) EDS spectrum with peaks labeled. Data collected in collaboration with Dr. Amin Azizi.

13.6 Determining the phase of the $ZrSe_2$ nanoribbons

One of the questions remaining for the $ZrSe_2$ NR is a matter of which phase the layered material prefers when encapsulated. As shown in the TaS_2 NR, defect states and periodic superstructures can be stabilized when confined to the nanometer scale, so it is perfectly reasonable to question which phase, 2-H or 1-T, the TMD would prefer when encapsulated. **Figure 13.6** shows the two phases that are commonly observed in TMD, both in plan-view and edge view. As discussed previously, $ZrSe_2$ in bulk prefers the 1-T phase, highlighted in **Figure 13.6b** and **13.6d**. However, other closely related TMD, such as TaS_2, prefer the 2-H phase, shown in **Figure 13.6a** and **13.6c**. The edge structure of each of these phases is shown as well, which will be analyzed in more detail alongside STEM images in later sections. In comparing the basal planes of **Figure 13.6** to the STEM imaging in **Figure 13.4**, specifically **Figure 13.4b**, there appears to be good match between the 2-H phase and the experimental images, with a nice

hexagonal lattice clearly visible. However, more structural analysis needs to be done, alongside more sample preparation, to determine what the true phase of the material is. There could also be multiple phases present if the energetics between the two systems are not significantly large.

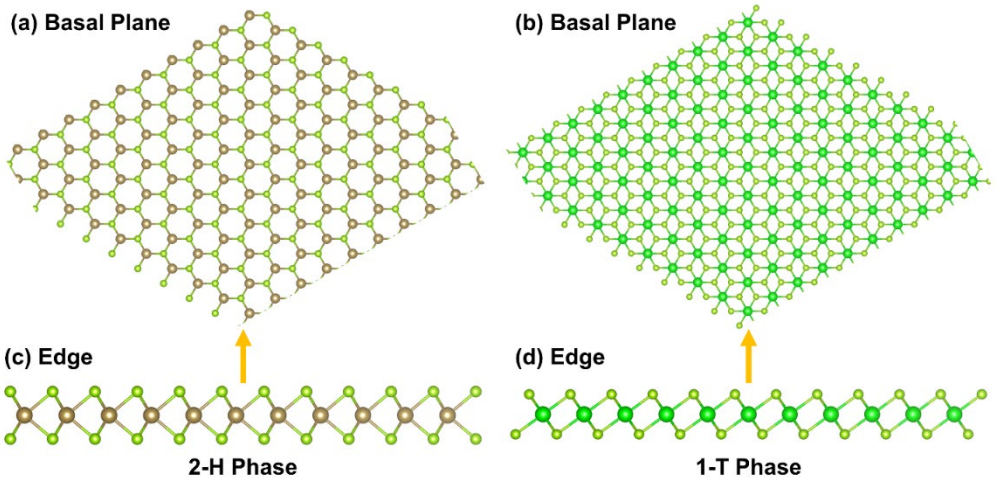

Figure 13.6 Two different phases observed in transition metal dichalcogenides. (a) Basal plane and (c) edge view of 2-H phase TaS_2, where a hexagonal lattice is readily apparent. Tantalum and sulfur atoms are represented by the gold and yellow spheres, respectively. (b) Basal plane and (d) edge view of 1-T phase $ZrSe_2$, where the transition metal atoms (bright green) form a nice 6-pointed star pattern. Zirconium and selenium atoms are represented by the green and yellow spheres, respectively.

In addition to the basal plane of the NR, we also observe many instances of the NR edge-on. **Figure 13.3d** shows one of the first observed instances of this edge-on view for the $ZrSe_2$ NR. As observed in **Figure 13.3d** and other images as well, some of NR appear to fold in on themselves, similar to a piece of paper being folded in half, where the edges of the NR become visible. **Figure 13.7** shows NR where the edges are more clearly visible with higher atomic resolution than **Figure 13.3d**. **Figure 13.7a** showcases another example of the folding phenomena, where the significant increase in contrast manifests from the increased sample thickness of viewing the NR along the edge of the plane. **Figure 13.7c** shows a schematic of these layers inside of a CNT. In **Figure 13.7b**, the edges of the NR are clearly resolved, allowing the determination that this NR is four layers thick based on the four sets of chalcogen sublattices present. Each set of sublattices have a separation of 0.6 nm, corresponding to the vdW spacing between TMD layers.

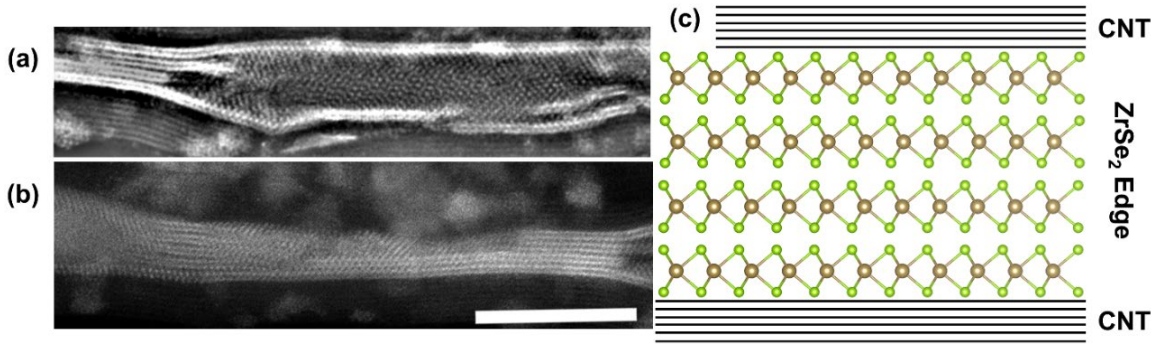

Figure 13.7 Edge structure of $ZrSe_2$ nanoribbons@CNT. (a) Bandpass-filtered STEM image of a folding $ZrSe_2$ nanoribbon. (b) STEM image of multiple layers of $ZrSe_2$ on edge, where total layer number appears to be 4 and 5. (c) Schematic of the CNT encapsulating several layers of $ZrSe_2$ and accommodating the vdW gap between layers. Zr and Se atoms are represented by gold and yellow green atoms, respectively, with the black lines indicating the walls of the CNT. Scale bar measures 10 nm.

13.6.1 Studying the edge structure of $ZrSe_2$ nanoribbons

The edges of the $ZrSe_2$ sheets could provide additional information into the phase of the material. As shown in **Figure 13.6**, the edge structure of the 2-H and 1-T phase is noticeably different, where the 2-H phase has more of a square structure, and the 1-T phase has more of a parallelogram structure. **Figure 13.8** examines the atomic edges of these layers in greater detail to see if we can make any clear observations about the phase of the material from these edge structures. **Figure 13.8a** shows a higher magnification image of the same edges from **Figure 13.7b**. Because there is well-defined atomic structure in our image, we can apply an FFT to determine the intensity of different frequencies within the image. **Figure 13.8b** shows the FFT of the selected area in **Figure 13.7a**, where we see the center zero frequency component, along with substantial intensity of non-zero frequencies roughly along the 45° line between the x and y axes (due to the orientation of the edges in the image). In **Figure 13.8b**, we also see very little signal of interest in the outermost portions. Therefore, we can apply a mask to the FFT, which is shown in **Figure 13.8c**, to remove unwanted portions of our image. The mask will allow us to ignore the zero-frequency component and the smallest frequencies on the outermost portions of the FFT (which corresponds mostly to random noise in our STEM images). This mask is how we produce the bandpass-filtered image (we are filtering out certain frequencies) as seen in **Figure 13.4b** and **13.7a**. After the mask is applied to the FFT in **Figure 13.8b**, we obtain the inverse FFT to produce the band-pass filtered image of the NR edges in **Figure 13.8d**. Spacing between layers is much more apparent now as we have removed random noise from the image, however we must be cautious in any measurements performed on these filtered images, as extraneous signal can be added or removed depending on how accurately our filtering was done.

The region of most interest in determination of phase is the structure within each layer, which has been selected in **Figure 13.8d**. Therefore, we need to build our understanding of how the edge structure seen in **Figure 13.6** would correspond to our STEM image seen in **Figure 13.8**. The first thing we notice is that this edge structure appears to be more square-like in appearance, as would be expected in the 2-H phase (**Figure 13.6c**). In the 2-H phase, the alignment of the selenium layers and zirconium center forms almost a straight line, where the Zr atom is slightly off-center, as seen in **Figure 13.6c**. The two layers of the brightest points would

correspond to the selenium layers, and the zirconium layer would be between these two layers. We then look at the structure within a sheet, as selected in **Figure 13.8d**. From the image in **Figure 13.8d**, the center region between the two layers appears to be slightly off center, but is much lower in intensity, and difficult to ascertain by eye what signal is there. A line scan within the sheet (between the two brightest points in the selected box) allows for further examination of the intensity of the structure, shown in **Figure 13.8e**. We see some slight signal between the two brightest points (around 0.4 nm in the line scan, the distance is arbitrary), which could correspond to the Zirconium atom between the chalcogen layers.

There is an important thing to note here, however: an absolute declaration about the phase of the material from the edge structure cannot be made. The edge structure merely adds supporting evidence that the 2-H phase could be stabilized in encapsulated $ZrSe_2$ NR. There are two main reasons to hold caution in absolute declaration from the edge structure. First, because the image has been band-passed filtered, a lot of signal from the image has been removed, with an assumption made that this signal is presumably due to random noise. More analysis on larger sample sizes would be needed to ensure the removed signal is of low significance. Second, the sample alignment can misconstrue observations made about the edge structure. Even in the edges from **Figure 13.8**, there are 4 distinct layers of $ZrSe_2$ within the image, but the structure of each layer differs from one another due to the alignment of each layer. A tilt-series of the NR edges would be necessary to determine the most suitable alignment for obtaining coherent signal from the edges. However, tilting of the encapsulated structures has proven incredibly difficult, so we rely on the random distribution of the NR to observe well-aligned specimen for measurement.

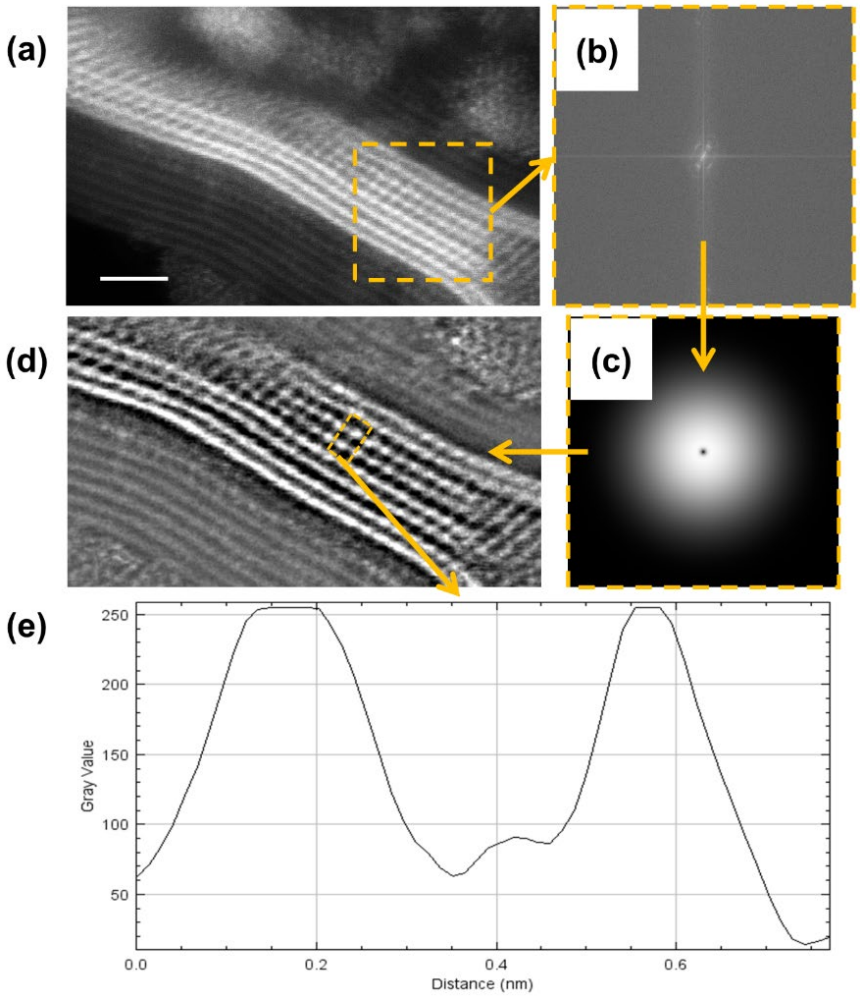

Figure 13.8 Analysis of the $ZrSe_2$ edge structure. (a) Normal STEM image obtained of the $ZrSe_2$ edges. (b) FFT of the edges from the STEM image. (c) The mask applied to the FFT to filter our image. (d) The final bandpass-filtered image showing stronger resolution between our bright and dark points. (e) Linescan within the $ZrSe_2$ layer. Scale bar measures 2 nm.

More experimental work needs to be done on the $ZrSe_2$ NR system to officially determine the isolated phase. However, initial results are very exciting, showing a potentially new phase of the $ZrSe_2$ system that has not been observed in bulk or monolayer before. In addition to the phase of the material, we have accessed NR of widths smaller than the critical 6 nm listed in the computational results from Li *et al.*, which suggests that creating a system with tunable bandgaps by controlling the width of a NR is well within experimental reality. The initial results shown here also support the broad applicability of the encapsulation technique to NR systems beyond the sulfides, which opens up the possibilities for the many other selenide-based TMD family members.

13.7 Characterizing the filling of $HfTe_2$ nanoribbons

13.7.1 Overview of the $HfTe_2$ nanoribbons

In addition to the $ZrSe_2$ NR synthesized and studied, we also pursued a telluride based TMD for encapsulation. **Figure 13.9** shows a transmission electron microscopy (TEM) image showing the $HfTe_2$ NR encapsulated within a CNT. In the micrograph, the parallel lines arise from the walls of the multiwalled nanotubes used in the synthesis, while the darker region in the center of the tubes is the inorganic lattice corresponding to the $HfTe_2$ NR. As shown in **Figure 13.9**, the synthesized NR have widths between 3.3 and 8 nm, although typical widths were on the order of 4 nm. The lengths of the NR appear to be much shorter than the $ZrSe_2$, consistently shorter than 100 nm. The nanoribbon widths are entirely dependent on the inner diameter of the CNT used, similar to other TMD systems studied. Also similar to TaS_2 and $ZrSe_2$, both the basal plane and edges of the NR were easily located and imaged.

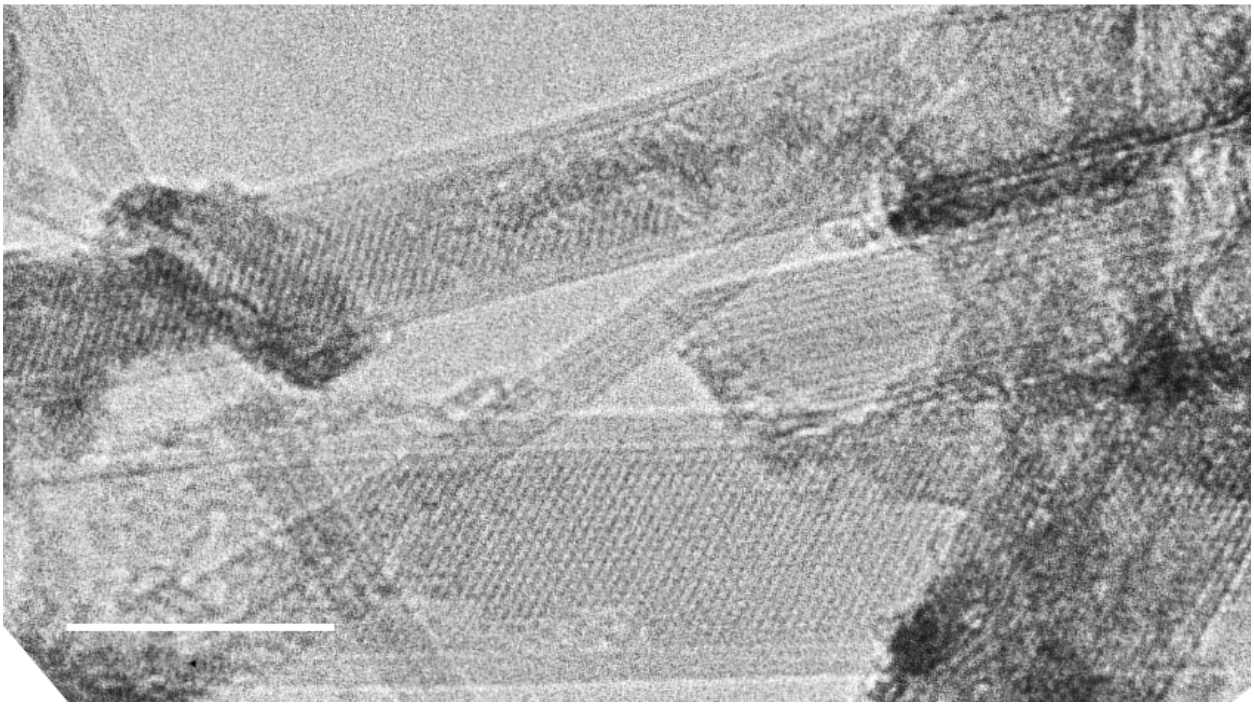

Figure 13.9 TEM of $HfTe_2$@CNT. (a) Low magnification TEM image of filled multiwall nanotubes. Periodic structure is observed in several of the MWCNT in our sample. Scale bar measures 10 nm. Data collected in collaboration with Derek Popple.

13.7.2 Studying the atomic structure of encapsulated $ZrSe_2$ nanoribbons

Once the dimensions of the NR were characterized, the sample was imaged via HAADF-STEM to gain greater insight into the atomic structure of the NR. Due to the greater resolution of the aberration-corrected microscope and the increased Z contrast characteristic to HAADF-STEM, the atomic structure of the NR is more easily visualized compared to the nanotube. **Figure 13.10** shows a couple of STEM images of the NR, along with a schematic of the encapsulated $HfTe_2$ NR, assumed to be 1-T phase. The sections of filled CNT contain NR with

pristine edges, as observed in **Figure 13.10**, where almost no distortion along the edge of the NR can be observed. This creates very crystalline and straight $HfTe_2$ NR, as opposed to the $ZrSe_2$ NR which tended to show curling and distortions along the edges in greater frequency.

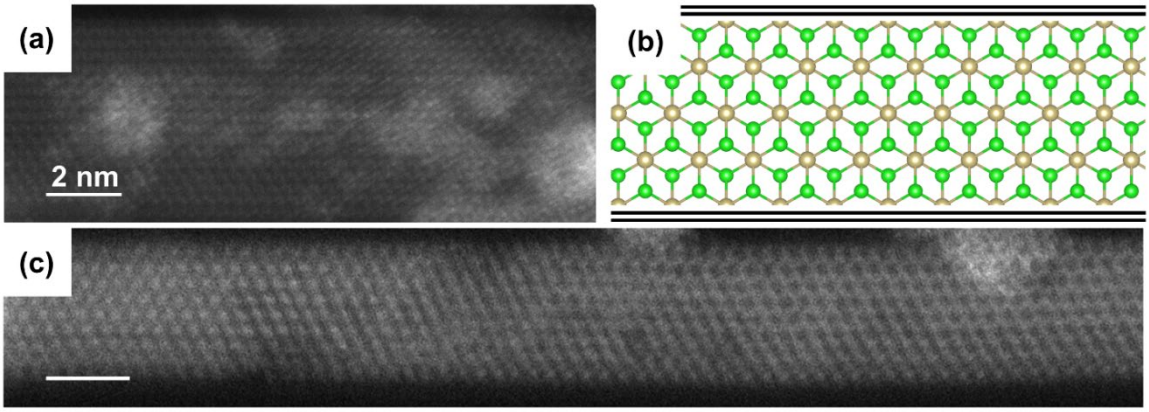

Figure 13.10 Basal plane structure of $HfTe_2$ nanoribbons@CNT. (a) STEM image of $HfTe_2$ nanoribbon. (b) Schematic of the 1-T phase $HfTe_2$ nanoribbon encapsulated in a double-walled CNT. Hf and Te atoms are represented by gold and green atoms, respectively, with the black lines indicating the walls of CNT. (c) Slightly rotated nanoribbon, where the left-most section appears to be most on-axis, and slightly rotates off axis along the nanoribbon axis. Scale bars measures 2 nm.

13.8 Determining the phase of the $HfTe_2$ nanoribbons

While the lengths of the $HfTe_2$ NR were relatively short in comparison to other TMD NR, the sections that were filled showed pristine atomic structures that could be easily analyzed in detail. **Figure 13.11** shows some standard analysis that can be done on the electron micrographs collected during the STEM imaging. **Figure 13.11a** is a band-pass filtered image of an encapsulated NR, and the corresponding FFT from the selected region shown in **Figure 13.11b**. Beautiful six-fold symmetry is immediately apparent, and the clean basal plane of the NR allows for further measurement by line scans to measure atomic spacing. In **Figure 13.11c**, the line scan of the selected row of atoms is shown, where the red arrows correspond to the peaks observed from Hf atoms, which have also been marked by red arrows on the atomic structure shown in **Figure 13.11d**. The experimentally measured spacing of the atoms is ~4.2 Å, with experimental error of ~ ± 0.2 Å. The measured atomic spacing in the calculated atomic structure shown in **Figure 13.11d** is 4.0Å, so the experimental spacing matches incredibly well with the calculated 1-T structure.

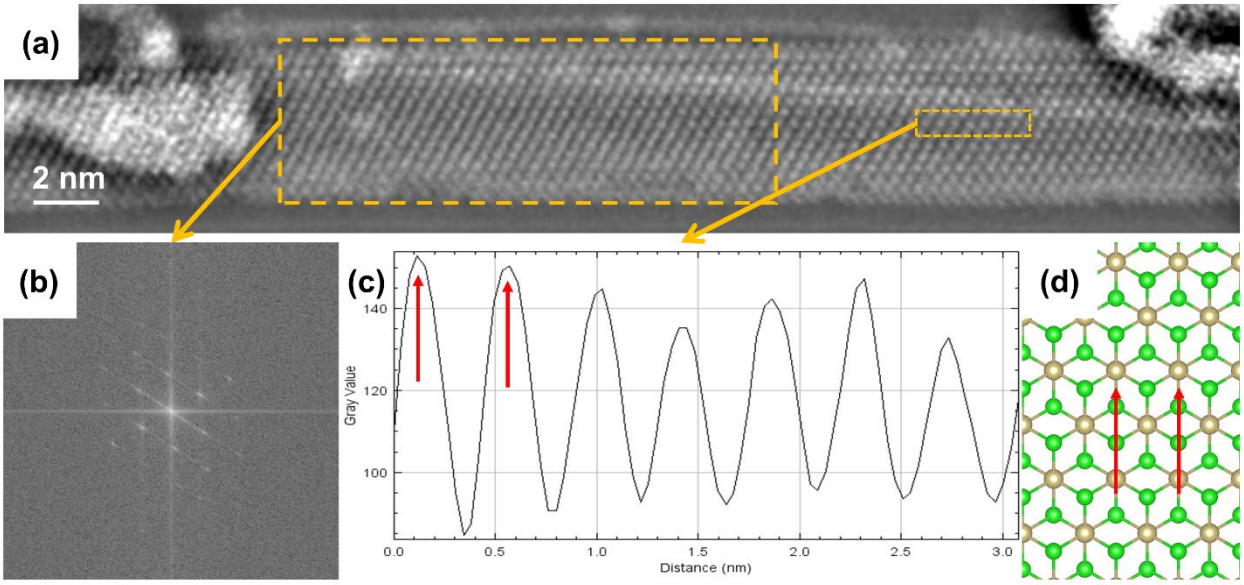

Figure 13.11 Analyzing the basal plane of $HfTe_2$@CNT. (a) Bandpass-filtered STEM image of an $HfTe_2$ nanoribbon, showcasing the hexagonal lattice of the basal plane. (b) FFT of the region encompassed by the dashed box, with 6-fold symmetry present. (c) Linescan of the selected region, with the location of Hf atoms indicated by the red arrows, which are also marked on the atomic model in (d). Hf and Te atoms are represented by gold and green atoms, respectively, with the black lines indicating the walls of CNT Scale bar measures 2 nm.

13.8.1 Studying the edge structure of $HfTe_2$ nanoribbons

In addition to the basal plane of the $HfTe_2$ NR, we also observe the edge of the NR. As discussed in the $ZrSe_2$ section, this edge structure can provide additional information about the phase of the TMD material within the CNT. **Figure 13.12** shows a folded NR and trilayer NR observed within the CNT. Many of the $HfTe_2$ NR observed were extremely crystalline in nature with very little deformation along the edges, so the frequency of edge structures observed was significantly fewer than that of the $ZrSe_2$ system. **Figure 13.12a** shows a NR that folds along its axis to eventually exhibit a bilayer edge structure. **Figure 13.12b** shows a trilayer system, with spacing between the layers of ~0.72 nm, in good agreement with the spacing of TMD layers in general. The edge structure observed in **Figure 13.12b** is shown as a schematic in **Figure 13.12c**. The structure seen here is very different than that of $ZrSe_2$ studied in **Figure 13.8**. Here, the spacing along the edge is incredibly tight, indicating a different alignment of the edge. This particular alignment can be observed in the atomic model of the 1-T phase, however it is possible to generate this exact same spacing and structure in the 2-H phase of TMD, so the edge structures currently observed for the $HfTe_2$ NR do not provide any additional information about the phase. However, atomic-scale imaging of the basal plane shows strong evidence supporting a 1-T phase of $HfTe_2$ NR encapsulated.

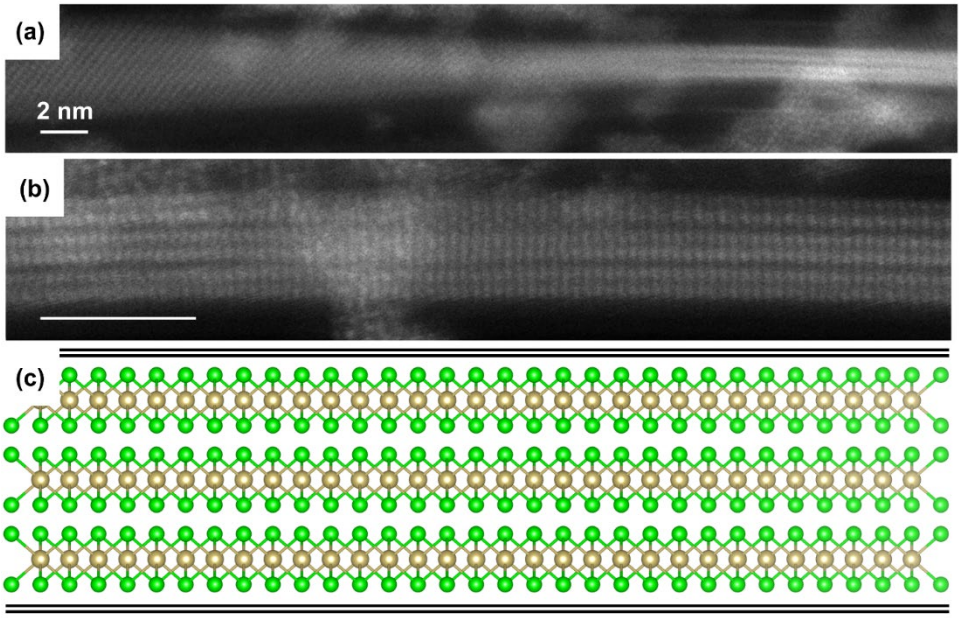

Figure 13.12 Edge structure of $HfTe_2$ nanoribbons@CNT. (a) STEM image of a folded nanoribbon, showing a bilayer structure after folding. (b) Trilayer $HfTe_2$ nanoribbon edge. (c) Schematic of the edge structure shown in a CNT. Hf and Te atoms are represented by gold and green atoms, respectively, with the black lines indicating the walls of CNT.

13.9 Conclusion

Here, we showed successful isolation of NR from members of the diselenide and ditelluride TMD family. The results shown here open the possibilities for the many other selenide- and telluride-based TMD family members to be isolated and studied as NR. Initial results on the $ZrSe_2$ NR system show a potentially new phase of the monolayer $ZrSe_2$ system. In addition to the phase of the material, we have accessed NR of widths smaller than the critical 6 nm listed in the computational results from Li *et al.*, which suggests that creating a system with tunable bandgaps by controlling the width of a NR is well within current experimental reality. Encapsulation of $HfTe_2$ NR seems to be a viable route to preferentially isolate a specific phase of the layered material, tending towards 1-T phase. Furthermore, $HfTe_2$ has yet to be fully realized in the monolayer limit (without chemical doping), but the encapsulation technique is proving to be an effective technique to reach that limit of $HfTe_2$ and study the monolayer limit. Wider CNT could be employed to see if larger $HfTe_2$ NR, approaching wide sheets, could be isolated at the few- or monolayer limit, to ease the study of the quantized system. The $ZrSe_2$ and $HfTe_2$ NR systems expand the study of TMD NR beyond that of the sulfide family, showcasing the importance and viability of the vapor-phase growth mechanisms for accessing the selenide and telluride families.

Chapter 14: A Culmination of Encapsulated Systems – Tuning $TaTe_x$ Structures Encapsulated within Carbon Nanotubes

Special thank you to Austin Culp, Dr. Mehmet Dogan, Dr. Philipp Pelz, and Dr. Colin Ophus for their assistance on this project.

Keywords: Tantalum Telluride, Carbon Nanotubes, Encapsulation, Transmission Electron Microscopy, Scanning Transmission Electron Microscopy, Morié Pattern, Nanoribbons, Chains

The previous chapters have discussed the various TMT and TMD species we have observed as encapsulated systems within carbon nanotubes and highlighted unique aspects of the isolated material. There have been several interesting structures observed, such as spiraling multi-chain systems, segmented chains, and periodic defect arrays. While these structures provide a lot of insight into the low-dimensional limit of the transition metal chalcogenide family, they were typically only associated with a single member of the transition metal chalcogenide family. Furthermore, the transition metal chalcogenide members studied typically preferred one stoichiometry over the other, forming either transition metal trichalcogenide chains *or* transition metal dichalcogenide nanoribbons. This chapter will explore the tantalum telluride material system, which exhibits multiple encapsulated structures based on the reaction conditions.

14.1 Motivation to tune encapsulated species

Control over material synthesis at the nanoscale allows for the stabilization of unique structures with novel material properties. While nanotubes provide excellent experimental control in encapsulating and confining materials down to the sub-nanometer size scale, typically there is only a single preferred structure that can be isolated. Here, however, we present an encapsulation study on the tantalum telluride material system, which exhibits a broader range of encapsulated structures. Excellent selectivity between isolating 1-Dimensional (1-D) chains of $TaTe_3$ or 2-D nanoribbons (NR) of $TaTe_2$ within the hollow cavity of carbon nanotubes (CNT) is achieved by tuning the synthesis reaction temperature. Transmission electron microscopy (TEM) and scanning transmission electron microscopy (STEM) reveal the detailed atomic structure of the encapsulated 1-D chains and 2-D NR. While the 1-D and 2-D structures of the TaTe system exhibit phenomena observed in other encapsulated transition metal chalcogenide family members, such as few-chain spiraling and multi-layer NR, we observe an entirely unexpected yet exciting moiré-like structure. We are currently pursuing atomic and electronic calculations of the $TaTe_2$ and $TaTe_3$ systems via density functional theory, as their atomic and electronic structure is not yet known. The $TaTe_x$ system explored here further expands the world of untouched but fascinating structures waiting to be stabilized, isolated, and studied at the atomic level.

14.2 Background on tantalum telluride

Isolating specific stoichiometries and structures of materials is one of the new driving forces behind material property design and control. One popular family of materials that are being extensively studied currently are transition metal chalcogenides, which, depending on their stoichiometry and structure, can be utilized as field-effect transistors, photodetectors, catalysts, or optoelectronics.[128,160,161,263–266] The transition metal chalcogenides can take on an abundance

of different stoichiometries and structures, but two of the more popular members are the transition metal dichalcogenides (TMD, chemical structure of MX_2, where M is a transition metal and X a chalcogen) and transition metal trichalcogenides (TMT, chemical structure of MX_3, where M is a transition metal and X a chalcogen).

Typically, most transition metal chalcogenide materials can adopt both the TMD and TMT stoichiometry, such as TiS_2 and TiS_3, $NbSe_2$ and $NbSe_3$, or $HfTe_2$ and $HfTe_3$. For many of these materials, targeting a specific stoichiometry, or selecting the TMD or TMT, can be relatively easily achieved by adjusting the reaction temperature and stoichiometric loading of reagents.[149,267,268] However, some material systems within the TMD/TMT family are not so easily separated, as is the case for Tantalum Telluride. Previous reports comment on the overall crystalline structure of the TMD and TMT system, alluding to the fact that they are layered structures similar to other members of the TMD and TMT family, but difficulty in isolating specific phases from the TaTe system through temperature or precursor loading prevented further study.[268,269]

Recent advancements in material stabilization and isolation via nanotube encapsulation provides an additional route for the selection of a specific stoichiometry in a material system, such as TaTe. Encapsulation within carbon nanotubes (CNT), for example, is possible for the TMD and TMT family due to the van der Waals (vdW) nature of their crystal structure, where the bulk crystal is comprised of smaller sub units held together by weak vdW forces.[109,110] The weak vdW structure of the crystal allows for isolation of the 2-D sheets as NR or 1-D chains down to a monolayer or single-chain limit within the CNT, even stabilizing previously unreported stoichiometries or structures in some material systems.[144,163,183,208,270] However, typically the encapsulation technique shows high preference for a single stoichiometry of the material system being studied, and tuning between different stoichiometries has proven challenging.[224,271]

Here, we report the successful targeted isolation of both $TaTe_3$ and $TaTe_2$ via encapsulation with CNT. The specific stoichiometry of the TaTe system grown in the confined space within the CNT can be preferentially selected and tuned through the overall reaction temperature of the synthesis. Encapsulation provides much greater experimental control over the obtained structure and allows for further characterization of the $TaTe_3$ and $TaTe_2$ in more detail than previously reported. As the synthesized material is protected by the CNT sheath, further characterization can be pursued via TEM and STEM. Not only is there very clear indication that the specific stoichiometries are distinctly isolated, but there is an additional structure observed exhibiting a unique and fascinating moiré-like structure. First-principles calculations are still being explored to uncover the atomic and electronic structure of the separated stoichiometries of $TaTe_2$ and $TaTe_3$.

14.3 Materials synthesis and structural characterization via electron microscopy

Multi-walled carbon nanotubes (CNTs) (Cheap tubes) were opened *via* oxidation at 515 °C for 1 hour in air, before the filling step. The encapsulated $TaTe_2$ NR, $TaTe_3$ chains, and $TaTe_x$ moiré structure are synthesized within CNTs using a similar procedure outlined for the growth of confined $NbSe_3$ and $HfTe_3$.[144,163] Stoichiometric quantities of Ta powder and Te shot (~450mg total), 1-2mg of opened MWCNT (CheapTubes, 90% SW-DW CNT), and ~5mg/cm^3 (ampoule volume) of I_2 are sealed under vacuum (~10^{-6} Torr) in a quartz ampoule. The ampoule is heated in a single-zone furnace at 600-900°C for 3 days, then cooled to room temperature over 1-5 days.

The filled CNTs are dispersed in isopropyl alcohol by bath sonication for 1 hour and drop-cast onto lacey carbon transmission electron microscope grids for imaging. Transmission electron microscope imaging was carried out on a JEOL 2010 microscope (80 keV accelerating voltage). Scanning transmission electron microscopy was completed at the National Center for Electron Microscopy at Lawrence Berkeley National Laboratory with assistance from Dr. Chengyu Song and Dr. Peter Ercius. The microscope used was the TEAM 0.5, which is a Titan 80-300 with an ultra-twin pole piece gap, DCOR probe aberration corrector and was operated at 80 kV and semi-convergence angle of 30 mrad. Images were acquired using the ADF-STEM detector with an inner angle of 60 mrad and a beam current to approximately 70 pA.

14.4 Encapsulated tantalum tritelluride

Selecting the trichalcogenides form within the TaTe material system can be achieved by lowering the overall reaction temperature to ranges within 600ºC. In other encapsulated tritelluride systems, the trigonal prismatic chains can exhibit themselves in the multi-,few- (2-4 chains), and single-chain limit.[144,163] While the multi-chain specimen retain the parallel alignment of the chains, few-chain specimen can exhibit a periodic structure, arising from the spiraling of chains about one another. **Figure 14.1** highlights the observed structures for the $TaTe_3$ system. **Figure 14.1a** showcases a multi-chain specimen encapsulated within a 9.4nm wide CNT, and associated atomic structures for the side view, where stronger, intrachain bonding is observed along the *b* axis, and the end view, where vdW gaps can be seen between the chains. **Figures 14.1b** and **14.1c** show the tell-tale few-chain spiraling specimen encapsulated within a 2.1nm and 2.3nm wide CNT, respectively.

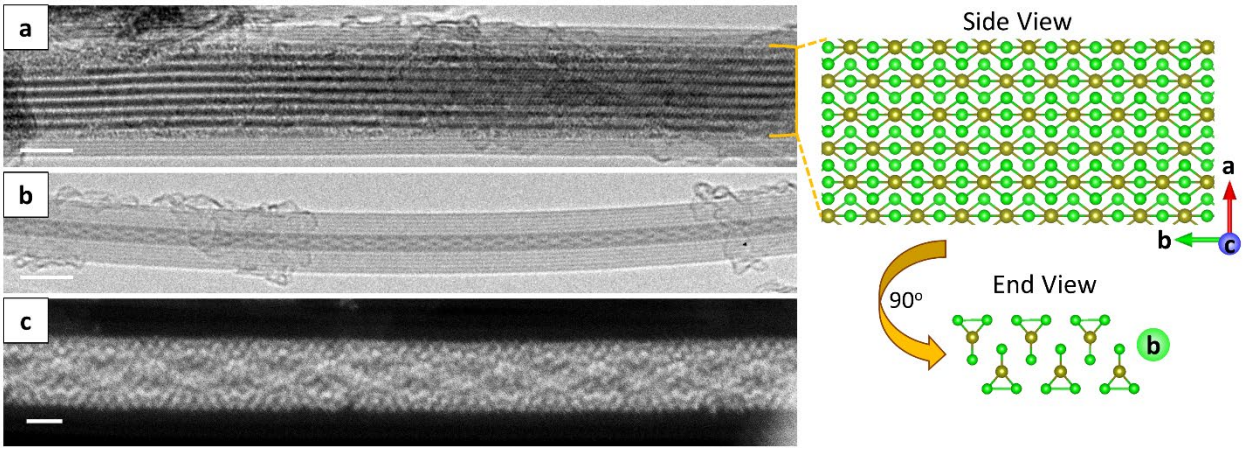

Figure 14.1 Electron microscopy images of encapsulated $TaTe_3$ chains. (a) TEM image of multi-chain $TaTe_3$. Atomic model shown to the right with a side view and end view of the trigonal prismatic chains. Ta and Te atoms are represented by gold and green spheres, respectively. (b/c) TEM and STEM images of spiraling few-chain $TaTe_3$. Scale bars measure (a/b) 5 and (c) 1 nm.

14.5 Encapsulated tantalum ditelluride

Selecting the dichalcogenide form within the TaTe system can be achieved through higher reaction temperatures, ranging from 800-900ºC. In the $TaTe_2$ system, we see clear examples of NR ranging from 3.5nm to 7.4nm in width. At the elevated reaction temperatures,

no TMT specimen are observed, indicating that the encapsulation coupled with higher temperatures solely favors the dichalcogenide phase of the TaTe system. The resulting NR are also encapsulated as both monolayers and bilayers, similar to other encapsulated NR species.[224] **Figure 14. 2** highlights the NR encapsulated within CNT and associated atomic models. **Figure 14.2a** shows a 7.4nm wide bilayer NR, which due to the extremely confined environment, begins to fold in on itself, displaying the edges of the $TaTe_2$ sheets, as detailed in the atomic model of the edge view of $TaTe_2$. **Figures 14.2b-d** are examples of 5.0nm, 4.8nm, and 6.4nm wide monolayer NR specimen, respectively, with the plan view of a NR shown in the atomic model. Interestingly, preliminary calculations show that the 1-T' phase of $TaTe_2$ is most stable, but the nanoribbons observed experimentally appear to be that of the 2-H phase, which is briefly explained in a later section.

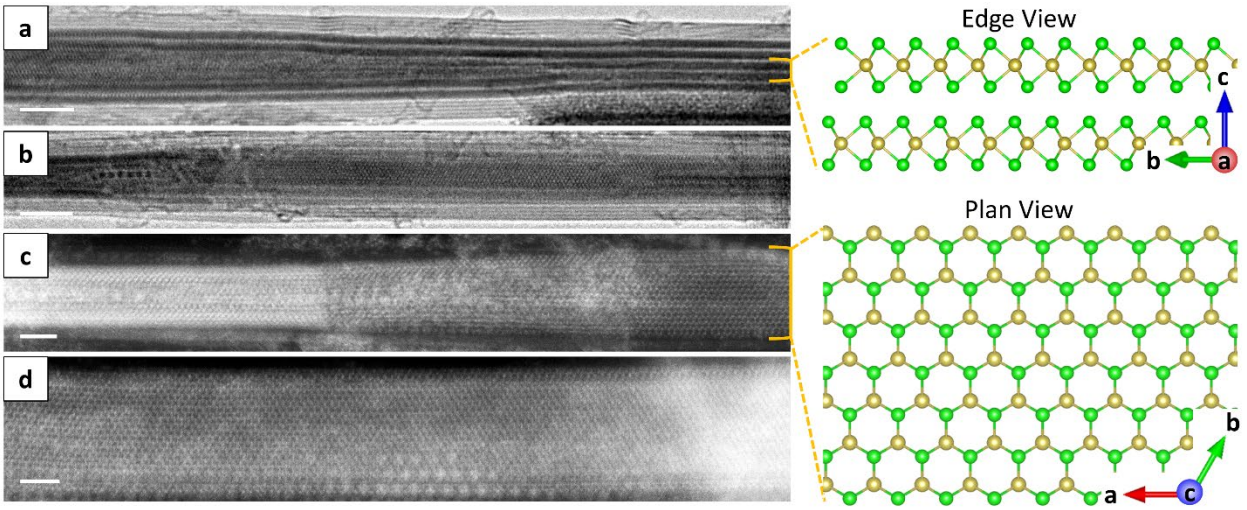

Figure 14.2 Electron microscopy images of encapsulated $TaTe_2$ nanoribbons. (a) TEM image of a curling, bilayer NR. Layer edges are clearly visible on the right-hand side of the image. Atomic model of the edge view shown to the right. Ta and Te atoms are represented by gold and green spheres, respectively. (b) TEM image of a monolayer NR. (c) STEM image of a monolayer NR. Atomic model of the plan view shown to the right. (d) STEM image of the basal plane of a flat monolayer NR. Scale bars measure (a/b) 5 nm and (c/d) 2 nm.

14.6 Encapsulated moiré structures

In conjunction with the NR observed at higher reaction temperatures, there emerged some unexpected, yet fascinating moiré-like structures stabilized within the CNT. The structure is not only stabilized in an encapsulated form, but highly reproducible and transferrable to varying pattern widths. Moiré specimen ranging from a single pattern up to five patterns wide can be found in the sample, with the moiré pattern retaining the same overall structure and spacing. This type of extended, coherent structure has not been observed in any highly confined material systems before. **Figure 14.3** highlights several examples of the moiré structure observed. **Figure 14.3a** shows a TEM image of a moiré structure roughly 3 patterns wide. **Figures 14.3b-d** each show the encapsulated moiré structure in increasing widths, from a single, double, and triple pattern wide, respectively. The corresponding widths of these structures are 2.6nm, 3.1nm, and 3.6nm, respectively, indicating the moiré structure itself is roughly 0.5nm in

width and grows in a quantized fashion, requiring select CNT of specific widths for each successive pattern added widthwise.

While the exact origin of the moiré-type patterned filling is still being examined, the patterns are strikingly similar to moiré patterns observed in bilayer systems of twisted TMDs as reported elsewhere.[272] However, a simple twisted bilayer system would not generate the edge structure observed in the experimental STEM images, so we are still studying various forms and iterations of such twisted systems and other multi-layered systems to elucidate the structure. One working hypothesis is that the ultra-confinement of the $TaTe_2$ layers forced them to reconstruct into a nanotube within the CNT. Preliminary results from ptychographic reconstruction, courtesy of Dr. Philipp Pelz and Dr. Colin Ophus, appears to show some amount of chirality, which further supports a chiral nanotube of $TaTe_2$ having formed. While a nanotube would account for the chirality of the structure, there is still some discrepancy in the overall intensity of the simulation vs. image, which could indicate the nanotube is collapsed. A secondary hypothesis, which supports both the edge and center structure observed, is some type of core-shell structure of $TaTe_2$, essentially a mix of a nanotube structure and additional layer(s) of $TaTe_2$ inside. The core-shell filling would probably result from some restructuring of the TaTe system into a slightly different stoichiometry other than 1:2, which has been observed in other systems.[22,273,274] We are still generating additional information from simulation and first-principle calculations to more conclusively solve the moiré-type filling.

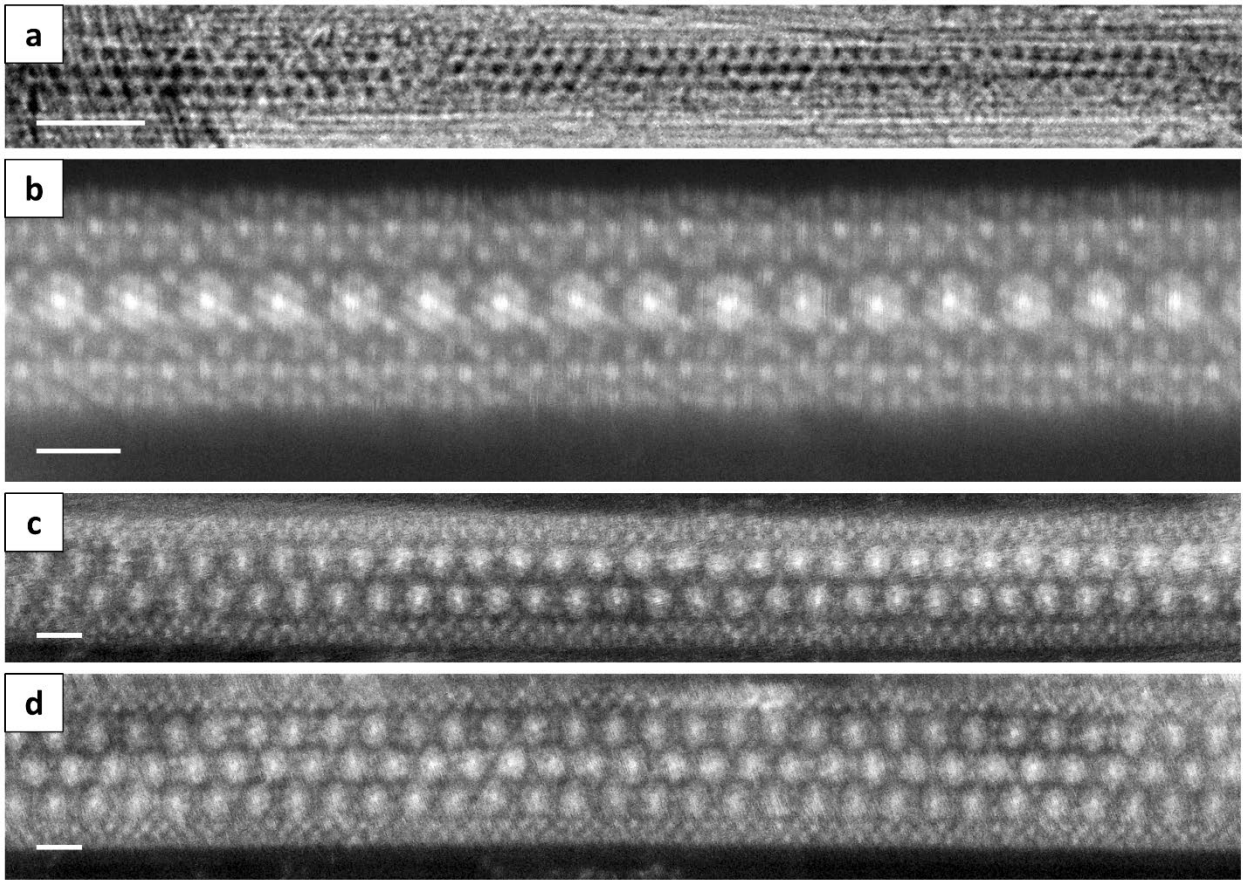

Figure 14.3 Electron microscopy images of the encapsulated moiré structure TaTe species. a) TEM image of the moiré structure about 3 patterns wide. b,c,d) STEM images of the moiré structure from increasing widths, from a single pattern, double pattern, and triple pattern wide, respectively. Scale bars measure (a) 5 nm and (b,c,d) 1 nm.

14.7 Atomic and electronic structure calculations

First-principles calculations provide insight into the atomic structure that gives rise to the moiré patterns observed, as well as the electronic structure of the new structure. Calculations are currently being performed by Dr. Mehmet Dogan, with supervision from Dr. Marvin Cohen, so current results will not be presented here as structures and additional variants are not completely relaxed. For the $TaTe_3$ chains, initial atomic structure calculations reveal a similar chain system to that of $NbSe_3$, where there are several distinct chain types in the bulk system.[148] As mentioned previously, $TaTe_2$ relaxes with significant stability in a 1-T' phase, similar to ReS_2, but with a trimer (instead of a dimer) distortion.[275] Interestingly, however, the observed phase in experimental STEM images is that of the 2-H phase, which could indicate dimension-dependent stability in the isolated $TaTe_2$ NR, where the additional confinement stabilizes a phase other than 1-T'. We are currently investigating how the dimensions of the layers of $TaTe_2$ affects stability, which will also provide insight into the type of underlying TaTe system in the moiré-type filling.

14.8 Conclusion

The TaTe system demonstrates significant material flexibility yet specificity in the encapsulation study presented above. Successful targeted synthesis of both $TaTe_3$ and $TaTe_2$ via encapsulation with CNT has been discussed in detail, with the specific stoichiometry of the TaTe system grown in the confined space of the CNT preferentially selected via the reaction temperature. While further study of the $TaTe_3$ and $TaTe_2$ system was a primary objected, an additional structure observed exhibited unique and fascinating moiré-like features. First-principles calculations are still being performed but are showing a rich landscape of phase stability for the $TaTe_2$ and $TaTe_3$ stoichiometries. Uncovering the stability of these narrow structures will provide further insight into the more interesting moiré patterns observed, deepening the area of study of novel and distinctive structures achievable through the encapsulated synthesis of the TMD and TMT material family.

Chapter 15: Continued Work – Atomic Confinement of Transition Metal Chalcogenides

Part II of this dissertation examined methods to tailor the properties of van der Waals (vdW) materials other than graphene and hexagonal boron nitride(h-BN). As the chemistries discussed in **Part I** are not easily applied to the material systems of interest, we instead turned to atomic confinement; a method that incorporates highly confined growth environments (as small as <1nm) for vdW-based materials to control the crystal structure of the encapsulated material. The materials of interest were the transition metal dichalcogenides (TMD) and transition metal trichalcogenides (TMT). TMD are similar to graphene and h-BN, in that their fundamental building blocks are atomically thin 2-D planes of atoms. TMT on the other hand, have an additional level of quantization, where their fundamental building blocks are atomically thin 1-D chains of atoms. The unifying factor between the TMD and TMT is their bulk crystalline form is comprised of low-dimensional building blocks held together by vdW forces. Because the vdW forces are comparatively weak to other types of bonding, these low-dimensional building blocks can be isolated from one another. Constraining the physical size of these crystalline solids can dramatically influence their electrical, optical, magnetic, thermal, and mechanical properties. The vdW limit of TMD and TMT are quantized in one or two dimensions, respectively, leading to strong structural, electronic, and phononic anisotropy.[6,148]

Chapter 8 discussed the first material I explored at its fundamental limit: $HfTe_3$. While bulk HfT_3 was rarely studied due to stability issues, the encapsulation technique utilized to isolate these 1-D structures simultaneously confined the chains, prevented oxidation in an air environment, and facilitated sample preparation for characterization *via* high resolution transmission electron microscopy (TEM) and scanning transmission electron microscopy (STEM). The inner diameter of carbon nanotubes (CNT) can be tuned to different sizes, allowing for control over the number of chains isolated. This allowed us to examine $HfTe_3$ specimen of many chains (~20), few chains (3 and 2), and even single isolated chains. While we have continued to push ahead in progress to experimentally examine the properties of these isolated chains, we started examining their properties via first-principles calculations. In our encapsulated $HfTe_3$ system, we found a coordinated interchain spiraling for triple and double chain $HfTe_3$ specimens, accompanied by a structural transition via a trigonal prismatic rocking distortion to a new, unreported crystal phase, concomitant with a metal-insulator transition, as the number of chains is decreased below four. $HfTe_3$ and $NbSe_3$ paved the way for the rest of the discoveries made in these encapsulated systems, as we got a first glimpse into the drastic atomic and electronic structural modifications that could be made by ultra-confinement of a transition metal chalcogenide material.

Chapter 9 dived into experimental attempts to continue the study of encapsulated and isolated TMT systems down to their vdW-limit. $HfTe_3$ is a single member of the TMT family, which are comprised of linear chain-like compounds with the chemical formula MX_3, where M is a transition metal (typically Group IVB or VB) and X is a chalcogen (S, Se, or Te). The high anisotropy in their crystal structure affects their electron transport properties, such as photoconductivity, charge density wave transitions, and superconductivity.[128,129,164] There are 11 total TMT members that have been studied in bulk form, while another 7 TMT members have not been synthesized or studied in any meaningful manner. This showcases just how large the potential for the TMT family is, and how diverse the atomic and electronic structures at the vdW limit, and associated properties, waiting to be uncovered truly are. We examined synthetic parameters for each TMT of interest, and we discussed the many triumphs and tribulations

encountered for each additional TMT member studied beyond $HfTe_3$. While there is much parameter space to explore to fine tune the conditions necessary for isolating each specific TMT member, there was great success in isolating $ZrTe_3$ chains, which could be a good candidate to explore other methods of characterizing the filled CNT, such as Raman spectroscopy.

Chapter 10 stemmed from the continued study of the $HfTe_3$ system. In an attempt to optimize the growth and filling of CNT with single-chain $HfTe_3$ for better imaging, we came across an entirely new low-dimensional form of the Hf-Te family. The new form consists of structurally coherent zero-dimensional "blocks", each comprised of two Hf atoms and nine Te atoms (i.e. Hf_2Te_9), arranged end-to-end in a *segmented linear chain*, with vdW bonds linking the blocks or chain segments. The segmented chain is stabilized by the interior of a CNT, which again facilitated experimental characterization. First principles calculations revealed an especially rich electronic structure for the segmented chain. The bands near the chemical potential are fully spin-polarized in one direction and *k*-dependent giant spin splitting (GSS) of the bands occurs due to one mirror symmetry which is broken by crystal momentum *k,* and another mirror symmetry which is preserved for all *k*. Calculated Zak phases of the bands suggest externally tunable topological invariance. The isolation of these segmented linear chains showed the potential of our encapsulation technique to access crystal systems that had not been successfully synthesized in bulk before.

Chapter 11 began to expand on this notion of encapsulating never-before-seen structures. As previously mentioned, there are 7 members of the TMT family that had not been successfully synthesized in bulk. However, from previous chapters, we have demonstrated how these TMT systems can undergo drastic atomic reconfiguration at the vdW limit. Applying this knowledge to some of the unreported TMT members, we successfully demonstrated the synthesis of the few- and single-chain limit of three new members of the quasi-1D TMT family, *via* our encapsulation technique within the hollow cavity of CNT. Capitalizing on the stabilizing factor of the nanotube sheath, we were able to access hitherto unseen compositions and crystal structures, specifically $NbTe_3$, VTe_3, and $TiTe_3$. We investigated the structures of the new materials with atomic-resolution electron microscopy, revealing helical twisting of chains in multi-chain specimens and, for the first time, an experimentally resolved trigonal antiprismatic rocking distortion in single chain specimen, as theoretically reported for single-chain $HfTe_3$. DFT calculations illuminated the electronic properties of single chains of the materials encapsulated in MWCNTs and quantified the stability of these materials in their bulk form and in the single-chain limit. We also began analyzing the Gibb's Free Energy of these systems, which shed additional light on the overall balance between the stability of the trichalcogenide systems vs. their dichalcogenide counterparts. The insight into the stability of the TMT vs. TMD explains some of the disparities in previous reports of synthesis and/or characterization of certain material families, such as the ones explored in **Chapter 9**. The work presented in **Chapter 11** laid fundamental groundwork for the study of confinement-stabilized non-equilibrium materials and their associated emergent physical phenomena.

Chapter 12 continued to expand the capabilities of the encapsulation technique to study highly confined material systems. Again, using chemical vapor transport and following specific temperature protocols, we were able to achieve encapsulated ribbon-like morphologies, rather than the typical linear-chain like morphologies we explored in **Chapters 8, 9, and 11**. These ribbons demonstrated the successful growth of 2H-TaS_2 nanoribbons (NR). We achieved TaS_2 NR with thicknesses down to the monolayer limit, widths as low as 2.5 nm, and lengths greater than 100 nm. The growth produced NR with controllable widths, clean NR surfaces and edges,

and enabled easy handling (e.g. solution-based post processing) for subsequent study of the structure. The detailed atomic registry of NR was elucidated with transmission electron microscopy and aberration-corrected annular dark-field scanning transmission electron microscopy. In addition to the pristine, clean NR, we also observed and investigated previously unknown and unique periodic atomic superstructures defined by ordered defect arrays. First-principles calculations revealed the presence of flat bands localized at the defect boundaries and edges. The discovery of the TaS_2 NR was exciting proof that we could now access a quasi-1-D morphology of the TMD family and had done so with a transferable and broadly deployable synthetic route toward ultra-narrow TMD NR growth for many members of the TMD family.

Chapter 13 explored the transferability of the encapsulation technique to other chalcogenide-based members of the TMD family. The first TMD member studied in this chapter was $ZrSe_2$, a semiconductor with previous theory studies showing a tunable bandgap if additional quantization can be imposed on the TMD sheet (forming a NR). So far, we have been able to access NR of widths smaller than the critical 6 nm listed in the computational results, which suggests that NR with tunable bandgaps is well within experimental reality. We also explored $HfTe_2$ NR, which could also benefit from more experimental work to increase the filling ratio of the CNT, as the overall length of the NR was considerably shorter than the TaS_2 and $ZrSe_2$ NR observed. However, impressive results have already been observed. While bulk $HfTe_2$ has been observed in both the 2-H and 1-T phase (and never in the monolayer limit), the encapsulation technique is proving to be a route to not only preferentially isolate a specific phase, but also reach the monolayer limit (without chemical doping). More importantly, the $ZrSe_2$ and $HfTe_2$ systems expand the study of TMD NR beyond that of the sulfide family, showcasing the importance and viability of the vapor-phase growth mechanisms for accessing the selenide- and telluride-based TMD NR families.

Chapter 14 presented a culmination of the encapsulated work discussed in **Part II**. This chapter reported the successful targeted isolation of both $TaTe_3$ and $TaTe_2$ via encapsulation with CNT. The specific stoichiometry of the TaTe system grown in the confined space within the CNT could be preferentially selected and tuned through the overall reaction temperature of the synthesis, allowing us (for the first time) to choose whether we isolated TMT chains or TMD nanoribbons. As the material grown is protected by the CNT sheath, further characterization can be pursued via TEM and STEM, where we not only saw there is very clear indication that the specific stoichiometries are distinctly isolated, but also uncovered an additional structure observed exhibiting a unique and fascinating moiré-like structure. While this project is still underway with a lot more to discover, we are currently pursuing 4-D STEM and ptychographic reconstruction to elucidate the more complex moiré-like structure. We are also performing first-principles calculations to study the TMT chains and TMD nanoribbons, as neither have every been studied in detail for the TaTe system. **Chapter 14** showed the true potential of our encapsulation technique, being utilized to study TMT chains, TMD nanoribbons, and a more complex and thoroughly unique moiré structure, all from the same material system.

Chapters 8-14 explored how constraining the dimensions of these 2-D and 1-D vdW materials down to "atomic thinness" resulted in various degrees of additional size quantization with profound consequences.[144,163,208,252,271] **Table 15.1** outlines the entire material family explored in **Part II** and associated discoveries for the Group IVB and VB TMD and TMT

explored in this dissertation. Included are the unique characteristics observed for each encapsulated species, whether it be an atomic structure distortion, electronic structure modulation, superstructures, or entirely new material system stabilized. The results presented in this dissertation highlight the exciting world of ultra-confined vdW materials waiting to be uncovered and studied, providing much-needed fundamental understanding about the atomic and electronic structure of crystalline solids at their atomic limit.

Table 15.1 The many combinations of TMD and TMT from the Group IV and V transition metal block. The di- and tri-chalcogenide are listed across the top for each transition metal, which are separated by bulk or the vdW (few- and single-chain limit or nanoribbon) form of material. Material discoveries where I was a primary or secondary researcher are listed in red font. All combinations have been listed for completeness, even if no bulk synthesis has been reported. The temperatures listed in the table are the transition temperatures.

		Chalcogen											
		S_3		S_2		Se_3		Se_2		Te_3		Te_2	
		Bulk	***Few and Single Chains***	*Bulk*	***Nanoribbon***	*Bulk*	***Few and Single Chains***	*Bulk*	***Nanoribbon***	*Bulk*	***Few and Single Chains***	*Bulk*	***Nanoribbon***
Group IV Transition Metal	**Ti**	Semicond.		Semimetal		No Reported Synthesis		CDW (200K)		No Reported Synthesis	**Semicond. (0.680eV) TAP Rocking Distortion**	Semimetal	
	Zr	Semicond.		Semicond.		Semicond.		Semicond.	**3-5nm, Tunable Bandgap**	SC (2K)	**Metallic, Spiraling few-chain**	Semimetal	
	Hf	Semicond.		Semicond.		Semicond.		Semicond.		SC (1.4-2K), CDW (70-93K)	**Metal-insulator Transition, Semicond., (1.10eV)**	Semimetal	**2-5nm Monolayer**
Group V Transition Metal	**V**	No Reported Synthesis		Metallic		No Reported Synthesis		CDW (110K)		No Reported Synthesis	**Semicond. (0.062eV) TAP Rocking Distortion**	Metallic	
	Nb	Semicond., CDW (450-475K)		SC (2-6K)		CDW (145K, 59K)	**Torsional Instability, Metallic**	CDW (26K), SC (7.2K)		No Reported Synthesis	**Semicond. (0.339eV) TAP Rocking Distortion**	SC (0.7K)	
	Ta	CDW (210-220K)		CDW (220, 280, 350K), SC (0.5-2.2K)	**3-5nm, Defect Array Structures**	SC (2.1K)		CDW (90K), SC (0.1K)		Reported Synthesis, No Characterization	**Spiraling few-chain**	CDW (170K)	**3-8nm, Moiré Super Structures**

Key: Semicond. = Semiconductor/Insulator; CDW = Charge Density Wave; SC = Superconducting; TAP = Trigonal Antiprismatic

While **Chapters 8-14** showed substantial progress in the overall synthesis and characterization of these atomically thin and narrow TMT and TMD species, there is still much work that can be done and that we are currently pursuing. The main push currently is to experimentally study the electronic structure of the species encapsulated within the CNT, which requires significant advancements in our ability to cross-correlate atomic-level imaging and device fabrication. Fortunately, with the help of Dr. Kyunghoon Lee, we have made incredible progress in our ability to make electrical contact with these encapsulated species.

Figure 15.1 shows an overview of standard TEM imaging, which shows a single chain of $NbSe_3$ encapsulated in a single wall CNT on a SiN substrate. Using alignment keys and numbered notation, we can mark exactly where the filled nanotube is, eventually patterning the very narrow channels shown in **Figure 15.1** as well. Some initial devices that have been built show very promising results in their measured resistance as a function of temperature, with reasonable contact resistance. Measuring the electronic properties of the encapsulated species is well within experimental expectations and will provide groundbreaking results in the fields of

quantized semiconductors, narrow charge density wave materials, and quasi-1-D superconductivity transitions. The world of encapsulated materials has proven to be a rich field of study, equally exciting and fascinating as the research that has been done on graphene and other related layered systems. From never-before-seen structural deformations (charge-induced torsional waves), to atomic-scale distortions (trigonal antiprismatic rocking), to metal-insulator transitions, to unreported crystalline structures, to periodic defect arrays, to moiré-like structures, the emergent phenomena seem endless and will prove to be an exciting area of study for years to come.

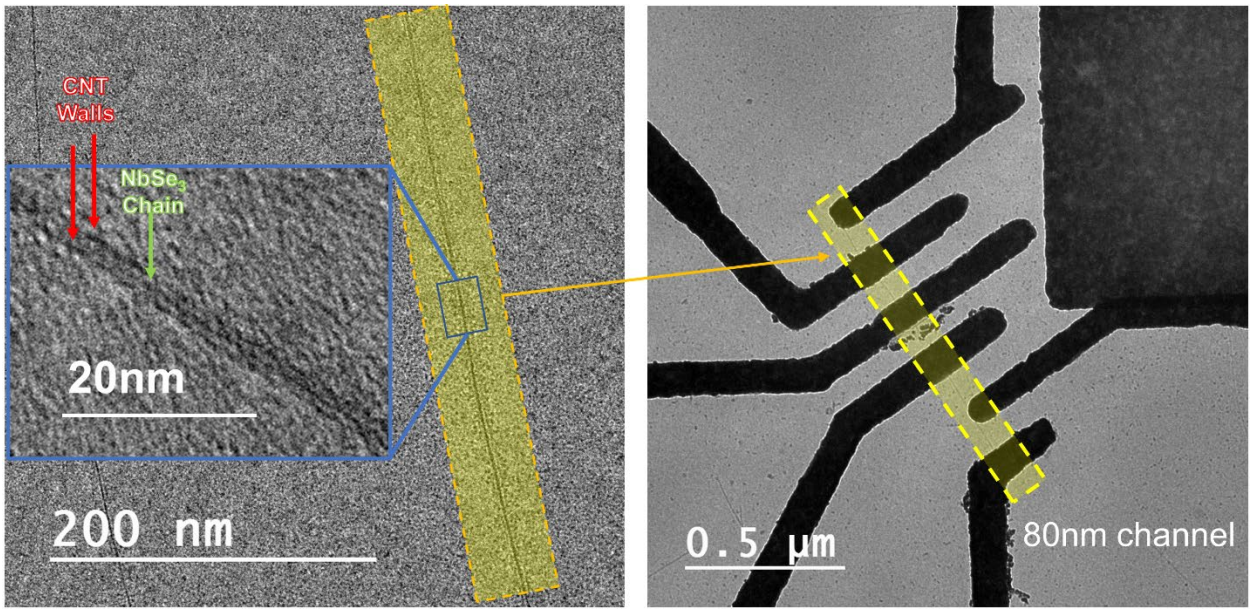

Figure 15.1 Overview of the cross-referencing between imaging and device contact deposition. Data collected in collaboration with Dr. Kyunghoon Lee.

References

(1) Németh, P.; Mccoll, K.; Smith, R. L.; Murri, M.; Garvie, L. A. J.; Alvaro, M.; Pécz, B.; Jones, A. P.; Corà, F.; Salzmann, C. G.; Mcmillan, P. F. Diamond-Graphene Composite Nanostructures. *Nano Lett.* **2020**, *20* (5), 3611–3619. https://doi.org/10.1021/acs.nanolett.0c00556.

(2) Yuan, Q.; Lin, C. Te; Chee, K. W. A. All-Carbon Devices Based on Sp 2 -on-Sp 3 Configuration. *APL Mater.* **2019**, *7* (3). https://doi.org/10.1063/1.5082767.

(3) Wang, J.; Ma, F.; Liang, W.; Sun, M. Electrical Properties and Applications of Graphene, Hexagonal Boron Nitride (h-BN), and Graphene/h-BN Heterostructures. *Mater. Today Phys.* **2017**, *2*, 6–34. https://doi.org/10.1016/j.mtphys.2017.07.001.

(4) Castro Neto, A. H.; Guinea, F.; Peres, N. M. R.; Novoselov, K. S.; Geim, A. K. The Electronic Properties of Graphene. *Rev. Mod. Phys.* **2009**, *81* (1), 109–162. https://doi.org/10.1103/RevModPhys.81.109.

(5) Yuk, J. M.; Kim, K.; Alemán, B.; Regan, W.; Ryu, J. H.; Park, J.; Ercius, P.; Lee, H. M.; Alivisatos, A. P.; Crommie, M. F.; Lee, J. Y.; Zettl, A. Graphene Veils and Sandwiches. *Nano Lett.* **2011**, *11* (8), 3290–3294. https://doi.org/10.1021/nl201647p.

(6) Geim, A. K.; Grigorieva, I. V. Van Der Waals Heterostructures. *Nature* **2013**, *499* (7459), 419–425. https://doi.org/10.1038/nature12385.

(7) Novoselov, K. S.; Geim, A. K.; Morozov, S. V.; Jiang, D.; Zhang, Y.; Dubonos, S. V.; Grigorieva, I. V.; Firsov, A. A. Electric Field Effect in Atomically Thin Carbon Films. *Science (80-.).* **2004**, *306* (5696), 666–669. https://doi.org/10.1126/science.1102896.

(8) Buscema, M.; Steele, G. A.; van der Zant, H. S. J.; Castellanos-Gomez, A. The Effect of the Substrate on the Raman and Photoluminescence Emission of Single Layer MoS2. *Nano Res.* **2014**, *7* (4), 561–571.

(9) Dean, C. R.; Young, A. F.; Meric, I.; Lee, C.; Wang, L.; Sorgenfrei, S.; Watanabe, K.; Taniguchi, T.; Kim, P.; Shepard, K. L.; Hone, J. Boron Nitride Substrates for High-Quality Graphene Electronics. *Nat. Nanotechnol.* **2010**, *5* (10), 722–726. https://doi.org/10.1038/nnano.2010.172.

(10) Iijima, S. Helical Microtubules of Graphitic Carbon. *Nature* **1991**, *354*, 744–752. https://doi.org/10.1016/j.carbon.2017.02.042.

(11) Charlier, J. C.; Blase, X.; Roche, S. Electronic and Transport Properties of Nanotubes. *Rev. Mod. Phys.* **2007**, *79* (2), 677–732. https://doi.org/10.1103/RevModPhys.79.677.

(12) Chopra, N. G.; Luyken, R. J.; Cherrey, K.; Crespi, V. H.; Cohen, M. L.; Louie, S. G.; Zettl, A. Boron Nitride Nanotubes. *Science (80-.).* **1995**, *269* (5226), 966–967. https://doi.org/10.1126/science.269.5226.966.

(13) Rubio, A.; Corkill, J. L.; Cohen, M. L. Theory of Graphitic Boron Nitride Nanotubes. *Phys. Rev. B* **1994**, *49* (7), 5081–5084. https://doi.org/10.1103/PhysRevB.49.5081.

(14) Fathalizadeh, A.; Pham, T.; Mickelson, W.; Zettl, A. Scaled Synthesis of Boron Nitride Nanotubes, Nanoribbons, and Nanococoons Using Direct Feedstock Injection into an Extended-Pressure, Inductively-Coupled Thermal Plasma. *Nano Lett.* **2014**, *14* (8), 4881–4886. https://doi.org/10.1021/nl5022915.

(15) Erickson, K. J.; Gibb, A. L.; Sinitskii, A.; Rousseas, M.; Alem, N.; Tour, J. M.; Zettl, A. K. Longitudinal Splitting of Boron Nitride Nanotubes for the Facile Synthesis of High Quality Boron Nitride Nanoribbons. *Nano Lett.* **2011**, *11* (8), 3221–3226. https://doi.org/10.1021/nl2014857.

(16) Windom, B. C.; Hahn, D. W. Raman Spectroscopy. *Wang Q.J., Chung YW. (eds) Encyclopedia of Tribology*; 2013; pp 1–12.
(17) Wu, J.; Lin, M.; Cong, X.; Liu, H.; Tan, P.; Lin, M. Raman Spectroscopy of Graphene-Based Materials and Its Applications in Related Devices. *Chem. Soc. Rev.* **2018**, 1822–1873. https://doi.org/10.1039/c6cs00915h.
(18) Ni, C. Scanning Electron Microscopy (SEM). *Wang Q.J., Chung YW. (eds) Encyclopedia of Tribology.*; 2013; pp 2977–2982.
(19) Nasrazadani, S.; Hassani, S. Modern Analytical Techniques in Failure Analysis of Aerospace, Chemical, and Oil and Gas Industries. *Handb. Mater. Fail. Anal. with Case Stud. from Oil Gas Ind.* **2016**, 39–54. https://doi.org/10.1016/B978-0-08-100117-2.00010-8.
(20) Qu, J.; MeyerIII, H. M. X-Ray Photoelectron Spectroscopy (XPS). *Wang Q.J., Chung YW. (eds) Encyclopedia of Tribology*; 2013; p 382.
(21) Wilson, N. R.; Pandey, P. A.; Beanland, R.; Young, R. J.; Kinloch, I. A.; Gong, L.; Liu, Z.; Suenaga, K.; Rourke, J. P.; York, S. J.; Sloan, J. Graphene Oxide: Structural Analysis and Application as a Highly Transparent Support for Electron Microscopy. *ACS Nano* **2009**, *3* (9), 2547–2556. https://doi.org/10.1021/nn900694t.
(22) Conrad, M.; Krumeich, F.; Reich, C.; Harbrecht, B. Hexagonal Approximants of a Dodecagonal Tantalum Telluride - the Crystal Structure of Ta21Te13. *Mater. Sci. Eng. A* **2000**, *294–296*, 37–40. https://doi.org/10.1016/S0921-5093(00)01150-3.
(23) Azizi, A.; Eichfeld, S.; Geschwind, G.; Zhang, K.; Jiang, B.; Mukherjee, D.; Hossain, L.; Piasecki, A. F.; Kabius, B.; Robinson, J. A.; Alem, N. Freestanding Van Der Waals Heterosturctures of Graphene and Transition Metal Dichalcogenides. *ACS Nano* **2015**, *9* (5), 4882–4890. https://doi.org/10.1021/acsnano.5b01677.
(24) Gorgolis, G.; Galiotis, C. Graphene Aerogels: A Review. *2D Mater.* **2017**, *4* (3). https://doi.org/10.1088/2053-1583/aa7883.
(25) Worsley, M. A.; Pauzauskie, P. J.; Olson, T. Y.; Biener, J.; Satcher, J. H.; Baumann, T. F. Synthesis of Graphene Aerogel with High Electrical Conductivity. *J. Am. Chem. Soc.* **2010**, *132* (40), 14067–14069. https://doi.org/10.1021/ja1072299.
(26) Worsley, M. A.; Shin, S. J.; Merrill, M. D.; Lenhardt, J.; Nelson, A. J.; Woo, L. Y.; Gash, A. E.; Baumann, T. F.; Orme, C. A. Ultralow Density, Monolithic WS_2, MoS_2, and MoS_2/Graphene Aerogels. *ACS Nano* **2015**, *9* (5), 4698–4705. https://doi.org/10.1021/acsnano.5b00087.
(27) Zhu, C.; Liu, T.; Qian, F.; Han, T. Y. J.; Duoss, E. B.; Kuntz, J. D.; Spadaccini, C. M.; Worsley, M. A.; Li, Y. Supercapacitors Based on Three-Dimensional Hierarchical Graphene Aerogels with Periodic Macropores. *Nano Lett.* **2016**, *16* (6), 3448–3456. https://doi.org/10.1021/acs.nanolett.5b04965.
(28) Harley-Trochimczyk, A.; Pham, T.; Chang, J.; Chen, E.; Worsley, M. A.; Zettl, A.; Mickelson, W.; Maboudian, R. Platinum Nanoparticle Loading of Boron Nitride Aerogel and Its Use as a Novel Material for Low-Power Catalytic Gas Sensing. *Adv. Funct. Mater.* **2016**, *26* (3), 433–439. https://doi.org/10.1002/adfm.201503605.
(29) Wang, J.; Liu, D.; Li, Q.; Chen, C.; Chen, Z.; Song, P.; Hao, J.; Li, Y.; Fakhrhoseini, S.; Naebe, M.; Wang, X.; Lei, W. Lightweight, Superelastic Yet Thermoconductive Boron Nitride Nanocomposite Aerogel for Thermal Energy Regulation. *ACS Nano* **2019**. https://doi.org/10.1021/acsnano.9b02182.
(30) Soleimani Dorcheh, A.; Abbasi, M. H. Silica Aerogel; Synthesis, Properties and

Characterization. *J. Mater. Process. Technol.* **2008**, *199* (1), 10–26. https://doi.org/10.1016/j.jmatprotec.2007.10.060.
(31) Turner, S.; Yan, W.; Long, H.; Nelson, A. J.; Baker, A.; Lee, J. R. I.; Carraro, C.; Worsley, M. A.; Maboudian, R.; Zettl, A. Boron Doping and Defect Engineering of Graphene Aerogels for Ultrasensitive NO_2 Detection. *J. Phys. Chem. C* **2018**, *122* (35), 20358–20365. https://doi.org/10.1021/acs.jpcc.8b05984.
(32) Hu, H.; Zhao, Z.; Wan, W.; Gogotsi, Y.; Qiu, J. Ultralight and Highly Compressible Graphene Aerogels. *Adv. Mater.* **2013**, *25* (15), 2219–2223. https://doi.org/10.1002/adma.201204530.
(33) Lei, W.; Mochalin, V. N.; Liu, D.; Qin, S.; Gogotsi, Y.; Chen, Y. Boron Nitride Colloidal Solutions, Ultralight Aerogels and Freestanding Membranes through One-Step Exfoliation and Functionalization. *Nat. Commun.* **2015**, *6*, 1–8. https://doi.org/10.1038/ncomms9849.
(34) Qian, Y.; Ismail, I. M.; Stein, A. Ultralight, High-Surface-Area, Multifunctional Graphene-Based Aerogels from Self-Assembly of Graphene Oxide and Resol. *Carbon*. March 2014, pp 221–231. https://doi.org/10.1016/j.carbon.2013.10.082.
(35) Turner, S.; Long, H.; Shevitski, B.; Pham, T.; Lorenzo, M.; Kennedy, E.; Aloni, S.; Worsley, M.; Zettl, A. Density Tunable Graphene Aerogels Using a Sacrificial Polycyclic Aromatic Hydrocarbon. *Phys. Status Solidi* **2017**, *1700203*, 1–6. https://doi.org/10.1002/pssb.201700203.
(36) Yao, B.; Chandrasekaran, S.; Zhang, H.; Ma, A.; Kang, J.; Zhang, L.; Lu, X.; Qian, F.; Zhu, C.; Duoss, E. B.; Spadaccini, C. M.; Worsley, M. A.; Li, Y. 3D-Printed Structure Boosts the Kinetics and Intrinsic Capacitance of Pseudocapacitive Graphene Aerogels. *Adv. Mater.* **2020**, 1906652. https://doi.org/10.1002/adma.201906652.
(37) Owuor, P. S.; Park, O. K.; Woellner, C. F.; Jalilov, A. S.; Susarla, S.; Joyner, J.; Ozden, S.; Duy, L.; Salvatierra, R. V.; Vajtai, R.; Tour, J. M.; Lou, J.; Galvão, D. S.; Tiwary, C. S.; Ajayan, P. M. Lightweight Hexagonal Boron Nitride Foam for CO_2 Absorption. *ACS Nano* **2017**, *11* (9), 8944–8952. https://doi.org/10.1021/acsnano.7b03291.
(38) Ashton, T. S.; Moore, A. L. Foam-like Hierarchical Hexagonal Boron Nitride as a Non-Traditional Thermal Conductivity Enhancer for Polymer-Based Composite Materials. *Int. J. Heat Mass Transf.* **2017**, *115*, 273–281. https://doi.org/10.1016/j.ijheatmasstransfer.2017.08.047.
(39) Pham, T.; Goldstein, A. P.; Lewicki, J. P.; Kucheyev, S. O.; Wang, C.; Russell, T. P.; Worsley, M. A.; Woo, L.; Mickelson, W.; Zettl, A. Nanoscale Structure and Superhydrophobicity of Sp^2-Bonded Boron Nitride Aerogels. *Nanoscale* **2015**, *7* (23), 10449–10458. https://doi.org/10.1039/c5nr01672j.
(40) Huang, H.; Shi, H.; Das, P.; Qin, J.; Li, Y. Y.; Wang, X.; Su, F.; Wen, P.; Li, S.; Lu, P.; Liu, F.; Li, Y. Y.; Zhang, Y.; Wang, Y.; Wu, Z.-S. Z.; Cheng, H.-M. H. The Chemistry and Promising Applications of Graphene and Porous Graphene Materials. *Adv. Funct. Mater.* **2020**, *30* (41), 1909035. https://doi.org/10.1002/adfm.201909035.
(41) Worsley, M. A.; Kucheyev, S. O.; Mason, H. E.; Merrill, M. D.; Mayer, B. P.; Lewicki, J.; Valdez, C. A.; Suss, M. E.; Stadermann, M.; Pauzauskie, P. J.; Jr, J. H. S.; Biener, J.; Baumann, T. F. Mechanically Robust 3D Graphene Macroassembly with High Surface Area. *Chem. Commun.* **2012**, 8428–8430. https://doi.org/10.1039/c2cc33979j.
(42) Worsley, M. A.; Charnvanichborikarn, S.; Montalvo, E.; Shin, S. J.; Tylski, E. D.; Lewicki, J. P.; Nelson, A. J.; Jr, J. H. S.; Biener, J.; Baumann, T. F.; Kucheyev, S. O. Toward Macroscale , Isotropic Carbons with Graphene- Sheet-Like Electrical and

Mechanical Properties. *Adv. Funct. Mater.* **2014**, 4259–4264. https://doi.org/10.1002/adfm.201400316.
(43) Witkowski, A.; Majkut, M.; Rulik, S. Analysis of Pipeline Transportation Systems for Carbon Dioxide Sequestration. *Arch. Thermodyn.* **2014**, *35* (1), 117–140. https://doi.org/10.2478/aoter-2014-0008.
(44) Moon, I. K.; Lee, J.; Ruoff, R. S.; Lee, H. Reduced Graphene Oxide by Chemical Graphitization. *Nat. Commun.* **2010**, *1* (6), 73. https://doi.org/10.1038/ncomms1067.
(45) Chen, W.; Yan, L. In Situ Self-Assembly of Mild Chemical Reduction Graphene for Three-Dimensional Architectures. *Nanoscale* **2011**, *3*, 3132–3137. https://doi.org/10.1039/c1nr10355e.
(46) Worsley, M. A.; Pham, T. T.; Yan, A.; Shin, S. J.; Lee, J. R. I.; Bagge-hansen, M.; Mickelson, W.; Zettl, A. Synthesis and Characterization of Highly Crystalline Graphene Aerogels. *ACS Nano* **2014**, No. 10, 11013–11022.
(47) Ming, W.; Bi, S.; Zhang, Y.; Yu, K.; Lu, C.; Fu, X.; Qiu, F.; Liu, P.; Su, Y.; Zhang, F. Bottom-Up Preparation of Fully Sp 2 -Bonded Porous Carbons with High Photoactivities. *Adv. Funct. Mater.* **2019**, *29* (14), 1808423. https://doi.org/10.1002/adfm.201808423.
(48) Yuen, S.; Ma, C. M.; Lin, Y.; Kuan, H. SCIENCE AND Preparation , Morphology and Properties of Acid and Amine Modified Multiwalled Carbon Nanotube / Polyimide Composite. **2007**, *67*, 2564–2573. https://doi.org/10.1016/j.compscitech.2006.12.006.
(49) Brunauer, S.; Emmett, P. H.; Teller, E. Adsorption of Gases in Multimolecular Layers. *J. Am. Chem. Soc.* **1938**, No. lc.
(50) Sing, K. S. W.; Everett, D. H.; Haul, R. A. W.; Moscou, L.; Pierotti, R. A.; Rouquerol, J.; Siemieniewska, T. Reporting Physisorption Data for Gas/Solid Systems with Special Reference to the Determination of Surface Area and Porosity. *Pure Appl. Chem.* **1985**, *57* (4), 603–619. https://doi.org/10.1351/pac198557040603.
(51) Pham, T.; Gibb, A. L.; Li, Z.; Gilbert, S. M.; Song, C.; Louie, S. G.; Zettl, A. Formation and Dynamics of Electron-Irradiation-Induced Defects in Hexagonal Boron Nitride at Elevated Temperatures. *Nano Lett.* **2016**, *16* (11), 7142–7147. https://doi.org/10.1021/acs.nanolett.6b03442.
(52) Alem, N.; Erni, R.; Kisielowski, C.; Rossell, M. D.; Hartel, P.; Jiang, B.; Gannett, W.; Zettl, A. Vacancy Growth and Migration Dynamics in Atomically Thin Hexagonal Boron Nitride under Electron Beam Irradiation. *Phys. Status Solidi - Rapid Res. Lett.* **2011**, *5* (8), 295–297. https://doi.org/10.1002/pssr.201105262.
(53) Guoxiu, W.; Juan, Y.; Jinsoo, P.; Xinglong, G.; Bei, W.; Hao, L.; Jane, Y. Facile Synthesis and Characterization of Graphene Nanosheets. *J. Phys. Chem. C* **2008**, *112* (22), 8192–8195. https://doi.org/10.1021/jp710931h.
(54) Eichler, J.; Lesniak, C. Boron Nitride (BN) and BN Composites for High-Temperature Applications. *J. Eur. Ceram. Soc.* **2008**, *28* (5), 1105–1109. https://doi.org/10.1016/j.jeurceramsoc.2007.09.005.
(55) Wu, K.; Wang, J.; Liu, D.; Lei, C.; Liu, D.; Lei, W.; Fu, Q. Highly Thermoconductive, Thermostable, and Super-Flexible Film by Engineering 1D Rigid Rod-Like Aramid Nanofiber/2D Boron Nitride Nanosheets. *Adv. Mater.* **2020**, 1906939. https://doi.org/10.1002/adma.201906939.
(56) Rousseas, M.; Goldstein, A. P.; Mickelson, W.; Worsley, M. A.; Woo, L.; Zettl, A. Synthesis of Highly Crystalline Sp^2-Bonded Boron Nitride Aerogels. *ACS Nano* **2013**, *7* (10), 8540–8546. https://doi.org/10.1021/nn402452p.

(57) Jiang, H.; Ma, L.; Yang, Q.; Tang, Z.; Song, X.; Zeng, H.; Zhi, C. Three-Dimensional Porous Boron Nitride Foam for Effective CO_2 Adsorption. *Solid State Commun.* **2019**, *294* (February), 1–5. https://doi.org/10.1016/j.ssc.2019.02.010.
(58) Bando, Y.; Golberg, D.; Mitome, M.; Kurashima, K.; Sato, T. C to BN Conversion in Multi-Walled Nanotubes as Revealed by Energy-Filtering Transmission Electron Microscopy. *Chem. Phys. Lett.* **2001**, *346* (1–2), 29–34. https://doi.org/10.1016/S0009-2614(01)00899-5.
(59) Han, W. Q.; Cumings, J.; Huang, X.; Bradley, K.; Zettl, A. Synthesis of Aligned $B_xC_yN_z$ Nanotubes by a Substitution-Reaction Route. *Chem. Phys. Lett.* **2001**, *346* (5–6), 368–372. https://doi.org/10.1016/S0009-2614(01)00993-9.
(60) Han, W.; Bando, Y.; Kurashima, K.; Sato, T. Synthesis of Boron Nitride Nanotubes from Carbon Nanotubes by a Substitution Reaction. *Appl. Phys. Lett.* **1998**, *73* (21), 3085–3087. https://doi.org/10.1063/1.122680.
(61) Han, W. Q.; Yu, H. G.; Liu, Z. Convert Graphene Sheets to Boron Nitride and Boron Nitride-Carbon Sheets via a Carbon-Substitution Reaction. *Appl. Phys. Lett.* **2011**, *98* (20). https://doi.org/10.1063/1.3593492.
(62) Han, W. Q.; Mickelson, W.; Cumings, J.; Zettl, A. Transformation of $B_xC_yN_z$ Nanotubes to Pure BN Nanotubes. *Appl. Phys. Lett.* **2002**, *81* (6), 1110–1112. https://doi.org/10.1063/1.1498494.
(63) Kagan, M. R.; McCreery, R. L. Reduction of Fluorescence Interference in Raman Spectroscopy via Analyte Adsorption on Graphitic Carbon. *Anal. Chem.* **1994**, *66* (23), 4159–4165. https://doi.org/10.1021/ac00095a008.
(64) Gutés, A.; Hsia, B.; Sussman, A.; Mickelson, W.; Zettl, A.; Carraro, C.; Maboudian, R. Graphene Decoration with Metal Nanoparticles: Towards Easy Integration for Sensing Applications. *Nanoscale* **2012**, *4* (2), 438–440. https://doi.org/10.1039/c1nr11537e.
(65) Yang, C.; Jiang, Q.; Li, W.; He, H.; Yang, L.; Lu, Z.; Huang, H. Ultrafine Pt Nanoparticle-Decorated 3D Hybrid Architectures Built from Reduced Graphene Oxide and MXene Nanosheets for Methanol Oxidation. *Chem. Mater.* **2019**, *23*. https://doi.org/10.1021/acs.chemmater.9b02115.
(66) Wu, J.; Liu, M.; Sharma, P. P.; Yadav, R. M.; Ma, L.; Yang, Y.; Zou, X.; Zhou, X. D.; Vajtai, R.; Yakobson, B. I.; Lou, J.; Ajayan, P. M. Incorporation of Nitrogen Defects for Efficient Reduction of CO_2 via Two-Electron Pathway on Three-Dimensional Graphene Foam. *Nano Lett.* **2016**, *16* (1), 466–470. https://doi.org/10.1021/acs.nanolett.5b04123.
(67) Perovic, M.; Qin, Q.; Oschatz, M. From Molecular Precursors to Nanoparticles—Tailoring the Adsorption Properties of Porous Carbon Materials by Controlled Chemical Functionalization. *Advanced Functional Materials*. Wiley-VCH Verlag October 9, 2020, p 1908371. https://doi.org/10.1002/adfm.201908371.
(68) Tian, W.; Zhang, H.; Duan, X.; Sun, H.; Shao, G.; Wang, S. Porous Carbons: Structure-Oriented Design and Versatile Applications. *Adv. Funct. Mater.* **2020**, 1909265. https://doi.org/10.1002/adfm.201909265.
(69) Xia, D.; Li, H.; Mannering, J.; Huang, P.; Zheng, X.; Kulak, A.; Baker, D.; Iruretagoyena, D.; Menzel, R. Electrically Heatable Graphene Aerogels as Nanoparticle Supports in Adsorptive Desulfurization and High-Pressure CO_2 Capture. *Adv. Funct. Mater.* **2020**, *30* (40), 2002788. https://doi.org/10.1002/adfm.202002788.
(70) Wu, Z. S.; Winter, A.; Chen, L.; Sun, Y.; Turchanin, A.; Feng, X.; Müllen, K. Three-Dimensional Nitrogen and Boron Co-Doped Graphene for High-Performance All-Solid-

State Supercapacitors. *Adv. Mater.* **2012**, *24* (37), 5130–5135. https://doi.org/10.1002/adma.201201948.
(71) Gong, Y.; Shi, G.; Zhang, Z.; Zhou, W.; Jung, J.; Gao, W.; Ma, L.; Yang, Y.; Yang, S.; You, G.; Vajtai, R.; Xu, Q.; Macdonald, A. H.; Yakobson, B. I.; Lou, J.; Liu, Z.; Ajayan, P. M. Direct Chemical Conversion of Graphene to Boron- and Nitrogen- and Carbon-Containing Atomic Layers. *Nat. Commun.* **2014**, *5*. https://doi.org/10.1038/ncomms4193.
(72) Putri, L. K.; Ng, B. J.; Ong, W. J.; Lee, H. W.; Chang, W. S.; Chai, S. P. Heteroatom Nitrogen- and Boron-Doping as a Facile Strategy to Improve Photocatalytic Activity of Standalone Reduced Graphene Oxide in Hydrogen Evolution. *ACS Appl. Mater. Interfaces* **2017**, *9* (5), 4558–4569. https://doi.org/10.1021/acsami.6b12060.
(73) Li, H.; Li, J.; Thomas, A.; Liao, Y. Ultra-High Surface Area Nitrogen-Doped Carbon Aerogels Derived From a Schiff-Base Porous Organic Polymer Aerogel for CO_2 Storage and Supercapacitors. *Adv. Funct. Mater.* **2019**, *29* (40), 1904785. https://doi.org/10.1002/adfm.201904785.
(74) Wu, J.; Pan, Z.; Zhang, Y.; Wang, B.; Peng, H. The Recent Progress of Nitrogen-Doped Carbon Nanomaterials for Electrochemical Batteries. *J. Mater. Chem. A* **2018**, *6* (27), 12932–12944. https://doi.org/10.1039/c8ta03968b.
(75) Lv, Q.; Si, W.; He, J.; Sun, L.; Zhang, C.; Wang, N.; Yang, Z.; Li, X.; Wang, X.; Deng, W.; Long, Y.; Huang, C.; Li, Y. Selectively Nitrogen-Doped Carbon Materials as Superior Metal-Free Catalysts for Oxygen Reduction. *Nat. Commun.* **2018**, *9* (1). https://doi.org/10.1038/s41467-018-05878-y.
(76) Xu, Y.; Deng, P.; Chen, G.; Chen, J.; Yan, Y.; Qi, K.; Liu, H.; Xia, B. Y. 2D Nitrogen-Doped Carbon Nanotubes/Graphene Hybrid as Bifunctional Oxygen Electrocatalyst for Long-Life Rechargeable Zn–Air Batteries. *Adv. Funct. Mater.* **2020**, *30* (6), 1906081. https://doi.org/10.1002/adfm.201906081.
(77) Inagaki, M.; Toyoda, M.; Soneda, Y.; Morishita, T. Nitrogen-Doped Carbon Materials. *Carbon*. Elsevier Ltd 2018, pp 104–140. https://doi.org/10.1016/j.carbon.2018.02.024.
(78) Zhu, J.; He, C.; Li, Y.; Kang, S.; Shen, P. K. One-Step Synthesis of Boron and Nitrogen-Dual-Self-Doped Graphene Sheets as Non-Metal Catalysts for Oxygen Reduction Reaction. *J. Mater. Chem. A* **2013**, *1* (46), 14700–14705. https://doi.org/10.1039/c3ta13318d.
(79) Sani, U.; Na'ibi, H. U.; Dailami, S. A. In Vitro Antimicrobial and Antioxidant Studies on N-(2- Hydroxylbenzylidene) Pyridine -2-Amine and Its M(II) Complexes. *Niger. J. Basic Appl. Sci.* **2018**, *25* (1), 81. https://doi.org/10.4314/njbas.v25i1.11.
(80) Zhao, J.; Ren, W.; Cheng, H. M. Graphene Sponge for Efficient and Repeatable Adsorption and Desorption of Water Contaminations. *J. Mater. Chem.* **2012**, *22* (38), 20197–20202. https://doi.org/10.1039/c2jm34128j.
(81) Inagaki, M.; Qiu, J.; Guo, Q. Carbon Foam: Preparation and Application. *Carbon*. Elsevier Ltd February 1, 2015, pp 128–152. https://doi.org/10.1016/j.carbon.2015.02.021.
(82) Sha, J.; Li, Y.; Villegas Salvatierra, R.; Wang, T.; Dong, P.; Ji, Y.; Lee, S. K.; Zhang, C.; Zhang, J.; Smith, R. H.; Ajayan, P. M.; Lou, J.; Zhao, N.; Tour, J. M. Three-Dimensional Printed Graphene Foams. *ACS Nano* **2017**, *11* (7), 6860–6867. https://doi.org/10.1021/acsnano.7b01987.
(83) Angizi, S.; Khalaj, M.; Alem, S. A. A.; Pakdel, A.; Willander, M.; Hatamie, A.; Simchi, A. Review—Towards the Two-Dimensional Hexagonal Boron Nitride (2D h-BN) Electrochemical Sensing Platforms. *J. Electrochem. Soc.* **2020**, *167* (12), 126513.

https://doi.org/10.1149/1945-7111/abaf29.
(84) Li, S.; Liu, F.; Su, Y.; Shao, N.; Yu, D.; Liu, Y.; Liu, W.; Zhang, Z. Luffa Sponge-Derived Hierarchical Meso/Macroporous Boron Nitride Fibers as Superior Sorbents for Heavy Metal Sequestration. *J. Hazard. Mater.* **2019**, *378* (October), 15–17. https://doi.org/10.1016/j.jhazmat.2019.05.062.
(85) Han, W. Q.; Brutchey, R.; Tilley, T. D.; Zettl, A. Activated Boron Nitride Derived from Activated Carbon. *Nano Lett.* **2004**, *4* (1), 173–176. https://doi.org/10.1021/nl034843a.
(86) Kozbial, A.; Zhou, F.; Li, Z.; Liu, H.; Li, L. Are Graphitic Surfaces Hydrophobic? *Acc. Chem. Res.* **2016**, *49* (12), 2765–2773. https://doi.org/10.1021/acs.accounts.6b00447.
(87) Shornikova, O. N.; Kogan, E. V.; Sorokina, N. E.; Avdeev, V. V. The Specific Surface Area and Porous Structure of Graphite Materials. *Russ. J. Phys. Chem. A* **2009**, *83* (6), 1022–1025. https://doi.org/10.1134/S0036024409060260.
(88) Chen, C.; Kennel, E. B.; Stiller, A. H.; Stansberry, P. G.; Zondlo, J. W. Carbon Foam Derived from Various Precursors. *Carbon N. Y.* **2006**, *44* (8), 1535–1543. https://doi.org/10.1016/j.carbon.2005.12.021.
(89) Alem, N.; Erni, R.; Kisielowski, C.; Rossell, M. D.; Gannett, W.; Zettl, A. Atomically Thin Hexagonal Boron Nitride Probed by Ultrahigh-Resolution Transmission Electron Microscopy. *Phys. Rev. B - Condens. Matter Mater. Phys.* **2009**, *80* (15), 1–7. https://doi.org/10.1103/PhysRevB.80.155425.
(90) Kim, K.; Lee, Z.; Malone, B. D.; Chan, K. T.; Alemán, B.; Regan, W.; Gannett, W.; Crommie, M. F.; Cohen, M. L.; Zettl, A. Multiply Folded Graphene. *Phys. Rev. B - Condens. Matter Mater. Phys.* **2011**, *83* (24), 245433. https://doi.org/10.1103/PhysRevB.83.245433.
(91) Singh, S. K.; Neek-Amal, M.; Costamagna, S.; Peeters, F. M. Thermomechanical Properties of a Single Hexagonal Boron Nitride Sheet. *Phys. Rev. B - Condens. Matter Mater. Phys.* **2013**, *87* (18), 1–7. https://doi.org/10.1103/PhysRevB.87.184106.
(92) Tsang, D. K. L.; Marsden, B. J.; Fok, S. L.; Hall, G. Graphite Thermal Expansion Relationship for Different Temperature Ranges. *Carbon N. Y.* **2005**, *43* (14), 2902–2906. https://doi.org/10.1016/j.carbon.2005.06.009.
(93) Thévenot, F. Boron Carbide-A Comprehensive Review. *J. Eur. Ceram. Soc.* **1990**, *6* (4), 205–225. https://doi.org/10.1016/0955-2219(90)90048-K.
(94) Zhang, W.; Yamashita, S.; Kita, H. Progress in Pressureless Sintering of Boron Carbide Ceramics–a Review. *Adv. Appl. Ceram.* **2019**, *118* (4), 222–239. https://doi.org/10.1080/17436753.2019.1574285.
(95) Perevislov, S. N.; Shcherbak, P. V.; Tomkovich, M. V. High Density Boron Carbide Ceramics. *Refract. Ind. Ceram.* **2018**, *59* (1), 32–36. https://doi.org/10.1007/s11148-018-0178-4.
(96) Domnich, V.; Reynaud, S.; Haber, R. A.; Chhowalla, M. Boron Carbide: Structure, Properties, and Stability under Stress. *J. Am. Ceram. Soc.* **2011**, *94* (11), 3605–3628. https://doi.org/10.1111/j.1551-2916.2011.04865.x.
(97) Suri, A. K.; Subramanian, C.; Sonber, J. K.; Ch Murthy, T. S. R. *Synthesis and Consolidation of Boron Carbide: A Review*; 2010; Vol. 55. https://doi.org/10.1179/095066009X12506721665211.
(98) Hayun, S.; Kalabukhov, S.; Ezersky, V.; Dariel, M. P.; Frage, N. Microstructural Characterization of Spark Plasma Sintered Boron Carbide Ceramics. *Ceram. Int.* **2010**, *36* (2), 451–457. https://doi.org/10.1016/j.ceramint.2009.09.004.

(99) Liu, T.; Luo, R.; Yoon, S. H.; Mochida, I. Anode Performance of Boron-Doped Graphites Prepared from Shot and Sponge Cokes. *J. Power Sources* **2010**, *195* (6), 1714–1719. https://doi.org/10.1016/j.jpowsour.2009.08.104.
(100) Wen, Z. H.; Han, Y. S.; Liang, L.; Li, J. B. Preparation of Porous Ceramics with Controllable Pore Sizes in an Easy and Low-Cost Way. *Mater. Charact.* **2008**, *59* (9), 1335–1338. https://doi.org/10.1016/j.matchar.2007.11.010.
(101) Lipp, A. Boron Carbide: Production, Properties, and Applications. *Tech. Rundschau* **1966**, *7*, 3–47.
(102) Yang, Z.; Zheng, Q.; Qiu, H.; LI, J.; Yang, J. A Simple Method for the Reduction of Graphene Oxide by Sodium Borohydride with CaCl2 as a Catalyst. *New Carbon Mater.* **2015**, *30* (1), 41–47. https://doi.org/10.1016/S1872-5805(15)60174-3.
(103) Eremeeva, Z. V.; Myakisheva, L. V.; Panov, V. S.; Lizunov, A. V.; Nepapushev, A. A.; Sidorenko, D. A.; Apostolova, E. V.; Mishunin, D. Y. Structure and Properties of the Boron Carbide Powder Obtained by the Mechanochemical Synthesis of the Carbon Char and Amorphous Boron Mix. *Inorg. Mater. Appl. Res.* **2019**, *10* (1), 49–52. https://doi.org/10.1134/S2075113319010088.
(104) Asadabad, M. A.; Eskandari, M. J. Transmission Electron Microscopy as Best Technique for Characterization in Nanotechnology. *Synth. React. Inorganic, Met. Nano-Metal Chem.* **2015**, *45* (3), 323–326. https://doi.org/10.1080/15533174.2013.831901.
(105) Yuan, L.; Wang, Y.; Cai, R.; Jiang, Q.; Wang, J.; Li, B.; Sharma, A.; Zhou, G. The Origin of Hematite Nanowire Growth during the Thermal Oxidation of Iron. *Mater. Sci. Eng. B Solid-State Mater. Adv. Technol.* **2012**, *177* (3), 327–336. https://doi.org/10.1016/j.mseb.2011.12.034.
(106) Hayun, S.; Weizmann, A.; Dariel, M. P.; Frage, N. Microstructural Evolution during the Infiltration of Boron Carbide with Molten Silicon. *J. Eur. Ceram. Soc.* **2010**, *30* (4), 1007–1014. https://doi.org/10.1016/j.jeurceramsoc.2009.09.021.
(107) Sun, Y.; Meng, Q.; Qian, M.; Liu, B.; Gao, K.; Ma, Y.; Wen, M.; Zheng, W. Enhancement of Oxidation Resistance via a Self-Healing Boron Carbide Coating on Diamond Particles. *Sci. Rep.* **2016**, *6* (February). https://doi.org/10.1038/srep20198.
(108) Azevedo, S.; De Paiva, R. Structural Stability and Electronic Properties of Carbon-Boron Nitride Compounds. *Europhys. Lett.* **2006**, *75* (1), 126–132. https://doi.org/10.1209/epl/i2006-10066-0.
(109) Manzeli, S.; Ovchinnikov, D.; Pasquier, D.; Yazyev, O. V.; Kis, A. 2D Transition Metal Dichalcogenides. *Nat. Rev. Mater.* **2017**, *2* (8), 17033. https://doi.org/10.1038/natrevmats.2017.33.
(110) Dai, J.; Li, M.; Zeng, X. C. Group IVB Transition Metal Trichalcogenides: A New Class of 2D Layered Materials beyond Graphene. *Wiley Interdiscip. Rev. Comput. Mol. Sci.* **2016**, *6* (2), 211–222. https://doi.org/10.1002/wcms.1243.
(111) Zhou, X.; Rodriguez, E. E. Tetrahedral Transition Metal Chalcogenides as Functional Inorganic Materials. *Chem. Mater.* **2017**, *29* (14), 5737–5752. https://doi.org/10.1021/acs.chemmater.7b01561.
(112) Kertesz, M.; Hoffmann, R. Octahedral vs. Trigonal-Prismatic Coordination and Clustering in Transition-Metal Dichalcogenides. *J. Am. Chem. Soc.* **1984**, *106* (12), 3453–3460. https://doi.org/10.1021/ja00324a012.
(113) Al-Hilli, A. A.; Evans, B. L. The Preparation and Properties of Transition Metal Dichalcogenide Single Crystals. *J. Cryst. Growth* **1972**, *15* (2), 93–101.

https://doi.org/10.1016/0022-0248(72)90129-7.
(114) Lévy, F.; Berger, H. Single Crystals of Transition Metal Trichalcogenides. *J. Cryst. Growth* **1983**, *61* (1), 61–68. https://doi.org/10.1016/0022-0248(83)90279-8.
(115) Lee, Y. H.; Zhang, X. Q.; Zhang, W.; Chang, M. T.; Lin, C. Te; Chang, K. Di; Yu, Y. C.; Wang, J. T. W.; Chang, C. S.; Li, L. J.; Lin, T. W. Synthesis of Large-Area MoS 2 Atomic Layers with Chemical Vapor Deposition. *Adv. Mater.* **2012**, *24* (17), 2320–2325. https://doi.org/10.1002/adma.201104798.
(116) Magda, G. Z.; Petõ, J.; Dobrik, G.; Hwang, C.; Biró, L. P.; Tapasztó, L. Exfoliation of Large-Area Transition Metal Chalcogenide Single Layers. *Sci. Rep.* **2015**, *5*, 3–7. https://doi.org/10.1038/srep14714.
(117) Roldán, R.; Castellanos-Gomez, A.; Cappelluti, E.; Guinea, F. Strain Engineering in Semiconducting Two-Dimensional Crystals. *J. Phys. Condens. Matter* **2015**, *27* (31). https://doi.org/10.1088/0953-8984/27/31/313201.
(118) Aminalragia-Giamini, S.; Marquez-Velasco, J.; Tsipas, P.; Tsoutsou, D.; Renaud, G.; Dimoulas, A. Molecular Beam Epitaxy of Thin $HfTe_2$ Semimetal Films. *2D Mater.* **2017**, *4* (1). https://doi.org/10.1088/2053-1583/4/1/015001.
(119) Chhowalla, M.; Shin, H. S.; Eda, G.; Li, L. J.; Loh, K. P.; Zhang, H. The Chemistry of Two-Dimensional Layered Transition Metal Dichalcogenide Nanosheets. *Nature Chemistry*. 2013, pp 263–275. https://doi.org/10.1038/nchem.1589.
(120) Furchi, M. M.; Polyushkin, D. K.; Pospischil, A.; Mueller, T. Mechanisms of Photoconductivity in Atomically Thin MoS2. *Nano Lett.* **2014**, *14* (11), 6165–6170. https://doi.org/10.1021/nl502339q.
(121) Bruix, A.; Füchtbauer, H. G.; Tuxen, A. K.; Walton, A. S.; Andersen, M.; Porsgaard, S.; Besenbacher, F.; Hammer, B.; Lauritsen, J. V. *In Situ* Detection of Active Edge Sites in Single-Layer MoS_2 Catalysts. *ACS Nano* **2015**, *9* (9), 9322–9330. https://doi.org/10.1021/acsnano.5b03199.
(122) Somoano, R. B.; Hadek, V.; Rembaum, A.; Somoano, R. B.; Hadek, V.; Rembaum, A. Alkali Metal Intercalates of Molybdenum Disulfide. **1973**, *58*. https://doi.org/10.1063/1.1679256.
(123) Cullen, P. L.; Cox, K. M.; Subhan, M. K. Bin; Picco, L.; Payton, O. D.; Buckley, D. J.; Miller, T. S.; Hodge, S. A.; Skipper, N. T.; Tileli, V.; Howard, C. A. Ionic Solutions of Two-Dimensional Materials. *Nat. Chem.* **2016**, *9* (3), 244–249. https://doi.org/10.1038/nchem.2650.
(124) Guo, Y.; Sun, D.; Ouyang, B.; Raja, A.; Song, J.; Heinz, T. F.; Brus, L. E. Probing the Dynamics of the Metallic-to-Semiconducting Structural Phase Transformation in MoS2 Crystals. *Nano Lett.* **2015**, *15* (8), 5081–5088. https://doi.org/10.1021/acs.nanolett.5b01196.
(125) Acerce, M.; Voiry, D.; Chhowalla, M. Metallic 1T Phase MoS2 Nanosheets as Supercapacitor Electrode Materials. *Nat. Nanotechnol.* **2015**, *10* (4), 313–318. https://doi.org/10.1038/nnano.2015.40.
(126) Chang, K.; Hai, X.; Pang, H.; Zhang, H.; Shi, L.; Liu, G.; Liu, H.; Zhao, G.; Li, M.; Ye, J. Targeted Synthesis of 2H- and 1T-Phase MoS2Monolayers for Catalytic Hydrogen Evolution. *Adv. Mater.* **2016**, *28* (45), 10033–10041. https://doi.org/10.1002/adma.201603765.
(127) Scott, R. A.; Jacobson, A. J.; Chianelli, R. R.; Pan, W.; Stiefel, E. I.; Hodgson, K. O.; Cramer, S. P. Reactions of MoS3, WS3, WSe3, and NbSe3 with Lithium. Metal Cluster

Rearrangement Revealed by EXAFS. *Inorg. Chem.* **1986**, *25*, 1461–1466.
(128) Island, J. O.; Molina-Mendoza, A. J.; Barawi, M.; Biele, R.; Flores, E.; Clamagirand, J. M.; Ares, J. R.; Sánchez, C.; Van Der Zant, H. S. J.; D'Agosta, R.; Ferrer, I. J.; Castellanos-Gomez, A. Electronics and Optoelectronics of Quasi-1D Layered Transition Metal Trichalcogenides. *2D Mater.* **2017**, *4* (2). https://doi.org/10.1088/2053-1583/aa6ca6.
(129) Li, J.; Peng, J.; Zhang, S.; Chen, G. Anisotropic Multichain Nature and Filamentary Superconductivity in the Charge Density Wave System HfTe3. *Phys. Rev. B* **2017**, *96* (17), 1–8. https://doi.org/10.1103/PhysRevB.96.174510.
(130) Hoffmann, R. How Chemistry and Physics Meet in the Solid State. *Angew. Chemie Int. Ed. English* **1987**, *26* (1), 846–878. https://doi.org/10.1521/00332747.1992.11024571.
(131) Wang, Y.; Xiao, J.; Zhu, H.; Li, Y.; Alsaid, Y.; Fong, K. Y.; Zhou, Y.; Wang, S.; Shi, W.; Wang, Y.; Zettl, A.; Reed, E. J.; Zhang, X. Structural Phase Transition in Monolayer MoTe2 Driven by Electrostatic Doping. *Nature* **2017**. https://doi.org/10.1038/nature24043.
(132) Jiang, L.; Zhang, S.; Kulinich, S. A.; Song, X.; Zhu, J.; Wang, X.; Zeng, H. Optimizing Hybridization of 1T and 2H Phases in MoS2 Monolayers to Improve Capacitances of Supercapacitors. *Mater. Res. Lett.* **2015**, *3* (4), 177–183. https://doi.org/10.1080/21663831.2015.1057654.
(133) Li, Y.; Wang, H.; Xie, L.; Liang, Y.; Hong, G.; Dai, H. MoS2 Nanoparticles Grown on Graphene: An Advanced Catalyst for the Hydrogen Evolution Reaction. *J. Am. Chem. Soc.* **2011**, *133* (19), 7296–7299. https://doi.org/10.1021/ja201269b.
(134) Tsai, M. L.; Su, S. H.; Chang, J. K.; Tsai, D. S.; Chen, C. H.; Wu, C. I.; Li, L. J.; Chen, L. J.; He, J. H. Monolayer MoS2 Heterojunction Solar Cells. *ACS Nano* **2014**, *8* (8), 8317–8322. https://doi.org/10.1021/nn502776h.
(135) Zhou, X.; Prikryl, J.; Krbal, M.; Macak, J. M.; Schmuki, P. Electrochemistry Communications Molybdenum Dichalcogenide Nanotube Arrays for Hydrogen-Evolution- Reaction Catalysis : Synergistic e Ff Ects of Sulfur and Selenium in a Core-Shell Tube Wall. *Electrochem. commun.* **2017**, *82* (August), 112–116. https://doi.org/10.1016/j.elecom.2017.08.004.
(136) Janisch, C.; Song, H.; Zhou, C.; Lin, Z.; Elías, A. L.; Ji, D.; Terrones, M.; Gan, Q.; Liu, Z. MoS 2 Monolayers on Nanocavities: Enhancement in Light–Matter Interaction. *2D Mater.* **2016**, *3* (2), 025017. https://doi.org/10.1088/2053-1583/3/2/025017.
(137) Mak, K. F.; Lee, C.; Hone, J.; Shan, J.; Heinz, T. F. Atomically Thin MoS_2: A New Direct-Gap Semiconductor. *Phys. Rev. Lett.* **2010**, *105* (13), 2–5. https://doi.org/10.1103/PhysRevLett.105.136805.
(138) Splendiani, A.; Sun, L.; Zhang, Y.; Li, T.; Kim, J.; Chim, C. Y.; Galli, G.; Wang, F. Emerging Photoluminescence in Monolayer MoS_2. *Nano Lett.* **2010**, *10* (4), 1271–1275. https://doi.org/10.1021/nl903868w.
(139) Onishi, S.; Jamei, M.; Zettl, A. Narrowband Noise Study of Sliding Charge Density Waves in $NbSe_3$ Nanoribbons. *New J. Phys.* **2017**, *19* (2). https://doi.org/10.1088/1367-2630/aa5912.
(140) Gately, R. D.; In het Panhuis, M. Filling of Carbon Nanotubes and Nanofibres. *Beilstein J. Nanotechnol.* **2015**, *6* (1), 508–516. https://doi.org/10.3762/bjnano.6.53.
(141) Pham, T.; Fathalizadeh, A.; Shevitski, B.; Turner, S.; Aloni, S.; Zettl, A. A Universal Wet-Chemistry Route to Metal Filling of Boron Nitride Nanotubes. *Nano Lett.* **2016**, *16* (1),

320–325. https://doi.org/10.1021/acs.nanolett.5b03874.
(142) Sloan, J.; Wright, D. M.; Bailey, S.; Brown, G.; York, A. P. E.; Coleman, K. S.; Green, M. L. H.; Sloan, J.; Wright, D. M.; Hutchison, J. L.; Woo, H.-G. Capillarity and Silver Nanowire Formation Observed in Single Walled Carbon Nanotubes. *Chem. Commun.* **1999**, No. 8, 699–700. https://doi.org/10.1039/a901572h.
(143) Chancolon, J.; Archaimbault, F.; Pineau, A.; Bonnamy, S. Filling of Carbon Nanotubes with Selenium by Vapor Phase Process. *J. Nanosci. Nanotechnol.* **2006**, *6* (1), 82–86. https://doi.org/10.1166/jnn.2006.17908.
(144) Pham, T.; Oh, S.; Stetz, P.; Onishi, S.; Kisielowski, C.; Cohen, M. L.; Zettl, A. Torsional Instability in the Single-Chain Limit of a Transition Metal Trichalcogenide. *Science (80-.).* **2018**, *361* (July), 263–266.
(145) Zhang, X. Characterization of Microstructures by Transmission Electron Microscopy. *Wang Q.J., Chung YW. (eds) Encyclopedia of Tribology*; 2013; pp 1–10.
(146) Li, W.; Ni, C. Electron Energy Loss Spectroscopy (EELS). *Wang Q.J., Chung YW. (eds) Encyclopedia of Tribology*; 2013; pp 940–945.
(147) Ahn, C. C. *Transmission Electron Energy Loss Spectrometry in Materials Science and The EELS Atlas*; Ahn, C. C., Ed.; Wiley, 2004. https://doi.org/10.1002/3527605495.
(148) Srivastava, S. K.; Avasthi, B. N. Preparation, Structure and Properties of Transition Metal Trichalcogenides. *J. Mater. Sci.* **1992**, *27* (14), 3693–3705. https://doi.org/10.1007/BF00545445.
(149) Brattas, Leif; Kjekshus, A. The Non-Metal Rich Region of the Hf-Te System. *Acta Chem. Scand.* **1971**, *25* (7), 2783–2784.
(150) Brattas, L.; Kjekshus, A. On the Properties of Compounds with the ZrSe3 Type Structure. *Acta Chemica Scandinavica*. 1972, pp 3441–3449. https://doi.org/10.3891/acta.chem.scand.26-3441.
(151) Denholme, S. J.; Yukawa, A.; Tsumura, K.; Nagao, M.; Tamura, R.; Watauchi, S.; Tanaka, I.; Takayanagi, H.; Miyakawa, N. Supplemental_Coexistence of Superconductivity and Charge-Density Wave in the Quasi-One-Dimensional Material HfTe3. *Sci. Rep.* **2017**, *7* (1987), 1–6. https://doi.org/10.1038/srep45217.
(152) Perdew, J. P.; Burke, K.; Ernzerhof, M. Generalized Gradient Approximation Made Simple. *Phys. Rev. Lett.* **1996**, *77* (18), 3865–3868. https://doi.org/10.1103/PhysRevLett.77.3865.
(153) Troullier, N.; Martins, J. L. Efficient Pseudopotentials for Plane-Wave Calculations. *Phys. Rev. B* **1991**, *43* (3), 1993–2006. https://doi.org/10.1103/PhysRevB.43.1993.
(154) Soler, J. M.; Artacho, E.; Gale, J. D.; García, A.; Junquera, J.; Ordejón, P.; Sánchez-Portal, D. The SIESTA Method for *Ab Initio* Order- *N* Materials Simulation. *J. Phys. Condens. Matter* **2002**, *14* (11), 2745–2779. https://doi.org/10.1088/0953-8984/14/11/302.
(155) Kleinman, L. Relativistic Norm-Conserving Pseudopotential. *Phys. Rev. B* **1980**, *21* (6), 2630–2631. https://doi.org/10.1103/PhysRevB.21.2630.
(156) Theurich, G.; Hill, N. A. Self-Consistent Treatment of Spin-Orbit Coupling in Solids Using Relativistic Fully Separable *Ab Initio* Pseudopotentials. *Phys. Rev. B* **2001**, *64* (7), 073106. https://doi.org/10.1103/PhysRevB.64.073106.
(157) Kleinman, L.; Bylander, D. M. Efficacious Form for Model Pseudopotentials. *Phys. Rev. Lett.* **1982**, *48* (20), 1425–1428. https://doi.org/10.1103/PhysRevLett.48.1425.
(158) Grimme, S. Semiempirical GGA-Type Density Functional Constructed with a Long-Range Dispersion Correction. *J. Comput. Chem.* **2006**, *27* (15), 1787–1799.

https://doi.org/10.1002/jcc.20495.
(159) Cohen, M. L.; Schlüter, M.; Chelikowsky, J. R.; Louie, S. G. Self-Consistent Pseudopotential Method for Localized Configurations: Molecules. *Phys. Rev. B* **1975**, *12* (12), 5575–5579. https://doi.org/10.1103/PhysRevB.12.5575.
(160) RadisavljevicB; RadenovicA; BrivioJ; GiacomettiV; KisA; Radisavljevic, B.; Radenovic, A.; Brivio, J.; Giacometti, V.; Kis, A. Single-Layer MoS2 Transistors. *Nat Nano* **2011**, *6* (3), 147–150. https://doi.org/http://www.nature.com/nnano/journal/v6/n3/abs/nnano.2010.279.html#supplementary-information.
(161) Lopez-Sanchez, O.; Lembke, D.; Kayci, M.; Radenovic, A.; Kis, A. Ultrasensitive Photodetectors Based on Monolayer MoS2. *Nat. Nanotechnol.* **2013**, *8* (7), 497–501. https://doi.org/10.1038/nnano.2013.100.
(162) Dolui, K.; Pemmaraju, C. Das; Sanvito, S. Electric Field Effects on Armchair MoS_2 Nanoribbons. *ACS Nano* **2012**, *6* (6), 4823–4834. https://doi.org/10.1021/nn301505x.
(163) Meyer, S.; Pham, T.; Oh, S.; Ercius, P.; Kisielowski, C.; Cohen, M. L.; Zettl, A. Metal-Insulator Transition in Quasi-One-Dimensional $HfTe_3$ in the Few-Chain Limit. *Phys. Rev. B* **2019**, *100* (4), 041403. https://doi.org/10.1103/PhysRevB.100.041403.
(164) Denholme, S. J.; Yukawa, A.; Tsumura, K.; Nagao, M.; Tamura, R.; Watauchi, S.; Tanaka, I.; Takayanagi, H.; Miyakawa, N. Coexistence of Superconductivity and Charge-Density Wave in the Quasi-One-Dimensional Material $HfTe_3$. *Sci. Rep.* **2017**, *7* (March), 1–6. https://doi.org/10.1038/srep45217.
(165) Xiong, W. W.; Chen, J. Q.; Wu, X. C.; Zhu, J. J. Visible Light Detectors Based on Individual $ZrSe_3$ and $HfSe_3$ Nanobelts. *J. Mater. Chem. C* **2015**, *3* (9), 1929–1934. https://doi.org/10.1039/c4tc02492c.
(166) Xiong, W. W.; Chen, J. Q.; Wu, X. C.; Zhu, J. J. Individual HfS_3 Nanobelt for Field-Effect Transistor and High Performance Visible-Light Detector. *J. Mater. Chem. C* **2014**, *2* (35), 7392–7395. https://doi.org/10.1039/c4tc01039f.
(167) Li, M.; Dai, J.; Zeng, X. C. Tuning the Electronic Properties of Transition-Metal Trichalcogenides via Tensile Strain. *Nanoscale* **2015**, *7* (37), 15385–15391. https://doi.org/10.1039/c5nr04505c.
(168) Liu, S.; Xiao, W.; Zhong, M.; Pan, L.; Wang, X.; Deng, H. X.; Liu, J.; Li, J.; Wei, Z. Highly Polarization Sensitive Photodetectors Based on Quasi-1D Titanium Trisulfide (TiS_3). *Nanotechnology* **2018**, *29* (18). https://doi.org/10.1088/1361-6528/aaafa2.
(169) Jin, Y.; Li, X.; Yang, J. Single Layer of MX3 (M = Ti, Zr; X = S, Se, Te): A New Platform for Nano-Electronics and Optics. *Phys. Chem. Chem. Phys.* **2015**, *17* (28), 18665–18669. https://doi.org/10.1039/c5cp02813b.
(170) Geremew, A.; Bloodgood, M. A.; Aytan, E.; Woo, B. W. K.; Corber, S. R.; Liu, G.; Bozhilov, K.; Salguero, T. T.; Rumyantsev, S.; Rao, M. P.; Balandin, A. A. Current Carrying Capacity of Quasi-1D ZrTe3 Van Der Waals Nanoribbons. *IEEE Electron Device Lett.* **2018**, *39* (5), 735–738. https://doi.org/10.1109/LED.2018.2820140.
(171) Ubaldini, A.; Jacimovic, J.; Ubrig, N.; Giannini, E. Chloride-Driven Chemical Vapor Transport Method for Crystal Growth of Transition Metal Dichalcogenides. *Cryst. Growth Des.* **2013**, *13* (10), 4453–4459. https://doi.org/10.1021/cg400953e.
(172) Wang, D.; Luo, F.; Lu, M.; Xie, X.; Huang, L.; Huang, W. Chemical Vapor Transport Reactions for Synthesizing Layered Materials and Their 2D Counterparts. *Small* **2019**, *15* (40), 1–12. https://doi.org/10.1002/smll.201804404.

(173) Lee, C.; Yan, H.; Brus, L.; Heinz, T.; Hone, J.; Ryu, S. Anomalous Lattice Vibrations of Single-and Few-Layer MoS2. *ACS Nano* **2010**, *4* (5), 2695–2700. https://doi.org/10.1021/nn1003937.
(174) Heeg, S.; Shi, L.; Pichler, T.; Novotny, L. Raman Resonance Profile of an Individual Confined Long Linear Carbon Chain. *Carbon N. Y.* **2018**, *139*, 581–585. https://doi.org/10.1016/j.carbon.2018.07.007.
(175) Heeg, S.; Shi, L.; Poulikakos, L. V.; Pichler, T.; Novotny, L. Carbon Nanotube Chirality Determines Properties of Encapsulated Linear Carbon Chain. *Nano Lett.* **2018**, *18* (9), 5426–5431. https://doi.org/10.1021/acs.nanolett.8b01681.
(176) Tschannen, C. D.; Gordeev, G.; Reich, S.; Shi, L.; Pichler, T.; Frimmer, M.; Novotny, L.; Heeg, S. Raman Scattering Cross Section of Confined Carbyne. *Nano Lett.* **2020**, *20* (9), 6750–6755. https://doi.org/10.1021/acs.nanolett.0c02632.
(177) Zhu, X.; Ning, W.; Li, L.; Ling, L.; Zhang, R.; Zhang, J.; Wang, K.; Liu, Y.; Pi, L.; Ma, Y.; Du, H.; Tian, M.; Sun, Y.; Petrovic, C.; Zhang, Y. Superconductivity and Charge Density Wave in ZrTe3-XSex. *Sci. Rep.* **2016**, *6*, 1–7. https://doi.org/10.1038/srep26974.
(178) Debnath, T.; Debnath, B.; Lake, R. K. Thermal Conductivity of the Quasi-1D Materials TaSe3 and ZrTe3. *Phys. Rev. Mater.* **2021**, 1–15.
(179) Simpson, J. R.; Roslyak, O.; Duque, J. G.; Hároz, E. H.; Crochet, J. J.; Telg, H.; Piryatinski, A.; Walker, A. R. H.; Doorn, S. K. Resonance Raman Signature of Intertube Excitons in Compositionally-Defined Carbon Nanotube Bundles. *Nat. Commun.* **2018**, *9* (1). https://doi.org/10.1038/s41467-018-03057-7.
(180) Bolotin, K. I.; Ghahari, F.; Shulman, M. D.; Stormer, H. L.; Kim, P. Observation of the Fractional Quantum Hall Effect in Graphene. *Nature* **2009**, *462* (7270), 196–199. https://doi.org/10.1038/nature08582.
(181) Novoselov, K. S.; Jiang, D.; Schedin, F.; Booth, T. J.; Khotkevich, V. V.; Morozov, S. V.; Geim, A. K. Two-Dimensional Atomic Crystals. *Proc. Natl. Acad. Sci. U. S. A.* **2005**, *102* (30), 10451–10453. https://doi.org/10.1073/pnas.0502848102.
(182) Nakata, Y.; Sugawara, K.; Chainani, A.; Yamauchi, K.; Nakayama, K.; Souma, S.; Chuang, P. Y.; Cheng, C. M.; Oguchi, T.; Ueno, K.; Takahashi, T.; Sato, T. Dimensionality Reduction and Band Quantization Induced by Potassium Intercalation in 1T-HfTe2. *Phys. Rev. Mater.* **2019**, *3* (7), 071001. https://doi.org/10.1103/PhysRevMaterials.3.071001.
(183) Nagata, M.; Shukla, S.; Nakanishi, Y.; Liu, Z.; Lin, Y. C.; Shiga, T.; Nakamura, Y.; Koyama, T.; Kishida, H.; Inoue, T.; Kanda, N.; Ohno, S.; Sakagawa, Y.; Suenaga, K.; Shinohara, H. Isolation of Single-Wired Transition-Metal Monochalcogenides by Carbon Nanotubes. *Nano Lett.* **2019**, *19* (8), 4845–4851. https://doi.org/10.1021/acs.nanolett.8b05074.
(184) Sato, M. Elastic and Plastic Deformation of Carbon Nanotubes. *Procedia Eng.* **2011**, *14*, 2366–2372. https://doi.org/10.1016/j.proeng.2011.07.298.
(185) Oh, S.; Choi, H. J. Orbital Angular Momentum Analysis for Giant Spin Splitting in Solids and Nanostructures. *Sci. Rep.* **2017**, *7* (1), 1–10. https://doi.org/10.1038/s41598-017-02032-4.
(186) Park, S. R.; Han, J.; Kim, C.; Koh, Y. Y.; Kim, C.; Lee, H.; Choi, H. J.; Han, J. H.; Lee, K. D.; Hur, N. J.; Arita, M.; Shimada, K.; Namatame, H.; Taniguchi, M. Chiral Orbital-Angular Momentum in the Surface States of Bi_2Se_3. *Phys. Rev. Lett.* **2012**, *108* (4), 1–5. https://doi.org/10.1103/PhysRevLett.108.046805.

(187) Manchon, A.; Koo, H. C.; Nitta, J.; Frolov, S. M.; Duine, R. A. New Perspectives for Rashba Spin – Orbit Coupling. *Nat. Publ. Gr.* **2015**, *14* (August), 871–882. https://doi.org/10.1038/nmat4360.
(188) Bihlmayer, G.; Rader, O.; Winkler, R. Focus on the Rashba Effect. *New J. Phys.* **2015**, *17* (5). https://doi.org/10.1088/1367-2630/17/5/050202.
(189) Gong, S. H.; Alpeggiani, F.; Sciacca, B.; Garnett, E. C.; Kuipers, L. Nanoscale Chiral Valley-Photon Interface through Optical Spin-Orbit Coupling. *arXiv* **2017**, *447* (January), 443–447.
(190) Jin, C.; Kim, J.; Iqbal Bakti Utama, M.; Regan, E. C.; Kleemann, H.; Cai, H.; Shen, Y.; Shinner, M. J.; Sengupta, A.; Watanabe, K.; Taniguchi, T.; Tongay, S.; Zettl, A.; Wang, F. Imaging of Pure Spin-Valley Diffusion Current in WS_2-WSe_2 Heterostructures. *Science (80-.).* **2018**, *360* (6391), 893–896. https://doi.org/10.1126/science.aao3503.
(191) Mulliken, R. S. Electronic Population Analysis on LCAO-MO Molecular Wave Functions. I. *J. Chem. Phys.* **1955**, *23* (10), 1833–1840. https://doi.org/10.1063/1.1740588.
(192) Hasan, M. Z.; Kane, C. L. Colloquium: Topological Insulators. *Rev. Mod. Phys.* **2010**, *82* (4), 3045–3067. https://doi.org/10.1103/RevModPhys.82.3045.
(193) Bradlyn, B.; Elcoro, L.; Cano, J.; Vergniory, M. G.; Wang, Z.; Felser, C.; Aroyo, M. I.; Bernevig, B. A. Topological Quantum Chemistry. *Nature* **2017**, *547* (7663), 298–305. https://doi.org/10.1038/nature23268.
(194) Cao, T.; Zhao, F.; Louie, S. G. Topological Phases in Graphene Nanoribbons: Junction States, Spin Centers, and Quantum Spin Chains. *Phys. Rev. Lett.* **2017**, *119* (7), 1–5. https://doi.org/10.1103/PhysRevLett.119.076401.
(195) Rizzo, D. J.; Veber, G.; Cao, T.; Bronner, C.; Chen, T.; Zhao, F.; Rodriguez, H.; Louie, S. G.; Crommie, M. F.; Fischer, F. R. Topological Band Engineering of Graphene Nanoribbons. *Nature* **2018**, *560* (7717), 204–208. https://doi.org/10.1038/s41586-018-0376-8.
(196) Delplace, P.; Ullmo, D.; Montambaux, G. Zak Phase and the Existence of Edge States in Graphene. *Phys. Rev. B - Condens. Matter Mater. Phys.* **2011**, *84* (19), 1–13. https://doi.org/10.1103/PhysRevB.84.195452.
(197) Fu, L.; Kane, C. L. Topological Insulators with Inversion Symmetry. *Phys. Rev. B - Condens. Matter Mater. Phys.* **2007**, *76* (4), 1–17. https://doi.org/10.1103/PhysRevB.76.045302.
(198) Zak, J. Berrys Phase for Energy Bands in Solids. *Phys. Rev. Lett.* **1989**, *62* (23), 2747–2750. https://doi.org/10.1103/PhysRevLett.62.2747.
(199) Lau, A.; Van Den Brink, J.; Ortix, C. Topological Mirror Insulators in One Dimension. *Phys. Rev. B* **2016**, *94* (16), 1–9. https://doi.org/10.1103/PhysRevB.94.165164.
(200) Van Miert, G.; Ortix, C. Excess Charges as a Probe of One-Dimensional Topological Crystalline Insulating Phases. *Phys. Rev. B* **2017**, *96* (23), 1–12. https://doi.org/10.1103/PhysRevB.96.235130.
(201) Lee, H. S.; Park, S.; Lim, J. Y.; Yu, S.; Ahn, J.; Hwang, D. K.; Sim, Y.; Lee, J. H.; Seong, M. J.; Oh, S.; Choi, H. J.; Im, S. Impact of H-Doping on n-Type TMD Channels for Low-Temperature Band-Like Transport. *Small* **2019**, *15* (38), 1–8. https://doi.org/10.1002/smll.201901793.
(202) Oh, S.; Lim, J. Y.; Im, S.; Choi, H. J. Stability, Efficiency, and Mechanism of n -Type Doping by Hydrogen Adatoms in Two-Dimensional Transition Metal Dichalcogenides.

Phys. Rev. B **2019**, *100* (8), 85416. https://doi.org/10.1103/PhysRevB.100.085416.
(203) Oh, S.; Crommie, M. F.; Cohen, M. L. Simulating the Nanomechanical Response of Cyclooctatetraene Molecules on a Graphene Device. *ACS Nano* **2019**, *13* (2), 1713–1718. https://doi.org/10.1021/acsnano.8b07781.
(204) Novoselov, K. S.; Geim, A. K.; Morozov, S. V.; Jiang, D.; Katsnelson, M. I.; Grigorieva, I. V.; Dubonos, S. V.; Firsov, A. A. Two-Dimensional Gas of Massless Dirac Fermions in Graphene. *Nature* **2005**, *438* (7065), 197–200. https://doi.org/10.1038/nature04233.
(205) Yang, B.; Liu, F.; Lagally, M. G. Local Strain-Mediated Chemical Potential Control of Quantum Dot Self-Organization in Heteroepitaxy. *Phys. Rev. Lett.* **2004**, *92* (2), 4. https://doi.org/10.1103/PhysRevLett.92.025502.
(206) Fu, L. Topological Crystalline Insulators. *Phys. Rev. Lett.* **2011**, *106* (10), 1–4. https://doi.org/10.1103/PhysRevLett.106.106802.
(207) Ando, Y.; Fu, L. Topological Crystalline Insulators and Topological Superconductors: From Concepts to Materials. *Annu. Rev. Condens. Matter Phys.* **2015**, *6* (1), 361–381. https://doi.org/10.1146/annurev-conmatphys-031214-014501.
(208) Pham, T.; Oh, S.; Stonemeyer, S.; Shevitski, B.; Cain, J. D.; Song, C.; Ercius, P.; Cohen, M. L.; Zettl, A. Emergence of Topologically Nontrivial Spin-Polarized States in a Segmented Linear Chain. *Phys. Rev. Lett.* **2020**, *124* (20). https://doi.org/10.1103/PhysRevLett.124.206403.
(209) Briggs, N.; Bersch, B.; Wang, Y.; Jiang, J.; Koch, R. J.; Nayir, N.; Wang, K.; Kolmer, M.; Ko, W.; De La Fuente Duran, A.; Subramanian, S.; Dong, C.; Shallenberger, J.; Fu, M.; Zou, Q.; Chuang, Y. W.; Gai, Z.; Li, A. P.; Bostwick, A.; Jozwiak, C.; Chang, C. Z.; Rotenberg, E.; Zhu, J.; van Duin, A. C. T.; Crespi, V.; Robinson, J. A. Atomically Thin Half-van Der Waals Metals Enabled by Confinement Heteroepitaxy. *Nat. Mater.* **2020**, *19* (6), 637–643. https://doi.org/10.1038/s41563-020-0631-x.
(210) Al Balushi, Z. Y.; Wang, K.; Ghosh, R. K.; Vilá, R. A.; Eichfeld, S. M.; Caldwell, J. D.; Qin, X.; Lin, Y. C.; Desario, P. A.; Stone, G.; Subramanian, S.; Paul, D. F.; Wallace, R. M.; Datta, S.; Redwing, J. M.; Robinson, J. A. Two-Dimensional Gallium Nitride Realized via Graphene Encapsulation. *Nat. Mater.* **2016**, *15* (11), 1166–1171. https://doi.org/10.1038/nmat4742.
(211) Flahaut, E.; Sloan, J.; Friedrichs, ⊥ S; Kirkland, A. I.; Coleman, K. S.; Williams, V. C.; Hanson, N.; Hutchison, J. L.; Green, M. L. H. Crystallization of 2H and 4H PbI 2 in Carbon Nanotubes of Varying Diameters and Morphologies. **2006**. https://doi.org/10.1021/cm0526056.
(212) Sloan, J.; Grosvenor, S. J.; Friedrichs, S.; Kirkland, A. I.; Hutchison, J. L.; Green, M. L. H. A One-Dimensional BaI2 Chain with Five- and Six-Coordination, Formed within a Single-Walled Carbon Nanotube. *Angew. Chemie Int. Ed.* **2002**, *41* (7), 1156–1159. https://doi.org/10.1002/1521-3773(20020402)41:7<1156::AID-ANIE1156>3.0.CO;2-N.
(213) Carter, R.; Sloan, J.; Kirkland, A. I.; Meyer, R. R.; Lindan, P. J. D.; Lin, G.; Green, M. L. H.; Vlandas, A.; Hutchison, J. L.; Harding, J. Correlation of Structural and Electronic Properties in a New Low-Dimensional Form of Mercury Telluride. *Phys. Rev. Lett.* **2006**, *96* (21), 1–4. https://doi.org/10.1093/analys/16.1.15.
(214) Spencer, J. H.; Nesbitt, J. M.; Trewhitt, H.; Kashtiban, R. J.; Bell, G.; Ivanov, V. G.; Faulques, E.; Sloan, J.; Smith, D. C. Raman Spectroscopy of Optical Transitions and Vibrational Energies of ∼1 Nm HgTe Extreme Nanowires within Single Walled Carbon Nanotubes. **2014**. https://doi.org/10.1021/nn5023632.

(215) Philp, E.; Sloan, J.; Kirkland, A. I.; Meyer, R. R.; Friedrichs, S.; Hutchison, J. L.; Green, M. L. H. An Encapsulated Helical One-Dimensional Cobalt Iodide Nanostructure. *Nat. Mater.* **2003**, *2* (12), 788–791. https://doi.org/10.1038/nmat1020.
(216) Gr̈ner, G.; Zettl, A.; Clark, W. G.; Thompson, A. H. Observation of Narrow-Band Charge-Density-Wave Noise in TaS3. *Physical Review B*. 1981, pp 6813–6815. https://doi.org/10.1103/PhysRevB.23.6813.
(217) Canadell, E.; Jobic, S.; Brec, R.; Rouxel, J. Electronic Structure and Properties of Anionic Mixed Valence and Layered $CrTe_3$: The Question of Extended Tellurium Bonding in Transition Metal Tellurides. *J. Solid State Chem.* **1992**, *98* (1), 59–70. https://doi.org/10.1016/0022-4596(92)90070-C.
(218) Jobic, S.; Brec, R.; Rouxel, J. Anionic Polymeric Bonds in Transition Metal Ditellurides. *J. Solid State Chem.* **1992**, *96* (1), 169–180. https://doi.org/10.1016/S0022-4596(05)80309-3.
(219) Lehn, J. M. Tellurium-Rich Tellurides. *Angew. Chemie Int. Ed. English* **1985**, *24* (10), 799–810.
(220) Kirkland, E. J. *Advanced Computing in Electron Microscopy*; Springer International Publishing, 2020. https://doi.org/10.1007/978-3-030-33260-0.
(221) Chen, P.; Pai, W. W.; Chan, Y. H.; Takayama, A.; Xu, C. Z.; Karn, A.; Hasegawa, S.; Chou, M. Y.; Mo, S. K.; Fedorov, A. V.; Chiang, T. C. Emergence of Charge Density Waves and a Pseudogap in Single-Layer $TiTe_2$. *Nat. Commun.* **2017**, *8* (1), 8–13. https://doi.org/10.1038/s41467-017-00641-1.
(222) Barajas-Aguilar, A. H.; Irwin, J. C.; Garay-Tapia, A. M.; Schwarz, T.; Paraguay Delgado, F.; Brodersen, P. M.; Prinja, R.; Kherani, N.; Jiménez Sandoval, S. J. Crystalline Structure, Electronic and Lattice-Dynamics Properties of $NbTe_2$. *Sci. Rep.* **2018**, *8* (1), 1–14. https://doi.org/10.1038/s41598-018-35308-4.
(223) Chen, H.; Li, Z.; Guo, L.; Chen, X. Anisotropic Magneto-Transport and Magnetic Properties of Low-Temperature Phase of $TaTe_2$. *Epl* **2017**, *117* (2). https://doi.org/10.1209/0295-5075/117/27009.
(224) Wang, Z.; Li, H.; Liu, Z.; Shi, Z.; Lu, J.; Suenaga, K.; Joung, S. K.; Okazaki, T.; Gu, Z.; Zhou, J.; Gao, Z.; Li, G.; Sanvito, S.; Wang, E.; Iijima, S. Mixed Low-Dimensional Nanomaterial: 2D Ultranarrow MoS_2 Inorganic Nanoribbons Encapsulated in Quasi-1D Carbon Nanotubes. *J. Am. Chem. Soc.* **2010**, *132* (39), 13840–13847. https://doi.org/10.1021/ja1058026.
(225) Bennett, P. B.; Pedramrazi, Z.; Madani, A.; Chen, Y.-C.; de Oteyza, D. G.; Chen, C.; Fischer, F. R.; Crommie, M. F.; Bokor, J. Bottom-up Graphene Nanoribbon Field-Effect Transistors. *Appl. Phys. Lett.* **2013**, *103* (25), 253114. https://doi.org/10.1063/1.4855116.
(226) Chen, Y. C.; De Oteyza, D. G.; Pedramrazi, Z.; Chen, C.; Fischer, F. R.; Crommie, M. F. Tuning the Band Gap of Graphene Nanoribbons Synthesized from Molecular Precursors. *ACS Nano* **2013**, *7* (7), 6123–6128. https://doi.org/10.1021/nn401948e.
(227) Tao, C.; Jiao, L.; Yazyev, O. V.; Chen, Y.-C.; Feng, J.; Zhang, X.; Capaz, R. B.; Tour, J. M.; Zettl, A.; Louie, S. G.; Dai, H.; Crommie, M. F. Spatially Resolving Edge States of Chiral Graphene Nanoribbons. *Nat. Phys.* **2011**, *7* (8), 616–620. https://doi.org/10.1038/nphys1991.
(228) Cai, J.; Pignedoli, C. A.; Talirz, L.; Ruffieux, P.; Söde, H.; Liang, L.; Meunier, V.; Berger, R.; Li, R.; Feng, X.; Müllen, K.; Fasel, R. Graphene Nanoribbon Heterojunctions. *Nat. Nanotechnol.* **2014**, *9* (11), 896–900. https://doi.org/10.1038/nnano.2014.184.

(229) Nguyen, G. D.; Tsai, H. Z.; Omrani, A. A.; Marangoni, T.; Wu, M.; Rizzo, D. J.; Rodgers, G. F.; Cloke, R. R.; Durr, R. A.; Sakai, Y.; Liou, F.; Aikawa, A. S.; Chelikowsky, J. R.; Louie, S. G.; Fischer, F. R.; Crommie, M. F. Atomically Precise Graphene Nanoribbon Heterojunctions from a Single Molecular Precursor. *Nat. Nanotechnol.* **2017**, *12* (11), 1077–1082. https://doi.org/10.1038/nnano.2017.155.
(230) Zhang, Z.; Xie, Y.; Peng, Q.; Chen, Y. A Theoretical Prediction of Super High-Performance Thermoelectric Materials Based on MoS_2/WS_2 Hybrid Nanoribbons. *Sci. Rep.* **2016**, *6* (1), 21639. https://doi.org/10.1038/srep21639.
(231) Botello-Méndez, A. R.; López-Urías, F.; Terrones, M.; Terrones, H. Metallic and Ferromagnetic Edges in Molybdenum Disulfide Nanoribbons. *Nanotechnology* **2009**, *20* (32), 325703. https://doi.org/10.1088/0957-4484/20/32/325703.
(232) Davelou, D.; Kopidakis, G.; Kaxiras, E.; Remediakis, I. N. Nanoribbon Edges of Transition-Metal Dichalcogenides: Stability and Electronic Properties. *Phys. Rev. B* **2017**, *96* (16), 165436. https://doi.org/10.1103/PhysRevB.96.165436.
(233) Li, Q.; Newberg, J. T.; Walter, E. C.; Hemminger, J. C.; Penner, R. M. Polycrystalline Molybdenum Disulfide (2H-MoS_2) Nano- and Microribbons by Electrochemical/Chemical Synthesis. *Nano Lett.* **2004**, *4* (2), 277–281. https://doi.org/10.1021/nl035011f.
(234) Pak, Y.; Kim, Y.; Lim, N.; Min, J. W.; Park, W.; Kim, W.; Jeong, Y.; Kim, H.; Kim, K.; Mitra, S.; Xin, B.; Kim, T. W.; Roqan, I. S.; Cho, B.; Jung, G. Y. Scalable Integration of Periodically Aligned 2D-MoS_2 Nanoribbon Array. *APL Mater.* **2018**, *6* (7), 076102. https://doi.org/10.1063/1.5038823.
(235) Li, Y.; Moy, E. C.; Murthy, A. A.; Hao, S.; Cain, J. D.; Hanson, E. D.; DiStefano, J. G.; Chae, W. H.; Li, Q.; Wolverton, C.; Chen, X.; Dravid, V. P. Large-Scale Fabrication of MoS_2 Ribbons and Their Light-Induced Electronic/Thermal Properties: Dichotomies in the Structural and Defect Engineering. *Adv. Funct. Mater.* **2018**, *28* (13), 1704863. https://doi.org/10.1002/adfm.201704863.
(236) Cheng, F.; Xu, H.; Xu, W.; Zhou, P.; Martin, J.; Loh, K. P. Controlled Growth of 1D $MoSe_2$ Nanoribbons with Spatially Modulated Edge States. *Nano Lett.* **2017**, *17* (2), 1116–1120. https://doi.org/10.1021/acs.nanolett.6b04715.
(237) Li, S.; Lin, Y. C.; Zhao, W.; Wu, J.; Wang, Z.; Hu, Z.; Shen, Y.; Tang, D. M.; Wang, J.; Zhang, Q.; Zhu, H.; Chu, L.; Zhao, W.; Liu, C.; Sun, Z.; Taniguchi, T.; Osada, M.; Chen, W.; Xu, Q. H.; Wee, A. T. S.; Suenaga, K.; Ding, F.; Eda, G. Vapour-Liquid-Solid Growth of Monolayer MoS_2 Nanoribbons. *Nat. Mater.* **2018**, *17* (6), 535–542. https://doi.org/10.1038/s41563-018-0055-z.
(238) Chowdhury, T.; Kim, J.; Sadler, E. C.; Li, C.; Lee, S. W.; Jo, K.; Xu, W.; Gracias, D. H.; Drichko, N. V.; Jariwala, D.; Brintlinger, T. H.; Mueller, T.; Park, H. G.; Kempa, T. J. Substrate-Directed Synthesis of MoS2 Nanocrystals with Tunable Dimensionality and Optical Properties. *Nature Nanotechnology*. Nature Publishing Group January 1, 2019. https://doi.org/10.1038/s41565-019-0571-2.
(239) Wang, Z.; Zhao, K.; Li, H.; Liu, Z.; Shi, Z.; Lu, J.; Suenaga, K.; Joung, S. K.; Okazaki, T.; Jin, Z.; Gu, Z.; Gao, Z.; Iijima, S. Ultra-Narrow WS_2 Nanoribbons Encapsulated in Carbon Nanotubes. *J. Mater. Chem.* **2011**, *21* (1), 171–180. https://doi.org/10.1039/c0jm02821e.
(240) Tsen, A. W.; Hovden, R.; Wang, D.; Kim, Y. D.; Spoth, K. A.; Liu, Y.; Lu, W.; Sun, Y.; Hone, J. C.; Kourkoutis, L. F.; Kim, P.; Pasupathy, A. N. Structure and Control of Charge

Density Waves in Two-Dimensional 1T-TaS_2. *Proc. Natl. Acad. Sci. U. S. A.* **2015**, *112* (49), 15054–15059. https://doi.org/10.1073/pnas.1512092112.
(241) Burk, B.; Thomson, R. E.; Clarke, J.; Zettl, A. Surface and Bulk Charge Density Wave Structure in 1T-TaS_2. *Science (80-.).* **1992**, *257* (5068), 362–364. https://doi.org/10.1126/science.257.5068.362.
(242) Sipos, B.; Kusmartseva, A. F.; Akrap, A.; Berger, H.; Forró, L.; Tutǐ, E. From Mott State to Superconductivity In-1T-TaS_2. *Nat. Mater.* **2008**, *7* (12), 960–965. https://doi.org/10.1038/nmat2318.
(243) Law, K. T.; Lee, P. A. 1T-TaS_2 as a Quantum Spin Liquid. *Proc. Natl. Acad. Sci. U. S. A.* **2017**, *114* (27), 6996–7000. https://doi.org/10.1073/pnas.1706769114.
(244) Ajayan, P. M.; Ebbesen, T. W.; Ichihashi, T.; Iijima, S.; Tanigaki, K.; Hiura, H. Opening Carbon Nanotubes with Oxygen and Implications for Filling. *Nature* **1993**, *362* (6420), 522–525. https://doi.org/10.1038/362522a0.
(245) Ophus, C. A Fast Image Simulation Algorithm for Scanning Transmission Electron Microscopy. *Adv. Struct. Chem. Imaging* **2017**, *3* (1), 1–11. https://doi.org/10.1186/s40679-017-0046-1.
(246) Hovden, R.; Tsen, A. W.; Liu, P.; Savitzky, B. H.; El Baggari, I.; Liu, Y.; Lu, W.; Sun, Y.; Kim, P.; Pasupathy, A. N.; Kourkoutis, L. F. Atomic Lattice Disorder in Charge-Density-Wave Phases of Exfoliated Dichalcogenides (1T-TaS_2). *Proc. Natl. Acad. Sci. U. S. A.* **2016**, *113* (41), 11420–11424. https://doi.org/10.1073/pnas.1606044113.
(247) Lazar, P.; Martincová, J.; Otyepka, M. Structure, Dynamical Stability, and Electronic Properties of Phases in TaS_2 from a High-Level Quantum Mechanical Calculation. *Phys. Rev. B - Condens. Matter Mater. Phys.* **2015**, *92* (22), 224104. https://doi.org/10.1103/PhysRevB.92.224104.
(248) Sanders, C. E.; Dendzik, M.; Ngankeu, A. S.; Eich, A.; Bruix, A.; Bianchi, M.; Miwa, J. A.; Hammer, B.; Khajetoorians, A. A.; Hofmann, P. Crystalline and Electronic Structure of Single-Layer TaS_2. *Phys. Rev. B* **2016**, *94* (8), 081404. https://doi.org/10.1103/PhysRevB.94.081404.
(249) Cai, J.; Ruffieux, P.; Jaafar, R.; Bieri, M.; Braun, T.; Blankenburg, S.; Muoth, M.; Seitsonen, A. P.; Saleh, M.; Feng, X.; Müllen, K.; Fasel, R. Atomically Precise Bottom-up Fabrication of Graphene Nanoribbons. *Nature* **2010**, *466* (7305), 470–473. https://doi.org/10.1038/nature09211.
(250) Ritter, K. A.; Lyding, J. W. The Influence of Edge Structure on the Electronic Properties of Graphene Quantum Dots and Nanoribbons. *Nat. Mater.* **2009**, *8* (3), 235–242. https://doi.org/10.1038/nmat2378.
(251) Chen, Y.; Cui, P.; Ren, X.; Zhang, C.; Jin, C.; Zhang, Z.; Shih, C. K. Fabrication of $MoSe_2$ Nanoribbons via an Unusual Morphological Phase Transition. *Nat. Commun.* **2017**, *8* (May), 1–9. https://doi.org/10.1038/ncomms15135.
(252) Cain, J. D.; Oh, S.; Azizi, A.; Stonemeyer, S.; Dogan, M.; Thiel, M.; Ercius, P.; Cohen, M. L.; Zettl, A. Ultra-Narrow TaS_2 Nanoribbons. *arXiv* **2020**.
(253) Liu, X.; Xu, T.; Wu, X.; Zhang, Z.; Yu, J.; Qiu, H.; Hong, J. H.; Jin, C. H.; Li, J. X.; Wang, X. R.; Sun, L. T.; Guo, W. Top-down Fabrication of Sub-Nanometre Semiconducting Nanoribbons Derived from Molybdenum Disulfide Sheets. *Nat. Commun.* **2013**, *4*, 1–6. https://doi.org/10.1038/ncomms2803.
(254) Rosenbach, D.; Oellers, N.; Jalil, A. R.; Mikulics, M.; Kölzer, J.; Zimmermann, E.; Mussler, G.; Bunte, S.; Grützmacher, D.; Lüth, H.; Schäpers, T. Quantum Transport in

Topological Surface States of Selectively Grown Bi2Te3 Nanoribbons. *Adv. Electron. Mater.* **2020**, *6* (8). https://doi.org/10.1002/aelm.202000205.
(255) Meyer, R. R.; Sloan, J.; Dunin-Borkowski, R. E.; Kirkland, A. I.; Novotny, M. C.; Bailey, S. R.; Hutchison, J. L.; Green, M. L. Discrete Atom Imaging of One-Dimensional Crystals Formed within Single-Walled Carbon Nanotubes. *Science* **2000**, *289* (5483), 1324–1327. https://doi.org/10.1126/science.289.5483.1324.
(256) Slade, C. A.; Sanchez, A. M.; Sloan, J. Unprecedented New Crystalline Forms of SnSe in Narrow to Medium Diameter Carbon Nanotubes. *Nano Lett.* **2019**, *19* (5), 2979–2984. https://doi.org/10.1021/acs.nanolett.9b00133.
(257) Mleczko, M. J.; Zhang, C.; Lee, H. R.; Kuo, H. H.; Magyari-Köpe, B.; Moore, R. G.; Shen, Z. X.; Fisher, I. R.; Nishi, Y.; Pop, E. HfSe2 and ZrSe2: Two-Dimensional Semiconductors with Native High-κ Oxides. *Sci. Adv.* **2017**, *3* (8). https://doi.org/10.1126/sciadv.1700481.
(258) Brauer, H. E.; Starnberg, H. I.; Holleboom, L. J.; Hughes, H. P. The Electronic Structure of ZrSe2 and CsxZrSe 2 Studied by Angle-Resolved Photoelectron Spectroscopy. *J. Phys. Condens. Matter* **1995**, *7* (40), 7741–7760. https://doi.org/10.1088/0953-8984/7/40/006.
(259) Li, S.; Zhou, M.; Wang, X.; Zheng, F.; Zhang, P. Tunable Direct-Indirect Band Gaps of $ZrSe_2$ Nanoribbons. *J. Appl. Phys.* **2018**, *124* (3). https://doi.org/10.1063/1.5036673.
(260) Yue, R.; Barton, A. T.; Zhu, H.; Azcatl, A.; Pena, L. F.; Wang, J.; Peng, X.; Lu, N.; Cheng, L.; Addou, R.; McDonnell, S.; Colombo, L.; Hsu, J. W. P.; Kim, J.; Kim, M. J.; Wallace, R. M.; Hinkle, C. L. HfSe2 Thin Films: 2D Transition Metal Dichalcogenides Grown by Molecular Beam Epitaxy. *ACS Nano* **2015**, *9* (1), 474–480. https://doi.org/10.1021/nn5056496.
(261) Roy, A.; Movva, H. C. P.; Satpati, B.; Kim, K.; Dey, R.; Rai, A.; Pramanik, T.; Guchhait, S.; Tutuc, E.; Banerjee, S. K. Structural and Electrical Properties of MoTe2 and MoSe2 Grown by Molecular Beam Epitaxy. *ACS Appl. Mater. Interfaces* **2016**, *8* (11), 7396–7402. https://doi.org/10.1021/acsami.6b00961.
(262) Adam, M. L.; Bala, A. A. Prediction of Phonon-Mediated Superconductivity and Charge Density Wave in Charge Doped 1T-$HfTe_2$. *Comput. Condens. Matter* **2021**, *26*, e00527. https://doi.org/10.1016/j.cocom.2020.e00527.
(263) Guo, J.; Li, F.; Sun, Y.; Zhang, X.; Tang, L. Oxygen-Incorporated MoS<inf>2</Inf> Ultrathin Nanosheets Grown on Graphene for Efficient Electrochemical Hydrogen Evolution. *J. Power Sources* **2015**, *291*, 195–200. https://doi.org/10.1016/j.jpowsour.2015.05.034.
(264) Li, Y.; Li, Y.; Araujo, C. M.; Luo, W.; Ahuja, R. Single-Layer MoS2 as Efficient Photocatalyst. **2012**, 2–8. https://doi.org/10.1039/C3CY00207A.
(265) Wang, Q. H.; Kalantar-Zadeh, K.; Kis, A.; Coleman, J. N.; Strano, M. S. Electronics and Optoelectronics of Two-Dimensional Transition Metal Dichalcogenides. *Nat. Nanotechnol.* **2012**, *7* (11), 699–712. https://doi.org/10.1038/nnano.2012.193.
(266) Yang, T.; Lin, H.; Loh, K. P.; Jia, B. Fundamental Transport Mechanisms and Advancements of Graphene Oxide Membranes for Molecular Separation. *Chem. Mater.* **2019**, *31* (6), 1829–1846. https://doi.org/10.1021/acs.chemmater.8b03820.
(267) Basuvalingam, S. B.; Zhang, Y.; Bloodgood, M. A.; Godiksen, R. H.; Curto, A. G.; Hofmann, J. P.; Verheijen, M. A.; Kessels, W. M. M.; Bol, A. A. Low-Temperature Phase-Controlled Synthesis of Titanium Di- And Tri-Sulfide by Atomic Layer Deposition. *Chem. Mater.* **2019**, *31* (22), 9354–9362. https://doi.org/10.1021/acs.chemmater.9b02895.

(268) Revolinsky, E., Brown, B. E., Beernsten, D. J., and Armitage, C. H. The Selenide and Telluride Systems of Niobium and Tantalum. *J. Less Common Met.* **1965**, 63–72.
(269) Brixner, L. H. Preparation and Properties of the Single Crystalline AB2-Type Selenides and Tellurides of Niobium, Tantalum, Molybdenum and Tungsten. *J. Inorg. Nucl. Chem.* **1962**, *24* (3), 257–263. https://doi.org/10.1016/0022-1902(62)80178-X.
(270) Splendiani, A.; Sun, L.; Zhang, Y.; Li, T.; Kim, J.; Chim, C. Y.; Galli, G.; Wang, F. Emerging Photoluminescence in Monolayer MoS 2. *Nano Lett.* **2010**, *10* (4), 1271–1275. https://doi.org/10.1021/nl903868w.
(271) Stonemeyer, S.; Cain, J. D.; Oh, S.; Azizi, A.; Elasha, M.; Thiel, M.; Song, C.; Ercius, P.; Cohen, M. L.; Zettl, A. Stabilization of $NbTe_3$, VTe_3, and $TiTe_3$ via Nanotube Encapsulation. *J. Am. Chem. Soc.* **2020**, 0–5. https://doi.org/10.1021/jacs.0c10175.
(272) Zhao, X.; Qiao, J.; Chan, S. M.; Li, J.; Dan, J.; Ning, S.; Zhou, W.; Quek, S. Y.; Pennycook, S. J.; Loh, K. P. Unveiling Atomic-Scale Moiré Features and Atomic Reconstructions in High-Angle Commensurately Twisted Transition Metal Dichalcogenide Homobilayers. *Nano Lett.* **2021**, *21* (7), 3262–3270. https://doi.org/10.1021/acs.nanolett.1c00563.
(273) Krumeich, F.; Conrad, M.; Nissen, H. U.; Harbrecht, B. The Mesoscopic Structure of Disordered Dodecagonal Tantalum Telluride: A High-Resolution Transmission Electron Microscopy Study. *Philos. Mag. Lett.* **1998**, *78* (5), 357–367. https://doi.org/10.1080/095008398177751.
(274) Conrad, M.; Krumeich, F.; Harbrecht, B. A Dodecagonal Quasicrystalline Chalcogenide. *Angew. Chemie - Int. Ed.* **1998**, *37* (10), 1383–1386. https://doi.org/10.1002/(sici)1521-3773(19980605)37:10<1383::aid-anie1383>3.0.co;2-r.
(275) Lin, Y.; Komsa, H.; Yeh, C.; Al, L. I. N. E. T. Single-Layer ReS_2: Two-Dimensional Semiconductor with Tunable In-Plane Anisotropy. *ACS Nano* **2015**, No. 11, 11249–11257.